LBL-4000
UC - 4 Chemistry
TID-4500-R62

NUCLEAR CHEMISTRY
Annual Report
1974

G. T. Seaborg, Director
B. G. Harvey, Deputy Director
Nuclear Chemistry Division

Editors: H. E. Conzett
N. M. Edelstein
C. F. Tsang

Lawrence Berkeley Laboratory
University of California
Berkeley, California

Work done under
U.S. Energy Research and Development Administration
Contract No. W-7405-eng-48

July 1975

Printed in the United States of America
Available from
National Technical Information Service
U.S. Department of Commerce
5285 Port Royal Road
Springfield, Virginia 22151
Price: Printed Copy $10.60; Microfiche $2.25

Contents

NUCLEAR REACTIONS AND SCATTERING

PHOTOELECTRON SPECTROSCOPY AND HYPERFINE INTERACTIONS

5. PHYSICAL, INORGANIC, AND ANALYTICAL CHEMISTRY

X-RAY CRYSTALLOGRAPHY

PHYSICAL AND INORGANIC CHEMISTRY

GEOCHEMISTRY

1. Nuclear Science

Nuclear Spectroscopy and Radioactivity

Nuclear Reactions and Scattering

Nuclear Theory

TABLE OF ISOTOPES PROJECT

E. Browne, J. M. Dairiki, R. E. Doebler, L. J. Jardine,*
C. M. Lederer, E. Leon, M. Rinneberg,† A. A. Shihab-Eldin,
V. S. Shirley and M. Whalley

As of December, 1974, the first compilation of 225 (of a total of 262) mass chains has been completed. In addition, 100 of these mass chains have been updated to a final 1974 cutoff date. This work represents a total compilation effort of 18.4 man-years since work on the 7th edition began in 1971.

Computer processing of the tabular data is in routine operation. The data for each mass chain are keyboarded and edited on the IRATE computer-terminal system.[1] Proof copy, including diagnostics on computer-detected errors in the data, is printed. The data are then proofread and edited, a second proof copy is produced and the corrections are checked. At a later date, after the mass chain has been updated to a final cutoff date, the new data are added, and any corrections to existing entries are made. (Most corrections at this stage involve only small changes in the data "flagging": e.g., an early γ-ray spectrum, superseded by a later measurement, is flagged to indicate that the data should not be printed, but that the reference(s) should be included under "other".)

Computer processing of level schemes is likewise in routine use. The output includes a semi-final plot for proofreading, diagnostics, and special tables useful for data checking. The latter include summaries of beta and alpha feeding and calculated log ft values or hindrance factors, tables and plots of transition energies vs level-energy differences, and lists of γ-ray properties (energy, intensity, multipolarity) reordered by energy. Level-scheme data are entered (on punched cards) only after final updating; the data are then processed, the plots proofread, and corrections made on the card decks.

Figure 1 shows the current status of these activities by mass chain. The totals are as follows:

First compilation completed	225
(Tabular data entered and proofread)	154†
Compilation updated to final cutoff date	104
(Tabular data entered and proofread)	73
(Level schemes entered and proofread)	79

A target date for final production of the 7th edition, July 1976, was set last year.[2] We hope to keep this date as nearly as possible. However, in the face of recent reduction in personnel on the project, some delay is unavoidable.

Level Scheme Formats

As described in the previous annual report,[2]

TABLE OF ISOTOPES-7th EDITION

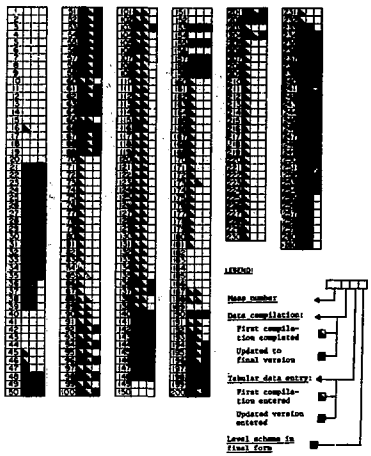

Fig. 1. Status of the mass-chain compilations for the 7th edition of the *Table of Isotopes*. Half-shaded boxes indicate first compilation only (mass chain not updated to final cutoff date) and tabular data entry of first compilation (see legend in lower right-hand corner). (XBL 755-1222)

level schemes will include a "skeleton scheme" for each mass chain and detailed schemes for each nucleus. The latter will consist of a decay scheme, including feeding from all radioactive parents, and a scheme summarizing the levels populated by all nuclear reactions. A sample set of detailed schemes for ^{197}Au is shown in Fig. 2. Reaction levels too numerous to display are noted in comments (see Fig. 2); hopefully the decay schemes can be shown in their entirety. Reaction schemes involving many γ-rays may also be abbreviated by omission of some of the γ-ray labels and/or by "stackplotting" of the γ-rays.

Table of Nuclear Moments

Two previous editions of this table, a standard reference on the subject, have been published as appendices to conference proceedings.[3] In 1974, production of the table was computerized by application of techniques developed for the *Table of Isotopes*. The data are entered in a readily updatable form on the IRATE system;[1] all information, including the introductory text, are input

TABLE OF NUCLEAR MOMENTS[1]

V.S. Shirley and C.M. Lederer

Table of Isotopes Project
Lawrence Berkeley Laboratory
Berkeley, California 94720

This table contains nuclear magnetic and quadrupole moments reported as of September, 1974. It supersedes the *Table of Nuclear Moments* published in the proceedings of the 1970 Rehovot Conference [CI70 Hyp Int 1255], and is similar to that table, except for changes described below.

The major innovation concerns a changeover from standard typing and printing methods to direct computer input and typography. The systems used for this purpose were developed in Berkeley, and are currently being used for several LBL projects, including production of the 7th edition of the *Table of Isotopes*. The systems' features include direct generation of final output on film, thorough checking of input data according to specified guidelines, and performance of certain calculations. For the *Table of Nuclear Moments*, the computer checked all data and references for correct syntax, calculated some of the moments from measured frequency or moment ratios, and applied diamagnetic corrections where appropriate.

Nuclear species for which moments are reported are identified in the first four columns of the table. The level-energy [illegible] blank for ground states. [illegible] gives energies (in units of keV) of the most excited states. Seven [illegible] are identified [illegible] ce energy [=E−BE(...)/A. Level [illegible] the [illegible]

TABLE OF NUCLEAR MOMENTS

Nucleus Z El A	Level energy	Half-life	Spin	μ [Standard] (nm)	Method (μ)	Reference (μ)	Q [Standard] (b)	Method (Q)	Reference (Q)
0 n 1		11.7 ± m	1/2	−1.913210 ±[illegible]	N	PR 104 283(56)			
1 H 1			1/2	+2.7928456 (1)	R	JPCR 2 663(73)			
2			1	+0.85743762 (^{2}H)	N	PC74 Fuller, PR 78 204(50)	+0.002875 ±[illegible]	MB,R	PRL 29 494(72) PR 57 577(40)
3		12.262 ± y	1/2	+2.978962014 ± (^{3}H)	N	PR 115 1012(59), PR 71 551(47)			
2 He 3			1/2	−2.12762493 ±[illegible] (^{3}H)	N	PR 185 1251(69)			
3 Li 6			1	+0.8220661 (^{6}Li)	N	INst 23a 1202(68), PL 25A 440(67), ORNL-1773(54)	+0.000644 ± [illegible] (^{6}Li)	MB	PR 133 1070(64)
7			3/2	+3.2564804 ± (^{7}Li)	N	INst 23a 1202(68), PL 25A 440(67), ORNL-1773(54)	−0.0366 ±[illegible]	MB,R	PR A4 251(71)
							−0.043 ±[illegible]	MB,R	PR B1 1025(70)
8		849 ± ms	2	1.65535 ±[illegible] +1.6532 ± +1.6532 ±	N/RD YadFiz 957(67) N/RD PR 175 1205(68)	PR C7 1273(73) N/RD	+0.053 ±[illegible]	AB	PR 153 1164(67)
4 Be 9			3/2	−1.17749 (^{9}Be)	N	[illegible]	[illegible]012	NR	PR 116 [illegible]
5 B			[illegible]	1.8055 ±[illegible]			[illegible]	AB,R	
				2.80065 (^{10}B)					

Journal-Code List

AdNP	Advan Nucl Phys (Ed. M. Baranger and E. Vogt. Plenum Press, New York)	JPCR	J. Phys. Chem. Ref. Data
AKyo	Annu. Rep. Res. Reactor Inst., Kyoto Univ.	JPJA	J. Phys. Soc. Jap.
AnP	Ann. Phys. (Paris)	JPJS	J. Phys. Soc. Jap., Suppl.
APAu	Acta Phys. Austr.	JPPa	J. Phys. (Paris) (name changed from J. Phys. Radium, 1961)
APLz	Ann. Phys. (Leipzig)	ND	Nucl. Data (section A: Nuclear Data Tables - superseded by At. Data and Nucl. Data Tables, Section B: Nuclear Data Sheets - supersedes obsolete Nucl. Data Sheets)
APPo	Acta Phys. Pol.		
ArkF	Ark. Fys. (superseded by Phys. Scr.)		
AR67 Hahlt	Hahn-Meitner-Inst. fuer Kernforschung, Berlin, Annual report (1967)	NIM	Nucl. Instrum. Methods (name changed from Nucl. Instrum. as of volume 4, 1959)
AR69 Hahlt	Hahn-Meitner-Inst. fuer Kernforschung, Berlin, Annual report (1969)	NInd	Nucl. Phys. and Solid St. Phys. (India), Section B.
AR71 Hahlt	Hahn-Meitner-Inst. fuer Kernforschung, Berlin, Annual report (1971)	NP	Nucl. Phys.
BAPS	Bull. Am. Phys. Soc., Ser. II	Nwis	Naturwissenschaften
Bk64 PAC	E. Karlsson, E. Matthias, and K. Siegbahn (editors), Perturbed Angular Correlations, North-Holland Publishing Co. (1964)	ORNL-OSPk	Oak Ridge National Lab., Oak Ridge, Tenn., Report
			Opt. Spektrosk. (Trans. Optics and Spectroscopy
SMBW-FB	[illegible]dung und Wissenschaft.		
[illegible]	[illegible]senschaftliche		[illegible]munication to G.H. Fuller [illegible]ed in ND A6 433 [illegible]tion in ND A6 475

Fig. 3. Sample sections of the 3rd edition of the *Table of Nuclear Moments*. These include introductory material (top), the table itself (middle), and the journal-code list (bottom). The entire 23-page table, including the two-page introduction and one-page journal-code list, was produced by computer.

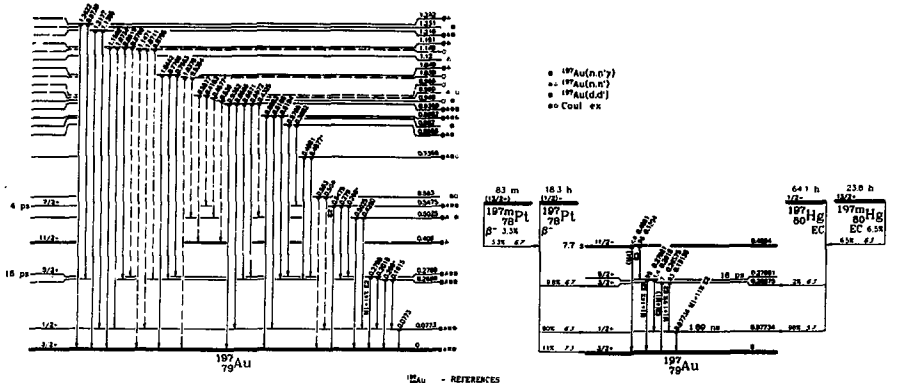

Fig. 2. Sample of detailed level schemes for ^{197}Au. (XBL 755-1224)

and edited in this manner. The 3rd edition was completed late in 1974; sample sections are shown in Fig. 3. This edition will again be published as part of a conference proceedings.[4] Future editions will be published at shorter intervals, possibly in a compilation journal.

Footnotes and References

*Present address: Argonne National Laboratory, Argonne, Illinois

†Present address: Hahn-Meitner Institute, Berlin, West Germany.

‡Tabular data for the remaining mass chains will be entered after the data have been updated to a final cutoff date.

1. E. Romascan, W. Greiman, C. M. Lederer and A. Allen, LBL-2366, p. 453 (1974).

2. E. Browne, J. M. Dairiki, R. E. Doebler, L. J. Jardine, C. M. Lederer, A. Shihab-Eldin, V. S. Shirley and M. Whalley, LBL-2366, p. 3 (1974).

3. a) V. S. Shirley, Proc. Int'l. Conf. Hyperfine Structure and Nuclear Radiations, Asilomar, Pacific Grove, Calif., p. 985 (1967); edited by E. Matthias and D. A. Shirley, North-Holland Pub. Co., Amsterdam (1968).

b) V. S. Shirley, Proc. Int'l. Conf. Hyperfine Interactions in Excited Nuclei, Rehovoth, p. 1255 (1970); edited by G. Goldring and R. Kalish, Gordon and Breach Science Pub., New York, London, Paris (1971).

4. V. S. Shirley and C. M. Lederer, in Proc. Int'l. Conf. Hyperfine Interactions Studied in Nuclear Reactions and Decay, Uppsala (1974); to be published (1975).

ALPHA DECAY STUDIES OF THE HIGH SPIN ISOMER OF BISMUTH-210

D. Tuggle, F. Asaro and I. Perlman*

^{210m}Bi is a metastable alpha emitter lying 270 keV above the ground state of ^{210}Bi and has a probable spin and parity of 9-. It decays principally by alpha particle emission but a small beta branching was reported.[1] In previous work[1-5] the alpha decay scheme was constructed from alpha singles, gamma singles, and a few alpha-gamma coincidence measurements. One author[2] reported that he had observed a parity forbidden alpha branching to the ground state of ^{206}Tl which has a spin and parity, 0-. Later data compilations[6] called the measurements doubtful.

In the present work the decay characteristics of ^{210m}Bi were carefully measured using a sample that had been chemically purified and highly enriched by mass separations. The ^{210m}Bi was produced by the reaction ^{209}Bi(n,γ)^{210m}Bi (σ_c = 19 mb).

The ground state of ^{210}Bi was also produced (σ_c = 15 mb). It decayed by β emission to ^{210}Po with the relatively short half life of 5 days. The ^{210}Po was removed from the bismuth by fractional distillation and solvent extraction. The ^{210m}Bi was separated from the ^{209}Bi in two mass separations. The first was conducted at Oak Ridge National Laboratory and the second at LBL. The separation at LBL produced an aluminum backed source of 20 μg of ^{210m}Bi containing less than 10% ^{209}Bi and with a total alpha activity of 25,000 dis/min.

The half life of ^{210m}Bi was measured using a bismuth sample that had not been mass separated, and had a ^{210m}Bi fraction measured as 0.13% by mass spectrographic analysis here at LBL. A known mass of this sample was deposited on a platinum disc by electrodeposition and the alpha activity was measured in a Frisch grid chamber. The alpha decay half life determined from this measurement is $(3.0 \pm .1) \times 10^6$ years (see Table 1).

Table 1. Comparison of decay values.

	Half life (present)	Half life (literature)	Branching ratio (present)
Alpha (total)	$(3.0 \pm .1) \times 10^6$ yr	3.55×10^6 yr[a]	
Beta	$> 1 \times 10^{12}$ yr	6×10^9 yr[b]	$< 3 \times 10^{-6}$
Alpha population (to ^{206}Tl ground state)	$> 3 \times 10^{12}$ yr	8×10^9 yr[a]	$< 1 \times 10^{-6}$

[a]Ref. 9 [b]Ref. 1 [c]Ref. 2

The beta decay branching was determined by measuring the amount of ^{210}Po alpha activity in the sample in equilibrium with ^{210m}Bi alpha activity. Our limit for this branching is much lower than previous values[1,2] and may represent a better chemical separation of ^{210m}Bi from the ^{210}Po formed from the initial decay of the 5-day ^{210}Bi ground state (see Table 1).

The alpha particle energies of ^{210m}Bi were measured with a surface barrier silicon detector with an active area of 150 mm^2. The conversion electrons in coincidence with alpha particles populating excited states in ^{206}Tl give spurious peaks at the sum energies. These spurious peaks can be reduced by decreasing the counting geometry for the alpha measurement or by bending the conversion electrons away from the detector with a magnetic field. Both techniques were used and an upper limit of 1×10^{-6} was set on the parity forbidden transition to the ground state of ^{206}Tl. Based on a Mang[7] type calculation of alpha decay rates, this limits the parity admixture in ^{210m}Bi to less than 10^{-4}. The energies and relative intensities of the alpha groups populating the excited states of ^{206}Tl were also measured and these are compared with previous work in Table 2.

Table 2. Alpha energies and relative abundances.

Energy (MeV)		Relative Abundance (%)	
Present	Literature[a]	Present	Literature[a]
4.224	--	0.01	--
4.414	4.400	0.3	0.19
4.579	4.568	0.5	0.96
4.564	4.550	4.8	3.74
4.905	4.896	39.4	40.4
4.941	4.935	55.0	54.6
5.201	5.201	$< 1 \times 10^{-4}$	0.04

[a]Ref. 2

The energies and relative intensities of the gamma rays associated with the alpha decay of ^{210m}Bi were measured with a Ge(Li) detector. The results of those measurements are compared with previously reported values in Table 3. The decay scheme of ^{206}Tl along with the low energy levels of ^{210}Bi and ^{210}Po are shown in Fig. 1.

Table 3. Gamma ray energies and intensities.

Energy		Relative Intensity	
Present	Literature[a]	Present	Literature[b]
266.7	265.7	100	100
305.1	304.8	55.7	54
330.4	329.1	1.3	1.1
344.7	344.0	1.4	1.4
369.1	369.6	1.4	1.3
535.0	(534)[c]	0.5	0.5
634.3	(634)[c]	0.3	0.02
648.6	649.8	7.0	5.6
731	--	--	--

[a]Ref. 3
[b]Ref. 2
[c]These two gamma rays were not observed by Ref. 3; the values given are for Ref. 2.

The branching ratios for the alpha decay of ^{210m}Bi to excited states of ^{206}Tl were calculated using a method developed by Mang.[7] Harmonic oscillator wave functions and the configurations of Kuo[8] were used. A radial parameter of 9.3 Fermis was chosen, and barrier penetration was calculated with a pure Coulomb potential between the alpha and the daughter nucleus. The values for the α and β size parameters used in the calculations were 0.17 and

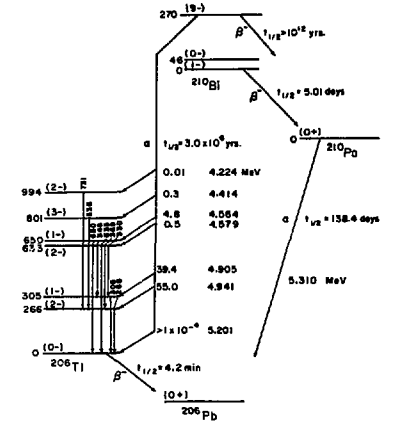

Fig. 1. (XBL 756-3316)

Table 4. Comparison of calculated and measured relative intensities.

Alpha energy (MeV)	^{206}Tl level (kev)	I( )	Experimental	Calculated
4.941	266	2-	55.0	82.6
4.905	305	1-	39.4	16.2
4.564	650	1-	4.8	1.1
4.579	635	2-	0.5	0.04
4.414	801	3-	0.3	0.002
4.224	994	2-	0.01	0.0006

0.47 Fm^{-2} respectively. The results of the calculations are listed in Table 4. The deviation in experimental and theoretical alpha abundances populating the higher excited states of ^{206}Tl becomes increasingly larger with excited state energy. This may indicate that Kuo's configuration mixing is inadequate.

We are indebted to Maynard C. Michel for his guidance in the mass separations and measurements.

Footnotes and References

*I. Perlman is currently is the Department of Archeometry of the Institute of Archeology of the Hebrew University in Jerusalem.

1. L. I. Rusinov, Y. N. Andreev, S. V. Golenetskii, M. I. Kislov and Y. I. Filimonov, J. Exptl. Theoret. Phys. 13, 707 (1961).

2. R. C. Lange, G. R. Hagee and A. R. Campbell, Nucl. Phys. A133, 273 (1969).

3. E. H. Spejewski, Nucl. Phys. A100. 236 (1967).

4. Y. I. Kharitonov, L. A. Sliv and G. A. Sogomonova, Nucl. Phys. 28, 210 (1961).

5. R. J. Walen and G. Bastin-Scoffier, J. de Phys. 20, 589 (1959).

6. M. B. Lewis, Nucl. Data Sheets, Sec. B, Vol. 5,6, 631 (1971).

7. H. J. Mang, Ann. Rev. Nucl. Sci. 14, 1 (1964).

8. T. T. S. Kuo and G. H. Harling, State Univ. of New York, Stony Brook, Naval Research Lab. Report NRL-2255 (1971).

9. R. C. Lange and G. R. Hagee, J. Inorg. Nucl. Chem. 31, 2297 (1969).

K-SHELL ELECTRON SHAKE-OFF ACCOMPANYING ALPHA DECAY

M. S. Rapaport, F. Asaro, and I. Perlman*

An electron ejected by the passage of an α particle through the Coulomb field shares in a complementary fashion in the α emission energy. The α spectrum associated with electron shake-off from a particular subshell will have a maximum energy equal to essentially the α particle energy without shake-off less the binding energy of the electron. The present work was undertaken to measure directly that part of the alpha spectrum connected with the electron shake-off effect in the K shell and to determine the differential shape of this spectrum and compare it with theoretical predictions. We hoped to improve the precision of previous measurements of the total K shell probability and delineate more clearly the discrepancy between experiment and the Migdal theory.

The general experimental procedure was to measure the alpha spectra of ^{210}Po and ^{238}Pu which were in coincidence with K x-rays. The K x-rays were detected with a solid state detector of pure Ge which had a full-width-at-half-maximum (FWHM) of 1.0 keV for a 122 keV γ-ray and an overall detection efficiency of 13.5% at that energy. The α particles were detected with Au-Si surface-barrier type detectors with geometries of about 2-5%.

The ^{238}Pu was purified by elution from an anion column and then vaporized in vacuum from a

tungsten filament onto a 0.002 inch thick mylar foil. The source which had been collimated to an area 5/16 inch in diameter during vaporization was invisible and had an activity of $\sim 1.2 \times 10^7$ α dis/min.

Two vials of ^{210}Po were purchased from New England Nuclear. The ^{210}Po was catalogued as carrier-free and of natural origin although investigation at the conclusion of the experiment showed it was prepared by the reaction and decay:

$$^{209}\mathrm{Bi}(n,\gamma)^{210}\mathrm{Bi} \xrightarrow[5\ day]{\beta^-} {}^{210}\mathrm{Po}\ .$$

The ^{210}Po from one of the vials was further purified by fuming to near dryness with concentrated HNO_3, loading onto a cation column (DOWEX 50) with .2 M HCl, washing with 2 M HNO_3, and eluting the ^{210}Po with 2 M HCl. The eluent was evaporated to dryness and vaporized like the ^{238}Pu onto a .002 inch thick mylar foil. The source was $\sim 1.7 \times 10^7$ α dis/min and was invisible.

The ^{238}Pu was measured in a coincidence unit for a total running time of 15 days. The α singles spectra were measured and recorded every day as were the coincident spectra. The γ singles spectra were monitored continuously. The α − K x-ray coincidence spectra for the one day runs were summed and this total spectrum is presented in Fig. 1. The abscissa is the analyzer channel in which the coincidences appeared, and it is roughly linear with the α particle energy. The ordinate is the total number of observed coincidences in the 15 day period. The highest energy peaks, α_0 and α_{44}, are due to accidental coincidences between the most intense α groups and radiation in the K x-ray gate. The most intense peak, α_{296}, is due to true coincidences with K x-rays from conversion of the 153 keV γ-ray and with the Compton background of this γ-ray in the K x-ray gate region.

The abundance of the α group associated with K shell shake-off is $(0.85 \pm 0.11) \times 10^{-6}$ per ^{238}Pu α particle.

The nomenclature for the normal α groups shown in Fig. 1 is the usual one with the energy of the excited state being a subscript to the α symbol, e.g. the ^{238}Pu α groups populating the 44 keV excited state in ^{234}U is designated ^{238}Pu α_{44} or simply α_{44}. We suggest for the α groups removing orbital electrons in their passage through the Coulomb field, that the shell designation of the electrons be added as a subscript before the excited state energy. Thus, the ^{238}Pu α group which populates the 44 keV state in ^{234}U and which also causes a K electron to be removed would be designated ^{238}Pu $\alpha_{K,44}$ or simply $\alpha_{K,44}$. To determine if these observed coincidences had the proper maximum energy for a ^{238}Pu α_0 particle which ejected a K electron with about zero kinetic energy we extrapolated their high energy side (Fig. 2) and that of ^{238}Pu α_0 to $\sim$ one quarter of their peak height. There was a difference in energy of 115 ± 10 keV which agrees with the K binding energy of uranium, 115.6 keV.

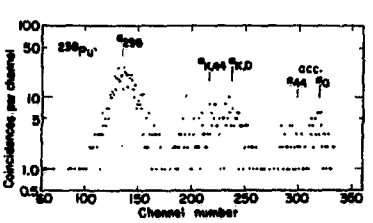

Fig. 1. ^{238}Pu α spectrum in coincidence with uranium K_β x-rays. (XBL 744-2875)

The ^{210}Po was also measured in the coincidence unit for a total running time of 15 days. The experiment was very similar to that for ^{238}Pu except that a larger fraction of the K x-ray peak could be used in the gate as there are no gamma rays in ^{210}Po decay near the gate energy. The various coincidence runs in the 15 day period were summed and the total spectrum is shown in Fig. 2. The highest energy peak, α_0, is due to accidental coincidences with the main α group.

By extrapolating the two peaks (Fig. 2) in the same fashion as for the ^{238}Pu experiment, we found the difference in energy was 88 ± 1 keV in excellent agreement with K shell binding energy of lead, 88.0 keV. The abundance of the particles associated with K shell shake-off is $(1.65 \pm .16) \times 10^{-6}$ per ^{210}Po α particle.

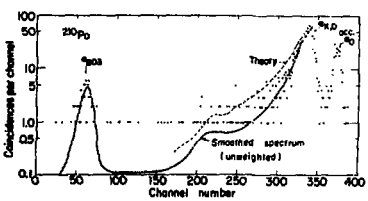

Fig. 2. ^{210}Po α spectrum in coincidence with lead K_α x-rays. Theoretical shape normalized to peak height. (XBL 744-2876)

According to Migdal's[1] theory the differential probability of ionizing one of the electrons may be expressed as

$$dP_{1s} = \frac{8v^2}{3(E_K - B)^4} \left| \langle k, \ell = 1 | \frac{1}{r^2} | 1s \rangle \right|^2 dE_k + \text{smaller terms}\ , \qquad (1)$$

where v is the velocity of the α particle, r is the radial distance from the nucleus, B is the binding energy of a 1s electron, ℓ is the angular momentum of the continuum states, E_k is the kinetic energy carried off by the ionized 1s electron and

Table 1. Probability of electron shake-off from the K shell.

Isotope	Ref.	Experiment	Stated Error	Theory (Hydrogenic)	Theory (H-F-S)
^{210}Po	6	1.5×10^{-6}	±33%		
	7	2.0	±16%		
	8	1.6	±31%		
	4	1.5	±27%		
	This work	1.65	±10%	2.67×10^{-6}	2.87×10^{-6}
^{238}Pu	15	0.51	±50%		
	This work	0.83	±13%	1.75×10^{-6}	1.66×10^{-6}

$k = \sqrt{2E_k}$. This equation is like Migdal's equation 15 except the summation over the angular part of wave function and of the two electrons has been carried out. The matrix element can be readily calculated with hydrogenic wave functions and the probability equation becomes

$$dP_{1s} = \frac{2^{11} v^2}{3z^6} \frac{e^{-\frac{4Z}{k} \arctan k/Z}}{\left(1 + \frac{k^2}{z^2}\right)^5 \left(1 - e^{-2\pi Z/k}\right)} dE_k \qquad (2)$$

where Z is the charge of the daughter nucleus. One gets the total ionization probability by numerical integration.

A more realistic set of wave functions would be of the self consistent type. We used the tabulated[2] Hartree-Fock-Slater central potentials to solve the Schrödinger equation for the continuum electrons and applied the Noumerov[5] integration method.

Table 1 summarizes the experimental results and our theoretical results on the shake-off effect in α decay.

Using our calculations of shake-off probability as a function of electron energy and the experimental average peak shape in the ^{210}Po α singles spectrum, we determined the shape of the α spectrum associated with the shake-off of K electrons which would be expected from Migdal's theory. The theoretical shape was normalized to the same peak height as the experimental curve and is shown as a dashed line in Fig. 2. The α singles spectrum had a small perturbation about 300 keV below the peak due to instrumental effects and this is reflected in both the calculations and the coincidence spectrum. As seen in Fig. 2, there is a definite discrepancy between the experimental and theoretical curves. The probability of electron shake-off decreases more rapidly than the theoretical prediction as the electron energy increases (i.e., as the α particle energy decreases). Ovechkin and Tsenter[4] observed the same effect in comparing electron energy measurements with Migdal's calculations, but the authors felt their experimental work was not sufficiently precise to indicate a definite discrepancy.

A distinctly different type of theoretical treatment was published recently by J. S. Hansen[5] after the present work was concluded. Hansen obtained a value of 2.02×10^{-6} for the total K shell ionization probability for ^{210}Po which is somewhat closer in agreement with the experimental result than any of the theoretical values. Although not discussed in the present work, Hansen's calculations for L and M shells were in far better agreement with the experimental results than any other theory.

After compilation of this work Briand et al[9] published a paper in which the α spectra associated with K shell shake-off was also measured.

Footnotes and References

*I. Perlman is now at the Hebrew University in Jerusalem.

1. A. Migdal, J. Phys. (USSR) 4, 449 (1941).

2. F. Herman and S. Skillman, Atomic Structure Calculations, Prentice-Hall, Inc. (1963).

3. J. M. Blatt, J. Comp. Phys. 1, 382 (1967).

4. V. V. Ovechkin and E. M. Tsenter, Soviet J. At. Energy (English transl.) 2, 344 (1957).

5. J. S. Hansen, Phys. Rev. A 9, 40 (1974).

6. M. A. Crace, R. A. Allen, D. West and H. Halban, Proc. Phys. Soc. (London) A64, 493 (1951).

7. W. C. Barber and R. H. Helm, Phys. Rev. 86, 275 (1952).

8. M. Riou, J. Phys. Rad. 13, 487 (1952).

9. J. P. Briand, P. Chevallier, A. Johnson, J. P. Rozet, M. Tavernier, and A. Touati, Phys. Rev. L33, 266 (1974).

THE ELECTRON-CAPTURE DECAY OF $^{206}Po^*$

L. J. Jardine† and A. A. Shihab-Eldin

Earlier investigations of electron-capture decay of ^{206}Po were carried out by Arbman[1] and Stoner[2] before high-resolution Ge(Li) detectors were available. More recent in-beam reaction studies[3,4] have provided some properties of the high-spin states of ^{206}Bi. Direct measurements of the alpha spectra of ^{210}At have also been made,[5] and we have recently[6] carried out the α-γ coincidence measurements of ^{210}At weak alpha decay branch to complement these recent studies of ^{206}Bi level structure.

We have remeasured the γ-ray singles and γγ coincidences following electron-capture decay of ^{206}Po using Ge(Li) detectors. Sources of 8.8 days ^{206}Po were obtained via the $^{209}Bi(p,4n)^{206}Po$ reaction. The targets were allowed to stand for several days following bombardment (at 37-42 MeV) until the ^{207}Po impurity had decayed away. This was then followed by chemical separation to remove the ^{207}Bi activity, in addition to the ^{205}Bi activity which grew in from the decay.

Gamma-ray singles spectra were obtained with a 35-cm^3 coaxial Ge(Li) detector (system resolution 2.6 keV (FWHM) at 1332 keV) and a 10 cm^3 planer Ge(Li) detector (system resolution 1.4 keV (FWHM) at 122 keV). Three parameter γ-γ coincidence measurements (E_1, E_2, Δt) were carried out with two 35-cm^3 coaxial Ge(Li) detectors. The width of the prompt time distribution was about 35 ns (FWHM). Approximately 50 coincidence sorts were performed at a resolving time of about 70 ns. Seventy-seven γ-ray transitions observed in the γ-ray singles were assigned to the electron-capture decay of ^{206}Po. Our results for the γ-ray energies are in rather good agreement with the transition energies determined from the internal conversion-electron measurements of Ref. 7 for transitions observed in both types of measurements. Multipolarities for many γ-rays were deduced from the comparison of experimental subshell ratios[7] and/or experimental conversion coefficients with theoretical values of Hager and Seltzer.[8] Conversion coefficients were calculated from the relative electron intensities of Ref. 7 and our relative γ-ray intensities.

Coincidence measurements and sum-difference relationships among γ-ray energies have been used to construct the scheme shown in Fig. 1. Spin and parity assignments are based upon log *ft* values of the electron-capture branches, transition multipolarities and previously reported data.[1-7] Also included in Fig. 1, are levels populated by the alpha decay of ^{210}At.[5,6] The decay scheme of Fig. 1 is substantially different than the previous one proposed by Arbman[1] because of the discovery[7] of an intense (93% of EC decays) 10.84 keV

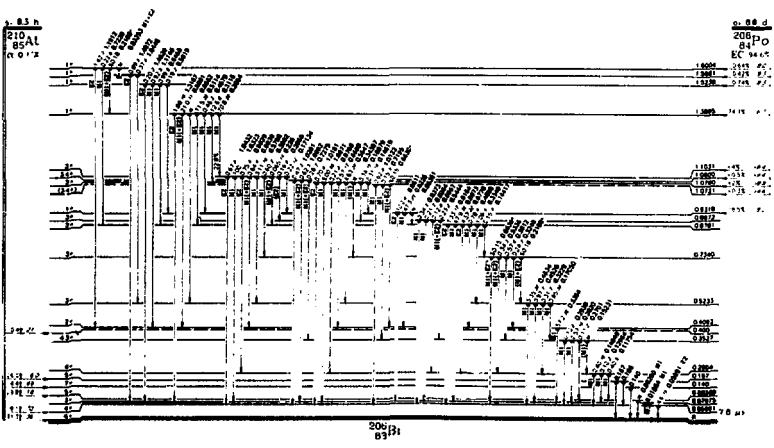

Fig. 1. Level scheme of ^{206}Bi. Relative photon intensities (with errors in italics) from the ^{206}Po decay are shown above the transitions. Relative alpha intensities from the ^{210}At decay and calculated alpha hindrance factors are shown. The absolute intensity of the 286.2 keV γ-ray was calculated from the level scheme to be 22.8 ± 2.0 photons per 100 decays of ^{206}Po. (XBL 7412-7847)

M1 transition depopulating a new 3^+ state at 70.8 keV.

No theoretical calculations of the level structure of ^{206}Bi have been made. However, its low-lying level structure might a priori be characterized by one (proton) particle-three (neutron) hole states arising from couplings of the (odd) 83rd proton with the (odd) 123rd neutron. To estimate qualitatively the number and type of such states, we show in Fig. 2 the experimental[9,10] states of ^{209}Bi and ^{205}Pb. The first three states of ^{209}Bi are due[9] to the proton single-particle orbitals of $1h_{9/2}$, $2f_{7/2}$, and $1i_{13/2}$. The four states ^{205}Pb at 0, 2.3, 270 and 1014 keV are due[10] predominantly to an odd neutron (or three-neutron holes) in the $2f_{5/2}$, $3p_{1/2}$, $3p_{3/2}$, and $1i_{13/2}$ single-particle orbitals, respectively. The remaining ^{205}Pb states shown are presumably of a more complex nature. If one now considers couplings of the $1h_{9/2}$ and $2f_{7/2}$ protons with the three neutron hole states of ^{205}Pb, the degenerate band structure shown in column 4 of Fig. 2 results. Finally, all known experimental states of ^{206}Bi are shown (with a shifted energy for the ground state) in the last column of Fig. 2. Relations between experimental levels and the 1p-3h configurations assumed responsible for it are indicated by dashed lines.

The rather low Q-value for the electron-capture decay of ^{206}Po helps to make an interpretation of the levels of ^{206}Bi easier as only five states receive any measurable direct electron-capture decay in the present level scheme. Electron-capture decays to these 1^+ states from the even-even 0^+ ground state of ^{206}Po proceed via an allowed beta transition. Subsequent γ-ray decay of these 1^+ states populates states of spin 2, 3, 4, and 5 until the 6^+ ground state is reached.

In Fig. 2 we have shown five possible (degenerate) multiplets formed from couplings of the odd proton and the odd neutron (or three-neutron holes) that give rise to 1^+ states in the energy range of interest. (It may only be fortuitous that five 1^+ states are presently experimentally identified.) The 1^+ state at 1389.5 keV receives most of the electron-capture decay and is believed to arise from the coupling of a $2f_{7/2}$ proton to the three-neutron holes with a configuration of the ground state of ^{205}Pb. Such a configuration of ^{206}Bi can be written explicitly as

$$(\pi(f_{7/2})\nu(f_{5/2})^{-1}(p_{1/2})^{-2})_{1^+} .$$

The 0^+ ground state of ^{205}Po is of a two proton-four neutron hole character with the probable dominant configuration

$$(\pi(h_{9/2})^2\nu(f_{5/2})^{-2}(p_{1/2})^{-2})_{0^+} .$$

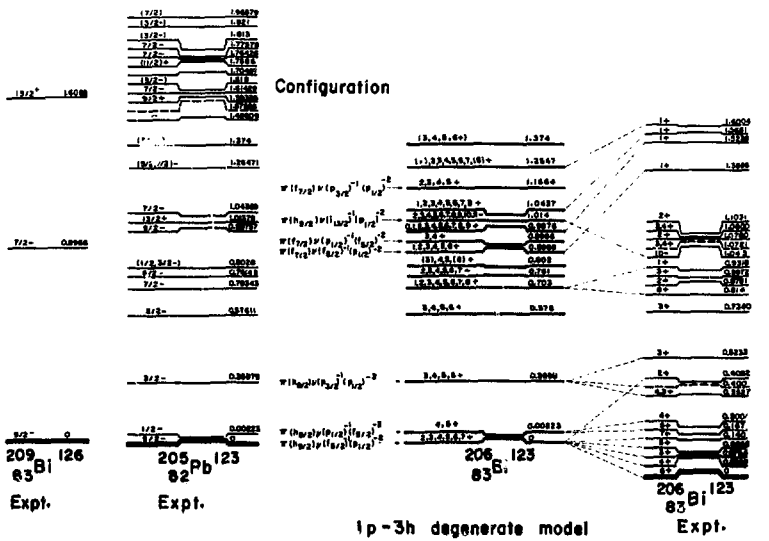

Fig. 2. Comparison of the experimental ^{206}Bi level scheme with the predictions of a simple coupling model. The experimental[12,13] states of ^{206}Bi and ^{205}Pb are used to estimate the energies and range of spins from multiplets formed from couplings of the odd proton and the three-neutron holes (1p-3h states) in ^{206}Bi. (XBL 7412-3385)

An allowed single-particle electron-capture decay of the type

$$\pi 2f_{7/2} \xrightarrow{EC} \nu 2f_{5/2}$$

can be used to explain the electron-capture decay to the 1^+ state at 1389.5 keV if the ground state wavefunction of ^{206}Po has a second component of the form

$$(\pi(f_{7/2})^2\nu(f_{5/2})^{-2}(p_{1/2})^{-2})_{0^+} \ .$$

Decay to the other 1^+ states in ^{206}Bi (with somewhat higher log ft values) probably proceeds via the same single-particle mechanism through admixtures of the

$$(\pi(f_{7/2})\nu(f_{5/2})^{-1}(p_{1/2})^{-2})_{1^+}$$

configuration present in the wavefunctions.

States assigned to the configurations

$$(\pi(h_{9/2})\nu(f_{5/2})^{-1}(p_{1/2})^{-2})_{2,3,4,5,6,7^+} \ ,$$

$$(\pi(h_{9/2})\nu(p_{1/2})^{-1}(f_{5/2})^{-2})_{4,5^+} \ , \text{ and}$$

$$(\pi(h_{9/2})\nu(p_{3/2})^{-1}(p_{1/2})^{-2})_{3,4,5,6^+}$$

are shown in Fig. 2. Calculations of electromagnetic transition probabilities and alpha decay rates using these assumed configurations for states of ^{206}Bi populated in the alpha decay of ^{210}At have previously been made.[6,11] The results indicated that agreement o. the theoretical calculations with existing experimental data could be obtained if some configuration mixing among these three configurations was allowed.

Finally the states in the energy range of 734.0 - 1103.1 keV are presumably of a rather complex structure and we cannot presently ascribe a specific configuration to these states using only qualitative arguments. However, two states observed[3,4] in recent in-beam experiments in this energy range merit some additional remarks. A 10^- isomer of 1 msec at 1043 keV has been assigned[12,13] the configuration

$$\pi(h_{9/2})\nu(i_{13/2})^{-1}(p_{1/2})^{-2} \ .$$

This is also consistent with the qualitative predictions of Fig. 2. Decay of this isomeric state to an 8^+ state at 814 keV has been observed. This 8^+ state, as suggested from Fig. 2, might arise from a coupling of a $h_{9/2}$ proton with a $7/2^-$ state of ^{205}Pb. The dominant configuration of the $7/2^-$ state of ^{205}Pb is expected to be of the type

$$(\nu(f_{5/2})^{-2}(p_{1/2})^{-1})_{7/2^-} \ ,$$

with perhaps the following internal coupling

$$(\nu((f_{5/2})^{-1}(p_{1/2})^{-1})_{2^+}(f_{5/2})^{-1})_{7/2^-} \ .$$

Thus the 8^+ state of ^{206}Bi might have a major component of the type

$$(\pi(h_{9/2})(\nu(f_{5/2})^{-2}(p_{1/2})^{-1})_{7/2^-})_{8^+} \ .$$

Perhaps these latter two states provide further evidence that the level structure of ^{206}Bi can be regarded as a series of one particle-three hole states, at least up to 1389 keV.

Footnotes and References

*Condensed from LBL-3447, to be submitted to Phys. Rev. C.

†Present address: Argonne National Laboratory, Argonne, Illinois.

1. E. Arbman, Nucl. Phys. 3, 625 (1957).

2. A. W. Stoner, Lawrence Berkeley Laboratory Report UCRL-3471 (1956).

3. Yu. N. Rakivnenko et al., Ukr. Fiz. Zh. 17, 1037 (1972).

4. U. Hagemann, K. H. Kaun, W. Neubert, W. Schulze, and F. Stary, Nucl. Phys. A197, 111 (1972).

5. N. A. Golovkov, Sh. Guetkh, B. S. Dzhelepov, Yu. V. Norseev, V. A. Khalkin, and V. G. Chumin, Izv. Akad, Nauk. SSSR (Ser. Fiz.) 33, 1622 (1969).

6. L. J. Jardine and A. A. Shihab-Eldin, Lawrence Berkeley Laboratory Report LBL-2943 (1974); Nucl. Phys. A244, 34 (1975).

7. M. Fujioka, M. Kanbe and K. Hisatake, Phys. Rev. Letts. 31, 114 (1973); K. Hisatake and M. Kanbe (private communications).

8. R. S. Hager and E. C. Seltzer, Nucl. Data A4, 1 (1968).

9. M. J. Martin, Nucl. Data 5, 287 (1971).

10. M. R. Schmorak, Nucl. Data 6, 425 (1971).

11. A. A. Shihab-Eldin, L. J. Jardin, and J. O. Rasmussen, Lawrence Berkeley Laboratory Report LBL-3409 (1974), (to be published in Nucl. Phys., 1975).

12. G. Schäfer, H. Hübel, C. Günther, A. Goldman, and D. Riegel, Phys. Lett 46B, 65 (1973).

13. T. W. Conlon, Nucl. Phys. A212, 531 (1973).

ALPHA DECAY OF ^{210}At TO LEVELS IN ^{206}Bi*

L. J. Jardine† and A. A. Shihab-Eldin

Alpha-gamma coincidence measurements were carried out for the weak alpha-decay branch of ^{210}At to supplement previous high resolution magnetic spectrometer measurements of the α spectra[1,2] The completed alpha decay scheme of ^{210}At and the recent detailed studies of the electron-capture decay of ^{206}Po[3,4] and the ^{205}Tl(α,3nγ) reaction[5,6] provide complementary information on the nature and decay characteristics of low-lying ^{206}Bi levels.

Astatine sources were produced at the 88-Inch Cyclotron via the ^{209}Bi(α,3n) reaction, followed by chemical purification and separation.

Three parameter (E_{α}, E_{γ}, Δt) coincidence measurements were carried out using a 10 cm^3 (active volume) Ge(Li) detector (1.5 keV (FWHM) resolution at 122 keV) and a 6 mm diameter Au-Si surface barrier detector (16 keV (FWHM) resolution at 4.8 MeV). Gates were set on the relatively intense three alpha groups α_{83}, α_{140} and α_{167}. The energies and relative intensities of the coincident γ-rays are given in Table 1. The relative intensities of the α_{83}, α_{140} and α_{167} groups calculated from the relative γ-ray intensities of Table 1 and the theoretical internal conversion coefficients, assuming the four γ-rays were of pure M1 multipolarity, gave good agreement with α-singles measurements of Ref. 1. This constitutes a weak argument supporting assignments of M1 multipolarity for these four transitions.

TABLE 1. γ-rays measured in coincidence with ^{210}At alpha particles.

γ-ray energy (keV)	Relative γ-ray intensity	α gate
83 ± 1	766 ± 153	α_{83}
140 ± 1	100	α_{140}
106 ± 1	272 ± 54	α_{167}
167 ± 2	174 ± 35	α_{167}

The ^{206}Bi level scheme deduced from our α-γ coincidence data is shown in Fig. 1. We have also included other known levels below 500 keV observed from the electron-capture decay of ^{206}Po [3,4] and the ^{205}Tl(α,3nγ) reaction[5,6] from which spin and parity assignments for all levels except those at 83 and 167 keV were derived. The decay characteristic of these two levels obtained in the present experiment together with the relative alpha decay rate calculations of Ref. 7 make a spin and parity assignment of 5$^+$ for both of these levels most probable.

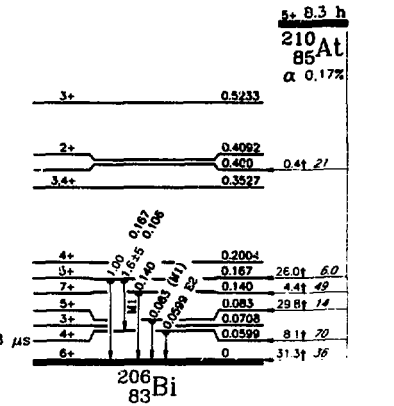

Fig. 1. Level scheme of ^{206}Bi. Relative alpha intensities,[1] relative photon intensities for the 167 keV level and calculated[8] alpha hindrance factors are also shown. Spins, parities and level energies below 0.524 MeV are shown as deduced from previous studies,[3-6] of the level structure.
(XBL 745-846A)

The ^{206}Bi nucleus with 123 neutrons and 83 protons is three neutron-hole and one proton removed from the magic ^{208}Pb core. Thus the lowest-lying states of ^{206}Bi are expected to be described (in zeroth order) by configurations resulting from the coupling of the $1h_{9/2}$ proton (^{209}Bi ground state) to the $5/2^-$, $1/2^-$ and $3/2^-$ three-neutron hole states in ^{205}Pb at 0.0, 23 and 263 keV, respectively. The configurations for these three multiplets are

$$[\pi(h_{9/2})\nu(f_{5/2})^{-1}\nu(p_{1/2})^{-2}]_{2,3,4,5,6,7^+},$$

$$[\pi(h_{9/2})\nu(p_{1/2})^{-1}\nu(f_{5/2})^{-2}]_{4,5^+}$$

and

$$[\pi(h_{9/2})\nu(p_{3/2})^{-1}\nu(p_{1/2})^{-2}]_{3,4,5,6^+}$$

respectively. The separation energies between the centers of mass of these three configurations are identical to the excitation energies of the first $5/2^-$, $1/2^-$ and $3/2^-$ states in ^{205}Pb. These small separations imply that the lower-lying states of spin and parity 4^+ and 5^+ must have rather extensive admixtures from the above three configurations, while the lowest states of spin and parity 2^+, 3^+, 6^+, and 7^+ are expected to be somewhat "purer" in character, belonging basically to a pure

$$[\pi(h_{9/2})\nu(f_{5/2})^{-1}\nu(p_{1/2})^{-2}]$$

configuration.

Relative alpha decay rate calculations[7] and electromagnetic transition rate calculations were carried out to test the above qualitative conclusions. To obtain agreement with experimental results it was found necessary to include admixtures from the above three configurations in describing the wave functions of the 4_1^+, 5_1^+, 5_2^+ and 4_2^+ states, with wave functions for 6_1^+, 3_1^+, 7_1^+ and 2_1^+ states limited to the pure

$$[\pi(h_{9/2})\nu(f_{5/2})^{-1}\nu(p_{1/2})^{-2}]$$

configuration.

In Table 2 we give a set of wave functions for the 6_1^+, 4_1^+, 7_1^+, and 5_2^+ states (obtained by trial and error) that correctly reproduces the experimental results from the α-decay studies when the relative alpha decay rates and electromagnetic transition rates are calculated. In Table 3 we show a comparison between calculated and experimental electromagnetic transition rates using the wave functions of Table 2.

In conclusion, both α- and γ-decay rate calculations indicated that an appreciable admixture from the

$$[\pi(h_{9/2})\nu(p_{3/2})^{-1}\nu(p_{1/2})^{-2}]$$

configuration, in addition to those from the

$$[\pi(h_{9/2})\nu(f_{5/2})^{-1}\nu(p_{1/2})^{-2}]$$

and

$$[\pi(h_{9/2})\nu(p_{1/2})^{-1}\nu(f_{5/2})^{-2}]$$

configurations are required for the description of the wave functions of the 4_1^+ and 5_2^+ states (and

TABLE 2. Wave functions for some ^{206}Bi states deduced from the electromagnetic transition probabilities calculations. These give consistent results with experiment when electromagnetic transition probabilities and α-decay rates are calculated.

Energy (keV)	J^π	configurations[a] $\lvert\pi(h_{9/2})\nu(f_{5/2})^{-1}(p_{1/2})^{-2}\rangle$	$\lvert\pi(h_{9/2})\nu(p_{1/2})^{-1}(f_{5/2})^{-2}\rangle$	$\lvert\pi(h_{9/2})\nu(p_{3/2})^{-1}(p_{1/2})^{-2}\rangle$
0	6_1^+	1.0		
60	4_1^+	$\sqrt{0.74}$	$-\sqrt{0.10}$	$-\sqrt{0.16}$
140	7_1^+	1.0		
167	5_2^+	$\sqrt{0.05}$	$\sqrt{0.67}$	$-\sqrt{0.28}$

[a]Numbers in the table represent the amplitudes of the configurations composing the state.

TABLE 3. Comparison of electromagnetic transition probabilities, using the wave functions of Table 2 in the decay of ^{206}Bi states with available experimental data.

Transition ($J_i \to J_f$)	E (keV)	Relative γ-ray branching intensity (expt.)	Multipolarity (expt.)	Theoretical transition probability[a] $T(\lambda) \times 10^{-9}$ sec^{-1} (M1 calc.)	(E2 calc.)	(expt.)
$5_2^+ \to 7_1^+$	27	n.o.[b]	(E2)	0	3.4×10^{-7}	
$5_2^+ \to 4_1^+$	107	1.6 ± 0.5	(M1)	3.00	2.5×10^{-4}	
$5_2^+ \to 6_1^+$	167	1.0	(M1)	1.16	5.8×10^{-3}	
$7_1^+ \to 6_1^+$	140	1.0	M1	6.63	0.013	
$4_1^+ \to 6_1^+$	60	1.0	E2	0	1.18×10^{-6}	$(1.2 \pm 0.1) \times 10^{-6}$

[a]The value for the oscillator parameter ν used in the calculation of T(E2) was 0.1659. Other parameters are discussed in the text.

[b]Transition was not observed.

also for the 4_1^+ and 5_1^+ states) in order to get agreement between theory and experiment. It will be interesting to find out if these qualitative conclusions will still be valid when theoretical wave functions in a larger and more realistic configuration space become available.

Footnotes and References

*Condensed from LBL-2943, Nucl. Phys. A244, 34 (1975).

†Present address: Argonne National Laboratory, Argonne, Illinois.

1. N. A. Golovkov, Sh. Guethk, B. S. Dzhelepov, Yu. V. Norseev, V. A. Khalkin, and V. G. Chumin, Izv. Akad. Nauk. SSSR (ser. fiz.) 33, 1622 (1969). (translated page 1489).

2. R. W. Hoff, Ph.D. Thesis, University of California, Radiation Laboratory Report UCRL-2325 (1953) unpublished.

3. M. Fujioka, M. Kanbe, and K. Hisataka, Phys. Rev. Lett. 31, 114 (1973); private communications, September 1973 and October 1973.

4. L. J. Jardine and A. A. Shihab-Eldin, Lawrence Berkeley Laboratory Report LBL-3447 (1974), unpublished, to be submitted to Phys. Rev. C.

5. U. Hagemann, K. H. Kaun, W. Neubert, W. Schulze and F. Stary, Nucl. Phys. A197, 111 (1972).

6. Y. M. Rakivnenko, O. P. Klyucharev, V. O. Lutsik, V. V. Ramaev, I. A. Ramanii, E. O. Skakun, G. T. Yatsenko, and K. S. Goncharov, Ukr. Fiz. Zh. 17, 1029 (1972).

7. A. A. Shihab-Eldin, L. J. Jardine, and J. O. Rasmussen, Lawrence Berkeley Laboratory Report LBL-2366 (1973), p. 175; ibid. LBL-3409 (1974), to be published in Nucl. Phys. A.

8. C. M. Lederer, Lawrence Berkeley Laboratory Report LBL-1996 (1973).

THE HALF-LIFE AND THE α-DECAY BRANCHING RATIO OF ^{207}Po*

B. Parsa† and S. S. Markowitz

^{207}Po was produced via ^{3}He activation of lead samples. Polonium was chemically separated from the irradiated targets. Gamma and α spectra were measured with Ge(Li) and surface-barrier α counters, respectively. The decay of the 992-keV γ-ray of ^{207}Po was followed and a half-life of 5.84 ± 0.07 hr was obtained for ^{207}Po. The α-decay branching of ^{207}Po was measured to be 0.0210 ± 0.0023 per cent.

Footnote and Reference

*Condensed version of J. Inorg. Nucl. Chem. 36, 1429 (1974).

†Visiting Fulbright-Hays Grantee. Permanent address: Tehran University Nuclear Center, Tehran, Iran.

ALPHA AND GAMMA BRANCHING IN 2-msec ^{213}Ra DECAY

D. G. Raich,† H. R. Bowman, R. E. Eppley,‡ J. O. Rasmussen, and I. Rezanka§

We have observed a direct α-branch in the 2.1 msec decay of ^{213m}Ra. The isomer was produced by bombarding a thin (∿ 0.6 mg/cm^2) isotopically enriched ^{204}Pb target with ∿ 60 MeV ^{12}C beams from the SuperHILAC. Recoil products were stopped in 2 atm of helium and jetted to a semiconductor detector. Transport and counting times in the millisecond region were achieved through the use of a very small volume He cell (∿ 1 cm^3) and short capillary, and a computer-based data collection system which, during the ∿ 20 ms interval between HILAC pulses, directed counting into a series of timed "buckets".

Three α-groups have been tentatively assigned to ^{213m}Ra decay, having energies of 8.47, 8.36, and 8.25 MeV in an intensity ratio of about 8:5:1. The assignment of the two stronger groups is fairly certain, and in particular it has been possible to rule out contributions from ^{214}Fr and ^{214m}Fr decay here. The existence and assignment of the weakest group is as yet less certain. These energies correspond to Q-values of 8.63, 8.52, and 8.41 MeV. Valli and Hyde's investigation[1] of 2.75 min ground-state ^{213}Ra α-decay likewise found three groups, corresponding to Q-values of 6.859, 6.750, and 6.645 MeV. From this we conclude that the isomeric state of ^{213}Ra must lie about 1770 keV above the ground state (see Fig. 1).

Such an assignment requires that we revise somewhat the ^{213}Ra level scheme and γ-ray tables that we put forth tentatively in last year's Annual Report,[2] and it supports some of the reservations expressed there. Additional γ-ray data from ^{206}Pb(^{12}C,5n)^{213}Ra experiments this year at Yale

lead to similar conclusions. Careful singles counting in the x-ray region fails to support our original inclusion of the 49 keV γ-ray, so that has been dropped. And γγt coincidence experiments show coincidences only between the three major γ-rays, 160.9, 546.3, and 1062.5 keV. The 210.5 keV γ-ray is not in coincidence, even though it tracks the others in excitation function and half-life; thus we believe it belongs to ^{209}Rn rather than ^{213}Ra. The resultant new level scheme is shown in Fig. 1.

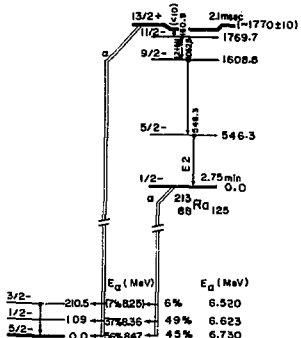

Fig. 1. Tentative level scheme to account for ^{213m}Ra decay data. (XBL 756-3317)

This new level scheme is capable of showing intensity balance down the γ-cascade, and it yields K-fluorescence of the right order of magnitude. Considering the 9/2- and 11/2- levels to be members of the $\pi(h_{9/2})^6\nu(p_{1/2})$ multiplet, it actually comes closer to following the trends of neighboring 125-neutron isotones. The introduction of an unobserved low-energy transition is a little distasteful, but there seems to be no other way of accounting for the halflife and α-energy data. The unobserved transition must be highly retarded, nevertheless, to give a 2.1 ms half-life; but if we consider the isomeric state to be primarily $\nu(i_{13/2})$, the configuration change required in going to the 11/2- level of the $\pi(h_{9/2})^6\nu(p_{1/2})$ multiplet could account for such retardation.

Work is continuing to more thoroughly check out additional consequences of this proposed level scheme.

Footnotes and References

*Final results will be submitted to Nucl. Phys. (anticipated 1975).

†Graduate student of Yale University, resident at LBL.

‡Present address: Monsanto Research Corp., Mound Laboratory, Miamisburg, OH 45342.

§Work performed at former Yale University HILAC facility. Present address: Research Laboratory, Xerox Corp., Rochester, NY 14600.

1. K. Valli, W. Treytl, and E. K. Hyde, Phys. Rev. 161, 1284 (1967); K. Valli and E. K. Hyde, Phys. Rev. 176, 1377 (1968).

2. D. G. Raich, J. O. Rasmussen, and I. Rezanka, Lawrence Berkeley Laboratory Nuclear Chemistry Annual Report 1973, LBL-2366 (1974), p. 16.

LEVELS OF ^{156}Dy AND DECAY SCHEME OF ^{156}Ho ISOMERS*

S. Iwata,† T. Tamura,‡ J. O. Rasmussen, and R. Needham§

Previous studies[1] have been made of the decay of ^{156}Ho, and they have shown population of daughter states up to spin 6. Ekström et al[2] have measured the spin of 56 min ^{156}Ho to be I = 1. The above facts suggest that there may be a short-lived higher-spin ground state that rapidly equilibrates with the 56 min, spin 1 isomer.

In earlier work at the Yale Heavy Ion Accelerator Laboratory we have studied the gamma spectra, mainly producing the activities by boron-11 bombardments of samarium oxide targets. In the summer of 1974 we made new studies, producing the activity by way of the parent erbium-156 by (^{12}C,3n) reaction on isotopically enriched ^{147}Sm oxide. This new work was done at the cyclotron of the Institute of Physical and Chemical Research (RIKEN), Japan.

We present in Fig. 1 a partial decay scheme extending the earlier work. Our γ-γ coincidence experiments were not very informative due to troubles from strong annihilation radiation. Thus, the assignments are mainly based on energy sums. That there is still more complexity to the decay is indicated by the table of additional gamma rays not fitted into the decay scheme.

We are especially grateful to Director H. Kimitsubo and colleagues of the Institute of Physical and Chemical Research, Wakai-shi, Saitama-ken, Japan, for making available their heavy-ion cyclotron and high-resolution gamma spectroscopic apparatus.

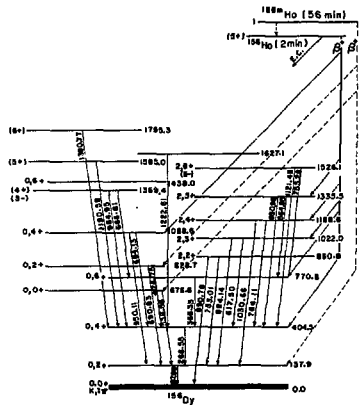

Fig. 1. Preliminary decay scheme of the ^{156}Ho isomers.

(XBL 756-3319)

TABLE 1. Unassigned high energy γ rays (keV) of ^{156}Ho.

1001.32(W)	1155.35(M)	1205.80(W)
1218.03(S)	1292.49(M)	1301.43(M)
1337.86(M)	1416.04(S)	1422.60(M)
1432.91(M)	1453.04(S)	1471.04(S)
1528.09(M)	1535.43(M)	1543.62(M)
1632.88(M)	1647.97(S)	1761.70(M)
1820.11(M)	1854.62(M)	2020.73(S)
2025.91(M)	2042.91(S)	2218.46(S)
2252.08(M)	2331.28(S)	2392.29(S)
2458.26(W)		

Intensity scale: (W) weak, (M) medium, (S) strong.

Footnotes and References

*Work supported in part by Kyoto University, by J.A.E.R.I., and by Japan Society for the Promotion of Science.

†Reactor Institute, Kyoto University, Kumatori, Japan.

‡Research Division, Japan Atomic Energy Research Institute, Tokai-mura, Japan.

§Present address: 34 Main Street, Malden, Mass.

NEW $i_{13/2}$ ISOMER $^{207}Rn^m$ AND ITS SPIN RELAXATION TIME IN LIQUID MERCURY*

I. Rezanka,† I. M. Ladenbauer-Bellis,† and J. O. Rasmussen

In the process of systematic investigation of nuclear isomers and their properties at Yale Heavy Ion Accelerator (HILAC), a previously unreported isomer $^{207}Rn^m$ was observed and its properties were studied.

The isomer was originally produced by bombardments of a thick natural Hg target with 120 MeV ^{12}C ions from the Yale HILAC.

In the study which followed, a thin (10 mg/cm^2) self-supporting Au target and ^{14}N ions with energies varying from 70 - 120 MeV were used. The γ and x rays were detected during and after the accelerator beam pulse by means of several Ge(Li) detectors ranging in size from 8 to 40 cm^3.

The standard beam duration of the HILAC is 2 ms and is followed by 98 ms beam-off period. However, for some of these experiments, the beam pulses were narrowed down to about 150 μs at the same repetition rate of 10 Hz. The data collection was performed under computer control and the PDP8/I computer was programmed for a wide variety of collection modes including a real-time analysis of the half-lives associated with different peaks of the spectrum. The photon radiations summarized in Table 1 are assigned to the isomer with a best

TABLE 1. Transitions in $^{207}Rn^m$ decay.

E (keV)	I_{photon} (% of decays)	$I_{transit}$ [a] (% of decays)
K x rays	77 ± 7	
234 ± 1	21 ± 5	126 ± 30
665.1 ± 0.1	98 ± 2	100[b]

[a]Assuming E2 and M2 multipolarities for the 234 and 665.1 keV transitions, respectively.

[b]Adopted value.

half-life value set at 181 ± 18 μs.

A prompt (within the resolving time of ≈40 ns) coincidence relation was established between the 665.1 keV γ line and the Rn Kx group when using a standard fast-slow coincidence circuitry and two Ge(Li) detectors with volumes 40 and 8 cm³, respectively. Consequently, the isomer is a Rn nuclide.

The mass number of the Rn isomer was determined as A = 207 by the measurement of relative excitation functions. Based on the coincidences observed in the decay of the isomeric state, between the 665.1 keV γ line and the Rn Kx rays, the two transitions connected with the isomer decay, 665.1 and 234 keV, appear to be in cascade. Furthermore, due to the observation of the 665.1 keV transition in the prompt gamma rays while the 234 keV γ line was not seen in beam at all, the 665.1 keV transition populates the ^{207}Rn ground state.

A (20 ± 15)% anisotropy in the beam direction, of the intensity of the 665.1 keV line was observed during the first 1 ms after the beam pulse when bombarding the thick Hg metallic target at room temperature with ^{12}C; by analogy with the relaxation time of ^{205}Pb^m in liquid Hg found[1] to be equal to 0.4 ± 0.2 ms, the relaxation time of Rn recoils could be expected to be comparable with the measurement time. The anisotropy indicated a quadrupole character of the 665.1 keV transition and its multipolarity was assigned as E2. The assignment of the M2 multipolarity of the 234 keV transition followed then from the measured γ- and x-ray intensities.

Considering the regular occurrence of the 5/2⁻ ground state for the nuclei with N = 121, the level scheme as shown in Fig. 1 was proposed and the isomeric level was assigned as the $i_{13/2}$ shell-model state.

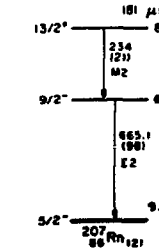

Fig. 1. Decay scheme of ^{207}Rn^m. (XBL 755-1223)

The hindrance factor of 530 for the delayed M2, 13/2⁺ → 9/2⁻ transition in ^{207}Rn was calculated by means of Weisskopf formula,[1] this value agrees well with the hindrance factors of 1500 and 290 calculated for the transitions of the same type observed[2] in ^{205}Po^m and ^{207}Po^m, respectively.

Footnote

*A more detailed report is in Phys. Rev. C10, 766 (1974).

†Heavy Ion Accelerator Laboratory, Yale University New Haven, CT 06520

HIGH-SPIN ROTATIONAL STATES IN ^{169}Hf FROM THE ^{159}Tb(^{14}N, 4nγ) REACTION AND DECAY OF ^{169}Ta*

E. der Mateosian,** I. Rezanka,† W. S. Ribbe,‡
I. M. Ladenbauer-Bellis,§ and J. O. Rasmussen¶

Studies of nuclear high-spin rotational states have led in recent years to the discovery of two new effects: sudden changes of the moment of inertia at high rotational velocities (backbending)[1,2] and the weakening of the coupling of the last odd particle to the core in unique parity states.[3,4] A complete understanding of both effects has not yet been achieved; both may be, in fact, related to Coriolis effects.[5] To arrive at a more definitive theoretical explanation, further experimental measurements are needed. The experimental studies should probably stress two directions: studying the nuclear high spin states in new nuclear species, and extending the knowledge about already investigated nuclei to even higher spin states. This study of ^{169}Hf has followed both lines.

The experimental work on this project was done as a cooperative effort of Yale Heavy Ion Accelerator, Lawrence Berkeley, and Brookhaven National Laboratories. The first experiments on this study were made at the Yale Heavy Ion Accelerator (HIA) where both the decay of ^{169}Ta and the in-beam gamma ray excitation functions of ^{169}Hf in the ^{159}Tb(^{14}N, 4n) reaction were studied. Following this preliminary in-beam spectroscopy, the final experiments on γγ-coincidences and angular distributions were done at the Brookhaven Laboratory tanden van de Graaf.

Although all the data are important for the level assignment and interpretation, the results of the coincidence experiment provided the most direct information about the rotational bands in ^{169}Hf. The coincidence results formed the main basis for the assignment of all rotational levels resulting from this study.

The three lowest levels of the 5/2⁻[523] rotational band were already assigned from the

^{169}Ta decay. Here, in the in-beam study, this band was also observed and identified up to considerably higher excitations. It was found that it consisted of two cascades with weak cross-feeding. The only $\Delta I = -1$ transitions positively observed here, are the two lowest ones; otherwise, only the $\Delta I = -2$ stretched transitions formed the band up to spins 31/2 and 29/2.

The two strong cascades shown in the coincidence spectra of Fig. 1 are obvious candidates for the decoupled positive parity band occurring regularly in odd-neutron rare earth nuclei.[6] This assignment follows both from their spacing and from their population patterns. The delayed coincidences of both cascades with the 28.8 keV, E1 transition ending in the ground state prove this assignment. Although such a band is a Coriolis mixture of several Nilsson orbitals originating in the $i_{13/2}$ shell model state, and the perturbation may be effective even for low rotational excitations, the prevailing single particle character for the low excitations should be $5/2^+[642]$. The spacings and intensities in the stronger of the cascades show, for example, that the 218.6 keV γ-line is the $17/2^+ \rightarrow 13/2^+$ transition; this, and the angular distribution enable us to assign this band starting with the $9/2^+$ level and extending reliably to spin 41/2 and tentatively to 49/2. The level scheme of ^{169}Hf resulting from this study is shown in Fig. 2.

Fundamental information can be obtained from the E2/M1 mixing amplitudes δ. This analysis is important for the assignment of the $5/2^+[512]$ band. Information of two kinds is available for this purpose: the results of the angular distribution measurements, and the cross-over-to-cascade branching ratios within the band. Generally the branching ratios yield more accurate absolute values of δ but cannot determine the sign, and the reliability hinges on the validity of the strong coupling model. The angular distributions determine the sign of δ unequivocally and its absolute value usually rather inaccurately, both in a model-independent way. Deduced mixing amplitudes are given in Table 1.

The mixing amplitude is strictly related to the nuclear g-factor by the relation

$$g_K - g_R = \frac{Q_0 E_\gamma}{1.073\ (I^2 - 1)^{\frac{1}{2}}} \frac{1}{\delta}\ , \qquad (1)$$

where Q_0 is the nuclear quadrupole moment in barns, E_γ the energy of the cascade transition in MeV, and I the initial spin. The value of 5.5 barns was taken for the value of Q_0, extrapolated from the tabulated B(E2) values of heavier Hf nuclei[8] according to the A-dependence of the $2 \rightarrow 0$ transitions in the doubly-even nuclei. The results of this determination are given in column 6 of

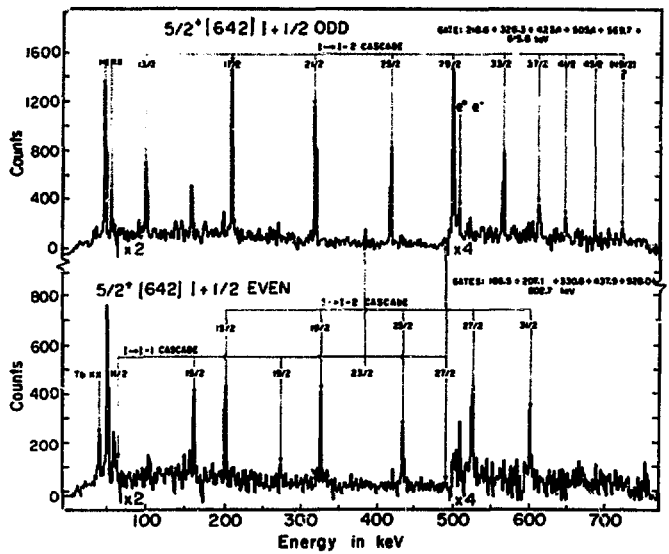

Fig. 1. Coincidence spectra added for the two cascades in $5/2^+[642]$ band; I + 1/2 odd in upper part, I + 1/2 even in lower part of the figure. (XBL 748-4005)

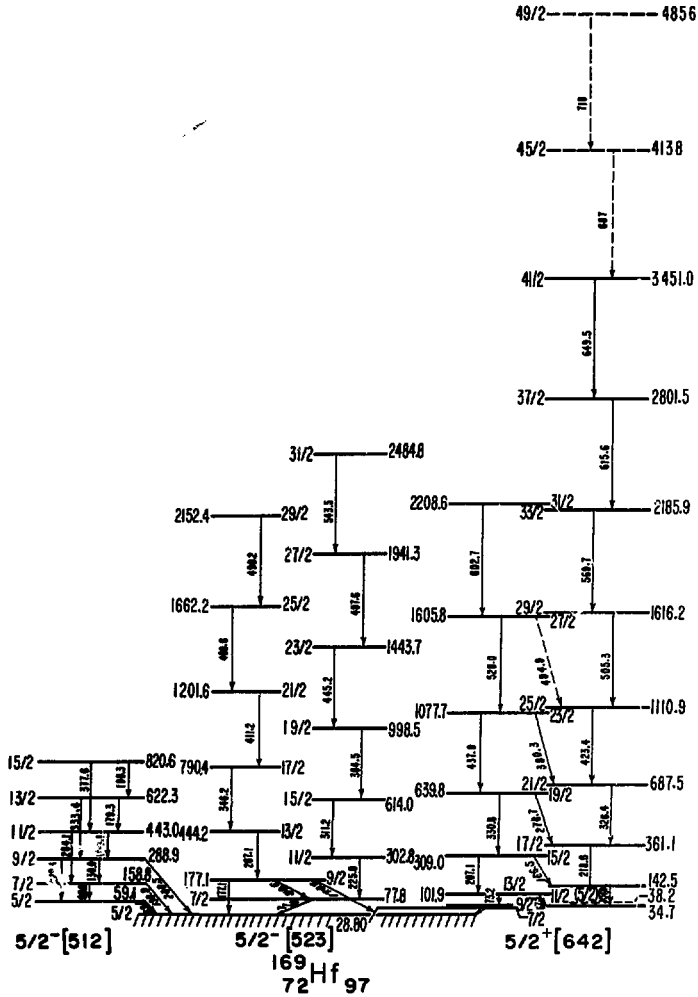

Fig. 2. ^{169}Hf scheme based on this study. (XBL 748-4004)

TABLE 1. Mixing amplitudes and g-factors in negative parity bands of ^{169}Hf.

Band	Initial spin	Mixing amplitudes, δ: From angular distribution	From branching ratio	Adopted value	$(g_K - g_R)_{exp}$	$(g_K - g_R)_{th}^{a}$
5/2⁻[523]	9/2		±0.70 ± 0.21[b]	-0.70 ± 0.21	-0.13 ± 0.04	-0.12
5/2⁻[512]	9/2	-4.0 to -0.05	±0.35 ± 0.10	-0.35 ± 0.10	-0.47 ± 0.15	-0.62
	11/2	-6.0 to -0.03	±0.22 ± 0.07	-0.22 ± 0.07	-0.66 ± 0.22	-0.62
	13/2	-10 to +0.02	±0.18 ± 0.05	-0.18 ± 0.05	-0.79 ± 0.26	-0.62

[a]Values of g_K extrapolated from Ref. 27, and g_R = +0.3 were used.
[b]From analysis of coincidence spectra.

Table 2, and in column 7 they are compared with the calculated[9] values. For that purpose, the value of 0.30 was used for g_R. The agreement appears to be good.

There is no abrupt change in moment-of-inertia at high spin in any of the bands measured here. This observation can be interpreted as favoring Stephens' and Simon's explanation[5] of backbending. If indeed the decoupled $i_{13/2}$ two-neutron band is responsible for the backbending in the ^{180}Hf, one would not expect the band in ^{169}Hf based on the $i_{13/2}$ neutron to backbend. On the contrary, the mixing with the three-neutron states of the same shell-model character would be strong, and the moment of inertia would change only gradually in the 5/2[642] band, as is observed here.

Footnotes and References

*A more complete report is published in Phys. Rev. C11, 1767 (1975).

**Present address: Brookhaven National Laboratory, Upton, New York 11973.

†Present address: Xerox Corporation, Rochester, New York.

‡Present address: Städt Rudolf-Virkchow Krankenhaus, Strahlungsabteilung, 1 Berlin 65.

§Present address: Heavy Ion Accelerator Laboratory, Yale University, New Haven, Connecticut 06520.

¶Present address: Lawrence Berkeley Laboratory, University of California, Berkeley, California 94720.

1. A. Johnson, H. Ryde, and J. Starkier, Phys. Letters 34B, 605 (1971).

2. A. Johnson, H. Ryde, and S. A. Hjorth, Nucl. Phys. A179, 753 (1972).

3. S. A. Hjorth, H. Ryde, K. A. Hageman, G. Løvhøiden, and J. C. Waddington, Nucl. Phys. A144, 513 (1970).

4. I. Rezanka, F. M. Bernthal, J. O. Rasmussen, R. Stokstad, I. Fraser, J. Greenberg, and D. A. Bromley, Nucl. Phys. A179, 51 (1972).

5. F. S. Stephens and R. S. Simon, Nucl. Phys. A183, 257 (1972).

6. F. S. Stephens, P. Kleinheinz, R. K. Sheline, and R. S. Simon, Nucl. Phys. A222, 235 (1974).

7. F. Boehm, G. Goldring, G. B. Hagemann, G. D. Symons, and A. Tveter, Phys. Letters 22, 627 (1966).

8. R. A. Sorenson, Rev. Mod. Phys. 45, 353 (1973).

9. I.-L. Lamm, Nucl. Phys. A125, 504 (1969).

HIGH-SPIN STATES IN ^{191,193,195}Au

P. O. Tjøm,* M. R. Maier,† D. Benson, Jr.,‡
F. S. Stephens and R. M. Diamond

A number of experimental studies have established the existence of decoupled bands in nuclei; these bands have been rather unambiguously identified in the neutron-deficient La and rare-earth nuclei, in the Hg region, and probably also in the Sr, Se, and Pd regions.[1] Here we will report on results from a study of the ^{191,193,195}Au nuclei.

In the Au nuclei a low-lying 11/2$^-$ state is known,[2] which at first might be thought to be the Ω = 11/2$^-$ Nilsson state, indicating a prolate deformation for these nuclei. Recent results show, however, that the nuclei in this mass region are oblate,[3-6] and if this is the case also for the Au nuclei, the Ω = 1/2 Nilsson orbital is closest to the Fermi surface and, within the context of the strong-coupling model, cannot explain the existence of the known low-lying 11/2$^-$ states. However, the model of a particle coupled to a rapidly-rotating non-spherical core[1,6] is consistent with the 11/2$^-$ assignment and with the observed band built on this state. The aim of the present study was to test insofar as possible the adequacy of such a rotation-aligned model for the negative-parity levels of this nucleus.

Several reactions have been used to populate states in ^{191,193,195}Au, i.e., Ir(α,xnγ)Au with 26, 29, and 42 MeV α beams and Os(^{7}Li,xnγ)Au with 50 and 58 MeV ^{7}Li beams. The targets were mounted on thin Al backings and were enriched in ^{191}Ir, ^{193}Ir, ^{190}Os and ^{192}Os. The Berkeley 88-Inch Cyclotron provided the alpha and ^{7}Li beams. The gamma-ray spectra were detected with one or two 8 cm^3 planar and one 30 cm^3 coaxial Ge(Li) detectors. The singles gamma-ray spectra were recorded both in-beam and off-beam, which make it possible to distinguish between prompt transitions and ones which are delayed by ≥ 5 ns. The angular anisotropies were measured with the detectors at 30° and 90° for the α reactions, and at 45° and 90° for the Li reactions. Gamma-gamma coincidence measurements were performed with both detectors at 90° relative to the beam direction.

The level schemes deduced for the ^{191,193,195}Au nucleus are shown in Fig. 1. The detailed experimental data are available in the published report of this work.[7] The favored bands in these Au nuclei are well established. Figure 2 shows the bands in comparison with the corresponding bands in doubly-even Pt and Hg nuclei. As seen from the figure, the 11/2$^-$ → 15/2$^-$ energy spacings are very close to the 0$^+$ → 2$^+$ energy spacing in the Hg isotopes, whereas the 0$^+$ → 2$^+$ energy spacing in the Pt isotopes are somewhat smaller. For the higher spins, the agreement between the energy spacings is also much better for Au and Hg than for Au and Pt. In the Pt isotopes, the number of empty levels available to the proton pairs is two rather than one, as it is for Hg and Au. This might be the reason for the greater similarity of the energy spacings in Au and Hg.

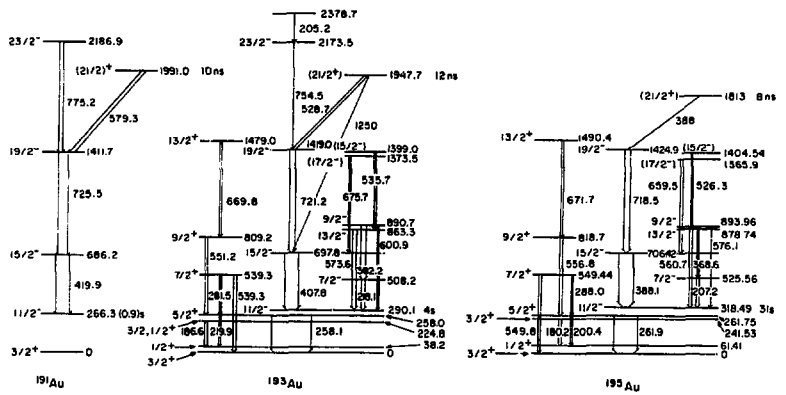

Fig. 1. The decay schemes for ^{191}Au, ^{193}Au, and ^{195}Au. The widths of the arrows indicate the relative intensities of the transitions following the (α,2nγ) reaction for ^{193}Au and ^{195}Au and the (Li,6n) reaction for ^{191}Au. (XBL 743-2493)

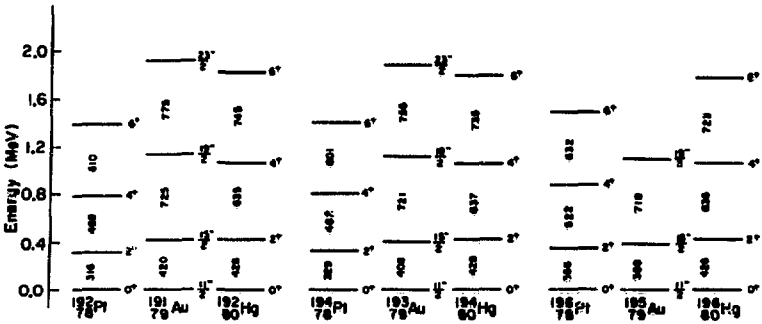

Fig. 2. The bands based on the 11/2⁻ state in the odd-mass Au nuclei compared to the ground-state bands in the adjacent Hg and Pt nuclei. (XBL 743-2491)

Apart from the decoupled band, levels having spins 7/2⁻, 9/2⁻, 13/2⁻, and 17/2⁻ are observed at excitation energies which do not differ more than 20 keV for ^{193}Au and ^{195}Au. From the study of the decay of ^{191}Hg, 7/2⁻, 9/2⁻, and 13/2⁻ levels are also observed in ^{191}Au at about the same excitation energy as in the other Au nuclei. Since these three Au nuclei are so similar, a comparison between the observed and calculated energy levels is only made for one case and this is shown for ^{195}Au in Fig. 3.

The calculation, similar to those previously made,[1] is based on a particle-plus-rotor model, using a perfect (rigid) rotor Hamiltonian for the core. Thus it does not include the possibility of asymmetric shapes, shape changes, vibrations, or large individual 2-qp components. All of these effects might be expected to occur in the Au region, so that the calculations in Fig. 3 should only be considered as a first approximation. The calculation has no parameters. The $\hbar^2/2\mathcal{I}$ and β values were derived from the average 2^+ energy in ^{194}Pt and ^{196}Hg according to expressions given in Ref. 1. This is about the same result one would get by basing these quantities on an average $\hbar^2/2\mathcal{I}$ value from the 2^+ and 4^+ states in ^{196}Hg.

Even with this relatively crude calculation the agreement between the experimental results and the calculation is rather convincing. The decoupled-band members (11/2, 15/2, and 19/2) reflect the core energies, and would be improved by using core spacings more realistic than those of the rigid rotor, as can be seen in Fig. 2. The 7/2 and 3/2 states are approximate members of this band, and this is the first time such low-spin states have been associated with a decoupled band. Their qualitative agreement with the calculation suggests that the rotation-aligned coupling scheme may apply to low-spin, as well as high-spin, states. The 13/2 and 17/2 states are members of the $\alpha = j - 1 = 9/2$ band (sometimes called the unfavored band), and the fact that this band lies considerably lower

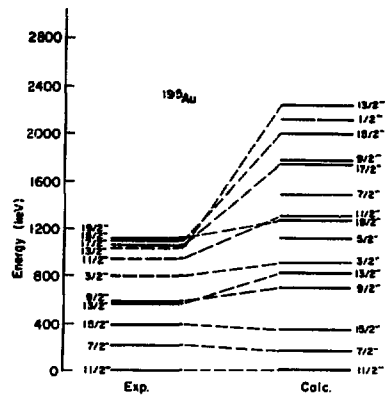

Fig. 3. A comparison of the observed negative-parity levels in ^{195}Au with those calculated from a particle-plus-symmetric-rotor model. The heavy, dashed lines indicate levels not observed in this work. (XBL 743-2492)

than calculated can be caused by non-axial shapes. Such shapes are likely to be important in the gold region as indicated by the low-lying second 2^+ states in the even-even Pt and Hg nuclei. The 9/2 state is an approximate member of this band. The second 11/2 and 15/2 states would belong to the $\alpha = 7/2$ band, and the second 13/2 state to the $\alpha = 5/2$ band. Figure 2 shows all the experimental negative-parity states below 1.25 MeV, and all the calculated ones below 2.3 MeV. The significant features of the comparison seem to us to be a) the

agreement in energy of the decoupled band and of the 6 or 8 lowest-energy states, and b) the occurrence, in general, of the correct states in the energy region shown. Calculations including shape asymmetry have been made,[8] and seem to provide a major improvement over the comparison in Fig. 3.

Two other kinds of levels are seen in these gold nuclei. Isomeric states with probable spins of $21/2^+$ are seen in all three nuclei, and probably result from the $h_{11/2}$ proton hole coupled with the well-known core 5^- states. While a plausible structure exists for these 5^- states, a number of unexplained features remain.[7] In addition, there are systematically occurring bands based on the low-lying positive-parity levels in these gold nuclei. These states are very likely based on the $s_{1/2}$ and $d_{3/2}$ orbitals, but the appropriate two-shell calculations are not available for comparison.

Footnotes and References

*On leave of absence from the Institute of Physics, University of Oslo, Norway.

†Present address: Physik Department E12, T. U. München, 8046 Garching Hochschulgelände, West Germany.

‡Present address: Department of Chemistry, Brookhaven National Laboratory, Upton, Long Island, N.Y. 11973.

1. F. S. Stephens, R. M. Diamond, J. R. Leigh, T. Kammuri, and K. Nakai, Phys. Rev. Letters 29, 438 (1972); see references in F. S. Stephens, Proceedings of the International Conference on Nuclear Physics, Munich, 1973, edited by J. de Boer and H. J. Mang, Vol. II, p. 367.

2. Nuclear Data Sheets 8, No. 5 (1972).

3. J. E. Glenn, R. J. Pryor, and J. X. Saladin, Phys. Rev. 188, 1905 (1969).

4. J. O. Newton, S. D. Cirilov, F. S. Stephens, and R. M. Diamond, Nucl. Phys. A148, 593 (1970).

5. K. Nakai, Phys. Letters 34B, 269 (1971).

6. F. S. Stephens, R. M. Diamond, D. Benson, Jr., and M. R. Maier, Phys. Rev. C7, 2163 (1973).

7. P. O. Tjøm, M. R. Maier, D. Benson, Jr., F. S. Stephens, and R. M. Diamond, Nucl. Phys. A231, 397 (1974).

8. J. Meyer ter Vehn, private communication (1974).

HIGH-SPIN EXCITATION MODES IN EVEN Hg NUCLEI*

D. Proetel,† R. M. Diamond, and F. S. Stephens

The mercury nuclei, with Z = 80, have only two protons less than the magic number 82 and lie in the transition region between the strongly deformed prolate rare-earth nuclei and the spherical lead nuclei. The heavier Hg isotopes are considered to be nearly spherical (vibrational) with small oblate deformation.[1] Negative-parity bands have been observed[2,3] in these nuclei starting at spin 5. The E2 transition probabilities[4,5] connecting the lowest members of these bands have strengths of about 30 s.p.u., indicating some collectivity. The negative parity, the fact that the lowest spin in the band is 5, and the occasionally very close spacing of the 5^- and 7^- members, however, suggest a single-particle nature for these states in which an $i_{13/2}$ neutron is coupled to a $p_{1/2}, p_{3/2}, f_{5/2}, \cdots$ neutron. In the very neutron-deficient mercury isotopes with A = 184 and 186, a change from small (probably) oblate deformation to large prolate deformation has been found[6] in the yrast states around spins 2 and 4, respectively.

The nuclei with A = 194, 196 and 198 have been studied following (α,xn); x = 3,4) reactions on enriched self-supporting platinum targets of approximately 5 mg/cm² thickness. The α beam was provided by the 88-Inch Cyclotron of the Lawrence Berkeley Laboratory. Excitation functions for the (α,3n) and (α,4n) reactions have been studied in the energy range between 34 and 50 MeV. The nucleus ^{188}Hg has been studied with the reactions ^{172}Yb(^{20}Ne,4n) at 104 MeV and ^{164}Dy(^{28}Si,4n) at 128, 135, and 144 MeV, and in the β decay of ^{188}Tl, which has been produced by bombarding ^{165}Ho with ^{28}Si and ^{159}Tb with ^{32}S. These heavy-ion beams were produced by the HILAC at the Lawrence Berkeley Laboratory. The time structure of the beams (pulse width ∿ 10 ns, distance between beam burst ∿ 150 ns at the cyclotron and ∿ 6 ms pulse width with a repetition rate of 36 sec^{-1} at the HILAC) were used to accumulate in-beam (IB) and off-beam (OB) spectra in order to determine isomeric transitions and short-lived activities. Approximate A_2 coefficients for the γ transitions were determined by measuring the anisotropy of the γ-ray emission at two angles in the reaction plane. Gamma-gamma coincidences were recorded between a coaxial and a planar Ge(Li) detector using conventional fast-slow coincidence techniques.

Low-lying levels in the three Hg isotopes with A = 194, 196 and 198 were known previously to the 6^+ and 7^- states,[2] and in ^{198}Hg to the 4^+ state.[7] Our experiments agree with all previous assignments, and add levels up to around spin 12 in both the positive- and the negative-parity bands. The decay schemes for the nuclei studied follow quite straightforwardly from the coincidence data, and are shown in Fig. 1. A great help in the case of ^{188}Hg is the γ spectrum from the β decay of ^{188}Tl which populates with decreasing intensity levels in ^{188}Hg up to the 8^+ state, and so determines the

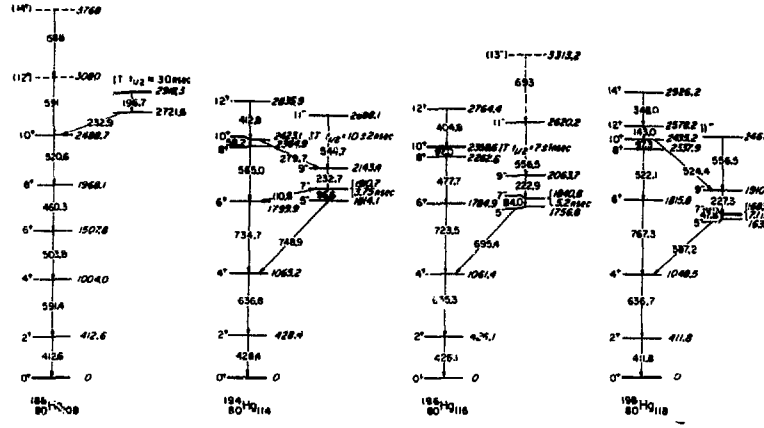

Fig. 1. The level and decay shcemes of the low-lying high-spin states in mercury nuclei with A = 188, 194, 196, and 198 as they follow from previous studies and the present work.
(XBL 743-2500)

sequence of these γ rays uniquely.

Information on the low-lying high-spin states is now available for almost all even-even and odd-A mercury nuclei from A = 184 through 200. The Hg nuclei with 190 ≤ A ≤ 200 are believed to be of oblate deformation, and the B(E2;$2^+ \rightarrow 0^+$) values indicate moderate collectivity in these nuclei, of a type historically called vibrational. However, the 10^+ states, with their small transition energies to the 8^+ states and their small B(E2;$10^+ \rightarrow 8^+$) values, seem to be mainly due to $(\pi i^2_{13/2})$ excitation. With the neutron-deficient Hg isotopes, A < 190, a very different transformation appears at higher spin. There is evidence for a change to large prolate deformation (small values of $\hbar^2/2\mathcal{J}$ and large B(E2) values) for states above a spin value which decreases with decreasing neutron number from 6^+ in ^{188}Hg to 2^+ in ^{184}Hg. Thus, the high-spin states of the yrast band show one type of behavior for A > 190, and a different type for A < 190. In either case, these nuclei with small deformation find it necessary to change the nature of their yrast band at higher spins, to either large prolate deformation (A < 190) or to a stretched pair of high-j particles (A > 190), in order to accommodate larger amounts of angular momentum more economically.

Finally, the negative-parity band built on the 5^- state shows both considerable collective quadrupole character (enhanced B(E2) values among the members) and a strong two-particle component, particularly of $[\nu i_{13/2}, \nu j]$. Some aspects of the levels (including having the natural parity members lowest and starting with 5^-) can be understood by shell-model calculations including residual interactions,[8] but the enhancement of the B(E2) values requires additional mixing of the states so obtained with each other, and with the collective motion of the core.[9]

Footnotes and References

*Condensation of LBL-2380.

†On leave from Sektion Physik, University of Munich.

1. D. Proetel, D. Benson, Jr., A. Gizon, J. Gizon, M. R. Maier, R. M. Diamond, and F. S. Stephens, Nucl. Phys. A226, 237 (1974).

2. R. F. Petry, R. A. Naumann, and J. S. Evans, Phys. Rev. 174, 1441 (1968).

3. J. C. Cunnane, R. Hochel, S. W. Yates, and P. J. Daly, Nucl. Phys. A190, 593 (1972); and S. W. Yates, J. C. Cunnane, R. Hochel and P. J. Daly, Preprint (1974).

4. H. Ton, G. H. Dulfer, J. Brasz, R. Kroondijk, and J. Blok, Nucl. Phys. A153, 129 (1970).

5. K. Krien, E. H. Spejewski, R. A. Naumann, and H. Hübel, Phys. Rev. C5, 1751 (1972).

6. D. Proetel, R. M. Diamond, P. Kienle, J. R. Leigh, K. H. Maier, and F. S. Stephens, Phys. Rev. Letters 31, 896 (1973); N. Rud, D. Ward, H. R. Andrews, R. L. Graham, and J. S. Geiger, Phys. Rev. Letters 31, 1421 (1973); and D. Protel, R. M. Diamond, and F. S. Stephens, Phys. Letters 48B, 102 (1974).

7. J. Burde, R. M. Diamond, and F. S. Stephens, Nucl. Phys. A92, 306 (1967).

8. The authors are indebted to Dr. M. Redlich for valuable discussions of this point.

9. Dr. Petr Vogel has made calculations embodying the essential features just described, and achieved qualitative agreement with experiment. Private communication, June, 1974.

DECOUPLED BANDS IN ODD-MASS MERCURY ISOTOPES*

D. Proetel,† D. Benson, Jr.,‡ A. Gizon,§ J. Gizon,§
M. R. Maier,¶ R. M. Diamond, and F. S. Stephens

The schemes of the low-lying high-spin states in mercury isotopes with A = 195, 197, and 199 have been studied by γ-ray spectroscopy following (α,xn) reactions on separated platinum targets. Excitation functions for the (α,3n) and (α,4n) reactions have been studied at seven different energies between 34 and 50 MeV, with α beams provided by the 88-Inch Cyclotron of the Lawrence Berkeley Laboratory. The time structure of the cyclotron beam (pulse width ∿ 10 nsec, distance between beam pulses ∿ 150 ns) was used to accumulate in-beam and off-beam spectra in order to determine isomeric transitions and short-lived activities. The anisotropies of the γ-ray angular distributions have been measured at 45° and 90° in the reaction plane. Conventional fast-slow coincidence techniques were used to record γ-γ coincidences between a planar and a coaxial Ge(Li) detector, both located at 90° with respect to the incident beam.

The decay schemes of the low-lying high-spin states in the three nuclei, ^{195,197,199}Hg are shown in Figs. 1-3. Although we are dealing with odd nuclei near the closed proton and neutron shells, the spectra of the odd-A Hg nuclei are relatively simple and remarkably similar to those of the adjacent even-even Hg nuclei. We observe a positive-parity band based on the $13/2^+$ state connected with stretched E2 transitions, and a presumably negative-parity band starting at $21/2^-$ which decays into the positive-parity band around spin 21/2. Figure 4 displays all available data on the 2^+, 4^+ and 6^+ states for even-even mercury nuclei and the $13/2^+$, $17/2^+$ and $21/2^+$ states in the odd-A mercury isotopes (solid bars) and the 5^- 7^-, and 9^- states

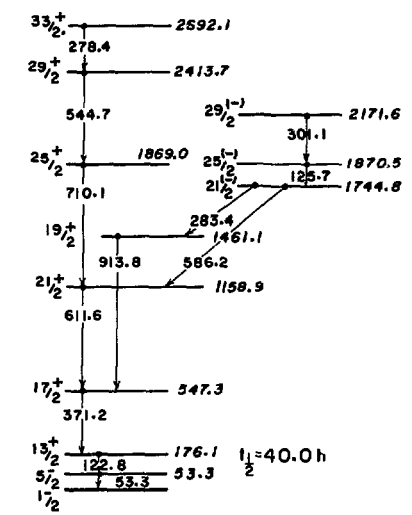

Fig. 1. Decay scheme for the low-lying high-spin states in ^{195}Hg. (XBL 741-2231)

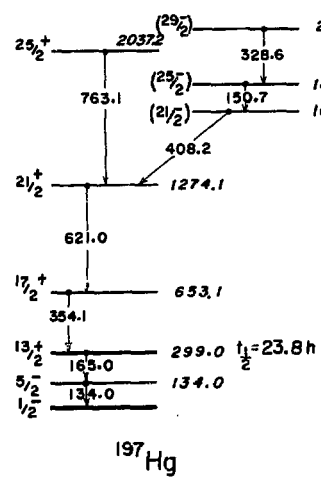

Fig. 2. Decay scheme for the low-lying high-spin states in ^{197}Hg. (XBL 741-2232)

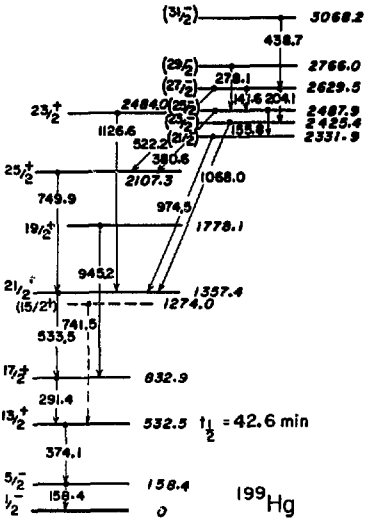

Fig. 3. Decay scheme for the low-lying high-spin states in ^{199}Hg. (XBL 741-2230)

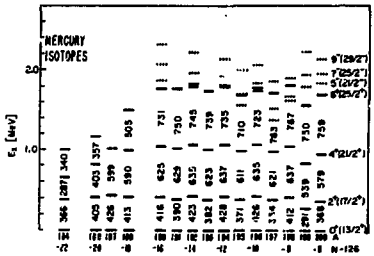

Fig. 4. Level systematics for the low-lying high-spin states in Hg isotopes with A = 184 through A = 200. Plotted are the 0^+, 2^+, 4^+, and 6^+ quasi-rotational states in the even-even and the $13/2^+$, $17/2^+$, $21/2^+$, and $25/2^+$ decoupled states in the odd-A nuclei (solid bars) as well as the 5^-, 7^-, and 9^- and $21/2^-$, $25/2^-$, and $29/2^-$ negative-parity states (dotted lines) in the even-even and odd-A nuclei, respectively. The spectra of the odd-A isotopes have been shifted in energy so that their isomeric $13/2^+$ states match up with the ground states in the even-even Hg isotopes. The numbers refer to the transition energies between the positive-parity states. The data on ^{191,192,193}Hg are from W. F. Davidson (private communication), the ones on ^{187}Hg are our own preliminary results. (XBL 741-2233)

together with the $21/2^{(-)}$, $25/2^{(-)}$ and $29/2^{(-)}$ states (broken bars) in the even-even and odd-A nuclei. (The spectra of the odd-A nuclei have been shifted so that the $13/2^+$ states match up with the 0^+ states in the even-even Hg nuclei.) A striking regularity is apparent in the 2^+, 4^+, and 6^+ states and the corresponding $13/2^+$, $17/2^+$ and $21/2^+$ states through a range of 14 neutron numbers. Clearly, decoupled bands are occurring in the odd-A Hg nuclei with spin sequences 13/2, 17/2 and 21/2 and energies very similar to the core energies in the even-even Hg isotopes. In the context of the rotation-alignment model[1,2] this implies oblate deformation for these nuclei, since for $\beta < 0$ the low Ω states of the $i_{13/2}$ subshell are close to the Fermi surface. For prolate deformation, one would expect a normal rotational band based on the $13/2^+$ state, with the usual spin sequence and energies approximately proportional to $I(I+1)$. Some of the unfavored states of the decoupled band ($\alpha = 11/2$) also seem to be seen, and their excitation energies follow qualitatively the predictions of the rotation-aligned coupling scheme. This provides additional evidence that this new coupling scheme may be a useful description for the low-lying high-spin states in these nuclei, and the large differences in energy between members of the multiplets show that weak-coupling schemes are invalid here. It appears that the strongly deformed (prolate) rare-earth region and the spherical lead region are connected by a transitional region with oblate deformation.

The observation of a probably negative-parity band in the odd-A mercury nuclei, starting at spin 21/2, strongly suggests that the excitation of a (decoupled) $i_{13/2}$ neutron hole plays a major role in the 5^-, 7^-, 9^-, ... bands recently discovered in the even-even mercury isotopes.

Footnotes and References

*Condensation of LBL-2349, see Nucl. Phys. A226, 237 (1974).

†On leave from: Sektion Physik der Universität München, 8046 Garching, West Germany.

‡Present address: Brookhaven National Laboratory, Upton, NY 11973.

§Present address: Institut des Sciences Nucleaires, BP 257, Grenoble 38044, France.

||Present address: Physik Department der TU München, 8046 Garching, West Germany.

1. J. R. Leigh, K. Nakai, K. H. Maier, F. Pühlhofer, F. S. Stephens, and R. M. Diamond, Nucl. Phys. A213, 1 (1973).

2. F. S. Stephens, Rev. Mod. Phys., in press.

LIFETIMES AND g-FACTORS IN DECOUPLED BANDS*

K. Nakai,† D. Proetel,‡ R. M. Diamond, and F. S. Stephens

Recently, a number of decoupled bands have been reported in odd-mass nuclei in various regions of the nuclear chart,[1] and an interpretation of these bands as examples of the rotation-aligned coupling scheme has been suggested.[2] If this interpretation is correct for nuclei in the "vibrational" regions, it indicates a greater importance of collective rotation than was previously thought to be likely in nuclei having such small deformations. Studies of the electromagnetic properties of these bands can be helpful in distinguishing among the possible coupling schemes, namely, weak, strong, and rotation-aligned.

The odd-mass Er isotopes were chosen for this first study because the lifetimes and the g-factors of the even-even Er nuclei are known,[3,4] and these are essential for comparison. Lifetimes of the $17/2\ (j+2)$ and $21/2\ (j+4)$ members of the decoupled bands in ^{157}Er and ^{159}Er have been measured using the recoil-distance Doppler-shift method. From the lifetimes determined for ^{157}Er, the g-factor of the $17/2^+$ state was calculated by analyzing time-integral PAD data taken during experiments to determine[4] g-factors in the even-even Er nuclei.

In the lifetime measurements, an ^{40}Ar beam from the Berkeley 88-Inch Cyclotron was used to bombard self-supporting targets of ^{122}Sn and ^{124}Sn about 850 μg/cm² thick. The beam energy was 171 MeV, near the maximum of the excitation functions for the (^{40}Ar,5n) reactions. Since some γ transitions of ^{158}Er were also seen in the spectra obtained, their lifetimes were determined for comparison with the previous results,[3] but the accuracy was poorer in these even-even measurements, because the beam energy was not optimized for the 4n reaction. The ratios, (unshifted intensity)/(unshifted + Doppler-shifted intensity), for the transitions of interest at each plunger distance were obtained and analyzed with a computer program that fits three cascading gamma transitions simultaneously, and allows for another cascade of three transitions to feed the group being determined. A plot of the experimental ratios vs plunger distance for ^{157}Er is shown in Fig. 1. The recoil velocity was determined to be $v/c = (2.10 \pm 0.02)\%$.

The B(E2) values obtained are compared with those in the neighboring even-even Er nuclei in Fig. 2. The B(E2) values in the odd-mass nuclei are considerably larger than the average values in the even-even nuclei. This indicates that the odd-mass states are not examples of weak coupling, as such a coupling scheme requires that these reduced transition probabilities be identical to those of the core, i.e., the neighboring even-even nuclei. However, both the rotation-aligned and the strong-

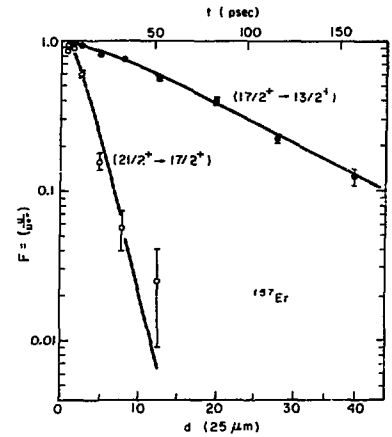

Fig. 1. The fraction of unshifted intensity, F, vs target-plunger distance for the $17/2 \rightarrow 13/2$ and $21/2 \rightarrow 17/2$ transitions of ^{157}Er. The distance is given in units of 25 μm, and a scale in psec is shown at the top. The lines are the computer fits to the data. (XBL 743-2672)

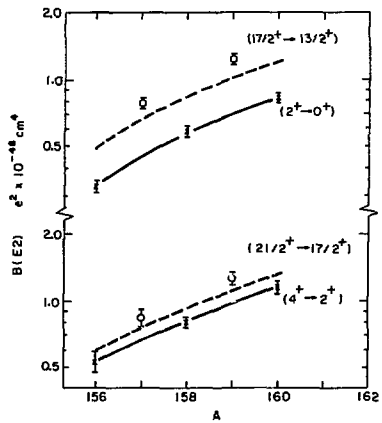

Fig. 2. Plots of B(E2) vs A. The solid curves correspond to weak-coupling (even-even) values, and the dashed curves to rotation-aligned ones. The crosses and circles correspond to measured values in even-even and odd-mass nuclei, respectively. (XBL 743-2671)

coupling schemes lead to larger B(E2) values, much closer to the observed ones.

To distinguish between these two possibilities, the results of an earlier time-integrated PAD measurement[4] of the g-factors in ^{156,158,160}Er, using the strong hyperfine field acting on the highly-charged ions recoiling into vacuum, was re-evaluated to also extract the g-factor of ^{157}Er. The result for the $17/2^+$ state of ^{157}Er is $|g| = 0.05 \pm 0.05$. This can be compared with the calculated values, using g_s(effective) = 0.6 g_s(free), g_R = 0.40, and g_ℓ = 0 for neutrons, weak coupling, -0.04; strong coupling, +0.18, +0.38, and +0.35 for K = 1/2, 3/2, and 5/2; and rotation-aligned, -0.02. So only the rotation-aligned wave functions give reasonable agreement for both types of measurement made here. The energy levels of these nuclei are also in best agreement with this scheme, though it is clearly only approximate, especially for ^{159}Er. These measurements are relatively easy to make, and can be applied rather generally to identify the type of coupling in particular nuclei. It will be interesting to make these measurements on other "decoupled" bands in regions of low deformation.

Footnotes and References

*Condensation of LBL-2389, see Phys. Rev. Lett. 32, 1380 (1974).

†Present address: Physics Department, University of Tokyo.

‡Present address: Physics Department, University of Munich.

1. F. S. Stephens, Proceedings of the International Conference on Nuclear Physics, Munich, August 1973, edited by J. de Boer and H. J. Mang (North Holland/American Elsevier, Amsterdam, 1973), p. 367, Vol. 2.

2. F. S. Stephens, R. M. Diamond, and S. G. Nilsson, Phys. Letters 44B, 429 (1973).

3. R. M. Diamond, F. S. Stephens, W. H. Kelly, and D. Ward, Phys. Rev. Letters 22, 546 (1949).

4. R. Nordhagen, G. Goldring, R. M. Diamond, K. Nakai, and F. S. Stephens, Nucl. Phys. A142, 577 (1970).

BACKBENDING AND ROTATION ALIGNMENT*

F. S. Stephens, P. Kleinheinz,† R. K. Sheline,‡ and R. S. Simon§

It is now clear that a rather sudden structural change occurs in the ground-state rotational band of a considerable number of rare-earth even nuclei at high angular momenta.[1,2] Early evidence for such a change came from the population patterns of such bands following (HI,xn) reactions,[3] but the conclusive step was the observation of irregularities in the rotational-energy spacings.[4] These irregularities are such that two or three rotational *transitions* in the region of I ∿ 12-20 become lower in energy with increasing I, whereas transitions above and below this I-region have the normal (rotational) monotonic increase in energy with I. If the moment-of-inertia, $\mathcal{I}$, is plotted against the square of the rotational frequency, ω^2, such a behavior produces a "backbending" curve (larger $\mathcal{I}$ but smaller values for ω^2). There has recently been considerable interest in determining the nature of the structural change responsible for this behavior. The purpose of this paper is to pursue the consequences of the "rotation-alignment" explanation for this change in order to see if it is consistent with relevant data in adjacent odd nuclei.

The underlying model for the effects we want to estimate here will be that suggested by Stephens and Simon[6] (SS). The basic proposal is that certain 2-quasiparticle states in even-even nuclei gain enough Coriolis energy by aligning their angular momenta with the rotation axis (rotation aligned) so that at high spin values they become the lowest states. At the beginning of the rare earth deformed region the 2-quasiparticle states involved would almost certainly be those from the $i_{13/2}$ shell. This alignment effect can be estimated using the SS model, however several parameters enter these calculations, which makes a unique prediction appear difficult. At this point it is useful to remember that most of the parameters entering into the 2-quasiparticle calculation for even nuclei also enter in much the same way into the 1-quasiparticle calculation of the lowest $i_{13/2}$ band in an odd nucleus. Such bands are observed throughout the rare-earth region and it seems clear that backbending in the even nuclei should be related to the characteristics of these bands in the adjacent odd nuclei if the rotation-alignment model is correct. We will make this comparison, first qualitatively for the whole rare-earth region, and then quantitatively for two pairs of nuclei.

If we look at the lowest $i_{13/2}$ band in an odd-neutron rare-earth nucleus one characteristic feature of the energies is the presence of a term whose sign alternates as I increases: this term has been called[7] the "signature" term. This alternation of energies is the beginning of the rotation-alignment process, and can be traced back to the Coriolis-induced amplitude of the Ω = 1/2 orbital in the wave function, and further, to its decoupling term. Thus, this signature term is related to the extent of alignment, though it is not a direct measure of it. Therefore, it would be of interest to compare the size of this term with the degree

of backbending in the adjacent even nuclei. In Fig. 1 we have plotted all the information on rotational levels of even nuclei in the rare-earth region from N ≈ 90 through Z ≈ 76. A figure similar in this respect has been given by Sorensen.[2] We have plotted in Fig. 2 the rotational levels of the lowest $i_{13/2}$ band in the odd-mass nuclei. The effects of the alternating energy term are apparent. The rotation-alignment model would imply some correlation between the size of the alternating energy term and backbending. Comparison of Figs. 1 and 2 suggests that this may well be the case, but a more quantitative comparison would be useful.

One of the effects that Coriolis mixing has on the levels of the lowest mixed band is a compression of the band; that is, an increase in the apparent moment of inertia. It is not difficult to arrive at a quantitative expression for the compression of the lowest $i_{13/2}$ band in the odd-neutron nuclei. If the band is decoupled (rotation aligned), then the I = 17/2 to 13/2 separation should be just the average I = 2 to 0 separation in the two adjacent even nuclei. Thus, the ratio, $6E(17/2 \to 13/2)/32E(2 \to 0)$, should be 6/32 = 0.188 if the band is decoupled. This ratio should be 1.00 if the band is not mixed at all. This "compression factor" for the odd nuclei has been included in Figs. 1 and 2, and we have drawn a rough contour line for a compression factor of 0.45. It is apparent that these numbers correlate rather closely with the size of the alternating energy term. Furthermore, the contour line approximately divides the backbending even nuclei from those that do not seem to backbend, though more data are badly needed in the lower right portions of Figs. 1 and 2. We find the correlation between compression factor and backbending, as indicated in Fig. 1, quite encouraging, and will now try to test these ideas by direct calculation.

The above discussion suggests that calculations of the type made by SS for the even nuclei should be first tested against the adjacent odd nuclei, and adjustments of the parameters be made, if necessary, in order to fit these odd nuclei. Thus, we start with an *a priori* estimate for the parameters, and an order for varying them until a satisfactory fit of each 1-quasiparticle band is achieved. Then this identical set is used for the 2-quasiparticle states in the adjacent even nuclei. Two sets of nuclei have been done: ^{161,162}Er in a backbending region, and ^{171,172}Hf in a non-backbending region. The details of the mathematical procedures are given in Ref. 5.

It seems possible to characterize the bands in the odd nuclei roughly by two features; a compression from the input $(\hbar^2/2\mathfrak{I})$, value and a magnitude for the energy oscillations. It is well known that both these quantities are too large if one does the Coriolis calculations with the *a priori*

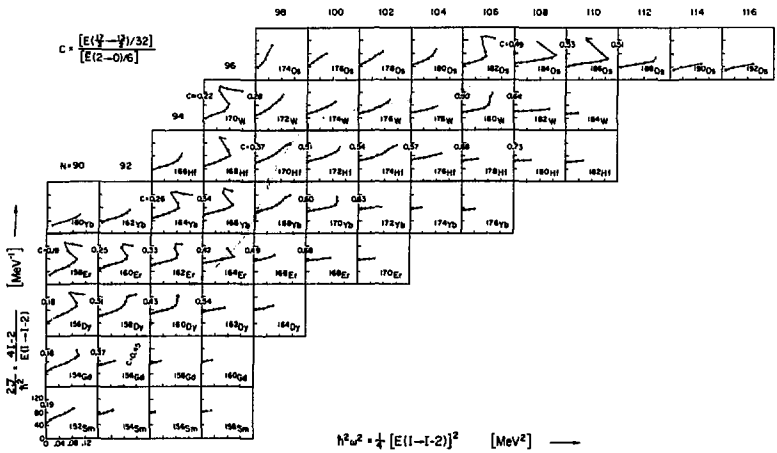

Fig. 1. Ground-band level energies in doubly-even rare earth nuclei. The plots give the moement-of-inertia $\mathfrak{I}$ versus the square of the rotational frequency ω^2, both quantities derived from the transition energy. In a few cases where more than one possible choice exists, the lowest-energy transition is always used. Tentatively assigned band members are indicated by an omitted dot. The compression factors C and the contour line for C = 0.45 are derived from the $17/2^+ \to 13/2^+$ level spacings observed in the odd-N nuclei (Fig. 2), and from the mean value $\bar{E}(2 \to 0)$ of the 2^+ energies in the adjacent even nuclei. The data references are given in Ref. 5.
(XBL 7312-6974)

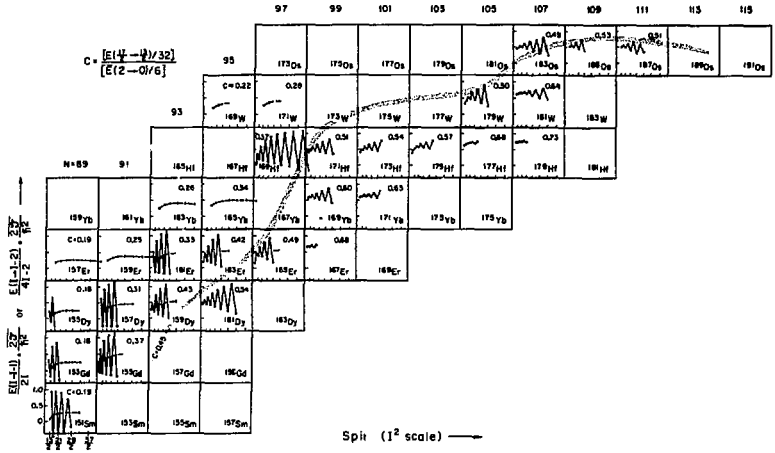

Fig. 2. The $i_{13/2}$ yrast level energies in odd-N rare-earth nuclei. The plots give the apparent $\hbar^2/2\mathcal{J}$ as derived from the transition energy (in units of the mean value of $\hbar^2/2\mathcal{J}$ in the neighboring doubly-even isotopes) *versus* the *square* of the spin of the upper level. In this plot an unperturbed rotational band gives a horizontal line (with the ordinate close to one), a band following the equation $E = AI(I+1) + BI^2(I+1)^2$ gives a straight line with the slope B. The compression factor C derived from the $17/2^+ \rightarrow 13/2^+$ transition energy is indicated for each nucleus. In several nuclei with N≤99 only one E2 cascade was observed, which establishes the energy-favored band members with I = j, j+2, ...; these points are connected by a broken line to indicate the absence of the alternate band members. (For illustrative purposes this is also done for several complete bands.) Dots are omitted for tentatively assigned band members. Reference to the original data is given in Ref. 5. (XBL 7312-6973)

parameters described. The Coriolis matrix elements must be reduced, and to do this we chose the form used by SS, which is decreasing f(U,V). We use:

$$f(U,V) = (U_1U_2 + V_1V_2)^n \quad \begin{cases} 1qp - 1qp \\ 2qp - 2qp \end{cases}, \quad (1)$$

where n is adjusted to fit the odd nucleus. Our procedure, therefore, was to fit the compression of the 1-quasiparticle band with n, and then fit the energy oscillation by varying ϵ_6 (the hexadecapole deformation). To obtain the fits shown in Fig. 3 for ^{161}Er and ^{171}Hf, only these two quantities had to be varied from the *a priori* input values (see Ref. 5). The results for the even nuclei are also shown in Fig. 3. They seem to us to be very encouraging, since there are no adjustable parameters in these cases. This kind of agreement between the calculated and observed behavior suggests both that the input parameters are behaving as we have proposed and that the basic ideas may be correct.

Both the qualitative survey and the detailed calculations we have made support the rotation-alignment explanation of back bending. It seems plausible that all the backbending in the rare-earth deformed region could be due to these $i_{13/2}$

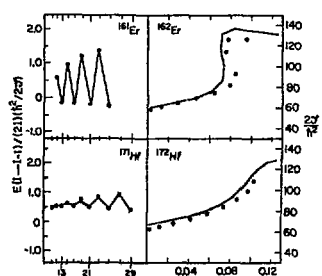

Fig. 3. A comparison of experimental (dots) and calculated (lines) properties of levels in the pairs of nuclei ^{161,162}Er and ^{171,172}Hf. The plots are of the same type as those in Figs. 1 and 2. The left side of the figure shows the fits obtained for the lowest $i_{13/2}$ band in the odd nucleus of each pair, and the right side shows the results for the doubly-even nucleus calculated using the same parameters. (XBL 736-3105)

2-quasiparticle states, though in the Os region it is quite possible that the $h_{9/2}$ proton shell is more important, or even that another process is involved.

Footnotes and References

*Condensation of LBL-1911.

†Present address: Los Alamos Scientific Laboratory, Los Alamos, NM 87544; supported by USAEC Contract AT-(40-1)2434 Florida State University.

‡Present address: Florida State University, Tallahassee, FL 32306.

§Present address: University of Munich.

1. A. Johnson and Z. Szymanski, Physics Reports 7C, 181 (1973).

2. R. A. Sorensen, Rev. Mod. Phys. 45, 353 (1973).

3. J. O. Newton, F. S. Stephens, R. M. Diamond, W. H. Kelly, and D. Ward, Nucl. Phys. A141, 631 (1970).

4. A. Johnson, H. Ryde, and J. Sztarkier, Phys. Letters 34B, 605 (1971).

5. Published in Nucl. Phys. A235, 235 (1974).

6. F. S. Stephens and R. S. Simon, Nucl. Phys. A183, 257 (1972).

7. A. Bohr and B. R. Mottelson, Nuclear Structure, (Benjamin, New York, Vol. 1, 1969), Vols. 2 and 3 to be published.

ANGULAR-MOMENTUM EFFECTS ON CONTINUUM GAMMA RAYS FOLLOWING HEAVY-ION REACTIONS*

P. O. Tjøm,† F. S. Stephens, R. M. Diamond, J. de Boer,‡ and W. E. Meyerhof§

The gamma-ray spectra following heavy-ion (HI, xn) reactions have two main features: discrete lines from heavily populated low-lying levels of the final product nuclei, and a continuum which presumably represents all the higher transitions, none of which has sufficient population to be resolved with present techniques. The present work, using p, ^{16}O, and ^{84}Kr projectiles, shows that large variations occur in the number of gamma rays in the continuum region depending mainly on the outgoing channel, and that this variation may be understood in terms of a simple model.

In our work it was essential to specify the reaction channel because many channels occur simultaneously in the reactions and a composite continuum of gamma rays would be difficult to interpret. Thus we measured the continuum in coincidence with known discrete transitions that specified particular channels, as was done by Sunyar.[1] For the discrete lines we used a 40 cc Ge(Li) detector at an angle of 90° to the incident beam direction and about 5 cm from the target. The continuum gamma-rays were detected in a 7.5 × 7.5 cm NaI crystal, 15 cm from the target, and at angles of 0°, 45°, and 90°. An absorber, consisting of 0.32 cm Pb and 0.32 cm Cu, was placed in front of the NaI detector, resulting in an overall detection efficiency that is very nearly constant for any gamma ray above 0.5 MeV. Since there are known discrete lines in the spectra of interest up to about 0.6 MeV, and since there are not likely to be many continuum gamma rays below this energy,[1] we took 0.6 MeV as the lower limit for measurements of the continuum.

Beams of 347 MeV ^{84}Kr provided by the Berkeley SuperHILAC were used to bombard targets of ^{62}Se (1.3 mg/cm^2) enriched to 97%. This produced the compound nucleus ^{166}Yb, and various discrete lines in the final nuclei $^{163}Yb(3n)$, $^{162}Yb(4n)$, and $^{161}Yb(5n)$ could be used as coincidence gates. A target of 99% enriched ^{150}Sm (1.4 mg/cm^2) was also bombarded at the Berkeley 88-Inch Cyclotron with 88 MeV ^{16}O to produce the same compound nucleus and products. Both targets were evaporated onto Pb backings about 25 μm thick, which stopped the beam and recoiling nuclei with no appreciable background. We also bombarded a ^{165}Ho target (220 mg/cm^2) with 25 MeV protons at the cyclotron in order to produce the compound nucleus ^{166}Er, and product nuclei $^{163}Er(3n)$ and $^{164}Er(2n)$. The average numbers of gamma rays, $\bar{N}_\gamma$, associated with each discrete line are given in Table 1.

The variations of $\bar{N}_\gamma$ in Table 1 are more than a factor of 10 overall, and nearly a factor of 3 in various $^{16}O + ^{150}Sm$ reactions alone. Such large variations are not likely to be caused simply by the difference in excitation energy resulting from different numbers of neutrons evaporated. This is shown by the $p + ^{165}Ho$ reaction, where a difference of one neutron causes a change of less than two gamma rays. It seems more likely that these large variations in $\bar{N}_\gamma$ result from angular-momentum effects. This can be tested by application of the simple sharp-cutoff model.[2] Using this model we could estimate the root-mean-square angular momentum, ℓ_{rms}, going into each reaction channel. To test whether the $\bar{N}_\gamma$ values from Table 1 correlate with these ℓ_{rms} values, we have plotted these quantities against each other in Fig. 1. For the $p + ^{165}Ho$ case, we took an average (weighted by the cross sections) for the 2n and 3n reactions of $\bar{N}_\gamma = 3$. It is quite apparent that a correlation

TABLE 1. Average number of continuum gamma-rays above 0.6 MeV.

E(keV)	$I_i \to I_f$	$^{84}Kr + ^{82}Se$ $\bar{N}_\gamma$	$^{16}O + ^{150}Sm$ $\bar{N}_\gamma$	E(keV)	$I_i \to I_f$	$p + ^{165}Ho$ $\bar{N}_\gamma$
	$^{162}Yb(4n)$				$^{163}Er(3n)$	
166	$2 \to 0$	11	8	127	$(13/2^+ \to 9/2^+)$	1.2
320	$4 \to 2$	14	10	165	$(15/2^+ \to 13/2^+)$	2.2
437	$6 \to 4$	12	9	171	$(13/2^- \to 11/2^-)$	2.3
521	$8 \to 6$	12	9	190	$9/2^- \to 5/7^-$	1.3
579	$10 \to 8$		9	213	$(15/2^+ \to 11/2^+)$	1.3
	$^{163}Yb(3n)$			218	$(17/2^+ \to 13/2^+)$	1.7
202	$17/2^+ \to 13/2^+$	20	14	236	$11/2^- \to 7/2^-$	1.6
345	$21/2^+ \to 17/2^+$	19	9		$^{164}Er(2n)$	
	$^{161}Yb(5n)$			208	$2 \to 0$	3.7
				314	$4 \to 2$	3.3
232	$17/2^+ \to 13/2^+$	10	5	410	$6 \to 4$	3.2

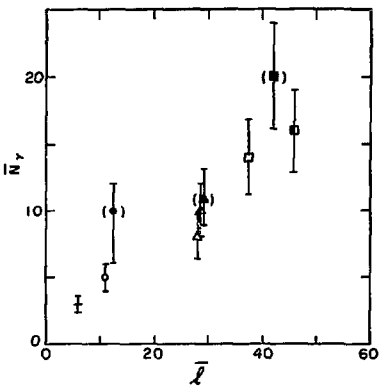

Fig. 1. The average number of continuum gamma rays (E_γ > 0.6 MeV) coincident with the lowest observed discrete transition ($2 \to 0$ or $17/2 \to 13/2$) vs the input ℓ_{rms} values. The cross is for the $^{165}Ho(p,xn\gamma)^{163,162}Er$ reaction and the circles, triangles and squares are for the 5n, 4n, and 3n reactions from $^{16}O + ^{150}Sm$ (open) and $^{84}K + ^{82}Se$ (solid). The parentheses on the $^{84}Kr + ^{82}Se$ data indicate that considerable uncertainty in the ℓ_{rms} values is introduced by the target thickness in this case. (XBL 746-3366)

exists in Fig. 1, although the relationship is not so good as to completely exclude the possibility of some other effects. For example, there is some suggestion that the $^{84}Kr + ^{82}Se$ reaction produces slightly more gamma rays than does the $^{16}O + ^{150}Sm$ reaction. Nevertheless, we conclude that most of the variation of $\bar{N}_\gamma$ is due to variation of the input angular momentum.

It is also interesting to consider whether there are enough gamma rays to carry of the rms ℓ-values. Figure 1 shows that an input angular momentum of 50ħ gives about 10 gamma rays. Since a multipolarity higher than E2 is not likely, this accounts for a maximum of 20ħ. However, the 4n reactions from both $^{16}O + ^{150}Sm$ and $^{84}Kr + ^{82}Se$ have at least five discrete gamma rays below 0.6 MeV which are known to carry off 10ħ. In the odd-mass cases (3n and 5n reactions) even more angular momentum is carried off by the discrete lines. Thus the $\bar{N}_\gamma$ values are consistent with the rms ℓ-values estimated from the sharp-cutoff model provided the continuum gamma rays are predominantly of the stretched ($I \to I-2$) E2 type. It is not yet clear whether the angular distributions are consistent with this requirement. The situation is somewhat relieved since the neutrons may carry off a few units of angular momentum, and there may be a few continuum gamma rays below 0.6 MeV.

Footnotes and References

*Condensed from Phys. Rev. Lett. 33, 593 (1974).

†On leave from the University of Oslo.

‡On leave from the University of Munich.

§On partial leave from Stanford University.

1. A. Sunyar, Proceedings of Heavy-Ion Summer Study, ORNL Report, CONF-720669, edited by S. T. Thornton (1972).

2. J. M. Blatt and V. F. Weisskopf, Theoretical Nuclear Physics (John Wiley & Sons, New York, 1952).

EVIDENCE FOR ASYMMETRIC SHAPES FROM HIGH-SPIN ODD-A SPECTRA*

J. Meyer ter Vehn,† F. S. Stephens, and R. M. Diamond

Rotational bands built on high-j states of unique parity in odd-A nuclei have a simple theoretical interpretation and can give rather detailed information about the nuclear shape and moments-of-inertia. In particular, this holds for nuclei with small deformations in the vicinity of closed shells in which the odd nucleon represents either a pure hole or a pure particle in the high-j orbital. It has been shown that a particle (hole) on a prolate (oblate) core tends to decouple from collective rotation by aligning its angular momentum to the rotation axis of the core.[1] This leads to decoupled bands with spin sequence j, j+2, j+4,... and energy spacings equal to those of the core. On the other hand, a hole (particle) in the prolate (oblate) core is strongly coupled and displays a normal rotational spectrum with spin sequence j, j+1, j+2,... .

The present calculation based on a single-j nucleon coupled to an asymmetric rotor shows that there is a continuous transition from decoupled to strongly coupled bands obtained by changing the shape asymmetry γ of the nucleus from prolate (γ = 0°) to oblate (γ = 60°) through a series of asymmetric shapes. In this transition, shown in Fig. 1 for a deformation $\beta \cdot A^{2/3} = 5$ and j = 11/2, many levels change energy rather sharply relative to others; for example, the "unfavored" states, I = 13/2, 17/2,... all drop considerably relative to the "favored" ones, I = 15/2, 19/2,... . This complex pattern of levels provides a severe test of the asymmetric rotor model, and one of the objectives is to apply this test to several nuclei in the Z = 80 region. It is also important to realize that some new types of information can be extracted from these odd-A spectra, provided the model is applicable. This is basically because the γ-dependence enters not only through the rotational Hamiltonian as in the even-even nuclei, but also through the Hamiltonian of the single particle. One can, therefore, easily differentiate between oblate and prolate shapes, and this determines γ in a range from 0 - 60° rather than only 0 - 30°. Furthermore, the level shifts, like the favored-unfavored one mentioned, are sensitive to the way the moments-of-inertia depend on shape, and thus can test the assumption of irrotational flow.

In Figs. 2 and 3, the calculation is compared with unique parity states in ^{187}Ir, ^{195}Au, and ^{197}Tl. The parameters β and γ are derived from the lowest excited states of adjacent even nuclei, also shown in the figures. None of the parameters is adjusted in the odd-A calculation. Compared with the calculation based on axially symmetric cores (γ = 0°,60°), the triaxial calculation leads to remarkably improved agreement with experiment, in particular concerning the position of unfavored

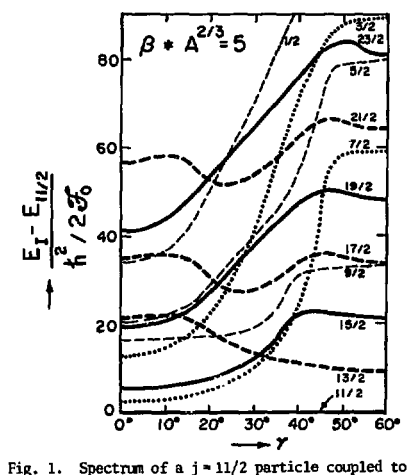

Fig. 1. Spectrum of a j = 11/2 particle coupled to an asymmetric rotor with all yrast levels I ≤ 23/2 as functions of γ. (XBL 743-2656)

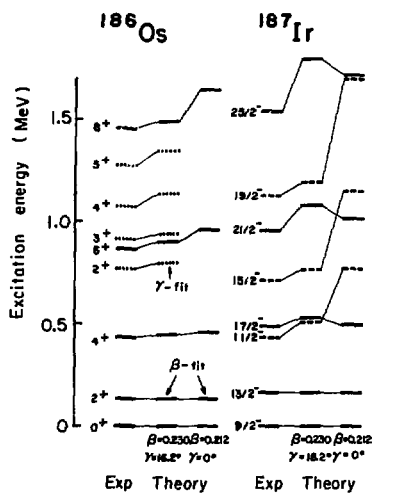

Fig. 2. Comparison of calculated and experimental spectra in ^{187}Ir with parameters β and γ fitted to ^{186}Os. (XBL 743-2655)

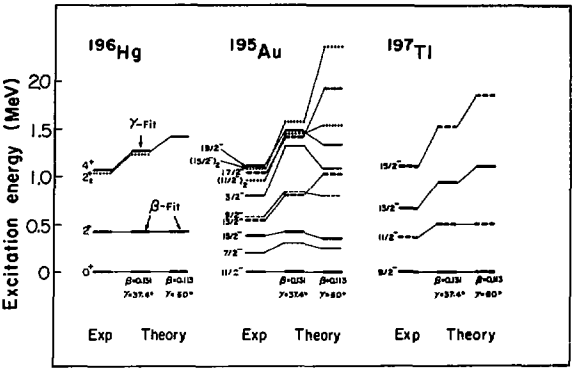

Fig. 3. Comparison of calculated and experimental spectra in ^{195}Au and ^{197}Tl with β and γ fitted to ^{196}Hg. (XBL 743-2653)

states. As seen for ^{195}Au, the second 11/2 and 15/2 states strongly support the assumption of shape asymmetry. It should be noticed that ^{195}Au and ^{197}Tl have the same core ^{196}Hg and the same parameters. For ^{195}Au a decoupled $h_{11/2}$-hole spectrum is obtained and for ^{197}Tl a strongly-coupled $h_{9/2}$-particle spectrum – in agreement with experiment. These results represent considerable evidence for triaxial deformations in these nuclei.

Footnotes and References

*Published in Phys. Rev. Lett. 32, 1383 (1974).

†On leave from Technische Universität München, Munich, West Germany.

1. F. S. Stephens, R. M. Diamond, J. R. Leigh, T. Kammuri, and K. Nakai, Phys. Rev. Lett. 29, 438 (1972).

INTERPRETATIONS OF LINE STRUCTURE IN DELAYED-NEUTRON SPECTRA

A. A. Shihab-Eldin, F. M. Nuh,* S. G. Prussin,* H. Franz,†
J.-V. Kratz,† K.-L. Kratz,† W. Rudolph,† and G. Herrmann

A dominant feature of all recently measured[1-4] high-resolution delayed neutron spectra (see Fig. 1) is prominent line structure with densities small compared to the expected level densities (e.g., the number of neutron lines for ^{85}As account for about 1% of the levels available through allowed β-decay.[5]) The line structure in ^{85}As and ^{135}Sb delayed-neutron spectra was shown[4] to account for the majority (≳ 60%) of the total neutron intensity. Statistical and possible systematic errors precluded a unique definition of the remaining intensity, although the presence of an underlying, continuous neutron distribution could not be ruled out. A second dominant feature of ^{85}As and ^{135}Sb spectra is the absence of appreciable neutron intensity above 1.6 MeV (^{85}As) and 2.0 MeV (^{135}Sb) even though larger ranges are possible for the neutron energies (large energy window, $(Q_\beta - B_n)$). Franz et al[4] demonstrated that this was mainly due to the dominance of neutron emission from intermediate levels to excited levels in the final residual nucleus. They also suggested that the extent of neutron decay of intermediate levels in ^{85}Se to more than one level in ^{84}Se is small.

Two possible interpretations of the line-structure in delayed-neutron spectra have been proposed so far. Shalev and Rudstam[2] suggested that for ^{87}Br and ^{137}I delayed-neutron spectra, the mean spacing of apparent neutron lines represents the true mean level spacing in the emitter nuclides (^{86}Kr and ^{136}Xe, respectively). They used these "experimental" mean level spacings to obtain a normalized set of level density parameters in both regions. These parameters were then used to calculate level densities for other neutron emitting nuclei (^{84}Se and ^{134}Te) that can then be used to predict the envelope of the energy distribution of delayed neutrons and the mean line spacing in their spectrum. They obtained fair agreement for ^{135}Sb

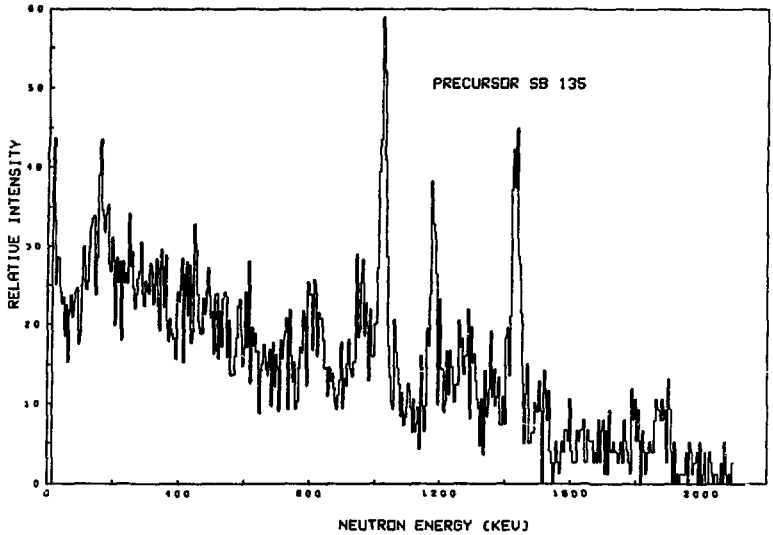

Fig. 1. Relative neutron intensity for ^{135}Sb, taken from Ref. 4. (XBL 755-1220)

and rather poor agreement for ^{85}As. The problem in their approach lies in the fact that the mean level spacing they derive from the line structure of the delayed-neutron spectrum is only an "effective" mean level spacing, (i.e., it is the mean level spacing for those states that are strongly fed by β-decay). Indeed for ^{85}As the peaks in the spectrum are much more widely spaced than can be accounted for by conventional spin-dependent level-density calculations with shell and pairing corrections[5] (the so-called "back-shifted" zero-order Fermi gas model). However, Huizenga and Moretto[6] have cautioned that for nuclei near closed shells, the magnitude and energy dependence of level densities, when calculated with a more realistic model (system of interacting fermions in shell-model states), can be quite different from the prediction of the previous model, especially at low excitation energies.

The second interpretation proposed was suggested simultaneously by Hansen[7] and by Karnaukhov et al[8] to explain the less pronounced line structure in delayed proton spectra. They interpreted the line structure as a statistical fluctuation resulting from the finite statistical distributions of parameters that determine the delayed-particle distribution (i.e., the beta strength function (S_β), delayed-particle width (Γ_p) and level density (ρ) in particle emitting nucleus). The application of this approach to the interpretation of line structure in measured delayed proton spectra seemed to be quite successful. The conditions for the applicability of this method are that $\Delta E >> D >> \Gamma$, where D is the mean level spacing ($1/\rho$) and ΔE is the particle spectrometer resolution.

In order to compare the line structure in the experimental delayed-neutron spectra with predictions of such a statistical model, we have followed the general method for non-overlapping levels discussed by Hansen[7] and Karnaukhov et al.[8] For neutron-emitting nuclides of interest, it was found that the condition $D>>\Gamma$ required for the validity of this method is not rigorously satisfied in the energy region of interest (above B_n) as can be seen from Table 1. However, this condition is sufficiently valid ($D \gtrsim 2\Gamma$) in the energy region of interest, that Erickson fluctuations are not significant.[9,10]

The expression for the variance in neutron intensities can be written out as:[7,8]

$$\mathrm{Var}\left(\frac{I_n(E)}{\bar{I}_n(E)}\right) = \frac{(2\ln)^{\frac{1}{2}} \cdot \pi^{\frac{1}{2}} \cdot (\Delta E)^{-\frac{1}{2}}}{\left[\sum_i \sum_f I_n^{if}(E_n)\right]^2} \times \sum_i \sum_f \left(I_n^{if}(E_n)\right)^2 \times D_i \cdot \alpha^{if}$$

TABLE 1. *Estimates of* $\left(\frac{\Gamma}{D}\right)$ *for daughters of the precursors* ^{87}Br *and* ^{85}As.

Precursor	Emitter B_n (MeV)	Emitter E_x (MeV)	Neutron energy E_n (MeV)	$J^\pi = 1/2^-$	Γ/D[a] $3/2^-$	$5/2^-$
^{87}Br	5.51	5.6	0.1	0.017	0.017	0.002
		6.5	0.9	0.0169	0.0169	0.004
^{85}As	4.1	4.2	0.1	0.016	0.016	0.024
		5.7	1.6	0.174	0.174	0.05
		6.3	2.2	0.317	0.317	0.239
		6.9	2.8	0.467	0.467	0.449

[a] D calculated using the level density formula of Gilbert and Cameron.[5] Γ calculated using the "Oxford Optical Code" by Wilmore.[12]

where

$$I_n(E_n) = \sum_i \sum_f \omega(I,I_i) \cdot I_\beta(E) \cdot \frac{\Gamma_n^{if}}{\Gamma^i} \quad ,$$

$$\alpha^{if} = 2 + 6\left[1 - 2\frac{\Gamma_n^{if}}{\Gamma^i} + \sum_{f'}\left(\frac{\Gamma_n^{if'}}{\Gamma^i}\right)^2\right] \quad ,$$

$$I_\beta(E) = S_\beta(E) \cdot f(Z,Q-E) \quad ,$$

ω is the beta decay partition function, $I_\beta(E)$ is the average beta intensity feeding levels at energy E in the intermediate nucleus, Γ_n^{if} is the partial neutron width from level i to level f in final nucleus, Γ^i is the total level (i) width, and f is the fermi function. Partial neutron widths were calculated using the expression

$$\Gamma_n^{if}(E_n) = \sum_\ell \frac{T_\ell(E_n)}{2\pi\rho(E_n)} \quad ,$$

where T_ℓ is the ℓ^{th} partial neutron transmission coefficient. These T_ℓ's were taken from optical-model calculations.[11,12] Level densities were calculated using the formulation of Gilbert and Cameron.[5]

The variance calculations were carried out for the ^{87}Br, ^{85}As, ^{135}Sb, and ^{137}I precursors. Neutron emission to four excited states in ^{84}Se and ^{134}Te and to two excited states in ^{136}Xe were included in the calculations. Only allowed β transitions were considered, and a constant beta intensity was assumed. This is not an unreasonable approximation, as it has been shown that the beta strength function for delayed-neutron precursors must have a reasonably strong energy dependence in the energy region of interest.[2,13,14] This yields a slowly varying beta intensity in the energy window $(Q - B_n)$, which can be approximated by a constant average value.

The calculated theoretical variance for all cases decreases smoothly with energy, with a small increase at an energy corresponding to the first excited state in the final daughter (if energetically accessible). In contrast, the experimental functions are relatively constant for ^{87}Br and ^{137}I, while showing a slowly increasing energy dependence for ^{85}As (Fig. 2) and a logarithmically

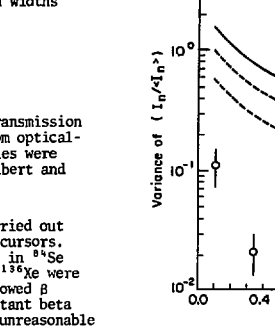

Fig. 2. Theoretical and experimental[18] fluctuations in the relative neutron intensity for the ^{85}As precursor. (XBL 756-3319)

increasing energy dependence for ^{135}Sb (Fig. 3). Thus there is general disagreement between the theoretical and experimental variances, especially for ^{85}As and ^{135}Sb. However, for ^{87}Br and ^{137}I, the large experimental variance uncertainties and the small energy window make the results of the comparison not as conclusive.

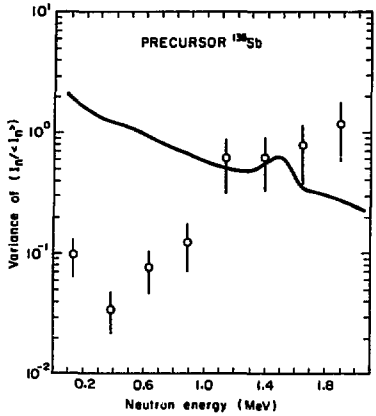

Fig. 3. Theoretical and experimental[18] fluctuations in the relative neutron intensity for the ^{135}Sb precursor. (XBL 756-3318)

The energy dependence of the calculated theoretical variance is directly proportional to the energy dependence of the average level density and therefore the increasing energy dependence of the experimental variance in ^{85}As and ^{135}Sb cannot be reconciled with predictions of the statistical model for non-overlapping levels. However, a combination of a decrease as a function of energy in the effective number of channels available for neutron emission and a breakdown of the condition $D \geq 2\Gamma$ (thus bringing in Ericson fluctuations) might explain such a behavior. The present calculations do not support this contention, though we cannot rule out this possibility completely and it is worthy of further investigation. The magnitude of the fluctuations was found to be strongly dependent upon the level density and only weakly dependent upon variations in the partial neutron width (as a result of variations in optical model parameters) and γ-decay width (which was held constant)[15].

We conclude from these comparisons and the experimental data that the β-strength function for levels in the energy range 5 - 8 MeV in the emitter nuclides ^{85}Se and ^{135}Te must possess strong local resonances not accounted for in the simple statistical model. Unless large, local fluctuations in the level density occur that are not contained in the normal level density formulations, the data indicate high selectivity in β decay and in the subsequent neutron emission to levels in the final nucleus, as evidenced by the lack of high-energy neutrons in ^{85}As and ^{135}Sb spectra.

These observations might be explained in terms of particle-hole structures involving the $d_{5/2}$ or $g_{9/2}$ proton orbitals. The last two neutrons in ^{85}As occupy the $d_{5/2}$ orbital just beyond the closed shell N = 50. A crude estimate locates the energy of the two-particle, one-hole configuration $[\pi(d_{5/2})^1(f_{5/2})^{-1};\nu(d_{5/2})^1]$ at 6 - 7 MeV in ^{85}Se, and the more complex structure resulting from decay of a $g_{9/2}$ neutron should lie within several MeV of this energy. It is possible that the selectivity in β decay is probing that part of the particle-hole structure in ^{85}Se contained in the antianalog state (AIAS) orthogonal to the analog state (IAS) of the ^{85}As ground state. Using the value of 110 MeV for the Lane potential,[16] the AIAS is calculated to lie near 6.3 MeV in ^{85}Se and should have its strength spread by strong coupling to core polarization states.[17] Since the strength of Gamov-Teller β decay to the AIAS is proportional to that of the $\Delta T = 1$, M1 γ-transition between the IAS and AIAS, this correlation may possibly serve as the basis for interpretation of the structure in the delayed-neutron spectrum from ^{85}As.

Finally, the present calculations depend upon the validity of many assumptions and approximations that were made to simplify the calculations. These need to be further investigated in detail. We are currently investigating the effect on the variance calculations of explicitly including a beta strength function proportional to level density, and calculating level densities using the more realistic model of interacting fermions in shell-model states.

Footnotes and References

*Department of Nuclear Engineering, University of California, Berkeley, California 94720.

†Institut für Kernchemie der Universität Mainz, D-65 Mainz, Germany.

1. S. Shalev and G. Rudstam, Phys. Rev. Lett. 28, 687 (1972).

2. S. Shalev and G. Rudstam, Nucl. Phys. A230, 153 (1974).

3. H. Franz, G. Herrmann, J.-V. Kratz, and K.-L. Kratz, J. Physique 33, C5, 31 (1972).

4. H. Franz, J.-V. Kratz, K.-L. Kratz, W. Rudolph, G. Herrmann, F. M. Nuh, S. G. Prussin, and A. A. Shihab-Eldin, Phys. Rev. Lett. 33, 859 (1974).

5. A. Gilbert and A. G. W. Cameron, Can. J. Phys. 43, 1446 (1965).

6. J. R. Huizenga and L. G. Moretto, Ann. Rev. Nucl. Sci. 22, 427 (1972).

7. P. G. Hansen, Adv. Nucl. Phys. 7, 159 (1973).

8. V. A. Karnaukhov, D. D. Bogdanov, and L. A. Petrov, Nucl. Phys. A206, 583 (1973).

9. M. G. Braga Marcazzan and L. M. Colli, Prog. Nucl. Phys. 11, 145 (1970).

10. P. J. Dallimore and I. Hall, Nucl. Phys. 88, 88 (1966).

11. N. Glendenning, "OPTIC Code", private communication (1965).

12. D. Wilmore, "Oxford Optical Programme", private communication by F. Hasan (1973).

13. A. C. Pappas and T. Sverdrup, Nucl. Phys. A188, 48 (1972).

14. K. Takahashi, Prog. Theor. Phys. 47, 1500 (1972).

15. A. G. W. Cameron, Can. J. Phys. 34, 666 (1956).

16. A. M. Lane, Nucl. Phys. 35, 676 (1962).

17. G. Vourvopoulos and J. D. Fox, Phys. Rev. 177, 1558 (1969).

18. F. M. Nuh, Ph.D. Thesis, Nuclear Engineering Department, University of California, Berkeley (1975).

MASS YIELD DISTRIBUTIONS IN THE REACTION OF ^{84}Kr IONS WITH ^{238}U*

J. V. Kratz,† A. E. Norris,‡ and G. T. Seaborg

Thick uranium targets were bombarded at the superheavy ion linear accelerator with 605 MeV ^{84}Kr ions, dissolved shortly after the end of bombardment, and separated chemically into 7 fractions[1] that were assayed for α-particle and γ-ray activities. We have measured cross sections for 129 isotopes. Through an interlaboratory collaboration a lanthanide-actinide fraction from an intense 24-h bombardment was radiochemically analyzed by the Los Alamos Scientific Laboratory nuclear chemistry group, which resulted in yield information on 27 additional nuclides.[2] The independent and cumulative yields are plotted versus mass number in Fig. 1(a). A detailed listing of the data and a description of their analysis will be given elsewhere.[4] The apparent scatter in the data in Fig. 1(a) occurs because independent yields, and even many of the cumulative yields, represent only a fraction of the total mass yields. Figure 1(b) is a contour map of the independent yields in a Z - A plane, indicating yield locations relative to the stability line. The pronounced structure revealed by the isopleths in the figure indicate that several yield distributions with different charge and mass dispersions, hence different origins, are superimposed on each other. To calculate the final mass yields, we integrated, at each mass number the Gaussian charge dispersion curves that were fitted to the data.[4] The final results are shown in Fig. 1(c).

Component A is determined by the yields of heavy-rare-earth nuclides and by the yields of very neutron-deficient Mo, Tc, Ag, In, Sn, Sb, I, and Cs isotopes. This component shows the expected characteristics of the binary fission product distribution originating from the fission of a composite nucleus. For component B, the heavy-mass branch is defined by the cumulative yields of neutron-rich nuclides peaking at A≈140. Figure 1(b) shows how distinctly the neutron-excess yields are separated from those of component A in this mass region. Guided by our results from the reaction ^{40}Ar on ^{238}U, where a low-energy fission of transfer products near ^{238}U was observed,[5] we assign this component to a double-humped low-energy fission product distribution. The light branch of this distribution was obtained by reflecting the well-defined shape of the heavy one, and its mass location was deduced from the cumulative yield balances for the isotopes ^{112}Pd, ^{111}Ag, and ^{107}Rh. From the observed charge distribution and the peak-to-valley ratio, we estimate an excitation energy of the fissioning nuclei of ~ 15 MeV. We find a value of 200 mb for the cross section of this transfer-induced fission as represented by component B. There should be a corresponding reduction in the heavy-rabbit-ear (component F) cross section as compared to its complementary light-rabbit-ear (component E) cross section; our measurements do show that component F has a cross section about 200 mb (actually 280 mb) smaller than component E.

After subtraction of contribution B from the yield data in the mass range $67 \leq A \leq 140$, we are left with yields that can be resolved into two Gaussian distributions [components C and D in Fig. 1(c)], peaking around A = 85 and A = 112. Distribution C [full width at half-maximum (FWHM) ≈ 20 mass units] is probably identical with the "quasi-Kr" events observed in Refs. 6 and 7. Apparently, the complementary "quasi-U" distribution is missing. Because much kinetic energy in the deep inelastic interaction of ^{84}Kr with the target nucleus goes into excitation, one would expect a high-energy cascade fission of the "quasi-U" nuclei leading to a symmetric fission product distribution centered slightly below A = 119. Actually, we do observe such a distribution (component D). From a mass and charge balance for the complete process – "quasi-fission" followed by a cascade fission of the "quasi-U" (which process might be termed "quasi-ternary-fission") – one can conclude that in the most probable interactions 13 neutrons and no protons are evaporated. The yield of component D is 840 ± 120 mb (200%), indicating that 67 - 100% of the "quasi-U" nuclei undergo fission. The shape and width of the distribution suggest that the average excitation energy of the "quasi-U" must have been ≥ 45 MeV.

The excess yields around A = 135 (component G)

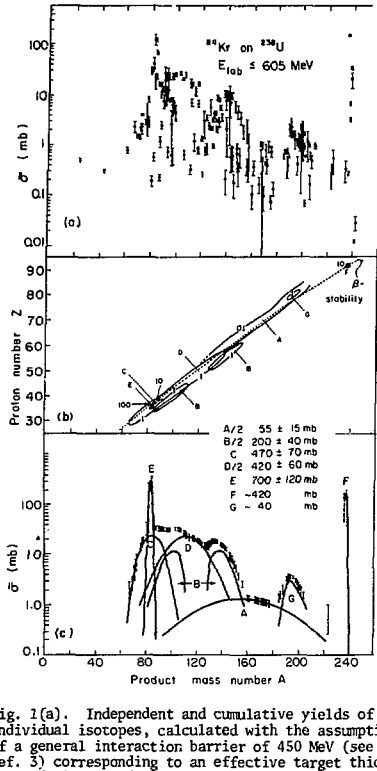

Fig. 1(a). Independent and cumulative yields of individual isotopes, calculated with the assumption of a general interaction barrier of 450 MeV (see Ref. 3) corresponding to an effective target thickness of 11.6 mg U/cm^2.

(b). Contour lines for equal independent yields in mb.

(c). Total integrated mass yields (upper and lower limits are indicated at those mass numbers for which experimental data were obtained) and their decomposition into individual components: (A) complete fusion-fission, (B) transfer-induced fission, (C) quasi-Kr, (D) cascade fission of the quasi-U, (E) and (F) transfer reactions ("rabbit ears"), (G) yields of their own origin.

(XBL 746-3449)

are unexplained. Suggested explanations such as target contamination and feeding of these mass chains by α-decay from higher masses can be excluded. We have also considered whether this peak might be a surviving nonfissionable tail (due to high fission barriers) at the light-mass-number end of the fissioning "quasi-U" distribution of nuclei. The primary "quasi-U" distribution (FWHM ≈ 20 mass units) could hardly extend into a mass region ~ 30 mass units below the target mass while still yielding cross sections of a few millibarns. Attempts to force a considerably broader complementary distribution through the mass yields around A = 185 resulted in an unreasonable imbalance in cross section for the quasi-ternary-fission process. We conclude, then, that the excess yield around A = 195, which we refer to as the "goldfinger", more likely originates from a hitherto unobserved reaction channel.

The paucity of data points between peaks F and G is due to the experimental difficulty of measuring the small yields of the predominantly short-lived isotopes in this region using radiochemical techniques.

As a consequence of the interpretation presented here, the total reaction cross section is the sum of the production cross sections for components A/2, C, E, and G: 1265 ± 205 mb. The mean geometrical cross section in the energy interval 450 to 605 MeV (lab) can be estimated as

$$\sigma_R = \pi R^2 \frac{\int_B^E (1 - B/E)dE}{E - B} = 1130 \text{ mb},$$

where B = 450 MeV,[3] E = 605 MeV, and R = 16.0 fm.

To conclude, we wish to point out that our analysis of the total mass yield distribution, and its decomposition into the components indicated in Fig. 1, is consistent with the results obtained for ^{84}Kr on ^{209}Bi in the kinematic coincidence experiments.[6,7] Our data confirm the assumption[6,7] that the quasi-Kr distribution is centered close to the projectile mass. It appears that > 92% of the Kr interactions with U in the investigated energy interval feed inelastic and deep inelastic reaction channels where only little mass transfer occurs. It is only in very few collisions (~ 4%) that a composite nucleus is formed.

Footnotes and References

*Condensed from LBL-2947, published in Phys. Rev. Letters 33, 502 (1974).

†On leave from Institut für Kernchemie, Universität Mainz, with a fellowship from Gesellschaft für Schwerionenforschung GSI, Darmstadt, Germany.

‡Los Alamos Scientific Laboratory, University of California, Los Alamos, New Mexico 87544.

1. J. V. Kratz, J. O. Liljenzin, and G. T. Seaborg, Inorg. Nucl. Chem. Lett. 10, 951 (1974).

2. B. P. Bayhurst, J. H. Cappis, W. R. Daniels, D. C. Hoffman, F. O. Lawrence, C. J. Orth, R. J. Prestwood, H. L. Smith, and Y. Wolfsberg, unpublished.

3. M. Lefort, C. Ngô, J. Péter, and B. Tamain, Nucl. Phys. A197, 485 (1972).

4. J. V. Kratz, A. E. Norris, and G. T. Seaborg, to be published.

5. J. V. Kratz, J. O. Liljenzin, A. E. Norris, I. Binder, and G. T. Seaborg, in Proceedings of the International Conference on Reactions Between Complex Nuclei, Nashville, Tennessee, 1974, edited by R. L. Robinson, F. K. McGowan, J. B. Ball, and J. H. Hamilton (North-Holland, Amsterdam, 1974), Vol. 1, p. 88.

6. F. Hanappe, M. Lefort, C. Ngô, J. Péter, and B. Tamain, Phys. Rev. Lett. 32, 738 (1974), and references therein.

7. J. Huizenga, K. Wolf, J. P. Unik, V. E. Viola, J. Birkelund, and H. Freiesleben, Phys. Rev. Lett. 33, 1105 (1974).

TRANSFER PRODUCTS RESULTING FROM THE HEAVY ION REACTION OF ^{40}Ar WITH ^{197}Au

I. Binder, R. J. Otto, M. M. Fowler, and D. Lee

As part of the on-going radiochemical study of heavy-ion reaction mechanisms,[1] the reaction of ^{40}Ar and ^{197}Au has been used to look at transfer products in the neighborhood of the target nuclide. This region is not readily accessible to particle identification techniques, and this radiochemical study will complement work already done[2] in studying products in the vicinity of the projectile. Precise isotopic distribution curves permitted by the sensitive radiochemical methods will aid in the calculation of cross sections in multi-element, mass distribution experiments. The gamma-ray analysis method used here permits resolution of nuclear isomers and determination of isomer ratios and some angular momentum effects. The yields in proximity to the target, ^{197}Au, will not be distorted by low-energy fission reactions found with a ^{238}U target.[3]

In this experiment gold foils (50 mg/cm^2) are bombarded with 340-MeV ^{40}Ar projectiles produced at the Berkeley SuperHILAC. Essentially all the reaction transfer products are caught within the foil. The foil is dissolved, and chemical separation schemes have been developed to quickly isolate Os, Au, Hg and Pb samples free of most interfering contaminants. Gamma-ray spectra are recorded for each of the samples, and the product nuclides are identified using half-life, gamma-ray energy and chemical information.[4]

The resulting plots of relative yield versus mass number (Fig. 1) appear to be rather Gaussian despite the interference of feeding from radioactive precursors to some of the yields. The center of the distribution is in the region of neutron-deficient isotopes, suggesting that substantial neutron evaporation has occurred. Given two possible isomeric states, the high-spin state (e.g., ^{199m}Hg, ^{183g}Os, ^{204m}Pb) is the favored product.

The gold isotopic distribution (Fig. 2) provides a special case. Two Gaussian curves seem to be superimposed. The broader, lower curve containing points for the high-spin isomers better corresponds to the curves obtained for the other elements.

Looking at Fig. 2, the narrow-A curve containing low-spin states of gold probably represents the "rabbit ears" of earlier studies[5] in which a few nucleons are transferred without much internal excitation. The wider, high-spin, neutron deficient curves seen for all the elements thus far investigated are likely due to deep-inelastic reactions in which more nucleons can be exchanged and there is a greater degree of internal excitation.

In examining the gamma rays from the various samples, some radiations could not be identified with any known nuclide. Interestingly, several gamma rays from the gold fraction seem to have similar half-lives (see Table 1). It is possible these originate from previously undiscovered isomers of gold. Heavy-ion reactions, in which much angular momentum can be brought in by the

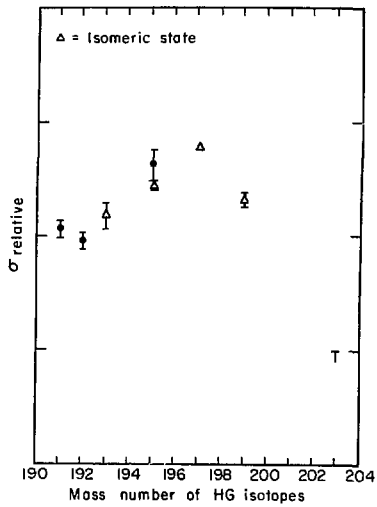

Fig. 1. Relative yields of Hg isotopes plotted vs mass number. (XBL 756-3321)

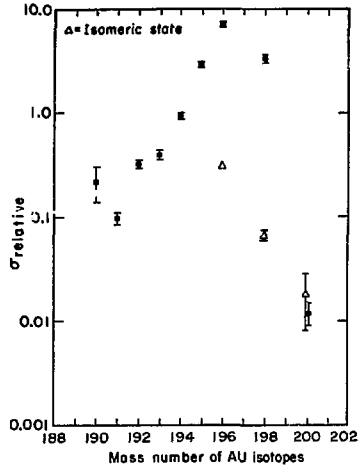

Fig. 2. Relative yields of Au isotopes plotted vs mass number. (XBL 756-3322)

projectile, may provide an important method for synthesizing high-spin states. This is worthy of further study.

TABLE 1. Energy and estimated $T_{1/2}$ for some unidentified activities.

E(keV)	$T_{1/2}$
158.7	56 days
211.7	60 days
499.5	5.2 hr
635.3	6.8 hr
1158.2	7.1 hr
1309.6	5.5 hr
1407.4	5.7 hr
1519.7	6.0 hr
1782.1	6.3 hr
1934.7	6.5 hr

References

1. R. J. Otto, M. M. Fowler, D. Lee, I. Binder, G. T. Seaborg, "Radiochemical Mass Yield Distribution Studies in the Reaction ^{40}Ar with ^{238}U and ^{209}Bi and 25.2 GeV ^{12}C with ^{238}U", in Section 1 of this Annual Report.

2. A. G. Artukh, G. F. Gridnev, V. L. Mikheev, V. V. Volkov, J. Wilczynski, Nucl. Phys. A215, 91 (1973); S. G. Thompson et al., LBL-2940.

3. J. V. Kratz, A. E. Norris, and G. T. Seaborg, Phys. Rev. Lett. 33, 502 (1974); "Mass-Yield Distributions in the Reaction of ^{84}Kr Ions with ^{238}U", in Section I of this Annual Report.

4. M. M. Fowler, D. Lee, R. J. Otto and I. Binder, "Computer Aided Analysis of Gamma-Ray Spectra", in Section IV of this Annual Report.

RECOIL RANGE STUDIES FROM REACTIONS OF ^{40}Ar WITH ^{209}Bi AND ^{232}Th

R. J. Otto, T. Raunemaa, M. M. Fowler, K. Williams, and G. T. Seaborg

Recoil range studies are a well-known and useful method of studying reaction mechanisms.[1] The stacked foil method inherently yields results that represent partial integrals of the energy and angular distributions of the reaction products. These results must then be fit with a postulated reaction model. Small and sometimes not so small differences seen with kinematic studies are lost; however, the important advantage of recoil range studies is that they can be used in conjunction with radiochemical methods.

A series of stacked recoil foil experiments were carried out at the SuperHILAC facility with 288-MeV ^{40}Ar ions on thin ^{232}Th targets and with 300-MeV ^{40}Ar ions on thin ^{209}Bi targets. The target geometry for the ^{40}Ar + ^{209}Bi experiments is shown in Fig. 1. The target geometry for the ^{40}Ar + ^{232}Th *experiments was the same as shown in* Fig. 1 except that the Th targets consisted of 0.2 to 0.7 mg/cm^2 of electrodeposited ThO_2 on a 0.075 mil Ni backing. Following the first Th experiment

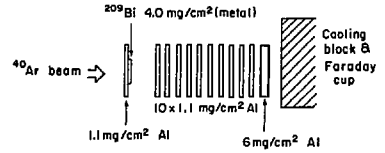

Fig. 1. Target geometry for ^{40}Ar + ^{209}Bi experiments. (XBL 756-3326)

the ThO_2 target and Ni backing were dissolved and chemical separations were done yielding a Ra,Ac fraction, a Th,Pa,U,Np fraction and a Pb,Bi,Po fraction. ^{223}Ra, ^{224}Ra, ^{225}Ra-^{225}Ac, and ^{226}Ac were found in the Ra,Ac sample based on the identification of the alpha particle energies associated with each decay chain. Peaks in the Th,Pa,U,Np fraction were seen with alpha energies corresponding to ^{226}Th and its alpha decay chain. The Pb,Bi, Po fraction contained a small amount of ^{212}Po resulting from the decay of ^{224}Ra, produced during the bombardment, and subsequent growth of ^{212}Pb prior to the chemical separation. In the following $^{40}Ar + ^{232}Th$ experiments the alpha activities of the target and recoil foils were determined directly. Alpha particle counts observed between 5.1 and 6.4 MeV were summed for each of the recoil foils. These energies, based on the chemical separations above, correspond primarily to ^{225}Ra, ^{225}Ac and ^{223}Ra transfer products. The relative distribution of these ^{225}Ra, ^{225}Ac and ^{223}Ra products in the forward recoil foils is shown in Fig. 2. The range distribution of Ra and Ac transfer products shown in Fig. 2 is consistent with the energy and angular distribution of the complementary quasi Ar products measured in the reaction of ^{40}Ar with ^{232}Th.[2,3] The small but significant fraction of transfer products with range of ~ 4.2 mg/cm^2 and corresponding to an energy equal to complete momentum transfer plus Coulomb repulsion could result from a deep inelastic process having a $1/\sin\theta$ angular distribution. This process is suggested in a kinematic study of the light quasi ^{40}Ar complements to Ra and Ac.[2,3]

One important object of these studies was to determine the usefulness of high resolution gamma-ray counting of the stacked Al recoil foils for identifying reaction mechanisms. Figure 3 shows the recoil range distributions of a transfer product (^{211}At) and complete fusion-fission or quasifission followed by fission of the heavy complement products (^{86}Zr, ^{120}Sb, ^{182}Re) from the reaction $^{40}Ar + ^{209}Bi$. The complete fusion-fission and/or quasifission followed by fission of the heavy complement products were identified on the basis of gamma-ray energy and relative intensity. The intensity of gamma-rays associated with fusion-fission or quasifission followed by fission of the heavy complement products is small relative to that associated with the $^{40}Ar + ^{27}Al$ transfer reaction product produced in the Al recoil foils and therefore a careful analysis of the gamma-ray spectra was needed. The computer code SAMPO[4] was used to identify the peak energies and absolute intensities

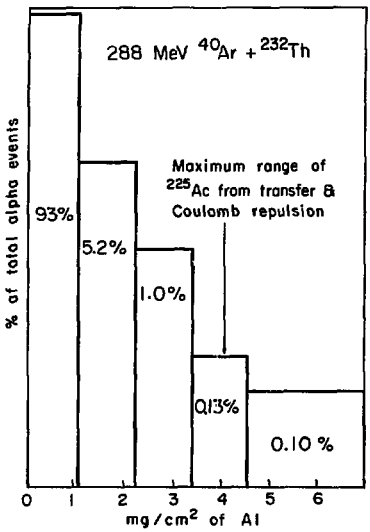

Fig. 2. Range distribution of alpha emitters with energies between 5.1 and 6.2 MeV produced in the reaction of 288 MeV ^{40}Ar with ^{232}Th. (XBL 756-3324)

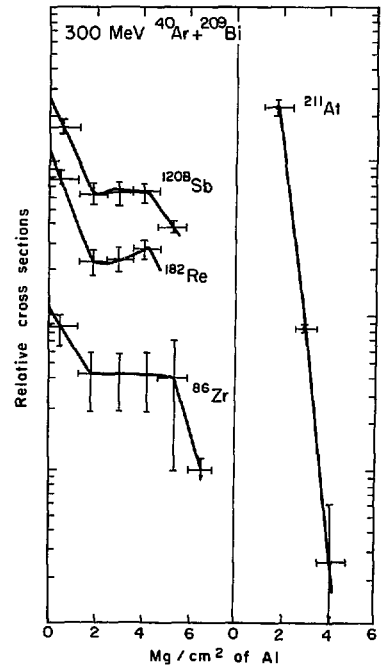

Fig. 3. Recoil range distribution of reaction products from 300 MeV ^{40}Ar with ^{209}Bi. (XBL 756-3325)

in the gamma-ray spectra from each of the recoil foils. The range distributions of the quasifission followed by fission of the heavy complement and/or complete fusion-fission products are clearly differentiated from those of the transfer products. These results will be used to correct cross sections from the mass yield studies of ^{40}Ar with ^{238}U and ^{209}Bi for recoil losses.[5] Using the stacked foil method along with radiochemistry and gamma-ray analysis, it may be possible to identify the reaction mechanism associated with the "goldfinger" phenomena, seen as excess yields around A ≈ 195, and reported by Kratz, Norris and Seaborg.[6]

References

1. J. M. Alexander, Nuclear Chemistry I, L. Yaffe, editor (Academic Press, New York, 1968), pp. 273-357.

2. A. G. Arkuth, G. F. Gridnev, V. L. Mikheev, and V. V. Volkov, Proceedings of the Nashville Conference on Reactions Between Complex Nuclei, June 10, 1974, Vol. 1, p. 87 (North-Holland and American Elesevier).

3. A. G. Arkuth, G. F. Gridnev, V. L. Mikheev, V. V. Volkov, and J. Wilczynski, Nucl. Phys. A215, 91 (1973).

4. J. T. Routti, UCRL-19452 (1969).

5. R. J. Otto, M. M. Fowler, D. Lee, I. Binder, and G. T. Seaborg, "Radiochemical Mass Yield Distribution Studies in the Reaction of ^{40}Ar with ^{238}U and ^{209}Bi and 25.2 GeV ^{12}C with ^{238}U", see Section I of this Annual Report.

6. J. V. Kratz, A. E. Norris, and G. T. Seaborg, Phys. Rev. Lett. 33, 502 (1974); see Section I of this Annual Report, "Mass Yield Distributions in the Reaction of ^{84}Kr Ions with ^{238}U".

RADIOCHEMICAL MASS YIELD DISTRIBUTION STUDIES IN THE REACTION OF ^{40}Ar WITH ^{238}U AND ^{209}Bi AND 25.2 GeV ^{12}C WITH ^{238}U

R. J. Otto, M. M. Fowler, D. Lee, I. Binder, and G. T. Seaborg

The radiochemical mass yield distribution of 605 MeV ^{84}Kr with ^{238}U reported by Kratz, Norris, and Seaborg[1] clearly distinguished five components. They were

1) transfer products showing as "rabbit ears" on the mass distribution curve (700 ± 120 mb);

2) "quasi-Kr" products centered at A ≈ 85 corresponding to the new "quasifission" reaction also observed by others in kinematic coincidence measurements (470 ± 70 mb) and the products from symmetric fission of their complements (420 ± 60 mb);

3) neutron-excess products from low-energy fission of Z ≈ 92 nuclides (200 ± 40 mb);

4) products from complete fusion-fission (55 ± 15 mb); and

5) unexplained neutron-deficient yields near gold at A ≈ 195 which we refer to as the "goldfinger" (~ 40 mb).

Thick depleted uranium (30 mg/cm^2) and bismuth (125 mg/cm^2) targets were bombarded with 340 MeV ^{40}Ar ions. The targets were subjected to a chemical group separation scheme developed by Kratz, Liljenzin and Seaborg,[2] with some small modifications to account for the differences in chemical properties of bismuth and uranium. The Ge(Li) gamma-ray counting and analysis used to identify and measure cross sections of the nuclides is the subject of another report.[3]

We have made a preliminary comparison of the independent and partial chain yields for the 340 MeV ^{40}Ar + ^{238}U reaction with those reported[2] for the 288 MeV ^{40}Ar + ^{238}U reaction. Based on this comparison and examination of the relative yields of nuclides as related to the valley of beta stability for the nuclides over the mass number range A ≈ 40 to A ≈ 92, the relative contribution of the complete fusion-fission process compared to other reaction channels is not as large as previously reported.[4]

In addition to the complete mass yield distribution studies of 340 MeV ^{40}Ar with thick ^{238}U targets, the isotopic distribution of I and Br isotopes from the same reaction with 212 to 288 MeV ^{40}Ar ions was determined. Figures 1 and 2 show the cross sections for the I and Br isotopes identified by gamma-ray energy and half life for ^{40}Ar with incident laboratory energies between 340 and 212 MeV. Since thick U targets were used, the cross sections represent integrated formation cross sections between the incident ion energy and the barrier, calculated to be 206 MeV (Lab) using r_0 = 1.4 fm. The Gaussian shaped curves drawn through points representing the yields of the neutron-deficient I isotopes represent best fits to the independent yield data in this region. The Gaussian-like isotopic mass yields probably result from quasifission followed by fission of the heavy complement (type 2 above) or from complete fusion-fission (type 4 above). The neutron-excess I and Br products are produced by low energy fission of nuclides with Z ≈ 92.

An analysis of the iodine isotopic distributions in terms of a complete fusion-fission mechanism may be made. Assuming that the neutron-deficient isotopic distributions in Figures 1 and 3 result from fusion-fission only, 15 ± 1 and 11 ± 1 neutrons would be emitted in the fusion-fission process from the ^{40}Ar + ^{238}U and ^{40}Ar + ^{209}Bi reactions, respectively. The relatively

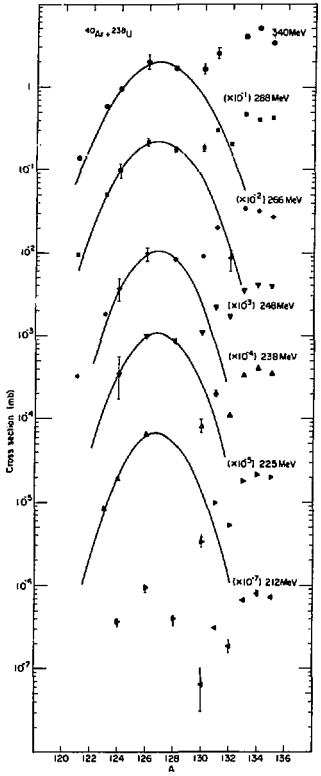

Fig. 1. Iodine isotopic yields from the reaction of ^{40}Ar with thick ^{238}U targets. (XBL 753-2565)

large neutron to proton ratio of the compound nucleus with respect to the neutron to proton ratio of stable Br isotopes would shift the center of the Br isotopic distributions to the neutron excess side of the valley of beta stability. Neutron deficient Br isotopes seen in Fig. 2 result from ^{40}Ar contamination trapped in the uranium metal target. The target arrangement did not allow for accurate beam intensity measurements. However, the cross section ratios shown in Fig. 4 provide information about the excitation functions of the I and Br isotopes independent of beam intensity and chemical yield. The ^{126}I to ^{135}I ratio indicates that the barrier is about 20 MeV higher for the fusion-fission or quasifission mechanism than for the transfer-reaction mechanism. The ratio of

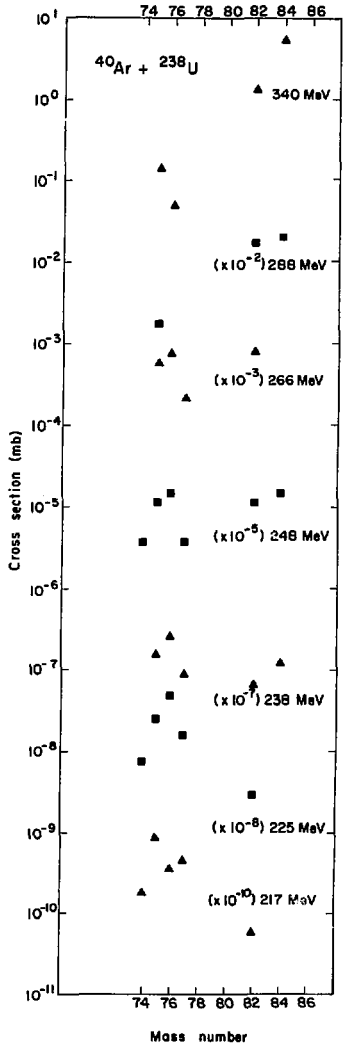

Fig. 2. Bromine isotopic yields from the reaction of ^{40}Ar with thick ^{238}U targets. (XBL 756-3315)

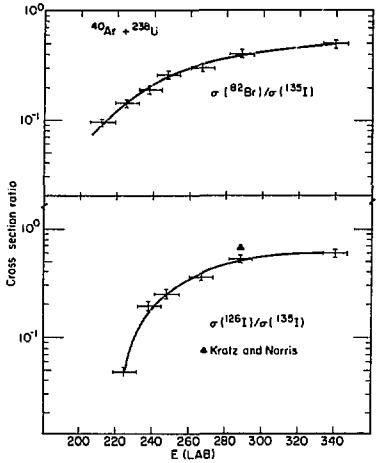

Fig. 4. Cross section ratios from the reaction of ^{40}Ar with ^{238}U plotted as a function of incident beam energy. The values plotted represent integral production cross section ratios for the reaction of ^{40}Ar with ^{238}U between the incident ion energy and the reaction barrier. (XBL 753-2559)

^{82}Br, an independent yield isotope, to ^{135}I, a cumulative yield isotope with a short-lived parent, is also shown in Fig. 4. Since ^{82}Br is produced in the transfer reaction mechanism as well as in the fusion-fission or quasifission mechanism, the evidence for a difference in barriers between the two type of reactions is not clearly seen.

The isotopic yields of I from 340 MeV ^{40}Ar with a thick ^{209}Bi are shown in Fig. 3. As expected, the low energy fission neutron-excess products are not seen. The Gaussian curve fit through the neutron-deficient I isotopes has the same width as was found with 340 MeV ^{40}Ar + ^{238}U but centered at A = 125.2 almost 1.5 mass units lower than the center for the ^{40}Ar + ^{238}U curves (Fig. 1).

A mass yield distribution study using relativistic heavy ions was also begun at the Bevalac. A ^{12}C beam intensity of $\sim 10^9$ particles/pulse was attained. The iodine isotopic yields from the reaction of 25.2 GeV ^{12}C with a 250 mg U target is shown in Fig. 3. The complete radiochemical separation used for the ^{40}Ar bombardments as described

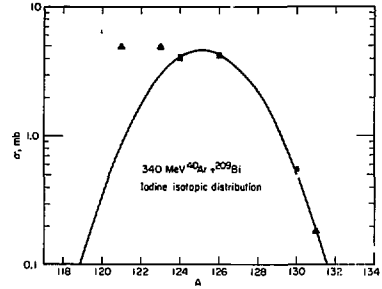

Fig. 3. Iodine isotopic yields from the reaction of 340 MeV ^{40}Ar with a thick ^{209}Bi target and from the reaction of 25.2 GeV ^{12}C ions with a ^{238}U target. (XBL 753-2560)

above was used with the 25.2 GeV ^{12}C + U experiment. Gamma-rays were seen for many nuclides between $Z \approx 20$ and $Z \approx 92$ with strong peaks for nuclides such as ^{28}Mg, ^{24}Na and neutron-excess low-energy fission products. An interesting comparison can be made between yields of cesium from 2.0 GeV protons on ^{238}U5 and the yields of iodine from this experiment. The comparison shows that, in the case of the iodine, there is an enhancement in the yields of neutron-deficient isotopes relative to that observed in the case of cesium.

References

1. J. V. Kratz, A. E. Norris, and G. T. Seaborg, Phys. Rev. Lett. 33, 502 (1974). See "Mass Yield Distributions in the Reaction of ^{84}Kr with ^{238}U", in Section I of this Annual Report.

2. J. V. Kratz, J. O. Liljenzin, and G. T. Seaborg, Inorg. Nucl. Chem. Lett. 10, 951 (1974).

3. M. M. Fowler, D. Lee, I. Binder, R. Otto, "Computer Aided Analysis of Gamma-Ray Spectra", in Section IV of this Annual Report. See also I. Binder, M. DiCasa, J. V. Kratz, J. O. Liljenzin, and A. E. Norris, Report LBL-2366, p. 451 (1973).

4. I. Binder, J. V. Kratz, J. O. Liljenzin, A. E. Norris, and G. T. Seaborg, Report LBL-2366, p. 61 (1973).

5. G. Friedlander, L. Friedman, B. Gordon, and L. Yaffe, Phys. Rev. 129, 1809 (1963).

EXCITATION FUNCTIONS OF COMPOUND NUCLEUS PRODUCTS FROM THE REACTION $^{40}Ar + ^{175}Lu$

J. R. Alonso, C. T. Alonso, A. Ghiorso,
J. M. Nitschke, and M. Nurmia

Introduction

One aspect of heavy ion physics that is receiving a great deal of current attention is the probability of compound nucleus formation using heavy beams on heavy targets. It is now clear that true compound nucleus formation does not occur as readily for very heavy projectiles as it does for the lighter projectiles, and that although full momentum transfer processes do occur with high probability the usual result is some form of composite system whose shape precludes the possibility of complete fusion into a compound nucleus.[1] Thus a study of the effect of projectile size and total system charge on compound nucleus formation by a direct observation of the complete fusion products has a direct bearing on, among other things, the probability of synthesis of transuranic and superheavy elements. In addition, the details of particle evaporation from compound nuclei produced with heavy beams are not well understood, and a measurement of the ratio of charged particle emission to neutron emission is important. Therefore we are undertaking a systematic study of compound nucleus formation and evaporation, starting with argon beams on progressively heavier targets. Preliminary results from the first study of this type are reported here.

For a direct and unambiguous detection of compound nucleus products it is important to work in a region where the neutron-evaporation products are isotopes of known alpha decay energies and half-lives. Thus the light actinium isotopes $^{210-213}Ac$ are the heaviest products that can be easily reached, implying that ^{175}Lu is the heaviest target that can be used with ^{40}Ar to observe (xn) products from a compound nucleus reaction. A detailed study of ^{175}Lu + ^{40}Ar can yield a good picture of many compound nucleus products, and ratios of (xn), (pxn), and (αxn) cross sections can be evaluated. The use of heavier targets such as ^{181}Ta can also yield compound nucleus information, but the important (xn)/(αxn) ratio cannot be measured because the light protactinium isotopes are too short-lived to be detected with our apparatus, or are unknown.

It is hoped that eventually an extrapolation of our measurements, together with those of Hahn et al[2] for lighter targets, will yield some trends that could give us some insight concerning the probabilities of compound nucleus formation for heavier beams on heavy targets.

Experiments

Our experimental techniques are the same as those used in our recent discovery of element 106.[3] These involve the transport of activity from the target area by an aerosol-gas stream to a low-background alpha counting area. Thin targets of metallic lutetium of thickness ~ 1 mg/cm^2 were evaporated on 2.7 mg/cm^2 aluminum backings. The argon beam energies ranged from 187 to 242 MeV. The energies were adjusted in gross steps by retuning the SuperHILAC and in fine steps by inserting degraders in the beam line. A solid state counter directly behind the target measured the attenuated beam after it had traversed both the degraders and the target.

Table 1 lists the alpha activities detected as well as the reaction which produced them. Note that some of the Fr products may have originated from the alpha decay of actinium parents, but the much higher yield of (αxn) to (xn) products implies that this effect is negligible. A typical alpha

TABLE 1.

Reactions	Activities	Half-life (sec)	Alpha energy (MeV)
(^{40}Ar,2n)	^{213}Ac	0.93	7.377
3n	^{212}Ac	0.80	7.362
4n	^{211}Ac	0.25	7.480
5n	^{210}Ac	0.35	7.482
p 2n	^{212}Ra	13	6.869
p 3n	^{211}Ra	15	6.910
p 4n	^{210}Ra	4.7	7.018
p 5n	^{209}Ra	3.8	7.008
α 2n	^{209}Fr	59	6.647
α 3n	^{208}Fr	52	6.647
α 4n	^{207}Fr	14.7	6.773

spectrum is shown in Fig. 1. This is a sum of the spectra observed in each detecting station around the periphery of the collecting wheel. Figures 2, 3, and 4 give excitation functions for the (xn), (pxn), and (αxn) products, respectively. These data are preliminary, with a fully computerized analysis still in progress. Figure 5 is a composite of the curves drawn through the experimental points. These excitation functions are broadened by about 5 - 10 MeV because of the energy dispersion of the beam in the degraders and the target.

Discussion

The parameters obtained from theoretical fits to these excitation functions reinforce our previous observation that our understanding of these processes is very limited. Two sets of calculations were performed. The first was a Sikkeland-type neutron evaporation calculation which does not include charged particle emission but does include nuclear deformation effects.[4] This code has proven to be very useful and quite accurate for transuranic element neutron evaporation cross sections

for projectiles up to neon. The second treatment utilized the code ALICE developed by M. Blann et al.[5] This code includes all modes of evaporation from the nucleus but does not include prompt or direct particle emissions.

The more efficient neutron evaporation code was used to undertake a search in the Wood-Saxon (r_o,d) parameter space for optimum values to fit the observed (xn) excitation functions. The optimum parameters were found to be r_o = 1.32 fm and d = 1.0 fm. In contrast, the parameters found by this code for transuranic element production with light projectiles were r_o = 1.25 fm and d = 0.5 fm. The implication is that for Ar + Lu the effective nuclear interaction radius is larger and the surface is more diffuse than for reactions involving lighter projectiles on heavier targets. Deformation effects are included in these calculations, so they cannot be responsible for the lower effective barriers.

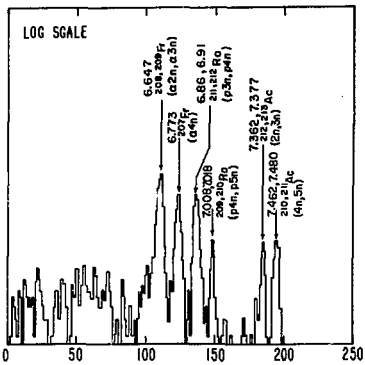

Fig. 1. Example of alpha spectrum obtained for the ^{40}Ar + ^{175}Lu reaction products. The peaks are labeled by energy (in MeV), parent isotope, and by particles boiled off from the compound nucleus to give each product. (XBL 756-3323)

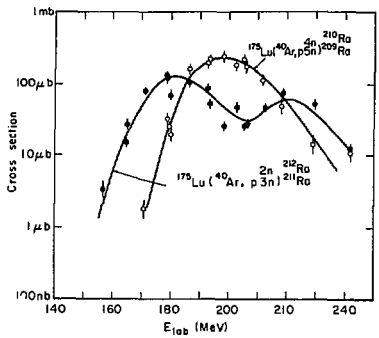

Fig. 3. Experimental excitation functions for $^{209-212}Ra$ isotopes, produced in (^{40}Ar,pxn) reactions. (XBL 756-3327)

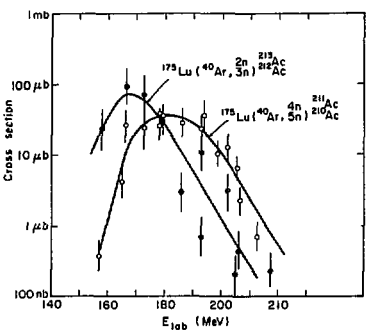

Fig. 2. Experimental excitation functions for $^{210-213}Ac$ activities, produced by pure neutron evaporation from the compound nucleus. (XBL 756-3330)

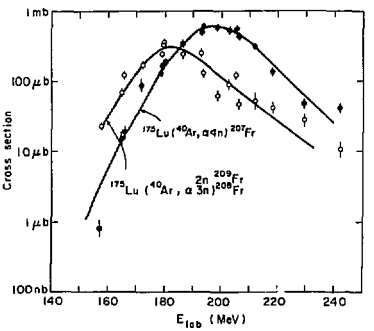

Fig. 4. Experimental excitation functions for $^{207-209}Fr$ isotopes produced in (^{40}Ar,αxn) reactions (XBL 756-3328)

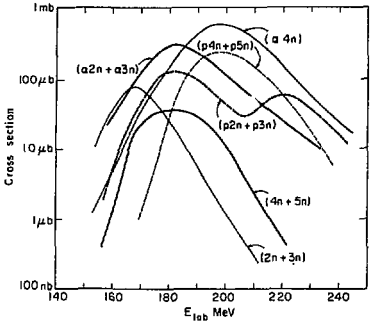

Fig. 5. Composite of experimental excitation function curves from Figs. 2-4. Experimental points have been left out for clarity. (XBL 756-3331)

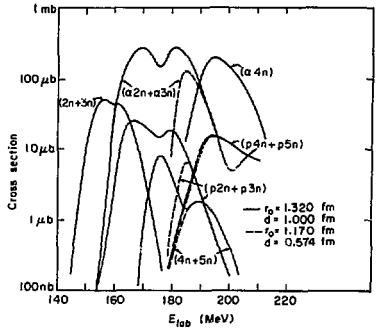

Fig. 6. Predictions for observed excitation functions made by the ALICE code of M. Blann et al,[5] using nuclear potential parameters of r_o = 1.32 fm, d = 1.0 fm, which best fit our observed reaction threshold. The dotted lines indicate the higher reaction barrier obtained for r_o = 1.17 fm, d = 0.574 fm, the parameters built into the code. (XBL 756-3329)

These parameters were used in the ALICE code with the results shown in Fig. 6. For comparison, the dotted lines show the predictions for the parameters (r_o = 1.17 fm and d = 0.574 fm) which are normally used with this code and which were selected on the basis of experimental data from the lower mass regions. Although there is similarity between theory and experiment (Figs. 6 and 5), the detailed agreement is poor. For example, the experimental excitation functions are much broader than the predictions, the observed (pxn) cross sections are about 10 times higher than predicted, and the (2n,3n) prediction peaks at too low an energy and is too strong with respect to the (4n, 5n) curve. Nevertheless, gross features are reproduced by the theory.

Using these parameters from the Ar + Lu reaction to predict cross sections for the $^{40}Ar + ^{208}Pb$ reaction yields cross sections for ^{245}Fm and ^{246}Fm which are at least three or four orders of magnitude too high compared to recent experimental results.[6] It is apparent that the region of targets from Lu to Pb sees the onset of one or more new mechanisms that are radically diminishing the probability of compound nuclear formation. Although the Ar + Lu parameters obtained here cannot be used to describe compound nucleus formation for heavier targets, perhaps an analysis of trends in the parameters themselves as a function of target size may lead to an extrapolation that has more validity. Further studies of this nature are in progress.

References

1. See for example, M. Lefort, Y. Le Beyec, and J. Peter, "Experimental Complete Fusion Results", Proceedings of International Conference on Reactions Between Complex Nuclei, Nashville, Tennessee, June 10-14, 1974.

2. R. L. Hahn et al., private communication.

3. A. Ghiorso, J. M. Nitschke, J. R. Alonso, C. T. Alonso, M. Nurmia, G. T. Seaborg, E. K. Hulet, and J. N. Lougheed, "Element 106", Phys. Rev. Lett. 33, 1490 (1974).

4. J. R. Alonso and J. O. Rasmussen, "Total Reaction Cross Sections for Heavy Ions", LBL-2366, p. 150 (1974).

5. M. Blann and F. Plasil, "ALICE: A Nuclear Evaporation Code", USAEC Report COO-3494-10 (1973); also W. G. Winn, H. H. Gutbrod, and M. Blann, Nucl. Phys. A18P, 423 (1972).

6. A. Ghiorso, private communication.

SEARCH FOR ^{260}Rf

M. Nurmia, E. K. Hulet,* K. Williams, and A. Ghiorso

We have continued our efforts to find the missing isotope ^{260}Rf. As in our earlier experiments[1] we have concentrated our work in the half-life range of 50 ms to one second because of the repeated claim[2] that ^{260}Rf has a half-life of 100 ms.

We bombarded a target of ^{249}Bk with ^{15}N ions in the rotating drum system described in Ref. 3. The reaction ^{249}Bk(^{15}N,4n)^{260}Rf is expected[4] to have a cross section of 14 nb at 82 MeV; this is in accordance with the measured production cross sections of neighboring nuclides.

No spontaneous fission activity with a half-life within the above limits was observed in these experiments, and we conclude that the half-life of ^{260}Rf is quite likely to be shorter than 25 ms.

Footnotes and References

*Lawrence Livermore Laboratory.

1. A. Ghiorso, Proceedings of the Welch Conference on Chemical Research, Huston, Texas, November 17-19, 1969; LRL Annual Report 1968 (UCRL-18667).

2. See, for instance, K. Bemis, Proceedings of International Conference on Reactions Between Complex Nuclei, Nashville, Tenn., June 10-14, 1974.

3. E. K. Hulet et al., Phys. Rev. Letters 26, 523 (1971).

4. J. Alonso, Gmelin's Handbuch der Anorganischen Chemie Vol. 71.

ELEMENT 106

A. Ghiorso, E. K. Hulet,* J. M. Nitschke, J. R. Alonso,
R. W. Lougheed,* C. T. Alonso, M. Nurmia, and G. T. Seaborg

The identification of new elements at the upper end of the periodic table is especially difficult because of extremely low production rates and because there are large uncertainties in predicting their nuclear properties. For these reasons, positive identification requires some means of determining the atomic number directly. Among the proven methods are (1) the measurement of distinctive K-x rays[1,2] following α-decay and (2) the establishment of a genetic link between an α-emitter of a new element and a previously identified daughter nuclide. Our identification of element 106 is based on the latter method because of its higher sensitivity. This method was also used in discovering α-emitting isotopes of rutherfordium (element 104)[3] and hahnium (element 105).[4] In the case of element 106, we have carried this method one step further by demonstrating that the granddaughter ^{255}No, $t_{1/2}$ = 3 min, E main alpha group 8.11 MeV (57%)[5,6,1] is in the chain of α-decay of ^{263}106. Thus, our proof for the atomic number of element 106 comes from demonstrating the following decay sequence: $^{263}106 \xrightarrow{\alpha} {}^{259}Rf \xrightarrow{\alpha} {}^{255}No \xrightarrow{\alpha}$.

These genetic relationships were established in two ways depending on whether or not the ^{263}106 α-particles escaped from their backing surface. (1) In the case where these particles were detected leaving the surface we observed with a certain probability in a time interval of 12 seconds the alphas of the 3-second daughter ^{259}Rf (E = 8.77 and 8.86 MeV) that also were directed outward; i.e., we observed the $^{263}106 \xrightarrow{\alpha} {}^{259}Rf \xrightarrow{\alpha}$ decay sequence. (2) In the case where the ^{263}106 alphas were directed into the backing surface (and hence were not detected), the recoil energy imparted to the daughter nucleus allowed it to escape from the surface and to be implanted in the face of an opposing detector. Upon periodically moving these detectors away from the original sources, the α-decay of daughter ^{259}Rf and the subsequent α-decay of the granddaughter were observed; i.e., we detected the $^{259}Rf \xrightarrow{\alpha} {}^{255}No \xrightarrow{\alpha}$ decay sequence. Considering the finite thickness of the deposits containing the ^{263}106 atoms, the considerable recoil energy required to transfer the observed number of daughter ^{259}Rf atoms to the detector faces could be furnished only by a preceding α-emitter. We thus were provided with a second genetic linkage to ^{263}106 by α-decay.

Our experimental apparatus is illustrated schematically in Fig. 1. The ^{18}O beam obtained from the SuperHILAC had an average current of 3×10^{12} ions/sec and was wobbled electromagnetically over the target area to prevent localized overheating of the target. The target was both edge-cooled by contact with a water-cooled copper block and gas-cooled by helium impinging on the aluminum target backing. The energy of the ^{18}O ion beam emerging from the target was determined by measuring the energy of these ions scattered from the target into a Si(Au) surface barrier detector placed at 30° to the beam axis.

The target was prepared by subliming 259 μg of ^{249}Cf as CfF_3 onto a 27 μg/mm^2 substrate of 99.999% pure Al. The ^{249}Cf, deposited over a 6.3 mm diam. area had an average surface density of 8.3 μg/mm^2. It was covered with a thin (0.3 μg/mm^2) layer of Al to prevent any transport of the californium to the detection system.

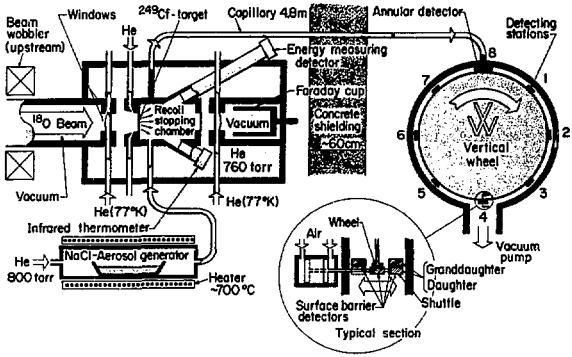

Fig. 1. Schematic representation of the experiment.
(XBL 748-3899)

Atoms of $^{263}106$ along with other transmutation products recoiled from the target into a stopping chamber and were swept by a flow of helium through Teflon tubing (4.8 m long, 1.24 mm inside diam.) into an adjoining counting area. The introduction of NaCl aerosol into the helium increased the transport efficiency to 80% or more. After a 0.1 sec transit time, the radioactive products which emerged from the Teflon tube were deposited onto the rim of a 45 cm diam. wheel which was rotated 45° each sec to collect a new deposit. Alpha particles from the deposits were then examined by a series of seven detecting stations each having 50 mm^2 Si(Au) surface barrier detectors positioned within 0.5 mm of the wheel rim. An eighth 100 mm^2 Si(Au) annular detector analyzed the α-activity of the deposit while it was being collected. Thus, each deposit was α-analyzed for seven sec (1 sec at each station) before it returned to the collecting position. Since new deposits were layered over the old, the wheel was advanced by 1.5° every 30 min to reduce the buildup of long-lived radioactivities in the deposits being analyzed.

If an α-particle from the decay of $^{263}106$ is observed, then another α-particle from the decay of its daughter, ^{259}Rf, should follow within a few daughter half-lives. Both events must originate from the same deposit, but they may be observed in separate detectors because the wheel advances the deposit every second. After considering the counting geometry and the decay and gating intervals we calculated a detection efficiency for these "mother-daughter" pairs of 28% compared to "mother only" events.

In addition to monitoring mother and daughter α-decays directly, we used a detector shuttle system (shown in the inset of Fig. 1) to detect daughters and granddaughters resulting from α-recoils. By moving the detectors away from the wheel, we could distinguish between recoil-implanted and wheel-borne ^{255}No and ^{259}Rf. Much larger amounts of these nuclides were made by direct nuclear reactions than by α-decay from $^{263}106$ and thus constituted a high background on the wheel. The set of seven detectors monitoring the wheel was shuttled every 6 sec to a low-background position facing seven stationary detectors, while another set of movable detectors resumed the monitoring of the wheel. In the event that a ^{259}Rf daughter had recoiled from the wheel onto a detector and we later observed α-decay of this daughter with the detector in the off-wheel position, this detector was not returned to the wheel position until 10 minutes had elapsed. This time period permitted an adequate opportunity for observing the subsequent α-decay of the 3-min granddaughter, ^{255}No.

Alpha and fission pulses from the detectors were amplified and passed through an analog-to-digital-converter to a PDP-9 computer. The computer recorded on magnetic tape all the event information, including α-energy, time, detector location, and wheel position. The PDP-9 also controlled the operation of the wheel and shuttle systems. We used off-line computer programs for correlating the arrival time of selected α-events with the time, α-energy, and detection location of other α-events. Using events in the ^{259}Rf energy region to define time origins, the intervals of 0 to 12 seconds and 50 to 62 seconds preceding these events were scanned for correlated decays. The first time range gave possible mother-daughter correlations, the second provided a good measure of the accidental background.

Earlier experiments performed in the Berkeley laboratory in 1970-71 had shown several promising mother-daughter events and daughter recoils. However, because of background radioactivities arising from Pb, Bi and Be in the target, these experiments were unable to provide sufficient proof of the atomic number. Our current α-spectra are virtually free of these background activities and show prominently only those α-emitters produced from the reactions of ^{18}O ions with ^{249}Cf.

The gross α-spectrum above 8 MeV, summed using the data from the wheel detectors, is shown in Fig. 2(a). Alpha groups at 8.77 and 8.86 MeV have been identified previously as belonging to ^{259}Rf.[3] We attribute most of the 87 events in the groups at 9.06 MeV and near 9.25 MeV to the α-decay of the new nuclide, ^{263}106. By means of a least-square analysis the number of these events observed at each wheel position (1 sec intervals) was found to decrease with a 0.9 ± 0.2 second half life.

The 9.06 and 9.25 MeV alphas are followed within 12 seconds by daughter alphas at 8.77 and 8.86 MeV, as shown in Fig. 2(b). The ratio of the time-correlated daughters to gross ^{263}106 events is roughly equal to the detection efficiency we derived for this process. An application of Poisson statistics indicates that, with 95% confidence,

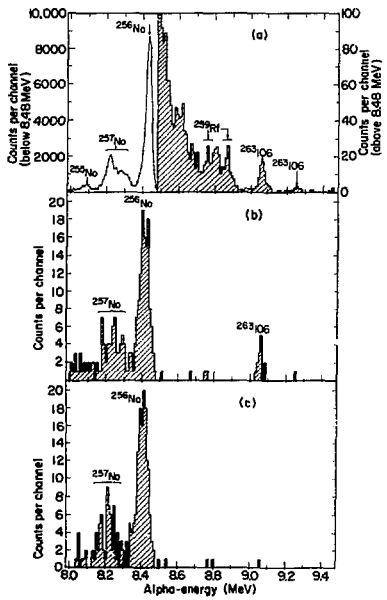

Fig. 2(a). Sum of alpha spectra from stations 1 through 7. The integrated beam intensity was 1.34×10^{18} particles of ^{18}O.

2(b). Alpha events in the *0 - 12 second interval* preceding ^{259}Rf events (8.65 to 8.91 MeV). The 12 second time interval represents four ^{259}Rf half lives.

2(c). Alpha events in the *50 - 62 second interval* preceding ^{259}Rf events. A 50-second time displacement was chosen to determine the accidental spectrum. Only one alpha event was found within the ^{263}106 energy region, as had been expected from Poisson statistics. (XBL 749-4129)

a maximum of 2.5 out of fourteen ^{263}106-^{259}Rf decay pairs might be attributed to accidentals. Random alphas occurring 50 - 62 sec before ^{259}Rf decay events are shown in Fig. 2(c). We infer from these data that the new activity decays by emission of 9.06 and 9.25 MeV α-particles to ^{259}Rf and, therefore, can belong only to ^{263}106.

Some 22 atoms of recoil-transferred ^{259}Rf were observed to decay in the off-wheel detectors. Shortly after such daughter events, granddaughter ^{255}No α-particles were detected in about a fifth of all off-wheel daughter decays. Considering the small number of granddaughters, this ratio may be expected from the ∿ 70% counting geometry and the ∿ 50% E.C. branching by ^{255}No.[7] In Table I we give a summary of all daughter-granddaughter and mother-daughter events.

From the rate of producing our new activity with α-energies of 9.06 and 9.25 MeV, we calculate a formation cross-section of ∿ 0.3 nb at an ^{18}O energy of 95 MeV. Very little of this activity was made by ^{18}O-ion beams of ∿ 91 and ∿ 100 MeV, which indicates a rather narrow excitation function. These preliminary measurements are consistent with our calculated excitation function for the ^{249}Cf(^{18}O,4n) reaction, which shows a half-width of 7 MeV and a maximum cross section of 0.2 nb.[8]

Spontaneous fission of ^{263}106 could not be determined because of interference from 2.7 hour ^{256}Fm, a spontaneous fission emitter produced in the bombardments. However, spontaneous fission is

TABLE 1.

Mother-Daughter Correlations			
^{263}106 E_α(MeV)	^{259}Rf E_α(MeV)	^{263}106 Station	Δt (sec) ^{259}Rf decay
9.03	8.85	1	3.6
9.04	8.85	2	10.5
9.04	8.91	1	1.2
9.05	8.74	2	2.2
9.05	8.77	5	0.9
9.05	8.85	1	1.0
9.06	8.70	2	3.0
9.06	8.72	1	2.5
9.06	8.75	3	1.6
9.06	8.78	1	6.4
9.06	8.78	3	9.4
9.08	8.74	1	2.1
9.08	8.76	7	0.3
9.25	8.88	1	3.5
Daughter-Granddaughter Correlations			
^{259}Rf E_α(MeV)	^{255}No E_α(MeV)	^{259}Rf Station	Δt (sec) ^{255}No decay
8.79	8.02	2	93.3
8.86	7.93	6	134.9
8.81	8.30	2	39.2
8.81	8.07	1	491.0

apparently not a major decay mode, since the α-events we observe account for a production cross section already larger than the calculated one.

During a recent visit by Soviet scientists to our laboratory, in which we exchanged information about "106" experiments, G. N. Flerov of the Dubna Laboratory reported the observation of spontaneous fission activities with half-lives of 4 - 10 milliseconds produced by bombarding $^{207,208}Pb$ with ^{54}Cr.[9] They attribute these activities to element 106. In view of the simultaneity of the experiments at the Dubna and Lawrence Laboratories, and their very different nature, we shall postpone suggesting a name for element 106 until the situation has been clarified.

Footnotes and References

*Lawrence Livermore Laboratory, Livermore, California 94550.

1. P. F. Dittner, C. E. Bemis, D. C. Hensley, R. J. Silva, and C. D. Goodman, Phys. Rev. Lett. 26, 1037 (1971).

2. C. E. Bemis, R. J. Silva, D. C. Hensley, O. L. Keller, J. Tarrant, L. Hunt, P. F. Dittner, R. Hahn, and C. D. Goodman, Phys. Rev. Lett. 31, 647 (1973).

3. A. Ghiorso, M. Nurmia, J. Harris, K. Eskola, and P. Eskola, Phys. Rev. Lett. 22, 1317 (1969).

4. A. Ghiorso, M. Nurmia, K. Eskola, J. Harris, and P. Eskola, Phys. Rev. Lett. 24, 1498 (1970).

5. G. N. Flerov, G. N. Akap'ev, A. G. Demin, V. A. Druin, Yu. V. Lobanov, and B. V. Fefilov, Yad. Fiz 7, 977 (1968); Soviet J. Nucl. Phys. 7, 588 (1968).

6. P. Eskola, K. Eskola, M. Nurmia, and A. Ghiorso, Phys. Rev. 62, 1058 (1970)

7. A. Ghiorso, et al., unpublished data (1971).

8. J. R. Alonso, "Production of Transuranic Elements in Charged Particle Reactions", in Gmelin Handbuch, Erg.-Werk, Bd. 7a, Transurane, Tl. A1, II, p. 28.

9. Yu. Ts. Oganessian, Yu. P. Tretyakov, A. S. Iljinov, A. G. Demin, A. A. Pleve, S. P. Tretyakova, V. M. Plotko, M. P. Ivanov, N. A. Danilov, Yu. S. Korotkin, and G. N. Flerov, JINR-D7-8099, Dubna. 1974.

SUPERHEAVIES IN NATURE – WHERE AND HOW TO LOOK*

M. J. Nurmia

It is not going to be easy to synthesize superheavy elements (SHE) – at best we might be able to make a few atoms the same way as, say hahnium, with the SuperHILAC or other machines.

However, if we were ever to find a single SHE nuclide in any natural source in the abundance of, say 10^{-16}, the whole picture would change. By working 100 kilograms of the material we would have some 10^{10} atoms – more than enough to prepare a large number of neighboring nuclei by neutron and charged-particle irradiation.

These "secondary" isotopes will generally have shorter half-lives and would thus provide sufficient activity for the study of the nuclear and chemical properties of the superheavy elements. They would also give rise to decay chains that would facilitate the study of the elements in the gap between the SHE's and hahnium. The rewards of success would thus be great, and we shall now look at the basic questions on how to improve the sensitivity of our search.

Most work so far has been based on two important assumptions:

1) The eka-element follows the chemistry of the lower homolog both in geochemical fractionation and in ordinary industrial processes. For example, one looks for eka-lead in either lead minerals or "pure" lead compounds.

2) The SHE either decays by SF or exists in secular equilibrium with a descendent that decays by SF.

Regarding the first assumption I would like to quote Darleane Hoffman, the discoverer of ^{244}Pu in nature.[1] She points out that even in that case it was very difficult to decide where to look for the highest geochemical enrichment of Pu, even though the chemistry of plutonium "has been rather well studied."

Regarding the second assumption it should be pointed out that an assumed primordial SHE is *not* likely to decay by spontaneous fission. A calculation by Fiset and Nix[2] that covers all nuclides with $172 \leq N \leq 191$ and $104 \leq Z \leq 130$ predicts that out of these 520 isotopes 15 would have a total half-life longer than 2 years. The half-lives of these 15 range up to 10^9 years, but only two of them, two isotopes of element 110, are predicted to have spontaneous fission as their main mode of decay. Even assuming for the considerable uncertainty of the predicted half-lives themselves, it appears likely that a long-lived primordial SHE would decay by alpha emission or electron capture and give rise to a family of one or more members before the chain is terminated in SF.

Most minerals are old enough so that there is a good chance for a secular equilibrium between the SHE and its descendants, but this condition

would not be fulfilled in case of industrial products and other such samples.

Of course, if the SHE has an essentially infinite half-life, it could only be detectable by methods such as mass spectrometer or activation analysis. As D. Hoffman[1] points out, it would be necessary to perform chemical concentration, i.e., a separation between SHE and its lower homolog.

I would suggest that we try to improve the sensitivity of our SHE search by abandoning the above assumptions and replacing them with specific assumptions regarding the SHE and its geochemical behavior.

At this point I would like to concentrate on one good possibility of a geochemical and physical distinction between a SHE and its lower homolog. The SHE is eka-mercury. In the group consisting of Zn, Cd and Hg, Cd is more volatile than Zn, and Hg is much more volatile than Cd.

Quantitative predictions can be made in the manner used for other SHE's by Keller et al.[3] but no matter how one extrapolates, eHg seems to be still more volatile than Hg. The trend of the chemical nobility of these elements is similar: Zn and Cd do not occur as metals in nature, but mercury is present in metallic form in minerals and as vapor in the atmosphere.

The amount of Hg in "unpolluted" air is given as 1 - 40 ng/m^3,[4] a concentration of $(1\text{-}8)\cdot10^{-12}$. In sea water the Hg concentration is 10 to 50 ng/l or $(1\text{-}5)\cdot10^{-11}$.

It is interesting to note that the Hg in the atmosphere may be largely of volcanic origin.[4,6] The same geochemical processes should work still more efficiently in the case of the more volatile and more noble eHg, if it is present in nature. eHg may actually resemble the heavy rare gases in its geochemical behavior and be preferentially concentrated in the atmosphere!

This offers many interesting possibilities for a search along the lines explored by Stoughton et al.[7] They used a neutron-multiplicity counter to look for spontaneous fissions in samples of crude xenon and silica gel from a commercial air liquefaction process, and also examined Au and Ag foils exposed to air flowing out of mercury mines. No SF activity was observed during a counting period of a few days.

Let us now consider the nuclear properties in some detail; this kind of evaluation can be made for other SHE's as well but I shall concentrate on eHg. Decay properties predicted for the longest-lived eHg isotopes by Fiset and Nix[2] are given in Table 1.

Table 1

A moderate "adjustment" of the alpha half-lives would evidently yield total half-lives sufficiently long so that some of the above isotopes could be present as primordial SHE's. There are at least two other possibilities.

TABLE 1. Longest-lived eHg isotopes.[6]

N	A	T_{SF}	T_α	Q_β MeV
178	290	79 d	180 d	--
179	291	$10^{4.5}$ y	6.4 y	0.2
180	292	$10^{3.6}$ y	98 y	--
181	293	$10^{9.1}$ y	$10^{5.6}$ y	--
182	294	$10^{8.5}$ y	$10^{4.5}$ y	--
183	295	$10^{14.5}$ y	$10^{6.4}$ y	--
184	296	$10^{14.4}$ y	$10^{5.4}$ y	--

First, SHE's may, after all, be produced in supernova explosions or other astrophysical processes and be arriving on the Earth as cosmic rays or cosmic dust some 10^3 to 10^6 years after their formation.[8] Relatively short-lived eHg isotopes may thus be present as "cosmic fallout" in the atmosphere or in the deep-sea sediments.

Second, eHg isotopes may be present as decay products of other SHE's. In this context we should pay particular attention to the suggestion of Meldner and Herrmann[9] that the longest-lived SHE isotopes may be of the odd-odd type and similar to ^{40}K and ^{50}V, both of which are long-lived in spite of their large beta-decay energy.

Some such odd-odd SHE candidates, taken from the table of Fiset and Nix,[2] are listed in Table 2.

Table 2

If eHg isotopes, such as those shown in Table 1, are present in nature, they are likely to decay by alpha emission forming ePt isotopes with various expected decay modes and half-lives up to $10^{4.5}$ years for ^{292}ePt.[2] In particular we *cannot* assume that samples of less than "geological" age contain the eHg in secular equilibrium with a descendant decaying by SF.

TABLE 2. Odd-odd SHE candidates.[2]

Element	N	A	T_{SF}	T_α	Q_β
107 eRe	183	290	$10^{11.8}$ y	$10^{17.5}$ y	3.7
109 eIr	181	290	$10^{5.3}$ y	$10^{6.9}$ y	2.2
	183	292	$10^{13.0}$ y	$10^{12.3}$ y	2.7
111 eAu	179	290	$10^{4.3}$ y	$10^{3.8}$ y	1.1
	181	292	$10^{9.1}$ y	$10^{4.2}$ y	1.3
	183	294	$10^{15.2}$ y	$10^{8.2}$ y	1.7
113 eTl	181	294	$10^{13.6}$ y	960 y	1.8
	183	296	$10^{18.9}$ y	$10^{5.3}$ y	1.2

The most attractive way to look for these isotopes is the mass spectrometer. The expected high volatility of eHg will cause some special problems but it will also provide an excellent way of concentrating and transferring samples.

In conclusion, then, I suggest that we look for eHg in natural sources using a good mass spectrometer. Of course I cannot guarantee success — but if we are always successful, then we are not tackling problems of the right kind!

Footnotes and References

*Condensed from a paper presented at the Nobel Symposium on "Superheavy Elements, Theoretical Predictions and Experimental Generation", Ronneby, Sweden, June 10-14, 1974; Physica Scripta 10A, 77 (1974).

1. D. C. Hoffman, Los Alamos Preprint LA-UR-73-251; D. C. Hoffman, F. O. Lawrence, J. M. Merewether and F. M. Rourke, Nature 234, 132 (1971).

2. E. O. Fiset and J. R. Nix, Nucl. Phys. A193, 647 (1972).

3. O. L. Keller, J. L. Burnett, T. A. Carlson, and C. W. Nestor, J. Phys. Chem. 74, 1127 (1970).

4. B. Z. Siegel, S. M. Siegel, and F. Thorarinsson, Nature 241, 526 (1973).

5. D. Gardner and J. P. Riley, Nature 241, 526 (1973).

6. A. Eshleman, S. M. Siegel, and B. Z. Siegel, Nature 233, 471 (1971).

7. R. W. Stoughton, J. Halperin, J. S. Drury, F. G. Perey, R. L. Macklin, R. V. Gentry, C. B. Moore, J. E. Noakes, R. M. Milton, J. H. McCarthy, and D. W. Sherwood, Nature Phys. Sci. 246, 26 (1973).

8. This mechanism has been considered for ^{244}Pu by K. Sakamoto (Nature 248, 130 (1974)).

9. H. Meldner and G. Herrmann, Z. Naturforsch. 24a, 1429 (1969).

THE VECTOR ANALYZING POWER IN d-p SCATTERING AT 45.4 MeV AND THE NUCLEON NUCLEON INTERACTION*

F. N. Rad, J. Birchall,† H. E. Conzett
S. Chintalapudi,‡ and R. Roy§

During the past few years, three-body calculations[1-5] have achieved notable success in fitting measured polarization observables[6-9] in elastic nucleon-deuteron scattering. These calculations, which use the Faddeev equations with separable nucleon-nucleon potentials, have been made with more and more complicated N-N interactions. The simple S-wave force had been sufficient to give agreement only with the differential cross-section data. The increasingly accurate and extensive polarization data, including nucleon and deuteron vector analyzing powers and deuteron tensor analyzing powers, have played a significant role in this theoretical refinement. It now seems possible to derive from such data, via the three-body calculations, information on the N-N interaction which, as yet, has not been available from N-N scattering experiments. The most recent calculations of Doleschall[5] show a surprisingly strong dependence of the nucleon and deuteron vector polarizations on variations of the input $^3S_1$ - $^3D_1$ N-N tensor interaction. We report here measurements of the deuteron vector analyzing power, iT_{11}, in d-p elastic scattering at E_d = 45.4 MeV, which can be compared directly with the calculated vector polarization at the equivalent nucleon energy E_N = 22.7 MeV.

Although it has been known[1-3,8] that the vector polarizations in N-d scattering are essentially due to the N-N P-wave interactions, there have been conflicting conclusions concerning the contribution to these polarizations from the tensor force. Pieper[4] reported only slight changes with the addition of the tensor force, and he suggested[10] that changes in the $^3S_1$ - $^3D_1$ potential would have little effect on the nucleon polarizations. This conjecture was based on Sloan and Aarons[1] result, which demonstrated that none of the N-d polarizations were very sensitive to changes in the $^3S_1$ - $^3D_1$ potential. However, that calculation did not include the P-wave interactions, so the calculated vector polarizations were unrealistically small. Doleschall's first calculation[3] showed a substantial change in the vector polarizations with the addition of the tensor force to the S and P-wave interactions, and his most recent calculation[5] shows that the vector polarizations are quite sensitive to the details of the $^3S_1$ - $^3D_1$ potential. It is just this sensitivity that offers the promise of providing information on the $^3S_1$ - $^3D_1$ n-p mixing parameter ε_1 and the $^1P_1$ phase shift, which are poorly determined from the phase shift analyses of n-p scattering data below 80 MeV.[11] Although Doleschall does not address this question, it seems clear that variations of ε_1 and the $^1P_1$ phase shift, in a search for improved fits to the vector polarization data, could result in a better determination of these parameters than has been possible from n-p scattering data.

Our experimental results are shown in Fig. 1, where the relative errors include the statistical error and a contribution of ± 0.004 which was determined from measured asymmetries with the beam polarization set to zero. In addition, there is a ± 3% normalization uncertainty from that of the

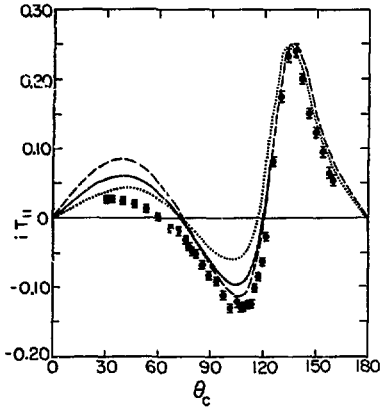

Fig. 1. The deuteron vector analyzing power, $iT_{11}(\theta)$, in d-p elastic scattering at E_d = 45.4 MeV. The curves are calculated results from Ref. 5 with different N-N interactions. Dotted line, set C (S and P-waves) + T4D tensor potential; dashed line, set C + T4M; solid line, set C + T4M + $^3D_2$. (XBL 744-2770A)

d-^{4}He analyzing power. Also shown in Fig. 1 are Doleschall's calculated results.[5] In this calculation he used an improved set of p-wave potentials which provide much better agreement with the two-nucleon p-wave phase shifts[11] for the lower energies which contribute in the three-nucleon calculation. Additionally, rank-2 tensor interactions were constructed in an attempt to simultaneously reproduce the $^3S_1$, $^3D_1$ phase shifts, the mixing parameter ϵ_1, and the deuteron properties. It was not possible to find a single rank-2 tensor force which satisfied all of these criteria, so two such sets were used. One, the T4D force, reproduced the low energy ($\lesssim$ 100 MeV) $^3D_1$ phase shifts but gave larger values of ϵ_1 than have been deduced from n-p scattering.[12] The other, the T4M force, reproduced the low energy ϵ_1 behavior but not that of the $^3D_1$ phase shifts. As shown in Fig. 1, the T4M force calculation is in good agreement with our data backward of $\theta_c \approx 80°$, but the agreement deteriorates at the forward angles. Even though the calculations are for n-d scattering they can be compared with our data since charge symmetry of the nuclear interaction provides equality of the n-d and p-d polarizations in the absence of Coulomb effects. Such effects have been demonstrated to be small near E_N = 22 MeV, in that the nucleon analyzing power in n-d[13] and p-d[6] scattering are equal within the experimental error. In a further effort to improve the agreement between experiment and theory for the proton analyzing power data, Doleschall also included a $^3D_2$ interaction. Computational limitations precluded the addition of a complete set of D-wave interactions. The results of that calculation with the T4M interaction, the T4M + $^3D_2$ result, is also shown in Fig. 1. Some improvement toward agreement is seen at the forward angles at the expense of a slightly poorer fit in the region θ_c = 85° to 115°. A very similar comparison between experiment and theory was found for the proton analyzing power data.[5]

The three-nucleon calculations represent major progress in predicting the polarization observables in N-d elastic scattering below 50 MeV. Small discrepancies remain with the vector polarizations in the forward angle region, which is just the region of greatest sensitivity to details of the $^3S_1$ - $^3D_1$ tensor interaction. Clearly, it would be most useful to do the calculation with a tensor force which simultaneously reproduces the N-N $^3D_1$ phase shift and the mixing parameter ϵ_1, for example, the rank-4 potential recently constructed by Pieper.[14]

Binstock and Bryan[11] have shown that the presently available n-p data (σ_{tot}, $d\sigma/d\Omega$, and P(θ)) near 50 MeV leave ϵ_1 undetermined between -10° to +3°. They also examined the sensitivity of other experimental observables to ϵ_1, and they found that the neutron-to-proton polarization transfer coefficient D_t combines fairly high sensitivity with reasonable experimental feasibility. A measurement of D_t to an absolute accuracy of ± 1% could determine ϵ_1 to about ± 1°. However, it should be possible in the three-nucleon calculation to fix $\delta(^3D_1)$ at the values determined from the n-p analyses and then to vary ϵ_1 in a search for improved fits to the p-d vector analyzing-power data. It seems quite possible that this procedure could provide a better determination of the low energy values of ϵ_1 than is feasible via the much more difficult n-p measurement of D_t. If this should prove to be so, one would, indeed, have deduced from the three-nucleon problem specific information about the two-nucleon interaction that has not yet been attainable.

Footnotes and References

*Condensed from publication in Phys. Rev. Letters 33, 1227 (1974).

†Present address: Physics Department, University of Basel, Switzerland.

‡Visitor from Bhabha Atomic Research Centre, Trombay, Bombay, India.

§National Research Council of Canada Post Doctoral Fellow.

1. J. C. Aarons and I. H. Sloan, Nucl. Phys. A182, 369 (1972); I. H. Sloan and J. C. Aarons, ibid A198, 321 (1972).

2. S. C. Pieper, Nucl. Phys. A193, 529 (1972).

3. P. Doleschall, Phys. Lett. 40B, 443 (1972); Nucl. Phys. A201, 264 (1973).

4. S. C. Pieper, Phys. Rev. C 6, 1157 (1972).

5. P. Doleschall, Nucl. Phys. A220, 491 (1974).

6. J. C. Faivre, D. Garreta, J. Jungerman, A. Papineau, J. Sura and A. Tarrats, Nucl. Phys. A124, 169 (1969).

7. R. E. White, W. Grüebler, V. König, R. Risler, A. Ruch, P. A. Schmelzbach and P. Marmier, Nucl. Phys. A180, 593 (1972).

8. J. S. C. McKee, H. E. Conzett, R. M. Larimer and Ch. Leemann, Phys. Rev. Lett. 29, 1613 (1972).

9. A. Fiore, J. Arvieux, Nguyen Van Sen, G. Perrin, F. Merchez, J. C. Gondrand, C. Perrin, J. L. Durand and R. Darves-Blanc, Phys. Rev. C 8, 2019 (1973).

10. S. C. Pieper, Phys. Rev. C 8, 1702 (1973).

11. M. H. MacGregor, R. A. Arndt and R. M. Wright, Phys. Rev. 182, 1714 (1969); R. A. Arndt, J. Binstock and R. Bryan, Phys. Rev. D 8, 1397 (1973); J. Binstock and R. Bryan, Phys. Rev. D 9, 2528 (1974).

12. The constrained solution values of ε_1 and $\delta(^1P_1)$ as given in Table VII, MacGregor et al., Ref. 11, were used.

13. J. J. Malanify, J. E. Simmons, R. B. Perkins and R. L. Walters, Phys. Rev. 146, 532 (1966); C. L. Morris, R. Rotter, W. Dean and S. T. Thornton, Phys. Rev. C 9, 1687 (1974).

14. S. C. Pieper, Phys. Rev. C 9, 883 (1974).

VECTOR-TO-VECTOR POLARIZATION TRANSFER IN DEUTERON-PROTON ELASTIC SCATTERING*

F. N. Rad, J. Birchall,† H. E. Conzett, and R. Roy‡

We report here on the first significant comparison between experimental and theoretically calculated vector-to-vector polarization transfer coefficients in nucleon-deuteron elastic scattering.

Considerable theoretical progress has been made recently in fitting the nucleon analyzing-powers measured in N-d elastic scattering at energies below 50 MeV.[1-3] These three-nucleon calculations, based on the Faddeev equations with separable nucleon-nucleon interactions, have also provided predictions of the deuteron vector and tensor polarizations and, more recently, of polarization transfer coefficients[4] at energies up to E_N = 23 MeV. Subsequent determinations of the deuteron analyzing-powers were in good agreement with the calculations.[5] These studies showed that the P-wave part of the N-N interaction was chiefly responsible for the vector analyzing power, whereas in addition, the two-body $^3S_1 - {}^3D_1$ tensor force was required in order to provide agreement with the observed tensor analyzing powers.

As a further test of the theoretical predictions, we report on measurements of the polarization of the recoil protons in d-p elastic scattering with incident 45.4 MeV vector polarized deuterons. These $^1H(\vec{d},\vec{p})^2H$ measurements provide determinations of the vector-to-vector polarization transfer coefficient, $K_y^{y'}(\theta)$, defined by the equation[6]

$$P_{y'} = \left(A_{y'} + \frac{3}{2} P_y K_y^{y'}\right)\Big/\left(1 + \frac{3}{2} P_y A_y\right), \quad (1)$$

where P_y is the polarization of the purely vector polarized incident deuteron beam, $P_{y'}$ is the observed polarization of the outgoing (recoil) proton, and A_y and $A_{y'}$ are, respectively, the deuteron vector analyzing power and the proton analyzing power in d-p elastic scattering. The Madison convention[7] is followed in defining the cartesian forms of the polarization and analyzing power, and the y and y' axes are taken along $\vec{k}_d \times \vec{k}_p$. From time-reversal invariance, the same coefficient describes the transfer of vector polarization in the inverse $^2H(\vec{p},\vec{d})^1H$ scattering process at the equivalent proton energy of 22.7 MeV.[6] Thus, our measurements can be compared directly with Pieper's[4] calculated $K_y^{y'}(\theta)$ at that energy.

Our experimental arrangement is shown in Fig. 1. The polarized deuteron beam from the Berkeley 88-inch cyclotron passed through a hydrogen gas target, positioned in a 36-inch diameter scattering chamber. Two silicon polarimeters, described in detail elsewhere,[8] were used to determine the

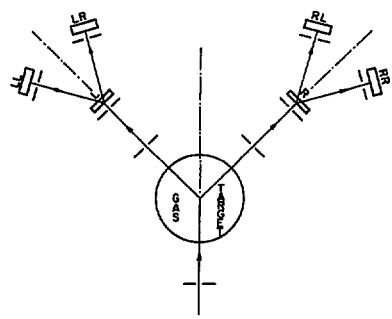

Fig. 1. Schematic diagram of the experimental arrangement, showing the left and right silicon polarimeters. The detectors labeled L and R are the left and right silicon analyzers, respectively. LL, LR, RL, and RR are the silicon side detectors of the polarimeters (XBL 7410-4413)

polarization of the scattered protons. They were positioned at equal scattering angles to the left and right of the beam axis. For each determination of $K_y^{y'}(\theta)$, data were taken with the spin vector of the beam orientated alternately up and down with respect to the scattering plane. The relative yield of elastic doubly-scattered protons into the LL detector of the silicon polarimeter is given by:

$$LL^{\pm} = (1 \mp 3/2\, p_y A_y)(1 + p_{y'} A_2) \quad , \qquad (2)$$

where the (+) and (-) superscripts correspond to the incident beam spin orientation of up and down, respectively, and A_2 is the silicon proton analyzing power in the second scattering.[9] Inserting $p_{y'}$ from Eq. (1),

$$LL^{\pm} = 1 \mp 3/2\, p_y A_y + A_2 A_{y'} \pm 3/2\, A_2 p_y K_y^{y'} \qquad (3)$$

From this and similar expressions for the relative yields $LR^{\pm}$, $RL^{\pm}$, and $RR^{\pm}$ one obtains

$$3/2\, p_y A_2 K_y^{y'} = \frac{(LL^+ - LL^-) - (LR^+ - LR^-)}{LL^+ + LL^- + LR^+ + LR^-} \qquad (4a)$$

$$= \frac{(RR^- - RR^+) - (RL^- - RL^+)}{RR^- + RR^+ + RL^- + RL^+} \qquad (4b)$$

$$= \frac{(LL^+ - RR^+) - (LR^+ - RL^+)}{LL^+ + RR^+ + LR^+ + RL^+} \qquad (4c)$$

$$= \frac{(RR^- - LL^-) - (RL^- - LR^-)}{RR^- + LL^- + RL^- + LR^-} \qquad (4d)$$

First order systematic errors due to instrumental asymmetries and beam misalignments were eliminated by averaging the values of $K_y^{y'}(\theta)$ from Eqs. (4a) and (4b), and similarly from Eqs. (4c) and (4d). The two average values obtained in this way agreed to within ± 0.006 at all angles. The effective proton analyzing power A_2 of the silicon polarimeter was determined with polarized protons elastically scattered from ^{4}He and ^{12}C, for which $K_y^{y'}(\theta) = 1.0$. With p_y known Eq. (4) then results in a value for A_2.

Our experimental results are shown in Fig. 2, where the errors indicated are purely statistical. The solid curve is Pieper's calculation, and it is seen that the agreement with experiment is excellent. Since this constitutes the first significant comparison between experimental and calculated polarization-transfer coefficients in N-d elastic scattering, this agreement represents yet another substantial success of the three-body calculations, particularly in view of the fact that there has been no adjustment of the two-body input parameters in order to fit these data.

Despite the excellent agreement between these experimental and predicted values of $K_y^{y'}(\theta)$, it recently has become clear that further calculations are necessary to address unresolved questions in

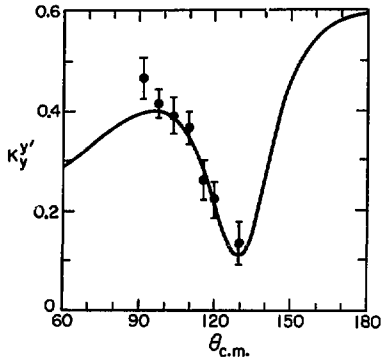

Fig. 2. The vector-to-vector polarization transfer coefficient, $K_y^{y'}(\theta)$, in d-p elastic scattering at E_d = 45.4 MeV. The solid curve is the calculated result from Ref. 4. (XBL 748-3862)

N-d scattering. Pieper compared his perturbative calculation[4] with Doleschall's exact calculation[2] for the same input N-N interactions, and he found that there were significant differences between the two calculations of the nucleon polarization near 23 MeV. In his most recent calculation, Doleschall[3] improved the P-wave and the $^3S_1 - {}^3D_1$ tensor interactions to give better agreement with the N-N phase-shift parameters. This resulted in improved fits to the nucleon and deuteron[10] vector analyzing-power data. An appropriate question, then, is the extent to which such improved N-N interactions would change the calculated values of $K_y^{y'}(\theta)$. As has been suggested,[10,11] an important program now is to specifically examine the sensitivities of the various analyzing-powers and polarization-transfer coefficients to the details of the input two-body interactions.

We are grateful to R. M. Larimer for her assistance during the course of the experiment.

Footnotes and References

*Condensed from publication in Phys. Rev. Letters 33, 1579 (1974).

†Present address: Physics Department, University of Basel, Switzerland.

‡National Research Council of Canada Post Doctoral Fellow.

1. S. C. Pieper, Nucl. Phys. A193, 529 (1973).

2. P. Doleschall, Nucl. Phys. A201, 264 (1973).

3. P. Doleschall, Nucl. Phys. A220, 491 (1974).

4. S. C. Pieper, Phys. Rev. C 8, 1702 (1973).

5. J. S. C. McKee, H. E. Conzett, R. M. Larimer and Ch. Leemann, Phys. Rev. Letters 29, 1613 (1972); A. Fiore, J. Arvieux, Nguyen Van Sen, G. Perrin, F. Merchez, J. C. Gondrand, C. Perrin, J. L. Durand and R. Darves-Blanc, Phys. Rev. C 8, 2019 (1973).

6. G. G. Ohlsen, Rep. Prog. Phys. 35, 717 (1972).

7. Polarization Phenomena in Nuclear Reactions, edited by H. H. Barschall and W. Haeberli (Univ. of Wisconsin Press, Madison, 1971), p. xxv.

8. J. Birchall, H. E. Conzett, W. Dahme, J. Arvieux, F. N. Rad, R. Roy and R. M. Larimer, Nucl. Instr. and Methods 123, 105 (1975).

9. For the spin-up orientation, the negative sign in the first term of Eq. (2), and correspondingly in the denominator of Eq. (1), results from the fact that the incident deuteron is scattered to the right, so p_y is opposite to $\hat{k}_i \times \hat{k}_f$.

10. F. N. Rad, J. Birchall, H. E. Conzett, S. Chintalapudi and R. Roy, Phys. Rev. Letters 33, 1227 (1974).

11. H. E. Conzett, Proc. Int'l. Conf. on Few Body Problems in Nuclear and Particle Physics, Laval University, Quebec, Canada (August 27-31, 1974), in press.

POLARIZATION EFFECTS IN THE NUCLEON-DEUTERON BREAKUP REACTION

H. E. Conzett, F. N. Rad, R. Roy,* and J. Birchall†

The present status of studies of polarization phenomena in the N-d breakup transition to three-nucleon final states is comparable to that which existed for the elastic channel almost ten years ago. That is, only a few experiments have been done which even show the presence of polarization effects, and theoretical interpretation and predictions via exact three-body calculations have not, as yet, been made. Such calculations[1] have been successful in fitting N-d breakup cross sections, but they have so far been limited to S-wave N-N input interactions. It appears that experimental evidence of significant polarization effects in the breakup channel are required in order to encourage, or even compel, the addition of the tensor force and P-wave contributions to these calculations.

Perhaps the first polarization effects seen in the breakup reaction below 100 MeV were those observed by Arvieux et al. in the reaction $D(\vec{p},2p)n$ at 10.5 MeV.[2] Their results are shown in Fig. 1. The open circles are their measurements of the proton analyzing power for the transition to the np final-state-interaction region of the 3-body continuum spectrum, in their case selected to be the region of relative np energies $E_{np} \leq 0.5$ MeV.

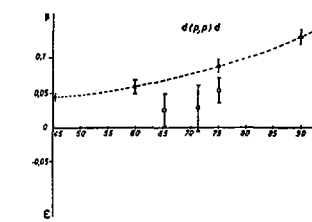

Fig. 1. Open circles: proton analyzing power in the $D(\vec{p},2p)n$ reaction at 10.5 MeV. Solid dots: proton analyzing power in $\vec{p}$-d elastic scattering at 11 MeV. From Ref. 2. (XBL 748-1345)

They noted, for comparison, the similarity of the trend of these data to that of the elastic channel analyzing power at 11 MeV, as shown by the solid dots connected by the dashed line. Recently, Blyth et al.[3] reported an investigation of the deuteron vector analyzing power at several angles in the same reaction $H(\vec{d},2p)n$, but now induced with a beam of 12.2 MeV vector polarized deuterons. Their reported values are all consistent with zero, within errors of ± 0.01 to ± 0.03, but it should be noted that in this case the elastic channel analyzing power at the nearby deuteron energy of 11.5 MeV has a maximum value of less than 0.05.[4] We have very recently obtained some results for the deuteron vector analyzing power in the same inelastic transition at E_d = 45.4 MeV. These are shown in Fig. 2. Again, for comparison, the elastic scattering analyzing power is shown as the smooth curve. Here the similarity between the inelastic and elastic analyzing powers is quite definite. This similarity is

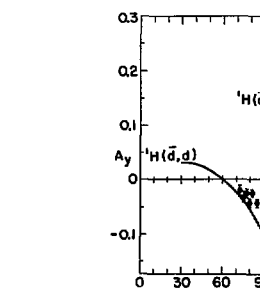

Fig. 2. Deuteron vector analyzing power in the $H(\vec{d},p)np$ reaction at E_d = 45.4 MeV. The c.m. production angle of np pairs with near-zero relative energy is θ_c. The smooth curve represents the $\vec{d}$-p elastic scattering analyzing power. (XBL 748-3890)

rather unexpected in view of the results that were reported by Brückmann et al., in their analysis of cross section data in this reaction at the slightly higher energy E_d = 52.3 MeV.[5] Their findings are displayed in Fig. 3. In their analysis they determined the separate contributions of n-p singlet and triplet pairs to the observed final-state-interaction peak at the relative n-p energy $E_{np} = 0$. These separate contributions are shown in the figure. The solid curve, which is in excellent agreement with the cross section for production of n-p triplet pairs, represents a Born approximation calculation in which the final state n-p wave function used was effectively that of a deuteron with binding energy $E_B \approx 0$. If triplet n-p production were the major contribution to the cross section, we could expect the similarity between inelastic and elastic vector analyzing powers. However, in just the backward angular region of maximum analyzing powers, Fig. 3 shows that the major cross section contribution is the production of n-p singlet pairs. Thus, one is led to the conclusion that the contribution to the inelastic analyzing power from the production of n-p singlet pairs has an angular distribution similar to that of the elastic analyzing power. Since Ebenhöh's three-body calculation[1] quite successfully reproduces the form of the singlet n-p contribution to the cross section shown in Fig. 3, it would be of considerable interest to add to such a calculation the N-N spin dependent interactions that are necessary for the calculation of these analyzing powers.

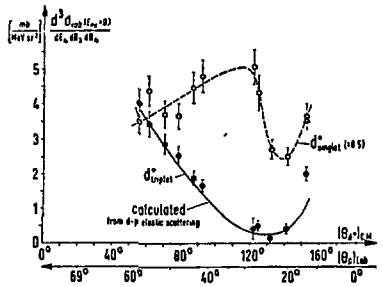

Fig. 3. H(d,2p)n cross sections at E_d = 52.3 MeV, from Ref. 5. (XBL 748-1344)

Footnotes and References

*National Research Council of Canada Post Doctoral Fellow.

†Present address: Physics Department, University of Basel, Switzerland.

1. R. T. Cahill and I. H. Sloan, Nucl. Phys. A165, 161 (1971); W. Ebenhöh, Nucl. Phys. A191, 97 (1972).

2. J. Arvieux, J. L. Durand, J. C. Faivre, D. Garreta, A. Papineau, J. Sura and A. Tarrats, Nucl. Phys. A150, 75 (1970).

3. C. O. Blyth, N. T. Okumasoglu, N. Berovic and J. S. C. McKee, Proc. Int'l. Conf. on Few Body Problems in Nuclear and Particle Physics, Quebec, Canada (August 27-31, 1974), in press.

4. R. E. White et al., Nucl. Phys. A180, 593 (1972).

5. H. Brückmann, W. Kluge, H. Matthäy, L. Schänzler and K. Wick, Nucl. Phys. A157, 209 (1970).

POLARIZATION PHENOMENA IN THE THREE-NUCLEON SYSTEM*

H. E. Conzett

There has been an impressive quantity and quality of polarization data acquired during the past few years on the mass 3 to mass 6 systems, essentially with beams of polarized protons and deuterons. I have chosen, in this paper, to limit the discussion of polarization effects to those of the three-nucleon system. I do this for two reasons: 1) There is now a rather extensive variety of experimental results on this system, and the ever more detailed three-body calculations of these polarization effects have been remarkably successful. Thus, a description of the past developments and present status of this research, in the detail that is warranted by this substantial progress, will take my allotted time. 2) Certainly a central role in this and in the past few-body conferences has been that of the "exact" three-body theory, which calculates the three-nucleon observables from the two-nucleon interaction. Thus, there is, so far, a natural separation between descriptions of three-nucleon data and those of mass 4 and higher. Polarization results are certainly important in the latter systems, but the appropriate theoretical descriptions are generally those of R-matrix analysis, and the direct connection to the nucleon-nucleon force is not made.

The first comparison, some 10 years ago, between the calculated[1] and experimental[2] proton analyzing power in N-d scattering below 100 MeV is shown in Fig. 1. This was at 40 MeV. This impulse-approximation calculation was quite inadequate to explain the data. In fact, the discrepancy between the experimental and the calculated results increased in going to the more complete versions of the calculation. Soon thereafter the early three-nucleon calculations, based on the Faddeev equations with simple S-wave nucleon-nucleon potentials, were very successful in fitting the elastic N-d

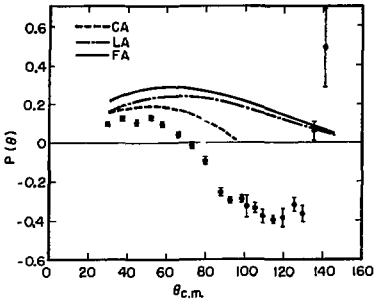

Fig. 1. The proton analyzing power in $\vec{p}$-d elastic scattering at 40 MeV. The experimental data are from Ref. 2, the theoretical curves from Ref. 1. (MUB-2813)

differential cross section data up to about 50 MeV. Since only S-wave forces were used, those calculations could not provide the observed polarizations. There was already a substantial amount of nucleon analyzing-power data up to 50 MeV and a few measurements of the deuteron vector and tensor analyzing powers at lower energies. Only within the past three years have more realistic N-N potentials been used in efforts to fit the polarization data. Aarons and Sloan[3] used a two-body force with separable terms corresponding to both the $^1S_0$ and the coupled $^3S_1 - {}^3D_1$ (tensor) interactions. This calculation gave deuteron tensor polarizations in qualitative agreement with experiment over the range E_N = 3-11 MeV. Soon thereafter Pieper[4] and Doleschall[5] independently included S- and P-wave interactions, and the improvement over the previous calculations of the vector polarizations was dramatic. The nucleon polarizations were in excellent agreement with the experimental data up to 14 MeV, and qualitative agreement was achieved beyond that to 40 MeV. Almost concurrently with these calculations, more precise determinations were made of the deuteron vector analyzing powers at E_d = 20 and 30 MeV,[6] and these were in good agreement with the calculations. These calculations have also provided very good fits to the recently measured tensor analyzing powers.[7]

At this point, then, these three-nucleon calculations had shown very considerable success in fitting the several available N-d elastic scattering observables. Also, it was clear that the polarization data required the use of the more realistic, i.e. more detailed and more complicated, N-N interactions, and thus provided the more sensitive and significant tests of the calculations. The conclusions then were that 1) the N-N P-wave interactions were chiefly responsible for the observed vector polarizations, whereas 2) the $^3S_1 - {}^3D_1$ tensor force was the source of the N-d tensor polarizations.

The stage was now ready for an examination of the *sensitivity* of the calculated N-d observables to changes in the N-N input interactions. Certainly, the first goal of the three-body theory has been to reproduce three-nucleon data with calculations that use two-nucleon forces. Clearly, a second goal is to pursue the possibility of deducing, from N-d scattering and the three-body calculations, information on the N-N interaction which has not been available from N-N scattering itself. Very recent investigations have suggested that this possibility exists. In contrast to the two quite definite conclusions noted above, there have been conflicting opinions concerning the effect of the N-N *tensor* force on the N-d *vector* polarizations. Pieper[8] reported only slight changes with the addition of the tensor force, and he suggested that changes in the $^3S_1 - {}^3D_1$ potential would have little effect on the nucleon polarization. This conjecture was based on Sloan and Aarons result,[9] which demonstrated that none of the N-d polarizations were very sensitive to reasonable changes in the tensor interaction. However, that calculation did not include P-waves, so the vector polarizations were unrealistically small. Doleschall's earlier calculation[5] showed a substantial change in the vector polarizations with the addition of the tensor force to the S- and P-wave interactions, and his most recent calculation[10] demonstrates that the vector polarizations are quite sensitive to the details of the $^3S_1 - {}^3D_1$ potential used. We very recently made measurements[11] at Berkeley of the deuteron vector analyzing power, iT_{11}, in d-p scattering at E_d = 45.4 MeV for direct comparison with the calculated vector polarization at the equivalent nucleon energy of 22.7 MeV. Our data are compared in Fig. 2 with the calculated results for the different N-N interactions. The dotted curve is the result with S- and P-waves plus one

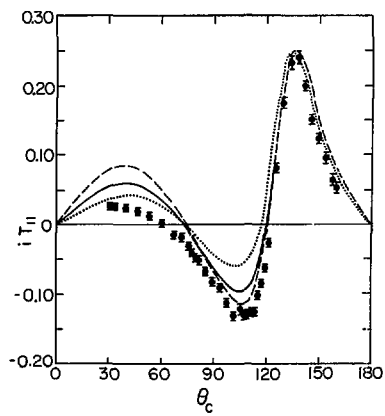

Fig. 2. The deuteron vector analyzing power, $iT_{11}(\theta)$ in d-p elastic scattering at 45.4 MeV. The curves are calculated results from Ref. 10 with different nucleon-nucleon interactions. (XBL 744-2770A)

tensor potential; the dashed line, with another; the solid line, with the addition of the $^3D_2$ terms to the second case. The angular region forward of $\theta_c = 120°$, wherein the remaining discrepancies between experiment and theory exist, is just the region of greatest sensitivity to the details of the $^3S_1 - ^3D_1$ tensor interaction. Clearly, it would be most interesting and useful to do the calculation with a tensor force which simultaneously reproduces the N-N $^3D_1$ phase shift and the mixing parameter ϵ_1.

I must now digress momentarily in order to connect these results with a problem of rather long standing in n-p scattering. MacGregor et al., in their phase shift analyses of n-p data five years ago, found that the $^1P_1$ phase shift $\delta(^1P_1)$ and the mixing parameter ϵ_1 were strongly correlated and poorly determined below 80 MeV.[12] Neither, in fact, was near the theoretical expectation. Arndt, Binstock and Bryan[13] have recently examined this problem in considerable detail near 50 MeV, including in their analyses some more recently available n-p data. They did not find a strong $\epsilon_1 - \delta(^1P_1)$ correlation. Concerning ϵ_1, they show that the present n-p data (σ_{TOT}, $d\sigma/d\Omega$, $P(\theta)$) near 50 MeV leave ϵ_1 undetermined between -10° to +3°. They also examine the sensitivity of other experimental observables to ϵ_1, and they find that the neutron-to-proton polarization transfer coefficient D_t combines fairly high sensitivity with reasonable experimental feasibility. With the assumed ± 0.01 absolute error on D_t, be assured that such an experiment, if reasonable, is difficult.

Let us return now to the three-nucleon calculation. In view of the demonstrated sensitivity of the vector polarizations to the N-N tensor interaction, it should be possible, with a tensor force which simultaneously reproduces the N-N $\delta(^3D_1)$ and ϵ_1, to vary ϵ_1 in a search for improved fits to the N-d vector analyzing power data. It seems possible that this procedure could more easily provide a better determination of the low energy values of ϵ_1 than is possible via the more difficult measurement of D_t. If this should prove to be so, one would indeed have deduced from the three-nucleon investigations specific information about the two-nucleon interaction that has not yet been attainable.

We have noted the considerable progress that has been made during the past two years in both the experimental and theoretical determinations of polarization observables in N-d elastic scattering. It seems to me that an important undertaking now is to specifically examine the sensitivities of the various analyzing powers and transfer coefficients to the details of the input two-body interactions; for example, sensitivity to variations of $\delta(^1P_1)$ and ϵ_1, and to the addition of a complete set of D-wave interactions in the exact calculation. This would provide invaluable guidance in the choice of further experiments, since it is clear that many of the polarization observables can now be measured to just about whatever accuracy is required for specific and detailed comparison with predictions.

Footnotes and References

*Excerpted from LBL-2995, Invited Paper, Proc. Int'l. Conf. on Few Body Problems in Nuclear and Particle Physics, Quebec, Canada (August 27-31, 1974), in press.

1. K. L. Kowalski and D. Feldman, Phys. Rev. 130, 276 (1963).

2. H. E. Conzett, H. S. Goldberg, E. Shield, R. J. Slobodrian and S. Yamabe, Phys. Lett. 11, 68 (1964).

3. J. C. Aarons and I. H. Sloan, Nucl. Phys. A182, 369 (1972).

4. S. C. Pieper, Nucl. Phys. A193, 529 (1972).

5. P. Doleschall, Nucl. Phys. A201, 264 (1973).

6. J. S. C. McKee, H. E. Conzett, R. M. Larimer and Ch. Leemann, Phys. Rev. Lett. 29, 1613 (1972).

7. A. Fiore, J. Arvieux, Nguyen Van Sen, G. Perrin, F. Merchez, J. C. Gondrand, C. Perrin, J. L. Durand and R. Darves-Blanc, Phys. Rev. C 8, 2019 (1973).

8. S. C. Pieper, Phys. Rev. C 6, 1157 (1972).

9. I. H. Sloan and J. C. Aarons, Nucl. Phys. A198, 321 (1972).

10. P. Doleschall, Nucl. Phys. A220, 491 (1974).

11. F. N. Rad, J. Birchall, H. E. Conzett, S. Chintalapudi and R. Roy, Phys. Rev. Lett. 33, 1227 (1974).

12. M. H. MacGregor, R. A. Arndt and R. M. Wright, Phys. Rev. 182, 956 (1969).

13. R. A. Arndt, J. Binstock and R. Bryan, Phys. Rev. D 8, 1397 (1973); J. Binstock and R. Bryan, Phys. Rev. D 9, 2528 (1974).

FINAL STATE INTERACTION IN THREE NUCLEON SYSTEM*

F. N. Rad, D. P. Saylor,† and Mahavir Jain‡

The dynamics of three-nucleon system, as well as the interaction between the particles on and off the energy shell can be studied by the processes leading to three nucleons in the final state. There are several approximate descriptions of the three-nucleon breakup process which are often used. Each is useful in providing an understanding of and insight into the qualitative features of the breakup process in a limited part of phase space. The final state interaction (FSI) mechanism is appropriate for understanding that part of the breakup spectrum in which one of the three outgoing pairs of nucleons has a low relative energy. Typically, the cross sections are enhanced. The FSI theory of Watson and Migdal is often used to describe these enhancements. Theoretical calculations[1] based on separable S-wave potentials give results in good agreement with the Watson-Migdal form of the final state peak. These calculations also predict a rather complex angular dependence of the FSI which may prove to be sensitive to the energy shell behavior assumed in the model.

Several attempts[2-5] have been made to estimate the size of model dependent effects in N-d breakup reactions. The recent results of Brayshaw[4] and of Haftel and Peterson[5] (HP) are of particular interest because these estimates were based on comparison of models which gave identical on-shell two-nucleon scattering. For $E_{cm} \leq 20$ MeV Brayshaw and HP have found that significant model dependent variations were restricted to three-body ^{2}S-waves. They also found that if it is required that the N-d doublet scattering length, a_2, is held fixed the remaining variability is much reduced. Brayshaw believes that his analysis indicates that the two nucleon observables and a_2 determine the low energy trinucleon reactions to high precision for any plausible interaction. It would be significant if this expectation were to be experimentally verified. The conclusions of HP are different from that of Brayshaw while they provide a basis for selecting experiments. HP have found substantial variability in the ^{2}S partial wave even with a fixed doublet scattering length. The sensitive region is concentrated where singlet FSI dominates. The variability in the amplitudes results in variations of the FSI angular distributions and spectra which are of sufficient magnitude to be significant experimentally. In regard to these HP expectations the experiment and analysis of Brückman et al.[6] (BKMSW) should be particularly valuable. They found that the breakup cross section in the np FSI region could be fitted very accurately by

$$\frac{d\sigma}{dS d\Omega_3 d\Omega_4} = \left[X^s_{np} F^s_{np} + X^t_{np} F^t_{np} \right] \rho_s ,$$

where F^s_{np} and F^t_{np} are the singlet and triplet Watson-Migdal enhancement factors. Empirically BKMSW have found that the triplet FSI angular distribution, $X^t_{np}(\theta_3)$, was the same as the experimental d-p elastic angular distribution and that the magnitude of the triplet FSI cross section could be successfully related to the elastic cross section. Their application of the Watson-Migdal analysis shows internal consistency with the np low-energy parameters. Other experiments which should be particularly valuable in isolating the np singlet FSI are the measurements of the vector to vector spin transfer parameters $K_y^{y'}$ in ^{1}H($\vec{d},\vec{p}$) and ^{2}H($\vec{p},\vec{p}$) for slightly inelastic p-d scattering. These experiments when combined with kinematically incomplete cross section measurements should allow one to extract $X^s_{np}(\theta_3)$. Assuming the validity of the Watson-Migdal analysis,

$$K_y^{y'} = \frac{{}^sK_y^{y'} X^s_{np} F^s_{np} + {}^tK_y^{y'} X^t_{np} F^t_{np}}{X^s_{np} F^s_{np} + X^t_{np} F^t_{np}}$$

where ${}^sK_y^{y'}$ and ${}^tK_y^{y'}$ are the spin-transfer parameters for the singlet and triplet components respectively. Using the simplified structure of the breakup amplitudes,[7] characteristic of the Amado model, it is easy to show that

$${}^sK_y^{y'} = 1 \quad \text{for} \quad {}^1\text{H}(\vec{d},\vec{p}), \text{ and } {}^1\text{H}(\vec{d},\vec{n})$$

$${}^sK_y^{y'} = -\frac{1}{3} \quad \text{for} \quad {}^2\text{H}(\vec{p},\vec{p}), \text{ and } {}^2\text{H}(\vec{p},\vec{n})$$

${}^tK_y^{y'}$ will depend on angle and energy but an implication of BKMSW is that ${}^tK_y^{y'}$ is nearly the same as the $K_y^{y'}$ parameters for elastic scattering. However in terms of the breakup amplitudes[7]

$${}^tK_y^{y'} = \frac{\frac{5}{2}|q|^2 - \frac{1}{12}|d_1|^2 - \frac{1}{4}|d_2|^2 - \frac{2}{3}\,\text{Re}\,q^* d_1 + \sqrt{\frac{4}{3}}\,\text{Re}\,q^* d_2 + \sqrt{\frac{1}{12}}\,\text{Re}\,d_1^* d_2}{2|q|^2 + \frac{1}{4}|d_1|^2 + \frac{3}{4}|d_2|^2 - \sqrt{\frac{3}{4}}\,\text{Re}\,d_1^* d_2} \quad \text{for } {}^1\text{H})\vec{d},\vec{p})$$

$${}^tK_y^{y'} = \frac{\frac{1}{9}|q|^2 + \frac{1}{36}|d_1|^2 + \frac{1}{12}|d_2|^2 + \frac{8}{9}\,\text{Re}\,q^* d_1 - \sqrt{\frac{64}{27}}\,\text{Re}\,q^* d_2 - \sqrt{\frac{1}{108}}\,\text{Re}\,d_1^* d_2}{3|q|^2 + \frac{1}{4}|d_1|^2 + \frac{3}{4}|d_2|^2 - \sqrt{\frac{3}{4}}\,\text{Re}\,d_1^* d_2} \quad \text{for } {}^2\text{H}(\vec{p},\vec{p})$$

where q is the amplitude for breakup in the quartet state (S = 3/2), and d_1 and d_2 are the doublet-state (S = 1/2) amplitudes in which the two identical nucleons are coupled to spin 1 or 0, respectively.

To a first approximation the slightly inelastic K_y' parameters can be computed on the basis of a decomposition of the breakup cross section similar to that of BKMSW and a measurement of the corresponding K_y' for elastic scattering. Thus a measurement of the K_y' parameters have additional interest in that they provide additional checks of the final state interaction theory. We are currently working on the theoretical predictions using a computer code which solves the three particle Faddeev equation for separable spin dependent S-wave nucleon nucleon interactions.[8]

Footnotes and References

*To be published in Proceedings of the Int'l. Conf. on Few Body Problems in Nuclear and Particle Physics, Quebec, Canada (27-31 August 1974).

†Physics Department, Worcester Polytechnic Institute, Worcester, Mass. 01609

‡Guest Scientist, Los Alamos Scientific Laboratory, University of Caliornia, Los Alamos, New Mexico 87544

1. R. T. Cahill and I. H. Sloan, Nucl. Phys. A165, 161 (1971); W. Ebenhöh, Proc. of the Int'l. Conf. on Few Particle Problems in the Nuclear Interactions, Los Angeles, California (1972) edited by Slaus et al. (North-Holland, Amsterdam, 1972), pp. 325-328.

2. W. M. Kloet and J. A. Tjon, Nucl. Phys. A210, 380 (1973).

3. Mahavir Jain, J. G. Roger and D. P. Saylor, Phys. Rev. Letters 31, 838 (1973).

4. D. D. Brayshaw, Phys. Rev. Letters 32, 382 (1974).

5. M. I. Haftel and E. L. Peterson, Bull. Am. Phys. Soc. 19, 505 (1974).

6. H. Brückman, W. Kluge, H. Mattäy, L. Schänzler and K. Wick, Nucl. Phys. A157, 209 (1970).

7. D. P. Saylor and F. N. Rad, Phys. Rev. C 8, 507 (1973).

8. Mahavir Jain and G. D. Doolen, Phys. Rev. C 8, 124 (1973).

POLARIZATION-ANALYZING POWER THEOREM FOR (p,n) TRANSITIONS BETWEEN MEMBERS OF AN ISOSPIN MULTIPLET*

H. E. Conzett

In a recent paper, Rohrer and Brown[1] reported measurements of the proton analyzing power, A(E,θ), in the ^{7}Li($\vec{p}$,n)^{7}Be reaction between E = 2.05 and 3.00 MeV. Their comparison with existing data[2] on the neutron polarization, P(E,θ), induced in the same reaction ^{7}Li(p,$\vec{n}$)^{7}Be with unpolarized protons, showed a near equality between P(E,θ) and A(E,θ). They suggested that the simplicity of this result indicated a simple explanation, which would have the further useful purpose of providing a means of optimizing the figure of merit, $P^2\sigma$, when using this reaction as a source of polarized neutrons at angles where no neutron polarization measurements exist, but for which A(θ) had been determined.

The purpose of this report is to provide the expected simple explanation for the near equality of P and A, which, in fact, applies to all (p,n) reactions that connect states that are members of an isospin doublet. The result follows from time reversal invariance and charge-symmetry of the interactions responsible for the reaction. Specifically, consider the reaction B(p,n)B' between nuclear states B and B'. The polarization-analyzing power† theorem for reciprocal or time-reversed reactions[4] provides that

$$P(E,\theta) \text{ in } B(p,\vec{n})B' \quad \text{is equal to} \quad A(E,\theta) \text{ in } B'(\vec{n},p)B \ . \tag{1}$$

Also, in the restricted case that B and B' are members of an isospin doublet (mirror states), charge-symmetry provides that

$$A(E,\theta) \text{ in } B'(\vec{n},p)B \quad \text{is equal to} \quad A(E,\theta) \text{ in } B(\vec{p},n)B' \ . \tag{2}$$

Therefore,

$$P(E,\theta) = A(E,\theta) \tag{3}$$

in the B(p,n)B' reaction. It is seen that this result follows from the fact that the inverse to the (p,n) reaction between members of an isospin doublet is, also, its charge-symmetric reaction. This argument can be extended to include a larger group of (p,n) reactions by imposing isospin conservation. The condition (2) then applies when B and B' are adjacent members of any isospin multiplet. Thus, the result (3) includes transitions between any two members, B and B', of an isospin multiplet that can be connected by the (p,n) or (n,p) reaction, i.e., for a $\Delta T_z = 1$ transition.

The exact equality (3) holds, of course, only under conditions of exact charge-symmetry or exact isospin conservation for the particular transition

considered. Since the weaker assumption of charge-symmetry is known to be better than that of charge independence in the nucleon-nucleon interaction, it is expected that (3) will be more nearly satisfied when B and B' are members of a doublet rather than members of a larger isospin multiplet.

Two examples of $P(E,\theta)$ and $A(E,\theta)$ measurements in (p,n) transitions between states which form an isospin doublet are the quoted ^{7}Li(p,n)^{7}Be data and the results from the ^{3}H(p,n)^{3}He reaction.[5] No such data seem to exist for transitions between members of a larger multiplet. The ^{7}Li(p,n)^{7}Be data indicate a possible deviation from the equality (3) at energies near 2.3 MeV, and the ^{3}H(p,n)^{3}He data show about a 17% relative difference between P and A in the energy range from 1.7 to 4.0 MeV. These deviations are not unexpected, since the Coulomb interaction breaks the exact charge symmetry between the states B and B'. That is, the radial wave function describing the neutron bound in B may be somewhat different from that of the proton bound in B', so the condition (2) is not exact; hence, the equality (3) is not exact. This circumstance might be considered a disadvantage. On the contrary, it offers the promise of a means to determine, for example, just such differences in nucleon bound state wave functions as are caused by the Coulomb interaction. Calculations should seek to explain the observed deviations from the P = A equality in terms of the Coulomb effect in breaking the exact charge-symmetry between the mirror states involved.

It should be noted that Ref. 5 presented a plausibility argument for P = A in the ^{3}H(p,n)^{3}He reaction based on P = A for elastic scattering and the quasi-elastic nature of the ^{3}H(p,n)^{3}He reaction.

Footnotes and References

*Published in Phys. Letters 51B, 4.5 (1974).

†We follow the Madison convention (Ref. 3) in the use of "analyzing power" rather than the less specific term "asymmetry".

1. U. Rohrer and L. Brown, Nucl. Phys. A217, 525 (1973).

2. A. J. Elwyn and R. O. Lane, Nucl. Phys. 31, 78 (1962); S. T. Thornton, C. L. Marris, J. R. Smith and R. P. Fogel, Nucl. Phys. A169, 131 (1971).

3. Polarization Phenomena in Nuclear Reactions, ed. by H. H. Barschall and W. Haeberli (Univ. of Wisconsin Press, Madison, 1971), p. xxv.

4. R. J. Blin-Stoyle, Proc. Phys. Soc. A65, 452 (1952); G. R. Satchler, Nucl. Phys. 8, 65 (1958).

5. R. C. Haight, J. J. Jarmer, J. E. Simmons and J. C. Martin, Phys. Rev. Letters 28, 1587 (1972); and references therein.

DEPOLARIZATION AND THE SPIN-SPIN INTERACTION IN p + ^{9}Be ELASTIC SCATTERING*

J. Birchall,† H. E. Conzett, J. Arvieux,‡ W. Dahme, R. M. Latimer

We report on definite evidence for the existence of a spin-spin term in the nucleon-nucleus optical model potential, which was first suggested by Feshbach.[1] For a nucleon of spin $\vec{\sigma}/2$ scattering from a nucleus of spin $\vec{I}$, both a spherically symmetric spin-spin term,

$$U_{SS}(r) = -V_{SS}\, F_0(r)\, \vec{\sigma} \cdot \vec{I} \quad , \qquad (1)$$

and a tensor term,[2] analogous to the classical potential between two magnetic dipoles

$$U_{ST}(r) = -V_{ST} F_T(r) \left[3(\vec{\sigma} \cdot \hat{r})(\vec{I} \cdot \hat{r}) - \vec{\sigma} \cdot \vec{I}\right]/2 \qquad (2)$$

may be present.

Several investigations have been made of the spin dependence of total cross sections of polarized neutrons on polarized ^{165}Ho and ^{59}Co in attempts to determine the strength of V_{SS} of the spherical interaction (1). The ^{59}Co results, summarized by Fisher et al.,[3] showed the larger effects. However, the information obtained on V_{SS} was ambiguous because the calculation, which followed the treatment of Davies and Satchler,[4] was unable to reproduce the energy dependence of the data from 0.3 to 8 MeV.

The presence of spin-spin effects can also be detected by measurements of the depolarization parameter D,[5] which has the value 1.0 for direct elastic scattering in the absence of a spin-spin interaction. Thus, deviations of D from unity can be evidence for the existence of such an effect. Batty and Tschalär[6] and Beurtey et al.[7] have measured D in the scattering of 50 and 20 MeV protons, respectively, from nuclei. Only the latter results showed values of D differing significantly from unity, but these measurements were for a single scattering angle.

In recent calculations Sherif and Hussein[8] have included both the spherical (1) and tensor (2) spin-spin terms in the optical potential. The depolarizations calculated with the spherical term alone were consistently different from the experimental values near 20 MeV, suggesting that contributions from the tensor term were important. These calculations showed that angular distributions of D were needed to determine the strength of the tensor interaction. They also showed that the

D-parameter was the elastic scattering observable most sensitive to the spin-spin interaction.

We have measured D at several angles in the elastic scattering of 25 MeV polarized protons from ^{9}Be. With an incident beam of polarization p_o, the polarization p_1 of the scattered protons is given by

$$p_1(\theta) = \left[A_1(\theta) + D(\theta)p_o\right]/\left[1 + p_o A_1(\theta)\right], \quad (3)$$

where $A_1(\theta)$ is the analyzing power of ^{9}Be. Both measured polarizations are perpendicular to the scattering plane and positive along the direction $\vec{k}_i \times \vec{k}_f$. The ^{9}Be target was approximately 1 MeV thick. The polarization $p_1(\theta)$ of the scattered protons was measured with a high efficiency, good resolution silicon polarimeter. It consisted of an analyzer in the form of a silicon detector and two side detectors positioned at left and right scattering angles of 27°. The analyzer detector was 1 mm thick, giving good scattering efficiency to the side detectors. The detectors in each combination of analyzer and side detector were operated in coincidence as a ΔE-E telescope, ensuring good intrinsic energy resolution and reduction of background. Thus, even though the analyzer was some 4.5 MeV thick to 23 MeV protons, resolution of 260-270 keV resolution was achieved in the polarimeter spectra at analyzer detector counting rates near 10^5/sec. The polarimeter was calibrated with protons of known polarization elastically scattered from ^{12}C. In the scattering from a spin-zero nucleus D has the value 1.0; so, with p_o and A_1 measured, p_1 is determined from eq. (3). The measured left-right asymmetry then determines the analyzing power of the polarimeter.

Our results are shown in Fig. 1. Deviations of D from unity are small but significant. The solid and dashed curves represent calculations by Sherif.[9] Both the depth, V_{SS} = 0.1 MeV, and a Woods-Saxon form for $F_o(r)$ were fixed from single-particle model estimates. For the tensor form, a Woods-Saxon form was taken for $F_T(r)$, and the depth V_{ST} was determined by fitting the single data point D(63.5°) = 1.040 ± 0.016 at 21.4 MeV. As

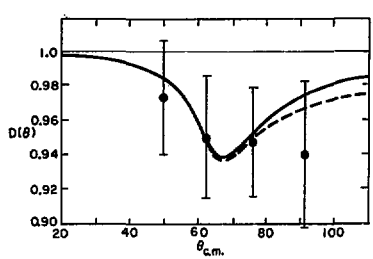

Fig. 1. Angular distribution of the D-parameter for p-^{9}Be elastic scattering at 25 MeV. The curves are calculated values from Ref. 9, the solid curve with V_{SS} = 0.1 MeV, V_{ST} = -3.75 MeV and the dashed curve with V_{SS} = 0.1 MeV, V_{ST} = +3.8 MeV.
(XBL 7410-4476)

seen in Fig. 1, these calculations at 25 MeV, with the same values of V_{SS} and V_{ST} that were used at 21.4 MeV, provide good fits to our data for either sign of V_{ST}. At 21.4 MeV the predicted[8] value of D(63.5°) was 1.0 for V_{ST} = 0, so these data clearly indicate the need for the tensor interaction term in the calculation. As was noted by Hussein and Sherif,[8] the magnitude of V_{ST} is much greater than expected, since Satchler's[10] estimate for ^{59}Co predicts the tensor strength to be weaker than that of the spherical interaction. It remains to be seen whether some other effect can explain the apparently large tensor strength.

The calculated results displayed in Fig. 1 show relatively little sensitivity to the sign of V_{ST}. However, the calculated D-parameter values in p-^{10}B scattering show much more sensitivity, so measurements there can provide more definite and detailed information on the spin-spin tensor interaction. We have recently made measurements[11] to compare with the p-^{10}B predictions, and these results and their analysis will be reported in forthcoming publication.

We are most grateful to W. Haeberli for his considerable contributions to the planning and the early stages of the experiment, and to H. S. Sherif for providing the calculated results at 25 MeV.

Footnotes and References

*Condensed from publication in Phys. Letters B53, 165 (1974).

†Present address: Physics Department, University of Basel, Switzerland.

‡Present address: Institute of Nuclear Science, University of Grenoble, France

§Present address: Physics Department, University of Munich, Garching, Germany.

1. H. Feshbach, Nuclear Spectroscopy, Part B, ed. by F. Ajzenberg-Selove (Academic Press, New York, 1960), p. 1033.

2. G. R. Satchler, Phys. Letters 34B, 37 (1971).

3. T. R. Fisher, H. A. Grench, D. C. Healey, J. S. McCarthy, D. Parks and R. Whitney, Nucl. Phys. A179, 241 (1972).

4. K. T. R. Davies and G. R. Satchler, Nucl. Phys. 53, 1 (1964).

5. L. Wolfenstein, Ann. Rev. Nucl. Sci. 6, 43 (1956).

6. C. J. Batty and C. Tschalär, Nucl. Phys. A143, 151 (1970).

7. R. Beurtey, P. Catillon and P. Schnabel, J. de Phys. 31 Suppl. C2, 96 (1970); P. Catillon, Polarization Phenomena in Nuclear Reactions, ed. by H. H. Barschall and W. Haeberli (Univ. of Wisconsin Press, Madison, 1971), p. 657.

8. H. S. Sherif and A. H. Hussein, Phys. Letters 41B, 465 (1972); A. H. Hussein and H. S. Sherif, Phys. Rev. C 8, 518 (1973).

9. H. S. Sherif, private communication

10. G. R. Satchler, Particles and Nuclei 1, 397 (1971).

11. J. Birchall, H. E. Conzett, F. N. Rad, S. Chintalapudi and R. M. Larimer, Bull. Am. Phys. Soc. 19, 477 (1974).

TWO PROTON TRANSFER ON ^{54}Fe STUDIED WITH HIGH ENERGY HEAVY ION REACTIONS (^{16}O, ^{14}C) AND (^{12}C, ^{10}Be)

H. Homeyer,* F. D. Becchetti,† B. G. Harvey, D. L. Hendrie, D. G. Kovar,‡ J. Mahoney and W. von Oertzen*

Two nucleon transfer reactions into ^{56}Ni have been studied by various groups using the ^{54}Fe(^{3}He,n)^{56}Ni [1-3] and the ^{58}Ni(p,t)^{56}Ni [4-7] reactions in order to determine energies and J^{π} values of the excited levels and to test nuclear models, especially the pairing vibrational model. In light ion reactions L = 0 and L = 2 transfers show up very strongly whereas higher angular momentum transfers are suppressed due to kinematic reasons and the J^{π} assignments for the respective levels are sometimes doubtful. The heavy ion reactions that should preferentially excite higher spin states have so far been greatly restricted by Q-window effects at low bombarding energy[8] or by poor energy resolution.[9]

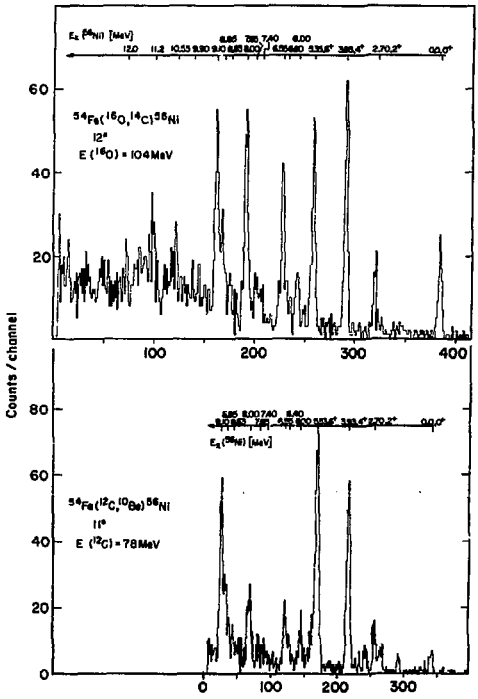

Fig. 1. Energy spectra of ^{54}Fe(^{16}O, ^{14}C)^{56}Ni, E(^{16}O) = 104 MeV and (^{12}C, ^{10}Be), E(^{12}C) = 78 MeV at 12° and 11° respectively. (XBL 7412-8353)

We report here high energy two proton transfer on ^{54}Fe using the reactions (^{16}O,^{14}C) at E_{16_O} = 104 MeV and (^{12}C,^{10}Be) at E_{12_C} = 78 MeV. Reaction products were analyzed in the focal plane of a dispersion matched magnetic spectrometer.[10] Position, time of flight (TOF), and specific energy loss (dE/dx) for each event were measured to allow complete particle separation for all reaction products considered. Details of the experimental setup are described in Ref. 11 and references therein. For the (^{16}O,^{14}C) reaction improved versions[12] of the dE/dx and TOF detectors were used.

Targets consisted of self-supporting isotopically enriched ^{54}Fe foils of ∿ 150 μg thickness. The energy resolution obtained was (90 - 150) keV for the (^{12}C,^{10}Be) reaction and (120 - 180) keV for (^{16}O,^{14}C), mainly due to target thickness. Energy calibration was performed relative to the elastically scattered particles swept across the focal plane by varying the magnetic field. This procedure reproduced the position of the ground state within 100 keV. The energies of the excited states were then taken relative to the ground state transition and were consistent to within 20 to 50 keV at all angles, depending only on the statistics of the levels.

Energy spectra of the reactions for (^{16}O, ^{14}C) and (^{12}C,^{10}Be) are shown in Fig. 1. The same levels or groups of levels are selectively excited in both heavy ion reactions up to 9 MeV excitation energy in ^{56}Ni. The relative intensities of the states, however, turn out to be considerably different in the two reactions. At some angles increased background at energies where excited ^{10}Be (2^+ at 3.37 MeV) or ^{14}C (6.09 MeV, 1^-, 6.59 MeV, 0^+) are expected was observed.

Fig. 2 shows the angular distributions of the ground state and the first three excited states in ^{56}Ni for the (^{16}O,^{14}C) reaction. They show a very pronounced L-dependence similar to those found in a recent (^{16}O,^{14}C) study on ^{40}Ca.[13]

Fig. 3 compares the integrated cross sections (integrated from 8° to 15° for (^{16}O,^{14}C) and 13° to 25° for (^{12}C,^{10}Be)) for the two heavy ion reactions with peak cross sections (0° for L = 0 and 20° for L = 2) obtained in (^{3}He,n) at E = 13 MeV[2] and a recent high resolution ^{58}Ni(p,t)^{56}Ni study[7] (peak cross sections). For the (p,t) reaction only those states are listed that had spin assignments. The density of levels populated by (p,t) above E_x = 6 MeV is so high that one can always find one state that lines up with one seen in the heavy ion reactions. Though at first glance it seems that the heavy ion reactions populate more or less the same states as (^{3}He,n), this is true only for the ground state and the first excited 2^+ state. Since the structure factors are the same for the three different two proton transfer reactions within a factor of 2,[11,14] it is mainly the kinematics that cause selective excitation of different levels in the respective reactions (see next section). In ^{58}Ni(p,t)^{56}Ni a $4^+/0^+$ doublet is found at 3.92/3.95 MeV. Comparing angular distributions and strength relative to the ground state transition it is immediately clear that we see the 4^+ state and (^{3}He,n) the 0^+, and L = 4 being highly suppressed

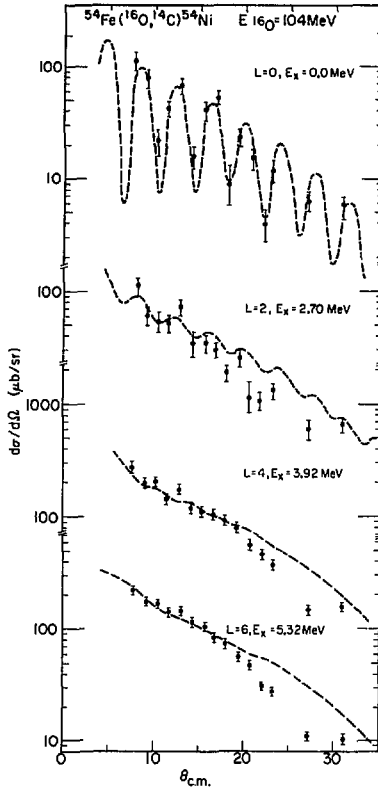

Fig. 2. Angular distributions for the ground state and the first three low lying states of ^{56}Ni from the (^{16}O,^{14}C) reaction. (XBL 7412-8355)

in (^{3}He,n) at 13 MeV incident energy. The same argument holds for the $6^+/2^+$ doublet at 5.34/5.35 MeV. Comparing intensities of neighboring states together with spins and L-values found in (p,t) and (^{3}He,n) leads to the assumption that all states above E_x = 6 MeV excited in the heavy ion reactions have spins larger than 3. Without going into details, two examples may be mentioned: In both (p,t) and (^{3}He,n) a 3^- state is found at E_x = 7.56 MeV. There is no evidence that we see a state at that energy, so the neighboring states at 7.4 and 7.6 MeV should not be the 0^+ and 2^+ seen in (^{3}He,n). Strong L = 2 transitions were observed in (^{3}He,n) at 9.4 and 10.8 MeV. We see no evidence for these states in the heavy ion spectra.

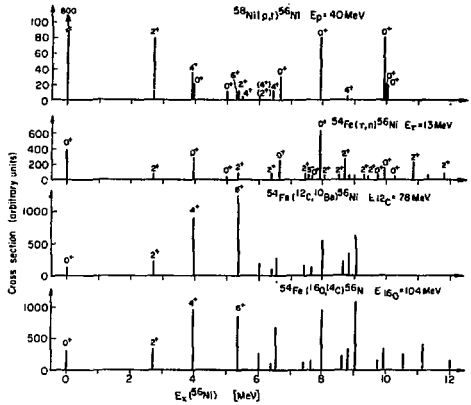

Fig. 3. Comparison of cross sections for two nucleon transfer reactions into Ni:
a) ^{58}Ni(p,t)^{56}Ni (peak cross sections)[7]
b) ^{54}Fe(^{3}He,n^{56}Ni (peak cross sections 0° for 0$^+$ and 20° for 2$^+$ and 3$^-$ states)
c) ^{56}Fe(^{16}O,^{14}C)^{56}Ni (integrated 8° - 15°)
d) ^{54}Fe(^{12}C,^{10}Be)^{56}Ni integrated 13° - 25°) (XBL 7412-8352)

Calculations were performed with the DWBA code BRUNHILD[15] taking recoil effects into account. The optical model parameters were chosen to fit the elastic cross section and the transfer to the low lying states reasonably well, and were: V = 100 MeV, W = 30 MeV, $r_{ov} = r_{ow} = 1.15$ fm, $a_v = a_w = .55$ fm. The form factor for the two proton transfer was constructed assuming the transfer of a two proton cluster in a relative s-state. The fits reproduce the experimental distributions fairly well for both reactions. Sample fits to the (^{16}O, ^{14}C) reaction are displayed with the data in Fig. 2.

The relative spectroscopic feature for the low lying states normalized to 1.0 for the transition to the 6$^+$ state at 5.3 MeV agree approximately with the errors for both heavy ion reactions and are also consistent with the 0$^+$ gs to 2$^+$, 2.7 MeV ratio extracted from (^{3}He,n). This indicates that the DWBA calculations account for the dominant kinematic effects involved in the different types of reactions, at least for the low excitation region.

Based on the empirical systematics and the DWBA results, we propose the J^π values for the excitation energies seen in Fig. 4. Comparison is made, where available, with the shell model calculations of Jaffrin.[16] It remains to make a

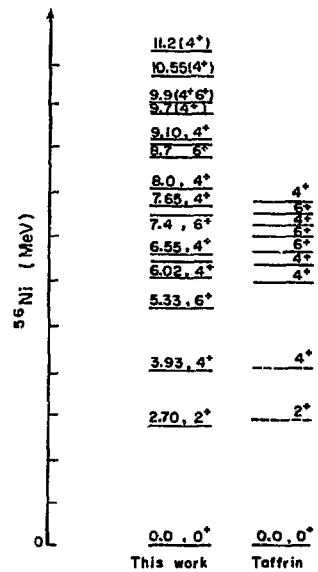

Fig. 4. Comparison of the experimental results of this experiment (energies and spins) with predicted shell model states of the study of Jaffrin.[22] (XBL 757-3436)

detailed comparison between theory and the full range of experimental results.

Footnotes and References

*Present address: Hahn-Meitner Institut, Berlin, Germany.

†Present address: University of Michigan, Ann Arbor, Michigan.

‡Present address: Argonne National Laboratory, Argonne, Illinois.

*Present address: Hahn-Meitner Institut, Berlin, Germany.

1. D. Evers, W. Assmann, K. Rudolph, S. J. Skorka, and P. Sperr, Nucl. Ph.. A198, 268 (1972).

2. H. Fuchs, K. Grabisch, D. Hilscher, U. Jahnke, H. Kluge, T. G. Masterson and H. Morgenstern, Phys. Lett. 49B, 447 (1974).

3. R. P. J. Winsborrow and B. E. F. Macefield, Nucl. Phys. A182, 481 (1972).

4. W. P. Alford, R. A. Lindgren and D. Elmore, Phys. Lett. 42B, 60 (1972).

5. W. G. Davies, J. E. Kitching, W. McLatchie, D. G. Montague, K. Ramavataram and N. S. Chant, Phys. Lett. 27B, 363 (1968).

6. G. Bruge and R. F. Leonard, Phys. Rev. C2, 220 (1970).

7. H. Nann and W. Benenson, Report MSUCL-136 (1974), to be published.

8. P. R. Christenson, V. I. Manko, F. D. Becchetti, and R. J. Nickles, Nucl. Phys. A207, 33 (1973).

9. F. Pougheon, P. Roussel, P. Colombani, H. Doubre and J. C. Roynette, Nucl. Phys. A193, 305 (1972).

10. B. G. Harvey, J. Mahoney, F. G. Pülhofer, F. S. Goulding, D. A. Landis, J. C. Faivre, D. G. Kovar, M. S. Zisman, J. R. Meriwether, S. W. Cosper and D. L. Hendrie, Nucl. Instr. and Meth. 104, 21 (1972).

11. F. D. Becchetti, D. G. Kovar, B. G. Harvey, D. L. Hendrie, H. Homeyer, J. Mahoney, W. von Oertzen and N. K. Glendenning, Phys. Rev. C9, 1543 (1974).

12. H. Homeyer, J. Mahoney and B. G. Harvey, Nucl. Instr. and Meth. 118, 311 (1974).

13. W. Henning, D. G. Kovar, B. Zeidman, and J. R. Erskine, Phys. Rev. Lett. 32, 1015 (1974).

14. B. Sørensen, Phys. Lett 53B, 285 (1974).

15. P. Braun-Munzinger, H. L. Harney and Wenneis, to be published.

16. A. Jaffrin, Phys. Lett. 32B, 6 (1970).

STUDY OF THE ^{142}Nd(^{18}O, ^{16}O) ^{144}Nd REACTION

K. Yagi,* B. Harvey, D. Hendrie, U. Jahnke,† C. Maguire, J. Mahoney and D. Scott

Two neutron pickup and stripping reactions, (p,t) and (t,p), on various rare earth nuclei have yielded very dissimilar excitation strengths for populating low-lying 2^+ excited states.[1] Recently it has been proposed that these results could be explained in the framework of the quadrupole pairing vibrational model.[2] A consequence of the theory is that two neutron stripping reactions on nuclei with neutron number N≥82 should strongly excite the lowest lying 2^+ residual state.

The heavy ion two neutron stripping reaction, ^{142}Nd(^{18}O,^{16}O)^{144}Nd, was studied at 99.2 MeV incident energy. The ^{16}O products were momentum analyzed in a magnetic spectrometer with a proportional counter-scintillator detector at the focal surface. Angular distributions were obtained for the ground and first excited state of ^{144}Nd, and for the ground state of ^{143}Nd in the (^{16}O,^{17}O) reaction as illustrated in Fig. 1. As expected, the 2^+ state is strongly excited, in fact, more strongly than the ground state. The angular width of the two neutron transfers is also wider than the one-neutron transfer. This is a consequence of the stronger binding of the two particle form factor giving a higher localization of the reaction region in radial and thus angular momentum space. The narrower angular momentum width of the reaction results in a broader angular distribution.

Calculations are now being made for this reaction, the same as for the ^{144}Nd(^{12}C,^{14}C)^{142}Nd experiment described elsewhere in this annual report.[3] In addition to the pairing correlations, second order processes may be interfering constructively with the direct transition and, hence, further enhancing the 2^+ yield.

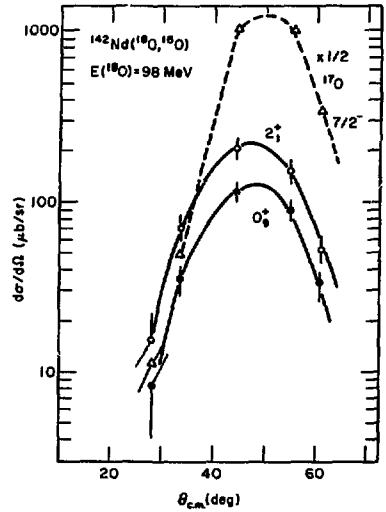

Fig. 1. The differential cross sections for the ^{142}Nd(^{18}O,^{16}O)^{144}Nd reaction leading to the ground and first 2^+ excited state (0.695 MeV). Also shown is the angular distribution for the ^{142}Nd(^{18}O,^{17}O)^{143}Nd reaction going to the $(7/2)^-$ ground state. (XBL 749-4270)

Footnotes and References

*On leave from Osaka University, Osaka, Japan.

†On leave from Hahn Meitner Institut, Berlin, Germany.

1. W. Oelert, G. Lindström and V. Riech, Nucl. Phys. A233, 237 (1974).

2. R. Broglia, O. Hansen and C. Riedel, Adv. in Nucl. Phys. 6, 287 (1973).

3. K. Yagi, D. L. Hendrie, L. Kraus, C. F. Maguire, J. Mahoney, D. K. Scott, Y. Terrien, T. Udagawa, K. S. Low and Tamura; contributors to this report.

ONE- AND MULTI-STEP PROCESSES IN THE ^{144}Nd(^{12}C, ^{14}C) REACTIONS*

K. Yagi,† D. L. Hendrie, L. Kraus,‡ C. F. Maguire, J. Mahoney, D. K. Scott, Y. Terrien,§ T. Udagawa,‖ K. S. Low‖ and T. Tamura‖

In previous work[1,2] on the ^{144}Nd(p,t)^{142}Nd reaction, the excitation of the ground (0_g^+) state, the first excited (2_1^+) state, the 2.98 MeV (0_2^+) state and the 3.49 MeV (2_2^+) state in ^{142}Nd (N = 82) was investigated. The purpose of the present work is to study these and additional states via the ^{144}Nd(^{12}C,^{14}C)^{142}Nd reaction. Our interests are to learn to what extent the light-ion and heavy-ion induced two-neutron pickup reactions are similar and to determine the effects of multi-step processes in heavy-ion transfer reactions.

The most remarkable feature found in the previous (p,t) work[1,2] was that the transitions to the 0_g^+, 0_2^+ and 2_2^+ final states were strong and were of one-step nature, while the transition to the 2_1^+ state was much weaker and also had an anomalous angular distribution markedly different from what was expected for a one step L = 2 transition. The difference in the behavior of the 2_1^+ and 2_2^+ transitions was attributed to the following distinct properties of those states.[2] The 2_2^+ state is a collective two-neutron hole state in the N = 82 closed shell, i.e., a second order quadrupole-pairing vibrational state[3] which can be excited strongly by a direct L = 2 type (p,t) reaction. On the other hand, the 2_1^+ state consists dominantly of a proton particle-hole quadrupole-vibrational configuration; thus a direct (p,t) process is substantially inhibited and higher order processes may contribute significantly. Indeed, the anomalous behavior of the 2_1^+ cross section, which defied explanation in terms of DWBA calculations, was well accounted for by coupled-channel Born approximation (CCBA) calculations, which took into account the effect of inelastic scattering.[2]

The ^{144}Nd(^{12}C,^{14}C) experiment was performed using a 78 MeV ^{12}C beam from the Berkeley 88-Inch Cyclotron. Reaction products were detected in the focal plane of a magnetic spectrometer.[4] Particle identification and energies of the reaction products were obtained by a combination of magnetic rigidity, dE/dx, total energy and time-of-flight. Angular distributions of the ^{14}C groups leading to 0_g^+, 2_1^+, 0_2^+, 2_2^+ states and a group at about 2.08 MeV consisting of 3_1^+, 4_1^+, 0_3^+ were measured from θ_{lab} = 8° to 55° in 2.5° steps.

Figure 1 gives the measured differential cross sections of the five ^{142}Nd groups, and one may conclude that the data have the following properties: 1) The 0_g^+, 0_2^+ and 2_2^+ states are excited strongly and have bell-shaped angular distributions which are characteristic of one-step transitions, with peaks appearing at $\theta_{cm} \approx 45°$;

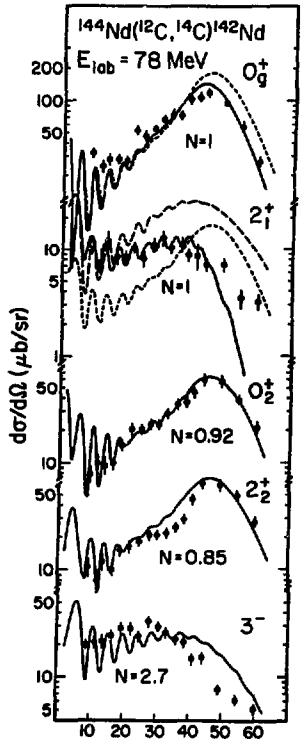

Fig. 1. Experimental and theoretical angular distributions of the ^{144}Nd(^{12}C,^{14}C) reaction at E_{lab} = 78 MeV. Each curve is labeled with a normalization factor N, so chosen that N = 1 for the 0^+_g state. (Without this renormalization, all the theoretical cross sections are to be reduced by a factor 9.)

2) The 2^+_1 transition is strongly inhibited and has a quite anomalous (flattened) angular distribution; 3) Below the excitation energy of 3.5 MeV, 0^+_g, 0^+_2 and 2^+_2 are the only states that are excited strongly, in spite of the fact that there are about 25 states in this energy range known from other experiments.[5] All these features are very much reminiscent of the situation for the (p,t) reaction.[1,2]

The cross section for the 0^+_g and 2^+_1 final states were obtained by performing exact finite-range (EFR)-CCBA calculations, in which $0^+ - 2^+$ Nd states were coupled in both incident and final channels, with β_2 = 0.125 and 0.096 for ^{144}Nd and ^{142}Nd, respectively. As seen in Fig. 1 good simultaneous fits to both bell-shaped 0^+_g and flattened 2^+_1 angular distributions are obtained. A corresponding EFR-DWBA cross section is also given by a dotted line for the 2^+_1 state, which is seen to have a completely different shape from the experimental angular distribution. The DWBA 0^+_g cross section, which is also given by a dotted line, will be discussed later.

It is worth emphasizing that not only the angular distribution, but also the relative magnitude of the EFR-CCBA 0^+_g and 2^+_1 cross sections were obtained correctly. It is worth noting further that the CCBA 2^+_1 cross section (solid line) was obtained as a result of destructive interference between the one-step DWBA process and the two two-step processes; $0^+_g(^{144}\text{Nd}) \rightarrow 0^+_g(^{142}\text{Nd}) \rightarrow 2^+_1(^{142}\text{Nd})$ and $0^+_g(^{144}\text{Nd}) \rightarrow 2^+_1(^{144}\text{Nd}) \rightarrow 2^+_1(^{142}\text{Nd})$. The 2^+_1 cross section given by a broken line was obtained by considering *only* these two-step processes. The very anomalous angular distribution results from this interference.

The calculation of the 0^+_2 and 2^+_2 cross sections was made in terms of EFR-DWBA, assuming that the excitation takes place only via pairing vibrational components in these states which have monopole and quadrupole nature, respectively.[6] As is expected the resultant cross sections (Fig. 1) are basically bell-shaped, and agree satisfactorily with experimental angular distributions. The relative normalization factors N = 0.92 and N = 0.85, respectively, for these two states are sufficiently close to unity, indicating that the wave functions we used to describe these two states are basically correct.

It should be finally noted that, both experimentally and theoretically, the peak of the bell-shaped angular distribution for the 0^+_2 state appears at 45°. On the other hand, the experimental peak for the 0^+_g state appears at 43°, i.e., a shift by 2° to forward angle takes place and our CCBA calculations explain this. The corresponding DWBA cross section, however, has the peak at 45° (in agreement with that for the 0^+_2 state) and the angular distribution (dotted line) fits the experiment rather poorly. The origin of the shift of 2° of the peak position in going from DWBA to CCBA is the destructive interference in the latter between the two-step 0^+_g (^{144}Nd) $\rightarrow 2^+_1(^{144}\text{Nd}) \rightarrow 0^+_g$ (^{142}Nd) amplitude and the one-step $0^+_g(^{144}\text{Nd}) \rightarrow 0^+_g$ (^{142}Nd) amplitude. This destructive interference is stronger (weaker) for partial waves whose orbital angular momentum ℓ is smaller (larger) than the grazing angular momentum ℓ_g. Thus, the effective value of ℓ_g for CCBA is larger than that for DWBA which results in the shift of the peak position to a smaller angle.

In summary, 1) The mechanism of the ^{144}Nd (^{12}C,^{14}C) reaction is quite analogous to that of the ^{144}Nd(p,t) reaction; 2) The comparison of the transitions to the two types of 2^+ states gives a definite evidence for the importance of two-step processes;[7,8] 3) Since the direct transfer signature for this system is a clear bell-shaped angular

distribution, the anomalous nature of the 2_1^+ excitation is much more conspicuous than that observed in the (p,t) case;[1,2] and 4) The coupling effect can be significant in predicting the correct angular distribution, in particular the peak position, even when the angular distribution has a simple bell shape. This was exemplified in our 0_g^+ cross section.

Footnotes and References

*Condensed from Phys. Rev. Letters 34, 96 (1975).

†On leave from Osaka University, Osaka, Japan.

‡On leave from CRN and Universite Pasteur, Strasbourg, France.

§On leave from CEN, Saclay, France.

‖Center for Nuclear Studies, University of Texas, Austin, Texas 78712.

1. K. Yagi, Y. Aoki, J. Kawa and K. Sato, Phys. Lett. 29B, 647 (1969).

2. K. Yagi, K. Sato, Y. Aoki, T. Udagawa and T. Tamura, Phys. Rev. Lett. 29, 1334 (1972).

3. A. Bohr, Proc. Int. Symposium on Nuclear Structure, Dubna, 1968 (IAEA, Vienna, 1968), p. 179.

4. B. G. Harvey, J. Mahoney, F. G. Pühlhofer, F. S. Goulding, D. A. Landis, J.-C. Faivre, D. G. Kovar, M. S. Zisman, J. R. Meriwether, S. W. Cosper and D. L. Hendrie, Nucl. Inst. Meth. 104, 21 (1972).

5. J. F. Lemming and S. Raman, Nuclear Data Sheets 10, 309 (1973).

6. The probability of the pairing vibrational components in 0_2^+ and 2_2^+ states we used are 73% and 75% respectively. These numbers were taken from the experimental fact that

$$\sigma(^{144}\mathrm{Nd}(p,t)^{142}\mathrm{Nd},0_2^+)/\sigma(^{142}\mathrm{Nd}(p,t)^{140}\mathrm{Nd},0_g^+) = 0.73$$

and

$$\sigma(^{144}\mathrm{Nd}(p,t)^{142}\mathrm{Nd},2_2^+)/\sigma(^{142}\mathrm{Nd}(p,t)^{140}\mathrm{Nd},2_1^+) = 0.75.$$

See Ref. 2 for the experimental data.

7. T. Tamura, K. S. Low and T. Udagawa, Phys. Lett. 51B, 116 (1974).

8. R. J. Ascuitto and N. K. Glendenning, Phys. Lett. 45B, 85 (1973).

OPPOSITE INTERFERENCE EFFECTS OBSERVED IN THE ^{148}Sm (^{18}O, ^{16}O) ^{150}Sm AND THE ^{150}Sm (^{16}O, ^{18}O) ^{148}Sm REACTIONS

C. Maguire, B. Harvey, D. Hendrie, H. Homeyer, U. Jahnke, J. Mahoney, D. Scott, and N. K. Glendenning

The presence of multi-step processes in heavy-ion transfer reactions has been confirmed in a number of recent experiments.[1] These reactions are extremely interesting because 1) experimentally the signature of multi-step transitions is very clear and 2) theoretically the effect of multi-step transitions is a sensitive function of the nuclear structure calculations for the target and residual systems. Depending on the nuclear structure model, the multi-step amplitudes may have the same or opposite sign as the pure direct amplitudes thus resulting in constructive or destructive interference respectively.[2]

Heavy-ion reactions on medium heavy nuclei ($A \approx 150$) are an excellent means of studying these processes because, as a function of angular momentum, the direct transition amplitudes typically have a broad peak about the grazing partial wave leading to classical bell-shaped angular distributions. The indirect amplitudes are more sharply peaked but still have their maxima at approximately the grazing partial wave. Since the indirect amplitudes can be of opposite sign to the direct, however, cancellations will occur leading to anomalously weakened, flat angular distributions.

The theoretical description of vibrational states, based on their microscopic description makes a very definite prediction that interference between direct and indirect modes will be of the opposite sense for stripping as compared to pickup reactions.[2] However, the question as to which case is the interference constructive and which case destructive, depends upon the relative importance of the so-called forward and backward going graphs. For nuclei close to closed shells, the forward-going graphs dominate. The tin isotopes are an example of this situation. There the stripping reaction leading to a vibrational state will exhibit destructive interference between the direct and indirect modes, while the pickup reaction will exhibit constructive interference as predicted by calculation[2] and confirmed by experiments.[3] The Samarium isotopes are rich in possibilities. At the light end, the neutron shell is near magic; a situation that is expected to lead to dominance of the forward-going graphs. In the middle, they have open shells in both neutrons and protons and moreover they span the transition region from vibrational to rotational nuclei. Both of these facts suggest the possibilities that the backward-going graphs may dominate the forward-going graphs. If they do then the sign of the interference is interchanged with respect to stripping and pickup reactions. In fact, this experiment exhibits just this opposite behavior for the spherical intermediate mass samarium isotopes as compared with tin.

The ^{150}Sm (^{16}O, ^{18}O) reaction was studied with a 104-MeV beam from the 88-Inch Cyclotron with the outgoing ^{18}O ions momentum-analyzed in a magnetic

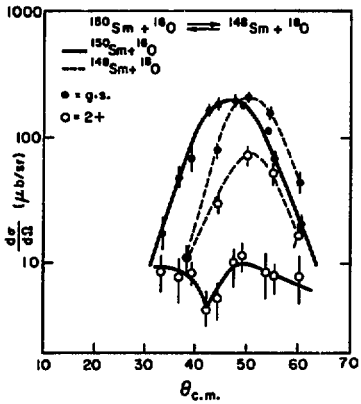

Fig. 1. Experimental angular distribution for the ^{148}Sm (^{18}O, ^{16}O) ^{150}Sm two-neutron stripping reaction and the reverse pick-up reaction. The lines through the data are to guide the eye.

(XBL 751-2144)

spectrometer and detected by in a solid state position-sensitive detector placed at the focal surface. Identification of the low yield ^{18}O group was exceptionally good as the detector afforded 600 keV total energy resolution and the nearest contaminant group, ^{15}N, was 5 MeV away on the low energy side. The ^{148}Sm (^{18}O,^{16}O) group was identified by Bρ, $\frac{dE}{dx}$, and TOF. (This system was not used in the (^{16}O,^{18}O) reaction because the high background of $^{16}O^{7+}$ inelastic events tails into the much lower yield $^{18}O^{8+}$ group.) The extracted angular distributions for the ground and first 2+ excited states are shown in Fig. 1. As in the tin data, three of the four angular distributions have a normal grazing angle shape, while the fourth is flattened and much weaker. Here, though it is the pick-up reaction that is anomalous, in tin it was the stripping reaction that had destructive interference.

Experiments are now planned for the ^{144}Sm(^{12}C, ^{14}C) ^{142}Sm two-neutron pick-up reaction. Because these isotopes have N = 82 and 80 respectively, the structure could revert to "forward" dominance gain, just as in the tin isotopes. Calculations will be performed for all these data to test nuclear structure models in the samarium isotopes.

References

1. K. Yagi, D. L. Hendrie, L. Kraus, C. F. Maguire, J. Mahoney, D. K. Scott, Y. Terrien, T. Udagawa, K. S. Low, and T. Tamura, Phys. Rev. Lett, 34, 96 (1975); K. Erb, D. Hanson, R. Ascuitto, B. Sorenson, J. S. Vaagen, and J. Kolata, Phys. Rev. Lett. 33, 1102 (1974).

2. R. J. Ascuitto and N. K. Glendenning, Phys.Lett. 47B (1973) 33.

3. B. G. Harvey, LBL-2366 (1974).

THE INTERFERENCE BETWEEN DIRECT AND INDIRECT MODES IN TWO-NUCLEON TRANSFER REACTIONS WITH HEAVY IONS

B. G. Harvey, D. L. Hendrie, U. Jahnke,* L. Kraus,† C. F. Maguire, J. Mahoney, D. K. Scott, Y. Terrien,‡ K. Yagi,§ and N. K. Glendenning

The presence of indirect transitions in two-neutron transfer reactions to vibrational states in the Sn isotopes has been predicted to have the interesting consequence that the interference between direct and indirect modes is destructive in stripping and constructive in pick-up.[1,2] This effect has not been demonstrated in conventional, light-ion induced reactions owing to the difficulty of performing inverse reactions of the type (p,t), (t,p) at the same center of mass energies, but the flexibility of heavy-ion induced transfer opens up several possibilities. Here we discuss the reactions $^{122}Sn(^{16}O,^{18}O)^{120}Sn$ and $^{120}Sn(^{18}O,^{16}O)^{122}Sn$ to the ground and lowest collective 2^+ excitations. The incident energies of 104 MeV for the ^{16}O beam and 99 MeV for the ^{18}O beam gave equal center of mass energies of 89 MeV for the reactions.

Some data for the $^{120}Sn(^{18}O,^{16}O)^{122}Sn$ reaction at 100 MeV were reported previously.[3] Since this reaction has a positive Q-value of 2.78 MeV, counter telescope techniques were adequate at backward angles to separate the 0^+ and 2^+ states from the intense elastic scattering. For more forward angle data (which is the important region for the indirect effects) and for the corresponding transitons in the inverse pick-up reaction $^{122}Sn(^{16}O,^{18}O)^{120}Sn$ the reaction products from 104 MeV ^{16}O and 99 MeV ^{18}O ions from the 88-Inch Cyclotron were detected with the Berkeley QSD magnetic spectrometer.

The differential cross sections for the two-neutron transfer reactions are shown in Fig. 1 along with the predictions of the reaction theory described in Refs. 1 and 2. The ground state transitions correspond to time-reversed reactions and are identical. (Absolute cross sections were measured for both reactions using the spectrometer; the data taken with the counter telescope for the (^{18}O, ^{16}O) reaction, were normalized to the spectrometer data for the ground state). The distributions for the ground states and for the 2^+ state in the pick-up reaction $^{122}Sn(^{16}O,^{18}O)^{120}Sn$ are all similar in shape, exhibiting a "bell-shaped" maximum at approximately $\theta_{CM} = 38°$, corresponding to a grazing collision in the combined Coulomb and nuclear fields.

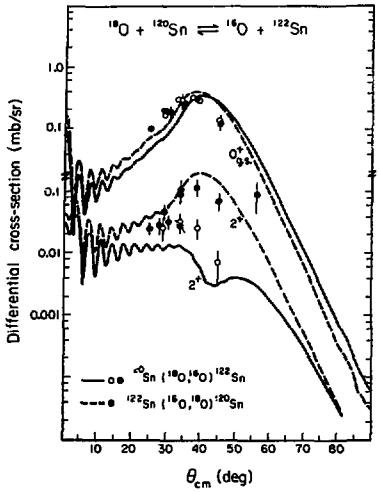

Fig. 1. The differential cross sections for ^{120}Sn $^{18}O,^{16}O)^{122}Sn$ and the reverse pick-up reaction. The solid line is the CCBA prediction for the stripping reactions, and the dashed line the fit to the pick-up reactions. The data designated with the dotted circles was taken at Berkeley, the open circles from Ref. 3. (XBL 751-2083)

This distribution is the well-known characteristic of a single-step, direct transition in heavy-ion induced transfer reactions at moderate energy above the Coulomb barrier. In the stripping reaction $^{120}Sn(^{18}O,^{16}O)^{122}Sn$ the 2^+ transition has a smaller cross section and shows no clear grazing maximum. Instead the cross section at forward angles is rather flat in excellent agreement with the predicted shape. To explain the contrasting behavior observed in the cross sections for stripping and pick-up to the vibrational states, we review the discussion of Refs. 1 and 2, by referring to Fig. 2. In the production of the 2^+ state, transitions 1 and 4 are indirect and are common to both the stripping and pick-up process, while 2 is the direct transition for pick-up and 3 is the direct transition for stripping. The amplitudes for these last two transitions have opposite sign according to the microscopic theory of vibrational states.[1,2] It is this opposite sign which leads to a constructive interference between the direct and indirect modes in the one reaction and destructive in the other. Destructive interference between two amplitudes, both of which are peaked near the grazing angle,[4] leads to distortion of the grazing peaked angular distribution, while a constructive interference retains the characteristic peak. The experimental cross sections for the 2^+ vibrational states obviously confirm the theory. That the two ground state cross

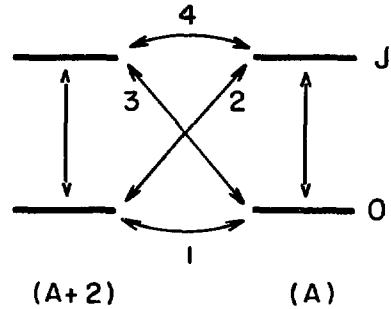

Fig. 2. Schematic diagram showing the different routes, direct and indirect, in a two-particle transfer reaction. (XBL 745-905)

sections are identical follows from the fact that they are time reversed reactions. That they also retain the characteristic grazing peak, undistorted by interference from higher order processes can also be understood in terms of Fig. 2. In this case, for either ground state transition, both 2 and 3 enter the two lowest order indirect modes, and since they have opposite signs they tend to cancel each other, resulting in little higher order contributions to the ground state cross sections. This explains why three of the cross sections have grazing peaked angular distributions while the fourth is distorted.

The coupled channels calculation described in Ref. 2 requires the deformation constants, both nuclear and Coulomb, to determine the strength of the inelastic excitations through which the indirect transitions proceed. These and the optical model potential parameters as well were obtained by fitting simultaneously the $^{18}O + ^{122}Sn$ elastic and first 2^+ inelastic angular distributions. These data were also taken with the QSD spectrometer. Table 1 lists the final parameters which give the fits illustrated in Fig. 3. When applied to the reaction calculation the predicted ground state yields were approximately a factor of 2.5 too low. The fits shown in Fig. 1 have been normalized to the experimental ground state cross section but the relative magnitudes predicted for the 0^+ to 2^+ cross sections are retained.

We have thus demonstrated here the predicted opposite interference characteristic between direct and indirect modes for the pick-up and stripping reactions. The opposite interference is associated with the underlying microscopic structure of the vibrational states. Heavy ion reactions such as these may prove to be a sensitive probe of inelastic modes of excitation which are not directly observable, and ultimately of deformation shapes and nuclear structure.

Table 1. Reaction parameters.

	Optical potential				Deformations		
Term	Depth	R_N	R_C	Diff	Nucleus	B_N	B_C
Real	87.9	1.203	1.2	0.502	^{120}Sn	0.13	0.09
Imag.	24.2	1.1[illegible]	---	0.67	^{122}Sn	0.124	0.095

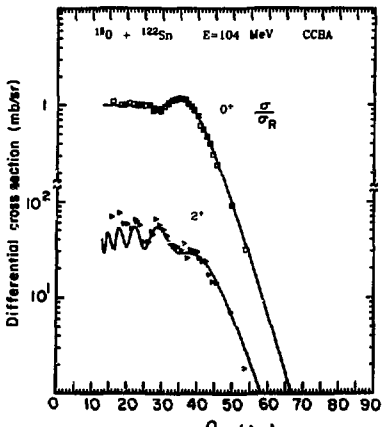

Fig. 3. The predicted fits to the ^{16}O + ^{122}Sn elastic and inelastic data based on the parameters of Table 1. (XBL 751-84)

Footnotes and References

*On leave from Hahn-Meitner Institut, Berlin, Germany.

†On leave from CRN and the Université Pasteur, Strasbourg, France.

†On leave from CEN, Saclay, France.

§On leave from Osaka University, Osaka, Japan.

1. N. K. Glendenning and R. J. Ascuitto, Symposium on Heavy-Ion Transfer Reactions, Argonne Informal Report PHY-1973B, p. 513.

2. N. K. Glendenning and R. J. Ascuitto, Phys. Lett. B47 (1973) 33.

3. N. Anyas-Weiss, et al., Proceeding of the International Conference on Nuclear Physics, eds. J. de. Boer and H. J. Mang (North Holland, 1973) Vol. 1, p. 485.

4. N. K. Glendenning, Classical and Quantum Mechanical Descriptions of Heavy-Ion Interactions in International Conference on Reactions between Complex Nuclei, Nashville, Tennessee, ed. by (Academic Press, 1974).

THE MULTINUCLEON TRANSFER REACTION $^{12}C(^{20}Ne, \alpha)^{28}Si$

D. K. Scott, D. L. Hendrie, U. Jahnke,* L. Kraus,†
C. F. Maguire, J. Mahoney, Y. Terrien,‡ and K. Yagi§

The excitation of new types of correlation in nuclear motion is an attractive possibility for direct multinucleon transfer reactions with heavy-ions. However when complete angular distributions were first measured for one such reaction, viz., $^{12}C(^{14}N,^{6}Li)\ ^{20}Ne$ at 76 MeV, it was found that the component for the direct transfer of eight nucleons was very small, and that the reaction was dominated by a compound mechanism.[1] Subsequently many reactions of this type have been successfully analyzed using Hauser-Feshbach theory.[2] It is now of interest to extend the study of multinucleon transfer reactions to higher energies in order to see if the direct transfer mechanism becomes significant.

We have commenced experiments on the $^{12}C(^{20}Ne, \alpha)^{28}Si$ reaction, in which the projectile has a large spectroscopic probability for decomposition in ^{16}O + α. Our aim was to see if direct transfer of ^{16}O onto the ^{12}C core might populate quasimolecular states in ^{28}Si, formed by the ^{16}O orbiting the ^{12}C core. So far such states have been observed as intermediate resonances in the excitation functions for elastic and inelastic heavy-ion scattering.

The experiments were performed at an incident

energy of 100 MeV and the α-particles were detected using the magnetic spectrometer. The spectrum in Fig. 1 shows that discrete states are observed superimposed on a large continuum (presumably from compound and break-up processes), beginning at 17-MeV excitation, of typical width 300 keV. If these states are populated by the decay of a high spin compound nucleus ^{32}S, which must be formed at an excitation of 56 MeV with $J \approx 26\hbar$, the decay would lead to differential cross sections symmetrical about 90° and of the form $1/\sin\theta$. Our preliminary data for $d\sigma/d\Omega$ indicate that the distributions are not of this form. The reaction was also studied at a lower incident energy of 93 MeV (corresponding to a change of 3.6 MeV in the center of mass) and over the excitation region up to 23 MeV the same set of states appear to be excited.

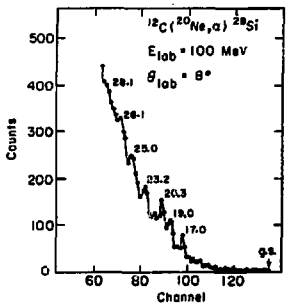

Fig. 1. Energy spectrum for the reaction $^{12}C(^{20}Ne, \alpha)\,^{28}Si$ at E_{lab} = 100 MeV and θ_{lab} = 8°.

(XBL 749-4234)

Hauser-Feshbach calculations will be undertaken to see of the observed cross sections (≈ 100 μb/sr could be accounted for on the model. However our initial conclusion is that multinucleon transfer reactions of the type (^{20}Ne, α) at high incident energies may have a sizeable direct component.

Footnotes and References

*On leave from Hahn-Meitner Institut, Berlin, Germany.

†On leave from CRN and Université Pasteur, Strasbourg, France.

‡On leave from CEN, Saclay, France.

§On leave from Osaka University, Osaka, Japan.

1. T. A. Belote, N. Anyas-Weiss, J. A. Becker, J. C. Cornell, P. S. Fisher, A. Menchaca-Rocha, A. D. Panagiotou, and J. K. Scott, Phys. Rev. Lett. 30, (1973) 450.

2. R. G. Stokstad, Reaction Between Complex Nuclei (Nashville, 1974), ed. by R. L. Robinson, F. K. McGowan, J. B. Ball, and J. H. Hamilton (North-Holland, 1974), p. 327 and references therein.

THE ENERGY VARIATION OF MULTINUCLEON TRANSFER REACTIONS WITH HEAVY IONS

D. K. Scott, D. L. Hendrie, U. Jahnke,* L. Kraus,†
C. F. Maguire, J. Mahoney, Y. Terrien,‡ and K. Yagi §

Recently it was discovered that two, three and four nucleon transfer reactions with heavy-ion beams of approximately 10 MeV/nucleon appear to be highly selective in exciting cluster states in light nuclei.[1] This observation is one of the promising aspects for spectroscopy with multinucleon transfer reactions induced by heavy-ions. Unfortunately the differential cross sections for heavy-ion transfer reactions at high energies are often rather poor signatures of the J-value of a state.[1] Here we describe a method of combining the high selectivity of the reactions with a study of the energy variation of the cross section over a wide range, to select systematically states of progressively higher spin in the cluster rotational band.

As a test case we chose the reaction $^{12}C(^{12}C, ^{9}Be)^{15}O$, since ($^{12}C$, ^{9}Be) has been shown to be very favorable for spatially symmetric ^{3}He transfer.[2] The reaction was studied at three bombarding energies, of 78, 104, and 187 MeV. The spectrum taken at 187 MeV, in Fig. 1, illustrates the pronounced excitation of states at 15.08 and 12.87 MeV, which have been assigned[4] $J^{\pi} = 13/2^{+}$ and $11/2^{-}$. On the cluster model these states correspond to ^{3}He orbitals L = 5 and 6, and are the upper members[3] of rotational bands with 2N + L = 6 and 5, where N is the number of nodes. As the incident energy is decreased, lower members of the bands are more strongly excited. This effect is illustrated in Fig. 2, which shows that at the lowest energy of 78 MeV, representative states of $J^{\pi} = 1/2^{-}$, $5/2^{+}$ and $13/2^{+}$ are excited with comparable intensity, but at 187 MeV there is a factor of 10^{3} between the $1/2^{-}$ and the proposed $13/2^{+}$ state. This variation if accounted for by reaction dynamics, can be used to infer J^{π} values.

We have used a semiclassical theory[1] to calculate the transition probability between cluster states in the projectile and residual nucleus, assuming straight line orbits. The results of the

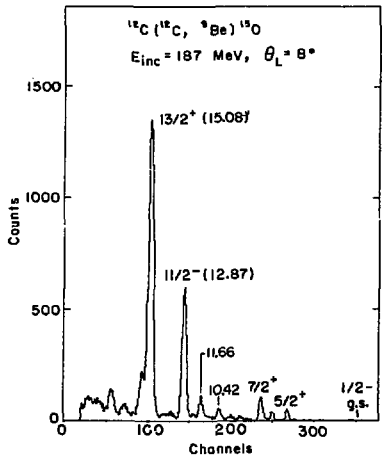

Fig. 1. Energy spectrum for the $^{12}C(^{12}C, ^{9}Be)^{15}O$ reaction at E_L = 187 MeV and θ_L = 8°.
(XBL 746-3473)

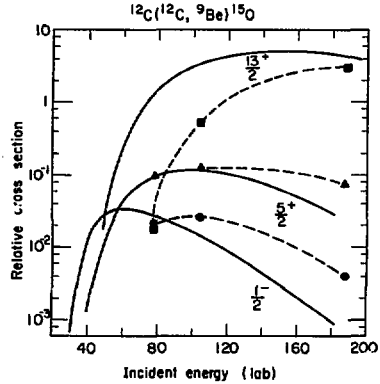

Fig. 2. Energy variation of cross sections for states of different J^π in the reaction $^{12}C(^{12}C,^{9}Be)^{15}O$. The dotted lines are to guide the eye through the experimental points, and the solid lines are the theoretical predictions of semiclassical theory. The hatched areas represent the predictions for the 1/2⁻ and 13/2⁺ states using zero range DWBA, arbitrary normalised to the 13/2⁺ state.
(XBL 749-4233)

calculation for the 1/2⁻, 5/2⁺, and 13/2⁺ states are shown in Fig. 2 by the solid lines. One overall normalization factor was applied to the data, and equal spectroscopic factors were assumed for all states. The general trend of the data is accounted for by the model, in particular the large enhancement of J^π = 13/2⁺ over 1/2⁻ at 187 MeV. It is found in fact that there is a systematic variation of the maximum in the cross section which moves progressively to higher energy the higher the J - value. For comparison we show the results of a "no-recoil" DWBA calculation for the 1/2⁻ and 13/2⁺ states. One set of optical parameters, obtained from a fit to elastic scattering data of $^{12}C + ^{12}C$ at 104 MeV, was used at all energies. This calculation is unable to accout for the enhancement of the 13/2⁺ state at high energy. Although better overall agreement for the energy variation of the 1/2⁻ state could probably be obtained by adjustment of the optical potentials, the proper account of the relative excitation of the states would be given only in a full finite-range calculation. The reason is that recoil effects dominate the three-nucleon transfer reaction at high energy. This involves the angular momentum carried by the transferred group of particles at the surface of the target nucleus, owing to the momentum in the motion of the projectile. At 187 MeV the associated angular momentum at forward angles is approximately 9ħ. The advantage of the semiclassical theory is its ability to make rapid surveys, with few arbitrary parameters.

Calculations using a folding potential model predict lower members of the 2N+L = 6 and 5 bands of J^π = 9/2⁺ and 7/2⁻ in the region of 11 and 10 MeV excitation,[3] respectively, which correspond to ^{3}He orbitals L = 4 and 3. Figure 1 shows that only two states are appreciably excited in this region, viz., at 10.42 and 11.66 MeV. The relative intensities reverse between 104 and 187 MeV, implying a higher orbital for the 11.66 MeV state. These states are therefore likely candidates for the 9/2⁺ and 7/2⁻ cluster states. This principle of energy variation is particularly useful for distinguishing two states of different spins close together in excitation energy. For states of better known spin, a case is illustrated in Fig. 3, which compares the excitation of two-proton "cluster" states of 3⁻ at 6.29 MeV and 4⁻ at 10.8 MeV, in the $^{12}C(^{12}C,^{10}Be)$ ^{14}O reaction at 114[1] and 187 MeV. The intensities of these L = 3 and L = 4 orbitals reverse at the higher energy. A further interesting case, beyond the range of the present experiments, is the 11/2⁺ and 9/2⁻ members of the bands which are the components of the 13/2⁺ and 11/2⁻ states, raised by the spin-orbit ^{3}He potential to over 20 MeV in excitation.

The location of these cluster states in mass 15, and in other regions of the periods table, possibly involving more massive clusters than ^{3}He or ^{4}He, is an interesting area of research for multi-nucleon transfer reactions with heavy-ion beams on high energy accelerators of readily variable energy. A fuller account of this work is given in Ref. 4.

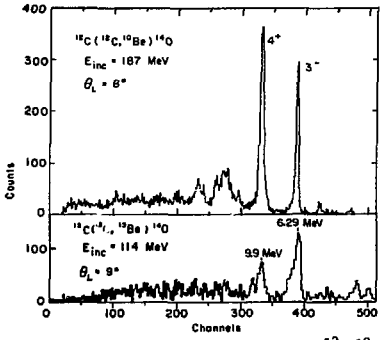

Fig. 3. Energy spectra for the reactions $^{12}C(^{12}C, ^{10}Be)^{14}O$ at 114 MeV and 187 MeV. (XBL 749-4231)

Footnotes and References

*Or. leave from Hahn-Meitner, Institut, Berlin, Germany.

†On leave from CRN and Université Pasteur, Strasbourg, France.

‡On leave from CEN, Saclay, France.

*On leave from Osaka University, Osaka, Japan.

1. N. Anyas-Weiss et al., Physics Reports 12C, 201 (1974).

2. D. Kurath and D. J. Millener, to be published.

3. J. P. Vary and C. B. Dover, Phys Rev. Lett. 31, 1510 (1973), and B. Buck, C. B. Dover, and J. P. Vary, to be published.

4. LBL Preprint-3445.

SPECTROSCOPY OF EXOTIC NUCLEI USING HEAVY-ION TRANSFER REACTIONS

D. K. Scott, B. G. Harvey, D. L. Hendrie, L. Kraus,†
C. F. Maguire, J. Mahoney, Y. Terrien,† and K. Yagi‡

The known limit of particle stability of neutron-excess nuclei extends far beyond the region accessible to nuclear spectroscopy in conventional light-ion induced reactions.[1] With the (t,p) reaction, nuclei only two neutrons removed from stable targets can be studied, whereas on the neutron deficient side of stability three and four neutron transfers are possible by the (^{3}He,^{6}He) and (^{4}He, ^{8}He) reactions. Comparable transfers to neutron-excess nuclei are made possible by heavy-ion reactions. Here we present our final results on a reaction for 3n stripping, the (^{11}B,^{8}B) reaction on targets of ^{26}Mg and ^{28}Si, both to provide a precise measurement of the mass-excess of the T_z = 5/2 nuclide ^{29}Mg for comparison with theoretical mass predictions, and to study the feasibility of using 3n transfer for studies of nuclear structure. The reactions ^{26}Mg(^{11}B,^{13}N)^{24}Ne and ^{26}Mg(^{11}B,^{11}C)^{26}Na also lead to exotic nuclei currently the object of nuclear model calculations,[2] and these were studied simultaneously. The experimental method and the advantages of detecting ^{8}B, were described in last year's Annual Report.[3] A more detailed account of this work is given in Ref. 4.

The prime objective of the present work was the precise mass measurement of ^{29}Mg. Although the masses of all T_z = 5/2 nuclides from ^{21}O to ^{35}P have recently been measured,[1] mainly by production in heavy-ion compound nuclear reactions followed by β-γ activity measurements, this technique was difficult to apply in the case of ^{29}Mg and resulted in a large error. The 3n transfer reaction is capable of high precision, but it is important to establish that the ground state of the reaction is populated. To clarify this point we studied the same reaction on ^{28}Si which differs from ^{26}Mg by the addition of a proton pair, and therefore the reaction might be expected to populate states with similar neutron structures. As Fig. 1(b) shows, the ground state of ^{31}Si is excited ($d\sigma/d\Omega \approx 80$ nb/sr), and we assume that the highest energy peak in the ^{29}Mg spectrum in Fig. 1(a) corresponds also to the ground state (here the cross section is only 15 nb/sr). The predicted location of the ground state from the mass-excess of Ref. 5 is also shown. Careful analysis of this peak, after corrections including energy

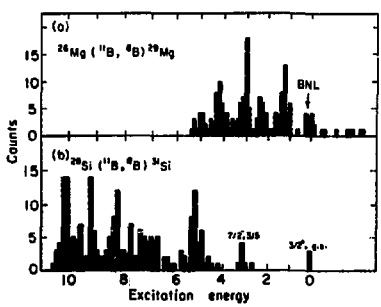

Fig. 1. Energy spectra for the reactions (a) ^{26}Mg(^{11}B,^{8}B)^{29}Mg and (b) ^{28}Si(^{11}B,^{8}B)^{31}Si induced by 86 MeV ^{11}B ions at 11°. The cut-off at ≈ 5 MeV excitation in ^{29}Mg is instrumental. The ground state predicted from the mass excess for ^{29}Mg in reference 7 is shown in (a). (XBL 744-2895)

losses in the target and "time-zero" foil, gave a Q-value of -19.72±0.05 MeV, corresponding to a mass-excess for ^{29}Mg of -10.75±0.05 MeV. The accuracy of the method, including the calibration of the magnetic field of the spectrometer, was checked using other reactions of known Q-value, e.g. (^{11}B, ^{13}N), which in some cases were measured with fields identical to that for the ^{26}Mg(^{11}B,^{8}B)^{29}Mg reaction. Our result is within the error of the mass-excess quoted in Ref. 5, of -10.589±0.400 MeV, differs by 0.83 MeV from the revised Garvey-Kelson prediction[6] and is in excellent agreement (within 50 keV) with the results of the modified shell-model predictive scheme of Jelley et al.[1,7]

The low cross section for 3n transfer follows the trend of high energy heavy-ion reactions of favoring the transfer of bound clusters. However the selectivity of the reaction shows that some correlation is still present. For example, in ^{31}Si only two states are populated in the first 4 MeV of excitation: the ground state, which has dominant structure $(s_{1/2})^2$ $(d_{3/2})$ both in the simple and the extended shell-model calculations,[8] and a state at 3.15 MeV of dominant structure $(s_{1/2})^2$ $f_{7/2}$. The reaction appears to proceed by direct transfer of a 2n cluster in an internal L=0, S=0, T=1 state, with the transfer of the third neutron to the lowest available orbitals. This interpretation is consistent with the absence of the 0.75 ($1/2^+$) and 1.70 MeV ($5/2^+$) states, which are accessible in direct 3n transfer only by the $(s_{1/2})$ $(d_{3/2})^2$ components[8] in the wave functions, for which the 2n cluster component is smaller. At higher excitation, in a region of level density greater than 15 levels/MeV, the few strongly observed states are likely to be associated with higher shell-model orbitals, and other cluster configurations.

The spectrum for ^{29}Mg in Fig. 2(a) has excited states at 1.38, 2.34, 3.07, and 4.27 MeV.(± 90 keV).

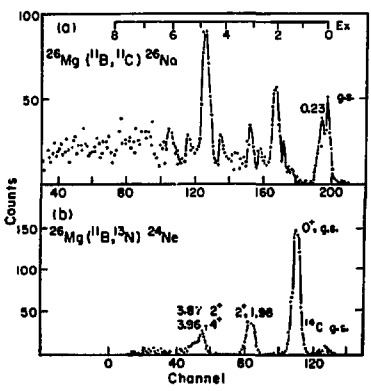

Fig. 2. Energy spectra for the reactions (a) ^{26}Mg(^{11}B, ^{11}C)^{26}Na and (b) ^{26}Mg(^{11}B,^{13}N)^{24}Ne induced by 86 MeV ^{11}B ions at 11°. (XBL 744-2897)

A recent calculation[2] of energy spectra of exotic nuclei in the sd-shell predicts positive parity configurations in ^{29}Mg of J^π = $1/2^+$, $5/2^+$, $7/2^+$, and $3/2^+$ at 0.02, 1.89, 2.53, and 3.19 MeV respectively. If the observed level at 1.38 MeV corresponds to the $5/2^+$ configuration, its strong excitation in ^{29}Mg compared to ^{31}Si implies that the overlap of the three neutrons with the ^{26}Mg and ^{28}Si is very different. Since ^{26}Mg and ^{28}Si have opposite deformations,[13] an alternative interpretation is that of transfer to different Nilsson orbitals.

In addition to ^{8}B, the reaction products ^{11}C and ^{13}N were clearly identified and the Q-values permitted all three ground states to be encompassed by the 25% energy bite of the focal plane detector. A spectrum for the ^{26}Mg(^{11}B,^{13}N)^{24}Ne reaction is shown in Fig. 2(b). Since ^{13}N has no particle stable excited states the reaction is favorable for spectroscopic studies of 2p pick-up. The cross section (80 μb/sr for the g.s.) is also substantially greater than that of the (^{6}Li,^{8}B) reaction.[1] On account of these advantages, and because the reaction is unusual in having comparable amplitudes for transfer of two protons in spatially symmetric and antisymmetric states,[10] this reaction may be suitable for determining the importance of the antisymmetric states.

The spectrum for the ^{26}Mg(^{11}B,^{11}C)^{26}Na reaction in Fig. 2(a) exhibits excited states at 0.23, 2.10, and 4.79 MeV. (±150 keV), although the latter two are somewhat ambiguous owing to the close proximity of ^{11}C excited states at 1.995 and 4.794 MeV. The selectivity of the reaction appears to be similar to that[11] of (^{7}Li,^{7}Be) and quite different from the (t,^{3}He) reaction,[12] which established excited states at 88, 241, and 420 keV. Although the detailed mechanism of these rearrangement reactions is poorly understood at present, it appears that the heavy-ion case preferentially excites high spin states.[13] A comparison of the quadruplet of levels near the ground state, excited in light- and heavy-ion induced reactions could possibly be used to infer the spin sequence, thereby distinguishing between rotational and shell model interpretations of ^{26}Na.

Footnotes and References

*On leave from CRN and Université Pasteur, Strasbourg, France.

†On leave from CEN, Saclay, France.

*On leave from Osaka University, Osaka, Japan.

1. "Exotic Reactions in the Light Elements", by J. Cerny in Proceedings of the Conference on Reactions Between Complex Nuclei (Nashville 1974), (North-Holland).

2. B. J. Cole, A. Watt and R. R. Whitehead, J. of Phys. A 7, 1399 (1974).

3. LBL Nuclear Chemistry Annual Report (1973), LBL Report-2366 (1974), p. 102 and p. 434.

4. D. K. Scott, B. G. Harvey, D. L. Hendrie, L. Kraus, C. F. Maguire, J. Mahoney, Y. Terrien, and K. Yagi, Phys. Rev. Lett. 33,1343 (1974) and LBL 2996.

5. D. R. Goosman, C. N. Davids, and D. E. Alburger, Phys. Rev. C8, 1331 (1973) and references therein.

6. C. Thibault and R. Klapisch, Phys. Rev. C9,798 (1974).

7. N. A. Jelley, J. Cerny, D. P. Stahel, and K. H. Wilcox, to be published.

8. B. H. Wildenthal, J. B. McGrory, E. C. Halbert, and H. D. Graber, Phys. Rev. C4, 1708 (1971).

9. D. Schwalm, A. Bamberger, P. G. Bizzeti, B. Povh, G.A.P. Engelbertink, J. W. Olness, and E. K. Warburton, Nucl. Phys. A192, 449 (1972).

10. D. Kurath, Comments on Nuclear and Particle Physics V, 55 (1972).

11. G. C. Ball, W. G. Davies, J. S. Forster, and J. C. Hardy, Phys. Rev. Lett. 28, 1068 (1972).

12. E. R. Flynn and J. D. Garrett, Phys. Rev. C9, 210 (1974).

13. D. Sinclair, private communication, 1974.

A MORE ACCURATE MASS FOR ^{8}He*

Joseph Cerny, N. A. Jelley,† D. L. Hendrie, C. F. Maguire,
J. Mahoney, D. K. Scott, and R. B. Weisenmiller

With the advent of large solid-angle magnetic spectrometers, multineutron transfer reactions, such as (α,^{8}He) or (^{3}He,^{8}He), producing highly neutron-deficient reaction products will be of increasing experimental interest. As an example, quite recently Robertson et al.[1] measured the masses of ^{8}C and ^{20}Mg via the (α,^{8}He) reaction on ^{12}C and ^{24}Mg. Since such studies rely directly on the previously measured[2-5] mass of ^{8}He, it was felt to be of interest to improve the accuracy of the earlier results.

Two different experimental approaches have been employed in determining the mass-excess of ^{8}He. Cerny et al.[2] utilized an 80-MeV alpha-particle beam and counter-telescope techniques to observe the ^{26}Mg(α,^{8}He)^{22}Mg reaction (Q-value ~ -45 MeV), obtaining a mass-excess for ^{8}He of 31.65±0.12 MeV. In addition, Batusov et al.[3] reported a mass-excess of 31.0±0.4 MeV for ^{8}He by observing in photographic emulsions the production (and decay) of ^{8}He nuclei produced by capture of stopped π$^-$ mesons in carbon and oxygen nuclei.

This reinvestigation of the mass-excess of ^{8}He again employed the ^{26}Mg(α,^{8}He)^{22}Mg reaction. An energy-analyzed 110.6 MeV α-particle beam from the 88-Inch Cyclotron was used to bombard a 1/2 mg/cm^2 ^{26}Mg target. Reaction products were detected at 10° lab with, at 1.4 msr solid angle, the focal plane of a magnetic spectrometer with a position sensitive proportional counter backed by a plastic scintillator.[6] Unambiguous particle identification was obtained by measuring Bρ (position), differential energy loss (ΔE/ΔX), time of flight (TOF) and the pulse height from a dynode of the scintillator (denoted E and proportional to energy, but with a further dependence on charge and mass).

The energy calibration of the focal plane was obtained by concurrently measuring ^{8}He events from the ^{26}Mg(α,^{8}He)^{24}Mg reaction. Transitions to the ^{24}Mg* (6.010 MeV) state[5] lie an amount equivalent to only ~ 200 keV away from the ^{26}Mg(α,^{8}He)^{22}Mg (ground state) reaction. The dispersion across the focal plane was obtained from the positions of the transitions populating the ^{26}Mg(α,^{8}He)^{24}Mg* (1.369, 4.123, and 6.010 MeV) states.

Figure 1 presents the energy spectrum from the ^{26}Mg(α,^{8}He)^{22}Mg reaction. As in the earlier experiment[2] at 80 MeV, transitions were observed to both the ground and the first excited state[5] of ^{22}Mg; the ground state cross section at 110.6 MeV was ~ 10nb/sr lab. A strong transition was also observed to a new state (or states) at 8.6 MeV excitation. This state should still be of T=1 character since Coulomb displacement energy calculations[6] place the lowest T=2 state in ^{22}Mg near 14.0 MeV excitation.

These results establish a new mass-excess for ^{8}He of 31.57±0.03 MeV (based on a ^{22}Mg mass-excess

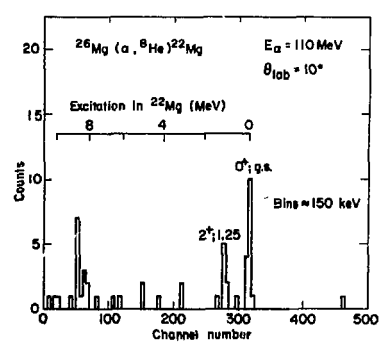

Fig. 1. The energy spectrum from the ^{26}Mg(α,^{8}He)^{22}Mg reaction at 10° lab using 110.6 MeV incident α-particles.

of -396±2 keV[7]), which agrees very well with the earlier measurements. ^{8}He is then bound by 2.17 MeV with respect to its lowest break-up channel of ^{6}He + 2n.

The mass of ^{8}He has considerable theoretical interest, initially because of questions of the possible existence of a bound state, and currently as one of the important tests of theories predicting binding energies of light nuclei, particularly with regard to the symmetry energy of the force employed. Table 1[8,9] presents results from a broad sample of these theoretical predictions of the mass-excess of ^{8}He (where applicable, calculations were updated using the 1971 atomic mass table[10]). Of the calculations prior to the first measurement of the mass-excess of ^{8}He, the approach of Goldanskii[9] and the intermediate coupling calculations of Barker[8] agree best with experiment. The more recent theoretical calculations of Barker[8] agree best with experiment. The more recent theoretical calculations generally predict masses for a number of even helium isotopes, in many cases so far subtantially disagreeing with experiment.

Table 1. Theoretical predictions of the mass-excess of ^{8}He.

[Experimental value = 31.57±0.03 MeV; unbound at 33.74 MeV]

Calculated mass-excess (Mev)	Type of calculation	Reference
32.2±0.4	Neutron pairing energy systematics	V. I. Goldanskii, Ref. 9.
34.2±2	Symmetry and pairing energy systematics	J. Jänecke, Nucl. Phys. 73, 97 (1965)
29.8	Independent particle model (recursion relations)	G. T. Garvey and I. Kelson, Phys. Rev. Letters 16, 197 (1966).
31.2	Intermediate coupling shell model	F. C. Barker, Ref. 8.
~ 30.6	Thomas-Fermi calculation	R. J. Lombard, Phys. Letters 35B, 493 (1971).
33.4	Constrained spherical Hartree-Fock calculation	X. Campi and D.W. Sprung, Nucl. Phys. A194, 401 (1972).
29.3	SU_4	C. Maguin, Nuovo Cimento 19A, 638 (1974).

Footnotes and References

*Condensed from LBL-2984. Phys. Rev. C (in press).

†Now at the Nuclear Physics Laboratory, University of Oxford, England.

1. R. G. H. Robertson, S. Martin, W. R. Falk, D. Ingham, and A. Djaloeis, Phys. Rev. Letters 32, 1207 (1974).

2. J. Cerny, S. W. Cosper, G. W. Butler, R. H. Pehl, F. S. Goulding, D. A. Landis, and C. Detraz, Phys. Rev. Letters 16, 469 (1966).

3. Yu. A. Batusov, S. A. Bunyatov, V. M. Sidorov, and V. A. Yarba, Phys. Letters 22, 487 (1966); and Sov. Journal of Nucl. Phys. 7, 20 (1968).

4. B. G. Harvey, J. Mahoney, F. G. Pühlhofer, F.S. Goulding, D. A. Landis, J. C. Faivre, D. G. Kovar, M. S. Zisman, J. R. Meriwether, S. W. Cooper, and D. L. Hendrie, Nucl. Instr. Methods 104, 21 (1972); H. Homeyer, J. Mahoney, and B. G. Harvey, ibid., 118, 311 (1974).

5. P. M. Endt and C. van der Leun, Nucl. Phys. A214, 1 (1973).

6. J. C. Hardy, H. Brunnader, J. Cerny, and J. Jänecke, Phys. Rev. 183, 854 (1969).

7. J. C. Hardy, H. Schmeing, W. Benenson, G. M. Crawley, E. Kashy, and H. Nann, Phys. Rev. C9, 252 (1974).

8. F. C. Barker, Nucl. Phys. 83, 418 (1966).

9. V. I. Goldanskii, Soviet Physics JETP 11, 1179 (1960).

10. A. H. Wapstra and N. B. Gove, Nuclear Data A9, 267 (1971).

^{7}Li + ^{7}Li REACTION STUDIES LEADING TO MULTI-NEUTRON FINAL STATES

Joseph Cerny, R. B. Weisenmiller, N. A. Jelley,† K. H. Wilcox, and G. J. Wozniak

Although there has been extensive historical interest in questions of the possible stability of ^{3}n or ^{4}n, and of the location of unbound resonances in these systems, no bound states nor uncontroversial multi-neutron resonance effects have so far been established in either of these systems (see Ref. 1 for a review of the 3n system; Ref. 2 for the 4n). Nonetheless, since certain heavy-ion reactions observing neutron-deficient reaction products afford a new look at these (and other[3]) multi-neutron final states, we have investigated one of the simplest of these systems, that of ^{7}Li + ^{7}Li → ^{12}C + 2n, ^{11}C + 3n, and ^{10}C + 4n. By also measuring the energy spectra and cross-sections of the boron isotopes in the better-established ^{12}B + d, ^{11}B + t and ^{10}B + ^{4}H channels (but ones in which the light product nuclei have lower T_z), one can hope to obtain some criteria by which to evaluate the yield in the carbon exit channels. Four of these reactions are discussed below; unfortunately, reactions on target contaminants precluded useful analysis of the ^{7}Li(^{7}Li, ^{12}C)2n and Li(^{7}Li,^{10}B)^{4}H results.

A beam of 79.6 MeV ^{7}Li^{+2} (~ 150 nA) from the Lawrence Berkeley Laboratory 88-Inch Cyclotron was used to bombard a 110 μgm/cm^2 ^{7}Li target. Reaction products were observed in two similar counter telescope systems placed at opposite sides of the beam. The data reported below came from the system placed at 7.4° (lab) with a 0.086 msr solid angle; it consisted of two transmission (ΔE) detectors, 18 and 14 μm thick (the first with subnanosecond pile-up rejection[4]), a 190 μm E detector, and a reject detector. Although equivalent results were obtained with the second system, which was placed at 9.6°, they were of poorer quality. Other experimental details were similar to those described previously;[5] a comparison of two particle identification signals was employed to reduce background, with a stringent comparison rejecting ~ 50% of the events traversing the telescope. Electronic and beam energy stability were monitored continuously, and the absolute beam energy was determined using a precision analyzing magnet.

Results from the ^{7}Li(^{7}Li,^{11}B)t and ^{7}Li(^{7}Li, ^{11}C) 3n reactions are compared in Fig. 1(a) and 1(b-c), respectively. Transitions to a number of the bound ^{11}B final states can be seen; in particular the ground state transition has a cross section of 23 μb/sr c.m. However, the ^{7}Li(^{7}Li,^{11}C) 3n data per se in Figs. 1(b) and 1(c) present no discernible structure. At this small forward angle the ^{11}C energy region that would correspond to a bound 3n system is free from reactions on target contaminants, and an upper limit of 70 nb/sr c.m. can be set for production of a bound ^{3}n. Two imperfect comparisons are available: this limit is a factor of ~ 300 less than the yield of the ^{12}B g.s. + t channel, and is a factor of ~12 less than the average yields of the ^{16}O(^{7}Li,^{11}C)^{12}B g.s. and ^{12}C(^{7}Li,^{11}C)^{8}Li g.s. reactions at forward angles (obtained from separate experiments). With regard

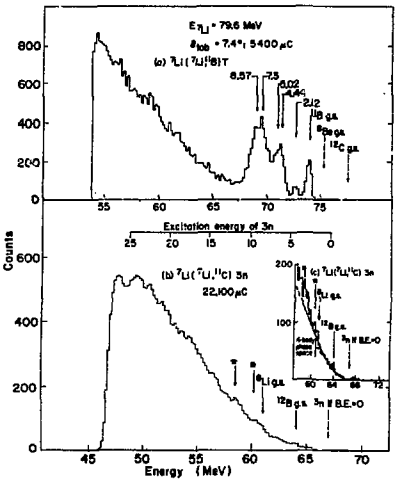

Fig. 1. Spectra from the ^{7}Li + ^{7}Li reaction at 79.6 MeV. (a) ^{7}Li(^{7}Li,^{11}B)t. Dashed arrows denote the expected location of contaminant reactions. (b) ^{7}Li(^{7}Li,^{11}C)3n. See (a). An arrow with an asterisk denotes the location of a known state from either a ^{12}C or ^{16}O contaminant. Also indicated is the ^{11}C energy that would correspond to transitions to a three neutron system with zero binding energy (B.E.). (c) A detail of the high-energy part of (b). (XBL 745-3298)

to those transitions corresponding to an unbound 3n system, one sees in Fig. 1(c) that the ^{11}C energy spectrum encompassing up to ~7 MeV excitation of three neutrons (before the bulk of the transitions from target contaminants begins) is well fit by four-body phase space.

Figure 2 presents an energy spectrum from the attempted three-proton transfer ^{7}Li(^{7}Li,^{10}C)4n reactions. Independent experiments on the ^{16}O(^{7}Li, ^{10}C)^{13}B and ^{12}C(^{7}Li,^{10}C)^{9}Li reactions successfully observed the transfer of three protons with comparable ground state cross sections, averaging ~450 nb/sr c.m. Peaks from reactions on these target contaminants account for the observed structure in the 4n continuum region of Fig. 2; the underlying background appears to be adequately fit by five-body phase space. Again, at this forward angle, contaminant reactions do not interfere in the region of the ^{10}C energy spectrum corresponding to

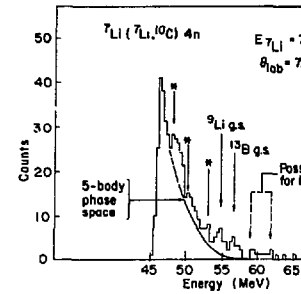

Fig. 2. An energy spectrum from the ^{7}Li(^{7}Li,^{10}C) 4n reaction at 79.6 MeV and 7.4°. Known contaminant reactions are indicated either explicitly or by an arrow with an asterisk. (XBL 745-3306)

transitions leading to a bound ^{4}n. (The known mass of ^{8}He sets an upper limit to the total binding energy of ^{4}n (see Ref.2).) The very minor background observed in this region arises from the ^{11}C "leak-through" remaining in this energy spectrum; however, it is still possible to set an upper limit of 30 nb/sr c.m. for the cross section of this reaction leading to a bound 4n system. The only available comparison is to note that this limit is a factor of ~15 less than the yield of the observed three-proton transfer reactions on ^{12}C and ^{16}O.

These results set stringent limits[1,2] in failing to observe transitions to a bound ^{3}n or ^{4}n; further, no resonance structure was evident in these heavy-ion studies of the unbound 3n and 4n systems. With the better particle identification and larger solid angles of magnetic spectrometers one would be more sensitive to bound ^{3}n or ^{4}n systems; and better data on the unbound 4n system (requiring rigid maintenance of the ^{7}Li target purity) would permit an interesting comparison with the ^{4}He(π^-,π^+)4n studies,[6] in which a possible final state interaction is observed between one neutron pair in the exit channel. Clearly the above approach can also be extended to search for bound or unbound structure in higher neutron configurations.

Footnotes and References

*Condensed from LBL-3407.

†Present address: Nuclear Physics Laboratory, University of Oxford, England.

1. L. M. Delves and A. C. Phillips, Rev. Mod. Phys. 41, 497 (1969). G. Paić, Few Particle Problems in the Nuclear Interaction, ed. I. Slaus, S. A. Moszkowski, R. P. Haddock, and W. H. T. van Oers (North-Holland Publ. Co., Amsterstam, 1972) p. 539.

2. S. Fiarman and W. E. Meyerhof, Nucl. Phys. A206, 1 (1973). Yu. A. Batusov, Zh. Ganzorig, L. Gumerova, I. V. Dudova, V. M. Sidorov, V. A. Khalkin, and D. Chultem, Dubna preprint P1-7475 (1973).

3. J. Cerny, Reactions Between Complex Nuclei, Vol. 2. ed. R. L. Robinson, F. K. McGowan, and J. B. Ball (North-Holland Publ. Co., Amsterdam, 1975).

4. J. D. Bowman, A. M. Poskanzer, R. G. Korteling, and G. W. Butler, Phys. Rev. C9, 836 (1974).

5. K. H. Wilcox, N. A. Jelley, G. J. Wozniak, R. B. Weisenmiller, H. L. Harney, and J. Cerny, Phys. Rev. Lett. 30, 866 (1973).

6. F. Becker and Yu. A. Batusov, Rivista del Nuovo Cimento, Ser. 2 1, 309 (1971), and references therein.

STUDY OF T=2 STATES IN ^{12}C AND ^{12}B

D. Ashery,* G. W. Goth,† G. J. Wozniak, M. S. Zisman, and J. Cerny

The double analog T=2 states in self-conjugate nuclei have been intensively investigated because of interest in the isospin multiplet mass relations and in isospin-forbidden decay properties.[1] The lowest 0$^+$ T=2 state in ^{12}C has been tentatively identified in the ^{14}C(p,t)^{12}C reaction[1,2] at an excitation energy of 27.50±0.1 MeV[1] and 27.595±0.02 MeV.[2] Attempts to form this state as a resonance in the ^{11}B+p, ^{10}B+d and ^{9}Be+^{3}He systems have failed.[3] In a recent study of the ^{10}Be(^{3}He,n)^{12}C reaction[4] a peak corresponding to an excitation energy of 27.611±0.020 MeV in ^{12}C, identified as the 0$^+$ T=2 state, was observed at 0° but not at any other angle.

In the present work the ^{14}C(p,t)^{12}C and ^{14}C(p,^{3}He)^{12}B reactions were studied at 54 MeV bombarding energy over the angular range of 14°-50° in the laboratory system. The target was prepared by passing ^{14}C-enriched methyl-iodide through an electrical discharge system. Details of this method are described elsewhere.[5] A 450 μg/cm^2 target, supported on a 560 μg/cm^2 gold foil was used in this experiment. The outgoing triton and ^{3}He particles were detected by two detector telescopes coupled to standard particle identification systems.

Figure 1 shows the triton and ^{3}He spectra obtained at 23° (lab). Two peaks are clearly observable in each spectrum, corresponding to excitation energies of 27.50±0.06 and 29.5±0.1 MeV in ^{12}C and of 12.8±0.06 and 14.9±0.1 MeV in ^{12}B. In Fig. 2 the angular distributions for these four states are

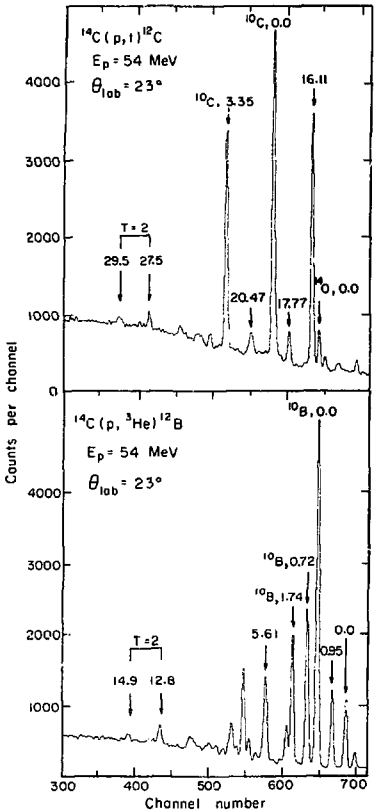

Fig. 1. Triton and ^{3}He energy spectra from the $^{14}C(p,t)^{12}C$ and $^{14}C(p,{}^{3}He)^{12}B$ at 23°. (XBL 754-2656)

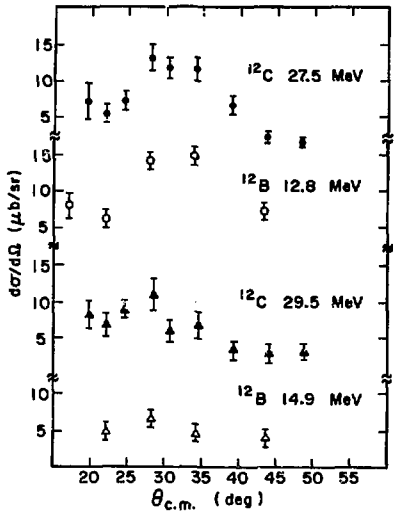

Fig. 2. Angular distributions of the T=2 states in ^{12}C and ^{12}B. (XBL 754-2655)

presented. There is an uncertainty of about 30% in the absolute cross sections, due mainly to uncertainties in target isotope enrichment. The state at 12.8 MeV in ^{12}B has been identified[1] as the lowest 0^+ T=2 state in this nucleus. The state at 27.5 MeV in ^{12}C, having the correct excitation energy and a similar angular distribution (consistent with an L=0 transition) is therefore identified as the lowest 0^+ T=2 state in ^{12}C. The ratio of cross-sections for the population of these two states is also consistent with the theoretical predictions.[6] The states at 14.9 MeV in ^{12}B and 29.5 MeV in ^{12}C are both at an excitation energy of about 2±0.1 MeV above the 0^+ T=2 state in their respective nucleus. In a recent study of the $^{14}C(^{18}O,{}^{12}Be)$ ^{20}Ne reaction[7] a state was observed in ^{12}Be at an excitation energy of 2.09±0.05 MeV. It is therefore suggested that these two states are both T=2 states, analogs of the 2.09 MeV state in ^{12}Be.

Footnotes and References

*On leave from Tel-Aviv University, Israel.

†Present address: Department of Chemistry, San Jose State University, San Jose, California.

1. J. Cerny, Annual Review of Nuclear Science, Vol. 18 (1968) 27.

2. P. H. Nettles, C. A. Barnes, D. C. Hensley, and C. D. Goodman, Bull. Am. Phys. Soc. 16, 489 (1971).

3. E. K. Warburton, H. M. Kvan, D. E. Alburger, and K. A. Snover, Phys. Rev. C6, 375 (1972) and references therein.

4. D. R. Goosman, D. F. Geesaman, F. E. Cecil, R. L. McGrath, and P. Paul, Phys. Rev. C10, 1525 (1974).

5. J. L. Gallant, Nuc. Inst. Meth. 102, 477 (1972).

6. J. Cerny and R. H. Pehl, Phys. Rev. Lett. 12, 619 (1964).

7. G. C. Ball, J. G. Costa, W. G. Davies, J. S. Forster, J. C. Hardy, and A. B. McDonald, Phys. Lett. 49B, 33 (1974).

IS (α, ^{8}Be) A DIRECT REACTION AT HIGH ENERGIES?

N. A. Jelley,* G. J. Wozniak, and J. Cerny

To conclusively determine the direct nature of the (α,^{8}Be) reaction near 65 MeV bombarding energy, an excitation function of the ^{12}C(α,^{8}Be)^{8}Be(gs) reaction was obtained. Measurements in small angular steps were taken over the maximum in the angular distribution at $\theta_{c.m.} \approx 35°$ (Ref.1) to see if the shape or magnitude changed substantially with bombarding energy. Data measured at E_α = 63.2, 65.2, 65.8, 66.6, 67.3 MeV are shown in Fig. 1. The angular width of each data point is ~1°, and the error bars shown are entirely statistical. Upon examining Fig. 1, it is clear that the magnitude of the differential cross section is a smooth and slowly decreasing function of the bombarding energy. The shape of the two observed maxima seems to also vary slowly with the incident energy.

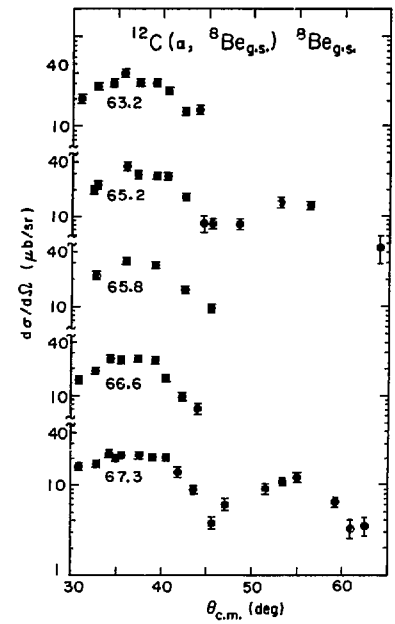

Fig. 1. Angular distributions of ^{8}Be nuclei emitted from the ^{12}C(α, ^{8}Be$_{g.s.}$) ^{8}Be$_{g.s.}$ reaction at E_α = 63.2, 65.2, 65.8, 66.6, and 67.3 MeV.

The above behavior is in marked contrast to that observed[2] at incident energies of 35.5-41.9 MeV for the differential cross sections for the ^{16}O(α,^{8}Be)^{12}C reactions to the ground and first excited state of ^{12}C. In the latter case, both the shapes and magnitudes of the cross sections changed substantially, causing Brown et al. to conclude that in this energy region statistical processes dominated direct ones. At the low bombarding energies of 12-26 MeV the ^{12}C(α,^{8}Be)^{8}Be reaction also seems to be dominated by compound processes.[3]

From the above, it seems that in the region of 20-40 MeV incident energies compound processes are important for the (α,^{8}Be) reaction mechanism, but at higher energies a direct mechanism is the major process, substantiating the conclusion of an earlier study.[1]

Footnote and References

*Present address: Nuclear Structure Lab, Kreble Road, Oxford, England.

1. G. J. Wozniak, N. A. Jelley, and J. Cerny, Phys. Rev. Lett. 31, 607 (1973).

2. R. E. Brown, J. S. Blair, D. Bodansky, N. Cue, and C. D. Kavaloski, Phys. Rev. 138, B1394 (1965).

3. P. Chevallier, F. Scheibling, G. Goldring, I. Plesser, and M. W. Sachs, Phys. Rev. 160, 827 (1967). P. Martin and T. R. Ophel, Nucl. Phys. A194, 491 (1972). F. Brochard, P. Chevallier, D. Disdier, G. Rudolf, and F. Scheibling, p. 204 in Proceedings of the Inter. Conf. on Nucl. Phys., ed. by J. de Boer and H. J. Mang (North-Holland 1973) Vol. 1.

α-TRANSFER STUDIES VIA THE (α, ^{8}Be) REACTION ON ^{15}N AND ^{14}N

G. J. Wozniak, N. A. Jelley,* and J. Cerny

An investigation of the α-cluster components in the ^{15}N and ^{14}N ground state wave functions was undertaken utilizing the (α,^{8}Be) reaction. Our ^{8}Be detection technique[1] was adapted[2] for use with a gas target through use of an unusual gas collimator, which consisted of two divided collimators in a standard pattern (see Fig. 1). As usual the front collimator defines the extent of the target and eliminates the possibility of detecting reaction products directly scattered from the cell entrance and exit. To reduce the singles counting rate in the twin ΔE detector, a 0.5-mm partition connected the posts of the two collimators. This partition eliminated particles that might otherwise have passed through different sides of the front and back collimators. In addition both the counter telescope and gas collimator were encased in an aluminum housing to shield the detectors from slit-scattered beam.

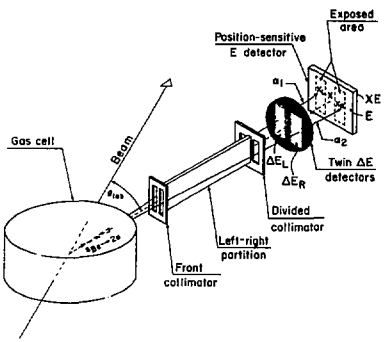

Fig. 1. A schematic diagram of a gas cell, the ^{8}Be gas collimator and ^{8}Be identifier.

(XBL 742-2319)

Using the above apparatus, the ^{15}N(α,^{8}Be)^{11}B reaction was studied at an incident energy of 72.1 MeV on an isotopically enriched (99%)$^{15}N_2$ gas target. Because of the small vertical size of the position sensitive detector, it was necessary to place the counter telescope close to the gas cell wall to obtain a sizeable detection efficiency. The large dE/dθ, poor position resolution (0.8 mm FWHM), and the extended target gave an experimental energy resolution of ~800 keV which is a factor of 2 worse than that attained with solid targets.

In Fig. 2 is shown a typical spectrum of the ^{15}N(α,^{8}Be)^{11}B reaction. The background level above

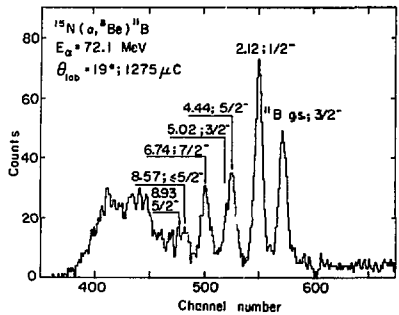

Fig. 2. A ^{8}Be energy spectrum from the ^{15}N(α,^{8}Be)^{11}B reaction at θ_{lab} = 19°. The locations of possible transitions to natural parity states below ~9 MeV are shown (see text). (XBL 746-3555)

the ground state is caused by intra-beam-burst pile up events which are not eliminated because subnanosecond pileup rejection was not employed. Strong transitions are clearly seen to the 3/2⁻ ground and 1/2⁻ 2.12 MeV states[3] of ^{11}B, which are consistent with their calculated α-structure factors.[3] The 5/2⁻ 4.44 MeV and 3/2⁻ 5.02 MeV levels are not resolved in this spectrum and were only resolved at θ_{lab} = 15°. However, from the measured excitation energy of 4.50±0.07 MeV for the third peak in the spectra, it seems that at all angles the 5/2⁻ state were populated stronger than the 3/2⁻ one. This is consistent with their theoretical α-structure factors.

No evidence was observed for transitions to the two positive parity states at 7.30 and 8.00 MeV. Thus a third positive parity level at 6.79 MeV was assumed not to be populated even though it could not be seen due to the strong transition to the 7/2⁻ level at 6.74 MeV. This 7/2⁻ state is made very strongly at θ_{lab} = 15°. There is also evidence that two states at 8.57 and 8.92 MeV are being made although their weak strength and the large background hindered their observation. Theoretical α-structure factors would indicate that they should be made with a strengtn similar to what was observed.

To calculate the experimental cross sections for the observed transitions, the probability of detecting a ^{8}Be nucleus from a gas target must be determined. This value was calculated by making a simple first order correction to the solid target detection efficiency and by using oxygen gas and

solid target data to normalize the cross sections. In Fig. 3 are shown angular distributions of the first four peaks shown in Fig. 2. As the ^{15}N ground state is spin 1/2 the transfers to all final states correspond to unique L values. Little structure is seen in these angular distributions; particularly noteworthy is the constrast between this L=0 transfer to the 1/2$^-$ 2.12 MeV state and the oscillating L=0 transfer to the ^8Be or ^{12}C ground states.[1] [The large angular acceptance (1.6° in the lab) of ^8Be events will tend to wash out minima.]

A brief survey of the (α,^8Be) reaction on a $^{14}N_2$ gas target was carried out at an incident energy of 72.1 MeV. In Fig. 4 is shown an energy spectrum taken at θ_{lab} = 18° with the predicted locations of transitions to T=0 states indicated. No evidence was observed for the excitation of the T=1 states occurring at 1.74 and 5.17 MeV in accordance with the ΔT=0 selection rule. Strong transitions were observed to the 3+ ground, 1+ 2.15-MeV, 2+ 3.59-MeV states and to a state at 6.07±0.06 MeV which are in qualitative agreement with calculated α-structure factors. The observed state at 6.07 MeV probably corresponds to the known 4$^+$ level at 6.02 MeV which has a large theoretical α-structure

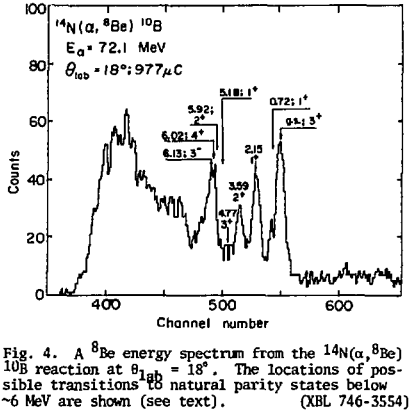

Fig. 4. A ^8Be energy spectrum from the $^{14}N(\alpha,^8Be)\,^{10}B$ reaction at θ_{lab} = 18°. The locations of possible transitions to natural parity states below ~6 MeV are shown (see text). (XBL 746-3554)

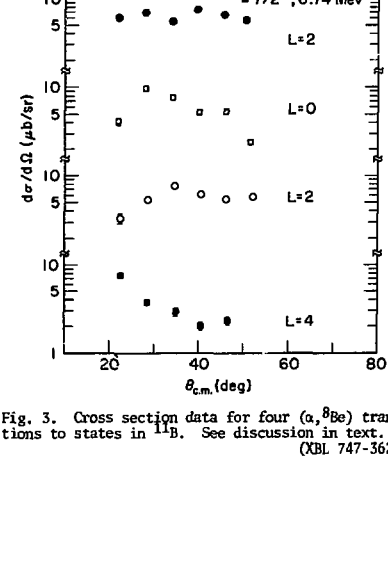

Fig. 3. Cross section data for four (α,^8Be) transitions to states in ^{11}B. See discussion in text. (XBL 747-3620)

factor. Weak transitions were observed to the 1$^+$ 0.72-MeV and 3$^+$ 4.77-MeV states and no evidence was observed for the excitation of the 1$^+$ 5.18-MeV state, which is consistent with their small theoretical α-structure factors. No evidence for the population of discrete states above ~6-MeV excitation energy was observed, however, the large level density and poor resolution hindered this search.

A systematic feature which emerged from a previous study of the (α, ^8Be) reaction on ^{11}B, ^{12}C, and ^{16}O was the strong population of only those states which are predicted to have significant α-structure factors. This selectivity is evident in the above study of ^{14}N and ^{15}N and is additional evidence that the (α, ^8Be) reaction proceeds via a simple α-cluster pickup process.

Footnote and References

*Present address: Nuclear Structure Lab, Kreble Road, Oxford, England.

1. G. J. Wozniak, N. A. Jelley, and Joseph Cerny, Phys. Rev. Lett. 31, 607 (1973).

2. G. J. Wozniak, N. A. Jelley, and Joseph Cerny, Nucl. Instr. and Meth. 120, 29 (1974).

3. F. Ajzenberg-Selove and T. Lauritsen, Nucl. Phys. A114, 1 (1968) and A227, 1 (1974).

4. D. Kurath, Phys. Rev. C7, 1390 (1973).

SPECTROSCOPIC STUDIES IN THE 1p-SHELL BY THE (^{6}Li, ^{8}B) REACTION

R. B. Weisenmiller, K. H. Wilcox, N. A. Jelley,*
G. J. Wozniak, D. Ashery,† and J. Cerny

Two-nucleon transfer reactions (such as (p,t), (p,^{3}He), (d,α), and their complementary stripping reactions) have been used extensively to study two-particle and two-hole states.[1] In light nuclei with an excess of protons or neutrons, Hartree-Fock calculations demonstrate that this type of correlation plays a major role in the effective nuclear interaction. Only with the advent of heavy ion beams has there been any practical reaction, such as (^{6}Li,^{8}B), to supplement the (^{3}He,n) reaction by probing two-proton-hole states in neutron-excess nuclei.

While a variety of possible heavy ion two-proton pick-up reactions are now feasible, the (^{6}Li,^{8}B) reaction presents the fewest experimental difficulties. Both ^{7}B and ^{9}B are particle unbound, thus allowing clean separation of the ^{8}B particles by particle identification with solid state detector telescopes. Since ^{8}B has no bound excited states, its energy spectra lack the shadow peak ambiguity of, e.g., the (^{18}O,^{20}Ne) reaction. Moreover, it is the lightest of the possible two-proton pick-up reactions and thus has the smallest kinematic effects (which are the major component of the energy resolution in the 1p-shell).

The general techniques of producing a lithium beam at the 88-Inch Cyclotron and the identification of the reaction products have been previously described.[3] Because of the highly negative Q-values of these reactions we used an 80 MeV beam to facilitate the detection of the ^{8}B exit particles. Due to the low cross sections of these reactions (see Table 1) a triple particle identifier was used to reduce the background. A telescope of 15, 10, and 200 μm (backed by a 1-mm reject detector) was typically used.

We decided to focus our study on the 1p-shell since the relevent two-nucleon fractional parentage coefficients and spectroscopic factors have been calculated[4] (see Table 1). In principle this allows a rather stringent test of the reaction mechanism as to the degree of single-step versus "multi-step" transfer of the two protons. Also this comparison could allow a better understanding of the effects of the projectile's structure, which is clearly more complicated than for the lighter two-nucleon transfer reactions. For example, ^{6}Li would be a ^{3}S(1$^+$) configuration and ^{8}B a ^{3}P (2$^+$) configuration, as calculated in a pure L·S coupling basis.[5] However, since this mass region is known to be better described by an intermediate coupling scheme,[6] not only do the projectile and ejectile spins enter in a complicated fashion, but the proton pair may also be transferred in a ^{1}D or ^{3}P relative state,[7] rather than a ^{1}S.

On T_z = 0 targets there is an obvious symmetry among the two-nucleon transfer reactions. An example of this symmetry is that the (p,t) reaction probes two-neutron-hole states in proton-excess nuclei, while the (^{6}Li,^{8}B) reaction probes two-proton-hole states in their mirror nuclei. This analogy is less than perfect because of the previously mentioned structural differences in the projectiles and also because of different kinematic effects in the two reactions. Figure 1 shows a typical spectrum of the ^{16}O (^{6}Li,^{8}B) ^{14}C reaction. It indicates the strong selectivity of this reaction. Besides the strong population of the g.s. 0$^+$ and the 2$^+$ state at 7.01 MeV, the other natural parity states are also populated (see Table 1). Compared to the (p,t) data,[8] both reactions show the same general selectivity. From this similarity it is possible to suggest the 8.32-MeV state as a 2$^+$, as the spacing between the lower 2$^+$ at 7.01 MeV and this state agrees well with the spacing of the analogous 2$^+$ states in ^{14}O (at 6.59 and 7.78 MeV). This assignment agrees with that from the ^{12}C (t,p) ^{14}C reaction,[9] but differs with the 1$^+$ assignment from neutron resonance work.[10] The population ratios of these two sets of states are different, however, since the upper 2$^+$ state is populated slightly more than the lower 2$^+$ state by the (p,t) reaction (see Table 1) while it is down a factor of four from the lower 2$^+$ state in the (^{6}Li,^{8}B) reaction. As the calculated spectroscopic factor for the predicted higher 2$^+$ state is almost six times larger than that for the lower 2$^+$ state, the anomalous population ratio of these states in the (p,t) data was explained by Fleming et al.[8] as being due to higher shell configuration mixing.

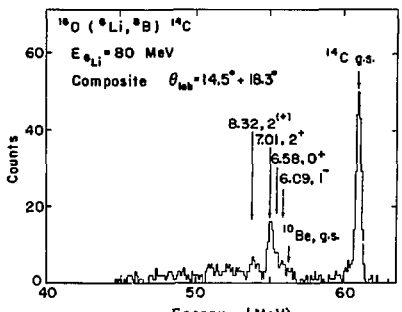

Fig. 1. Energy spectrum from the reaction ^{16}O (^{6}Li,^{8}B) ^{14}C obtained from a partially oxidized ^{142}Nd target. Spectra were collected at θ_{lab} = 14.5° (8550 μC). The 18.3° data were kinematically shifted to correspond to the 14.5° data and added to them.
(XBL 7412-7823)

Table 1. Comparisons of (^{6}Li, ^{8}B) data with both analogous (p,t) data and with Cohen and Kurath calculations.

Final nucleus	J^{π}	Excitation energy (MeV) Known levels	Excitation energy (MeV) Predicted levels[4]	Peak cross sections (^{6}Li, ^{8}B) (μb/sr c.m.)	Integrated cross sections (p,t) (mb)	Spectroscopic[4] factors SMAG	Spectroscopic[4] factors DMAG[a]
^{14}C	0^-	g.s.[b]	g.s.	19.4±1.6[c]	388.5[d]	2.21	
	1^-	6.09		1.5±0.6			
	0^+	6.58		2.0±0.6			
	3^-	6.73					
	0^+	6.89					
	2^+	7.01	6.83	4.3±1.0	242.2		12.72
	2^-	7.34					
	$(1,2)^+$	8.32	15.19	1.0±0.6	323.2		2.28
	etc.						
^{8}Li	2^+	g.s.[e]	g.s.	3.0±0.3[f]	117[g]		0.73
	1^+	0.981	0.91	1.1±0.2			0.00
	3^+	2.26	1.63	9.6±0.5	225	0.75	1.31
	etc.						
^{9}Li	$(3/2)^-$	g.s[e]	g.s.	1.7±0.2[h]		0.67	1.44
	$(1/2)^-$	2.69	3.88				0.03
	$(5/2)^-$ [i]	4.31	3.79	0.4±0.1			0.51
	$(3/2)^-$ [i]	5.4	4.88	0.2±0.1		0.14	0.06
	$(7/2)^-$ [i]	6.41	6.18	0.5±0.1			0.00
^{11}Be	$1/2^+$	g.s.[j]					
	$1/2^-$	0.320	g.s.	2.38±0.2[k]		1.96	
	$(1/2,3/2)^{\pm}(5/2)^+$	1.785					
	$(1/2,3/2)^{\pm}(5/2)^+$	2.69	2.60($3/2^-$)	0.5 ±0.3			0.19
	$(1/2,3/2)^{\pm}(5/2)^+$	3.41					
		3.89	4.98($5/2^-$)	0.75±0.2			1.84
		3.96					
	etc.		5.25($3/2^-$)				1.40

[a] Defined in Ref. 3; SMAG is the L = 0 transfer magnitude and DMAG is the L = 2 transfer magnitude.

[b] F. Ajzenberg-Selove, Nucl. Phys. A152, 1 (1970).

[c] $\theta_{lab} = 11.7°$.

[d] Integrated from 13 to 65° (Ref. 8)

[e] F. Ajzenberg-Selove and T. Lauritsen, Nucl. Phys. A227, 1 (1974).

[f] $\theta_{lab} = 9.7°$.

[g] Integrated from 15 to 50° (tabulated in S. Kahana and D. Kurath, Phys. Rev. C3, 543 (1971) (based on Ref.11).

[h] $\theta_{lab} = 15.0°$.

[i] Assignment suggested in Ref. 12.

[j] F. Ajzenberg-Selove and T. Lauritsen, Nucl. Phys. A114, 1 (1968).

[k] $\theta_{lab} = 9.7°$.

Figure 2(a) shows a spectrum of the ^{10}B (^6Li,^8B) ^8Li results. These data show the same general selectivity as the analogous (p,t) data.[11] For both reactions, this is one of the few targets in the 1p-shell in which an excited state is populated more strongly than the ground state. Another typical spectrum is given in Fig. 2(b), which shows the ^{11}B (^6Li,^8B) ^9Li reaction. These results can be compared to the data from the ^7Li (t,p) ^9Li reaction populating the same final nucleus.[9,12] The state at 2.69 MeV is weakly populated in the (t,p) reaction and populated slightly, if at all, in the (^6Li,^8B) reaction. From the population ratio of this state relative to the ground state, it has been assigned tentatively as a $1/2^-$ state.[12] While it is impossible to conclude anything definite about this state from our data without using a DWBA analysis to remove any kinematic effects of the reaction, the $1/2^-$ state does have a very low spectroscopic factor for population by two-proton pick-up reactions.[4] An alternative explanation would be that it is a positive parity state. If a simple pair transfer mechanism is postulated, then the (^6Li,^8B) reaction on odd mass 1p-shell targets should only populate negative parity states. The (t,p) reaction does not have this inherent selectivity since it can also populate positive parity states with higher shell configurations.

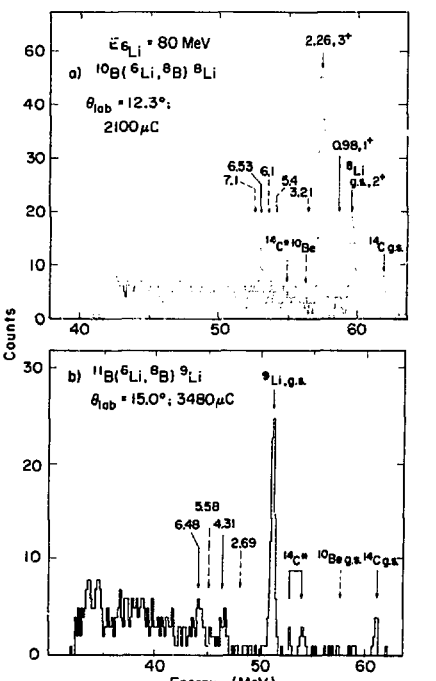

Fig. 2. Energy spectra from: (a) the $^{10}B(^6Li,^8B)$ ^8Li reaction at θ_{lab} = 12.3°; and (b) the $^{11}B(^6Li,^8B)$ ^9Li reaction at θ_{lab} = 15.0° (3480 μC).
(XBL 7412-8399)

This effect is demonstrated in Fig. 3 for the ^{13}C (^6Li,^8B) ^{11}Be reaction. In ^{11}Be it is known that the ground state is a $1/2^+$ state and the first excited state (at 0.32 MeV) is a $1/2^-$ state.[13] This unusual level ordering was predicted by Talmi and Unna[14] as a consequence of the two-body component of the residual interaction depressing the energy of the $1/2^+$ state. These data show the $1/2^-$ state is populated strongly, while the $1/2^+$ g.s. is populated weakly if at all.

The angular distributions of the (^6Li,^8B) reaction are monotonically decreasing with angle. This is consistent with the cross sections being peaked near the grazing angle (as is the case for the $^{142}Nd(^6Li,^8B)^{140}Ce$ data for the ground state transition), which on these light targets is at an inaccessibly forward angle. Also, a J = 0 transfer has a steeper envelope than a higher J transfer. While one would hope eventually to extract spectroscopic information from this reaction, presently high-energy lithium beams are a novelty and optical model parameters are nonexistent. This precludes a really meaningful comparison between the calculated spectroscopic factors[3] and experimental data at this time. However, even by qualitative comparisons to existing two-nucleon transfer data it is possible to extend our knowledge and understanding of the states in neutron-deficient nuclei.

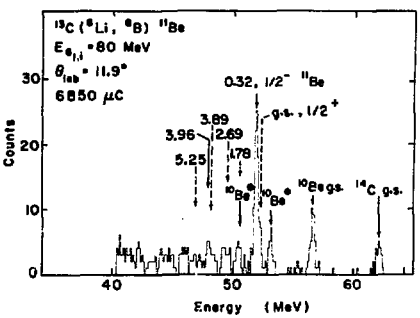

Fig. 3. Energy spectrum from the reaction ^{13}C (^6Li, ^8B) ^{11}Be at θ_{lab} = 11.9° (6847 μC).
(XBL 7412-7822)

Footnotes and References

*Present address: Nuclear Physics Laboratory, University of Oxford, England.

†On leave from the Tel Aviv University, Israel.

1. e.g. The Symposium on Two-Nucleon Transfer and Pairing Excitations, Argonne Physics Division Informal Report PHY-1972H (1972); Norman K. Glendenning, in Nuclear Spectroscopy and Reactions, Part D, edited by Joseph Cerny (Academic Press, N.Y., 1975).

2. G. Ripka, Advances in Nuclear Physics, Vol. 1, edited by M. Baranger and E. Vogt (Plenum Press, N. Y., 1968).

3. K. H. Wilcox, N. A. Jelley, G. J. Wozniak, R. B. Weisenmiller, H. L. Harney, and Joseph Cerny, Phys. Rev. Lett. 30, 866 (1973).

4. S. Cohen and D. Kurath, Nucl. Phys. A141, 145 (1970).

5. F. C. Barker, Nucl. Phys. 83, 418 (1966).

6. D. Kurath, Phys. Rev. 101, 216 (1956); S. Cohen and D. Kurath, Nucl. Phys. 73, 1 (1965).

7. D. Kurath, Comments on Nuclear and Particle Physics V2, 55 (1972).

8. D. G. Fleming, J. C. Hardy, and Joseph Cerny, Nucl. Phys. A162, 225 (1971).

9. R. Middleton and D. J. Pullen, Nucl. Phys. 51, 63 (1964).

10. H. O. Cohn, J. K. Blair, and H. B. Willard, Phys. Rev. 122, 534 (1961).

11. G. T. A. Squier, A. R. Johnston, E. W. Spiers, S. A. Harbison, and N. M. Stewart, Nucl. Phys. A141, 158 (1970).

12. P. G. Young and R. H. Stokes, Phys. Rev. C4, 1597 (1971).

13. F. Ajzenberg-Selove and T. Lauritsen, Nucl. Phys. A114, 1 (1968).

14. I. Talmi and I. Unna, Phys. Rev. Lett. 4, 469 (1960).

CROSS SECTION LIMITS FOR THE PRODUCTION OF SOME HIGHLY NEUTRON-EXCESS S AND Cl ISOTOPES

K. H. Wilcox, N. A. Jelley,* R. B. Weisenmiller, and J. Cerny

The predictions of mass excesses of light nuclei by various models may diverge substantially as we leave the line of β-stability.[1] There has consequently been a considerable interest in measuring mass excesses of very neutron-rich isotopes in the lower-Z nuclei in order to test the theoretical assumptions underlying these models. Due to the successful observation[2] of ^{43,45,46}Ar via the (α,^{9}Be), (α,^{7}Be) and (^{6}Li,^{8}B) reactions on ^{48}Ca, we have irradiated a 400 μg/cm^2 ^{48}Ca target with a 110-MeV α beam and observed the ^{8,10,11}B and $^{10-13}$C exit particles, which populate the residual nuclei ^{44,42,41}Cl and $^{42-39}$S, respectively. Ground state Q values for these reactions vary from about -20 to -44 MeV.

The three-counter, double particle identification technique[3] was used to observe boron isotopes at angles of 10° and 30° in the laboratory system and carbon isotopes at 10° and 35°. No positively-identifiable peak was seen for the formation of the ground state of any of the Cl or S isotopes. Figure 1 shows the energy spectra obtained from ^{10}B exit particles detected at 10° and 30°, and from ^{8}B particles at 30°. The expected positions of the ^{42}Cl and ^{44}Cl ground states are indicated.

The energy region of interest for ^{8}B and ^{10,11}C at 10° was obscured by the large contribution from ^{12}C and ^{16}O contaminants on the target.

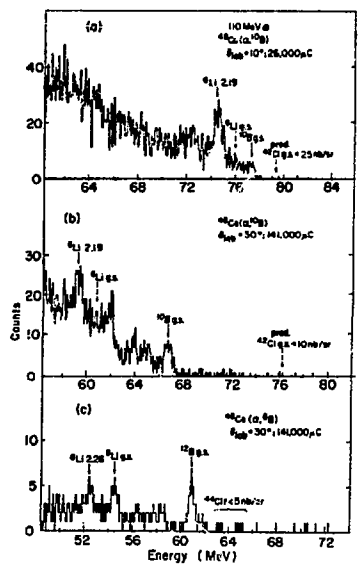

Fig. 1. Energy spectra for the ^{48}Ca(α, ^{10}B)^{42}Cl reaction at (a) 10° and (b) 30°, and (c) the ^{48}Ca(α,^{8}B)^{44}Cl reaction at 30°. (XBL 745-3296)

For the other reactions, however, the background level was very low, permitting the determination of strict upper limits for the cross sections of these reactions populating the ground state. Upper limits for formation of the Cl isotopes were from 15 to 30 nb/sr at 10° and from 5 to 10 nb/sr at 30°. Limits for the S isotopes were about 5 nb/sr at 10° and ranged from 1 to 10 nb/sr at 35°. The very large angular momentum mismatches involved (5-8ħ as calculated semi-classically, including the Coulomb potential) may have contributed to extremely low cross sections for many of these reactions.

Footnotes and References

*Present address: Nuclear Physics Laboratory, University of Oxford, England.

1. N. A. Jelley, J. Cerny, D. P. Stahel, and K. H. Wilcox, Phys. Rev. C11, 2049 (1975).

2. N. A. Jelley, K. H. Wilcox, R. B. Weisenmiller, G. J. Wozniak, and J. Cerny, Phys. Rev. C9, 2067 (1974).

3. F. S. Goulding, D. A. Landis, J. Cerny, and R. H. Pehl, IEEE Trans. Nucl. Sci. 13, 514 (1966).

PREDICTIONS OF THE MASSES OF VERY NEUTRON-EXCESS LIGHT NUCLEI

N. A. Jelley,* Joseph Cerny, D. P. Stahel, and K. H. Wilcox

Over the last few years the masses of many very neutron-rich light nuclei[1] ($T_z \geq 5/2$, $A < 50$) have been determined. On comparing these results with theoretical predictions based on the transverse relation of Garvey-Kelson,[2,3] poorer agreement is generally found than was the case for nuclei nearer β-stability. For example, in the s-d shell there are several $T_z = 5/2$ nuclei for which there is a significant discrepancy (> 500 keV) between the experimental and the calculated mass-excess.

Following the simple shell model approach of Goldstein and Talmi,[4] we have derived[5] an alternative scheme, similar in approach to the method of Garvey et al.[2] but taking more explicit account of shell effects, which more successfully accounts for many of the observed masses of neutron-excess light nuclei. The mass of a nucleus, M(Z,N), with m_i protons in the j_i shell and n_k neutrons in the higher j_k shell, is given by what will be denoted the modified shell model mass equation:

$$M(Z,N) = U(Z) + W(N) + \sum_{ik} m_i n_k V(j_i j_k) \quad [m_i n_k \text{ even}], \tag{1}$$

where U(Z) and W(N) are arbitrary functions of the number of protons and neutrons, respectively, and the sum $\sum_{ik}$ is over the neutron-proton interaction $V(j_i j_k)$.

Equation (1) is similar to the Garvey-Kelson transverse mass equation[2]:

$$M(Z,N) = F(Z) + G(N) + H(A) \tag{2}$$

where F, G and H are arbitrary functions of the number of protons, neutrons and nucleons, respectively. Comparison of these equations shows that the two methods differ mainly in their parameterization of the residual neutron-proton interaction. In the method of Garvey et al.[2] much of this interaction is given by the function H(A), while in Eq. (1) more explicit account is taken of shell structure by the term $\sum_{ik} m_i n_k V(j_i j_k)$. Also, implicit in Eq. (2) is the assumption that the residual neutron-proton interaction is independent[6] of T_z. These different assumptions allow the transverse mass equation to be more general than the modified mass equation, both in predicting masses of odd-odd nuclei and in being able to predict masses farther from stability. In both cases predictions are carried out by determining the parameters of the mass equations by a least-squares fit to known masses.

As a means of comparing these two approaches when applied to light neutron-rich nuclei, the masses of the $T_z = 5/2$ nuclei in the s-d shell have been predicted, and their relative agreement with the experimental values is shown in Fig. 1. Transverse mass equation predictions were taken from the calculations of Thibault and Klapisch[5], who included as input from the s-d shell only known $T_z \leq 2$ nuclei. For the other predictions the modified mass equation was used except for the values for ^{21}O and ^{23}F, where the simple shell model[7] was employed, since insufficient masses are known for Eq. (1) to be used. Only known non-odd-odd

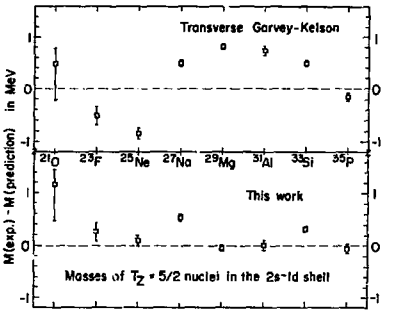

Fig. 1. Two comparisons of the differences between experimental and predicted mass-excesses for the $T_z = 5/2$ nuclei in the 2s-1d shell. See text.
(XBL 745-3304A)

Table 1.
Comparisons with experiment of the predictions of the transverse (T) and the modified (M) mass-equations.

				Mass Excess (MeV±MeV)			Binding Energy (MeV)					
							1 Neutron			2 Neutron		
				Experimental	Calculated		Experimental	Calculated		Experimental	Calculated	
Z	N	EL	A		T	M		T	M		T	M
2	6	HE	8	31.57±.03	31.57	31.51	2.61			2.17		
2	7	HE	9	U ≡ unbound	42.61	43.49		-2.97	-3.85		- .36	
2	8	HE	10	U	51.00	52.34		- .32	- .78		-3.29	-4.62
3	7	LI	10	U	33.25			- .21			3.84	
3	8	LI	11	40.94±.08	40.94	41.14				.17		
3	9	LI	12	U	52.94			-3.93			-3.55	
4	8	BE	12	25.03±.05	25.02	24.75	3.22			3.72		
4	9	BE	13	U	35.39	34.60		-2.31	-1.77		.94	1.84
4	10	BE	14	B ≡ bound	40.72	41.09*		2.74	1.58		.44	- .20
5	9	B	14	23.66 ±.03	23.66		.98			5.86		
5	10	B	15	B	28.75	29.89		2.97			3.97	2.66
5	11	B	16	U	37.97			-1.14			1.83	
6	11	C	17	B	21.27	20.86		.50	.90		4.75	5.34
6	12	C	18	B	25.50	24.57		3.84	4.36		4.34	5.27
7	12	N	19	B	16.27	15.32		5.07			7.74	8.51
7	13	N	20	B	21.60			2.75			7.82	
8	13	O	21	$\left(9.3^{+.3}_{-.7}\right)$	8.74	8.39+		3.08	3.48		10.80	11.09
8	14	O	22	$\left(11.5^{+.2}_{-.5}\right)$	9.42	9.35+		7.39	7.11		10.47	10.59
8	15	O	23	B	15.48	15.40		2.01	2.02		9.40	9.13
9	14	F	23	3.36±.17	3.40	3.36	7.54			12.74		
9	15	F	24	B	8.04			3.44			10.89	
10	15	NE	25	-2.16 ±.10	-1.95	-2.12	4.28			13.15		
10	16	NE	26	B	.17	- .27		5.95	6.23		9.89	10.43
11	15	NA	26	-6.90 ±.02	-6.94		5.62			14.63		
11	16	NA	27	-5.62 ±.06	-5.71	-5.73	6.79			12.41		
11	17	NA	28	-1.14 ±.08	-1.02		3.59			10.38		
11	18	NA	29	2.65 ±.10	2.32	2.66	4.28			7.87		
11	19	NA	30	8.37 ±.20	8.50		2.35			6.63		
11	20	NA	31	(10.6 ±.8)	12.70	14.38		3.87			5.76	4.42
11	21	NA	32	(16.4 ±1.1)	21.02			- .25			3.62	
11	22	NA	33	B	26.90			2.19			1.94	
12	17	MG	29	-10.75±.05	-10.70	-10.75	3.80			12.31		
12	18	MG	30	B	- 9.37	- 9.21		6.75	6.54		10.56	10.42
13	18	AL	31	-15.01±.10	-15.00	-15.05	7.19			12.94		
13	19	AL	32	B	-11.14			4.21			11.50	
14	19	SI	33	-20.57 ±.05	-20.71	-20.67	4.55			13.76		
14	20	SI	34	B	-20.57	-20.32		7.93	7.72		12.77	12.42
15	20	P	35	-24.5[illegible] ±.08	-24.90	-24.81	8.45			14.74		
15	21	P	36	B	-20.88			4.05			12.46	
16	23	S	39	B	-23.07	-23.21		4.33	4.35		12.24	12.31
16	24	S	40	B	-22.50	-22.64		7.50	7.51		11.83	11.85
17	24	CL	41	B	-27.43	-27.39		7.84			13.65	13.67
17	25	CL	42	B	-24.68			5.32			13.16	

*Assumed value, see text.

†Calculated using simple shell model. See Ref. 4.

$T_z \leq 2$ nuclei, together with ^{29}Na, with configurations $\pi p_{1/2}\ \nu d_{5/2}$, $\pi d_{5/2}\ \nu s_{1/2}$, $\pi d_{5/2}\ \nu d_{3/2}$ and $\pi s_{1/2}\ \nu d_{3/2}$ were included as input. (The mass of ^{29}Na determines the interaction parameter $V(\pi d_{5/2}\ \nu d_{3/2})$.) As seen in Fig. 1, considerably better agreement was obtained with the approach of this work than with the transverse mass equation; quantitatively the rms deviations between experiment and calculation are 260 keV and 620 keV, respectively (excluding the mass of ^{21}O because of its large error). Another example is discussed in Ref. 8 where the masses of the argon isotopes $^{43-46}$Ar are compared with the predictions of Eqs. (1) and (2); better agreement is also found using Eq. (1).

Table 1 presents predictions of mass excesses and one- and two-neutron binding energies of selected neutron-excess nuclei at or just beyond the limits of current investigation obtained through a recalculation with Eq. (2), the transverse mass equation, as well as with Eq. (1), the modified mass equation, denoted T and M, respectively. Experimental values are given when available (see Ref. 6 for sources) and those nuclei only known to be bound or unbound are indicated by the symbol "B" or "U". A complete tabulation of the results is given in Ref. 7.

Calculated T and M values in Table 1 arise from a least-squares fitting program which employed with equal weight the appropriate particle-stable nuclei[11] with $N \geq Z$ whose mass-excesses are known to $\leq$ 200 keV; those known with less accuracy were not used in these calculations and are shown in the table enclosed in parentheses. All known nuclei (271) with $2 \leq Z \leq 35$ and $4 \leq N \leq 50$ were used in obtaining the transverse mass equation values. Compared to the recent calculation,[5] the ten known s-d shell, $T_z \geq 5/2$ nuclei given in Table 1 were the additional nuclei included. For Eq. (1) the known non-odd-odd nuclei (74) with configurations $\pi p_{3/2}\ \nu p_{1/2}$, $\pi p_{3/2}\ \nu d_{5/2}$, $\pi p_{1/2}\ \nu d_{5/2}$, $\pi d_{5/2}\ \nu s_{1/2}$, $\pi d_{5/2}\ \nu d_{3/2}$, $\pi s_{1/2}\ \nu d_{3/2}$ and $\pi d_{5/2}\ \nu f_{7/2}$ were employed. In Eq. (1) lack of sufficient known masses required assumed values for the mass-excesses of ^{21}O, ^{22}O and ^{14}Be: for ^{21}O and ^{22}O the simple shell model[7] was used and (to determine the interaction parameter $V(\pi p_{5/2}\ \nu d_{5/2})$ the mass-excess of ^{14}Be (known to be bound)[12] was taken to equal ^{12}Be + 2n = 41.09 MeV, close to the value obtained with the transverse equation of 40.72 MeV.

In order to compare how well these two approaches account for known masses, one can evaluate the rms deviation in each case. For nuclei with $2 \leq Z \leq 17$ the transverse mass equation yields an rms deviation of 220 keV and the modified mass equation 200 keV. Though these values are very similar it does not necessarily follow that the predictive validity of the two approaches will be the same (compare the results in Fig. 1).

From Table 1 it can be seen that the differences between the T and M approaches observed in the s-d shell for the $T_z = 5/2$ nuclei persist to lighter nuclei, since the predictions for ^{13}Be, ^{15}B and ^{19}N differ by more than 750 keV. Those nuclei lying on the edge of stability as predicted by this recalculation with the transverse equation differ from those of Ref. 3, which did not employ any $T_z \geq 5/2$ nuclei from the s-d shell, in that a) ^{23}N, ^{26}O, ^{40}Mg, ^{43}Al and ^{48}Si are predicted to be the last nucleon-stable isotopes, compared[3] to ^{25}N, ^{28}O, ^{42}Mg, ^{45}Al and ^{46}Si; and b) ^{28}F, ^{29}Ne and ^{37}Mg are predicted to be the first unbound isotopes, compared[3] to ^{30}F, ^{34}Ne and ^{41}Mg. Results from the modified mass equation are less extensive than those from the transverse equation, generally not predicting the edge of stability; however, for the lighter nuclei ^{26}O is calculated by Eq. (3) to be unbound by 240 keV, predicting ^{24}O as the last stable oxygen isotope. Also ^{29}F is calculated to be unbound to 2n decay by 910 keV, compared to the prediction of the transverse equation that it is bound by 770 keV.

The approach employing the modified mass equation described above appears to be a useful alternate predictive scheme for the masses of very neutron-excess light nuclei. Further mass measurements of nuclei far from stability such as, for example, the nucleon-stable isotopes ^{15}B and ^{19}N will afford particularly interesting new comparisons of this method and that of Garvey et al.[2] with experiment.

Footnotes and References

*Present address: Nuclear Physics Laboratory, University of Oxford, England.

1. J. Cerny, Reactions Between Complex Nuclei, Vol. 2, ed. R. C. Robinson, F. K. McGowan and J. B. Ball (North-Holland Publ. Co., Amsterdam, 1975.

2. G. T. Garvey, W. J. Gerace, R. L. Jaffe, I. Talmi and I. Kelson, Rev. Mod. Phys. 41, S1 (1969).

3. C. Thibault and R. Klapisch, Phys. Rev. C9, 793 (1974).

4. S. Goldstein and I. Talmi, Phys. Rev. 105, 995 (1957).

5. N. A. Jelley, Joseph Cerny, D. P. Stahel, and K. H. Wilcox, Phys. Rev. C11, 2049 (1975).

6. J. Jänecke and H. Behrens, Phys. Rev. C9, 1276 (1974).

7. N. A. Jelley, J. Cerny, D. P. Stahel, and K. H. Wilcox, Lawrence Berkeley Laboratory Report LBL-3414.

8. N. A. Jelley, K. H. Wilcox, R. B. Weissmiller, G. J. Wozniak and J. Cerny, Phys. Rev. C9, 2067 (1974).

9. R. Klapisch, C. Thibault, C. Rigand, A. M. Poskanzer, L. Lessard, and W. Reisdorf, Inter. Conf. on Nucl. Physics, Munich, Vol. 1, ed. J. de Boer and H. J. Mang (North-Holland Publ.Co., Amsterdam, (1973) 325 and private communication (to be published).

10. A. G. Artukh, G. F. Gridnev, V. L. Mikheev, V. V. Volkov, and J. Wilczynski, Nucl. Phys. A192, 170 (1972).

11. Masses were generally taken from A. H. Wapstra and N. B. Gove, Nucl. Data A9, 265(1971). References to most new masses of interest are given in Table 1; a few other new or revised masses (for ^{34}P, ^{38}S, $^{43-46}$Ar, and ^{58}Mn) are cited in Ref. 7. In addition, in order to determine all of the parameters, it was necessary to use the mass of the particle-unstable nuclide ^{7}He.

12. J. D. Bowman, A. M. Poskanzer, R. G. Korteling and G. W. Butler, Phys. Rev. C9, 836 (1974).

A SEARCH FOR ^{53}Ni

D. J. Vieira, R. A. Gough, and J. Cerny

The series of A = 4n + 1, T_z = - 3/2 beta-delayed proton emitters is known[1,2] from ^{9}C to ^{49}Fe. To extend the series to heavier nuclei a pulsed beam experiment was performed in search of ^{53}Ni.

A 1.2-mg/cm^2 natural calcium target at a target angle of 70° was bombarded with a 65-MeV $^{16}O^{+5}$ beam provided by the 88-Inch Cyclotron. A slotted rotating wheel[3] was used to control the pulsing of the beam and to shield the detector while the target was being irradiated. After an irradiation time of 150 msec the beam was turned off and an 18 μm ΔE - 107 μm E counter telescope was used to detect particles passing from the target through a slot in the wheel. During the 200 msec counting period, events which were in fast ΔE-E coincidence (2τ = 30 nsec) were fed into a particle-identifier; those which identified as protons were stored in an analyzer as a function of time.

The delayed proton spectrum obtained after 12,900 μC is shown in Fig. 1. The large group at E_p(Lab) = 1.56 MeV results from the direct proton decay of ^{53}Co^m produced by the ^{40}Ca(^{16}O,p2n)^{53}Co^m reaction.[4] This group was useful as an internal monitor and as an energy calibration point. Other calibration points were obtained from the production of ^{41}Ti by bombardment of Ca with 29.5 MeV ^{3}He. The observed half-lives of ^{41}Ti and ^{53}Co^m were 84±3 msec and 257±15 msec, respectively. These agree well with the previous measurements of 80±1 msec[5] and 247±12 msec.[4]

A new and very weak activity was observed at an energy of 1.88±0.05 MeV (lab) after correcting for energy losses in the target and detector dead layers. The half-life exhibited by this group is 45±15 msec, thereby precluding the possibility that the events result from pile-up associated with the decay of ^{53}Co^m. Furthermore, the half-life is distinctly different from the 75±10 msec[6] half-life of ^{49}Fe which can be produced at this energy by the ^{40}Ca(^{16}O, α3n) reaction. Two small groups labeled in Fig. 1 by dashed arrows are believed to be delayed protons emitted from ^{29}S which are produced via the ^{16}O (^{16}O,3n) reaction on the slight oxygen contaminant present in the target. Other possible impurity reaction products are unable to account for this new activity since the energy and half-life of this group are not compatible with the known properties of any other delayed proton precursors.

The 1.88±0.05 MeV activity is consistent, however, with beta-delayed proton emission expected from ^{53}Ni produced by the ^{40}Ca(^{16}O,3n) reaction. A preliminary decay scheme is presented in Fig. 2. The figure shows the super-allowed beta decay of ^{53}Ni to the lowest T = 3/2 state in ^{53}Co, which in turn proton decays to the first excited state in ^{52}Fe. Decay to this 2+ state rather than to the ground state was assumed since this gave the best agreement between the excitation energy of the T = 3/2 state of ^{53}Co and its mirror state in ^{53}Fe. Further support is given by the fact that both ^{45}Cr and ^{49}Fe show similar preference for decay to the 2+ state. Based on this assumption no evidence for decay to the ground state of ^{52}Fe was observed (see Fig. 1). Using the masses of the analogue states of ^{53}Co and ^{53}Fe, together with the ground state mass of ^{53}Mn, the isobaric multiplet mass equation predicts the mass excess for ^{53}Ni to be -29.48±0.19 MeV. This agrees with the Coulomb energy predictions of -29.654±0.009 MeV.[7]

Due to the contrast in magnitude of the ^{53}Co^m group compared to the ^{53}Ni group, it is interesting to compare the observed production ratio to the predicted ratio. Using the evaporation code GROGI2[8] the cross section ratio of ^{53}Co^m to ^{53}Ni at this

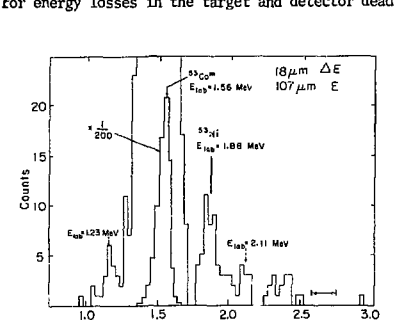

Fig. 1. An identified-proton energy spectrum resulting from the bombardment of Ca with 65 MeV ^{16}O. The two groups labeled with dashed arrows are believed to arise from the decay of ^{29}S (see text). The horizontal arrows denote the proton energy region of possible transitions to the ^{52}Fe *ground state* following the decay of ^{53}Ni.

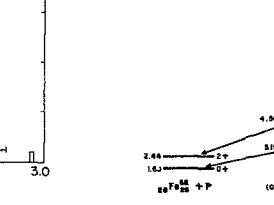

Fig. 2. The proposed decay scheme of ^{53}Ni. The bold faced arrow represents the proton decay of ^{53}Co^m, while the normal arrows represent the β-delayed proton decay of ^{53}Ni. (XBL 743-613)

energy was calculated to be ~6,500:1. Assuming the branching ratio for proton decay of $^{53}Co^{m}$ is 1.5%,[4] and a branching ratio for ^{53}Ni of 65%,[9] the experimental cross section ratio turns out to be ~11,000: 1. Considering the large uncertainties in both the experimental and theoretical ratios, this difference is not unreasonable. Thus, all the results indicate this new activity can be attributed to the β^+ delayed proton decay of ^{53}Ni.

Footnotes and References

1. J. C. Hardy, Nucl. Data A11, 327 (1973).

2. K. P. Jackson, J. C. Hardy, A. Schmeing, R. L. Graham, J. S. Geiger, K. W. Allen, Phys. Lett., 49B 341 (1974).

3. Similar to the rotation wheel used in reference 4 except with a much larger solid angle of 0.4 sr.

4. J. Cerny, R. A. Gough, R. G. Sextro and J.E. Esterl, Nucl. Phys. A188, 666 (1972).

5. R. G. Sextro, R. A. Gough, and J. Cerny, Nucl. Phys. A234, 130 (1974).

6. J. Cerny, C. N. Cardinal, H. C. Evans, K. P. Jackson, and N. A. Jelley, Phys. Rev. Lett. 24, 1128 (1970).

7. J. Jänecke, Nucl. Phys. A114, 433 (1968).

8. J. Gilat, GROGI2, Brookhaven National Laboratory Report No. BNL50246 (1970) unpublished.

9. Assuming a log ft = 3.3 for the superallowed beta transition, the observed delayed protons could account for approximately 65% of the total decays.

ARGON-INDUCED TRANSFER REACTIONS AT COULOMB BARRIER ENERGIES

R. C. Eggers,* J. O. Rasmussen, and W. S. Ribbe†

In the last few years there have been some theoretical investigations on semi-classical transfer theory (SCTT) for calculating heavy-ion transfer reactions at near Coulomb barrier energies.[1] While it is generally conceded that the methods under investigation lack some of the rigor of the coupled channel Born approximation (CCBA) or the distorted wave Born approximation (DWBA) methods, the attempt is to retain most of the essential features while reducing the computational complexities of the traditional methods. Perhaps the most important advance of the theory was the powerful addition theorem developed by Buttle and Goldfarb which reduced the complexities of the six-dimensional T-matrix integral into a product of two three dimensional integrals.[2] The authors of the SCTT have extended this work to simplify the calculation of the more complex of the two integrals by assuming a classical hyperbolic orbit for the projectile. Both of these simplifications depend quite heavily on the fact that the incident energy is low.

We have made experimental measurements which can be compared to these theories and we can probe the limitations of the theories. Our experiments were done with a small 11.7 cm diameter scattering chamber lined with aluminum catcher foils. The foils were gamma counted off-line after irradiation with an argon beam from the SuperHILAC. We used the intensity of the known gamma-ray lines of radioactive nuclei in the region around Argon to pick out the various products and calculate the cross-section based on the Faraday reading and the efficiency of the gamma-ray counter. Principal products observed were ^{41}Ar, ^{39}Cl and ^{38}S. We ran at 183 MeV and 209 MeV with thin targets of 91 g/cm^2 and 400 g/cm^2 for tantalum and gold, respectively. Our foils were divided into 30 degree conical sections for the angular distribution determinations. Table 1 summarizes the reaction cross-section for the gold and tantalum experiments.

TABLE I

THE FIRST LINE FOR EACH PRODUCT GIVES THE REACTION
THE PRODUCT OBSERVED IN THE FIRST ONE OF THE TWO GIVE
THE SECOND LINE GIVES CENTER OF MASS ANGLES FOR THE REACTION
THE THIRD LINE FOR EACH PRODUCT GIVES THE DIFFERENTIAL CROSS-SECTION IN MB/SR

LAB ANGLES FOR ALL PRODUCTS ARE GIVEN ON THE NEXT LINE									
0.- 15.	15.- 45.	45.- 75.	75.-105.	105.-135.	135.-165.	165.-175.	TARGET		
197 AU(40 AR,4P) AR	196 AU			TOTAL=11.9±1.3*			183 MEV		
8.- 18.	18.- 53.	53.- 88.	88.-118.	118.-144.	144.-168.	168.-175.	TARGET		
0.+ .77	0.+ .70	.077+.052	.40+ .04	2.05+ .12	2.77+ .21	2.50+1.25	.43+.08		
197 AU(40 AR,4N) AR	196 AU			TOTAL=32.9±1.3			209 MEV		
8.- 18.	18.- 53.	53.- 88.	88.-118.	118.-144.	144.-168.	168.-175.	TARGET		
1.68+ .97	.60+ .20	4.09+ .27	2.85+ .29	1.13+ .21	.67+ .15	0.+ 2.1	5.4+ .3		
197 AU(40 AR,3P) CL	198 HG			TOTAL=7.08±1.23			183 MEV		
8.- 18.	18.- 53.	53.- 88.	88.-118.	118.-144.	144.-168.	168.-175.	TARGET		
4.94+4.88	7.+ .108	0.+ .192	0.+ .882	1.28+ .28	2.64+ .25	0.19+5.98	0.+ .150		
197 AU(40 AR,3N) CL	198 HG			TOTAL=17.8±1.53			209 MEV		
8.- 18.	18.- 53.	53.- 88.	88.-118.	118.-144.	144.-168.	168.-175.	TARGET		
9.16+1.28	0.+ .129	1.46+ .20	1.90+ .10	1.22+ .12	1.42+ .15%	0.+ 4.32	1.6+ .12		
197 AU(40 AR,2N) CL	199 TL			TOTAL=7.08±1.03			183 MEV		
8.- 18.	18.- 53.	53.- 88.	88.-118.	118.-144.	144.-168.	168.-175.	TARGET		
1.68+2.05	0.+ .097	1.+ .089	0.+ .064	0.+ .185	.95+ .19	0.+2.25	0.+ .15		
197 AU(40 AR,1N) CL	199 TL			TOTAL=6.12+ .70			209 MEV		
8.- 18.	18.- 53.	53.- 88.	88.-118.	118.-144.	144.-168.	168.-175.	TARGET		
0.+1.06	0.+ .107	.714+ .120	.472+ .059	.282+ .146	0.+ .194	1.43+1.68	1.41+ .19		
181 TA(40 AR,4N) AR	180 TA			TOTAL=18.8±1.40			183 MEV		
8.- 18.	18.- 54.	54.- 88.	88.-118.	118.-144.	144.-168.	168.-175.	TARGET		
28.+ 2.	.42+ .19	.50+ .17	1.40+ .15	3.4+ .4	4.49+ .49	2.31+.98	2.19+ .13		
181 TA(40 AR,3N) TA			TOTAL=44.1±4.78			209 MEV			
8.- 18.	18.- 54.	54.- 88.	88.-118.	118.-144.	144.-168.	168.-175.	TARGET		
24.+ 4.	1.47+ .49	10.1+ 1.0	.00+ .20	.55+ .22	0.+1.01	0.+ 5.11	1.89+ .33		
181 TA(40 AR,2N) CL	182 W			TOTAL=12.7±4.18			183 MEV		
8.- 18.	18.- 54.	54.- 87.	87.-117.	117.-144.	144.-168.	168.-175.	TARGET		
17.+ 4.7	0.+ .66	0.+ .30	3.08+ .42	2.74+ .44	0.+ .34	0.+8.24	2.92+ .030		
181 TA(40 AR,2N) CL	182 W			TOTAL=24.+-4.+.72			209 MEV		
8.- 18.	18.- 54.	54.- 87.	87.-117.	117.-144.	144.-168.	168.-175.	TARGET		
0.+5.30	0.+ .356	5.48+1.18	.945+ .274	0.+ .440	2.42+1.16	0.+14.9	4.75+ .249		
181 TA(40 AR,3S) S	183 RE			TOTAL=5.08±1.86			183 MEV		
8.- 18.	18.- 54.	54.- 87.	87.-117.	117.-144.	144.-168.	168.-175.	TARGET		
0.+3.06	0.+ .114	0.+ .281	.268+ .120	1.45+ .166	1.30+ .359	0.+ .76	.40+ .43		
181 TA(40 AR,3N) S	181 RE			TOTAL=.89±3.05			209 MEV		
8.- 18.	18.- 54.	54.- 87.	87.-117.	117.-144.	144.-168.	168.-175.	TARGET		
0.+2.99	.181+ .248	0.+ .767	0.+ .144	0.+ .292	0.+ .930	0.+7.03	.484+ .26		

* ALL TOTALS EXCLUSIVE OF THE 0-15 DEGREE SECTION

To compare with the SCTT we show in Fig. 1 the angular distribution for the most prominent product, ^{41}Ar, for both energies and both targets. The angular distribution of the theory is given an arbitrary scaling factor, since there are good reasons to expect that it won't be quantitative in this respect.[3]

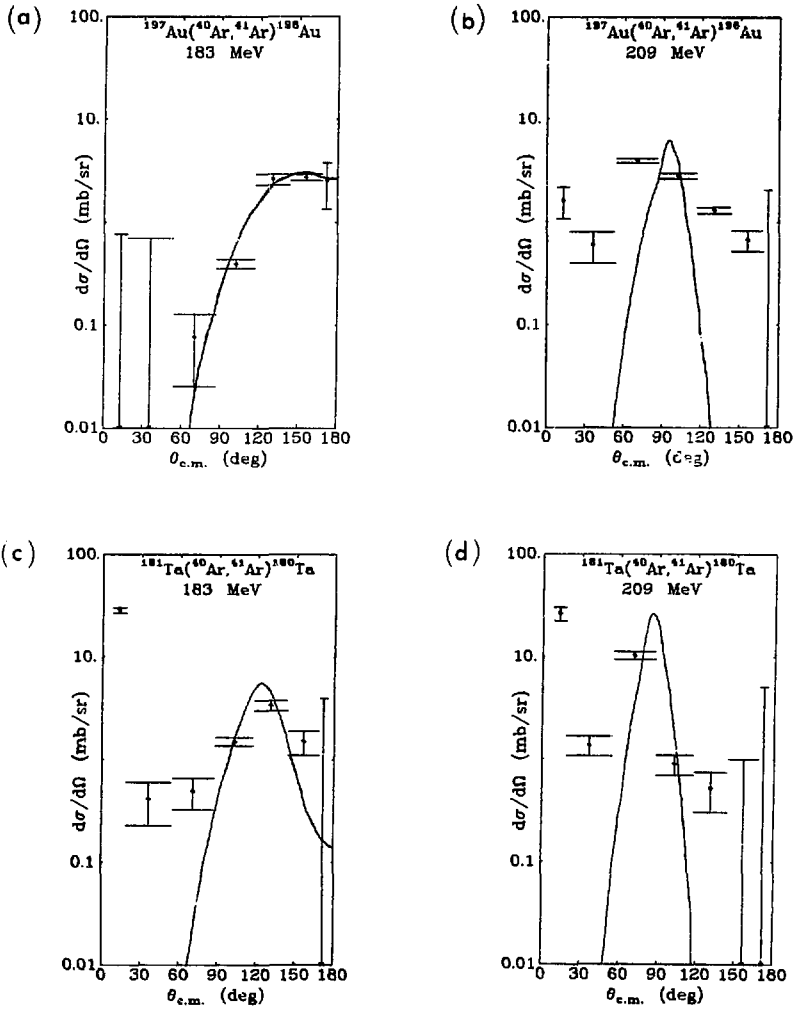

Fig. 1. Experimental and theoretical angular distributions of the neutron pick-up reaction by ^{40}Ar bombardment of gold and tantalum targets. Experimental results are given by the points and represent yield summed over all bound states in the radioactive product ^{41}Ar. The theoretical curves are semi-classical transfer theory coupled with optical model calculations following formulas of Alder et al.[1] The absolute normalization of the theoretical curves is arbitrary. (XBL 743-2714, XBL 743-2715, XBL 743-2711, XBL 743-2712)

As is readily apparent the SCTT only works well at or below the Coulomb barrier, which occurs for the lower energy on gold. The other three cases correspond to energies up to a few tens of MeV above the barrier. For these above-barrier cases a "background" cross-section not strongly dependent on angle arises. (We are cautious about the high points at the most forward angle, since it is possible that some beam particles hit the catcher foil.) The general picture of Wilczynski may fit our observations.[4] At or below barrier only quasi-elastic transfers with minimal internal excitation occur, peaking at the semi-classical grazing angle, according to the SCTT. At higher energies for impact parameters decreasing from the grazing values, translational energy may be lost to internal excitation and these inelastic products are sprayed to angles increasingly forward of the grazing peaks. It was not feasible for us to measure energies of the products, so we cannot directly test the interpretation that the broadly distributed products are lower energy than the grazing peaks.

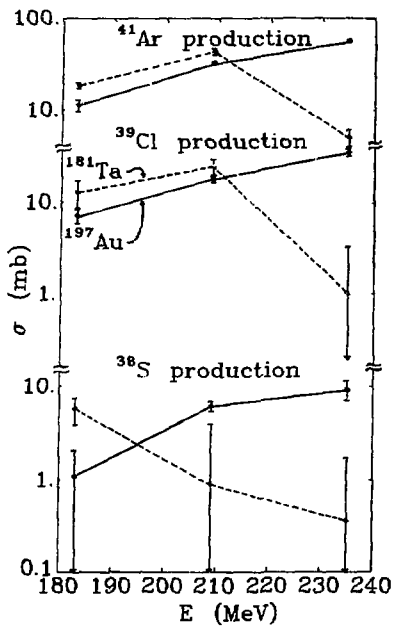

Fig. 2. Angle-integrated cross sections for observed transfer reactions or a function of bombarding energy of ^{40}Ar beam. (XBL 748-3859)

One other interesting aspect of our data is that it shows preliminary evidence for the conjectured effect of deformation on heavy-ion reactions. Of course, the absolute cross-sections are subject to the uncertainty that impurities in the argon beam could give erroneous Faraday readings. Figure 2 shows the excitation function for these reactions and demonstrates a steeper threshold for the spherical gold nucleus than for the deformed tantalum. It is reasoned that this effect comes from the tips of the deformed nucleus which, because they stick further out, can make reaction at lower energy where the projectile does not approach the nucleus so closely. One other feature of these excitation functions, that is, why the higher energy point for the ^{38}S excitation function drops is not fully understood.

Our conclusion is that the theory that we are comparing with here, the SCTT, is probably quite good for total transfer near the Coulomb barrier, but products with broad angular distribution appear as soon as the energy is increased very much. This most likely is due to internal excitation, as some theorists now are calculating by friction terms in the classical trajectories.

Footnotes and References

*Present address: Cyclotron Laboratory, Texas A.&M. University, College Station, Texas.

†Present address: Stadt Rudolf-Virkchow Kranken-

Nucl. Phys. A191, 399 (1972).

1. K. Alder, R. Morf, M. Pauli and D. Trautmann, Nucl. Phys. A191 399 (1972).

2. P. J. A. Buttle and L. J. Goldfarb, Nucl. Phys. 78 409 (1966).

3. J. S. Blair, R. M. DeVries, K. G. Nair, A. J. Blatz, and W. Reisdorf, Phys. Rev. C10 1856 (1974).

4. J. Wilczynski, Phys. Lett. 47B, 124 (1973).

CROSS SECTIONS OF (p,pxn) REACTIONS ON ^{208}Pb

H. Kawakami,* M. Koike,* K. Komura,* N. Yoshikawa,*
M. Sakai,* and J. O. Rasmussen†

The 52-MeV extracted proton beam from the synchrocyclotron at the Institute for Nuclear Study (INS), University of Tokyo, was used to irradiate enriched ^{208}Pb at 24-, 36-, 44- and 52-MeV. The incident proton energy was adjusted by carbon plate absorbers. The average beam current was about 1 nA. The target used was metallic foil of an enriched isotope (99.9%) of ^{208}Pb. A target foil of 8.3 mg/cm^2 thickness (for the excitation function) was prepared by electrodeposition. A thicker one used for the life-time measurement at 44 MeV was made by rolling and was 12.8 mg/cm^2 thick.

The Ge(Li) detector used was 40 cm^3 in effective volume. The energy resolution was 2.5 keV (FWHM) at 1.33 MeV. The detection efficiency E_γ was calibrated with IAEA standard sources ^{137}Cs and ^{60}Co placed at the target position. Overall errors for the cross sections were estimated to be 25%. The γ-ray spectra were analyzed with an automatic peak search program. The computer used was the TOSBAC 3400 at INS. The FM cyclotron pulse width of 0.078 ms was used with delayed gamma rays counted in the 1.06 ms interval between beam pulses.

The delayed 802.9-keV ($2_1^+ - 0_g^+$) γ-rays were counted from 0.053 to 0.352 ms (0.299 ms) in the decay curve after the beam pulse. The prompt γ-rays have completely decayed out earlier than 0.053 ms. The cross section for formation of the 0.12 ms 7-isomer at 2.2 MeV in ^{206}Pb, was calculated from the intensity of the 802.9-keV gamma ray. The excitation curve for the reaction ^{208}Pb(p,p2n)^{206}Pb measured through the 802.9 keV ($2_1^+ - 0_g^+$) γ-ray is shown in Fig. 1.

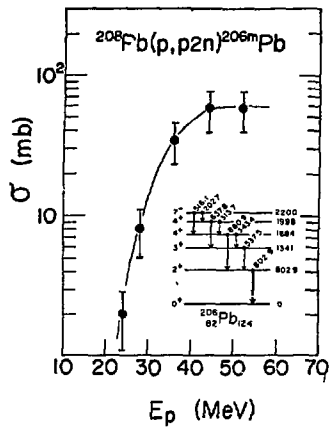

Fig. 1. Excitation function for the 7-isomeric state of ^{206}Pb. (XBL 756-1714)

^{208}Pb(p,pn)^{207}Pb Excitation Function

The excitation function for the reaction ^{208}Pb(p,pn)^{207m}Pb ($i_{13/2}$ isomer of 0.80-sec half-life at 1.623 MeV) was measured with the 1063.7- and 569.8-keV γ-gamma rays. The half-life of this state has been reported to be 800 ms. The decay correction was not made for the calculation of the cross sections, since this half-life 800 ms is much longer than the duty cycle. The excitation function obtained is shown in Fig. 2.

Discussion

The p,pn cross sections at relativistic energies have long been something of a mystery in that they are substantially larger than theory. The theoretidal calculations of sophisticated Monte Carlo cascade evaporation type are satisfactory for most observed reactions but not p,pn. We speculated that some direct excitation by p,p' to states above the neutron binding energy might play a role.

As a basis for possible future higher-energy studies we felt p,pn excitation functions at lower

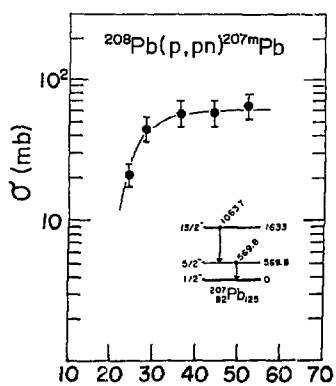

Fig. 2. Excitation function for the 13/2-isomeric state of ^{207}Pb. (XBL 756-1715)

energy would be useful. The lack of a distinct peak and the flatness of excitation functions at higher energy clearly shows the direct interaction nature. The cross sections are surprisingly large for such partial yields to high spin isomers, but high neutron pick-up cross sections by heavy ions on ^{208}Pb have been noted earlier.

Footnotes

*Institute for Nuclear Studies, University of Tokyo, Tanaski, Tokyo, Japan.

+Lawrence Berkeley Laboratory, summer visitor at INS, Tokyo; travel supported by the Japan Society for Promotion of Science.

X RAY MEASUREMENTS OF ANGULAR DISTRIBUTIONS IN HEAVY ION REACTIONS

J. Moulton, R. Babinet,
L. G. Moretto, and S. G. Thompson

Heavy ion reactions in which the projectile kinetic energy is distributed over the single particle and the collective modes of a compound nucleus, are expected to produce CM angular distributions symmetric around 90°. These distributions approach 1/sinθ for reactions proceeding with large angular momentum and breaking up into large fragments. Our group has investigated angular distributions in several heavy ion systems, using solid state and gas (E - ΔE) detectors.[1] (Projectiles: N, Ne, Ar. Targets: Cu, Ag, Au. Energies: 7 to 12 MeV/nucleon). In these experiments the resolution of individual atomic numbers is limited to Z less than 36. Significant asymmetry is observed, the angular distributions being forward peaked, especially for fragments close in Z to the projectile. Because of this deviation from symmetry about 90°, it is important to pursue these experiments further.

This report discusses preliminary results of a technique which measures the relative angular distributions for heavier fragments (Z > 40). A thin metal target is suspended inside a small cylinder, which has been lined with 3 to 5 mil Al foil. A carbon collimator is attached, and the assembly is placed in the Faraday cup of a scattering chamber. (This set-up allows us to carry out two simultaneous experiments: one in the scattering chamber and one in the Faraday cup). The reaction products emitted from the metal target are embedded in the Al foil. After 24 to 48 hours of bombardment, the target assembly is removed, and the Al foil is cut into strips concentric with the beam path. Strips upstream of the target cover backward angles, while strips downstream cover forward angles. The geometry of the inside of the cylinder determines the exact angles subtended. Each strip contains either the isotopes emitted in the solid angle subtended by the strip, or their decay products. The fragments are quite excited, coming from a compound system whose temperature was 2 to 3 MeV.[2] Early evaporation of several neutrons leading to beta decay and K capture is expected, so that X-ray emission can be observed. The characteristic X rays can then be measured, in order to determine the relative cross section as a function of angle for each Z. The X ray intensity is measured three times from each strip over a period of 10 to 14 hours after removal from the beam. One strip is used as a standard and measured 10 to 12 times during the counting period, to establish a decay curve for each peak. Intensities can then be extrapolated to

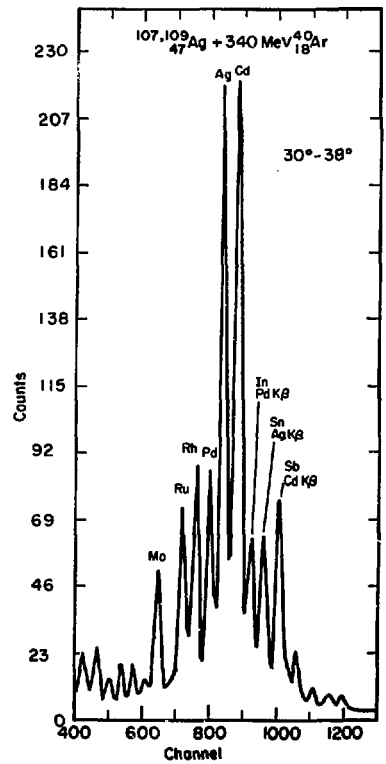

Fig. 1. X-ray spectra from 340 MeV Ar on Ag. Peak labels indicate Kα line unless otherwise indicated. (a) 30° - 38° lab angles. (b) 12° - 30° lab angles. Note the absence of products above Sb in (a). (XBL-752-2383)

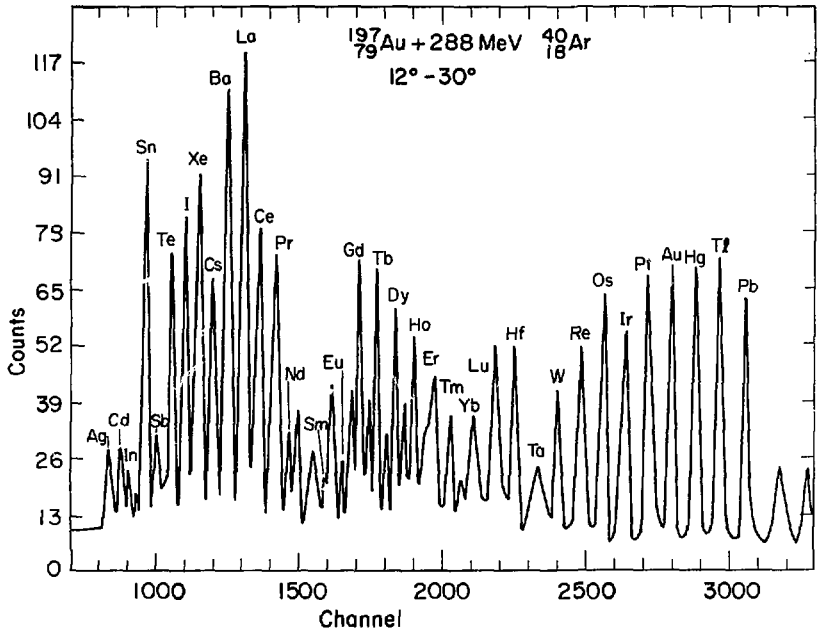

Fig. 2. X-ray spectrum from 288-MeV Ar on Au. 12° - 30° lab angles. Peak labels indicate main ($K\alpha_1$) component. Unlabeled peaks are $K\alpha_2$ or $K\beta$ peaks. All elements from Ag to Pb are present except Pm. (XBL 752-2384)

an arbitrary zero time. The yields for each element observed are compared from one strip to the next, to establish a relative cross section as a function of angle. While the shape of the angular distribution can be determined, the absolute magnitude of the cross section can not be established readily. This is because the population of fragments of a given Z consist of several isotopes, each decaying with a different half life, and with different branching ratios for K capture vs beta emission; gamma decay vs internal conversion; and X-ray fluorescence vs Auger decay. Thus the relation between X-ray yield and the actual cross section is very complex. A further complexity is that the population of one Z is fed by beta decay of neighboring elements, which in turn are fed likewise.

Data have been collected for three systems, and analysis is now in progress. The systems are: 340-MeV Ar on Ag, 288-MeV Ar on Au, and 175-MeV Ne on Au. Fragments below Z = 40 are poorly detected because of the low efficiency of detection of weak (less than 15 keV) X rays, and the short counting times necessitated by numerous Al strips. The Ar on Ag system produced little information of interest: the large CM velocity resulted in the high-Z cross section being peaked very much forward, so little activity behind 30° was observed (other than from quasi-elastic few particles transfer, see Fig. 1). The 288-MeV Ar on Au system yielded activity from all elements between Ag and Pb, covering lab angles 12° to 78°. A typical X-ray spectrum is shown in Fig.2. More backward angles were not measured. The 175-MeV Ne on Au system produced only low activity because of low Ne beam current, but foils subtending forward angles (12°-30°, 30°-38°) and backward angles (150°-168°, 142°-150°) appeared to display comparable activity for Z's somewhat above symmetric division. Except for quasi-elastic transfer products around Au, other products were not observed. Quantitative analysis of this data is not yet complete.

References

1. S. G. Thompson et al., "Macroscopic Aspects of Heavy Ion Reactions", UCRL-2940.

2. Calculated as $T = (E^*/8)^{1/2}$.

PARTICLES EMITTED IN THE INTERACTION OF Cu WITH ^{20}Ne AT 252-MeV BOMBARDING ENERGY

R. Jared, L. G. Moretto, R. Babinet, J. Galin, J. Hunter,
R. Schmitt, J. Moulton, and S. G. Thompson

The interest in studying this reaction is quite similar to that illustrated for the reaction of Ag + Ne. An added advantage is that with the available Z resolution (Z ≈33) the charge distribution can be determined up to and beyond the symmetric splitting (Z = 19 - 20). A slight disadvantage arises from the unfavorable kinematics which compresses all the cross sections in the forward direction and prevents the detection of large Z's at large c.m. angles. The experimental equipment used in this study is the same as that used in the Ag + Ne case.

In Fig. 1 the cross sections are shown as a function of Z for various laboratory angles. It is interesting to notice that the charge distributions appear to be fairly flat; very little increase is seen in the cross sections close to the symmetric splitting, while the cross sections appear to increase substantially for Z < 10 at the very forward angles. This is mainly due to the very dramatic forward peaking occurring for atomic numbers below 10. In Fig. 2, the center of mass angular distributions are shown for the various atomic numbers. As in the case of Ag + Ne, the angular distributions for Z < 10 are very strongly forward peaked. At the extreme forward angles there is some contribution due to the quasi-elastic component of the cross section. Nevertheless, there is no doubt that the relaxed component is also strongly forward peaked. The rapid damping of the forward peaking for Z < 10, visible in Ne + Ag, is also visible here. Still, the symmetric splitting occurs at Z = 19 - 20 and therefore only very close to the symmetric division does one observe an angular distribution possibly consistent with 1/sinθ.

As in many other cases one has here very strong evidence of incomplete relaxation in the mass/charge asymmetry degree of freedom. In fact, it is not clear whether there is any compound nucleus cross section at all hidden in the present data. Thus it is very important for the understanding of these data to revise and extend the current theories on reaction mechanisms.

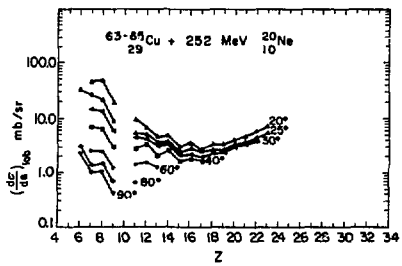

Fig. 1. Cross sections as a function of Z for various laboratory angles. (XBL 752-2299)

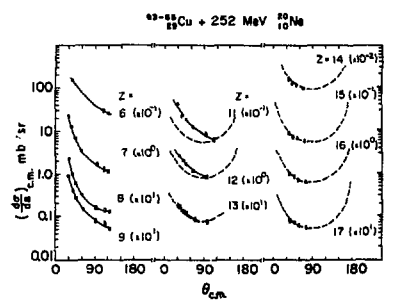

Fig. 2. Center of mass angular distribution for various Z's. (XBL 752-2300)

PRELIMINARY STUDY OF THE PARTICLES EMITTED IN THE REACTION BETWEEN Cu AND 288-MeV AND 340-MeV ^{40}Ar

L. G. Moretto, R. C. Jared, R. Babinet, J. Galin,
J. Hunter, and S. G. Thompson

This combination of target and projectile has been briefly investigated in our survey carried out throughout the periodic table. The purpose of this investigation is to learn about the broad systematics of the heavy ion reaction. The kinetic energy distribution shows the now familiar two components: the high energy quasi-elastic component and the low energy relaxed component. The overall charge distributions appear to be fairly similar to those observed in the Ar + Ag reactions. The main features (Fig. 1) are: an overall increase of the cross section with increasing Z as one moves towards symmetric splitting; a minimum in the cross section at and around Z = 9; and an increase of the cross section for lower atomic numbers. Furthermore, the cross section presents an even-odd alternation, also typical of similar reactions. The unfavorable kinematics make it hard to obtain complete angular distributions.

In conclusion, the present reaction appears to be consistent in its features with the Ar + Ag reaction, without indicating any special new feature.

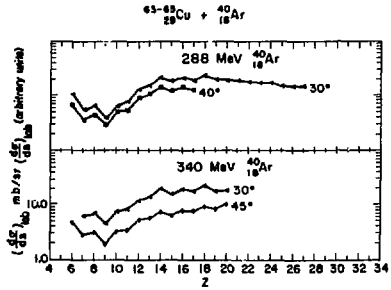

Fig. 1. Cross section as a function of atomic number for various lab angles at 288-MeV and 340-MeV bombarding energy. (XBL 752-2303)

STUDY OF THE RELAXATION PROCESSES IN THE REACTION BETWEEN ^{107,109}Ag AND ^{20}Ne AT 175 MeV AND 252 MeV

R. Babinet, J. Galin, M. Fowler, R. Jared,
J. Hunter, L. G. Moretto, and S. G. Thompson

As it has previously been shown for the Ag + ^{14}N system[1], an important fraction of the reaction cross section is associated with products whose charges range from Z = 1 to Z ≃ 18 with kinetic energies which remind us of the fission process. However the angular distributions of most of these products are not symmetric about 90° c.m. Instead, the angular distribution is more strongly peaked forward than backward, thus indicating that we are dealing with a much faster reaction mechanism than that associated with the formation of a completely equilibrated compound nucleus. The asymmetric angular distribution of the products observed previously by bombarding Ag with ^{14}N is the indicator of a process occurring in a time scale smaller than the rotational period of the system (10^{-21} to 10^{-20} sec).

The reason for choosing a Ne induced reaction on Ag to be compared with N-induced reactions on Ag, is the following. The difference of 6 nucleons out of 122 does not change the composite system significantly. However the mass or charge asymmetry of the entrance channel is quite different in the two systems. If this mass (or charge) asymmetry degree of freedom were completely relaxed during the equilibration process, one should not observe any significant difference in the relative abundance of the products obtained in both reactions. On the other hand, if the mass asymmetry degree of freedom were not completely equilibrated, the mass/charge asymmetry of the entrance channels should be reflected in the Z distribution of the products. Indeed, a glance at the potential energy of the composite system versus asymmetry shows (Fig. 1) that the injection point for the N + Ag system is located on a steep potential energy slope, while it appears to be close to the maximum in the Ne + Ag system. If the products are to be emitted very rapidly before completion of the relaxation process, most of them should be found in elements below Z = 7 in nitrogen induced reactions and more evenly distributed around Z = 10 in neon induced reactions.

The thin (~ 300 μg/cm^2) self supporting natural silver targets were bombarded with the ^{20}Ne beam obtained from the 88-Inch Cyclotron and the bombarding energies were 175 MeV and 252 MeV. At both energies Ne^{6+} ions were accelerated in order to avoid possible $^{12}C^{3+}$ or $^{16}O^{4+}$ contaminations which are likely with $^{20}Ne^{5+}$ beams.

The reaction products were identified by means of two ΔE-E telescopes. The ΔE counter is an ionization chamber filled with either a methane-argon mixing or pure methane under a well stabilized pressure of 6 to 8 cm of mercury. The ionization

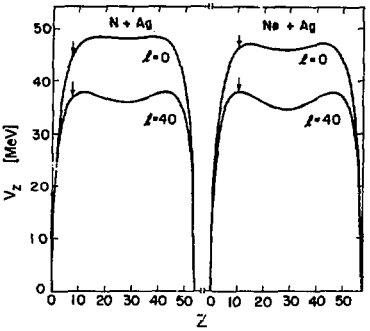

Fig. 1. Potential energy of the combined system as a function of the atomic number of one of the fragments for Ag + ^{14}N and Ag + ^{20}Ne. The injection point is indicated by means of an arrow.
(XBL 752-2308)

chamber allows us to carry out the Z identification up to Z ≈ 32 - 34.

The observed kinetic energy distributions contain a high energy component (quasi-elastic) and a low energy component close to the Coulomb barrier (relaxed). The quasi-elastic component prevails close to the grazing angle and for Z's close to that of the projectile (Fig. 2). At angles different from the grazing angle, the relaxed component, in which we are specifically interested, is the only component observed.

Angular distributions have been measured in the range 15° < θ lab < 155°. However, due to the thickness of the ΔE counter (~1 mg/cm^2(Ar·CH_4) or ~ 0.5 mg/cm^2CH_4) there is an energy threshold in the detection of the different products. Thus, for obvious kinematical reasons, the range of identified products without low energy cut off is typically Z = 5-30 at θ = 20° and only Z = 5-10 for θ = 150°. Therefore, as shown in Fig. 3, we are able to measure angular distributions ranging at least from forward to 90° c.m. for 20 Z's between Z =5 and Z=24. In Fig. 3 only the cross sections for the relaxed component are given where it can be separated from the quasi-elastic component. This explains why experimental values are missing around the grazing angle for the projectile's neighbors.

The angular distributions exhibit roughly the same patterns as the N induced reactions (Fig. 4). For the atomic numbers below the projectile and slightly above, a strong forward peaked distribution is observed, while for the highest atomic numbers the angular distribution is consistent with a 1/sinθ distribution.

A glimpse at the potential energy versus asymmetry indicates that the system is driven more rapidly toward larger than smaller asymmetries. Therefore if the separation of the system were

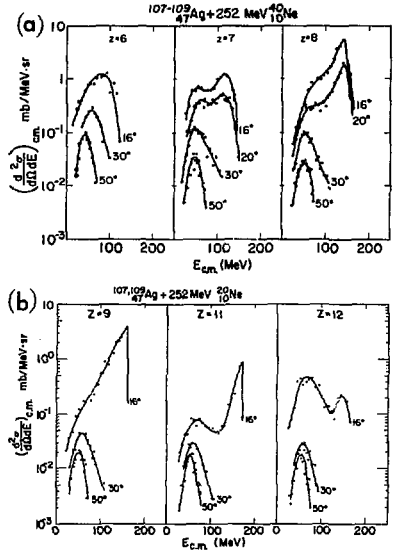

Fig. 2. Examples of kinetic energy distributions. The quasi-elastic and the relaxed components are visible. (XBL 748-4081, XBL 748-4082)

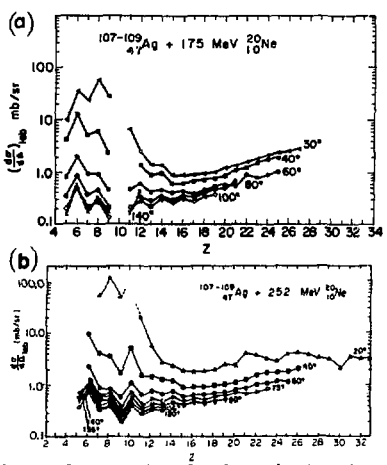

Fig. 3. Cross sections for the production of particles of various atomic numbers at different angles. (XBL 752-2310, XBL 7412-8427)

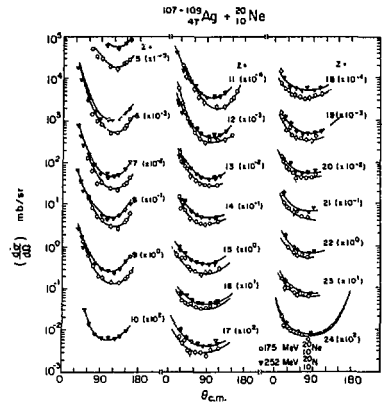

Fig. 4. Center of mass angular distributions for various Z's at 170 MeV and 250 MeV bombarding energies. (XBL 752-2309)

achieved in a time much shorter than the rotation period, most of the products would be lighter or slightly heavier than the projectile and would be emitted in the forward direction. On the contrary it takes a longer time for the system to evolve toward a more symmetric configuration. Following the angular distributions from Z = 11 up to Z = 24 a change toward a 1/sinθ distribution appears gradually, indicating that the time needed by the former projectile in order to gain 5 or 6 charges is of the order of magnitude of the rotation period.

A comparison between the angular distributions at the two bombarding energies shows a stronger forward peaking of the distribution at the lower energy. This might indicate a difference in the ℓ waves involved in such interactions. At the higher energy the average ℓ value appears to be higher than at the lower energy, thus increasing the mean rotation velocity and allowing more particles to be emitted backward.

As long as the angular distributions are very strongly forward peaked, there is no way to evaluate and compare the relative cross sections integrated over θ for a given Z and for the two energies. But from Z = 15 or 16 to Z = 24, the cross sections tend to become very close in value at both energies.

The last point worth emphasizing is related to the relative cross sections of the products at different angles (Fig. 3). In contrast with the N induced reactions there is no tremendous increase of the cross section around and specially below the Z of the projectile. This points out the particular influence of the entrance channel in the interactions, strongly indicating a partial relaxation of the charge (or mass) asymmetry degree of freedom.

In conclusion, it has been shown how the study of angular distributions of the products is a very convenient way to obtain information regarding the time involved in the interactions under study. However as soon as the times involved become larger than the rotational period we are no longer able to distinguish between only several or a multitude of rotational periods. As a consequence the 1/sinθ dependence cannot be considered, as it has been often in the past, as the signature of compound nucleus formation.

In the case of Ne induced reactions on Ag, at both energies a complete equilibration of all the degrees of freedom of the system followed by the emission of a particle with Z ≥ 5 seems very improbable. Instead most of these products are emitted by a composite system which is not completely relaxed in all its degrees of freedom.

References

1. S. C. Thompson, L. G. Moretto, R. C. Jared, R. P. Babinet, J. Galin, M. M. Fowler, R. C. Gatti and J. Hunter, LBL-2940, June 1974.

STUDY OF THE FRAGMENTS EMITTED IN THE INTERACTION BETWEEN Ag AND ^{40}Ar AT 288-MeV AND 340-MeV BOMBARDING ENERGY

J. Galin, R. Babinet, M. Fowler, R. Jared, R. Gatti, S. G. Thompson, and L. G. Moretto

The previous study of 288-MeV Ar induced reactions on Ag has been completed and extended to a higher bombarding energy (340-MeV). The increase in bombarding energy has two effects. The first is to increase the reaction cross section by opening new entrance channels associated with higher ℓ waves. The second is to increase the available energy and thus the nuclear temperature for those processes where a complete relaxation of the kinetic energy occurs. Also, the choice of a very high bombarding energy is very helpful in separating the relaxed from the quasi-elastic component of the kinetic energy distributions.

The experimental set-up is similar to that described for the experiments carried out at the 88-Inch Cyclotron. The experiment at 288-MeV Ar was performed with a ΔE proportional counter. With such a device it was not possible to resolve products above Z = 18. The higher energy experiment was performed with a ΔE ionization chamber with superior performance which allowed us to attain good atomic number resolution up to Z = 32.

Some examples of the kinetic energy distributions illustrating the presence of both high energy (quasi-elastic) and low energy (relaxed) components are shown in Fig. 1.

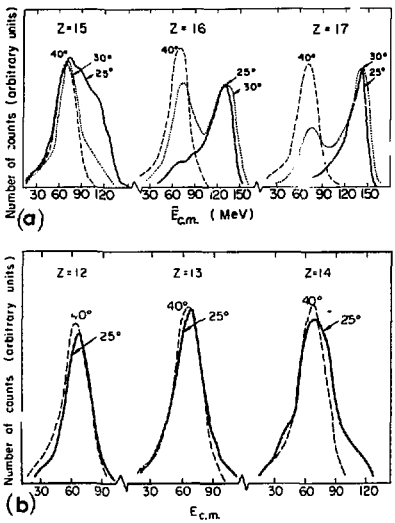

Fig. 1. Examples of kinetic energy distributions at 288-MeV bombarding ener
(XBL 744-2775, XBL 744-2774)

The cross sections as a function of Z for various laboratory angles are shown in Fig. 2. These cross sections do not contain the quasi-elastic components of the cross section. The corresponding center of mass angular distributions are shown in Fig. 3. One can notice that the cross sections are very similar at both energies for Z's close to the projectile, while around Z = 8 the cross sections at 340-MeV are 50 to 80% higher than at 288-MeV. The cross sections tend to increase with increasing Z. This is in definite contrast both with the Ne + Ag case and the N + Ag case. In the first case the cross sections are quite constant and in the second case the cross sections actually decrease with Z. The angular distributions are more forward peaked than backward peaked for all the Z's, more forward peaked close to Z = 18. The excess forward peaking shows that the decay occurs in a time comparable to the rotational period (10^{-20}, 10^{-21} sec). The decreased forward peaking for products farther removed from the projectile indicates that the products close to the projectile are populated sooner than those farther removed from it and consequently can be emitted sooner.

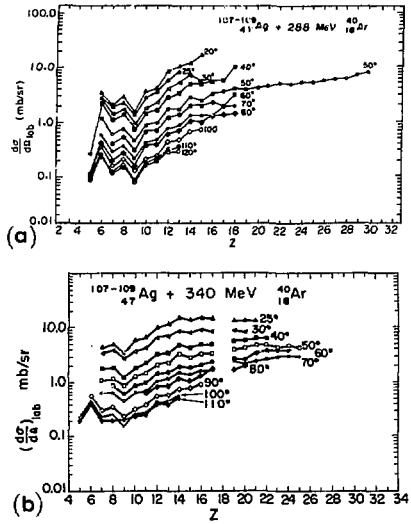

Fig. 2. Cross sections as a function of Z for various laboratory angles at 288-MeV and 340-MeV bombarding energy. (XBL 7411-8216A, XBL 752-2301)

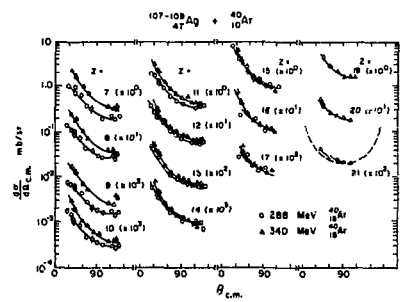

Fig. 3. Center of mass angular distributions for various Z's at 288-MeV and 340-MeV bombarding energy. (XBL 752-2302)

In conclusion, the evidence seems to support the hypothesis of a short-lived intermediate complex (instead of a compound nucleus) that decays before all the degrees of freedom, in particular the mass asymmetry degree of freedom, have had the time to undergo complete relaxation.

COINCIDENCE EXPERIMENT IN THE REACTION ARGON (340 MeV) ON SILVER, USING A SOLID STATE POSITION SENSITIVE DETECTOR AND A PARTICLE TELESCOPE

R. Babinet, Z. Fraenkel, P. Russo, R. Jared,
L. G. Moretto, and S. G. Thompson

Coincidence experiments with and without a position sensitive detector (PSD) have been used in the early study of the fission-like process observed in heavy ion reactions.[1,2,3] In a typical experiment both energies and angles of the two complementary fragments are measured. From these measurements the two-dimensional mass-energy distribution of the products may be deduced, provided several a priori assumptions on the process itself are made. However, even if these assumptions were justified, this general approach suffers, in the case of heavy ion reactions, from uncertainties associated mainly with a large center of mass motion and, with the poor knowledge of surface barrier detector response to heavy ions, especially with a PSD. On the other hand, through the recently developed ionization ΔE counter telescope,[4] which allows charge determinations up to 30 or more, detailed information regarding both the quasi-elastic and the relaxed components in heavy ion reactions has been obtained from measurements on the light fragment alone,[5] independently of any constraint on other products of the reactions. Information on correlated distributions may be obtained, with no loss of efficiency, by combining these two techniques. The information on the charge of the light fragment is expected to improve greatly the quality of such experiments. In this framework, we have considered first the hypothesis of binary division. The main evidence for binary division in the relaxed component of heavy ion reaction cross sections comes from the kinetic energy of the light fragments. Previous experimental results[5] indicate that the average kinetic energies of all products detected, except for a few Z's around the projectile Z where a high energy component associated with the transfer of a few nucleons is present, are consistent with the energy expected from the Coulomb repulsion of two complementary fragments. However, a systematic shift of the average kinetic energy by a few MeV seems to show up between forward and backward angles in the angular distribution, thus indicating that the assumption of a binary division should be much more carefully checked. In order to investigate this point, we have started at the SuperHILAC, a coincidence experiment between an ionization telescope and a position sensitive detector (PSD). We were then able to measure the energy and identify the charge of the light fragment as well as to determine the energy and the position of the heavy partner in the PSD.

The ORTEC position sensitive detector used in this experiment is 7 mm high and 45 mm wide, giving an angular acceptance of 24° in the reaction plane. Protection against beam induced electron background was obtained by magnetic deflection which we have found more effective and more convenient than an electrostatic shielding. The ionization telescope has been described elsewhere.[4] Improvement in the collection time for the ΔE signal with no loss of resolution has been obtained using pure methane (in place of argon + methane) as gas for the ionization part of the telescope. The 340-MeV Ar beam with an intensity of about 2×10^{10} pps was used to bombard a 300 μg self-supporting silver target. Precision pulses were recorded in and out of the beam pulse during the run in order to check for pile-up effects. The position signal of the PSD was calibrated using a collimator with seven holes, the distance between the center of two consecutive holes was 5 mm. The linearity of the position signal as a function of the energy signal was found to be excellent, while on the other hand the differential linearity of the position signal as a function of the true position in the detector for a given energy is about 13% between hole No. 1 and hole No.7. This can be easily corrected for, once measured, but it has nevertheless been ignored in the preliminary analysis of the data. A summary of the results is presented in Table 1 for four different sets of PSD and ionization telescope angles. The last two columns refer to the distribution of the

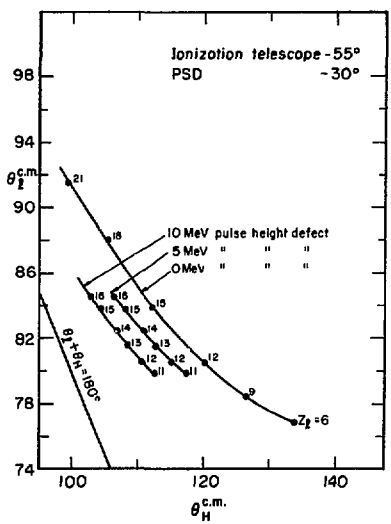

Fig. 1. Center of mass angle for the light fragment versus that of the heavy fragment. The three curves correspond to three different pulse height defects in the position sensitive detector (0, 5 and 10 MeV). The Z of the light fragment for each point is written next to it. (XBL 752-2387)

Table 1.

Z_ℓ	$\bar{E}_\ell^{cm}$	σ_{E_ℓ}	$\bar{E}_h^{cm}$	σ_{E_h}	$\bar{\theta}_h^{lab}$	σ_{θ_h}	N_ℓ	$\overline{\theta_\ell^{cm}+\theta_h^{cm}}$	$\sigma_{\theta_\ell+\theta_h}$	$\sigma_{\theta_\ell+\theta_h}$
10	55.5	10.0	15.4	4.8	23.7	4.8	390	192.0	9.8	PSD angle: 30°
11	57.1	10.5	16.5	4.5	25.4	4.7	494	192.9	9.0	Telescope angle: 40°
12	56.4	8.6	17.6	4.8	27.4	4.7	590	191.8	9.2	
13	60.2	10.7	19.5	4.7	30.5	4.0	659	189.3	8.1	
14	60.4	10.8	20.8	4.2	31.8	3.8	868	188.8	8.7	
15	61.1	9.9	21.5	3.8	33.2	3.3	655	187.4	7.4	
16	60.0	9.6	22.0	3.7	33.9	3.3	641	187.0	7.5	
18	63.5	12.3	32.2	5.8	42.8	4.3	1661	188.6	6.6	PSD angle: 50°
19	62.5	11.0	33.2	6.2	44.2	4.6	1587	187.8	5.8	Telescope angle: 40°
20	61.2	10.6	34.6	6.4	45.5	4.5	1844	187.8	5.5	
21	59.5	10.8	3 9	7.0	47.2	4.5	1763	187.7	5.8	
22	56.8	10.1	38.6	7.2	48.6	4.5	2037	187.8	5.7	
23	54.7	10.1	40.7	7.2	50.0	4.4	1962	187.9	6.0	
24	52.0	10.1	41.9	7.6	50.9	4.3	1814	187.9	5.8	
25	50.1	9.1	44.2	7.7	51.9	4.0	1930	188.1	5.9	
26	47.9	8.3	45.4	7.7	52.4	3.9	1953	187.7	5.8	
11	56.8	8.8	13.8	5.4	24.1	4.9	340	198.0	11.5	P. angle: 30°
12	58.1	9.4	15.7	5.4	26.4	4.9	552	196.5	10.3	Telescope angle: 55°
13	58.8	9.7	17.9	5.9	28.7	4.8	623	194.9	9.8	
14	60.0	10 6	19.7	5.7	30.5	4.4	829	193.6	8.7	
15	60.1	11.4	21.7	6.3	31.8	4.3	738	192.9	9.2	
16	60.0	10.3	23.1	5.9	33.4	3.8	837	191.6	7.9	
24	53.0	8.7	36.4	6.6	40.4	3.4	1268	192.0	6.8	PSD angle: 50°
25	51.9	9.1	38.3	6.8	41.0	3.6	1216	192.5	7.6	Telescope angle: 55°
26	49.2	8.5	39.4	7.2	40.9	3.6	1243	192.8	7.4	
27	46.6	8.3	41.4	7.4	41.2	3.7	1319	193.4	7.4	Experimental detection threshold of the light fragment energy for $Z \geq 27$.
28	46.0	7.1	43.1	7.2	41.5	3.8	1263	193.1	7.0	
29	44.7	6.6	44.8	7.7	41.6	3.8	1127	194.1	7.1	
30	42.9	5.7	46.4	7.9	41.5	3.8	1558	194.3	6.9	

Z_ℓ: Z of the light fragment.

$\bar{E}_\ell^{cm}$ σ_{E_ℓ}: Average and variance of the center of mass light fragment energy distribution.

$\bar{E}_h^{cm}$, σ_{E_h}: Average and variance of the center of mass heavy fragment energy distribution.

θ_h σ_θ : Average and variance of the heavy fragment lab angle distribution.

N_ℓ: Number of coincidences recorded for this particular Z.

$\overline{\theta_\ell^{cm}+\theta_h^{cm}}$, $\sigma_{\theta_\ell+\theta_h}$: Average and variance of the distribution of the sum of the c.m. light and heavy fragment angles.

sum of the c.m. angles for the two fragments. The average $\theta_\ell^{cm} + \theta_h^{cm}$ should evidently be 180° for a binary process. The discrepancy (~15°) between this value and the measured one is expected to be accounted for by neutron evaporation and pulse height defect. The influence of the pulse height defect is shown on Fig. 1, where the c.m. light fragment angle is plotted versus that of the heavy fragment for different pulse height defects. (A value of 6 MeV was measured for silver ions of 30 MeV and the adopted value in Table 1 is 5 MeV.) No attempt has been made yet to correct for neutron evaporation. The variance of the distribution $(\theta_\ell^{cm} + \theta_h^{cm})$ is rather broad. If this is associated with neutron (or particle) evaporation, a similar width should be observed in the azimuthal distribution. More over, such a broad distribution in azimuthal angle also means that we lose many coincidence events (compared to the singles rate), due to pure geometrical effects. Thus a more quantitative analysis of the data (comparison of the coincidence events cross section with single event cross section) requires the knowledge of the azimuthal distribution. We have just made such a measurement and some results are shown in Figs. 2 and 3. The width of the azimuthal distribution is substantially lower than that observed for the radial angular distribution. However, the variance of this last distribution includes a contribution from the $\theta_\ell^{cm} + \theta_h^{cm}$ as a function of the number of evaporated neutrons, and this is expected to broaden the distribution. Indeed this could even give some measure of the distribution of the evaporated neutrons.

In summary, preliminary results indicate that the hypothesis of binary division is well founded, and that a more quantitative result can be obtained. However, the energy dependent efficiency of coincidence detection, not only complicates the analysis of the data but also introduces some imprecision in the results. More striking is the indirect information on the neutron evaporation, which seems to be produced in this experiment. It is clear that such results would be of great interest for the general understanding of the deep inelastic process. In this respect, we conclude that this type of experiment seems very appealing.

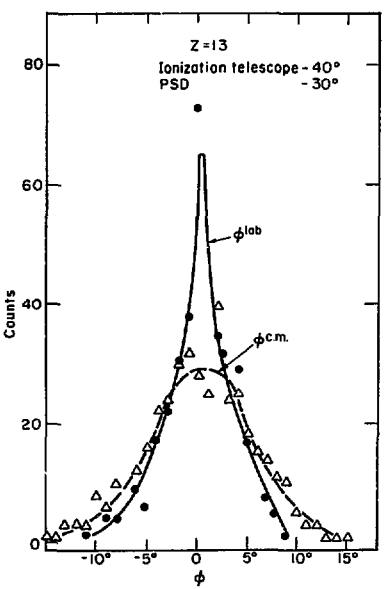

Fig. 2. Azimuthal angular distributions in the Laboratory and center of mass systems. (XBL 752-2386)

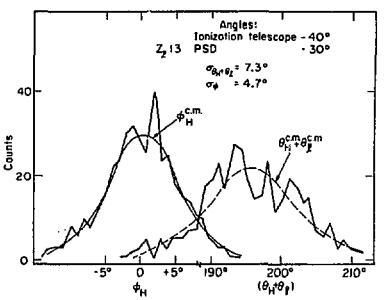

Fig. 3. Comparison between the azimuthal angular distribution of the heavy fragment and the associate radial distribution for the sum of the c.m. angles of the two fragments. (XBL 752-2385)

References

1. F. Hanappe, C. Ngô, J. Péter and B. Tamain, Proceedings of the Third IAEA Symposium on the Physics and Chemistry of Fission, IABA,-3M 174-42, Vol. 2, p. 289. International Atomic Energy Agency, Vienna 1974.

2. R. Plasil, R. L. Ferguson, Ibid., IAEA - SM 174-71 Vol. 2, p. 319.

3. K. L. Wolf, J. P. Unik, J. R. Huizenga J. Birkelund, H. Freiesleben and V. Viola, Phys. Rev. Lett. 33, 1105 (1974).

4. M. Fowler R. C. Jared, Nucl. Instr. Meth. 124, 341 (1975).

5. See papers in this annual report.

STUDY OF THE FRAGMENTS EMITTED IN THE INTERACTION BETWEEN ^{197}Au AND ^{40}Ar AT 288-MeV AND 340-MeV BOMBARDING ENERGY

L. G. Moretto, R. Babinet, J. Galin, R. Schmitt, Z. Fraenkel,
R. Jared, J. Hunter, and S. G. Thompson

The study of the reaction products obtained in the bombardment of Ag with N, Ne and Ar projectiles has shown the following systematics. A large fraction of the cross section has completely relaxed kinetic energy distributions. The same component of the cross section is characterized by an excess forward peaking, more enhanced for products close to the projectile. The excess forward peaking disappears more rapidly for fragments with Z larger than that of the projectile than for fragments with Z smaller than that of the projectile. For instance, in the Ne induced reaction, the angular distributions are already consistent with $1/\sin\theta$ 5 atomic numbers above that of the projectile (at $Z = 15$). This is presumably due to the fact that the entrance channel asymmetry corresponds to a potential energy of the intermediate complex sloping in the direction of increasing asymmetrics. The diffusion process is expected to drive the system rapidly in the direction of decreasing potential energies, leading to a rapid decay and to a forward peaking of the fragments with Z's lower than that of the projectile. The diffusion also spreads slowly towards higher potential energies thus allowing the system to emit fragments with Z's larger than that of the projectile over a longer time span and with a symmetric angular distribution. The choice of Au as a target should reverse the above situation to some extent. The injection asymmetry corresponds now to a potential energy sloping towards symmetry. Therefore one should expect a substantial excess in forward peaking which is retained well above the projectile. Furthermore, the bombardment of a Au target has an additional purpose. With such a heavy target one should obtain nuclei with fission barriers much lower than with an Ag target. A very large cross section for fission as understood in the traditional sense should be observed. On the other hand, if a large excess forward peaking should be observed over a large range of products, one should be led to believe that indeed a new process distinct from the traditional compound nucleus process is involved in the reactions. The experiments have been carried out at 288 MeV and at 340 MeV with a set-up similar to that used in Ne and Ar induced reactions on Ag.

Close to the grazing angle it is sometimes easy to single out the relaxed component of the kinetic energy since two distinct peaks (quasi-elastic and relaxed) are observed (see Fig. 1). One must notice that the quasi-elastic contribution is not the same below and above the projectile. The quasi-elastic cross section is vanishing and can be neglected with regard to the relaxed component for $Z \geq 21$, at all angles. But for Z's as low as 12 or even lower, the energy spectra exhibit a much broader FWHM and a higher mean energy in the forward direction than in the backward direction, well outside the grazing angle. Thus here observes indeed a higher energy component which seems to be added to the relaxed one. Yet it is quite puzzling to consider the exchange of

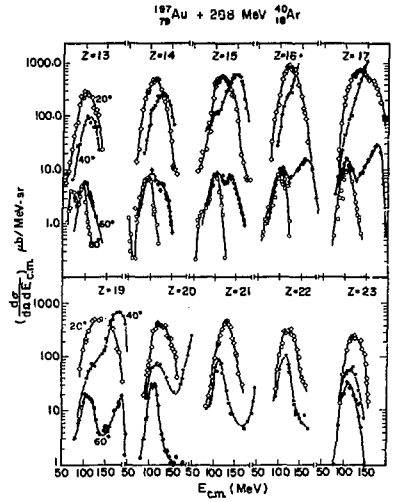

Fig. 1. Some examples of kinetic energy distributions. (XBL 752-2304)

12 nucleons (6 protons and a similar number of neutrons) or more as a quasi-elastic phenomenon. For $Z = 7$ or 8 the energy spectra remain the same inside the grazing angle as they are well outside this angle.

Furthermore the most probable energies appear to be slightly shifted toward higher values (several MeV) when observing the products more and more forward. This seems to occur for all the products, although it is more difficult to reach such a conclusion for the products affected by the quasi-elastic contribution. Thus for the products emitted in the forward direction the energy thermalization process is not as complete as it is elsewhere. That gives a more accurate idea of the time needed for the kinetic energy to attain complete relaxation. It is actually more than a quarter or even half the time of a rotation period.

It is clearly seen in Figs. 2 and 3 that the relative cross section of the products is strongly dependent on the bombarding energy. It is interesting to notice that above the projectile, higher cross sections are found for the lower bombarding energy. The increase of bombarding energy results

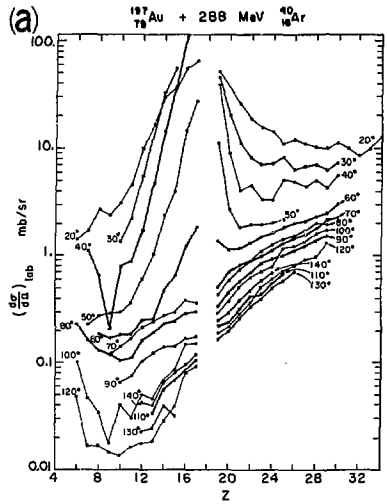

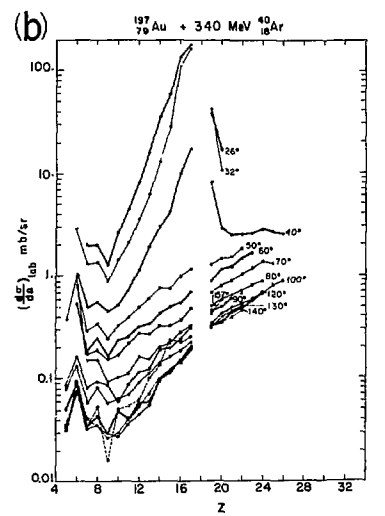

Fig. 2. Dependence of the cross section upon Z for various laboratory angles at two bombarding energies. (XBL 752-2305) (XBL 752-2306)

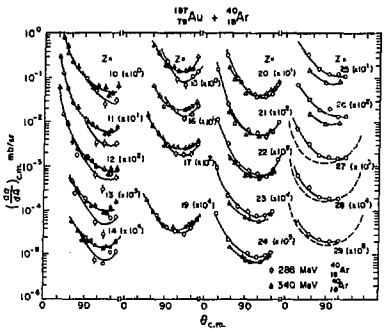

Fig. 3. Center of mass angular distributions for various atomic numbers at the two bombarding energies. (XBL 752-2307)

in an increase in the temperature of the composite system. This has the effect of smoothing the differences in the potential energy of the system. Therefore the relative distribution of the products is expected to be also smoothed by an increase in the energy, as observed.

Concerning the angular distributions (Fig. 3), several comments must be given. Distributions are more forward than backward peaked and nowhere has a 1/sinθ distribution been found as it was for example in the case of Ne induced reactions on Ag. In the case of 288-MeV Ar on Au this means in particular that all the fragments up to Z = 29 (and consequently a mass around 65) cannot be accounted for in terms of the fission of a completely relaxed compound nucleus as has been done so far.

Furthermore, the retained forward peaking up to Z = 29 indicates that the system is diffusing, as expected, on a downward sloping potential energy, towards symmetry.

PRELIMINARY STUDIES ON THE REACTION Cu + ^{84}Kr AT 606-MeV BOMBARDING ENERGY

L. G. Moretto, R. Babinet, R. Jared, R. C. Gatti, J. Moulton, and S. G. Thompson

A very preliminary investigation of the reaction between Cu and 606 MeV ^{84}Kr has been carried out. The purpose of this study is to compare both the particle cross sections and their kinetic energies with the reaction Ag + ^{40}Ar at 288-MeV bombarding energy. The combined system is the same in both cases. The differences in the center of mass energy are minor. The main differences are of course in the angular momentum and especially in the entrance channel mass-charge asymmetry.

The data have been collected with particle telescopes described in the Ne + Ag reaction report. The experimental results show an amazing similarity between the two reactions. In Fig. 1 the center of mass kinetic energy distributions for a Z = 16 fragment obtained from both reactions is shown. The two peaks appear to be identical within the experimental uncertainty. This is not too surprising, in as far as these "relaxed" components in the kinetic energy distribution find their origin in the Coulomb repulsion of the two fragments. More surprising is the similarity of the two reactions in the cross sections as a function of the fragment Z (Fig. 2). The cross section appears to increase with increasing atomic number and is modulated by the usual even-odd effect. A full comparison of the two reactions is possible only after many more angles are measured and a complete angular distribution is available.

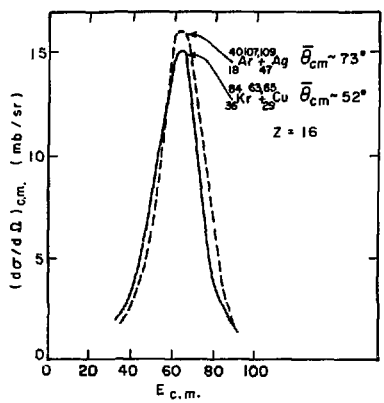

Fig. 1. Comparison of the c.m. kinetic energy distributions for Z = 16 in the reaction Ar + Ag and Cu + Kr. (XBL 745-3211)

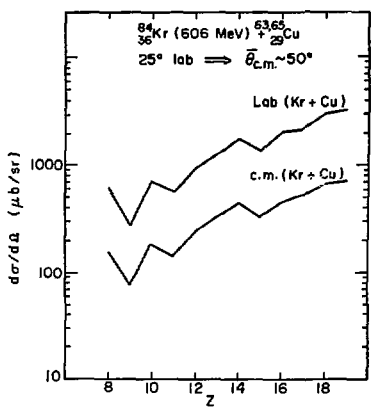

Fig. 2. Lab and c.m. cross section as a function of atomic number. (XBL 745-3210)

FISSION EXCITATION FUNCTIONS IN MEDIUM-HEAVY NUCLEI

L. G. Moretto, R. C. Gatti,
R. P. Schmitt, and S. G. Thompson

The measurement of fission barriers is important in the study of smoothly varying nuclear properties such as those described by the liquid drop and droplet models. A straightforward and powerful technique for obtaining fission barriers is through the analysis of excitation functions.

Since fission barriers tend to decrease with increasing Z^2/A (neglecting shell effects), many of the heavier elements have already been studied. The virgin territories lie in the region around $^{208}_{87}Pb$, in the area just preceding it and extending into the lanthanide region. It is the purpose of this work to fill in some of the gaps around $^{208}_{82}Pb$ remaining from our previous work and to extend the measurements into the rare earth region. A good deal of data has already been taken using ^4He and to a lesser extent ^1H projectiles on various targets.

In order to obtain meaningful results, targets free of heavy element contamination (e.g., ^{232}Th, ^{238}U) must be used. The Hg isotopes are well suited for use in this instance because their low boiling point allows them to be vaporized relatively free of contamination. Despite the obvious difficulty involved, targets have been prepared by first amalgamating the Hg with Ag and then covering the target with thin layers of Pd which does not form an amalgam but does prevent evaporation of the Hg.

The experimental apparatus is depicted in Fig. 1. The beam enters the chamber from the left through an isolation foil and the two Geneva wheels in which various degrading foils are mounted. The beam then passes through a long collimator 3mm in diameter, strikes a thin (> 1 mg/cm^2) target mounted at 45° with respect to the beam direction and is collected in a Faraday cup. Fission events are recorded using 1-cm^2 mica detectors mounted 1 inch from the center of the chamber and at 135° with respect to the beam axis. There are four such detectors, any of which can be rotated into position without breaking the vacuum.

The angular distribution for the binary fission of a rotating nucleus is approximately proportional to $(\sin\theta)^{-1}$ where θ is not close to either 0° or 180°. Such an angular distribution yields the same integrated cross section as an isotropic distribution normalized at 140.5°. Because of the kinematical shift and the deviation form $(\sin\theta)^{-1}$, we chose to position the track detectors at 135° in the lab. The geometry factor of this configuraiton is easily obtained using a Au target because the ^1H + Au and ^4He + Au systems have been well studied.

The experimental data as it exists at present are shown in Fig. 2. All the excitation functions are seen to rise rapidly with increasing excitation energy. One striking feature of the data is the behavior of the Hg isotopes. The cross sections are depressed dramatically as the magic numbers N = 126 and Z = 82 are approached, thus beautifully illustrating the effect of shell closure on the fission barrier height. The Hg isotopes are very interesting for quite another reason: after taking neutron binding energies into account, one can obtain a direct estimate of the cross section for first chance fission in several different cases. The inclusion of a ^{198}Hg target will serve to improve the data in this respect.

The data obtained from the study of ^1H-induced fission are still in the preliminary stages. Upon its completion, a great deal will have been added to our understanding of smoothly varying nuclear properties not to mention a very close look at the closed neutron and proton shells at N = 126 and Z = 82 respectively.

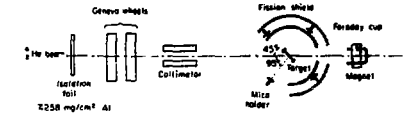

Fig. 1. Experimental apparatus. (XBL 742-2460)

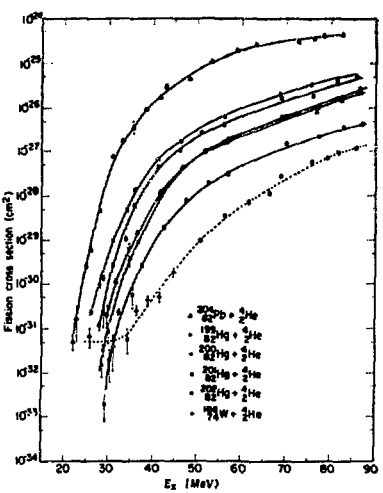

Fig. 2. Fission cross sections as a function of excitation energy. (XBL 752-2378)

References

1. L. G. Moretto, S. G. Thompson, J. Routti, and R. C. Gatti, Phys. Letters 38B, 471 (1972).

2. L. G. Moretto, Invited Paper presented at the Third Symposium on the Physics and Chemistry of Fission, Rochester, New York, August 13-17, 1973; Lawrence Berkeley Laboratory Report LBL-1914.

COMPLETE FUSION CROSS SECTIONS FOR THE ^{20}Ne + ^{238}U SYSTEM

V. E. Viola, Jr.,* A. M. Zebelman, R. G. Sextro, W. G. Meyer,† and R. G. Clark†

The complete fusion and total reaction cross sections for collisions between 175- and 252-MeV ^{20}Ne ions and ^{238}U have been measured at the 88-Inch Cyclotron in order to study the dependence of σ_{CF}/σ_R as a function of excitation energy. Here we define σ_{CF} as the cross section for fission resulting from reactions in which there is complete transfer of projectile linear momentum to the target-projectile system; σ_R is the total nuclear reaction cross section. The fission-fragment angular correlation technique was used to determine complete fusion cross sections. Both planar and non-planar measurements were performed using a position-sensitive semiconductor detector (PSD) covered with a multi-slit collimator. The planar correlation function for 175-MeV ^{20}Ne + ^{238}U is shown in Fig. 1;

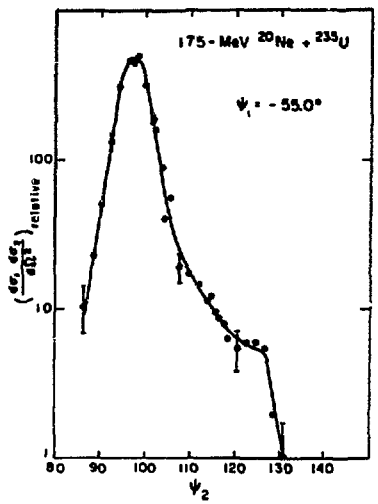

Fig. 1. Fragment angular correlation from fission of ^{238}U with 175-MeV ^{20}Ne ions. A defining detector (ψ_1) was placed at -55.0° with respect to the beam axis and correlated fragments (ψ_2) were observed with a PSD placed at appropriate angles. Data represent only planar contributions to the correlation function. (XBL 757-3437)

here a defining detector was placed at -55.0° and the PSD at appropriate correlation angles. The non-planar correlation functions are found to be much broader at correlation angles near 170-180° (ψ_2=115 -125°), indicating a larger contribution from incomplete fusion events than indicated in the planar correlation function.

Total reaction cross sections were determined in two ways: 1) by measuring the total fission cross section[1] and, because of the very high fissionability of ^{238}U, assuming $\sigma_R = \sigma_{CF}$; and 2) by measuring the elastic scattering of ^{20}Ne and determining σ_R using the 1/4- point recipe based on Fresnel scattering theory.[2] Elastic scattering data were also obtained using a position-sensitive detector, and plots of $\sigma_{elastic}/\sigma_{Rutherford}$ are shown in Fig. 2 as a function of center of mass angle. From the elastic scattering data we obtain the following total nuclear reaction cross sections, σ_R, and maximum angular momentum values, ℓ_{max}: at 175-MeV,

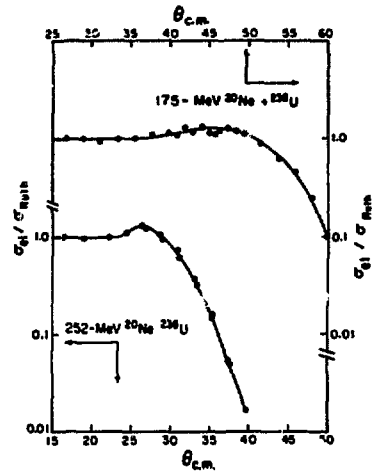

Fig. 2. Ratio of elastic scattering (σ_{el}) to Rutherford scattering cross section (σ_{Ruth}) as a function of center-of-mass angle for 175-MeV ^{20}Ne ions incident on ^{238}U (upper curve) and 252-MeV ^{20}Ne ions on ^{238}U (lower curve). (XBL 757-3438)

σ_R = 1900 mb and ℓ_{max} = 91.8, and at 252-MeV, σ_R = 2810 and ℓ_{max} = 134. Preliminary analysis of the angular correlation results at 175-MeV yields a value of σ_{CF}/σ_R = 0.75±0.05. This value corresponds to a critical angular momentum, ℓ_c = 76.5. This is to be compared with a value of ℓ_c = 84.5 derived previously with 208-MeV ^{20}Ne ions and a ^{238}U target.[3] The dependence of the ratio σ_{CF}/σ_R and ℓ_c on excitation energy will be studied using current potential model predictions.[4] The elastic scattering data are also being analyzed in terms of Fresnel scattering theory and various heavy ion optical model potentials.

Footnotes and References

*Permanent address: University of Maryland, College Park, Md.

†University of Maryland, College Park, Md.

1. V. E. Viola, Jr. and T. Sikkeland, Phys. Rev. 128, 767 (1962).

2. W. E. Frahn, Phys. Rev. Lett. 26, 358 (1971); Ann. Phys. 72, 524 (1972).

3. T. Sikkeland and V. E. Viola, Jr., Proc. of 3rd Conf. on Reactions between Complex Nuclei (U. of California Press, Berkeley, 1963) p. 232.

4. J. Wilczyński, Nucl. Phys. A216 (1973); R. Bass, Phys. Lett. 47B, 139 (1973); D.H.E. Gross and H. Kalinowski, Phys. Lett. 48B, 302 (1974); J. Galin, D. Guerreau, M. Lefort and X. Tarrago, Phys. Rev. C9, 1018 (1974).

COUNTER EXPERIMENTS IN THE THIN TARGET AREA AT LAMPF

G. W. Butler,* D. G. Perry,* A. M. Poskanzer,
J. B. Natowitz,† F. Plasil,‡ and L. P. Remsberg§

A collaborative effort has been initiated to conduct counter experiments in the main proton beam line at the Los Alamos Meson Physics Facility. The 800-MeV proton beam, with present intensity of 10 μA, irradiates a uranium target 3.5 mg/cm^2 thick. Fragments were identified by ΔE-E silicon counter telescopes located 4.6 m from the target. Energy spectra have been measured for He, Li, Be, and B fragments at 45°, 90°, and 135° to the beam. It is expected that the data will be useful in describing the low deposition energy production of these fragments for comparison to higher energy reactions at the Bevatron and Bevalac.

Preliminary results, when compared to the previous work with 5-GeV protons,[1] indicate that the energy spectra peak at higher kinetic energies and fall off more steeply above the peak.

A second experiment, utilizing a silicon ΔE-E-TOF telescope,[2] was installed at 90° to the beam and some test data were taken. Both the time of flight between the ΔE and E detectors and the time of the ΔE signal relative to the RF of the linac were recorded. At LAMPF the proton beam comes in 0.2 ns wide bursts every 5 ns. It is planned to use the time of flight between the silicon detectors to sort out which beam micropulse the fragment came from. Thus it should be possible to do TOF identification from the RF over a 4-1/2 meter flight path.

Footnotes and References

*Los Alamos Scientific Laboratory.

†Texas A & M University.

‡Oak Ridge National Laboratory.

§Brookhaven National Laboratory.

1. A. M. Poskanzer, G. W. Bulter, and E. K. Hyde, Phys. Rev. C3, 882 (1971).

2. G. W. Butler, A. M. Poskanzer, and D. A. Landis, Nucl. Instru. Methods 89, 189 (1970), and newer fast electronics designed by D. A. Landis.

FRAGMENTS FROM URANIUM IRRADIATED BY 2.1 GeV/NUCLEON DEUTERONS AND ALPHA PARTICLES*

A. M. Zebelman, A. M. Poskanzer, J. D. Bowman,†
R. G. Sextro, and V. E. Viola, Jr.‡

An aspect of high energy proton reactions with complex nuclei that has emerged recently is that the gross features of this interaction are independent of proton bombarding energy from a few GeV up to 300 GeV.[1] That is, it appears that above a few GeV, increasing the proton energy does not deposit any more energy in the target nucleus. The orientation of the present work is to determine if the gross features change when one keeps the energy of the projectile at a few GeV/nucleon but increases the mass of the projectile. The preliminary results of Sullivan et al.[2] indicate that significant changes occur. We have previously made extensive studies of the energy spectra and angular distributions of He through Mg fragments from heavy targets irradiated by high energy protons.[3,4] This work shows that the energy spectra of the products Li and heavier are sensitive indicators of high deposition energies in the nucleus. Thus a comparison of the energy spectra of these fragments produced by heavy ions and protons should bear on the problem of energy deposition. In the present work energy spectra and crude angular distributions were measured for He to B fragments from a uranium target irradiated by the 2.1 GeV/nucleon deuteron and alpha beams from the Bevatron. In order to allow a careful comparison with proton-induced reactions, data were remeasured with the same equipment using 4.9 GeV protons. Most of the experimental details are described more fully in Ref. 3. In general, the detector telescopes used consisted of a transmission ΔE detector, and E detector, and an anti-coincidence detector.

The energy spectra from the alpha particle reactions and the proton reactions are shown in Fig. 1. The peak cross sections of the proton-induced reactions have been normalized to those of the alpha-induced reactions in order to illustrate the more prominent high energy tails and somewhat increased yields at low energies in the alpha data. The data show gross features already noted for proton irradiations:[3]

1) The peaks in the spectra shift towards higher energy as the atomic numbers of the fragments increase, in accord with an increasing Coulomb barrier.

2) The spectra of the neutron-deficient isotopes ^{6}Li and ^{7}Be exhibit more prominent high energy tails than do the other isotopes of these elements.

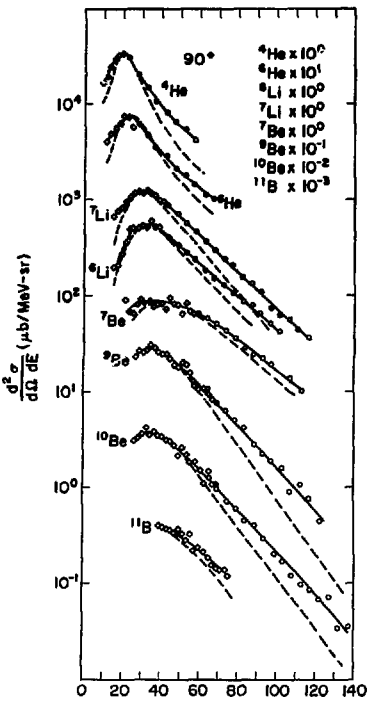

Fig. 1. Laboratory energy spectra at 90° for alpha and proton irradiations. The incident proton data are shown as dashed curves and have been normalized at their peaks to the incident alpha data.
(XBL 745-2985)

Laboratory angular distributions are shown in Fig. 2. Shown with the proton-induced data are the previously published data[3] at five angles, showing that a straight line through the data is adequate for integration. The distributions were integrated according to the straight lines drawn between the data points to give the total cross sections listed in Table 1.

As in Ref. 3 an attempt was made to fit the energy spectra in terms of an evaporation model in order to extract certain parameters, such as effective Coulomb barriers and apparent nuclear temperatures. The parameters obtained with incident protons were consistent with those obtained previously.[3]

From the analysis of the alpha induced data it was found that the fragments are forward peaked in the system of the emitting nucleus and that this effect is more pronounced than observed previously

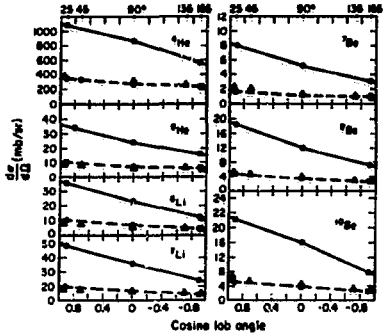

Fig. 2. Laboratory angular distributions for alpha- and proton-induced reactions. The dashed lines go through the incident proton data. The circles are from the present work while the data represented by triangles come from Ref. 3. (XBL 745-2985)

Table 1. Total cross sections for the alpha-induced reactions and ratio of alpha- and deuteron-induced reactions to proton induced reactions.

Isotope	σ_α (mb)	σ_α/σ_p	σ_d/σ_p
^{4}He	10600	2.9	1.4[a]
^{6}He	310	3.1	1.5[b]
^{6}Li	297	3.3	1.3[b]
^{7}Li	650	3.8	1.5[a]
^{8}Li	≈210	4.2[b]	1.2[b]
^{9}Li	≈ 60	3.8[b]	1.5[b]
^{7}Be	67	4.3	1.5[a]
^{9}Be	157	3.4	1.3[a]
^{10}Be	196	4.0	1.6[a]
^{11}Be	≈ 21	4.3[b]	
^{12}Be	≈ 11	4.5[b]	

[a]Based solely on the 90° differential cross sections.

[b]Based solely on the ratios of peak areas in the 90° particle spectra.

with incident protons.[3] Additionally, it was found that the effective Coulomb barriers that were already anomalously low with incident protons, have dropped another 15% for incident alphas; the apparent temperatures, which were unbelievably high for incident protons, have climbed another 1-1/2 MeV on the average for incident alphas; and finally, the smearing parameters, which describe the dispersion in the Coulomb barrier, have increased almost a factor of 2.

In summary, we find that although the cross sections for the production of fragments from uranium are a factor of 1.5 higher with deuterons than with protons, the energy spectra of these fragments are not significantly different. However, in the interaction of alpha particles with uranium there are many indications of increased deposition energy. The cross sections for producing the fragments are a factor of 3 to 4 higher. The effective Coulomb barriers are lower, the apparent temperatures are higher, the smearing of the energy spectra has increased, and the angular distributions are more forward peaked.

Footnotes and References

*Condensed from LBL-3427, Physical Review C, 11, 1280 (1975).

†Present address: Los Alamos Scientific Laboratory, Los Alamos, NM 87544.

‡Permanent address: University of Maryland, College Park, MD 20742.

1. S. K. Chang and N. Sugarman, Phys. Rev. C9, 1138 (1974). Y.W. Yu and N. T. Porile, Phys. Rev. C10, 167 (1974).

2. J. D. Sullivan, P. B. Price, H. J. Crawford, and M. Whitehead, Phys. Rev. Letters 30, 136 (1973).

3. A. M. Poskanzer, G. W. Butler, and E. K. Hyde, Phys. Rev. C3, 882 (1971).

4. E. K. Hyde, G. W. Butler, and A. M. Poskanzer, Phys. Rev. C4, 1759 (1971). R. G. Korteling, C. R. Toren, and E. K. Hyde, Phys. Rev. C7, 1611 (1973).

STUDIES AT THE BEVATRON OF FRAGMENTS FROM C, Al, Ag, AND U TARGETS OBSERVED WITH A GASEOUS ΔE COUNTER

R. G. Sextro, A. M. Zebelman, and A. M. Poskanzer

Previous counter telescope studies of fragments from the high energy proton bombardment of Al (Ref. 1), Ag (Ref. 2), and U (Ref. 3) targets have been restricted in the range of fragment energies observed because of the low energy cut-off caused by the thickness of the ΔE counter. Only the high energy tails were observed for all fragments from the Al target and for the fragments heavier than C from the Ag and U targets. This caused serious omissions in both the energy spectra and the cross-sections.

In the present experiment we have used a thin gaseous ionization counter as a ΔE detector, along with a 100 μm E detector in a counter telescope to study fragments from C, Al, Ag, and U targets. While the previous measurements had low-energy cut-offs ranging from 1.5 MeV/nucleon for the lighter fragments to 2.5 MeV/nucleon for the heavier fragments, the present data extend down to 0.6 MeV/nucleon for all fragments observed.

The ionization counter was adopted from one designed by Fowler and Jared,[4] and used successfully in studies of heavy-ion induced reactions. Fragments entered the gas counter through an 8-mm diameter entrance window of 50 μg/cm² Formvar (supported by a wire grid), traversed a 7.1 cm flight path through an Ar-CH_4 gas mixture (P-7) at 50 Torr pressure, and struck the E detector located inside the gas. The total gas thickness of ∿ 0.76 mg/cm² is equivalent to ∿ 3 μm of silicon. The first stage of the preamplifier was located inside the gas counter, giving a typical ΔE pulser resolution of 16 - 20 keV FWHM. The gas flowed continuously through the counter at ∿ 0.6 Torr-liters/sec, and the pressure was stabilized to within ± 1% using a Cartesian manostat on the counter exit. The coincidence time resolution between the ΔE and E counters was measured to be 160 nsec FWHM for the 8-mm diameter window, and was found to be a direct function of the size of the window. This is consistent with the expected electron drift velocities in the gas.

The measurements consisted of three sets of experiments. The first used the 4.9 GeV proton beam to bombard self-supporting C (68 μg/cm² polystyrene) and Al (168 μg/cm²) targets. Energy spectra for all products were obtained at 20, 45, 90, 135, and 160°. The second set of experiments used a 2.1 GeV proton beam on the same targets, but with energy spectra acquired only at 20, 90, and 160°. The final part used the 4.9 GeV proton beam to irradiate Ag and U targets. For the former (530 μg/cm² self-supporting Ag), energy spectra for fragments from B to Ar were observed only at 90°. More complete information was obtained for the U target (715 μg/cm² as UF_4 on 0.25 mil Mylar), with energy spectra for N to Ar fragments observed at 20, 90, and 160°.

A ΔE vs E spectrum is shown in Fig. 1 for the Al target. Element ridges can be clearly seen for He up to Na, with an indication of some Mg events. The maxima in the ridge lines for the low energy heavy elements is caused by the neutralization of the atoms as they slow down. Resolving elements at energies below the maxima may be difficult. An indication of the elemental resolution from the analog particle identifier (PI) can be obtained by restricting the fragment energies to a fairly narrow band above 5 MeV. Such a spectrum is shown in Fig. 2.

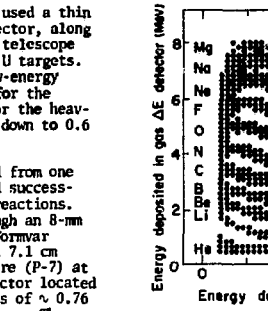

Fig. 1. Two-dimensional plot of ΔE vs E showing distinct ridges for different elements. The contour level has been adjusted for each element separately for clarity. (XBL 757-3446)

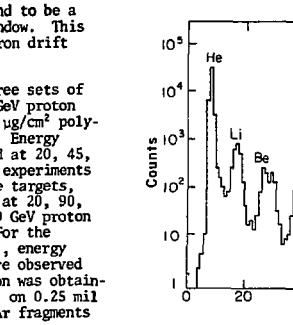

Fig. 2. Analog particle identifier spectrum for fragments with energies between 5 and 10 MeV. (XBL 757-3447)

elements heavier than Ne are off-scale to the right.

Currently off-line digital PI techniques are being used to attempt to separate isotopes for the very light fragments, and to achieve element resolution independent of particle energy for all fragments. It is anticipated that energy spectra and cross-sections will then be obtained. The data from Al + 2.1-GeV p will be compared to cascade evaporation calculations. The data from C + 2.1-GeV p will complement the results of Cork et al,[5] where a hydrogen [$(CH_2)_n$ - C difference] target was bombarded with a 2.1 GeV/nucleon C beam. All of the light target data will be of interest to astrophysics, and the heavy target data to the study of high deposition energies in high energy nuclear reactions.

References

1. A. M. Poskanzer, G. W. Butler, and E. K. Hyde, unpublished data.

2. E. K. Hyde, G. W. Butler, and A. M. Poskanzer, Phys. Rev. C4, 1754 (1971); R. G. Korteling, C. R. Toren, and E. K. Hyde, Phys. Rev. C7, 1611 (1973).

3. A. M. Poskanzer, G. W. Butler, and E. K. Hyde, Phys. Rev. C3, 882 (1971).

4. M. M. Fowler and R. C. Jared, Nucl. Instrum. Methods 124, 341 (1975); see also Sec. 4 of this Annual Report.

5. P. Lindstrom, D. Greiner, H. Heckman, B. Cork, and F. Bieser, LBL-3650 (Feb. 1975); D. Greiner, P. Lindstrom, H. Heckman, B. Cork, and F. Bieser, LBL-3651 (Mar. 1975).

CROSS SECTIONS ABOVE 0.3 GeV FOR (p,2p) REACTIONS OF ^{48}Ti AND ^{74}Ge

N. P. Jacob, Jr. and S. S. Markowitz

This work reports the results for (p,2p) excitation functions of ^{48}Ti and ^{74}Ge, both medium mass nuclei amenable to analysis without chemical separation. Since the predominant mechanism for (p,2p) reactions involves a "quasi-free" knockout[1] of a target proton, it has been used to illustrate free-pp scattering structure in the (p,2p) excitation functions determined by activation. The purpose of this particular study was to supplement the several prior excitation function studies[2-4] and gain a more complete notion of the systematic variation of free-particle structure in such reactions.

The targets for this work were prepared by high temperature vacuum evaporation of enriched $^{48}TiO_2$ (99.13%) and $^{74}GeO_2$ (94.5%) to thicknesses of 0.7-1.5 mg/cm^2 on 0.0013- cm aluminum foil. All targets were activated in the internal proton beams of the Lawrence Berkeley Laboratory (184-Inch Synchrocyclotron at energies from 0.3 GeV to 0.73 GeV, and the Bevatron for energies from 1.0 GeV to 4.6 GeV. Subsequent gamma ray counting of the foils with high resolution Ge(Li) detectors and analysis by computer code permitted cross sections to be calculated. The details of the experimental procedure are described elsewhere.[5]

The final (p,2p) cross sections are summarized in Table 1 and plotted as a function of incident proton energy in Fig. 1. The cross sections for the monitor reaction $^{27}Al(p,3pn)\ ^{24}Na$ used to calculate the reaction cross sections were taken from the review article of Cumming.[6] The uncertainty quoted with each (p,2p) result is the mean standard deviation and is derived from the individual determinations.

As seen from Fig. 1 and Table 1, the phenomenon of quasi-free pp scattering is observed for these medium mass nuclei. Previously measured (p,2p) excitation functions in the FeV energy

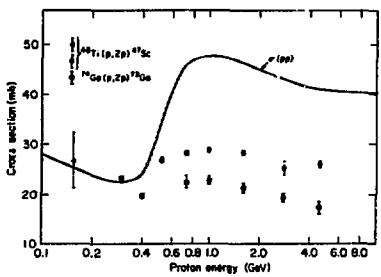

Fig. 1. Excitation functions for the ^{48}Ti (p,2p) ^{47}Sc and ^{74}Ge (p,2p)^{73}Ga reactions. The open circle at 0.155 GeV is taken from Ref. 7. The total cross seciton for pp scattering is also plotted for comparison. Below 0.5 GeV, the free-particle curve was taken from Ref. 8 and above 0.5 GeV, the data from Ref. 9 were used. (XBL 7410-4498)

region have also reflected the rise in cross section between 0.4 and 1.0 GeV, corresponding to an increase in the free-particle pp cross section over the same energy region.[2-4]

In Table 2, the ratio of the cross section at 1.0 GeV to that at 0.4 GeV for prior and present work is summarized. The increases in relative cross section observed in the present study are in good agreement with that determined by Reeder[4] for the $^{25}Mg(p,2p)\ ^{24}Na$ reaction. From the tabulated results, we note that the cross section or "reduced free-pp" ratio has a roughly constant mean value

Table 1. Reaction cross sections. All free pp cross sections are obtained from Ref. 6, unless indicated otherwise.

Energy (GeV)	$^{48}Ti(p,2p)^{47}Sc$ Individual Cross Sections (mb)	$^{48}Ti(p,2p)^{47}Sc$ Average±s.d. (mb)	$^{74}Ge(p,2p)^{73}Ga$ Individual Cross Sections (mb)	$^{74}Ge(p,2p)^{73}Ga$ Average±s.d. (mb)	Free pp (mb)	Monitor Cross[b] Sections (mb)
0.300±0.012	23.3,22.9,22.8, 22.9,24.5	23.3±0.7			22.9±1.5[a]	10.1±7%
0.400±0.016			19.4,20.2	19.8±0.6	24.0±1.0[a]	10.5
0.520±0.022	27.3,25.5,27.8, 26.9	26.9±1.0			34.0±0.2	10.7
0.730±0.029	27.9,26.4,26.1, 29.5	28.5±0.7	23.9,21.2	22.6±1.9	46.0±0.1	10.8
1.00±0.01	29.4,28.8	29.1±0.4	23.5,22.3	22.9±0.8	47.5±0.1	10.5
1.60±0.02	28.8,28.1	28.5±0.5	21.9,20.7	21.3±0.8	46.4±0.1	10.0
2.80±0.03	25.5,23.9	25.2±1.8	18.8,20.0	19.4±0.8	43.0±0.1	9.2
4.62±0.05	25.4,26.6	26.0±0.8	19.5,16.1	17.3±1.7	40.9±0.1	8.8

[a] Ref. 8.

[b] Ref. 6.

Table 2. Ratio of (p,2p) cross section at 1.0 GeV to the cross section at 0.4 GeV for various targets.

Reaction	$\sigma_{1.0}/\sigma_{0.4}$	Reference
free pp	1.98±0.08	8,9
$^{25}Mn(p,2p)^{24}Na$	1.19±0.05	4
$^{48}Ti(p,2p)^{47}Sc$	1.17±0.02	Present Work[a]
$^{57}Fe(p,2p)^{56}Mn$	1.40±0.31	2[b]
$^{68}Zn(p,2p)^{67}Cu$	1.46±0.22	2[b]
$^{74}Ge(p,2p)^{73}Ga$	1.16±0.05	Present Work
$^{142}Ce(p,2p)^{141}La$	1.47±0.13	5

[a] Cross section at 0.4 GeV is interpolated from excitation function.

[b] This ratio represents $\sigma_{0.72}/\sigma_{0.42}$.

of 1.31 ± 0.06 for the reactions. This fact may imply that an increasing nuclear surface, where simple knockout reactions are thought to occur, may nearly compensate for particle attenuation scattering, which would also increase with mass number.

To date, there exists no (p,2p) cross section calculations in the literature above the meson threshold of about 370 MeV. The results of such a calculation would be of considerable interest in demonstrating the theoretical behavior of (p,2p) cross sections in the GeV energy region.

Therefore, as part of this study, (p,2p) cross sections were calculated for ^{48}Ti and ^{74}Ge up to 1.0 GeV incident proton energy using the Monte Carlo intranuclear cascade model of Harp[10] coupled to the evaporation code of Dostrovsky et al.[11] The cascade model allows for inelastically produced (3,3) isobars and their subsequent interaction or decay in the nucleus. Only single isobar production is considered and thus cross section values above 1.0 GeV, where double pion production and double isobar formation become a possibility, were not calculated.

A plot of experimental and calculated values is presented in Figs. 2 and 3. Calculated (p,pn) cross sections are included for comparison.

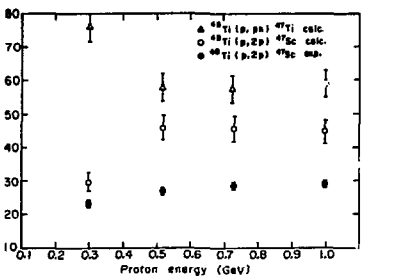

Fig. 2. Calculated and experimental (p,2p) cross sections for the ^{48}Ti (p,2p) ^{47}Sc reaction. The ^{48}Ti (p,pn)^{47}Ti cross sections, calculated using the same model (Ref. 10) are also added to the plot for comparison. (XBL 747-3690)

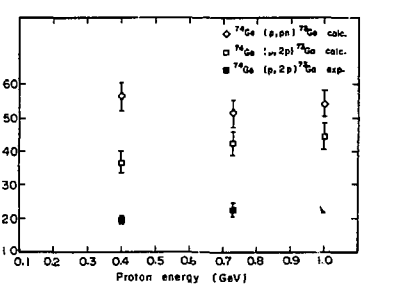

Fig. 3. Calculated and experimental (p,2p) cross sections for the ^{74}Ge (p,2p) ^{73}Ga reaction. The ^{74}Ge (p,pn)^{73}Ge cross sections, calculated using the same model (Ref. 10), are also added to the plot for comparison. (XBL 74703691)

A concise summary of experimental and theoretical work emphasizing excitation function shapes and trends is illustrated in Fig. 4. The "experimental" and "calculated (p,2p) curves" were obtained by normalizing the ^{74}Ge(p,2p) ^{73}Ga results to the ^{48}Ti(p,2p) ^{47}Sc results up to 1.0 GeV. In a similar fashion, the (p,pn) Monte Carlo results for the ^{74}Ge were normalized to those for ^{48}Ti to yield the smooth "calculated (p,pn) curve." Plotted at the bottom is the free-pp cross section over the same energy region. This normalization analysis leads to the following immediate conclusions. 1) The experimentally observed rise in σ(p,2p) for ^{48}Ti and ^{74}Ge between 0.3 GeV and 1.0 GeV is substantially smaller than predicted by the Monte Carlo calculation. Quantitatively, the relative increases in σ(p,2p) are (25 ± 3)% experimentally compared to (51 ± 19)% theoretically. 2) The experimental and theoretical σ(p,2p) rise is significantly smaller than the σ(pp) rise over the same energy region. These observations may be interpreted as evidence for attenuation of the incoming projectile and outgoing particles by nuclear matter matter. 3) Although the shapes not only of the two experimental (p,2p) excitation functions but also of the theoretical (p,2p) excitation functions are similar, the normalizations show the ^{48}Ti (p,2p) ^{47}Sc experimental cross sections to be systematically about 27% larger than those for the ^{74}Ge (p,2p) ^{73}Ga reaction. The Monte Carlo calculations predict a σ(p,2p) increase for ^{48}Ti in the same direction, but only of 6%. 4) The "calculated (p,pn) curve" shows a significant drop above 0.3 GeV as opposed to rising "experimental" and "calculated (p,2p)" curves. Calculations also predict a large (p,pn) cross section for ^{48}Ti than for ^{74}Ge by about 11%.

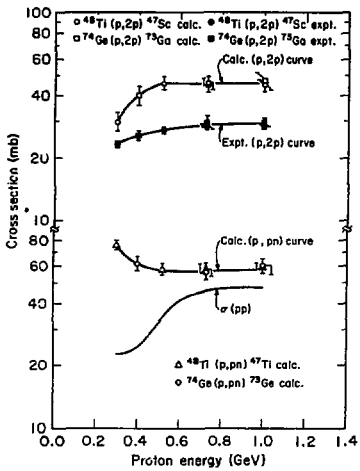

Fig. 4. Comparison of cross section changes and excitation function shapes. The "experimental" and "calculated (p,2p) curves" were obtained by normalizing the ^{74}Ge (p,2p)^{73}Ga results to the ^{48}Ti (p,2p)^{47}Ge were normalized to those for ^{48}Ti to yield the smooth "calculated (p,pn) curve". Plotted at the bottom is the free pp cross section over the same energy region. (XBL 7410-4099)

Footnotes and References

*Condensed from LBL-2381. Phys. Rev. C11, 541 (1975).

1. J. R. Grover and A. A. Caretto, Jr., Ann. Rev. Nucl. Sci. 14, 51 (1964).

2. P. L. Reeder, University of California, Lawrence Radiation Laboratory Report, UCRL-10531, unpublished (1962).

3. S. Meloni and J. B. Cumming, Phys. Rev. 136, B 1359 (1964).

4. P. L. Reeder, Phys. Rev. 178, 1795 (1969).

5. N.P. Jacob, Jr. and S. S. Markowitz, Phys. Rev. C 11, 541 (1975).

6. J. B. Cumming, Ann. Rev. Nucl. Sci. 13, 261 (1963).

7. J. P. Cohen, G. Albuoy, and N. Poffe, J. Phys. (Paris) 26, 427 (1965).

8. V. S. Barashenkov and V. M. Maltsev, Fortschr. Physik 9, 549 (1961).

9. D. V. Bugg, D. C. Salter, G. H. Stafford, R. F. George, K. F. Riley, and R. J. Tapper, Phys. Rev. 146, 980 (1966).

10. G. D. Harp (Phys. Rev. C, 10,2387 (1975). This program is an extension to 1.0 GeV of the model developed by G. D. Harp, K. Chen, G. Friedlander, Z. Fraenkel, and J. M. Miller, Phys. Rev. C 8, 581 (1973).

11. I. Dostrovsky, Z. Fraenkel, and G. Friedlander, Phys. Rev. 116, 683 (1959).

NUCLEAR REACTIONS OF C, Al, AND F WITH RELATIVISTIC HEAVY IONS AT THE BEVALAC

D. L. Murphy and S. S. Markowitz

A new area of experimental physics has been opened by the successful acceleration of heavy ions to relativistic energies at the Bevalac (0.25 - 2.1 GeV/nucleon). The study of the interaction of relativistic nuclei with simple and complex nuclei is an area which promises to be a stimulating new region of nuclear research, pertinent to elementary particles, nuclear structure, and astrophysics.[1,2,3]

Early studies of the reactions of relativistic heavy ions have indicated that significantly different processes are important compared to those at 10 MeV/nucleon. For example, fragmentation of projectiles has been observed[4] to lead to particles of lower mass and charge which have very nearly the same velocity and direction as the incident ion. Heckman et al. found also that the spectra and relative yields of projectile fragmentation products do not appear to depend on the target nucleus. They interpret these results in terms of two concepts from the theory of multiparticle reactions at high energy, limiting fragmentation and factorization. Limiting fragmentation states that, at high energies, the production cross section for the ith fragment is independent of energy. Factorization states that in the inclusive reaction,

$$A + B \rightarrow X + \text{anything},$$

the partial cross sections factor according to the rule

$$\sigma^{*}_{AB} \rightarrow \gamma^{*}_{A}\,\gamma_{B},$$

where the function γ^{*}_{A} depends only on the beam nucleus and γ_{B} only on the target nucleus.

Cumming et al.,[5] in their comparison of the relative product yields for the spallation of Cu induced by 3.9-GeV ^{14}N and 3.9-GeV protons, said the results of their study could be considered as giving support to the factorization hypothesis.

In order to further test the applicability of these hypotheses to nucleus-nucleus collisions in the GeV/nucleon energy region, a study of target fragmentation has begun by looking at specific inclusive reactions which lend themselves to observation after irradiation. For example, the inclusive reaction

$$X + {}^{12}C \rightarrow {}^{11}C + \text{anything},$$

where X = relativistic heavy ion, can be studied via conventional β-counting. Light targets such as Al, F, and C have been used since the induced activities are primarily β-emitters with resolvable half-lives. Gamma spectroscopy has been utilized to study the few long-lived emitters which can be produced in the interaction of the relativistic heavy ion with the light target nuclei. Beam monitoring is done with a gas ionization chamber, whose characteristics we spent some time studying.

Some preliminary results of a 2.1 GeV/nucleon ^{12}C bombardment are presented in Table 1 and compared with proton results. Experiments have been performed with ^{20}Ne (0.4 GeV/nucleon), ^{14}N (1 GeV/nucleon), and ^{40}Ar (1.8 GeV/nucleon).

Before any definite conclusions can be drawn, these reaction cross sections must be determined for more heavy ions. In addition, they will be measured at several different incident energies in order to determine if the region of limiting fragmentation has been reached.

Table 1. Formation cross sections (in mb) for 2-GeV/nucleon p and ^{12}C.[a]

	protons[b]	^{12}C
$\sigma_C(^{11}C)$	27.2	68
$\sigma_C(^{7}Be)$	10.5	20
$\sigma_F(^{18}F)$	24.0[c]	58
$\sigma_F(^{13}N)$	-	8
$\sigma_{Al}(^{24}Na)$	9.5	16
$\sigma_{Al}(^{22}Na)$	12.3[d]	29
$\sigma_{Al}(^{18}F)$	7.3	21
$\sigma_{Al}(^{13}N)$	1.3[d]	8
$\sigma_{Al}(^{11}C)$	5.2[d]	16
$\sigma_{Al}(^{7}Be)$	7.8[e]	22

[a]The convenient notation $\sigma_Z(Y)$ denotes the cross section for the producing of Y from the target Z.
[b]Results normalized to Al monitor cross section of 9.5 mb from Ref. 6.
[c]Ref. 7 [d]Ref. 8 [e]Ref. 8, 2.9 GeV.

References

1. H. H. Heckman, Lawrence Berkeley Laboratory Report LBL-2052 (1973).

2. H. M. Steiner, Lawrence Berkeley Laboratory Report LBL-2144 (1973).

3. E. K. Hyde, Lawrence Berkeley Laboratory Report LBL-3049 (1974).

4. H. H. Heckman, D. E. Greiner, P. J. Lindstrom, F. S. Beiser, Phys. Rev. Lett. 28, 926 (1972).

5. J. B. Cumming, P. E. Haustein, R. W. Stoenner, L. Mausner, and R. A. Naumann, Phys. Rev. C 10, 739 (1974).

6. J. B. Cumming, Ann. Rev. of Nucl. Science 13, 261 (1963).

7. S. S. Markowitz, F. S. Rowland, and G. Friedlander, Phys. Rev. 112, 1295 (1958).

8. J. B. Cumming, J. Hudis, A. M. Poskanzer, and S. Kaufman, Phys. Rev. 128, 2392 (1962).

EXCITATION FUNCTIONS FOR SIMPLE PION INDUCED NUCLEAR REACTIONS ON ^{14}N, ^{16}O, AND ^{19}F

N. P. Jacob, Jr., and S. S. Markowitz

The use of π mesons in nuclear reaction studies has proved to be a valuable tool in elucidating the mechanism of these reactions at high energies. In contrast to the relatively structureless nucleon-nucleon cross sections, pion-nucleon cross sections display several broad resonances. This picture is illustrated in Fig. 1, showing the well studied T = 3/2, J = 3/2 resonance at ~ 180 MeV (also referred to as the (3,3) resonance) and several smaller resonances at 600 and 900 MeV incident π-energy. Therefore, the significance of these resonances in the study of pion interactions with nuclei may manifest itself in two ways 1) The excitation functions for knockout type reactions of the form $(\pi,\pi N)$, where N is the nucleon removed, should exhibit these structures if a pion-nucleon initial interaction has occured. 2) The ratio of π^- to π^+ induced cross sections leading to the same product in knockout reactions would yield some additional insight into reaction mechanisms. For example, the ratio

$$\sigma\,{}^{A}X(\pi^-,\pi^-n)^{A-1}X]\,/\,\sigma[{}^{A}X(\pi^+,\pi N)^{A-1}X]$$

determined experimentally would be anticipated to be approximately equal to the ratio of free particle cross sections $\sigma(\pi^+p)/\sigma(\pi^-p) = \sigma(\pi^-n)/\sigma(\pi^+n)$, according to a simple impulse approximation picture. The most famous case is at the (3,3) resonance where the reactions

1. $\pi^+ + p \rightarrow \pi^+ + p$
2. $\pi^- + p \rightarrow \pi^- + p$
3. $\pi^- + p \rightarrow \pi^0 + n$

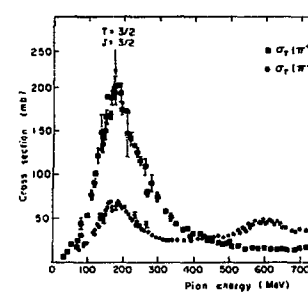

Fig. 1. The total free-particle πN cross sections. (XBL 754-2685)

are in the ratio 9:1:2. Since $\sigma(\pi^+p) = \sigma(\pi^-n)$ and $\sigma(\pi^-p) = \sigma(\pi^+n)$ by charge symmetry, the ratio $\sigma(\pi^-n)/\sigma(\pi^+n) = 9/(1+2) = 3$ at 180 MeV.

Thus, the ratio of π^- to π^+ induced neutron knockout cross sections at about 180 MeV incident energy should be about 3.

The pioneering work of Reeder and Markowitz[1] demonstrated the appearance of the (3,3) resonance in the $^{12}C(\pi^-,\pi^-n)^{11}C$ excitation function. The first preliminary investigation using positive and negative pions on light nuclei was first performed by Chivers et al.[2] This particular work found the surprising result that the $\sigma_{\pi^-}/\sigma_{\pi^-}$ ratios for $(\pi,\pi n)$ reactions of ^{12}C, ^{14}N and ^{16}O were all 1 ± 0.1 at 180 MeV rather than the predicted simple impulse approximation value of 3. A number of theoretical models incorporating contributions from inelastic scattering and final state interactions were proposed to explain this deivation, but none satisfactorily could produce the ratio of 1.[2-6]

The aim of this project, then, was multifold: 1) to recheck the activation results of Chivers for $(\pi,\pi n)$ reactions on ^{14}N and ^{16}O, both N = Z nuclei. 2) To search for appearance of the (3,3) resonance in the light nuclei ^{14}N, ^{16}O and ^{19}F. And 3) to provide an extensive set of $\sigma_{\pi^-}/\sigma_{\pi^+}$ ratios for ^{14}N and ^{16}O (N = Z) and for ^{19}F ($N \neq Z$) for theoretical interpretation. These light nuclei were chosen as targets because the constituent nucleons are essentially all on the "surface" region, where knockout reactions are thought to occur.

This work was performed at two national laboratories. The initial phase of research used the secondary pion beams at the Lawrence Berkeley Laboratory 184-Inch Synchrocyclotron. Secondary pion fluxes averages 10^5/sec. The pion work was completed in conjunction with a pion monitoring experiment at the new Clinton P. Anderson Meson Physics Facility at Los Alamos, New Mexico. While fluxes in the future are expected to reach a conservative 10^9 π/sec, the work here was performed at fluxes of $5 \times 10^5\pi$/sec or greater. Several exposures with $10^7\pi$/sec were made.

The targets used in this work took the form of discs, generally 1½ - 2 inches in diameter and from 1/8 - ½ inch thick. Thicknesses were varied with increasing or decreasing flux to achieve greater counting rates and to study the effect of potential secondary contributions to the final cross section from thick targets. Primary targets for ^{19}F, ^{14}N,

and ^{16}O were, respectively, discs of CF_2, machined BN, and boric acid H_3BO_3 in a thin aluminum can. Usually only 1 target was run at a time. In order to monitor the beam, a plastic scintillator or polyethylene disc equal in size to the target was exposed simultaneously. Subsequent counting of the monitor and target discs with a 511-511 keV coincidence detector and least squares fitting of decay curves permitted reaction cross section to be calculated.

The excitation functions are shown graphically in Figs. 2-4. The cross sections for the monitor reaction $^{12}C(\pi, \pi N)^{11}C$ used to calculate the reaction cross sections were accurately redetermined by the Los Alamos Nuclear Chemistry pion-monitoring group.[7] Horizontal error bars are root-mean-square combinations of π energy resolution and loss in energy from face of target to its center. Vertical error bars are statistical in nature.

As seen from Figs. 2-4, the (3,3) resonance is preserved in the $(\pi,\pi n)$ reactions on these light nuclei. Plendl et al.[8] observed a resonance in the $^{19}F(\pi^-,\pi^-n)$ reaction that is about 25% lower in cross section and much narrower than this work. Hogstrom et al.[9] finds a resonance in the $^{19}F(\pi^+,\pi^+N)\ ^{18}F$ reaction, but also too narrow. Based on the struck nucleon momentum, it can be shown that the free-particle πN resonance should be broadened 100 MeV, from about 150 MeV to 250 MeV, for $(\pi,\pi N)$ reactions in light nuclei.[1]

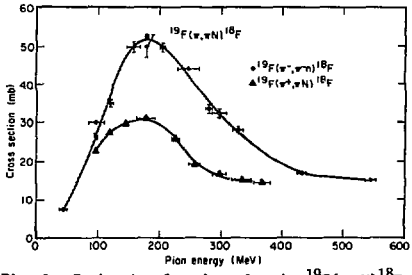

Fig. 2. Excitation functions for the $^{19}F(\pi,\pi N)^{18}F$ reactions. (XBL 755-2872)

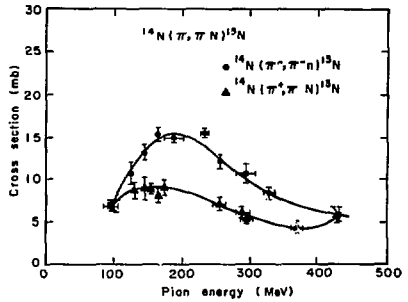

Fig. 3. Excitation functions for the $^{14}N(\pi,\pi N)^{13}N$ reactions. (XBL 755-2866)

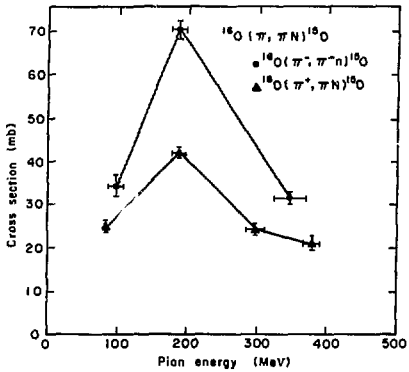

Fig. 4. Excitation functions for the $^{16}O(\pi,\pi N)^{15}O$ reactions. (XBL 755-2870)

The most serious disagreement with Chivers et al.[2] is noted. The $\sigma_{\pi^-}/\sigma_{\pi^+}$ ratios at the (3,3) resonance at 180 MeV for all $(\pi,\pi n)$ reactions on the light nuclei studied in the present work are 1.7 ± 0.2 as compared to the 1.0 ± 0.1 ratio of Chivers et al.[2] Also in disagreement are the magnitudes of the $^{14}N(\pi,\pi n)\ ^{13}N$ cross sections, which are a factor of 4 lower in this work. The results in this report are believed to be consistent with the phenomenon that excited states of ^{13}N are unbound. Therefore, only formation of ^{13}N in its ground state is observed.

An important preliminary theory has recently been advanced by Sternheim and Silbar[10] to explain the present $\sigma_{\pi^-}/\sigma_{\pi^+}$ cross section ratios as a function of energy. Their work begins with the assumption, originally made by Hewson,[4] that the following single-nucleon knockout reactions can occur in the nucleus:

Primary Interaction	Outgoing Particles	Relative Cross Section to Give Observed Product
π^-n	$\begin{bmatrix}\pi^-n\\ \pi^-p\end{bmatrix}$ (N.C.E.)	$\sigma_1(1-X)$
π^-p	$\begin{bmatrix}\pi^0n\\ \pi^-p\\ \pi^-n\end{bmatrix}$ (N.C.E.)	$\sigma_2 X$
π^+p	$\begin{bmatrix}\pi^+p\\ \pi^+n\end{bmatrix}$ (N.C.E.)	$\sigma_1 X$
π^+n	$\begin{bmatrix}\pi^0p\\ \pi^+n\\ \pi^+p\end{bmatrix}$ (N.C.E.)	σ_3 $\sigma_2(1-X)$

where $\sigma_1 = \pi^- + n \to \pi^- + n = 9$ (relative units)

$\sigma_2 = \pi^+ + n \to \pi^+ + n = 1$

$\sigma_3 = \pi^+ + n \to \pi^0 + p = 2$

and X = probability of a nucleon charge exchange ($n \to p$, $p \to n$), N.C.E. Then, for producing a $(\pi,\pi n)$ product

$$R = \sigma_{\pi^-}/\sigma_{\pi^+} = \frac{\sigma_1 - X(\sigma_1 - \sigma_2)}{\sigma_2 + \sigma_3 X(\sigma_1 - \sigma_2)} = \frac{9-8X}{3+8X}.$$

Sternheim and Silbar[10] have included in the above possible channels the (π^+,π^+N) depletion reaction. Then

$$R = (9-8p)/(3+6p)$$

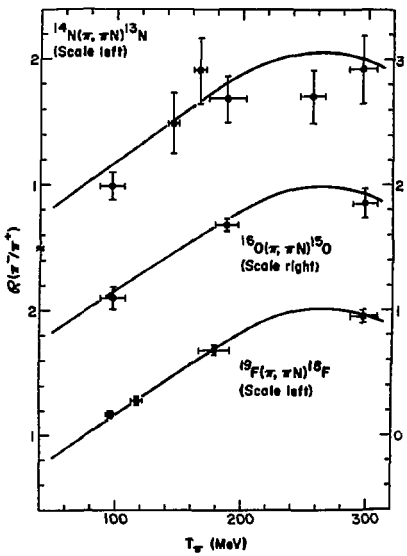

Fig. 5. Comparison between experimental and theoretical cross section ratios. Solid line represents the calculation, and filled circles are experimental. (XBL 756-1572)

Where p = probability of a nucleon charge exchange (following Sternheim-Silbar notation) and

$$p(T_\pi) = \tfrac{1}{2}\{1 - \exp[-A\rho_0\, \sigma_{NCE}(T_\pi)p(T_\pi)]\}$$

where

A = mass number of target
ρ_0 = nuclear density
$\sigma_{EX}(T_\pi)$ = nucleon charge exchange cross section as a function of pion kinetic energy, T_π
$D(T_\pi)$ = distance traveled by the initially struck nucleon as a function of pion kinetic energy T_π.

The above expression is slightly modified for N=Z nuclei. The details of its derivation are described elsewhere.[10]

The theoretical $\sigma_{\pi^-}/\sigma_{\pi^+}$ ratios predicted by the above simple model are compared with the experimental ratios for each target nucleus in Fig. 5. Within experimental error, agreement between theory and experiment is very good. Some deviation from the theory is found for the case of $^{19}F(\pi^-,\pi^-n)^{18}F$ at lower energies.

On the basis of this good agreement, we conclude that the nucleon charge exchange model for $(\pi,\pi N)$ reactions neatly accounts for experimental $\sigma_{\pi^-}/\sigma_{\pi^+}$ ratios. This theory, in addition, lends credence to the possibility of "unclean" knockout contributing significantly to any type of knockout reaction.

Footnotes and References

1. P. L. Reeder and S. S. Markowitz, Phys. Rev. 133, B639 (1964).

2. D. T. Chivers et al., Nucl. Phys. A126, 129 (1969)

3. V. M. Kolybasov, Phys. Letters 27B, 3 (1968).

4. P. W. Hewson, Nucl. Phys. A133, 659 (1969).

5. D. Robson, Ann. Phys. 71, 277 (1972).

6. R. Seki, Nuovo Cimento 9, 235 (1972).

7. B. J. Dropesky, G. W. Butler, C. J. Orth, R. A. Williams, G. Friedlander, M.A. Yates, and S. B. Kaufman, Phys. Rev. Letters, 34, 821 (1975).

8. H. S. Plendl et al., Nucl. Phys. B44, 413 (1972).

9. K. R. Hogstron et al., Nucl. Phys. A125, 598 (1973).

10 M. Sternheim and R. R. Silbar, Phys. Rev. Letters 34, 824 (1975).

DROPLET MODEL DESCRIPTION OF NUCLEAR MASSES, FISSION BARRIERS AND RADII*

W. D. Myers

In our earlier work[1,2] we had fitted a more or less conventional liquid drop model mass formula to the smooth mass surface that results when shell corrections (of the type proposed by Swiatecki[3]) are applied to the experimental masses. Besides the usual liquid drop model terms (which are the volume energy, symmetry energy, surface energy, Coulomb energy and the empirical even-odd mass correction) a surface symmetry energy and Coulomb diffuseness correction were used. Liquid drop model fission barriers were also compared with experiment as a part of the fitting procedure. The inclusion of fission barriers permits more accurate determination of the separate values of the Coulomb and surface energy coefficients, which are highly correlated in a fit to ground state masses alone. In this way the separate values of these two coefficients can be more accurately determined. We found that the Coulomb energy coefficient (which is inversely proportional to the nuclear radius constant r_o) determined in this way differs by 6-10% from that obtained in electron scattering measurements of nuclear sizes. A real discrepancy was seen to exist since both methods were expected to be accurate to one or two percent.

In Ref. 4 we undertook a study to determine whether this discrepancy might not be due to the omission of higher order terms (such as compressibility and surface curvature effects) in the liquid drop model. The droplet model was developed in the course of our investigation of these higher order terms and some preliminary applications of it have already been made.

The purpose of the present work is to determine the droplet model coefficients by fitting to masses, fission barriers, and radii. The predictions of the model are then compared with experiment to give an indication of its range of applicability. One gratifying result of this work is the apparent resolution of the radius constant discrepancy mentioned above. The value of this constant obtained in the droplet model fit no longer differs from that obtained in electron scattering experiments.

The primary data employed for the determination of the droplet model coefficients were the experimental atomic masses with $A \geq 10$. These were supplemented by 62 experimental fission barriers, 109 ground state deformations and 6 nuclear charge radii. The actual fit was weighted 3/4 to the masses and 1/4 to the fission barriers. If we had given each datum equal weight the large number of masses would have dominated leaving the barriers with little influence on the results. The radii were only used in the fitting procedure for rounding off the final set of coefficients. The deformations are determined largely by the coefficients in the shell effect function whose values were taken from our previous work.[2] The resulting droplet model predictions for all of these quantities are discussed in the following sections.

Mass Differences

One way of displaying the differences between the experimental masses and the theoretical predictions is to plot the individual mass differences versus the neutron number as is done in Fig. 1.

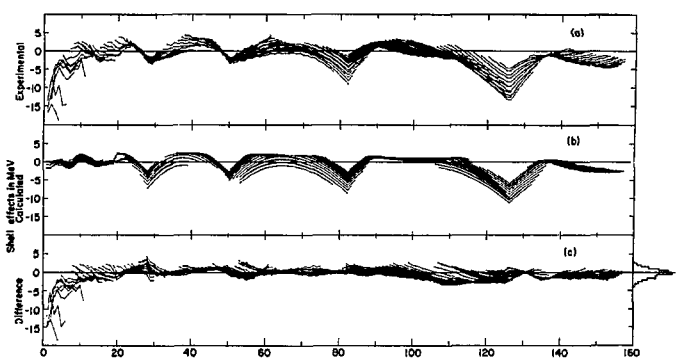

Fig. 1. The experimental and calculated shell effects and their difference are shown as functions of the neutron number. Isotopes of an element are connected by a line. The large negative deviations at the beginning of the periodic table are for nuclei outside of the fit region, which began at $A = 10$. A small histogram to the right of part (c) shows how the final errors are distributed for nuclei in the fit region. The substantial weight given to fitting fission barriers is presumably responsible for pulling the error distribution slightly to one side so that the mass residuals are not equally distributed about zero. (XBL 7412-8341)

This plot, which should be compared with similar ones in our previous work,[2] shows how poor our shell correction function is at the end of the rare earth region. The agreement between our shell function and the experimental one is also poor for the heavy elements. Microscopic methods for calculating shell effects such as the Strutinsky procedure were expected to give a better account of these features but their overall agreement with experiment was found to be about the same.

Fission Barriers

In Fig. 2(a) the experimental fission barriers have been plotted relative to the ground state mass. The droplet model saddle masses for the same nuclei are shown in Fig. 2(b) and the residual errors in Fig. 1(c). The calculated values are seen to differ from the experimental ones in a systematic (almost linear) way as one moves through the periodic table. If we had included shell corrections at the saddle point our calculated values would have agreed better in the actinide region but would not have changed much for the lighter nuclei. Negative values of the curvature correction coefficient, and a modified type of surface energy function[3] were both found effective in reducing the differences in saddle masses but they made the fit to ground state masses worse. So far no satisfactory explanation for these deviations has been found.

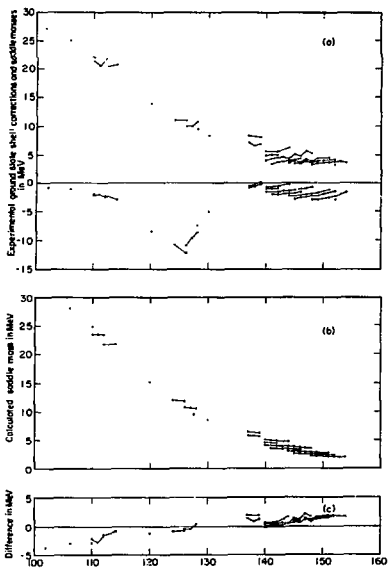

Fig. 2. Experimental and calculated saddle masses and their differences plotted against neutron number N. (XBL 7412-8338)

Deformations

As in our previous work one of the results of the calculation of shell effects is a prediction of nuclear ground state deformations. During the fitting procedure the calculated values were compared with the experimental ones. Figure 3 shows that there is rough agreement between theory and experiment for nuclei in the rare-earth and actinide regions. The main deviations seems to be associated (as with the mass deviations) with the inability of our shell correction function to adequately portray the behavior of nuclei at the upper end of the rare-earth region.

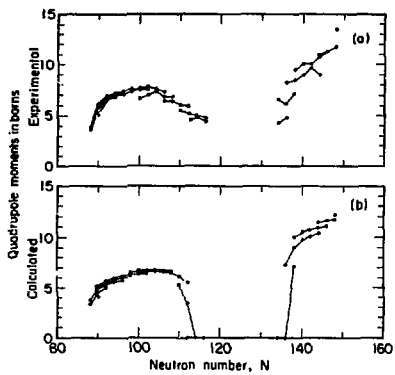

Fig. 3. Calculated and experimental quadrupole moments for nuclei in the rare-earth and actinide region are plotted against neutron number. (XBL 7412-8335)

Radii

The droplet model parameters chosen to give the best fit for masses and fission barriers also lead to predictions of nuclear charge radii in quite good agreement with experiment. The droplet model fit seems to have resolved the discrepancy that existed between the nuclear radius constant inferred from a liquid drop model fit to masses, and that obtained from electron scattering measurements of nuclear charge radii. Figure 4 shows how the effective sharp radii of the neutron and proton distributions are expected to vary for nuclei along beta-stability and how these radii are related to the radius constant r_0.

Remarks

The differences that remain when the droplet model is used to calculate ground state masses seem to be due to inadequate shell corrections, but this is not the case for fission barriers. For barriers, the differences vary smoothly as one

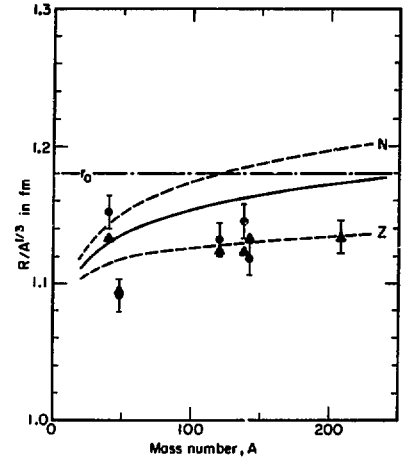

Fig. 4. Various quantities characteristic of the radial extent of spherical nuclei are plotted versus the mass number A. The dashed lines labeled N and Z correspond to the droplet model predictions for the quantities ($R_n/A^{1/3}$) and ($R_z/A^{1/3}$) for nuclei along the bottom of the valley of beta-stability. The solid line, which is the weighted mean of the neutron and proton lines, represents the value of ($R/A^{1/3}$) for the total nucleon density. The solid dots correspond to the experimental values of ($R_z/A^{1/3}$). Solid triangles indicate the droplet model value of ($R_z/A^{1/3}$) for these same nuclei. For comparison a dot-dashed line is drawn across the figure at 1.18 fm which is the value of r_0 determined by the fitting procedure.

(XBL 7412-8333)

moves up the periodic table indicating that some effect of a statistical nature may still be missing.

In so far as some of the coefficients we have evaluated here (the volume energy coefficient, symmetry energy coefficient, surface energy coefficient and nuclear radius constant, for example) are constants of nature, we feel that they are probably more accurately determined from the experimental data than was possible with the liquid drop model. When the droplet model is used there is less need for these coefficients to assume slightly incorrect values to compensate for missing higher order terms. The droplet model also provides a more accurate way for extrapolating far from beta-stability because of the higher order effects that are included. Since a number of higher order shape dependencies (such as the shape dependence of the Coulomb redistribution energy or surface symmetry energy) are included, the droplet model will be important in calculations of heavy-ion collisions where highly distorted shapes are involved.

Footnote and References

*Condensed from LBL-3428.

1. W. D. Myers and W. J. Swiatecki, Nucl. Phys. 81, 1-60 (1966).

2. W. D. Myers and W. J. Swiatecki, Nuclides Far Off the Stability Line, Proc. of the Lysekil Symposium, 1966, Arkiv Fysik 36, 343-352 (1967).

3. W. J. Swiatecki, Proc. Conf. on Nuclidic Masses, Vienna, 1963, ed. by W. H. Johnson, Jr. (Springer-Verlag, Wein-New York, 1964) p. 58.

4. W. D. Myers and W. J. Swiatecki, Ann. Phys. (N.Y.) 55, 395-505 (1969).

5. H. J. Krappe and J. R. Nix, Proc. Third Int. Conf. on Physics and Chemistry of Fission, (IAEA, Vienna, 1974) paper IAEA-SM-174/12.

MACROSCOPIC ASPECTS OF HEAVY-ION REACTIONS*

W. D. Myers

The overall status of the macroscopic approach to heavy-ion reactions was reviewed to determine how much progress has been made in this field and the range of applicability of the calculations that have been undertaken. The rate at which publications employing this approach are appearing in the scientific literature seems to be growing exponentially for a number of different reasons. (For recent reviews see refs. [1-3].) The most important is the increasing experimental interest in these reactions associated with the search for superheavy elements and the availability of new heavy-ion accelerators. Another reason is that, not only is a macroscopic approach possible (because both the target and projectile are composite systems with $A \gg 1$), but classical or semi-classical methods are applicable as well (because the "action" $\gg \hbar$).

Much of the work going on is at the relatively primitive stage of trying to establish plausible links between phenomena which actually require a dynamical description (such as compound nucleus formation for a particular target, projectile combination, energy and angular momentum) and some feature of the one dimensional (radial separation) potential energy (i.e., does the potential contain a minimum in which the system may be trapped, etc.).

Various attempts are now being made to include dynamical effects. Progress along these lines is based on the familiar procedure of: 1) choosing the degrees of freedom, 2) formulating the equations of motion (inertias, and forces both conservative and non-conservative), 3) performing the (classical or quantum mechanical) calculations for determining

the dynamical evolution of the system, and 4) comparing the results with experiment, after which one re-cycles through from the beginning as new and previously unexplained phenomena are observed.

Degrees of Freedom

The most ambitious calculations being undertaken seek to describe the collision behavior by numerically following the time evolution of a set of fluid elements initially distributed over a grid so as to represent the incoming ions.[4] Substantial simplification occurs if the nuclear shapes are parameterized. One seeks to employ a multi-dimensional family of shapes that is flexible enough to represent the natural dynamical evolution of the system but has as few parameters as possible. It has often been stressed that at least three degrees of freedom are absolutely essential if the parametrization is to be generally applicable. These are: 1) a separation or elongation coordinate, 2) a necking or fragment distortion coordinate, and 3) a mass asymmetry coordinate. In addition to the shape, other degrees of freedom may be important under certain circumstances.

The ultimate simplification occurs if the nuclear density distributions are simply "frozen" in their original form and are constrained to remain unchanged during the collision. This severe limitation on the degrees of freedom allowed (only the distance between the nuclei and their angular orientation need be considered) drastically restricts the range of applicability of the model. None the less, most of the semi-classical calculations of heavy-ion reactions have employed this model because of its tractability. The scope of the model is generally tested against the experimental results and other degrees of freedom are sometimes introduced as perturbations to explain some particular result.

Frozen Density Distributions

Once the distance between the nuclei and their orientations have been chosen as the only degrees of freedom to be treated explicitly (by freezing the densities), the next step is to formulate the equations of motion. Classical mechanics often applies and the inertial parameters are often taken to be the reduced mass of the system and the rigid body moments of inertia. For both the conservative and non-conservative forces that act a wide variety of somewhat similar alternatives have been proposed.

Partly because these approaches are all so similar we have no strict criteria for choosing between them. However, there are some purely geometrical considerations that one should be aware of and one unifying principle that would greatly simplify these calculations if it were more widely employed.

a. Geometrical Considerations. The error most commonly made in these calculations is to assume that some radial location (such as the half density point or the optical potential *half value point*) is strictly proportional to $A^{1/3}$. The principle of nuclear saturation, which forms the basis for such assumptions, should be more closely adhered to. It is based on the observation that the bulk density in the central region of nuclei throughout the periodic table is nearly constant. If this is the case then only the equivalent sharp radius R is proportional to $A^{1/3}$. For a spherical density distribution with a diffuse surface, purely geometrical considerations govern the relationship between this quantity and the location of the point at which the density has *half its central value*.

In a similar way, misleading results can be obtained if the half-value point of the single particle optical potential is assumed to be proportional to $A^{1/3}$ rather than relating its location to the density distribution of the nucleus it is supposed to represent.

b. Proximity Force Theorem. The potential between various sizes of target and projectile interacting via a two-body force can be expressed in terms of a single universal function which is easily obtained. This is because of the fact that,

> "The force between rigid gently curved surfaces is proportional to *the potential* per *unit* area *between* flat surfaces."

This theorem and its applications to heavy-ion potentials is discussed further elsewhere in this report (also see Annual Report 1973).

Static and Dynamic Considerations

The gross features of heavy-ion elastic scattering are described rather well by assuming that all the incoming projectiles whose energy and angular momentum permit them to pass over (or penetrate through) the barrier in the potential energy are removed from the entrance channel. For light projectiles and energies not too far above the Coulomb barrier most of the nuclei which pass over the barrier actually combine with the target to form a compound nucleus. For these systems the hollow in the one-dimensional potential energy disappears when the incident angular momentum is too large, and the compound nucleus cross-section seems to be limited by the critical angular momentum at which this occurs.

Even though absorption (and hence compound nucleus formation) is almost synonymous with trapping for lighter mass projectiles, substantial difficulties arise when the mass asymmetry between target and projectile is reduced. We have to extend our thinking to the other essential degrees of freedom if we want to understand the origin of these difficulties.

Figure 1, which includes a "necking" degree of freedom $\tilde{\alpha}_4$ as well as a separation coordinate $\tilde{\alpha}_2$, serves to remined us that the two fragment valley of two colliding nuclei does not lead directly to the ground state configuration of the compound system. Indeed, if the trapping configuration corresponds to a point in this two-dimensional space like like the one labelled A then no hope of compound nucleus formation exists unless enough additional energy is added to drive the system over the intervening ridge toward the spherical ground state at point H. Even then a compound nucleus might not result because the energy in the collective degrees of freedom would be sufficient to bring the system out over the fission barrier at point S.

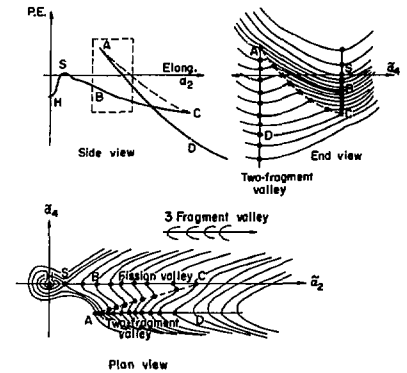

Fig. 1. See text. (XBL 7111-4852)

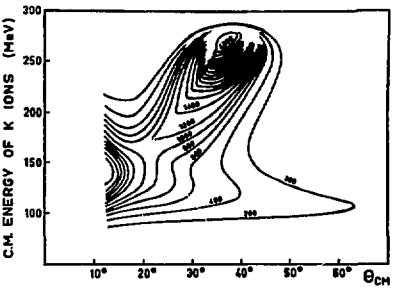

Fig. 2. The yield contours for the reaction $^{232}Th(^{40}Ar,K)$, E_{lab} = 388 MeV are plotted against the center-of-mass energy and deflection angle. (XBL 746-963)

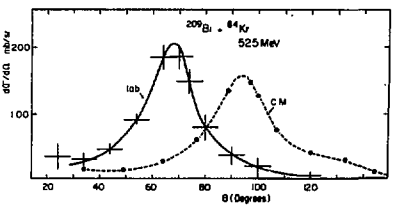

Fig. 3. The angular distribution of products from the indicated reaction that have an energy much lower than the incident energy. The energy observed is approximately that of Coulomb repulsion from a configuration of contact with the target nucleus. (XLB 746-966)

New Phenomena

The considerations of the previous section make it abundantly clear that when heavier projectiles are used compound nucleus formation is no longer expected to be the primary result of bringing two nuclei into contact. A host of new phenomena are expected to arise because the time constants for various types of collective motion (rotation, vibration, neck healing, mass asymmetry, etc.) are roughly comparable. Of course this is also true for lighter projectiles, but the interchange of energy among the various collective degrees of freedom and the damping into intrinsic states is not experimentally observable because the end result of the collision is usually a compound nucleus. The important difference is that systems formed with heavier projectiles are expected to re-disintegrate giving us the opportunity to observe the consequences of interaction of the various degrees of freedom during the collision.

In the scattering of ^{40}Ar on ^{232}Th at a center of mass energy of 331 MeV the emerging K nuclei (one proton and perhaps a few neutrons are picked up from the target) have the energy and angle distributions shown in Fig. 2.[5] This kind of distribution might be generated by viscous forces acting on projectiles that pass close to the nucleus. Trajectories corresponding to impact parameters smaller than those that lead to grazing collisions will not only be slowed down but will also be deflected forward to smaller angles.

When the periods for vibration (or neck healing) and rotation become comparable certain types of focusing can take place. Figure 3 is the angular distribution of light products (assumed to be similar to the ^{84}Kr projectile) scattered from ^{209}Bi having energies distinctly lower than the bombarding energy.[6] These products seem to correspond to collisions where radial motion of the incoming projectile is completely stopped and the system rotates with the incident angular momentum while some other collective vibration (such as neck healing and reforming) takes place. The vibration and rotation rates for different incident angular momentum seem to be correlated in such a way as to focus all the products into a rather narrow range of forward angles.

Footnote and References

*Condensed from LBL-2945, to be published in the Proceedings of the International Conference on Reactions between Complex Nuclear, Nashville, Tenn., June 1974.

1. M. Blann, Proceedings of the International Conference on Nuclear Physics, Munich, August 1973, North-Holland Publishing Co.

2. F. Plasil, Paper DB2, American Physical Society Meeting, Washington, D.C., April 1974.

3. A. Fleury and J. M. Alexander, preprint, May 1974.

4. Carol Alonso, Nuclear Chemistry Annual Report 1973, LBL-2366.

5. J. Wilczynski, Phys. Letters 45B, 484 (1973).

6. F. Hanappe, M. Lefort, C. Ngô, J. Peter, and B. Tamain, Phys. Rev. Letters 32, 738 (1974).

A CLASSIFICATION OF HEAVY ION REACTIONS

C. F. Tsang

The availability of heavy ion beams has opened up many new areas of research in heavy ion reactions. New phenomena, such as deep inelastic collisions, have been observed and well established processes, such as compound nucleus formation, are being studied in greater detail. Hence it is useful to have at the back of one's mind a picture classifying these processes with different designations. This not only helps to clear up confusions in discussions (so that we know we are referring to the same or different processes), but also provides a general background from which appropriate models may be constructed for each phenomenon.

Figure 1 was developed* for this purpose. It is based on a macroscopic view of the collisions between heavy nuclei. The two major elements entering into the construction of the figure are the energy of collision and the impact parameter. The macroscopic approach to heavy ion physics is discussed elsewhere in this annual report, as well as in other well known references.[1] Figure 1 illustrates the six major processes that may occur when two heavy nuclei collide--this is what we call "the six-fold way." When the impact parameter is large, the nuclei do not even touch each other and all that may happen are Rutherford scattering and Coulomb excitations. This may be called "Distant Collision." As we decrease the impact parameter, the two nuclei begin to touch; i.e., the tails of the respective density distributions overlap each other. This is the "Grazing Collision," an example of which is the one or two nucleon transfer reactions. When the impact parameter is decreased further and the collision energy is large enough (higher than the Coulomb barrier energy), solid contact may be made, by which we mean that, for instance, the half-density points of the respective density distributions overlap each other. At this point, depending on collision conditions, two things may happen. If the energy is larger then the binding energy of the projectile or target, we have what we call the "Hit-and-Run Collision", examples of which are Poskanzer's target fragmentation, Heckman's projectile fragmentation for relativistic heavy ions, as well as Miller's experiments with lighter ions at non-relativistic energies. If the energy of collision is not too large, then there is a possibility for the system to get stuck, which means that in a velocity distribution (or rapidity diagram), instead of the two sharp peaks corresponding to the initial velocities of the colliding nuclei there is now only one bump. Now the controlling factor is the neck degree of freedom. If the neck growth is slower than the separation (or fission) speed, we have "the Two-body System" where the two bodies are quite distinguishable even though significant nucleon-transfer may have taken place. An example is given by experiments of Volkov, Huizenga, Moretto, Wolf, and others. It is referred to by a variety of names: deep-inelastic reactions, relaxed peaks, and strongly damped processes, which all refer to the same thing. On the other hand if the neck growth degree of freedom is faster, then we may obtain a fused system, which means that in a spatial distribution, instead of two bumps centered around the respective centers of mass of the two nuclei, there is now only one broad bump, and the two nuclei are no longer distinguishable from each other. On a potential energy surface such a system is well within the scission point. However, depending on the dynamical conditions, the system may or may not be trapped in the compound nucleus well in the potential energy surface. We call the system not trapped in the well the composite system, which may divide with mass distribution essentially symmetric. Some memories of the entrance channel may remain, in which case the products may be distinguished from ordinary compound nucleus fission by their angular distributions. Examples of "Composite Systems" are found in experiments of Lefort, Blann, Plasil, and others. They are sometimes referred to as fusion-fission products. For a system trapped in the compound nucleus well we have the "Compound System" which may de-excite by evaporation of a few particles or undergo the well-known compound nucleus fission. These are studied in the experiments of Flerov, Ghiorso, Stephens, Lefort, Natowitz, and others.

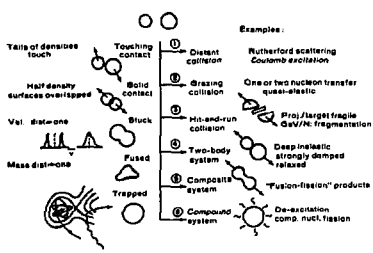

Fig. 1. The six-fold way.

While the classification in Fig. 1 cannot claim to take into account many detailed dynamical aspects of the heavy ion collisions, it is useful to relate the many possible processes in a simple and intuitive way, and to provide a background for detailed studies of these processes.

Footnote and References

*The work was done in collaboration with W. J. Swiatecki.

1. See contributions of W. D. Myers and N. K. Glendenning in this annual report. See also W. J. Swiatecki, Phys. Rep. 4, 325 (1972); Journal de Phys. Colloque C5, Supp. 8-9, 33, C5-45 (1972); Invited talk at Nobel Symposium Ronneby, Sweden, June 1974.

EXACT TREATMENT OF THE DWBA BY ANALYTIC MEANS FOR PARTICLE TRANSFER BETWEEN HEAVY IONS*

N. K. Glendenning and M. A. Nagarajan

Introduction

Reactions between complex nuclei in which one or several nucleons are transferred to form discrete states in the product nuclei are though to be direct reactions, analogous to light ion reactions such as the (d,p) reactions.[1] In this case, in lowest order, the reaction may be computed by the distorted wave Born-approximation (DWBA).

The DWBA involves the evaluation of multidimensional integrals, which is difficult because the integrands consist of products of a number of functions which depend on different vector coordinates, with, however, only several of them being independent. In the case of light nuclide reactions, such as (d,p), the evaluation is simplified by neglecting the effect of the finite size of the light nuclide (d in the case of (d,p) reaction). For reactions between complex nuclei, the neglect of their finite size is not justified, however. In addition to this, the small de Broglie wavelength of typical heavy-ion reactions requires that the particular dependence of the functions in the integrand on their vector coordinates be retained with an accuracy commensurate with the wavelength. Evaluation of the integrals which approximate the vector dependences of the integrands while retaining the finite range[2] are referred to as no-recoil approximations. (The zero-range approximation of the integrals automatically neglects recoil.)

There appear to be three distinct approaches to evaluating the DWBA integral without making either the zero-range or recoilless approximation. These are usually referred to as "exact", the sense of the word being that any errors are due to the finite accuracy of the numerical methods, and not to the neglect of physical effects. One approach evaluates directly the multidimensional integral. A second approach employs a Legendre expansion in two vectors by which the angle integrals can then be done in closed form. There remains a double-radial integral. The third approach expands the functions of the dependent coordinates in terms of functions for which a separation into the independent coordinates is possible. The most transparent way of achieving this is the expansion of the distorted waves on a plane wave basis. Then the coordinates separate trivially.

So far the direct evaluation of the multidimensional integrals for heavy ion reactions has been done only for angular momentum transfer equal to zero, perhaps because the method takes much computer time. Computer programs based on the second approach also have turned out to be costly to execute. In this connection, Low and Tamura have discussed how to choose the integration regions judiciously so as to save computer time, apparently at the cost of accuracy in absolute, though not in relative, cross sections. Of the third approach, the expansions of Sawaguri and Tobocman converge slowly and have consequently been applied only to light systems (N + 0). The expansion in plane waves used by Charlton has been thus far applied only to very light ion reactions.

In view of the above critique there is evidently a need for a fast and accurate method of evaluating the DWBA integrals. We propose the method discussed in detail in the next section, which appears to us to be a fast method, and one in which the convergence with respect to recoil angular momentum can be exploited. The method is based first on the existence of an addition theorem for the product of a spherical Bessel function and spherical harmonic, analoguous to that for a Hankel function. This addition theorem which is the vehicle for the separation of coordinates, can be exploited by representing the functions whose coordinates are to be separated, by a Fourier-Bessel series. Our approach belongs to the third category mentioned above. A virtue of our particular formulation is that the recoil angular momentum appears as the natural expansion parameter. This fact can be exploited in numerical calculations by truncating the series when satisfactory convergence is achieved.

The DWBA amplitude for the reaction is involves the evaluation of an integral like

$$t \equiv \int\int \psi^{(-)*}_{k_p}(\underline{R}_p)\, \phi^{*}_{L_2 S_2 J_2 M_2}(\underline{R}_{AN})\, V(R_{PN}) \times \phi_{L_1 S_1 J_1 M_1}(\underline{R}_{PN})\, \psi^{(+)}_{k_D}(\underline{R}_D)\, d\underline{R}_D\, d\underline{R}_{PN}. \qquad (1)$$

The difficulty mentioned above of evaluating this six-dimensional integral is now apparaent. The coordinates of integration, $\underline{R}_D$ and $\underline{R}_{PN}$, appear as arguments of only three of the functions, but appear in the other two in the combinations (see Fig. 1):

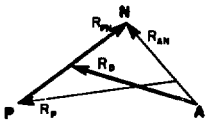

Fig. 1. The coordinates for the reaction A + (N+P) → (A+N) + P, with D = N+P, B = A+N. We choose to represent all vectors in terms of the two shown by heavy lines. (XBL 745-3031)

$$R_P = \frac{A}{B} R_D - \frac{N}{B}\frac{M}{D} R_{PN} ,$$

$$R_{AN} = R_D + \frac{P}{D} R_{PN}. \qquad (2)$$

(In this context we use A to denote the mass of nucleus A etc., and M denotes the total mass.) The recoilless approximation consists in neglecting the second term on the right side of R_P. Aside from the trivial scaling factor A/B, the arguments of two distorted waves are then the same. This simplifies the integration very much. However, this neglect would be justified only when $\psi_{k_p}(R_p)$ varies slowly over distances

$$d = \frac{N}{D}\frac{M}{B} r_D \qquad (3)$$

where we use r_D to denote the radius of D which is the approximate bound on R_{PN} imposed by the presence of $V(R_{PN})$ in (1). Hence recoild effects will be small only if the de Broglie wavelength $\lambda = 1/k_p$ is large compared to d, i.e.,

$$x \equiv \frac{N}{D}\frac{M}{B} k_p r_D << 1. \qquad (4)$$

This inequality is rarely satisfied (see Table 1).

To evaluate the integral (1) without making the zero-range or recoilless approximation, we seek to express the functions $\psi(R_D)$ and $\phi(R_{AN})$ each as the product of a function of R_D and of R_{PN}. To this end we first introduce, as usual, the partial wave expansions

$$\psi^{(+)}_{k_D}(R_D) = 4\pi \sum_{L_D\mu_D} e^{i\sigma_D} i^{L_D} F_{L_D}(k_D,R_D) Y^{\mu}_{L_D}(\hat{k}_D) Y^{\mu_D}_{L_D}(\hat{R}_D)$$

$$\psi^{(-)*}_{k_p}(R_p) = 4\pi \sum_{L_p\mu_p} e^{i\sigma_p} i^{-L_p} F_{L_p}(k_p,R_p) Y^{\mu_p}_{L_p}(\hat{k}_p) Y^{\mu_p *}_{L_p}(\hat{R}_p) \qquad (5)$$

$$\text{If } F_{L_p}(k_p,R_p) = \sum_n a_n^{L_p} j_{L_p}(\alpha_n^{L_p} R_p) \quad (0 \le R_p \le R_m). \qquad (6)$$

We show in Fig. 2 how accurately a typical partial wave can be represented by a five - and ten-term series of this type.

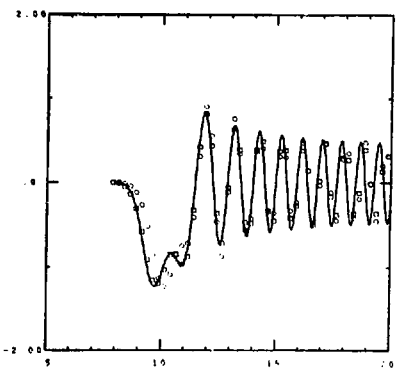

Fig. 2. A typical scattered wave function corresponding to ℓ = 84 in an inelastic channel 2⁺ of $^{18}O + ^{120}Sn$) is shown by solid line. The best five- and ten-term Bessel series, Eq. (6), fitted to the function over the region 0 ≤ R ≤ 15F are shown by circles and squares respectively. (XBL 756-1558)

Table 1. For a few typical reactions the parameter x which gives a measure of the importance of recoil (Eq. 4) is listed. The largest recoil angular momentum ℓ_R is given by $\sqrt{\ell_R(\ell_R+1)} = x$ which for such a rough estimate we solve as $\ell_R \simeq x$.

	E_{Lab} (MeV)	$x \simeq \ell_R$
$^{13}C(^{12}C,^{13}C)^{12}C$	87	2
$^{208}Pb(^{16}O,^{15}N)^{209}Bi$	104	2
$^{120}Sn(^{18}O,^{16}O)^{122}Sn$	100	4
$^{12}C(^{20}Ne,^{16}O)^{16}O$	78	5

Similarly, if we denote the radial part of $\phi_{L_2S_2J_2}(R_{AN})$ by $u_{L_2J_2}$

$$\phi_{L_2S_2J_2}(R_{AN}) = u_{L_2J_2}(R_{AN})[Y_{L_2}(\hat{R}_{AN}),S_2]_{J_2}$$

we can expand it

$$u_{L_2 J_2}(R_{AN}) = \sum_m b_m^{L_2} j_{L_2}(\beta_m^{L_2} R_{AN}). \quad (7)$$

The addition theorem is written for these as

$$j_{L_p}(\alpha R_p) Y^*_{L_p \mu_p}(\hat{R}_p) = \sum_{\ell_p \ell_R} A_{\ell_p \ell_R L_p} (-)^{\ell_p} j_{\ell_p}(\alpha_B^A R_D) \times j_{\ell_R}(\alpha_D^N \beta_B^M R_{PN}) \left[Y_{\ell_p}(\hat{R}_D) Y_{\ell_R}(-\hat{R}_{PN}) \right]^*_{L_p \mu_p} \quad (8)$$

and

$$j_{L_2}(\beta R_{AN}) Y_{L_2 M_2}(\hat{R}_{AN}) = \sum_{\Lambda \ell} A_{\Lambda \ell L_2} (-)^{\Lambda} j_\Lambda(\beta R_D) \times j_\ell(\beta_D^P R_{PN}) \left[Y_\Lambda(\hat{R}_D) Y_\ell(R_{PN}) \right]_{L_2 M_2}.$$

Now the angular integrals in (1) can be done in closed form, and the radial integrals reduce to a sum of products of one dimensional integrals of the form,

$$\int_0^{R_m} j_{\ell_R}(\alpha_n^{L_p} \beta_D^N r) j_\ell(\beta_m^{L_2} \beta_D^P r) V(r) u_{L_1 J_1}(r) r^2 \, dr \times \int_0^{R_m} j_{\ell_p}(\alpha_n^{L_p} \beta_B^A R) j_\Lambda(\beta_m^{L_2} R) F_{L_D}(k_D, R) R^2 \, dr. \quad (9)$$

The main result of our paper is expressed in here. The six-fold integral representing the t-matrix has been reduced to products of two one-dimensional integrals.[1]

It is a convenient feature of this formalism that the recoil angular momentum appears explicitly because we anticipate that this quantity is restricted to small values. Thus, the convergence in this variable can be exploited in numerical calculations to reduce the number of integrals (9) that need to be evaluated. It therefore appears that we have developed a method for evaluating the direct reaction amplitude for heavy ion reactions that will prove to be fast and therefore economical.

Footnote and References

*Abridged version of LBL-2378, in press in Nuclear Physics.

1. For a review and references to the literature see N. K. Glendenning, One and Two Nucleon Transfer Reactions, in Nuclear Spectroscopy, edited by J. Cerny (Academic Press to be published).

2. P. J. A. Buttle and L. J. B. Goldfarb, Nucl. Phys. 78, 409 (1966).

HOW WELL CAN THE INTERACTION BETWEEN HEAVY IONS BE DETERMINED BY ELASTIC AND INELASTIC EXPERIMENTS?*

N. K. Glendenning

It has been asserted that the elastic scattering cross section for heavy ions is sensitive only to the tail region of their mutual interaction. The opinion has also been expressed that inelastic scattering would provide a more sensitive probe. Here we intend to determine more precisely what can be learned from these reactions. The existence of the grazing angle in the classical deflection function for scattering from a potential provides a hint as to how to proceed. This angle is the invariant quantity that all potentials must possess if they are to reproduce this feature of the cross sections. Accordingly we focus on the penetration depth $D(\ell_g)$ of the grazing orbit, ℓ_g. Taking the $^{18}O+^{120}Sn$ scattering at E = 100 MeV (lab) as a concrete example, this depth turns out to be about 12 F.

We adopt as a standard potential one suggested by Becchetti (the 40-MeV potential of the table). The value of this potential at the above mentioned grazing distance is 0.36 MeV. We generate set of potentials which pass through this point, and lie within something like ±30% of the standard potential within an internal of ±1 F around the grazing distance. There is a continuous infinity of potentials having such a specification, of which the tail region of a few are shown in Fig. 1, while a larger selection is shown in Table 1. (The parameters refer to a Woods-Saxon form.) For each real potential we have used a search routine to provide an imaginary part of the potential such that all potentials yield the indistinguishable cross sections down to several orders of magnitude below the peak. The compacted elastic cross sections for the two extreme potentials listed in the table are shown in Figs. 2 and 3 at two different energies. In addition we show the cross sections for exciting the 2^+ state in tin. It is evident that the cross sections are indistinguishable even for the extreme potentials of Table 1 down to several orders of magnitude

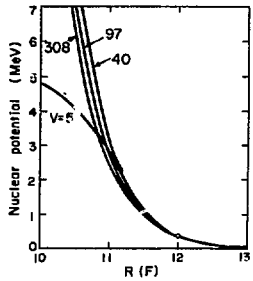

Fig. 1. The tail region of the real part of potentials which, together with the imaginary parts listed in Table 1, yield elastic cross sections which are indistinguishable. The central value of the depth is in each case indicated and can be used to identify the corresponding entry in Table 1. These are members of a continuum of potentials. V can have any value lying between these curves, and possibly beyond. (XBL 745-3282)

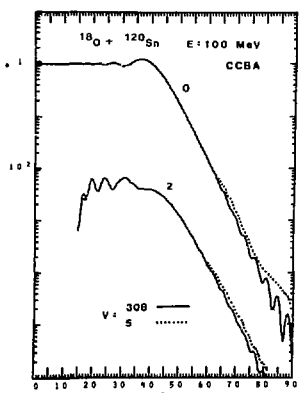

Fig. 2. Elastic and inelastic 2^+ cross section for 100-MeV $^{18}O + ^{120}Sn$ cannot distinguish between the two extreme potentials of Table 1 (first and last entry). The two scales refer to the two curves. For the inelastic cross section, our calculation for $\theta \leq 15°$ is inaccurate because only the contributions for $\ell \leq 215$ and $R \leq 30$ F were computed at this energy. Cross sections throughout are in mb/sr. (XBL 745-915)

below the peak. We may conclude therefore that unless it becomes possible to make very precise measurements for very low cross sections, neither the

Table 1. A selection from a continuum of potentials which yield elastic scattering cross sections which are indistinguishable for 100-MeV $^{18}O + ^{120}Sn$. Reaction cross sections are equal within ~3%. In each case the Coulomb radius is $r_C = 1.2$. The 40-MeV potential is our standard one.

V	r_V	a_V	W	r_W	a_W	σ_R
-308	1.125	0.52	- 8.9	1.334	0.5323	1600
			-48.5	1.203	0.5716	
-214	1.125	0.55	- 8.18	1.368	0.5433	1820
-149	1.19	0.5	- 8.44	1.337	0.5224	1795
- 98	1.22	0.5	- 7.404	1.354	0.4936	1785
			-33.34	1.232	0.5001	1745
- 67	1.24	0.5	- 5.673	1.378	0.5119	1695
- 40	1.31	0.45	-15	1.31	0.45	1760
- 24	1.32	0.48	- 4.866	1.401	0.4631	1790
- 10.7	1.39	0.45	- 6.063	1.385	0.4179	1780
- 5.49	1.46	0.38	- 7.763	1.424	0.3276	1790

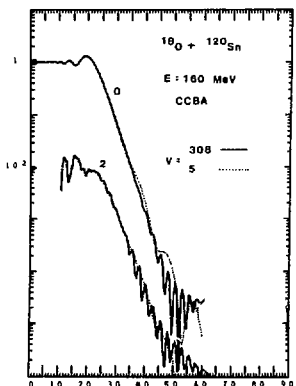

Fig. 3. Elastic and inelastic cross sections for 160-MeV $^{18}O + ^{120}Sn$ cannot distinguish between the two extreme potentials of Table 1 (first and last entry). (XBL 745-912)

elastic nor inelastic cross sections provide more than a very approximate specification of the interaction in the tail response. That is to say, no potential falling within the wide bounds between the curves of Fig. 1 can be distinguished save by the most precise of elastic or inelastic experiments.

Footnote

*Excerpted from an Invited Paper in Proceedings of International Conference on Reactions Between Complex Nuclei, Nashville, Vo. 2; ed. by R. L. Robinson et al. (North Holland, Amsterdam, 1974) p. 137.

TWO-NUCLEON TRANSFER BETWEEN HEAVY IONS, DEEP ORBITS AND SECONDARY PEAKS*

N. K. Glendenning

We learned in the preceding paper that neither elastic nor inelastic cross sections carry information about the interaction between nuclei except in the tail region. A consideration of the form factors for various reactions between nuclei reveals that several nucleon transfer should be more sensitive to the interior region. Indeed for two nucleon transfer, the form factor is peaked at a separation distance of the centers corresponding to a total immersion of one nucleus within the other (Fig.8). Whether the nuclei in such close collisions survive to emerge again in simple direct reaction channels with sufficient probability to be observed is as yet an unsettled question. If they do, the carry information about that region, and we must learn how to interpret it.

For orientation we consider first the two extreme potentials of Table 1 of the preceding paper whose elastic and inelastic cross sections were compared at two energies in Figs. 2 and 3 of that paper and found to be indistinguishable under usual experimental conditions. In contrast the two-neutron transfer cross sections leading to the ground and 2^+ states in ^{122}Sn are very different and easily distinguished at angles away from the grazing angle (Fig. 1). At this point we emphasize that the grazing angle is ideal for determining spectroscopic information in transfer reactions, because it depends so weakly on the interaction. However, it is only by making measurements away from the grazing angle that information about interior conditions can be determined. The S-matrix at E = 100 MeV for the ground state transition for both potentials are shown in Fig. 2 and reveal a very large contribution coming from small angular momentum collisions in the case of the deep potential. Whether such a large contribution for strongly overlapping collisions is realistic we cannot tell from either elastic or inelastic experiments, but the opportunity for learning this is certainly afforded by transfer reactions. In addition to plotting the amplitude of S, which most transparently reveals the important regions of ℓ, we have also plotted S itself in the complex plane and joined these points. The

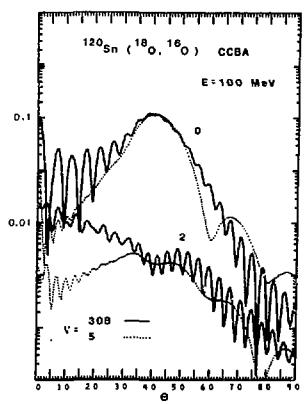

Fig. 1. Cross sections for two-neutron transfer to the ground and 2^+ vibrational state easily distinguish between the two extreme potentials of Table 1 of the preceding paper. The two scales refer to the two states. (XBL 745-914)

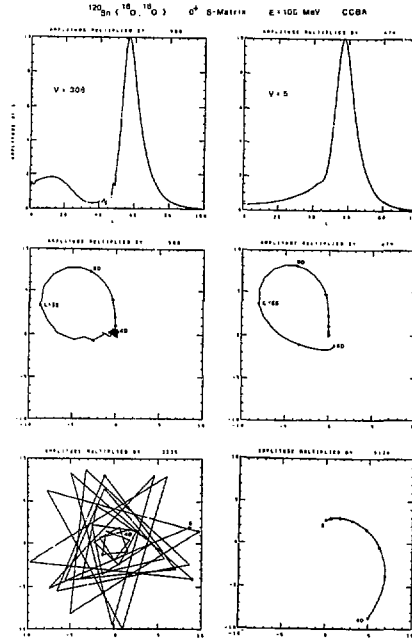

Fig. 2. The S-matrix for the ground state transfer are compared for the two extreme potentials. The corresponding cross sections are in Fig. 1. The amplitude of S is plotted in the top part of the figure, and S iteself is plotted in the complex plane in the bottom part. Note the resonant behavior in the lower ℓ region in the case of the deep potential, signalled by the rapid rotations. (XBL 745-903)

resonant behavior of the deep potential signified by the rapid rotation of the trajectory around the origin is in contrast with the shallow potential. These are potential or shape resonance like those known from neutron scattering. This behavior appears also in the elastic S-matrix but since it is in the low ℓ-region, where S is several orders of magnitude less than inity, it does not manifest itself in elastic scattering, but rather in several nucleon transfer reactions.

Perhaps it is not so surprising that such different potentials as the two compared above could be distinguished. Therefore, we turn our attention to two which are more conventional. The one is the standard that we adopted at the beginning of this article and which was the basis for the potentials of Table 1 in the preceding paper. It was employed by Becchetti in the O + Pb reaction. The other one is due to Morrison which he used for O + Ca. They are labeled B and M in Table 1 of this paper. It may be noticed that the Morrison potential is very similar to one (97) in Table 1 of the preceding

Table 1. The Becchetti and Morrison potentials and their reaction cross sections at two energies. The primed potentials have weaker absorption. Fairwise they have close to the same reaction cross sections. Coulomb radius parameter is $r_c = 1.2$. (Energy, length and cross sections are quoted in MeV, F and mb.)

	V	r_0	a	W	σ_R	
					E = 100	E = 160
B	- 40	1.31	0.45	-15	1760	2525
M	-100	1.22	0.5	-40	1750	2510
B'	- 40	1.31	0.45	-10	1720	2465
M'	-100	1.22	0.5	-27	1700	2450

paper, and it is not surprising therefore that they cannot be distinguished by elastic and inelastic scattering. In fact, the two-neutron transfer reaction at E = 100 MeV shown in Fig. 3 does not distinguish between them either. The S-matrix for the Becchetti potential reveals no interior contributions. Only a narrow band of angular momenta centered at the critical angular momentum ℓ_c are important. Knowing that the imaginary potential is poorly determined we have reduced it for both potentials but in such a way that the reaction cross sections remain about equal for the two potentials. This roughly insures that we are dealing with equivalently absorbing potentials. They are labeled B' and M' in Table 1. All four yield indistinguishable elastic and inelastic cross sections, and even at the reduced absorption we cannot distinguish easily the two-neutron transfer cross sections (Fig. 4).

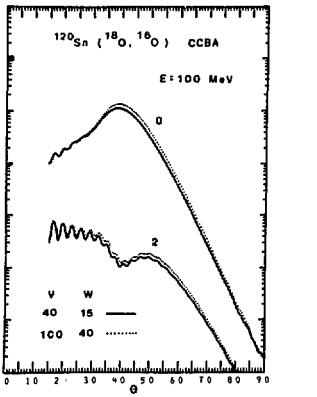

Fig. 3. Cross sections for two-neutron transfer to the ground and 2^+ vibrational state. The two cases refer to the Becchetti and Morrison potentials of Table 1. (XBL 745-913)

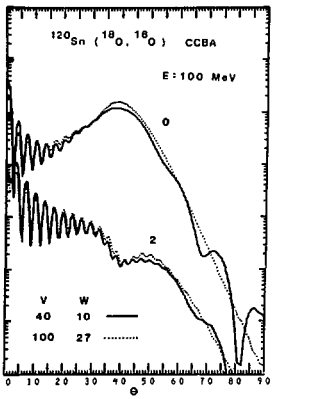

Fig. 4. Cross sections for two-neutron transfer to the ground and 2^+ vibrational state computed for the reduced absorptions indicated by potentials B' and M' in Table 1. Experiment could not easily distinguish between these. (XBL 745-911)

At this point we turn to the classical orbits to assist us in deciding what to look for that can distinguish between these two potentials. Their

classical deflection functions are compared in Fig. 5 at several energies. It can be seen that for $\ell > \ell_c$ they give rise to the same classical cross section. However, the inner region below ℓ_c is different in the two cases. Such differences are obscured in the quantum elastic and inelastic scattering by the imaginary potential, even when it is week.

Our attention is attracted by the flat regions around $\ell \sim 30$ in the case of 160-MeV scattering because flat regions of the deflection function give rise to large cross section, there being many waves that scatter near the same angle. Classically, therefore, the deep potential would produce a peak at $\theta \simeq 15°$, while the shallow potential would produce a peak at $\theta \simeq 45°$. Since the grazing angle, $\theta_g \simeq 23°$ is so far forward at this energy the presence of a secondary peak at 15° is likely to be obscured. However, because the cross section normally drops off quickly beyond θ_g, the secondary peak at $\theta = 45°$ produced by the weak potential may be observable if absorption is not so strong as to damp altogether the interior partial waves. It turns out that for the absorption strengths originally quoted for the Becchetti and Morrison potentials, the secondary structure is not visible. However, the two-nucleon transfer cross sections shown in Fig. 6 clearly distinguish between the deep and shallow potentials for the case of weaker absorption. In particular for the shallow potential we see the secondary peak at $\theta \sim 45$ as anticipated from the classical discussion. The corresponding S-matrix is shown in Fig. 7 and here we see, again in agreement with the classical picture, a subsidiary peak at $\ell \sim 30$.

Thus by this consideration of classical scattering, we have been led to suggest how two-nucleon transfer reactions may be used to distinguish between potentials which are equally acceptable as far as elastic and inelastic scattering is concerned. For this is possible, however, the absorption must not be too strong (unless the real potentials are extreme such as 308 and 5 in Table 1 of the preceding paper. We note in this connection that the reduction in W shown in Table 1 does not reduce the reaction cross section proportionally. We saw in Table 1 of the preceding paper a selection of potentials which are equivalent for elastic and inelastic

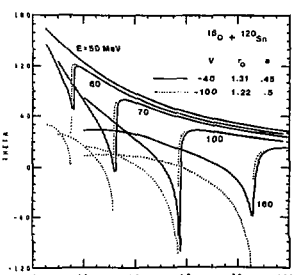

Fig. 5. Deflection function at several energies are compared for the potentials indicated. The singularities mark the value of the critical angular momentum at each energy. The grazing angle θ_g and angular momentum ℓ_g correspond to the maximum just above ℓ_c in each case. (XBL 745-930)

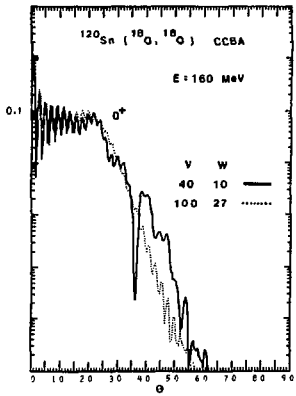

Fig. 6. Cross section for two-neutron transfer to the ground state computed at E = 100 MeV for the Becchetti and Morrison potential with reduced absorption (B' and M') of Table 1. Note the secondary structure in the one case occurring at $\ell = 45°$ in correspondence with the classical deflection function of Fig. 5, which predicts such a peak arising from deep orbits around $\ell \sim 30$. (XBL 745-917)

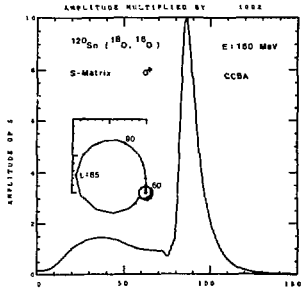

Fig. 7. S-matrix at E = 160 MeV for the ground state two-neutron transfer corresponding to the Becchetti potential with weak absorption (B' in Table 1). Note the broad structure around $\ell = 30$. Corresponding cross section is in Fig. 6. Inset shows S plotted inthe complex plane from $\ell = 60$. (XBL 745-931)

scattering. Therefore, we add that for potentials with a real depth somewhat weaker than the Becchetti potential, the secondary peak would move to larger angles, and in the reverse direction for stronger ones. The appearancd in experiment of such a secondary peak would indicate that the absorption is "weak" and the real potential shallow. The absence of such a peak would be inconclusive.

We have seen a sample of two-nucleon cross sections which are widely different, depending upon the potential acting between the nuclei at distances corresponding to appreciable overlap. The differences show up at angles away from the grazing angle. This is natural, of course, since the grazing angle is so called because it is only modestly perturbed by the nuclear field. A reexamination of our figures reveals how important it is to perform measurements at small angle intervals and with good resolution and statistics. This make the experiments slow, but they should prove very rewarding. Clearly much more information is potentially available here than is elastic or inelastic experiments. Of course, the latter play their role in defining the strength of the inelastic branch of multiple-step transfer amplitudes. But they carry very little information about the nuclear field that is unique.

I stress that the attention to two-nucleon transfer and the tin isotopes is for illustrative purposes only. For other multi-nucleon transfer reations, and for other mass region the same type of classical analysis is expected to be fruitful.

Footnote

*Excerpted from an Invited Paper in Proceedings of International Conference on Reactions Between Complex Nuclei, Nashville, Vol. 2; ed. by R. L. Robinson et al. (North Holland, Amsterdam, 1974) p. 137.

TWO-FOLD NATURE OF COULOMB-NUCLEAR INTERFERENCE IN HEAVY ION INELASTIC SCATTERING

N. K. Glendenning

The so-called Coulomb-nuclear interference phenomenon has been a subject of a number of experimental papers and has also been discussed in theoretical papers. In some of the latter papers, wave interference explanation of the phenomenon given that, together with the opposite source of the nuclear and Coulomb parts of the interaction, yields an explanation of the phase relationship observed in oscillations in the elastic and inelastic cross sections.[1] The experimental papers often allude simply to a cancellation arising from the opposite source of the fields.[2]

Actually there are in fact two distinct aspects of the phenomenon. The wave interference aspect can be understood in terms of the deflection function shown in Fig. 1. The position is indicated of three orbits, 1,2, and 3, all of which scatter to the same angle. The outer most one, labeled 1, can excite the nucleus only through the long-range quadrupole component of the Coulomb field, whereas orbits 2 and 3 penetrate to the region where the nuclear field is strong. The superposition principle ensures the interference of the amplitude of such waves and it is the opposite sense to the elastic scattering.

The second aspect could be called the impulse cancellation effect. Along certain orbits in a very narrow band of angular momenta the integrated effect of the alternating sign of the Coulomb-nuclear-Coulomb quadrupole field sums to a negligible impulse. This appears explicitly in an examination of the S-matrix for the inelastic process shown in Fig. 2. There the amplitude, and S-itself, plotted in the complex plane, is shown for a pure Coulomb and a pure nuclear quadrupole field in the second and third columns of the figure. An examination of S in the complex plane reveals that for

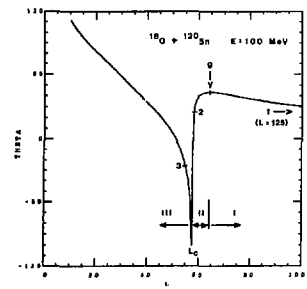

Fig. 1. Deflection function from which the classical scattering angle of a trajectory with angular momentum ℓ can be read for 100 MeV $^{18}O + ^{120}Sn$. The back scattering for small ℓ is caused by the repulsive Coulomb core which at this energy is not surmounted. The singularity occurs at the critical angular momentum ℓ_c. The three regions I, II, and III correspond to orbits which i) turn away from the nucleus, ii) turn partly around the edge of iii) plunge through the surface into the interior.

partial waves in the vicinity of $\ell = 60$ the Coulomb and nuclear contributions are in opposite quadrants. This leads to their approximate cancellation indicated in the first column of the figure by the sharp minimum in the amplitude of S, and the twist in S itself.

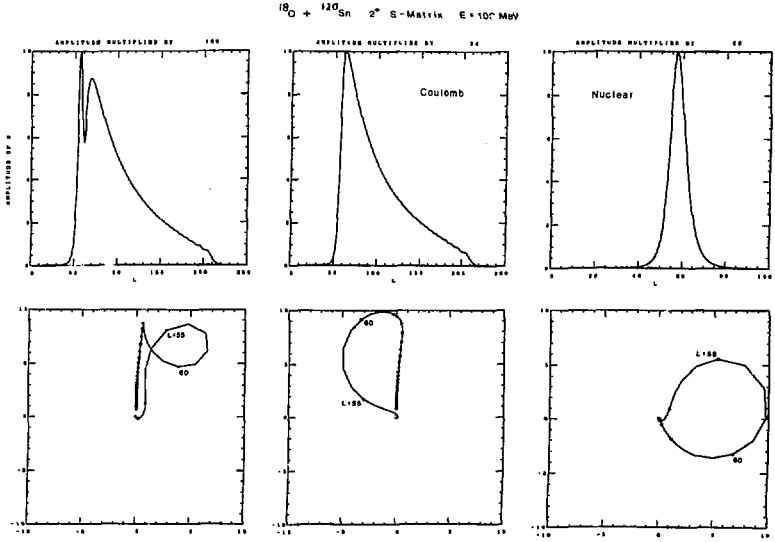

Fig. 2. For inelastic scattering to the collective 2^+ state the amplitude of the S-matrix are shown for the complete process and for pure nuclear and pure Coulomb excitation. Below, the S-matrices themselves are plotted in the complex plane as points, which are joined. Dots mark intervals of 5 units. The vector sum of the nuclear and Coulomb parts at corresponding ℓ yield (to lowest order) the complete S. The points corresponding to ℓ = 55 and 60 are marked and the others can be located by counting. Note that the ℓ-scale for the nuclear S amplitude is expanded. In the first part of the figure, it is the spike at $\ell \sim 57$. Also note the slow convergence of high ℓ as revealed by the density of points and their slow approach to the origin. (XBL 745-902)

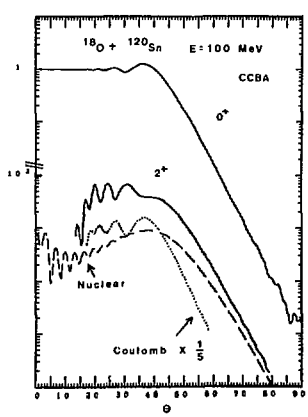

The corresponding cross sections for the separate contributions and combined Coulomb and Nuclear excitation are shown in Fig. 3, where the elastic and inelastic cross sections are seen to be out of phase in the region of angles less than the grazing one, as discussed above. Of course the uncertainty relationship existing between ℓ and θ does not permit the location in angle of the impulse cancellation with any precision because of the narrowness of the minimum in S (Fig. 2). It is manifest in an overall reduction of the cross section in a broad θ region as compared to pure Coulomb excitation.

Fig. 3. The phase relation between elastic and inelastic cross sections can be seen. Pure nuclear and Coulomb excitation cross sections for the 2^+ state are also shown. (Cross sections are in mb/sr.) (XBL 756-1559)

References

1. R. A. Malfleet, S. Landdowne, and V. Rostokin, Phys. Letters 44B, 238 (1973).

2. R. Videbalk, I. Chernov, P. R. Christensen, and E. E. Gross, Phys. Rev. Letters 28, 1072 (1973).

QUANTAL ANALOG OF THE CLASSICAL DEFLECTION FUNCTION FOR HEAVY ION COLLISIONS

N. K. Glendenning

A fascinating aspect of heavy ion reactions that has been discussed at length is the usefulness of classical ideas in understanding the quantum mechanical description of the reaction and in some cases the relationship of the physical assumptions made in a quantum calculation and the cross section details. Not only this, but classical physics can sometimes be used to suggest what kind of experiments need to be performed to settle specific questions.[1]

An essential part of the classical description is the deflection function, which is a plot of the scattering angle in a collision as a function of the impact parameter, or equivalently the angular momentum of the relative motion. A recent paper has questioned the relevance of this classical quantity in interpreting heavy ion reactions, and has shown examples where the classical deflection function and its quantal analog do not correspond very closely. This would be disappointing development if it were generally, or unqualifiedly true. It is our aim here to investigate the question in detail.

We first define what is meant by the quantal analogue of the deflection function. The scattering amplitude for any (non-elastic) process contains, aside from geometrical factors, a sum over

$$e^{i(\sigma_\ell + \sigma_{\ell'})} S_{\ell',\ell} Y_\ell^m(\theta,\phi)$$

where σ_ℓ and $\sigma_{\ell'}$ are Coulomb phase shifts for the incident and exit channels and $S_{\ell',\ell}$ is the S matrix, the amplitude in the exit channel ℓ' per unt incident flux in the incident channel ℓ. We define the amplitude and phase of S by

$$S_{\ell',\ell} = \eta_{\ell',\ell} \exp(2i\delta_{\ell',\ell}).$$

By replacing the spherical harmonic by its assymptotic expression valid for large ℓ, one finds that the above product involves

$$\eta_{\ell',\ell} [\exp(i\phi^+_{\ell',\ell}) + \exp(i\phi^-_{\ell',\ell})].$$

where

$$\phi^\pm_{\ell',\ell} = 2\theta - \frac{\pi}{4}(2\delta_{\ell',\ell} + \sigma_\ell + \sigma_{\ell'}).$$

For large ℓ the exponentials are rapidly oscillating functions of θ. The main contribution to the sum of which the above is a term (aside from other factors irrelevant to our argument) therefore comes about when the phase is stationary; i.e.,

$$\frac{d}{d\ell}\phi^\pm_{\ell',\ell} = 0.$$

This gives us

$$\theta = \frac{d}{d\ell}(2\delta_{\ell',\ell} + \sigma_\ell + \sigma_{\ell'})$$

which we refer to the quantal analogue of the deflection function. It is understood to be a function of ℓ.

Harney et al.[2] compared the above analogue computed for elastic scattering from a complex potential with the classical deflection function computed from the real part of the potential. Such a comparison is made in Fig. 1 for two different absorption strengths the potential 1 of Table 1. Indeed one sees that there is very little resemblance. If however instead of making the comparison for the quantum elastic scattering, it is made for some other quasi-elastic process such as two-neutron transfer, then one finds as in Fig. 2 a greater similarity when the absorption is not too strong. The reason why the disagreement in the elastic channel is so pronounced is clear. The quantum elastic channel has in it the shadow scattering arising from the black sphere caused by the absorbing complex potential. It is only by going to non-elastic channels that we can avoid this highly non-classical deflection functions resemble each other. The resemblance is in some case more pronounced than in others. If the absorption is too strong, there is little resemblance. Otherwise only in the region of the critical angular momentum does the quantum result differ from the classical. In particular the rainbow angle is preserved, as is the shoulder above the critical angular momentum. Interestingly, in connection with the predictions made in "Two-Nucleon

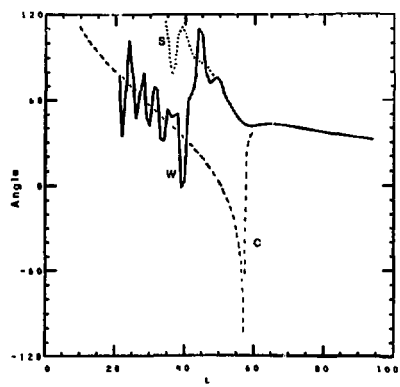

Fig. 1. For the elastic channel in $^{18}O+^{120}Sn$ at E = 100 MeV the quantal deflection functions for a weak (W) and strong (S) absorbing potential is compared with the classical result (C). (XBL 753-681)

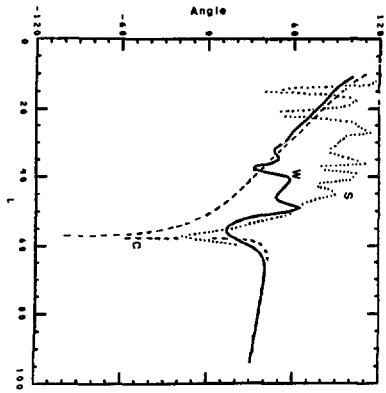

Fig. 2. For the two nucleon transfer channel $^{18}O_{0^+} + ^{120}Sn \rightarrow ^{16}O_{0^+} + ^{122}Sn$ (2^+) the quantal deflections functions for a weak (W) and strong (S) absorbing potential are compared with the classical result (C) at E = 100 MeV. (XBL 753-683)

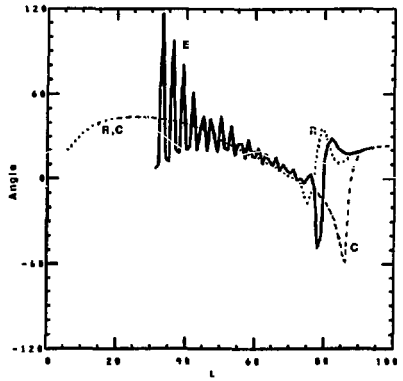

Fig. 3. For E = 160 MeV the quantal deflection functions in the elastic (E) and two nucleon transfer channel (R) referred to in Fig. 2 are compared for weak absorption with the classical result (C). (XBL 753-685)

Transfer Between Heavy Ions, Deep Orbits and Secondary Peaks," we compare the quantum and classical deflection functions at E = 160 MeV in Fig. 3. In the region of the critical angular momentum the correspondence is poor, but for the reaction, the quantal deflection function traces the classical function very accurately in the regions where it is flat. These are precisely the important regions since they yield relatively large contributions to the cross section.

We conclude that the classical deflection function provides quite an accurate picture of its quantal analogue in the regions where it is of greatest interest, namely the flat regions corresponding to large cross section. Therefore we can continue to take advantage of this as a device both for understanding as well as predicting phenomena in heavy ion collisions.[1]

References

1. N. K. Glendenning, International Conference on Reactions Between Complex Nuclei, Nashville (North Holland) p. 137 (1974).

2. H. L. Harney, P. Brown-Munzinger, and C. K. Gelbke, Z. Physik 269, 339 (1974).

A SEPARABLE EXPANSION FOR THE NUCLEAR FORM FACTORS

M. A. Nagarajan and W. L. Wang

We discuss a technique to obtain a separable expansion for the nuclear form factors. The form factors $F(\vec{k}',\vec{k})$ for a local density $\rho(\vec{r})$ is generally a function of the momentum transfer $\vec{q} = \vec{k}' - \vec{k}$, where $\vec{k}'$ and $\vec{k}$ are two momenta:

$$F(\vec{q}) = \int e^{-i(\vec{k}'-\vec{k})\cdot\vec{r}} \rho(\vec{r}) d\vec{r} \, . \qquad (1)$$

We shall show that a good approximation may be devised to represent such a form factor in terms of products of functions depending on $\vec{k}$ and $\vec{k}'$ separately.

For density distribution of interest, we may write

$$\rho(\vec{r}) = \rho_0(r) + \sum_I \rho_I(r) \, Y^*_{I0}(\hat{r}), \qquad (2)$$

where $\rho_0(r)$ is the spherical density and $\rho_I(r)$ are the multiple density distributions of order I. The form factors for $\rho(\vec{r})$ of Eq. (2) may be written as

$$F(\vec{q}) = \sum_{\substack{\ell,\ell' \\ m,m' \\ I,M}} C(\ell,\ell',m,m',I,M)\ \lambda_I^{\ell\ell'}(k,k')\ Y_{\ell m}(\hat{k}) \times Y^*_{\ell' m'}(k'), \qquad (3)$$

where we have lumped all the angular momentum coefficients in the factor C; $\lambda_I^{\ell\ell'}(k,k')$ is defined as

$$\lambda_I^{\ell\ell'}(k,k') = \int_0^\infty j_\ell(kr) j_{\ell'}(k'r) \rho_I(r) r^2 dr, \qquad (4)$$

where $j_\ell(x)$ are the spherical Bessel functions of order ℓ.

We observe that the integral in Eq. (4) may be cut off at some radius, say R, where the radial density becomes negligibly small. Within such a finite domain, i.e., $r \leq R$, we introduce the Fourier-Bessel expansion for $j_\ell(kr)$[1]

$$j_\ell(kr) = \sum_{n=1}^{N} A_n^\ell(k) j_\ell(\alpha_n^\ell r) \qquad \text{for } 0 \leq r \leq R, \qquad (5)$$

where $\alpha_n^\ell R$ is the n-th zero of the spherical Bessel function of order ℓ. The expansion coefficients $A_n^\ell(k)$ may be obtained in an analytic form. Using Eq. (5), we find the following separable form for $\lambda_I^{\ell\ell'}(k,k')$:

$$\lambda_I^{\ell\ell'}(k,k') = \sum_{\substack{m=1 \\ n=1}}^{M} A_n^\ell(k) A_m^{\ell'}(k') K_I(\alpha_n^\ell, \alpha_m^{\ell'}), \qquad (6)$$

where

$$K_I(\alpha_n^\ell, \alpha_m^{\ell'}) = \int_0^R j_\ell(\alpha_n^\ell r) j_{\ell'}(\alpha_m^{\ell'} r) \rho_I(r) r^2 dr. \qquad (7)$$

Equations (6) and (7) give us the desired separable representation for the nuclear form factor.

We now compare our results obtained with a finite number of terms in Eq. (6) to the exact results from Eq. (4). The convergence is generally quite good. We find it convenient to tabulate our results for two values of k and k'. The results are shown in Tables 1 and 2 for two typical nuclear density distributions. More detailed numerical studies are given in Ref. 2.

Table 1. The values of $\lambda_I^{\ell\ell'}(k,k')$ for I = 0-4. The nuclear density distribution is the Woods-Saxon form. The radius r is taken to be 4 fm and the diffuseness a = 0.6 fm. N is the order of expansion used in Eq. (5). The values given are calculated from Eq. (6) for N = M = 6, 10, and 14. The exact values are obtained by numerical integration in Eq. (4). In this Table, k = 1.0 fm^{-1} and k' = 1.0 fm^{-1}.

ℓ	N=6	N=10	N=14	Exact
0	0.07493	0.07493	0.07493	0.07492
1	0.07318	0.07306	0.07301	0.07300
2	0.05814	0.05813	0.05812	0.05811
3	0.03235	0.03230	0.03229	0.03228
4	0.01295	0.01281	0.01277	0.01276

Table 2. The values of $\lambda_{I=2}^{\ell\ell'}(k,k')$ for k = 0.5 fm^{-1} and k' = 1.5 fm^{-1}, for I = 2 (Quadrupole) derivative Woods-Saxon density with r_o = 4 fm and a = 0.6 fm. The density is not normalized, but is taken to be $\rho_{I=2}(r) = (r_o/\rho_o)\frac{d\rho_o(r)}{dr}$. The values of N are the order of expansion in Eq. (7) with M = N. The exact values are obtained from Eq. (4).

ℓ	ℓ'	N = 6	N = 10	N = 14	Exact
0	2	0.1999	0.19999	0.1998	0.1995
	1	-1.842	-1.857	-1.859	-1.853
1	3	1.537	1.531	1.531	1.526
	0	0.3552	0.3761	0.3756	0.3738
2	2	-0.7736	-0.7919	-0.7921	-0.7888
	4	1.513	1.514	1.513	1.505
	1	-0.2331	-0.2268	-0.2265	-0.2220
3	3	0.01569	0.01116	0.01148	0.009036
	5	0.6825	0.6822	0.6820	0.6809
	2	-0.1071	-0.1069	-0.1068	-1059
4	4	0.1072	0.1064	0.1064	0.1050
	3	-0.01179	-0.01200	-0.01204	-0.01243
5	5	0.04218	0.04195	0.04193	0.04182

References

1. M. Abramowitz and I. A. Stegun, Handbook of Mathematical Functions, National Bureau of Standards Publication (1970).

2. M. A. Nagarajan and W. L. Wang, Phys. Rev. C10, 2206 (1974).

COUPLED-CHANNEL PION-NUCLEUS CHARGE EXCHANGE REACTIONS

M. A. Nagarajan and W. L. Wang

In this report, we discuss a coupled-channel approach to pion-nucleus charge-exchange reactions near the (3,3) resonance region. These processes are of particular interest because they are dominated by the Δ(1231) isobar formation in the nucleus. In the distorted wave Born approximation (DWBA), the effects of the (3,3) resonance on the single and double charge exchange reactions have been studied in detail.[1] Within similar approximations, we show that the channel coupling effects may also be treated without much complication. The simplifying hypotheses are quite similar to these used in the isobar-doorway model,[2] which was used in the DWBA calculation of Ref. 1.

We first discuss a coupled-channel formalism using the concept of isobar-doorway states in the elastic and charge exchange channels. We use an adiabatic approximation to simplify our coupled equations, and obtain a formal expression of the T-matrix in terms of a resonant and a nonresonant contributions. We then explicitly introduce the approximations of the isobar-doorway model and obtain solutions of the coupled-channel equations algebraically in a closed form. The resonant couplings may be treated exactly by an N-point integration, or approximately by introducing a separable expansion of the particle wave nuclear form factors.[3]

It is of interest to study the effects of the channel couplings on the elastic and charge exchange scattering by comparing the result of the present formulation with the DWBA as proposed in Ref. 1. We should note, however, that the coupled-channel formalism here depends on the "exact resonance" approximation. Otherwise, the two formalisms are identical. We may diminish the uncertainty due to the exact resonance approximation by applying the theory to larger nuclei, and study the true channel-coupling effects.

References

1. M. A. Nagarajan and W. L. Wang, Lawrence Berkeley Laboratory Report LBL-2934 (1974); Phys. Rev. C10, 2125 (1974).

2. L. S. Kisslinger and W. L. Wang, Phys. Rev. Letters 30, 1071 (1973).

3. M. A. Nagarajan and W. L. Wang, LBL-2986; Phys. Rev. C10, 2206 (1974).

HEAVY ION INDUCED TRANSFER REACTIONS LEADING TO WEAKLY BOUND FINAL STATES

M. A. Nagarajan

The theory of nucleon transfer leading to unbound states in light ion induced reactions has been formulated by Huby et al.,[1] and by others.[2] The method that has been used is either to describe the unbound state as a quasibound state or, if the unbound state is in the vicinity of a resonance, to describe it as a Gamow state. Both of the methods lead to an expression for the transition amplitude which resembles the one for transfer to bound states. In light ion reactions, one further assumes a zero range approximation which simplifies the evaluation of the cross-section considerably.

In the case of heavy ion induced transfer reactions, the zero range approximation is not applicable. One thus has to face the problem of evaluating ingegrals which are two dimensional. In the early application of the distorted wave Born approximation (D.W.B.A.) to heavy ion induced reactions, Buttle and Goldfarb[3] invoked a "no-recoil" approximation, which involves eliminating all terms of the order of the ratio of masses of the transferred nucleon to either of the cores. This approximation allows one to evaluate the two dimensional integral in two parts, firstly, the evaluation of the form factor and secondly the evaluation of the distorted wave integral. The no-recoil approximation was equivalent to assuming the transfer of the nucleon to occur when the two nuclei were at rest relative to one another. Recently the problem of neutron transfer to unbound states has been studied by Baur and Trautman,[4] who explicitly calculated the features of Sub Coulomb transfer. During recent years, experiments[5] have indicated the nonadequacy of the no-recoil approximation, and approximate[6] and exact[7] calculations of recoil corrections have been made. These calculations exhibit the importance of the translational motion of the transferred nucleon.

In the present note, we wish to extend the theory of transfer to weakly bound final states incorporating the finite range and the recoil effects.

For the sake of simplicity, we shall use the notation of Buttle and Goldfarb [3] and represent the reaction as

$$\underbrace{(c_1+n)}_{a_1} + c_2 \rightarrow \underbrace{(c_2+n)}_{a_2} + c_1 .$$

The co-ordinate system will be identical to that of ref. 3. The DWBA transition amplitude of the transfer is given by

$$T_{fi}(\vec{k}_f,\vec{k}_i) = \langle \psi_{a_2\alpha_2}(\xi_1 n)\Phi_{c_1\gamma_1}(\xi)\chi^{(-)}(\vec{k}_f,\vec{r}_f)|V_{c_1 n}(r_1)|\chi^{(+)}(k_i,r_i)\Phi_{c_2\gamma}(\xi)\psi_{a_1\alpha_1}(\xi_1 n)\rangle .$$

One can integrate over the internal co-ordinates of the cores introducing the spectroscopic factors as follows:

$$\langle \psi_{a_2\alpha_2}(\xi_1 n)|\Phi_{c_2\gamma_2}(\xi)\rangle \equiv \int d\xi \psi^*_{a_2\alpha_2}(\xi_1 n)\Phi_{c_2\gamma_2}(\xi)$$

$$= \theta^{1/2}_{j_2\ell_2} \sum_{\lambda_2\sigma_2} \langle c_2\gamma_2 j_2\varsigma_2|a_2\alpha_2\rangle \langle \ell_2\lambda_2 s_2\sigma_2|j_2\varsigma_2\rangle \times U_\ell(r_2)\, Y_{\ell_2\lambda_2}{}^*(\hat{r}_2)\, \chi^+_{s_2\sigma_2}(s) \qquad (2)$$

and a similar expression for the parentage expansion of the projectile wave function $\psi_{a_1\alpha_1}(\xi_1 n)$. In Eq. (2), the function $\chi_{s_2\sigma_2}(s)$ is the spin wave function of the nucleon in the residual nucleus, and $\theta^{1/2}_{j_2\ell_2}$ is the spectroscopic factor. The transition amplitude becomes

$$T_{fi}(\vec{k}_f,\vec{k}_i) = \theta^{1/2}_{j_1\ell_1}\theta^{1/2}_{j_2\ell_2} \sum_{\substack{\lambda_1\lambda_2 \\ LM}} (-)^{\ell_1-s-\varsigma_1} \frac{\hat{j}_1\hat{j}_2}{s\,\ell} U(\ell_2 j_1 \ell_2 j_2; SL)$$

$$\times \langle j_1 -\varsigma_1 j_2 \varsigma_2 | LM\rangle \langle \ell_1\lambda_1 LM|\ell_2\lambda_2\rangle$$

$$\times \langle c_1\gamma_1 j_1\varsigma_1|a_1\alpha_1\rangle \langle c_2\gamma_2 j_2\varsigma_2|a_2\alpha_2\rangle \qquad (3)$$

$$\times \int d^3r_1 \int d^3r_2\, \chi^{(-)*}(\vec{k}_f,\vec{r}_f) U_\ell(r_2)$$

$$\times\ Y_{\ell_2\lambda_2}{}^*(\hat{r}_2) V(r_1) U_{\ell_1}(r_1)$$

$$\times\ Y_{\ell_1\lambda_1}(r_1)\, \chi^{(+)}(\vec{k}_i,\vec{r}_i) .$$

To derive Eq. (3), we have assumed that the interaction $V(r_1)$ is spin independent.

If the nucleon is very weakly bound in the residual nucleus, one would expect that, in view of the strong absorption in the elastic channels, the transfer would occur in the asymptotic region of the nucleon wave function in the final nucleus. One could therefore approximate the function $U_{\ell_2}(r_2)$ by a spherical Hankel function, i.e.,

$$U_{\ell_2}(r_2) \simeq N_{\ell_2} h^{(1)*}_{\ell_2}(ix_2 r_2) \qquad (4)$$

where the decay constant X_2 is defined by

$$\frac{h^2 x_2^2}{2m} = \varepsilon_2 \qquad (5)$$

ε_2 being the separation energy. One can use the addition theorem

$$h^{(1)*}_{\ell}(ix_2 r_2)\, Y_{\ell_2\lambda_2}{}^*(\hat{r}_2)$$

$$= \sqrt{4\pi} \sum_{\substack{\ell\lambda \\ \ell'\lambda'}} i^{\ell'-\ell-\ell_2} \frac{\hat{\ell}\,\hat{\ell}_2}{\hat{\ell}_1} \langle \ell\lambda\ell_2\lambda_2|\ell'\lambda'\rangle \times \langle \ell 0 \ell_2|\ell' 0\rangle\, j^*_{\ell'}(ix_2 r_1) \times\ Y_{\ell'\lambda'}{}^*(\hat{r}_1) h^{(1)*}_{\ell}(ix_2 r) Y_{\ell\lambda}(\hat{r}) . \qquad (6)$$

We now define what we refer to as weak binding. The integration over the r_1 is restricted by the range of the interaction $V(r_1)$. One would expect it to be of order of the radius of the projectile. We use the criterion

$$x_2 R_1 < 1, \qquad (7)$$

where R_1 is the radius of the projectile, to define weak binding. If Eq. (7) is satisfied, one can verify that in Eq. (8), the spherical Bessel functions satisfy the condition

$$j^*_{\ell'}(ix_2 r_1) \simeq \delta_{\ell' 0} . \qquad (8)$$

$$h^{(1)*}_{\ell_2}(ix_2 r_2) Y_{\ell_2 r_2}{}^*(\hat{r}_2) = (-)^{\ell_2} h^{(1)*}_{\ell_2}(ix_2 r) Y_{\ell_2\lambda_2}{}^*(\hat{r}) . \qquad (9)$$

Equation (9) implies that under the weak binding condition, Eq. (7), the wave function of the nucleon in the final nucleus has no component in the

direction of r_1, and that in the no-recoil approximation the transfer amplitude would identically vanish or be extremely small.* This is a particular case where the reaction proceeds entirely through the effect of recoil.

At high energies, where one could expect the diffraction model to be valid, the integrals considerably simplify. We use the model of Dodd and Greider[8] for simplicity. The elastic scattering wave function is described by

$$\chi^{(+)}(\vec{k}_i,\vec{r}_i) = \exp(i\vec{k}_i,\vec{r}_i)\ \theta(r_i). \tag{10}$$

Where $\theta(r_i)$ vanishes in the region of overlap of the ions and in the shadow region. With the use of Eqs. (9) and (10) the integral in Eq. (3) becomes

$$(-)^{\ell_2} N_{\ell_2} \int \hat{dr}_1\, e^{-i\vec{k}_R\cdot\vec{r}_1}\, V(r_1)\, U_{\ell_1}(r_1) \times \int d\vec{r}\, e^{i\vec{q}\cdot\vec{r}}\, h^{(1)*}_{\ell_2}(i\chi_2 r) Y^{*}_{\ell_2\lambda_2}(\hat{r})\ \theta(r). \tag{11}$$

Where

$$\vec{q} = \vec{k}_i - \frac{M_{c_2}}{M_{a_2}}\vec{k}_f \tag{12a}$$

and

$$\vec{k}_R = m\left(\frac{\vec{k}_i}{M_{a_1}} + \frac{\vec{k}_f}{M_{a_2}}\right). \tag{12b}$$

It can be verified that $\vec{k}_R$ is the recoil momentum, and the first integral in Eq. (11) is the Fourier transform of the product of the potential and the projectile wave function. The differential cross section becomes

$$\frac{d\sigma}{d\Omega} = \frac{\mu_i\mu_t}{(2\pi\hbar^2)^2}\frac{k_t}{k_i}\frac{(2a_1+1)}{(2c_2+1)} \times \frac{(4\pi)}{(2S+1)(2\ell_2+1)} \times \theta_{\ell_1 j_1 \theta_{\ell_2 j_2}} (N_{\ell_2})^2\, |G_{\ell_1}(k_R)|^2 \sum_{\lambda_2} |\beta_{\ell_2\lambda_2}|^2. \tag{13}$$

Where

$$G_{\ell_1}(k_R) = \int_0^\infty r_1^2 dr_1 j_{\ell_1}(k_R r_1)\, V(r_1)\, U_{\ell_1}(r_1) \tag{14a}$$

and

$$\beta_{\ell_2\lambda_2} = \int d^3r\, e^{i\vec{q}\cdot\vec{r}} h^{(1)*}_{\ell_2}(i\chi_2 r) Y_{\ell_2\lambda_2}(\hat{r})\ \theta(r). \tag{14b}$$

Equation (13) is valid for transfer of particles with intrinsic spin of 1/2 or 0. The factorization of the cross-section into the two terms $G_{\ell_1}(k_R)$ and $\beta_{\ell_2\lambda_2}$ is characteristic of a reaction of the type (p,2p). If the final binding energy is small, the final channel behaves like a three body channel and the result in Eq. (13) is not surprising.

The above treatment can also be applied to reactions where the transferred particle is in a resonant state in the final system. An example of this type would be one where one the two ions in the final system is ^{8}Be, which is composed of two alpha particles in a s-wave resonance at about 90 keV above the threshold. The wave function of the particle will then be of the form

$$U_{\ell_2}(r_2) = N_{\ell_2}\frac{\sin(k_2 r_2 + \delta)}{k_2 r_2} \tag{15}$$

which satisfies an addition theorem similar to Eq. (6), and the final result would be identical.

In order to obtain the simple result of Eq. (13), we had ignored the dependence of the distorted wave integral, $\beta_{\ell_2\lambda_2}$ on χ_2. If the transfer process is assumed to be peripheral, the distorted wave integral is dependent upon χ_2 approximately as $1/(\chi_2 R)^{\ell+1}$ where ℓ is the angular momentum transfer and R is the sum of radii of the ions. The dependence of the nuclear overlap integral on χ_2 on the other hand can be approximated as $(\chi_2 R_1)^{\ell'}$. Hence, the contribution from the higher order term will be of the order of R_1/R of the leading term calculated in Eq. (11). If the target is heavy in comparison with the projectile, the ratio R_1/R is likely to be small. The feature of factorization of the differential cross section expressed by Eq. (13) would result if the masses of the projectile and target are very different and if the Q of the reaction is close to the optimum value. The latter condition is necessary if one assumes the reaction to be peripheral.

Footnote and References

1. R. Huby and J. R. Mines, Rev. Mod. Phys. 37,406 (1965); R. Huby, Nucl. Phys. A138, 442 (1969); R. Huby, Phys. Letters 33B, 323 (1970); B. J. Cole, R. Huby, and J. R. Mines, Phys. Letters 33B, 320 (1970).

2. C. M. Vincent, Phys. Rev. 175, 1309 (1968); T. Berggren, Nucl. Phys. A109, 265 (1968); J. Bang and J. Zimanyi, Nucl. Phys. A139, 534 (1969).

3. P. J. A. Buttle and L. J. B. Goldfarb, Nucl. Phys. 78, 409 (1966).

4. G. Baur and D. Trautmann, Nucl-Phys. A211, 333 (1973).

5. D. G. Kovar et al., Phys. Rev. Lett. 29, 1023 (1972); 30, 1075 (1973).

6. D. M. Brink, Phys. Lett. 40B, 37 (1972); M. A. Nagarajan, Nucl. Phys. A196, 34 (1972); A209, 485 (1973); A. J. Baltz and S. Kahana, (to be published).

7. R. Bock and H. Yoshida, Nucl. Phys. A189, 177 (1972).

8. L. R. Dodd and K. R. Greider, Phys. Rev. 180, 1187 (1969).

PION-NUCLEUS CHARGE EXCHANGE REACTIONS IN THE ISOBAR-DOORWAY MODEL

M. A. Nagarajan and W. L. Wang

In this work, we discuss the application of the isobar-doorway model[1] to the charge exchange reactions. It is appropriate to recall the main ideas of the model. One separates the pion-nucleon interaction into a resonant and a nonresonant part. One assumes that the resonant part of the interaction creates an isobar compound state, i.e., a nucleon hole and a Δ particle in the target. One further assumes that the scattering and reaction phenomena are largely determined by the detailed properties of the isobar is formed in the elastic channel and then decays into both elastic and inelastic channels. The doorway state picture emerges if one assumes that the coupling between the elastic and inelastic channels is solely through the isobar compound state.

The formalism we present in the following section will be applicable to elastic (leading to the ground state of the final nucleus) as well as inelastic charge exchange reactions, leading to quasi-bound excited states of the final nucleus. Breakup of the final nucleus is considered only through a parameterization of the omitted channels. The formalism is within the spirit of the usual DWBA calculations where the initial and the final states wave functions are assumed to be determined from the elastic scattering experiments in the respective channels. In our model, we obtain such elastic scattering wave functions from the isobar-doorway model.

For SCX (Single Charge Exchange) reaction, we consider the following process:

$$\pi_1 + A_1 \longrightarrow \pi_2 + A_2 \qquad (1)$$

where 1 and 2 denote the initial and final charge states of the pions. The incident channel has a π_1 (π^+ or π^-) interacting with the target nucleus A_1; the outgoing channel has a π_2 (generally π^0 for SCX reactions) with the residual nucleus A_2. The Hamiltonian of the system may be written as

$$H = H_0 + K_\pi + V \qquad (2)$$

where $H_0(r_1, r_2 \cdots r_A)$ is the baryon Hamiltonian with baryon coordinates $r_1, \cdots r_A$. The baryon Hamiltonian also describes the motion of the excited state of the nucleon (i.e., isobar). We allow at most one isobar in the system. In Eq. (2), the pion kinetic energy operator is K_π and the π-nucleus interaction is V. This π-nucleus interaction V describes the elastic scattering as well as the charge exchange process, along with all other reactions. We may separate this interaction into two parts:

$$V = V_0 + V_R \qquad (3)$$

where the non-resonant interaction V_0 contains operators of the following form

$$V_0 = f_{\pi N}\, a_\pi^+ a_N^+ a_N a_\pi \qquad (4)$$

with $f_{\pi N}$ as the strength of the interaction (a_π^+ and a_N^+ are creation operators of a pion and a nucleon, respectively). The Coulomb interaction is included in V_0. The resonant interaction V_R has the following form

$$V_R = G_{\pi N\Delta}\, a_\Delta a_N^+ a_\pi^+ + \text{h. c} \qquad (5)$$

where $G_{\pi N\Delta}$ depends on the coupling strength and the quantum numbers of π, N and Δ. The nonresonant interaction contains the π-nucleon s-wave and T = 1/2 p-wave interactions. The resonant interaction is the T = 3/2 p-wave interaction.

To formulate our problem, it is useful to use the projection-operator techniques of Feshbach. We have two charge states in the P-space, so we separate the P-space into two parts: P_1 and P_2, which project onto the initial and the final nuclear states, respectively. We next define the Q-space operator, Q, which projects onto the isobar-doorway states $|\phi_{n\alpha}>$. We finally define the q-space operator, Q, which projects onto the rest of the Holbert space (the compound inelastic states). In order to exhibit the important dynamical effects of the isobar resonance, we choose to introduce a distorted wave Born approximation (DWBA) for the T-matrix. The DWBA SCX amplitude is defined as

$$T = < \chi_2^{(-)} | \mathcal{H}_{21} | \chi_1^{(+)} > ,$$

where the distorted wave functions $|\chi_1^{(\pm)}>$ are the

homogeneous solutions of

$$(E - \mathcal{H}_{ii})|\chi_i^{(\pm)}\rangle = 0 \qquad i = 1,2$$

where $\mathcal{H}_{ij} = P_i \mathcal{H} P_j$ and

$$\mathcal{H} = H + H(E - \tilde{H}_{QQ})^{-1} H,$$

with

$$\tilde{H}_{QQ} = H_{QQ} + H_{Qq}(E - H_{qq})^{-1} H_{qQ}.$$

Formally our results so far are rather similar to the (p,n) reactions. However, for the case of pion-nucleus charge exchange reactions, both the wave functions $|\chi^{(\pm)}\rangle$ and the interaction $\mathcal{H}_{21}$ have strong energy dependence due to the (3,3) resonance. The fact that the π-nucleus interaction is strong and resonating indicates important initial- and final-state interactions.

We shall not discuss the details of the formulation here. They may be found in Ref. 2. However, it is appropriate to summarize our results as follows.

We have extended the isobar-doorway model for pion-nucleus scattering to the charge exchange reactions. We have shown that energy dependence of the SCX and DCX reaction amplitude in DWBA may be conveniently separated from the parts which contain nuclear structure information. The energy dependence depends on the pion optical potential, or the self-energy effects in the nuclear medium; it is therefore shown to be closely related to the elastic scattering amplitude.

Within the model, the single and double charge exchange reactions may be treated on the same footing as the elastic scattering with common factors depending only on the energy and therefore may be consistently described by a simple parametrization from the energy dependence of the total cross sections. These factors may eventually be evaluated by a more detailed interaction model, such as a microscopic theory where the motion of the isobar is explicitly taken into account. The model we present is general enough to allow variations in the detailed assumptions of the pion-nucleon interaction in the medium.

The same procedure as described in this work may also be applied to separate the resonant and nonresonant components in an optical-model calculation. This separation of the optical potential, of course, is an extension of the usual DWBA calculation; for the case of pion-nucleus scattering, this approach may be useful in order to gain more insight into the roles of the (3,3) resonance in the optical potential. However, this type of optical-model approach will be formally equivalent to our formulation if the optical-model wave functions used are obtained from formally exact optical potentials, since our wave function formally contain all orders of multiple scattering.

Finally, we would like to point out that our model has the distinctive feature of displaying explicitly the roles of the (3,3) resonance in the reaction dynamics, including the initial and final state interactions. The effect of the nonresonant background interactions is also properly retained in the formalism.

References

1. L. S. Kisslinger and W. L. Wang, Phys. Rev. Letters 30, 1071 (1973).

2. M. A. Nagarajan and W. L. Wang, Phys. Rev. C10, 2125 (1974).

FACTORIZATION IN RELATIVISTIC HEAVY-ION SCATTERING

W. L. Wang

We have calculated the total cross sections for relativistic nucleus-nucleus scattering in the Glauber theory and conclude that there will be no factorization, due to the short-range nature of nucleon-nucleon interaction as compared to the sizes of the colliding nuclei. In the optical limit, the elastic scattering amplitude $F_{AB}(\vec{q})$ is given as,[1]

$$F_{AB}(\vec{q}) = \frac{ik}{2\pi} \int d^2\vec{b}\, \exp(i\vec{q}\cdot\vec{b}) \times \{1 - \exp(iv \int d^2\vec{b}' T_A(\vec{b}') T_A(\vec{b}-\vec{b}'))\} \tag{1}$$

where q is the momentum transfer and k is the incident momentum. The two-dimensional densities $T(\vec{b})$ are related to the nuclear density distribution $\rho(\vec{r})$ by

$$T_A(\vec{b}) \int_{-\infty}^{\infty} \rho_A(\vec{r} \equiv \vec{b} + \vec{z})\, dz, \tag{2}$$

where $\rho_A(\vec{r})$ is normalized to unity. The interaction parameter x is related to the nucleon-nucleon total cross section σ_{nn} by

$$x = \frac{(i+\alpha)}{2} AB\, \sigma_{nn}, \tag{3}$$

where A and B are the mass numbers of the colliding nuclei, α is the ratio of real to imaginary parts of the nucleon-nucleon elastic scattering amplitude. In our calculation we use $\sigma_{nn} = 44.5$ mb and $\alpha = -0.2$. The nuclear density distribution $\rho(\vec{r})$ is taken to have the spherical Woods-Saxon form.

For simplicity, we define the "factorizability" Γ_{AB} for A-B scattering as

$$\Gamma_{AB} = \frac{(\sigma_{AB})^2}{\sigma_{AA}\,\sigma_{BB}} \qquad (4)$$

where σ_{AB} is the total cross section for A-B scattering. We may obtain the total cross sections from $F_{AB}(\vec{q})$ of Eq, (1) through the optical theorem.

We now show our results of the total cross section as a function of the effective radius

$$R_{eff} = r_o(A^{1/3} + B^{1/3}) \qquad (5)$$

with $r_o = 1.25$ fm. From these results, it is clear that the Glauber theory gives qualitatively the same results as predicted by a simple black-sphere model.

In the case of the black-sphere model, the factorizability becomes

$$\Gamma_{AB} = \frac{(1 + \gamma_{AB})^4}{16\gamma_{AB}^2} \qquad (6)$$

where γ_{AB} is the ratio of the radii of the two nuclei

$$\gamma_{AB} = R_A/R_B \qquad (7)$$

We now show the results of σ_{AB} and Γ_{AB} from our numerical calculations (using Eqs. (1) and (4)) in Table 1, where we also list the factorizabilities as obtained from the black-sphere model, (6) and (7).

As concluding remarks, we would like to note that Eq. (1) is obtained with an explicit assumption that the range of nucleon-nucleon interaction (the interaction radius) is much smaller than the nuclear radius. This is the reason that the relative sizes of the colliding objects remain important and the scattering process is still determined by the geometrical properties of the objects. It is therefore clear that there will be no strict $\Gamma_{AB} = 1$ factorization in the nucleus-nucleus scattering as long as the sizes of the colliding objects remain much larger than the range of nucleon-nucleon interaction.

Table 1. Total Cross Section and Factorizability. Nucleus-nucleus total cross sections (fm^2) calculated in the optical model. The average nucleon-nucleon cross section $\bar{\sigma}_{nn} = 44.5$ mb and $\alpha = -0.2$ (see Eq. (3)). The nuclear density is of a Fermi distribution. The factorizability (the lower left table) is defined by Eq.(4). The values in the parentheses are from Eqs, (6) and (7).

B \ A	4	12	16	27	32	40	88	208
4	35.2	89	104	164	200	221	315	502
12	1.52 (1.29)	148	165	260	321	341	443	659
16	1.63 (1.41)	0.97 (1.01)	189	298	369	389	493	720
27	2.34 (1.80)	1.40 (1.08)	1.44 (1.04)	326	405	424	523	754
32	2.78 (2.03)	1.70 (1.14)	1.76 (1.08)	1.01 (1.01)	409	428	530	762
40	2.93 (2.21)	1.66 (1.18)	1.69 (1.11)	1.15 (1.02)	0.94 (1.001)	474	577	819
88	3.64 (2.98)	1.71 (1.40)	1.66 (1.28)	1.08 (1.10)	0.88 (1.05)	0.91 (1.03)	775	1051
208	5.18 (4.44)	2.12 (1.81)	1.98 (1.61)	1.26 (1.29)	1.03 (1.20)	1.02 (1.15)	1.03 (1.04)	1383

Reference

1. W. Czyż and L. C. Maximon, Ann. Phys. (N.Y.) 52, 59 (1969).

CHARGE TRANSFER IN HIGH-ENERGY ATOMIC COLLISIONS*

M. Kleber† and M. A. Nagarajan

Introduction

The theory of charge transfer in high-energy atomic collisions has remained an intriguing problem over a long period of time. Different methods have been used to predict electron transfer cross sections, but the success in explaining cross sections does not by itself constitute a criterion of the validity of a theory. In fact, Greider and Dodd[1] have pointed out that the DWBA is questionable *as a first approximation to rearrangement scattering.* In this note, we show that the conditions for the validity of DWBA are considerably relaxed in the high-energy limit.

The Formalism

In DWBA, the prior form of the transition amplitude is given by

$$T_{f_i} = \int d\vec{r}_a \, d\vec{r}_b \, \chi^{(-)*}_{\vec{k}_f}(\vec{r}_f) \, \psi_f^*(\vec{r}_b) \times V_i \, \psi_i(\vec{r}_a) \, \chi^{(+)}_{\vec{k}_i}(\vec{r}_i) \qquad (1)$$

In Eq. (1), $\vec{r}_a$ and $\vec{r}_b$ are respectively the coordinate vectors of the electron relative to the residual particle (target minus electron) and to the positive ion. $\psi_i(\vec{r}_a)$ and $\psi_f(\vec{r}_b)$ represent the bound states of the electron in its initial and final system. $\chi^{(+)}_{\vec{k}_i}(\vec{r}_i)$ and $\chi^{(-)}_{\vec{k}_f}(\vec{r}_f)$ describe the relative motion of the colliding particles in the initial and final states, $\vec{r}_i$ and $\vec{r}_f$ being the respective channel vectors. The Coulomb interaction between the positive ion and the residual particle (target minus electron) is explicitly utilized in constructing the distorted wave functions $\chi^{(+)}_{\vec{k}_i}(\vec{r}_i)$ and $\chi^{(-)}_{\vec{k}_f}(\vec{r}_f)$. The perturbation causing the transition is therefore

$$V_i = Z^{(f)}_{eff} \frac{e^2}{r_b} \qquad (2)$$

where $Z^{(f)}_{eff}$ is the effective charge of the positive ion, and V_i denotes the Coulomb interaction between the electron and the positive ion.

In momentum space, Eq. (1) reads

$$T_{f_i} = \int d\vec{p}_i \, d\vec{p}_f \, \psi^{(-)*}_{\vec{k}_f}(\vec{p}_i) \, \psi^{(+)}_{\vec{k}_i}(\vec{p}_i) \times \tilde{\phi}_f^*\left(\frac{M_2}{M_2+m}\vec{p}_f - \vec{p}_i\right) \phi_i\left(\vec{p}_f - \frac{M_1}{M_1+m}\vec{p}_i\right) \qquad (3)$$

M_1, M_2 and m refer to the masses of the target, the projectile and the electron respectively.

In the high-energy limit the momentum wave functions $\psi^{(+)}_{\vec{k}_i}(\vec{p}_i)$ and $\psi^{(-)}_{\vec{k}_f}(\vec{p}_f)$ are strongly peaked around $\vec{p}_i = \vec{k}_i$ and $\vec{p}_f = \vec{k}_f$, respectively. If at these values of the momenta the functions ϕ_i and ϕ_f are not zero, one may replace the variables $\vec{p}_i$ and $\vec{p}_f$ in ϕ_i and ϕ_f by the values $\vec{k}_i$ and $\vec{k}_f$. The resulting expression for the transition amplitude becomes

$$T_{f_i} = (2\pi)^3 \, \phi_i\left(\vec{k}_f - \frac{M_1}{M_1+m}\vec{k}_i\right) \tilde{\phi}_f^*\left(\frac{M_2}{M_2+m}\vec{k}_f - \vec{k}_i\right) \chi^{(-)*}_{\vec{k}_f}(\vec{r}=0) \, \chi^{(+)}_{\vec{k}_i}(\vec{r}=0). \qquad (4)$$

The assumption used in deriving Eq. (4) is that the momentum distribution of the bound states is much wider and more slowly varying than the spread of the scattering wave packets. If the bound state wave function has nodes, the peaking approximation becomes invalid in the vicinity of the nodes, but it should not affect the evaluation of the total cross section. In order to verify the nature of the spreading of the scattering wave packet, we used the representation of $\psi_{\vec{k}}(\vec{p})$ given by Bethe and Salpeter,[2] which is valid at high energies, and found that even after the subtraction of the delta function term, $\delta(\vec{k}-\vec{p})$, the remaining term is still very strongly peaked over $\vec{p} = \vec{k}$.

The transition amplitude, Eq. (4), depends upon the value of the scattering wave functions at $r = 0$. At $r = 0$, these functions are dominated by the Coulomb repulsion between target and projectile. At these distances, the effect of the electron-ion interaction is negligible, and the question of the best auxiliary potential, which according to Greider and Dodd[1] is important for the convergence of the DWBA, does not enter into Eq. (4).

Using the result that

$$\left| \chi^{(\pm)}_{\vec{k}}(\vec{r}=0) \right|^2 = \frac{2\pi\eta}{\exp(2\pi\eta)-1} \qquad (5)$$

where η is the Sommerfeld parameter

$$\eta = Z_i \, Z_f \frac{e^2}{\hbar v} \qquad (6)$$

with Z_i and Z_f representing the nuclear charges of the colliding particles and v their relative velocity, one obtains for the total cross section

$$\sigma = \sigma^{BK} \left[\frac{2\pi\eta}{\exp(2\pi\eta) - 1} \right]^2 \qquad (7)$$

where σ^{BK} is the Brinkman-Kramers cross section. The effect of screening on the estimate of the cross section was investigated in the case of proton-hydrogen atom collision. A screened Coulomb potential[3] of the form

$$U(\tau) = \exp(-\alpha r) \frac{e^2}{r} \left(1 + \frac{\alpha r}{2}\right) \qquad (8)$$

where α is twice the inverse Bohr radius, was used to calculate the scattering wave functions. It was found that at a proton energy of 100 keV, the cross section showed a 1% deviation from Eq. 7).

In the one-electron approximation, the average Brinkman-Kramers cross section for an electron capture from a hydrogen-like target from an initial state with principal quantum number n_i into an empty hydrogen-like shell of principal quantum number n_f is given by (McDowell and Coleman, page 379).[4]

$$\sigma^{BK} = \frac{2^{18}\pi\, k^8 \kappa_i^5 \kappa_f^5 n_f^2}{5[k^4 + 2k^2(\kappa_i^2 + \kappa_f^2) + (\kappa_i^2 - \kappa_f^2)^2]^5} \qquad (9)$$

where

$$k = mv/\hbar \qquad (10)$$

and

$$\kappa_a = \frac{mc^2}{\hbar c} \frac{Z_{eff}^{(a)} e^2}{\hbar c} \frac{1}{n_a} \quad ; \quad a = i,f.$$

Approximation (7) should remain valid as long as the electron cloud does not get deformed during the collision with the ion, i.e., if

$$\pi\eta \leq 1. \qquad (11)$$

Comparison With Experiment

The total cross section for electron capture at high energies is obtained by summing σ^{BK} in Eq. (9) over all values of n_f and by inserting the result in Eq. (7). For a proton incident on hydrogen, the condition $\pi\eta \leq 1$ means that (7) should be valid for proton energies exceeding 250 keV. In Figs. 1 and 2, the theoretical predictions are shown for the reaction

$$H^+ + H(1s) \longrightarrow \sum_{n,\ell} H(n\ell) + H^{+\cdot}$$

Also plotted are the experimental results for protons incident on H_2 multiplied by 0.5. It is, however, not obvious that the hydrogen molecule could be considered as equivalent to two independent hydrogen atoms. Tuan and Gerjuoy[9] showed that in the high-energy limit the ratio of charge transfer from atomic hydrogen to charge transfer from H_2 tends towards a value between 0.6 and 0.7. In spite of the scatter in the experimental points, we can see from the figures that a scaling factor between 0.6 and 0.7 will improve the agreement between the high-energy DWBA (7) and the measured capture cross sections.

In order to avoid the problem of scaling factors, we investigated the nonresonant electron capture in proton-helium collisions:

$$H^+ + He(1s^2) \longrightarrow \sum_{n,\ell} H(n\ell) + \sum_{n'\ell'} He^+(n'\ell').$$

In this reaction the high-energy approximation (7) should be valid for proton energies exceeding 1000

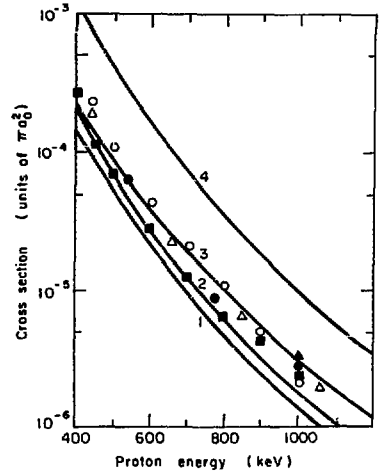

Fig. 1. Total cross sections for electron capture by protons from atomic hydrogen. Curve 1: Impulse approximation.[10] Curve 2: Continuum distorted wave method.[11] Curve 3: High-energy DWBA limit (Eq. (11)). Curve 4: Brinkman-Kramers approximation (Eq. (13)). Experimental results: ■ Ref. 12, △ Ref. 8, ▲ Ref. 13, ○ Williams 1967, ● Ref. 14. (XBL 757-3503)

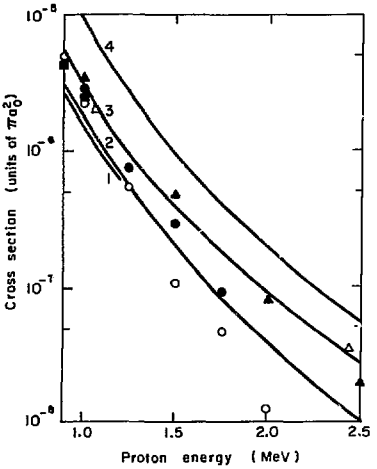

Fig. 2. Total cross sections for electron capture by protons from atomic hydrogen. Details as in Fig. 1. (XBL 757-3502)

keV. We note that the simultaneous transfer of one He electron and the Coulomb excitation of the remaining electron is not included in DWBA, but as a second-order process it should not be important at high impact energies. By comparison with correlated two-electron wave functions, Bransden and Sin Fai Lam[6] found that the single-electron wave function which belongs to $Z_{eff} = 1.6875$ is adequate for the calculation of electron capture in helium. We therefore used this effective charge to calculate the intrinsic momentum κ_i. The calculated cross sections are compared with the experimental cross sections in Table 1.

Table 1. Total cross sections σ^{BK} (Eq. (13)) and σ (Eq.(11)) for electron capture by protons from helium.

E	σ^{BK}	σ	σ(experiment)	Ref.
1.063	$11.3^{-5\dagger}$	1.22^{-5}	$(2.9\pm0.4)^{-5}$	8
2.45	11.8^{-7}	2.91^{-7}	$(3.2\pm0.4)^{-7}$	8
2.99	3.81^{-7}	1.08^{-7}	$(1.2\pm0.1)^{-7}$	8
5.41	12.4^{-9}	4.97^{-9}	$(5.4\pm0.6)^{-9}$	8
6.45	4.42^{-9}	1.93^{-9}	$(2\pm0.4)^{-8}$	9
10.5	2.52^{-10}	1.32^{-10}	$(1.2\pm0.4)^{-10}$	9

Proton energy E in MeV, cross sections in 10^{-16}cm^2.

†The superscript indicates the power of ten by which the number is to be multiplied.

Conclusion

The non-relativistic high-energy DWBA approximation reproduces very well the experimental situation in the energy ranges under consideration. This agreement is, of course, no proof for the reliability of the theory. Nevertheless, it should be realized that the DWBA capture rate in the case of 10.5 MeV protons on He is in accordance with the result of more advanced scattering methods as described by Begum et al.[7] The high-energy electron transfer is not only a test for the correctness of the scattering theory used in a calculation, but it simultaneously probes the asymptotic tail of the momentum distribution of the bound electron. Since Hartree-Fock calculations are not very sensitive to the asymptotic region of the electron momentum distribution, the reliability of theoretical capture cross sections for complex targets will be obscured at high energies.

Footnotes and References

*Abstracted from Journal of Physics B (Atomic and Molecular Physics).

†Physik-Department, Technische Universität München 8046 Garching, Germany.

1. K. R. Greider and L. R. Dodd, Phys. Rev. 146, 671-5 (1966).

2. H. A. Bethe and E. E. Salpeter, Encyclopedia of Physics, Vol. 35, (Springer, Berlin, 1957) p. 131.

3. J. D. Jackson, Classical Electrodynamics (Wiley, New York, 1962) p. 24.

4. M.R.C. McDowell and J. P. Coleman, Introduction to the Theory of Ion-Atom Collisions (North Holland, Amsterdam, 1970).

5. T. F. Tuan and E. Gerjuoy, Phys. Rev. 117, 756-63 (1960).

6. B. H. Bransden and L. T. Sin Fai Lam, Proc. Phys. Soc. 87, 653-5 (1966).

7. S. Begum, B. H. Bransden, and J. Coleman, J. Phys. B: Atom. Molec. Phys. 6, 837-840 (1973).

8. L. M. Welsch, K. H. Berkner, S. N. Kaplan, and R. V. Pyle, Phys. Rev. 158, 85-92 (1967).

9. K. H. Berkner, S. N. Kaplan, G. A. Paułika, and R. V. Pyle, Phys. Rev. 140, A729-31 (1965).

10. J. P. Coleman and M.R.C. McDowell, Proc. Phys. Soc. 85, 1097-108 (1965).

11. A. Salin, J. Phys. B: Atom. Molec. Phys. 3, 937-51 (1970).

12. C. F. Barnett and H. K. Reynold, Phys. Rev. 109, 355-9 (1958).

13. U. Schryber, Helv. Phys. Acta 40, 1023-51 (1968).

14. L. H. Toburen, M. Y. Nakai, and R. A. Langley, Phys. Rev. 171, 114-22 (1968).

THE NUCLEAR SEYLER-BLANCHARD MODEL IN THE HARTREE APPROXIMATION

J. Randrup*

Introduction

The nuclear model introduced by Seyler and Blanchard[1] in 1961 has proved a very useful tool for the study of macroscopic properties of nuclei. The model is based on a simple phenomenological two-nucleon interaction (often referred to as the Seyler-Blanchard interaction),

$$V_{12} = -\,Cg\left(\frac{r_{12}}{a}\right)\left(1 - p_{12}^2/b^2\right) \qquad g(r) = \frac{e^{-r}}{r}\,. \qquad (1)$$

Here r_{12} is the distance between the two interacting nuclei and $\vec{p}_{12} = \vec{p}_1 - \vec{p}_2$ their relative momentum. The spatial part of the Seyler-Blanchard interaction is a Yukawa function of range a. The interaction strength C depends on whether the two nucleons are 'like' (i.e., two neutrons or two protons) or 'unlike' (i.e., a neutron and a proton). In addition, the strength of the interaction depends on the relative momentum p_{12} of the two nucleons; it becomes weaker as p_{12} increases and for some value b (the 'saturation' momentum) it changes from attractive to repulsive.

The fact that one wishes to extract information about the *macroscopic* nuclear properties only, permits the use of relatively simple approximations for the treatment of the associated many-body problem. Up to now, the model has been studied almost exclusively within the Thomas-Fermi approximation. This approximation leads to a very simple description of the nuclear system.

The Seyler-Blanchard model, in its Thomas-Fermi formulation, has a wide range of applicability, and because of its great mathematical simplicity it is a very helpful tool for the study of macroscopic nuclear properties. It is obvious, however, that in the nuclear surface region, where the potential varies rapidly, the Thomas-Fermi approximation is rather crude as it neglects the phase correlations imposed by the surface as well as the penetration of particles into the classically forbidden region. Considering the great virtue of the model, it is valuable to clarify, in a quantitative way, how much a more proper treatment of the quantum-mechanics would affect the results.

We have studied the Seyler-Blanchard model within the Hartree approximation. At the same time the model is formulated in more general terms so that it applies also to the general situation of non-static systems. The Hartree approximation treats the quantum-mechanics in an exact way, within the restriction that the many-particle system be described by a product wave function. Like the Thomas-Fermi approximation, the Hartree approximation neglects effects associated with the correlation between individual particles, and it constitutes a natural basis for studying the macroscopic properties of a quantum system.

The development of the Seyler-Blanchard model in the Hartree approximation provides us with a possibility for determining the accuracy of the Thomas-Fermi approximation for nuclear matter. Moreover, it makes it possible to obtain more accurate values for the various macroscopic nuclear properties, as for example, those represented by the Droplet-Model coefficients.[2]

In addition to thus yielding a more detailed insight into the properties of isolated static nuclear systems, the development of the model presented here has importance for more general situations encountered, for example that of two colliding nuclei.

Quantization

The quantization of the Seyler-Blanchard interaction is rather straightforward, the only problem being associated with the proper quantum representation of the momentum-dependent part, p^2g Cr). The apparent ambiguity (whether to choose $\frac{1}{4}(p^2g+gp^2)$ or $\vec{p}g\vec{p}$ or some combination) may be eliminated after a closer analysis of the situation. The crucial point is the requirement that the resulting expression for the interaction-energy density continues the momentum distribution of the system only in terms of the total local momentum, which is the only measurable quantity. This requirement leads to the result that the momentum-dependent part of the Seyler-Blanchard interaction should be quantized as the average of the two alternatives mentioned above; this may be written $p^2g \to \frac{1}{4}\{\vec{p}, \{\vec{p},g\}\}$, where $\{a,b\} = \frac{1}{2}(ab-ba)$ is the anti-communicator.

We can not here go into further details of the Hartree formulas but we mention below some results for semi-infinite nuclear matter.

Density Profiles

For the parameter values specified in Ref. 2 we have calculated the self-consistent solution to the derived Hartree equations. In Fig. 1 we display the resulting matter density distribution $\rho(x)$. For comparison we also show the corresponding density distribution as obtained in the Thomas-Fermi approximation. The two densities are plotted such that their surface locations x_s coincide. The Hartree density exhibits two new features relative to the Thomas-Fermi density. One is the tail outside the system due to the finite depth of the nuclear potential. The other feature is the density ripples due to the phase correlations imposed by the presence of the surface.

We observe that the Thomas-Fermi density represents the average trend of the Hartree density quite well, being most markedly off in the tail region. The surface diffuseness, measured in terms of the 10-90% distance, increases by around 11% from 3.17a

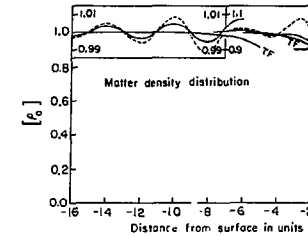

Fig. 1. Matter density distributions in units of the bulk density ρ_0. The smooth curve is the Thomas-Fermi result and the oscillating curve is the Hartree result. The dashed density corresponds to an infinite wall located such that the wiggles are in phase with the Hartree wiggles deep inside the system. The scale has been enlarged by a factor of ten for $x < -7a$ in order to exhibit the density wiggles. (XBL 749-4326)

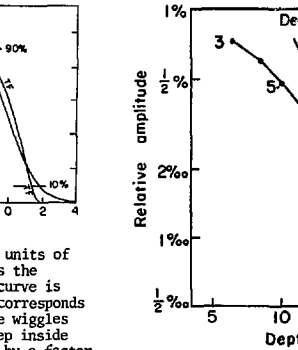

Fig. 2. Doubly logarithmic plot of the relative amplitude of the Hartree density wiggles as function of the depth. The straight lines corresponds to the inverse square dependence pertaining to an infinite wall while the curved line joins the actual results, from the third to the seventeenth undulation. The vertical scale extends from 0.01 to 0.0005. (XBL 749-4319)

to 3.51a. This increase is almost entirely due to the density tail which moves the 10% point outwards by 0.46a. The 90% point is almost unaffected by the quantization because it happens to be located right between two oscillations. We observe that the amplitudes of the ripples are considerably smaller than those corresponding to a sharp surface. This is due to the diffuse surface. This is due to the diffuse surface which disturbs to some extent the perfect phase correlations of the wave functions at the surface and thereby inhibits the undulations. However, as one goes away from the surface region deeper into the system the effect of the surface profile is felt to a decreasing extent and the wiggles become more and more similar to those pertaining to a sharp wall. This phenomenon is illustrated in Fig. 2 where we have plotted the amplitude versus the depth from the surface. Thus the asymptotic behavior does not depend on the detailed profile of the surface but follows in general the infinite-wall expression.

This fact has some impact on the possibility of describing the density profile in terms of surface moments along the lines suggested by Stissmann for finite nuclei.[3] The nuclear density profile is described in terms of surface moments of the density distributions, the surface diffuseness being given in terms of the second moment, the surface skewness (flare) in terms of the third moment, and so on. Any two distributions may then be compared by comparing their respective surface moments. However, as we have seen above, the density amplitudes are asymptotically inversely proportional to the square of the depth. It follows that all higher moments, from the second and up, are not mathematically well defined. In fact, they all exhibit an oscillatory behavior as function of the lower limit of the integral (the cut-off depth x_c), the corresponding amplitude being constant for the second moment, increasing linearly for the third moment, and so on. Hence it is not possible to directly extract the surface-moment information about a semi-infinite quantum density distribution. For real nuclei, of course, the problem does not occur because of the finite size. But it is of general interest to study semi-infinite systems. And since this type of density ripple is a quite general feature in a Hartree description of such system, it would be desirable to generalize the concept of surface moments to cover this case as well. Such a generalization could conceivably be brought about by defining some appropriate averaging procedure by which the convergence would be ensured. In doing so one might benefit from the general knowledge of the behavior of the ripples in the asymptotic limit.

In Fig. 3 we have made a similar plot of the kinetic-energy densities obtained in the Hartree

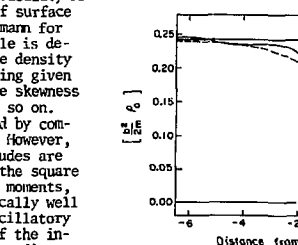

Fig. 3. Kinetic-energy density distributions in units of $b^2/2m\ \rho_0$. The full curve is the Hartree result and the dashed curve the Thomas-Fermi result. (XBL 749-4325)

and Thomas-Fermi approximations. We observe here in particular how the kinetic-energy density is negative in the outer surface region. But apart from this region it follows rather closely the oscillations of the matter distribution plotted in Fig. 1.

Surface Energy

For the self-consistent Hartree solution we have calculated the surface-energy density distribution $a_s(x)$. The surface energy represents the binding-energy deficit due to the presence of a surface for the system. Hence $a_s(x)$ is given by

$$a_s(x) = e(x) - \frac{e_o}{\rho_o}\rho(x) \qquad (2)$$

where $e(x)$ is the total energy density and $\rho(x)$ the matter density. The subscripts o refer as usual to the bulk values. The surface-energy coefficient a_s is the integral of this density, multiplied by the 'nucleon' surface area,

$$a_s = 4\pi r_o^2 \int_{-\infty}^{\infty} a_s(x)\, dx. \qquad (3)$$

In Fig. 4 we show the calculated surface-energy density together with the one pertaining to the Thomas-Fermi system. Figure 5 shows the decomposition of these densities into their kinetic and interaction parts. For the Hartree system those latter partial densities exhibit oscillations in the deeper part of the system. They are opposite to each other so that the combined density $a_s(x)$ has considerably smaller oscillations. The Thomas-Fermi densities all go to zero at the end-point $x_o = 1.90a$ while the Hartree densities extend out in the tail region. We notice that in this region the two parts tend to cancel each other resulting in a rather negligible, slightly negative, value of the total surface-energy density.

The kinetic-energy contribution to the surface-energy density is negative (apart from the small bulk oscillations). Its behavior in the tail region reflects the fact that it is very advantageous for a particle to be in this region as it has here

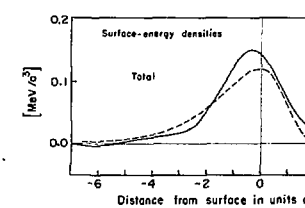

Fig. 4. Surface-energy density distributions in units of MeV/a³. Full line: Hartree, dashed line: Thomas-Fermi. (XBL 749-4324)

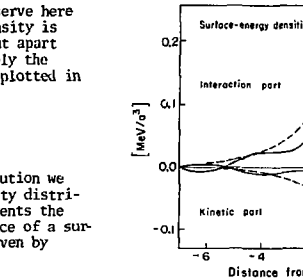

Fig. 5. Kinetic and interaction parts of the surface-energy density distributions displayed in Fig. 4. (XBL 749-4323)

very small or even negative kinetic energy. Further inside the system the Hartree contribution is less negative than the Thomas-Fermi contribution. This is due to the quantum localization effect which prohibits low-momentum particles from getting as close to a potential wall as high-momentum particles. This exclusion of the low-momentum particles from the potential surface results in a relative excess of high-momentum particles and a corresponding higher kinetic energy in that region. In the Thomas-Fermi approximation, with its phase averaging, this effect is not taken into account. In the extreme case of a sharp wall, the kinetic-energy contribution to the surface energy would be positive; the fact that it remains negative in the actual case is due to the diffuseness of the surface.

The interaction-energy contribution to the surface-energy density follows more closely the Thomas-Fermi curve, with some wiggles reflecting the matter-density oscillations relative to the Thomas-Fermi density. For example, the fact that $a_x^{int}(x)$ is smaller than the Thomas-Fermi curve on the inside slope (around-3a) is a consequence of the first density hump which brings the density closer to the ideal bulk value and consequently lowers the energy deficit. In the tail region there is an appreciable contribution because the particles here are not very well bound. As we noticed, it so happens that this contribution to a large extent cancels the kinetic-energy gain in the tail.

The curve for the total surface-energy density then follows rather well the Thomas-Fermi curve. The largest deviation occurs near the peak and from the discussion above it follows that this increase should be mainly ascribed to the lack of low-momentum particles near a quantum surface.

The integrated quantities corresponding to the various densities discussed above are listed in Table 1. For the surface-energy coefficient a_s we find a 10% increase from the Thomas-Fermi value of 18.56 MeV to 20.51 MeV. In an earlier study by Köhler[4] of nuclear many-body calculations it is stated that the surface-energy coefficient would increase by 3.3±1 MeV. This trend is confirmed by

Table 1. Various characteristic surface quantities as obtained within the Thomas-Fermi and Hartree approximations. The quantities are: 10-90% surface diffuseness of matter density, the similar diffuseness based on the second surface moment, the kinectic part of the surface-energy coefficient, the interaction part, the total surface-energy coefficient, the 10-90% diffuseness of the mass function, and the 10-90% diffuseness of the potential. The last colouum shows the relative change (in percent) in going from the Thomas-Fermi to the Hartree approximation.

Quantity		Thomas-Fermi	Hartree	Change [%]
$t_{10\text{-}90}$	[a]	3.17	3.51	10.7
b	[a]	1.39	1.47	5.8
a_s^{kin}	[MeV]	-16.22	-16.88	4.1
a_s^{int}	[MeV]	34.79	37.38	7.4
a_s	[MeV]	18.56	20.51	10.5
$t^B_{10\text{-}90}$	[a]	4.30	4.95	15.1
$t^U_{10\text{-}90}$	[a]	4.55	5.10	12.1

the present more accurate finding that the increase is 1.95±0.01 MeV; because of the large error quoted by Köhler we do not attempt a detailed comparison.

Our study of the semi-infinite nuclear system may be concluded by the following remarks. For the various density distributions. the Thomas-Fermi approximation yields a good average representation of the Hartree results. This supports the application of the Thomas-Fermi approximation for studies of macroscopic nuclear properties. In this connection we recall the criterion derived in Ref. 2 that the Thomas-Fermi approximation yields the correct density to within 10% provided $|\nabla\rho|/\rho^{4/3} \lesssim 10$. In the nuclear case this relation holds good through the surface region out to a point where the density has dropped to one-sixth of its central value.[2] Our results, displayed in Figs. 1 and 3, are seen to confirm this criterion which was obtained on the basis of a study of linear potentials.[5] Furthermore, we can state that the Thomas-Fermi approximation underestimates the surface diffuseness as well as the surface energy by around 10%. This could be roughly compensated for by increasing the range parameter a by this relative amount (keeping the value of Ca^3 constant) when using the Thomas-Fermi approximation.

Footnotes and References

*On leave from the University of Aarhus, Aarhus, Denmark.

1. R. G. Seyler and G. H. Blanchard, Phys. Rev. 124, 227 (1961).

2. W. D. Myers and W. J. Swiatecki, Ann. Phys. 55, 395 (1969).

3. G. Süssmann, "Description of the Nuclear Surface by Moments," Lawrence Berkeley Laboratory Reprint LBL-1615 (1973).

4. H. S. Köhler, Nucl. Phys. A139, 353 (1969).

5. W. J. Swiatecki, Proc. Phys. Soc. A68, 285 (1955).

NUCLEAR HYDRODYNAMICS

C. T. Alonso

The incoming data from very heavy ion experiments have indicated that the collisions of heavy nuclei may be strongly influenced by macroscopic dynamic effects.[1] Exciting prospects are associated with future studies of the bulk properties of heavy, almost macroscopic drops of the unique nuclear fluid. Thus it is of interest to investigate whether the techniques of classical hydrodynamics can describe the bulk flow of very heavy nuclei. During the past ten years dynamic studies of nuclear fission, assuming irrotational and inviscid flow, have been carried out by Nix and his collaborators.[2] In this decade we are interested in nuclear collisions, which probably involve rotational as well as viscous flow, and new methods for solving the corresponding flow equations are needed. Therefore we have developed a numerical solution of the Navier-Stokes equation that describes the rotational or irrotational flow of charged viscous drops scaled to nuclear dimensions.[3] The computer code SQUISH that performs this numerical calculation can simulate the surface oscillations, fissions, and fusions of classical charged liquid drops. The free surface of these drops is not restricted by any parameterization and therefore it can assume any shape necessary for the solution of the differential flow equations. In particular it should be able to follow distorted collisions of liquid drops.

In previous papers we have discussed certain aspects of the rheological properties of the nuclear liquid.[3,4] We have concluded that slow processes involving many nucleons like fission and fusion should be described by a liquid model. The nuclear drop is an emerging hydrodynamic system; that is, heavy ion accelerator experiments can lie in the transition regions between the quantum mechanical and the classical and between the microscopic and the macroscopic. Therefore we should expect that our classical macroscopic model will need quantum-mechanical or microscopic adjustment in certain cases. Our primary purpose is to explore how far a full hydrodynamical treatment can be taken in the description of nuclear processes. It is interesting to note

that recent studies in the field of molecular dynamics have indicated that small systems containing several hundred particles pass into the hydrodynamic regime much faster than had been previously thought.[5] This may indicate that a hydrodynamic nuclear model will be more appropriate than has been anticipated.

In cases where a hydrodynamic model applies, the transport coefficient of greatest interest is the viscosity because of its sensitive microscopic origins. The nuclear viscosity is probably highly temperature dependent. In Fig. 1 on the left is shown the observed temperature dependence of the neutral Fermi liquid He^3, which is not dissimilar to the nuclear liquid. On the right of Fig. 1 is a speculation concerning the temperature dependence of the viscosity of nuclear matter. At low temperatures the pairing correlation in nuclear matter may introduce a superfluid component that brings the viscosity down. This could mean that cold processes like spontaneous nuclear fission have an effective viscosity that is quite different from hot processes like accelerator collisions.

In the spirit of the classical macroscopic assumption, we have carried out a full solution of the Navier-Stokes equation for a charged viscous liquid drop. The hydrodynamic equations and surface boundary conditions have been described in a previous report.[3,4] In Fig. 2 is illustrated the

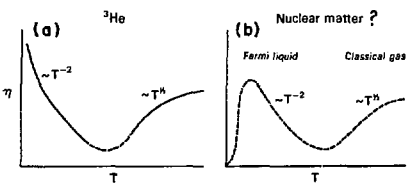

Fig. 1. (a) Measured temperature dependence of the viscosity of the Fermi liquid He^3. (b) Speculation of the temperature dependence of the viscosity of nuclear matter. A superfluid component could force the viscosity to zero at low temperatures.
(XBL 749-4939)

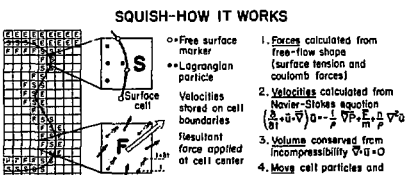

Fig. 2. A schematic description of how the two-dimensional code SQUISH solves the finite-difference equations for fluid flow while satisfying the boundary conditions at the free surface of a viscous incompressible liquid. (XBL 748-4016)

numerical solution as it is carried out by the code SQUISH. An axially symmetric drop is placed on a fixed Eulerian mesh, and movable Lagrangian particles representing liquid volume elements are injected into the drop at t = 0. The code calculates the Coulomb forces and the surface tension from the free surface and its derivatives, which are obtained from a cubic spline fit on a special set of Lagrangian markers that follow the free surface. The method of G.B. Foote is used for applying the surface tension to the drop.[6] We have used the SMAC method of Harlow and Amsden for the hydrodynamic solution.[7] In this method the mesh is first adjusted to contain the correct vorticity and then the code deposits the correct velocities on the cell boundaries. The particles are moved according to the weighted local velocities, the time is incremented by a small step dt, and in this manner the program cycles, tracing out the flow of the drop as a function of time.

Our studies of drop dynamics fall into three categories: 1) surface oscillations, 2) fissions, and 3) fusions. In order to check the accuracy of the code we have relied heavily on experimental and theoretical research from such other fields as meteorology, fluid dynamics, astrophysics, and even space science. In Fig. 3, for example, are two frames of colliding water drops filmed in the Skylab space station. Conversely, we find that this code has applications in all of these fields.

Surface oscillations have been described in previous reports.[3,4] We find that our code obeys the Rayleigh theory quite well and that it can reproduce such quantities as the critical viscosity, the period, the damping, and the amplitude with good accuracy for both charged and uncharged drops. We are presently using the code as a research tool to study the effects of short-time solutions of

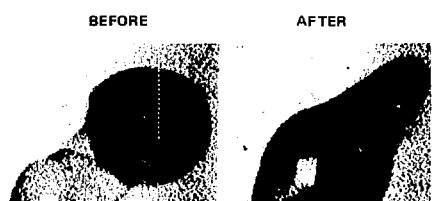

Fig. 3. Colliding water drops in the Skylab space station. This system soon fused into a stable compound drop. (CBB 751-454)

Rayleigh oscillations as well as studies of the flow in large-amplitude oscillations for which no theory exists. In Figs. 4 and 5 are shown the underdamped and overdamped motions of an uncharged ^{152}Sm nucleus, and in Fig. 6 is the underdamped oscillation of a charged ^{152}Sm nucleus.

Fission studies of charged drops that move beyond the saddle point are harder to check because there are no direct experimental data for comparison. We have available only the inviscid calculations of Nix[2] and some asymptotic data from nuclear fission experiments. Due to practical limitations involving the expense of running the code, we can make numerical simulations only in a certain range of viscosities that includes the critical viscosity for surface oscillations. Therefore we cannot simulate the inviscid Nix calculations directly. By increasing the charge on a drop we can determine the atomic number at which it stops oscillating and starts to fission, and we do find that the code predicts correct saddle point charges. In Fig. 7 are shown two fission simulations initiated at rest beyond the saddle point and using the two viscosities that produced the underdamped and overdamped oscillations of Fig. 4 and 5. We find that at these viscosities this highly charged drop (Z=160, A=300) does not scission but elongates with a thin cylindrical neck. Similar recent simulations of real

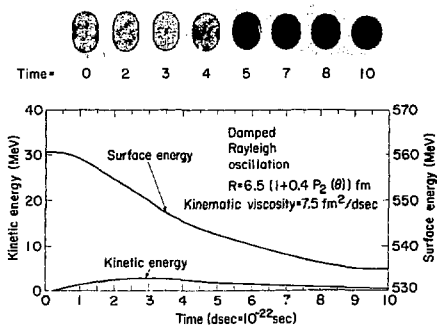

Fig. 4. Underdamped surface oscillations of a viscous liquid drop scaled to the dimensions of uncharged ^{152}Sm nuclei. (XBB 748-5739)

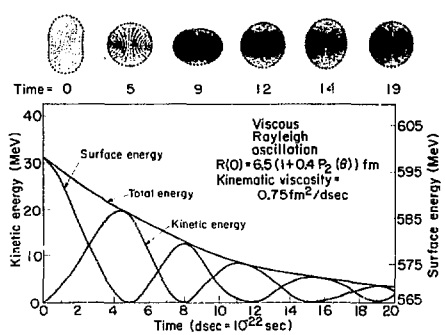

Fig. 5. Overdamped surface oscillations of the drop represented in Fig. 4. The viscosity has been increased by a factor of ten. (XBB 748-5740)

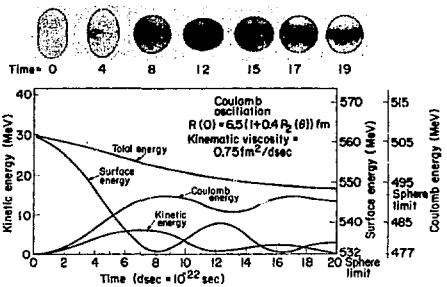

Fig. 6. Underdamped surface oscillations of a charged ^{152}Sm nuclear drop. (XBB 748-5738)

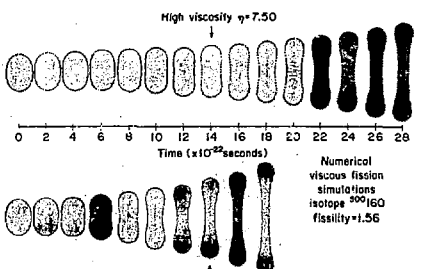

Fig. 7. Simulations of nuclear fission of the mythological isotope 160^{300}, which was started at rest with a shape outside the saddle shape. The drop on the top is ten times more viscous than the drop on the bottom. The central time scale applies to both simulations. (XBB 749-5975)

nuclei indicate that these viscous drops also do not achieve scission at the times predicted by Nix for inviscid drops. This results in a lower fragment velocity at infinity, and preliminary results indicate that the lowered velocities do not correspond to experimental velocities. The problem of viscous fission is still under study at this time.

Fusion studies such as that shown in Fig. 8 are also under way. There are no experimental or theoretical data for comparison except some generalized results from heavy ion accelerator collisions. Our preliminary observation from fusion simulations is that colliding viscous drops develop a lot of heat in their fusing neck that causes them to lose their forward momentum before they have fused to within the saddle shape, with the result that they do not fuse into a stable compound drop but rather break up after a short time. The implication for heavy ion physics is that nuclear drops would not fuse to make compound nuclei if their viscosity is appreciable.

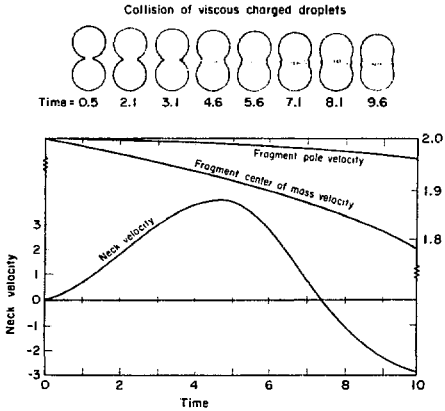

Fig. 8. Preliminary simulation of the fusion of two viscous charged drops. (XBL 746-3368)

References

1. W. D. Myers, "Macroscopic Aspects of Heavy Ion Reactions", Proceedings of the International Conference on Reactions Between Complex Nuclei, Nashville, Tennessee, June 10-14, 1974.

2. J.R. Nix, "Further studies in the liquid drop theory of nuclear fission," Nuc Phys. A130, 241 (1969); also A. J. Sierk and J.R. Nix, "Dynamics of fission and fusion with applications to the formation of superheavy nuclei", LA-UR-73-931, (1973).

3. C. T. Alonso, "The Dynamics of Viscous Nuclear Drops," LBL-2992 (1974).

4. C. T. Alonso, "The Dynamics of Charged Viscous Liquid Drops," LBL- 2366 (1973).

5. B. J. Alder, "Computer dynamics," Ann Rev. Phys. Chem. 24, 325 (1973).

6. G. B. Foote, A numerical method for studying liquid drop behavior", J. Comp. Phys. 11, 507 (1973).

7. A.A. Amsden and F.H. Harlow, "The SMAC Method: A Numerical Technique for Calculating Incompressible Fluid Flows," LASL-LA-9370, (1970).

SIMILARITIES AND DIFFERENCES BETWEEN VOLUME-CHARGED (NUCLEAR) DROPS AND CHARGED CONDUCTING (RAIN) DROPS*

C. F. Tsang

The liquid drop model of nuclear fission was suggested thirty five years ago. The model has been very useful for the understanding of nuclear fission data and has recently been found to be an important element in what has come to be known in nuclear physics as the Strutinsky method by which the predictions on the masses and stability of the yet-undiscovered superheavy nuclei are made.

With all that has been developed in the nuclear fission problem, it would be interesting to apply it to actual macroscopic rain drops which are electrically conducting and consider their shapes of equilibrium. This has the great advantage over the nuclear case that direct measurements in the laboratory on a drop can be made. Besides studying the rain drops on its own merit, a parallel theoretical and experimental study of the conducting drop may also throw light on the nuclear drop. Of course properties of the charged conducting drop is not a new area of study. In 1882, Lord Rayleigh[1] published a paper on the stability of a charged conducting drop under small oscillations. Other studies are made more recently.[2] However, in the present work we make a close comparative study of the nuclear drop and the rain drop using methods developed in the liquid drop theory of nuclear fission.

It is straightforward to apply the methods developed in nuclear fission theory to the study of a charged conducting drop. Thus the fissility parameter x can be defined similarly as the ratio of the Coulomb energy to twice the surface energy for a sphere with given charge and volume. The equation for the energy excess ξ over a spherical drop will be the same as for the volume charged drop case. Of

course, the Coulomb energies will now be evaluated on the assumption that the drop is conducting.

Three simple similarities may be pointed out.

(a) For $x = 0$, there is no charge on the drop so that the equilibrium shapes are the same whether the drop is conducting or not. Also, it turns out nontrivially that as in the case of a volume charged drop, $x = 1$ represents the transition point where the spherical drop is stable for $x < 1$ and is unstable for $x > 1$.

(b) A second similarity is apparent if we look at the energy difference ξ_R between the initial and the final state when the drop is divided into equal spheres. It has been shown by Swiatecki that for a volume charged drop.

$$\xi_R = (n^{1/3} - 1) + 2x\,(n^{-2/3} - 1).$$

When we make a similar study for a conducting drop, we get a completely identical equation and the corresponding disucssions are applicable. The reason is that only spherical shapes are involved in both the initial and final states, and the Coulomb energy of a volume charged sphere (which is $3/5\ Q^2/R$) and that of a conducting sphere (which is $1/2\ Q^2/R$) differ by only a numerical factor, 6/5, that is the same for both states.

(c) It also turns out that the Coulomb energy of a volume charged ellipsoid and that of a conducting ellipsoid is given by

$$E_c = \frac{1}{4} Q^2 \int_0^\infty [(a^2+\lambda)(b^2+\lambda)]^{1/2}\, d\lambda$$

so that

$$B_c = \frac{E_c}{E_c^{(0)}} = \frac{1}{2} R \int_0^\infty [(a^2+\lambda)(b^2+\lambda)(c^2+\lambda)]^{1/2}\, d\lambda$$

where a, b, and c are the lengths of the axes of an ellipsoid and $E_c^{(0)}$ is Coulomb energy of a sphere with same volume and charge. This integral may be carried out analytically in the case of a spheriod where two of the axes are equal. B_c for a volume charged case is given by exactly the same formula. Hence, if we make the drop to take on only ellipsoidal shapes, then any conclusions about the statics of the volume charged drop will be true for the conducting drop.

The first difference between the volume charged drop and a conducting drop can be found if we consider the division of the drop into two unequal spheres at an infinite distance apart, one with volume βV and the other with volume $(1-\beta)V$. In Fig. 1 is plotted the energy change ξ_R between the initial and final states as a function of β for various values of the fissility parameter x. For $\beta = 0$ and $\beta = 1$ we get a sphere with volume V which is just the initial state. For $\beta = 0.5$, we get two equal spheres. The energy change turns out to be zero at $x = 0.35$ for $\beta = 0.5$. For a conducting drop Fig. 2 is found.

We note that here again the energy is zero at $x = 0.35$ for $\beta = 0.5$. However, except for the points at $\beta = 0$, 0.5, and 1.0 the curves in the two figures are very different. A potential minimum for a volume charged drop occurs at $\beta = 0.5$ for $x > 0.2$, but a potential maximum for a conducting drop occurs at $\beta = 0.5$ for all x values less than one. In the latter case minima occur at points where the fragments are unequal.

The major reason for the above differences is that the charge to mass ratio for a volume charged drop is a constant, but for a conducting drop it is not required to be a constant. This is also the

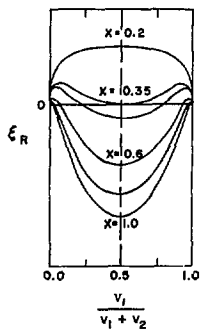

Fig. 1. The energy change in the division of a volume-charged drop into two spheres as a function of the fractional volume of one of the spheres for various values of x. (XBL 694-2458)

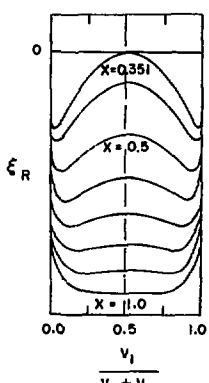

Fig. 2. Same as Fig. 1 for the case of a charged conducting drop. (XBL 694-2459)

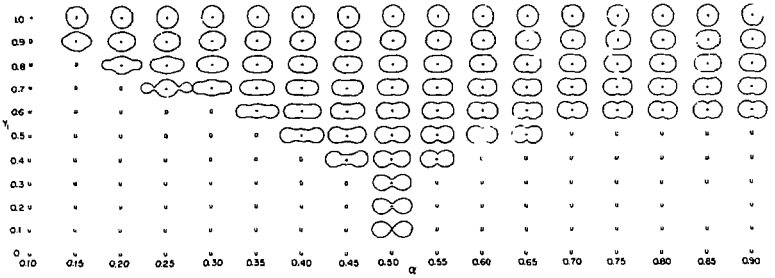

Fig. 3. *Shapes in the symmetry N = 3 family of equipotential surfaces.* (XBL 693-2278)

underlying cause for the second difference that appears when we try to find the configuration with the absolute lowest energy for a drop with a given fissility parameter x. For a volume charged drop, this configuration is n equal droplets at infinity and the number n depends on the x values of the drop. One would at first expect that the same conclusion might hold for a conducting drop. But, as it can be shown, for a conducting drop, the configuration at the lowest energy is one with all the charges Q on the drop taken off and distributed among many infinitesimal droplets at infinity. The total energy of the droplets may be made to vanish and only the surface energy of the original drop is left.

In our work we next try to determine the equilibrium shapes of a charged conducting drop to be compared with those for a volume-charged drop.

The calculation of the Coulomb energy of a conducting drop with an arbitrary shape is in general a difficult problem. However, it can be side-stepped by requiring the drop to assume a prescribed family of shapes, in fact, making the calculation of its Coulomb energy a trivial matter. It is well-known from the theory of electrostatics that the electric potential due to a system of charges (total charge Q) at any point on a given equipotential, is the same as that due to a charged conductor with the shape of this equipotential having a charge Q. Hence, if we require the drop to assume the shape of an equipotential of potential α, its Coulomb energy is just 1/2 αQ. If R is the radius of a sphere that has the same volume as the drop and possesses the same amount of charge, its Coulomb energy is 1/2 Q^2/R. Hence we get

$$B_c = \alpha R/Q.$$

The surface energy relative to that of the sphere, B_s, can simply be found by calculating the area numerically. Hence for a given fissility x the energy of the drop is calculated, and equilibrium shapes, whose energies are stationary, are then determined numerically.

For illustration, the shapes of equipotentials that enclose three equal points charges are shown in Fig.3, where the volumes of the shapes have been normalized to the same value. The symmetric equilibrium shapes of a charged conducting drop we calculated based on a family of shapes generated by two, three up to six point charges are shown in Fig. 4. The abscissa gives the fissility parameter x from 0 to 1. The ordinate gives R_{MIN}/R and R_{MAX}/R as a measure of the shape, where the minimum radius R_{MIN} is

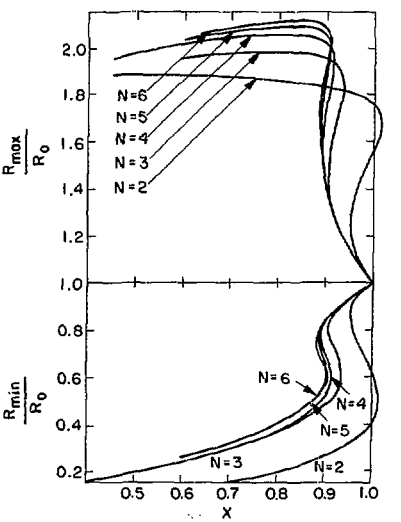

Fig. 4. The maximum and minimum radii of the symmetric saddle point shapes of a charged conducting drop as a function of the fissility parameter x. Different curves correspond to the restriction to different families of shapes indicated by the values of N. (XBL 694-2462)

the minimum radius of the neck of the drop and the maximum radius R_{MAX} is the distances from the center of the neck (at its minimum radius) to the ends of the drop.

Let us take the N = 6 curves at its face value and examine its main features. As the value of x goes from 1 toward small x values, the equilibrium shape elongates from a sphere, i.e., R_{MAX}/R increases with decreasing x in the region near x = 1. This is in constrast to cases of small x values ($x \lesssim 0.7$) where R_{MAX}/R is slowly decreasing with decreasing values of x. The shapes in the latter case are long and look like a dumbbell. Similar to the volume charged drop case there exists a region where there is a rapid change of shape, but it occurs at $x \approx 0.9$ in the present case. Actually the curve for R_{MAX}/R even turns back at x = 0.887 and again at x = 0.906. However, we are able to show, by an independent variational test, that our results in this region are much less reliable than regions with larger or smaller x values, so that the double turn may be spurious. (It is interesting to note that similar uncertainty once existed in the volume charged case).

The nature of these equilibrium shapes may be found by looking at the signs of the second derivatives of their energy with respect to all the parameters. The following results are found when the shapes are restricted to only the degrees of freedom that allow reflection symmetric shapes. For $1 > x > 0.887$ the energy of the drop is a maximum in one degree of freedom, but a minimum in the other symmetric degree of freedom. Between the bends, for $0.887 < x < 0.906$, the energy is a minimum. For values of x smaller than 0.906, it is again a maximum in one degree of freedom. With respect to the degrees of freedom that describe reflection asymmetric deformation, the energy of the drop is a minimum from x = 1 to $x \approx 0.892$. From $x \approx 0.892$ to $x \approx 0.68$, it is a maximum in one degree of freedom. Below $x \approx 0.68$ it appears to be a maximum in two degrees of freedom. Hence, the equilibrium point is a saddle from x = 1 to $x \approx 0.892$. From $x \approx 0.892$ to x = 0.887 it is a mountain top (unstable in more than one direction). Between the bends at $x \approx 0.887$ and $x \approx 0.906$ it is again a saddle. For x smaller than 0.906, it turns out to be a mountain top also. As discussed before the shapes close to x = 1 is fairly well determined, but at the bends the results are not reliable.

In conclusion, it is interesting to note that even some ninety years after Lord Rayleigh's study of a charged conducting drop, the whole problem is still a very open subject. The present calculations have been able to determine the saddle points of a charged conducting drop for values of x from 0.892 to 1 where they are reflection symmetric. But for the region up to 0.892, one is still very ignorant of the saddle point shapes and energies of a charged conducting drop.

Footnote and References

*Condensed version of LBL-2970. Invited paper at the International Colloquim on Drops and Bubbles at Pasadena, California, August 28-30, 1974.

1. Lord Rayleigh, Phil. Mag. XIV, 184 (1882).

2. B. Vonnegut and R. L. Neubaeur, J. Collid. Sci. 7, 616 (1952). S. A. Ryce and R. R. Wymah, Can. J. Phys. 42, 2185 (1964). S. A. Ryce and D. A. Partiarche, Can. J. Phys. 43, 2192 (1965). S. A. Ryce, Nature 1343 (1966).
Proceedings of the International Symposium on Electrodynamics at Massachusetts Institute of Technology, March 31-April 2, 1969). (International Unions of Theoretical and Applied Mechanics, Pure and Applied Physics).
P. R. Brazier-Smith, M. Brook, J. Latham, C. P. R. Saunders, and M. H. Smith, Proc. Roy. Soc. A322, 523 (1971). P. R. Brazier-Smith, Phys. Fluids 14, 1 (1971). P. R. Brazier-Smith, Quart. J. R. Met. Soc. 98, 434 (1972). C.P.R. Saunders and B. S. Wong, J. Atmos. Terr. Phys. 36, 707 (1974).

FURTHER STUDIES ON PROXIMITY FORCES

J. Randrup, W. J. Swiatecki,* and C. F. Tsang

For certain physical systems such as homogeneous solids, fluids or the heavier atomic nuclei, made up of elements interacting by short-range forces and possessing a surface region which is thin compared to the size of the obejct under consideration (leptodermous systems), the potential energy of the system may be decomposed into a volume term and a surface term. The surface term is proportional to the area of the surface bounding the object. For a simply-connected system the above decomposition is accurate if the principal radii of curvature of the surface are everywhere much larger than the thickness of the surface region. Moreover, when this condition is satisfied, correction terms to the surface energy (such as the curvature correction) may be derived by expansions in powers of the ratio of the thickness of the surface to the size of the system, thus making the expression for the potential energy even more accurate. Such a series expansion has been useful in discussing the average binding energies (masses) of atomic nuclei, and one might have thought that, apart from effects associated with the discreteness of nucleons (shell effects) there was no more to the problem of average nuclear energies than the calculation of the above series expansions to a sufficiently high order. This is not the case. Thus, when the surface of the system becomes contorted into features whose characteristic dimensions are of the order of the thickness of the surface region itself, the above series expansions become useless. This failing is by no means of merely academic interest: it may be serious for a system with a thin neck, on the verge of dividing into two fragments (as in nuclear fission),

or in the case of two sub-systems about to come into contact (as in collisions between heavy nuclei). In the latter case in particular, when the system is not simply-connected, a calculation of the surface energies of the two pieces, no matter how accurately it is corrected for the curvatures of the two surfaces, can never give rise to the (strong) attraction that in practice appears when the two surfaces approach to within a distance comparable with the surfaces thickness.

Various attempts to remedy these failings have been made in the past. They range from microscopic computer calculations on individual pairs of nuclei (by Greiner and collaborators[1] and Brueckner and collaborators[2]) through various folding prescriptions where a more or less realistic potential well is folded into a more or less realistic density distribution[3,4] to direct estimates of certain aspects of the nucleus-nucleus force in terms of the experimentally known surface-energy coefficient.[5]

In line with the latter developments we have found it possible to derive simple expressions for the additional potential energy (or forces) associated with certain of the more important types of violently contorted surfaces, which should enable one to complement in a useful way the usual series expansions of the nuclear energy. We shall call these additional forces "Proximity Forces" because they arise from the proximity of elements of the contorted surface, the contortion being such that different pieces of the surface actually face each other across a small gap or crevice. In particular we have derived a theorem that makes it possible to relate (approximately) the interaction between two finite nuclei to the interaction between two flat parallel slabs of semi-infinite nuclear matter--a problem that is simpler, and can be solved (in a suitable approximation) once and for all.

The Proximity Force Theorem states that, under certain assumptions, the force F(s) between curved surfaces, as a function of the least separation s, is proportional to the interaction potential per unit area e(s) between two flat surfaces, the proportionality factor being 2π times a certain mean radius of curvature characterizing the two surfaces at the point of closest approach. The theorem was proved and discussed in the last year's Annual Report. The result may be expressed as follows:

$$F(s) = -\frac{dV_p}{ds} = 2\pi \bar{R}\, e(s),$$

where, in the case of two spherical surfaces with radii C_1 and C_2, the mean curvature radius $\bar{R}$ is given by

$$\bar{R} = \frac{C_1 C_2}{C_1 + C_2},$$

a kind of "reduced radius" of the two spheres (like a reduced mass $M_1M_2/(M_1+M_2)$. Thus the Proximity Potential is given by

$$V_p(s) = 2\pi \bar{R}\, \varepsilon(s) \text{ where } \varepsilon(s) = \int_s^\infty e(s')ds'. \quad (1)$$

Caution should be exercised in using the Proximity Theorem. The proper domain of applicability of the theorem derived above is to the mapping of the average nuclear potential energy (for not too small systems) in a small sub-space of the total configuration space, defined by specifying certain deformation co-ordinates. In trying to compare the potential V_p directly with results of nucleus-nucleus scattering experiments one should remember that nuclei are not undeformable, so that at each instant of time, the formula show up in scattering experiments at sufficiently high energies (especially in grazing collisions) where there might not be enough time during the collision for the nuclear density distributions to deform appreciably. It might also be argued that in the analysis of elastic nucleus-nucleus collisions a formula based on the assumption of undeformability is actually the relevant one, since any excitation of the degrees of freedom of the individual nuclei would tend to take the system out of the channel for elastic scattering.

A second reservation on the indiscriminate use of Eq. (1) stems from the assumption that C_1 and C_1 should be much larger than the thickness of the nuclear surface. Even for heavy nuclei this condition is not satisfied very accurately, and when one of the nuclei is as light as oxygen or neon, serious corrections to Eq. (1) might be expected.

In this connection it seemed for a while, as a result of comparisons of our Proximity Force Theorem with calculations of Krappe and Nix,[5] that even though correct in principle the theorem might be useless in practice for applications to nuclei, because actual nuclear radii are not sufficiently large compared to the diffuseness of the surface. These difficulties and their resolution are illustrated by the following considerations.

In Ref. 3 Krappe and Nix give a formula for the interaction potential between two non-overlapping sharp spheres of radii R_1 and R_2 whose volume elements interact by a Yukawa attraxtion of a certain strength (sa, K) and range a. We rewrite the formula as follows

$$V = -16\pi a^2\gamma\left(\frac{R_1}{a}\cosh\frac{R_1}{a} - \sinh\frac{R_1}{a}\right)\left(\frac{R_2}{a}\cosh\frac{R_2}{a} - \sinh\frac{R_2}{a}\right) \quad (2)$$
$$\cdot \frac{\exp[-(R_1+R_2+s)/a]}{(R_1+R_2+s)/a}.$$

Here γ stands for $2\pi a^4K$ and, as shown by Krappe and Nix, this is the surface energy per unit area associated with the sharp surface and the Yukawa interactions underlying their model. The separation between the two sharp surfaces is denoted by s. When R_1 and R_2 are sufficiently large compared to a the conditions for the validity of the Proximity Force Theorem are satisfied and, as remarked by Krappe and Nix, the limiting form of V

$$V \to -4\pi\gamma \frac{R_1R_2}{R_1+R_2} a\, e^{-s/a}, \quad (3)$$

is, indeed, in accordance with our theorem since the interaction energy per unit area between two Krappe-Nix semi-infinite systems with flat surfaces can be shown to be given by

$$e(s) = -2\gamma\, e^{-s/a}. \qquad (4)$$

If, however, one attempts to use Eq.(3) as an approximation to Eq.(2) for values of $R_{1,2}/a$ of the order of two to four, one finds discrepancies of the order of a factor of three to two! (The Krappe-Nix range a is of the order of 1-1.5 fm; it should not be confused with the range a in the Seyler-Blanchard model [8], whose value is about 0.6 fm.) This poor accuracy of Eq.(3) was traced to the fact that the relevant effective radius of a Krappe-Nix sphere (i.e., or a sharp density distribution of radius R generating a diffuse potential well), is significantly smaller than R, and by applying the Proximity Theorem to these effective objects with smaller radii a dramatic improvement was obtained.

The crux of the matter is that the location of the profile of the potential well of a Krappe-Nix sphere (as given by the half-value radius or Suss-mann's central radius C_V) is inside the density radius R as is seen from the formula

$$C_V = R\left[1 - \frac{b^2}{R^2} + \cdots\right].$$

Here b is the Süssmann width of the diffuse potential surface. In the Krappe-Nix case it can be shown to be given by $b^2 = 2a^2$.

The location of the effective profile of a Krappe-Nix sphere [taken as the mean between the density and potential profiles because the density and potential enter symmetrically in the formula $\int V\rho$ for the (interaction) energy] is therefore

$$C_{effective} = \frac{1}{2}(C_V + C_\rho) = R\left(1 - \frac{a^2}{R^2} + \cdots\right). \qquad (5)$$

(Note that in the case of the density the half-value or central radius C_ρ is equal to R because the diffuseness is zero.)

Applying the Proximity Force Theorem to the effective spheres with radii given by Eq. (5) we find

$$V_p = -4\pi\, a\gamma\, \frac{\left(R_1 - \frac{a^2}{R_1}\right)\left(R_2 - \frac{a^2}{R_2}\right)}{R_1 - \frac{a^2}{R_1} + R_2 - \frac{a^2}{R_2}}\, \exp\left(-\frac{s}{a} - \frac{a}{R_1} - \frac{a}{R_2}\right)$$

to be compared with the exact result Eq. (2). Figure 1 shows the comparison for the case of equal spheres $R_1 = R_2 = R$. In that case the Krappe-Nix interaction V and the Proximity Potential V_p may be written as

$$V/4\pi a^2\gamma = -4\,(\rho - \sinh\rho)^2\, \frac{e^{-\sigma-2\rho}}{\sigma+2\rho}$$

and

$$V_p/4\pi a^2\gamma = -\frac{1}{2}\left(\rho - \frac{1}{\rho}\right) e^{-\sigma-(2/\rho)},$$

where $\rho = R_1/a = R_2/a$, and $\sigma = s/a$.

On the left in Fig. 2 these expressions are plotted as functions of the separation s/a for

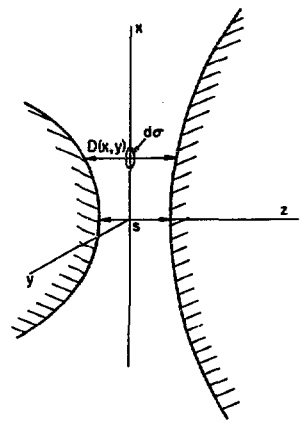

Fig. 1. Two curved surfaces whose distance of closest approach is s (along the z-axis). The gap width D(x,y) is a function of the transverse coordinates x and y. (XBL 7412-8381)

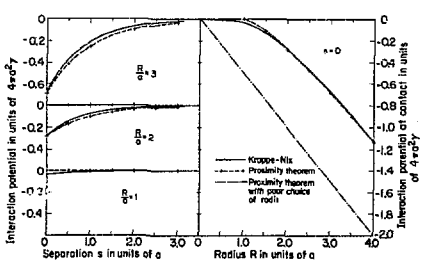

Fig. 2. A comparison of the exact interaction between two equal Krappe-Nix spheres (solid lines) and the approximation resulting from the Proximity Theorem applied to properly chosen effective spheres (dashed lines and crosses). The dot-dashed line corresponds to a poor choice for the radii of the interacting objects. (XBL 7412-8382)

three radii: R/a = 3, 2, 1. At contact (s = 0) the Krappe-Nix potential V and Proximity Potential Vp are reasonably close; the former then falls off somewhat more rapidly with s than the latter. On the right the values of V and Vp at contact are compared as a function of R/a. The Proximity Potential is zero at R/a = 1 whereas the exact result has a small tail extending to R/a = 0. Otherwise the correspondence between the two curves is close. The dot-dashed curve is given by Eq. (3). It eventually achieves the correct limiting value, but is useless for R/a ~ 2-4. We made similar comparisons of V and Vp for unequal spheres with a ratio of radii 2:1 and the close agreement was preserved.

These comparisons illustrate the importance of recognizing the proper location of the surface profiles of the curved objects to which the Proximity Theorem is being applied. This has to do with the importance of properly matching the parallel flat surfaces (underlying the Proximity Theorem) to the profiles of the curved surface elements that the flat surfaces are supposed to represent. In the Krappe-Nix case this proper matching makes all the difference between the theorem being a useless curiosity, or providing a semi-quantitative tool for predicting in certain cases the results of a calculation without carrying out the somewhat involved multiple integrations associated with folding in (Yukawa) interactions. We should remark, however, that the Krappe-Nix case, with a sharp density but a diffuse potential, is a situation that exaggerates this aspect of the problem. It is only because the density is sharp that its profile stays at R, whereas the potential profile moves in by b^2/R as the surface is curved. In a self-cohesive system (such as a nucleus), where the density generates the potential and the potential determines the density in a self-consistent way, the widths of the potential and density profiles are approximately equal, and so the density and potential profile locations do not move appreciably with respect to each other as the surface is curved. Applying the Proximity Theorem simply to the density radii C_ρ, as was done implicitly, should then be a fairly adequate procedure.

Concerning the relation of our Proximity Potential to nucleon-nucleon potentials obtained by folding (either using schematic models of the Brink-Rowley [4] type) the most important difference is that the Proximity Potential takes account of the saturating character of nuclear interactions (built into the Proximity Theorem by way of the saturating properties of the semi-infinite systems). The non-saturating folding procedures of the Brink-Rowley type tend to give potentials much too deep by the time the two nuclei are in contact. In the Krappe-Nix case the potential is effectively normalized to give the right attraction at contact (by adjusting the properties of the Yukawa force so that it reproduces the surface tension coefficient). The non-saturating character is then in evidence in a more subtle failing of the force function, namely in that e(s) in Eq. (4) is not a minimum near s = 0, and consequently that V in Eq. (2) does not have a point of inflexion near contact.

Footnote and References

*LBL Theory Group.

1. W. Greiner, Proceedings of Heavy-Ion Summer Study at Oak Ridge National Laboratory, June 12-July 1, 1972, p. 1.

2. K. A. Brueckner, J. R. Buchler, S. Jorna, and R. J. Lombard, Phys. Rev. 171, 1188 (1968).

3. H. J. Krappe and J. R. Nix, Proceedings of the Third IAEA Symposium on Physics and Chemistry of Fission, Rochester, New York, August 1973, p. 159.

4. D. M. Brink and N. Rowley, Nucl. Phys. A219, 79 (1974); R. A. Broglia and A. Winther, Phys. Reports 4, 153 (1972).

5. J. Wilczynski, Nucl. Phys. A216, 386 (1973); R. Bass, Phys. Lett. 47B, 139 (1973).

POTENTIAL ENERGY SURFACES

J. P. Blocki*

Great progress has been made in heavy ion physics during the last few years. On the one hand a lot of experiments have been done using many different combinations of target-projectile systems with different relative angular momenta and energies. On the other hand there are many theoretical descriptions that attempt to interpret the results of these experiments and predict some main features of heavy ion collisions, such as probabilities of scattering (elastic and deep inelastic) and formation of compound systems. However, it has been found that there is a lack of some basic calculations, namely of potential energy surfaces for different target-projectile combinations. This should obviously be a starting point in all theoretical considerations. In this note we intend to describe our approach to the solution of this fundamental problem.

The basic model assumed for calculation of the potential energy is a simple liquid drop model (Coulomb plus surface terms). The shape of the drop is described by three smoothly joined portions of quadratic surfaces of revolution, which are two spheres connected by hyperboloidal (spheroidal) neck (see Fig. 1).

The equation for a drop surface in a cylindrical coordinates system is written as:

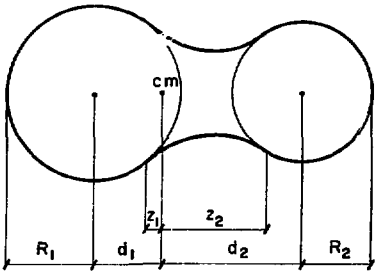

Fig. 1. An illustration of a shape described by two spheres connected by hyperboloidal neck.
(XBL 757-3507)

$$\rho^2 \begin{cases} R_1^2 - (z - d_1)^2 & -d_1 - R_1 \leq z \leq Z_1 \\ a + bz + cz^2 & Z_1 \leq z \leq Z_2 \\ R_2^2 - (z - d_2)^2 & Z_2 \leq z \leq d_2 + R_2 \ . \end{cases} \qquad (1)$$

There are seven parameters describing the shape (R_1, R_2, d_1, d_2, a, b, c), four of which can be eliminated by imposing the constancy of the volume, the smooth connection between surfaces at points Z_1 abd Z_2, and fixed position of the center of mass. Essentially, there remain three independent degrees of freedom in describing the shape and it was decided to choose for these: asymmetry

$$A = M_1/(M_1+M_2) = R_1^3/(R_1^3 + R_2^3),$$

where M_1 and M_2 are the masses of two separated fragments, distance between spheres centers $D = d_2 - d_1$, and so called "neck variable" $\sigma = \Delta V_{neck}/V_o$, which is the excess of the volume of the hyperboloidal (spheroidal) neck over the nominal one expressed in units of total volume V_o. By nominal volume of the neck we understand the volume that corresponds to the overlapping volume of two spheres. To make the situation more clear the family of shapes for asymmetry A = 0.2 is presented in Fig. 2.

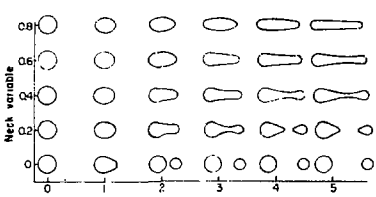

Fig. 2. The family of shapes for asymmetry A = 0.2 (the R in the figure is the radius of the compound sphere). (XBL 757-3497)

The potential energy is parametrized additionally by the fissionability parameter x, which essentially defines the proportion in which Coulomb and surface terms should be mixed in total energy E

$$E = B_s - 1 + 2x\,(B_c - 1) \qquad (2)$$

where B_s and B_c are the ratios of surface and Coulomb energies respectively, to those of the compound sphere and E is expressed in units of surface energy of the compound sphere.

We decided to present the results of our calculations of E in the form of the sets of two-dimensional plots $E = E(\sigma, D)$, for definite values of asymmetry A and x. An example of such a plot for A = 0.2 and x = 0.7 is shown on Fig. 3.

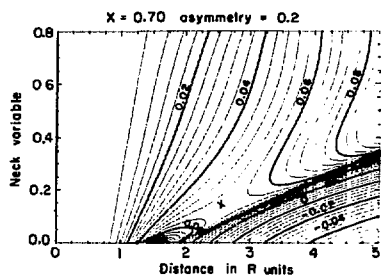

Fig. 3. Plot of potential energy surface for asymmetry A = 0.2 and fissionability parameter x = 0.7.
(XBL 757-3501)

The distance between the sphere's centers D is expressed in units of the radius R of the compound sphere. The saddle point for fission was indicated by x. The big mountain around $\sigma = 0$ and $D \approx 1.55$ corresponds to the barrier for fusion in head-on collisions of two nuclei. Looking at this plot, one could make the first estimate as to what the probability of the compound system formation in head-on collisions is, and at the same time what the competition of fission process is. It is obvious, that in order to make this last estimation one should have the whole set of plots for all different values of asymmetry A at fixed x, as the fission process may lead to other more energetically convenient values of asymmetry. Besides, to answer the questions of fusion probability and fusion-fission competition more precisely the problem of dynamics should be solved.

Nevertheless, it is hoped, the calculations of the potential energy surfaces presented here will be helpful to experimentalists as a guide for determining values of potential energies in various heavy ion experiments, while they should also be a base for further theoretical considerations.

Footnote

*On leave from Institute of Nuclear Research, Poland.

A SIMPLE MODEL FOR DEEP-INELASTIC HEAVY ION SCATTERING

F. Beck*

INTRODUCTION

The occurrence of highly inelastic direct scattering in heavy ion reactions well above the Coulomb barrier represents a new and outstanding gross feature of such reactions: when summed over relatively narrow distributions of charge- and mass-transfers in the reaction products the deep inelastic events peak at a (kinetic) energy-loss of the order of 100 MeV, well separated from the quasi elastic scattering. In some cases there is also a peaking in the angular distribution at a scattering angle somewhat smaller than the grazing angle.[1-4]

It has been pointed out by several authors[5] that heavy ion reactions well above the Coulomb barrier can be treated in a classical approximation. Quantum corrections to the so derived classical cross sections then show up in typical oscillations, or in rainbow scattering, in regions where the classical trajectories vary strongly with the impact parameter. They can be treated in a semiclassical way by amending the classical trajectories with WKB phases and constructing a scattering amplitude.[6,7] In deep inelastic heavy ion scattering, however, one sums over a large member of reaction channels, and quantum effects wash out completely. Thus a purely classical treatment, in terms of a classical deflection function $\vartheta(b)$, seems sufficient, from which the scattering cross section is derived according to

$$\frac{d\sigma}{d\Omega} = \frac{b}{\sin\vartheta} \cdot \left|\frac{db}{d\vartheta}\right| . \qquad (1)$$

In such a description the inelasticity is introduced by assuming, in addition to the conservative Coulomb and nuclear forces, a friction force representing statistically the transfer of kinetic energy to internal excitations of the reaction partners.

The heavy ion reaction cross sections have been studied in a classical dissipative treatment by several authors.[8-11] The models discussed so far are characterized by (a) a rather strong nuclear attraction inside the Coulomb barrier (of the order of the nucleon-nucleus potential), (b) a friction form-factor which peaks in the nuclear surface, and, in one case,[8] extends well to separation distances outside the nuclear interaction region and (c) the same forces are assumed for the entrance and exit channels. The deep inelastic events are then attributed to "negative angle scattering", and the cross section rises continuously to the quasi-elastic peak near the grazing angle. Thus in this form the model is unable to separate the deep inelastic scattering in energy or angular distribution from the quasi elastic scattering, contrary to the observations.

In the schematic calculation reported here no precise fit to experimental data is intended. The emphasis lies rather in employing a fairly simple, analytically solvable, scattering problem, and to study the influence of various assumptions about the nuclear interactions. On the other hand, the model is flexible enough to include, and to vary, the main qualitative features of the conservative and dissipative forces along a prescribed trajectory in the entrance and exit channels of heavy ion collisions.

The Scattering Model

The schematic model is characterized by three features which differ to some extent from previous calculations: (a) the interactions and interaction radii differ in the entrance and exit channels. Bondorf[12] already pointed out that the formation of a neck has to be expected in heavy ion scattering forming a strongly interacting contact area which allows considerable mass-, charge-, and energy-transfer between reaction partners.[13] (b) The interaction potential for heavy ions inside the touching radius is shallow due to the strong Coulomb repulsion and may even become repulsive in the density overlap region. (c) Energy dissipation is only present in the interaction region. Thus the friction force is exactly zero before touching in the entrance channel and after scission in the exit channel.

For the sake of generating analytically simple soluble equations of motion the potentials $V(r)$ of the conservative forces $F^C(r)$ are either step potentials or vary $\sim r^{-1}$ (modified Coulomb potentials; r is the distance between centers of gravity of the two fragments).

The friction is assumed to be purely radial and the corresponding force is

$$F^d(r) = -\lambda \sqrt{8\mu}\, \frac{1}{r^2}\frac{dr}{dt}; \quad \mu = \frac{M_1 M_2}{M_1+M_2} \qquad (2)$$

in the regions where dissipation is present. The choice of the friction form factor $\sim r^{-2}$ is again dictated by practical arguments of solubility may be even not so unphysical. The practical action of that force is anyhow restricted to the nuclear surface (cf. Fig. 5).

With these assumptions four radial regions can be defined:

Region I: Entrance channel: $r_{in} > R_i$

$$V(r) = \frac{q^2}{r}\ ;\ q^2 = Z_i Z_2 e^2$$
$$F^d = 0$$

Region II: Entrance channel: $R_i < r_{in} < R_c$

$$V(r) = f_{ni}\frac{q^2}{r} + c_i$$
$$F^d(r) = -\ \lambda_i \sqrt{8\mu}\, \frac{1}{r^2}\frac{dr}{dt}$$

Region III: Exit channel: $R_c < r_{out} < R_{sc}$

$$V(r) = f_{ni}\frac{q^2}{r} + c_o$$

$$F^d(r) = -\lambda_o\sqrt{8\mu}\,\frac{1}{r^2}\,\frac{dr}{dt}$$

Region IV: Exit channel: $r_{out} > R_{sc}$

$$V(r) = \frac{q^2}{r}$$

$$F^d = 0$$

The substitutions $d\theta = [L/mr^2]\cdot dt$, which follows from the integration of the tangential equation (L = const, no tangential friction!), and $Y(\theta) = 1/r(\theta) + \mu\cdot f_{ni}\cdot q^2/L^2$ lead to the radial equation in the form (prime denotes differentiation with respect to θ)

$$Y'' - 2\,\frac{\lambda}{b\cdot E_{cm}^{1/2}}\,Y' + Y = 0 \qquad (3)$$

which has solutions in terms of elementary functions. The total scattering solution results from continuation of the individual solutions through regions I - IV.

Choice of Potential Parameters

The two deep inelastic scattering experiments that have been discussed in most of the theoretical work so far are chosen also in this calculation as a basis for comparison:

(A) $^{84}Kr + ^{209}Bi$ at $E_{cm} = 374$ MeV[3,4]

(b) $^{40}Ar + ^{232}Th$ at $E_{cm} = 331$ MeV[1] .

The radius parameters R_i, R_{sc} and the potential steps at $r = R_i$ were taken from a liquid drop calculation of nuclear energies including a neck degree of freedom.[14] The liquid drop parameters are those given by Myers and Swiatecki at the Lysekill Conference.[15] In addition to this a repulsive core was introduced to represent the increase in energy where the densities overlap strongly. It consists of an adjustable soft core and a hard core at $r = R_c$.

The resulting model potentials are shown in Figs. 1 and 2, respectively, for the two compound systems, and for three different choices of the soft core strength.

Results

The results of the model calculation are presented in Figs. 3 to 7. The deflection functions (Figs. 3 and 6) show that the assumptions in this model lead to a separation of the deep inelastic peak from the quasi-elastic scattering. The discontinuity in the deflection functions near the grazing impact parameter results from the discontinuity in the potential at $r = R_1$.

The cross sections show in the Kr case a pronounced angular peaking below the grazing angle

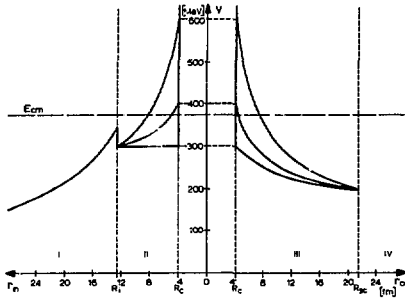

Fig. 1. Potentials of the conservative force in the regions I - IV for the system $^{84}Kr + ^{209}Bi$ and three different choices of the soft core (V_{R_c} = 300, 400, 600 MeV, resp.). The entrance channel coordinate, r_{in}, is plotted to the left, the exit channel coordinate, r_{out}, to the right. (XBL 745-829)

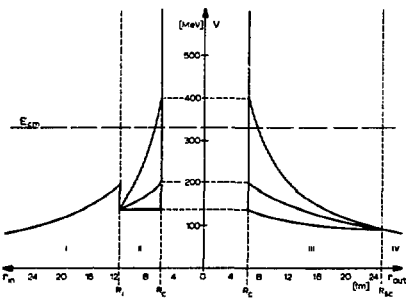

Fig. 2. The same as Fig. 1 for the system $^{40}Ar + ^{232}Th$. (XBL 754-828)

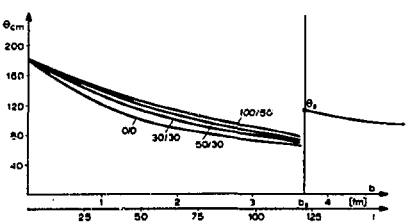

Fig. 3. Deflection functions $\Theta(b)$, resp. $\Theta(\ell)$ with $\ell = 2\cdot b$) for the system $^{84}Kr + ^{209}Bi$ at E_{cm} = 374 MeV. The parameters are the friction constants λ_i/λ_0 in units $MeV^{1/2}\cdot fm$. The soft core has the value V_{R_c} = 400 MeV. (XBL 754-827)

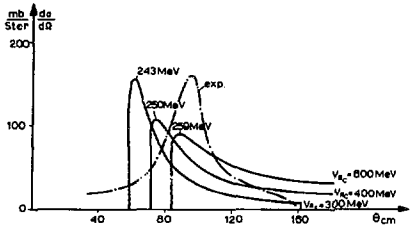

Fig. 4. Differential cross section for deep inelastic scattering; $^{84}Kr + ^{209}Bi$ at E_{cm} = 374 MeV. λ_i = 100 $MeV^{1/2}.fm$, λ_0 = 100 $MeV^{1/2}.fm$. The cross section is plotted for different strengths of the soft core and the final energies at the peak value are also indicated. The dot-dashed curves give the experimental results, ref.3). (XBL 754-826)

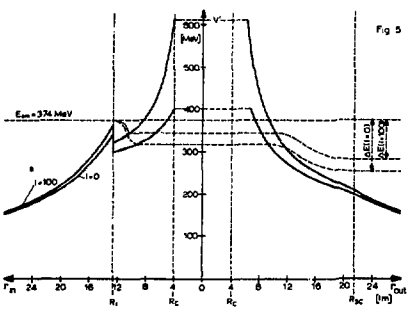

Fig. 5. The effective potential $V'(r) = V(r) + \hbar^2 l^2/2\mu r^2$ for two differents values of $l(=L/\hbar)$ and the energies of the corresponding trajectories. The origin of the focussing and the importance of the difference in the entrance and exit channel potentials for a relatively small spread in the energy loss can be seen from this picture. The example is $^{84}Kr + ^{209}Bi$. (XBL 754-825)

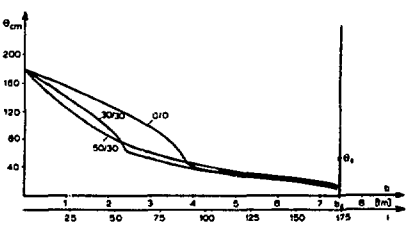

Fig. 6. The same as Fig. 3 for the $^{40}Ar + ^{232}Th$ reaction at E_{cm} = 331 MeV; V_{R_c} = 200 MeV. (XBL 754 824)

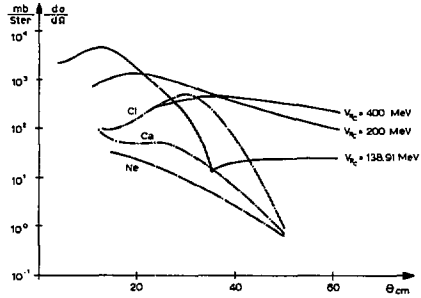

Fig. 7. The same as Fig. 4 for $^{40}Ar + ^{232}Th$. E_{cm} = 331 MeV; λ_i = 50 $MeV^{1/2}.fm$, λ_0 = 30 $MeV^{1/2}.fm$. The experimental cross sections are given for selected reaction products. (XBL 754-823)

while in the Ar + Th system the peak has moved to forward angles and is no longer pronounced. No negative angles are involved in the scattering, due to the rather shallow nuclear potentials resulting from the liquid drop fit.

The observed inelasticity can be achieved by fixing the friction constant to the weak friction case (in the terminology of Bondorf et al.[9]). The friction force (2) can be written in the form

$$F^d(r) = -\lambda \frac{\sqrt{8\mu c^2}}{R_i^2} \left(\frac{R_i}{r}\right)^2 \frac{v_r}{c} . \qquad (4)$$

For $v_r \simeq 0.05.c$ (at the Coulomb barrier), and $r = R_i$ one has the following correspondence in the Kr + Bi case

$$\lambda = 50\ MeV^{1/2} \cdot fm \leftrightarrow F^d(R_i) \simeq 10\ MeV/fm$$

$$\lambda = 250\ MeV^{1/2} \cdot fm \leftrightarrow F^d(R_i) \simeq 51\ MeV\ fm .$$

The employed friction force constants are all in the range 30 $MeV^{1/2}fm \leq \lambda \leq 100\ MeV^{1/2}.fm$.

Conclusion

The schematic model that was investigated here shows that the characteristic features of deep inelastic heavy ion scattering can qualitatively be reproduced if a difference between entrance and exit channels together with the rather shallow nuclear potentials expected for heavy ions because of Coulomb and density overlap effects are employed.

In contrast to purely elastic scattering where the interior region is masked by strong absorption in the surface, deep inelastic heavy ion

scattering offers a unique experimental tool to investigate the nuclear potential energy landscape in the vicinity of the fusion-fission valley.

Footnote and References

*On leave from Institut für Kernphysik, Technische Hochschule Darmstadt, 61 Darmstadt, Germany.

1. A. G. Artukh, G. F. Gridney, V. L. Mikheev, V. V. Volkov, and J. Wilczynski, Nucl. Phys. A215 91 (1973).

2. M. Lefort, C. Ngo, J. Peter, and B. Tamain, Nucl. Phys. A216 166 (1973).

3. F. Hanappe et al., Proc. Int. Conf. on Reactions between Complex Nuclei, Vol. 1, North-Holland (1974) p. 116.

4. J. Huizenga, Talk presented at the GSI Seminar, Darmstadt (1974).

5. For a discussion of this approximation see, for example, R. A. Broglia and A. Winther, Physics Reports 4, 153 (1972).

6. K. W. Ford and I. A. Wheeler, Ann. Phys. (N.Y.) 7, 259, 287 (1959).

7. W. H. Miller, Advan. Chem. Phys. 25, 69 (1974).

8. D. H. E. Gross and H. Kalinowski, Phys. Lett. 48B 302 (1974).

9. J. P. Bondorf et al., Preprint, Copenhagen (1974).

10. C. F. Tsang, LBL-2028 (1974).

11. J. R. Nix, private communication (1975).

12. J. P. Bondorf, Proc. Int. Conf. on Reactions between Complex Nuclei, North-Holland (1974).

13. W. Nörenberg, Report to the Int. Workshop on Gross Properties of Nuclei and Nuclear Excitations, Hirschegg (1975).

14. J. Blocki and W. J. Swiatecki, this Annual Report, and private communication.

15. W. D. Myers and W. J. Swiatecki, Arkiv Fysik 36 343 (1967).

THEORETICAL ESTIMATES OF SPONTANEOUS-FISSION HALF-LIVES FOR SUPERHEAVY ELEMENTS

J. Randrup, S. E. Larsson,* P. Möller,*
A. Sobiczewski,† and A. Tuksiak†

Introduction

The first extensive and realistic estimates of the stability of super-heavy elements (SHE) was given by the Berkeley-Lund-Warsaw group[1,2] in 1968 on the basis of the modified-oscillator (M.O.) model. Since then, many other calculations (which we do not attempt to review here) have been made on the stability of this region of nuclei. In particular, we may refer to similar studies made by Fiset and Nix[3,4] using the Folded-Yukawa (F.Y.) single-particle model and by Brack et al.[5] using a Woods-Saxon type of potential. These calculations suggest considerably longer half-lives than those of Refs. 1 and 2.

Progress has been made on several crucial points involved in such calculations. Firstly, the description of the smooth macroscopic part of the deformation energy is now more detailed and has reached a higher degree of sophistication in the recently developed shape-dependent droplet model of Myers and Swiatecki.[6] Secondly, detailed studies[7,8] of the fluctuating microscopic-correction energy have now established that the fission of SHE may proceed through axially asymmetric shapes with a corresponding reduction of the fission barrier by up to a few MeV. As an alternative to a multi-dimensional barrier-penetration treatment, considered by Pauli[9] and Szymański,[10] we have taken a semi-empirical approach to the problem. In an earlier study we found that the observed spontaneous-fission half-lives could be well reproduced in terms of such an approach,[11,12] and it is believed that such a method which appears reliable just outside the presently known actinide region may also be used for an extrapolation to the superheavy region.

These developments make it desirable to reconsider the stability question for the SHE's. Furthermore, it has been realized that the single-particle potential parameters, in particular the spin-orbit coupling strength used in the original study,[1,2] probably should be slightly modified also to account for information from the spherical Pb region. In the present calculations the spontaneous-fission half-lives are calculated on the basis of the recently introduced semi-empirical approach[11] with the smooth inertial-mass function refitted as in Ref. 12.

Calculation of Fission Barriers

The calculations have been carried out within the framework of the M.O. model, as described in Ref. 7. However, we have here considered two alternative sets of single-particle potential-parameters. One is the conventional "A = 298" set of Ref. 2 (here denoted by SPL-1) based on a linear extrapolation through known deformed regions while the other set (SPL-2) corresponds to a somewhat reduced spin-orbit coupling strength as the spherical Pb region indicates.[13] We have investigated a

spin-orbit coupling strength κ reduced by 15% with $\mu' = \kappa\mu$ fixed). See Table 1. Calculations based on the previous parameter set are given for comparison. For the macroscopic part of the energy we use the shape-dependent droplet model with the newly determined values of the coefficients.[6]

Table 1. Alternative single-particle potential-parameters for the superheavy region of nuclei.

	κ_p	μ_p	κ_n	μ_n
SPL-1	0.0534	0.686	0.0634	0.256
SPL-2	0.0454	0.807	0.0539	0.301

Spherical Shape. Since the superheavy region largely consists of near-spherical nuclei, the subshells corresponding to purely spherical shapes deserve particular attention. Figure 1 displays the proton and neutron single-particle levels for the two alternative parameter sets SPL-1 and SPL-2. For the protons the Z = 114 gap is slightly reduced in going from SPL-1 to SPL-2 due to the reduced 2f and 1i spin-orbit splittings. For neutrons the main effect is the opposite one. A decrease in κ actually increases the N = 184 gap as the $h_{11/2}$ state is raised. The N = 184 gap thereby becomes more pronounced at the expense of the N = 196 gap. The resulting spectra, both for neutrons and protons, are more similar to those obtained by Fiset and Nix[3] in the F.Y. model. The extracted microscopic-correction energies are displayed in Fig. 2. The shape of the superheavy island is mainly determined by these ground state energies.

Deformed Shapes. We now proceed to study the potential energy for deformed shapes. Single-particle levels are calculated in the $(\varepsilon,\varepsilon_4)$ plane in a 90-point grid: $\varepsilon = -0.05(0.05)0.80$, $\varepsilon_4^* = -0.08(0.04)0.08$ where $\varepsilon_4^* = \varepsilon_4 + \frac{0.11}{0.85}\varepsilon$. Deformation-energies are determined by means of the Strutinsky shell-correction method[13,14] The pairing strength G is assumed independent of deformation.

From the deformation-energy surfaces we construct one-dimensional fission-barriers by smoothly joining the minima and saddle points with polynomials of degree three. These polynomials are calculated as functions of r, the center-of-mass separation coordiante. One or more additional points beyond the last barrier peak are also used in the construction of the fission barriers (this procedure is described in Ref. 11). These barriers are subject to corrections, taken from Ref. 8, due to the axial-asymmetry degree of freedom. The resulting fission barrier heights, with corrections from ε_4 and γ included,[8] are displayed in Fig. 3.

Inertial-Mass Parameters. The spontaneous-fission decay, in parallel with the alpha decay mode, plays a decisive role in determining the total half-lives for the SHE's. We have employed two alternatives for the calculation of spontaneous-fission half-lives. Rather than taking an average value of the inertial-mass parameter B, we have considered the deformation dependence.

The hydrodynamical method, based on the use of a smooth semi-empirically determined inertial-mass function, was found to give very satisfactory

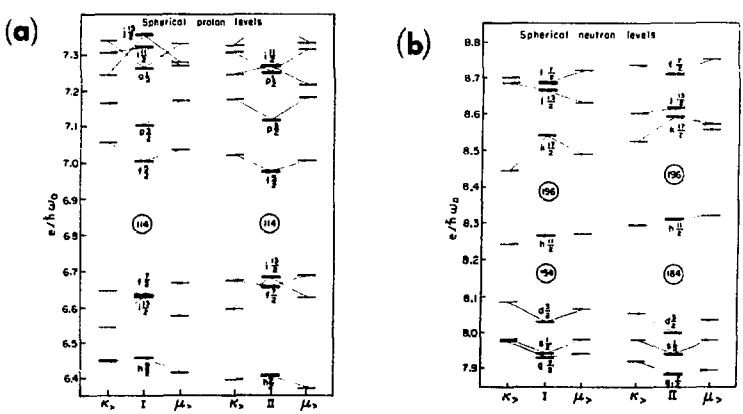

Fig. 1. Single-particle levels for spherical shape. Left-hand sides are obtained with the parameter choice SPL-1 and the right-hand sides with SPL-2. Independent variations of the parameters κ and μ have been performed. The levels labeled $\kappa_>$ correspond to a 10% increase in κ (keeping μ fixed) and $\mu_>$ indicates a similar 10% increase of μ with κ fixed.
(XBL 743-2729, XBL 743-2728)

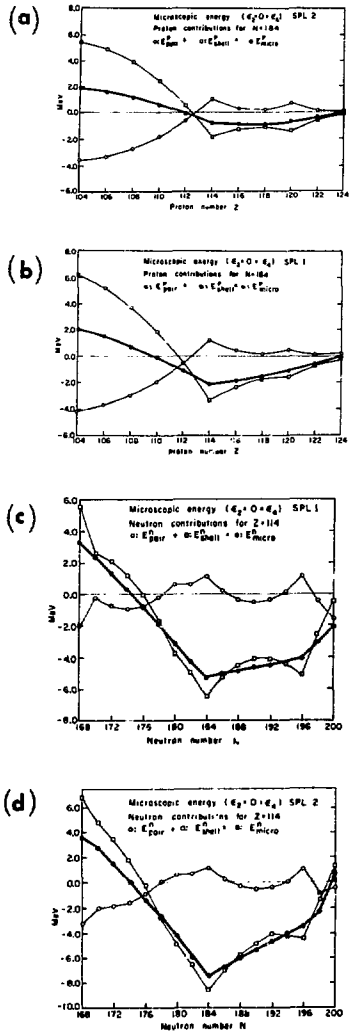

Fig. 2. Microscopic-correction energies as composed of the pairing-correction energies and the Strutinsky shell energies. These energies have a rather smooth A dependence.
(XBL 743-2723,XBL 743-2724, XBL 743-2725, XBL 743-2727)

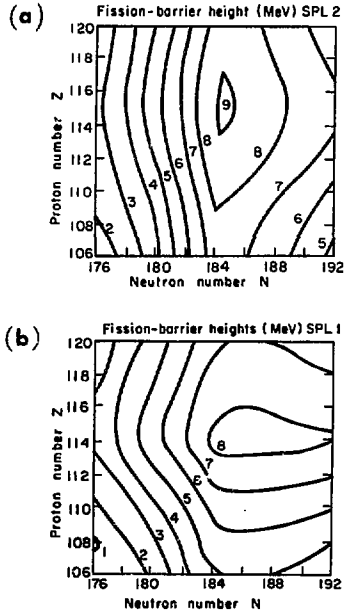

Fig. 3. Fission barrier heights (in MeV), according to the sets SPL-1 and SPL-2, with the axial-asymmetry correction included.
(XBL 743-2733,XBL 743-2734)

results in the actinide region. Actually, the spontaneous-fission half-lives were there reproduced to within a factor of 80 on the aver e.[12]

In this semi-empirical approach the inertial-mass function is assumed to be described by the following expression

$$B_r = \left[1 + k \frac{17}{15} e^{-(r-\frac{3}{4}R_0)/d} \right]. \qquad (1)$$

The inertial mass is defined in terms of the center-of-mass separation coordinate r. Furthermore, μ is the reduced mass of the two-fragment system and d the fall-off parameter indicated by irrotation-flow calculations. In a recent investigation for the actinides the factor k was determined from a fit to the half-life data as $k = 10.0$. This k-value is assumed to hold for the SHE's as well.

As is shown in Ref. 11 a relatively good reproduction of the actinide fission half-lives may

be obtained by using microscopically calculated inertial-mass parameters renormalized through one common a posteriori common factor (of around 0.8). A preliminary estimate indicates that the predicted fission half-lives in the superheavy region calculated by use of the microscopic inertias renormalized, by a factor 0.8, differ from those calculated by use of the semi-empirical inertias by less than a factor 100. A more detailed calculation based on the microscopic inertias is in progress.

Results and Discussion

In summary, the following conclusions can be drawn: 1) The shape of the superheavy island depends extensively on the single-particle parameter set used and considerably less on which of the two alternative inertias is used for the calculation of the half-lives. 2) For SPL-1 the island extends "eastwards" or towards N-values in excess of N = 184, as a consequence of the significant N = 196 gap while the SPL-2 results (see Figs. 3 and 4) exhibit a larger similarity with the results of Ref. 3. In fact, the island exhibits a rather strong alignment along N = 184. 3) When comparing the half-lives based on the use of the extrapolated smooth inertias with those based on microscopic calculations we find in a preliminary estimate that they differ by less than a factor 100. This discrepancy may be taken as a measure of the uncertainty in the theoretical half-life estimates. 4) The SPL-1 half-lives are around four orders of magnitude shorter than the SPL-2 results in the island center.

The (in our opinion) most reliable fission half-life estimate, based on the single-particle scheme SPL-2, and the semi-empirically calculated inertia values predicts for $^{298}114$ a fission half-life of 10^8 years. These half-lives are somewhat shorter than the previous estimates of Nilsson et al.[2,16,17] and in particular Nix et al.[3,4] and Brack et al.[5] Part of these differences is due to the inclusion of the γ-corrections which reduces the barrier heights by 1-2 MeV.

In the superheavy region the alpha process is a progressively important competing mode of decay. From the calculated ground-state energies the alpha half-lives may be estimated.[19] The combined alpha and fission half-lives are shown in Fig. 4. The decrease in alpha stability with increasing Z has the consequence that the nucleus with the longest total half-life is $^{294}110$ rather than $^{298}114$ with a total half-life of 10^5 years.

Accepting the present calculations at their face value, it appears excluded that one should be able to find SHE's in terrestial matter.

Two recently studied effects, not included in these calculations, appear to work in the direction to increase the half-lives. One represents the Coulomb shell-corrections associated with the non-homogenous charge distribution. The other derives from the inclusion of non-isotropic terms in the pairing matrix elements. These effects are expected to adjust the estimates somewhat upward (see Ref. 20) in the vicinity of $^{298}114$.

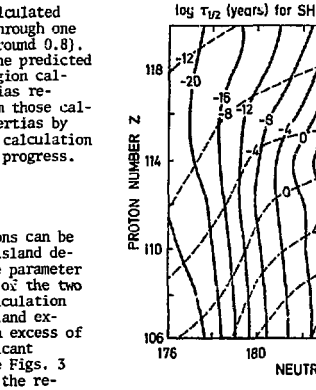

Fig. 4. Combined diagram of half-lives with respect to spontaneous fission and alpha decay, as obtained for the parameter set SPL-2 with the semi-empirical fission inertial-mass function and the alpha half-life formula of Taagepera and Nurmia.[19]

Footnotes and References

*Department of Mathematical Physics Lund Institute of Technology Lund, Sweden

†Institute for Nuclear Research Hoza 69 Warsaw, Poland.

1. S. G. Nilsson, J. R. Nix, A. Sobiczewski, Z. Szymański, S. Wycech, C. Gustafson, P. Möller, Nucl. Phys. A115, 545 (1968).

2. S. G. Nilsson, C. F. Tsang, A. Sobiczewski, Z. Szymański, S. Wycech, C. Gustafson, I.-L. Lamm, P. Möller, and B. Nilsson, Nucl. Phys. A131, 1 (1969).

3. E. O. Fiset and J. R. Nix, Nucl.Phys. A192, 647 (1972).

4. J. R. Nix, Ann. REv. Nucl. Sci. 22 (1972).

5. M. Brack, J. Damgaard, A. S. Jensen, H. C. Pauli, V. M. Strutinsky, and C. Y. Wong, Rev. Mod. Phys. 44, 320 (1972).

6. W. D. Myers, and W. J. Swiatecki, Ann. of Phys. 55, 395 (1970); Berkeley Preprint LBL-1937 (1973) to be published.

7. S. E. Larsson, and G. Leander, Physics and Chemistry of Fission, IAEA, Rochester, 1973.

8. S. E. Larsson, P. Möller, and S. G. Nilsson, Contribution to this Symposium.

9. H. C. Pauli, Contribution to this Symposium.

10. Z. Szymański, Contribution to this Symposium.

11. J. Randrup, C. F. Tsang, P. Möller, S. G. Nilsson, and S. E. Larsson, Nucl. Phys. A217, 221 (1973).

12. J. Randrup, S. E. Larsson, and A. Sobiczewski, to be submitted to Phys. Rev. C, 1974.

13. V. M. Strutinsky, Nucl. Phys. A95, 420 (1967).

14. V. M. Strutinsky, Nucl. Phys. A122, 1 (1968).

15. A. Sobiczewski, Z. Szymanski, S. Wyceck, S. G. Nilsson, J. R. Nix, C. F. Tsang, C. Gustafson, P. Möller, and B. Nilsson, Nucl Phys. A131, 67 (1969).

16. C. F. Tsang, and S. G. Nilsson, Nucl. Phys. A140, 289 (1970).

17. T. Johansson, S.G. Nilsson, and Z. Szymański, Ann. Phys. 5, 377 (1970).

18. I. Ragnarsson, and S. G. Nilsson, private communication, 1973.

19. B. Taagepera, and M. Nurmia, Ann. Acad. Sci. Fennicab, ser. A VI, 78, 1 (1961).

10. S. E. Larsson, G. Leander, and I. Ragnarsson, Contribution to this Symposium.

STUDIES IN THE SUPERFLUID ENHANCEMENT OF FISSION BARRIER PENETRATION

L. G. Moretto, R. P. Babinet, and J. J. Sventek

A description of some preliminary work in this area has been already published. After a brief review, we wish to describe extensions which have been made.

We are attempting to determine the effect of the pairing interaction on the penetrability of fission barriers in the WKB approximation. It is well known that the gap parameter Δ is usually determined by minimizing the expectation value of the BCS Hamiltonian with respect to Δ:

$$\frac{\partial \langle H \rangle}{\partial \Delta} = 0. \tag{1}$$

Equation 1 is usually referred to as the Gap Equation. The gap parameter is then a constant Δ_0 which characterizes the stationary nucleus. When dealing with barrier penetration, the assumption of constant Δ_0 is no longer valid, since the penetrability is determined from a dynamical principle (the Least Action Principle), while the value of Δ_0 was determined from static considerations. It seems that the gap parameter Δ should be defined *in the framework* of the more general dynamical principle.

In the WKB approximation, the penetrability is given by $P = \exp(-2S/\hbar)$. The action integral S is given by:

$$S = \int_a^b \sqrt{2B(V-E)}\, d\alpha \tag{2}$$

where α is the deformation coordinate, a and b are classical turning points, B is the inertia associated with the coordinate α, V is the potential energy, and E is the total energy. This expression depends upon the gap parameter Δ through both the inertia B and the potential V.

The Least Action Principle requires that the path taken by the system in getting from point a to point b be such that S is an extremum, i.e., $\delta S = 0$. In our case, S will be a minimum.

Our task is to find the path $\Delta(\alpha)$ that minimizes Eq. (2), which can be formally rewritten as:

$$\int_a^b F(\Delta(\alpha),\ \dot{\Delta}(\alpha), \alpha)\, d\alpha \tag{3}$$

where $\dot{\Delta}(\alpha) = \frac{d\Delta(\alpha)}{\alpha}$. The differential equation for $\Delta(\alpha)$ that minimizes Eq. (3) is:

$$\frac{d}{dt}\left(\frac{\partial F}{\partial \dot{\Delta}}\right) - \frac{\partial F}{\partial \Delta} = 0. \tag{4}$$

This is Euler-Lagrange Differential Equation well known in the calculus of variations. In our particular case,

$$F = \sqrt{2(B_{\alpha\alpha} + 2\, B_{\alpha\Delta}\dot{\Delta} + B_{\Delta\Delta}(\dot{\Delta})^2)(V-E)},$$

where the $B_{i,j}$'s are the elements of the inertia tensor, each of which depends upon α and Δ, as does V. After carrying out the necessary straightforward algebra in Eq. 4, we get the following differential equation for Δ:

$$0 = f_1(\alpha,\Delta)\, \ddot{\Delta} + f_2(\alpha,\Delta)\, (\dot{\Delta})^3 + f_3(\alpha,\Delta)\, (\dot{\Delta})^2 + f_4(\alpha,\Delta)\, \dot{\Delta} + f_5(\alpha,\Delta) \tag{5}$$

where

$$f_i(\alpha,\Delta) = \begin{cases} 2\epsilon(ac-b^2) & i=1 \\ \epsilon(bc_\Delta - 2cb_\Delta + cc_\alpha) - \epsilon_\Delta bc + \epsilon_\alpha c^2 & i=2 \\ \epsilon(ac_\Delta - 2bb_\Delta - 2ca_\Delta + 3bc_\alpha) - \epsilon_\Delta[2b^2+ac] + 3\epsilon_\alpha bc & i=3 \\ \epsilon(-ca_\alpha + 2bb_\alpha + 2ac_\alpha - 3ba_\Delta) + \epsilon_\alpha[2b^2+ac] - 3\epsilon_\Delta ab & i=4 \\ \epsilon(-aa_\Delta + 2ab_\alpha - ba_\alpha) - \epsilon_\Delta a^2 + \epsilon_\alpha ab & i=5 \end{cases}$$

and $a = B_{\alpha\alpha}$, $b = B_{\alpha\Delta}$, $c = B_{\Delta\Delta}$, $\varepsilon = V\text{-}E$,

$$x_\alpha = \frac{dx}{d\alpha} \text{ and } x_\Delta = \frac{dx}{d\Delta} \text{ for } x = a,b,c, ,$$

$$\ddot{\Delta} = \frac{d^2\Delta}{d\alpha^2}, \quad \dot{\Delta} = \frac{d\Delta}{d\alpha}.$$

Once we know the functional forms of $B_{\alpha\alpha}$, $B_{\alpha\Delta}$, $B_{\Delta\Delta}$, and V on α and Δ, we can solve the differential equation by the normal numerical methods after we specify the value of Δ at the two endpoints. When considering spontaneous fission, it would seem reasonable that the value of Δ when the fissioning system enters and leaves the barrier should be the one determined by the Gap Equation, Δ_0.

For the calculations below the following forms have been used:

$$B_{\alpha\alpha} = \frac{k_\alpha}{\Delta^2}, \quad B_{\Delta\Delta} = \frac{k_\Delta}{\Delta^2}, \quad B_{\nabla\Delta} = 0,$$

$$V(\alpha,\Delta) = V_0(\alpha) + g(\Delta-\Delta_0)^2.$$

The inertias have been obtained from the cranking model and the potential has been approximated to second order in $(\Delta-\Delta_0)$.

In Fig. 1 a single-humped potential barrier $V_0(\alpha)$, and the corresponding $\Delta(\alpha)$ from solving Eq. 5 are shown. The value of Δ is quite enhanced as we proceed into the barrier, and the corresponding enhancement of the penetrability over that when Δ is constant is approximately a factor 10^9. Figure 2 shows a barrier similar to that of an actinide nucleus, and the corresponding $\Delta(\alpha)$ from Eq. 5. The gap parameter tends to follow the general form of $V_0(\alpha)$. In this case, the penetrability is enhanced approximately by a factor of 10^{13} over that obtained when Δ is a constant.

The code used to solve Eq. 5 is now used with the potential energies and mass parameters calculated from a Nilsson Hamiltonian including pairing and with the Cranking model expressions for the mass parameters. Further studies of the type of enhancement in barrier penetrability described here are planned for these more realistic potentials and mass parameters.

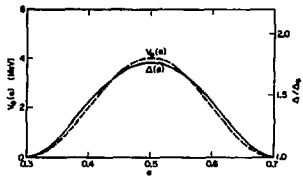

Fig. 1. Single-humped fission barrier and dynamical value of the gap parameter as a function of deformation. (XBL 752-2379)

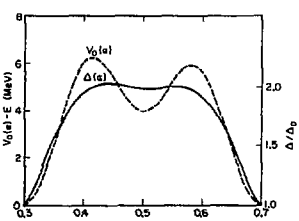

Fig. 2. Double-humped fission barrier and dynamical value of the gap parameter as a function of deformation. (XBL 752-2380)

References

1. L. G. Moretto and R. P. Babinet. Large superfluidity enhancement in the penetration barrier, Phys. Lett. 49B 147 (1974).

A THEORETICAL APPROACH TO THE PROBLEM OF PARTIAL EQUILIBRATION IN HEAVY ION REACTIONS

L. G. Moretto and J. S. Sventek

The present work is concerned with explaining the observed features of the "relaxed" or "deep-inelastic" cross section observed in heavy ion reactions by many groups.[1-3] The main features of this large fraction of the total reaction cross section are:

1) Fully relaxed kinetic energy spectra,
2) A mass-charge asymmetry distribution not wholly consistent with statistical equilibrium, and
3) Center-of-mass angular distributions which are forward peaked and whose forward peaking depends upon the distance in atomic number between the emitted fragment and the projectile.

These general features appear to be consistent with the following qualitative, three-step mechanism:

1. Promptly after the initial collision, friction brings the two nuclei to rest one with respect to the other, while the initial kinetic energy is dissipated into the internal degrees of freedom, leading to the formation of an intermediate complex of well-defined asymmetry.

2. A diffusion process leads to the exchange of particles between the two touching fragments, thus generating a time-dependent distribution in the asymmetry of the intermediate complex.

3. The complex decays randomly with a time constant comparable to or shorter than the rotational time.

The central aspect of the model is the diffusion of the intermediate complex along the asymmetry degree of freedom. The time-dependent-population $\phi_Z(t)$ of the macroscopic state whose asymmetry is characterized by the atomic number Z of one of the fragments, can be described by a Master Equation:

$$\dot{\phi}_z = \sum_{z'} (\Lambda_{zz'} \phi_{z'} - \Lambda_{z'z} \phi_z).$$

Using Golden Rule No. 2, we can express the macroscopic transition probabilities ($\Lambda_{zz'}$) in terms of the microscopic transition probabilities ($\lambda_{zz'}$) and the level density of the macroscopic states (ρ_z) as:

$$\Lambda_{zz'} = \lambda_{zz'} \rho_z .$$

The level density of the intermediate complex is a function of the excitation energy of the complex, which is equal to the total energy minus the potential energy necessary to form the intermediate complex. Due to the finite transfer rate between the two fragments in contact, the $\lambda_{zz'}$'s must obey some sort of a sum rule, and for lack of better knowledge, we assume

$$\lambda_{zz'} = \lambda_0 / [\rho_z \rho_{z'}]^{\frac{1}{2}} .$$

The level densities can be expanded as follows

$$\rho(E-V_z) = \rho(E) e^{-V_z/T}$$

where

$$T^{-1} = \left. \frac{d \ln \rho(x)}{dx} \right|_{x = E}$$

to give the final version of our Master Equation:

$$\dot{\phi}_z = \lambda_0 \sum_{z'} e^{(V_z + V_{z'})/2T} \left[\phi_{z'} e^{-V_z/T} - \phi_z e^{-V_{z'}/T} \right].$$

We assume that the sum over Z' is limited to $Z \pm 1$, since the temperatures commonly encountered (2 - 3 MeV) are sufficiently high to rule out 2nd and higher order correlations among transferred particles.

The potential energies V_z used are liquid drop potential energies for saddle point shapes of a given asymmetry. The potential energies are calculated by means of the liquid drop model using a rigid body moment of interia. Types of saddle point shapes considered to date include touching spheres, touching spheriods, and spheres connected by an hyperboloid of revolution. The diffusion constant λ_0 should be shape dependent, and we assume it to be proportional to the cross-sectional area of the neck through which particles are expected to diffuse.

For the initial part of the mechanism, we assume that after the collision, the target and projectile slip over each other by an angle θ_S, which is proportional to the tangential velocity at point of impact. The kinetic energy is dissipated as the slippage takes place. After the slippage, the complex rotates with the rigid moment of inertia.

In the final stage, we assume that, after a given contact time t, the fragment is emitted at an angle θ with a new $Z = Z_{exit}$. This information allows one to calculate the impact parameters b which satisfy these conditions. The final cross section is given by:

$$\frac{d\sigma_z}{d\Omega}(\theta) = \int_0^\infty \frac{dt}{T} e^{-t/T} \left\{ \sum \phi_z(b,t) \frac{bP(b)}{\left| \sin\theta \frac{d\theta}{db} \right|} \right\}$$

where T is the mean lifetime of the complex and the sum is carried over the aforementioned b values. The quantity P(b) or P(ℓ) represents the probability ($0 \leq P \leq 1$) that a given ℓ-wave will lead to a reaction of the kind we have described. It seems safe to assume that P(ℓ) will be substantially different from zero for rather large ℓ-waves, since the low ℓ-waves are certainly associated with the formation of a compound nucleus, and thus responsible for the evaporation residue cross section. The highest ℓ-waves are associated with direct or quasi-elastic cross sections. We have made the rather bold assumption that no sizeable amount of fission is present in the reaction cross section, since, for low ℓ-waves, the fission barrier is large and, for high ℓ-waves, the compound nucleus is not formed. We establish P(ℓ) from the experimental data.

Using this formalism, we have tried to fit the data for Ag + 288-MeV Ar. We have used a step function for P(ℓ), with slighly rounded edges, the lower bound defined by the evaporation residue cross section of 670 mb,[4] and the upper bound defined by the sum of the evaporation residue and relaxed cross sections, which is ~ 2000 mb.

Figure 1 is a plot of the potential energy, V_z, measured with respect to the rotating ground state, as a function of asymmetry (here specified by the Z of one fragment) for three representative ℓ-waves in the reaction $^{107,109}Ag$ + 288-MeV ^{40}Ar. The arrows show where the system starts, its diffusion along the mass asymmetry coordinate. It seems apparent that the system is more likely to

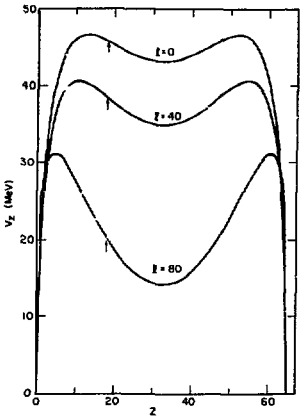

Fig. 1. Potential energy V_Z as a function of Z for the system $^{107,109}Ag + ^{40}Ar$. (XBL 752-2381)

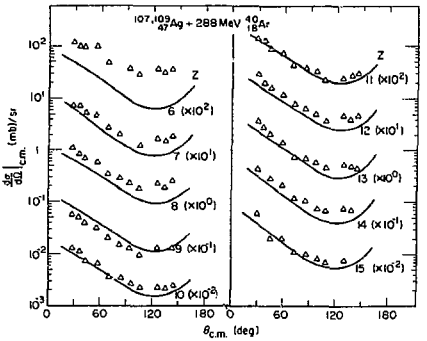

Fig. 2. Comparison of experimental cross section (Δ) with theoretial cross sections calculated for the system $^{107,109}Ag$ + 288 MeV ^{40}Ar. (XBL 752-2382)

diffuse towards symmetric fragments, and that this tendency is larger for higher ℓ-waves.

Figure 2 is a comparison of experimental relaxed cross sections (triangles) with the cross sections calculated using this theory. The values of the previously defined parameters that went into this calculation are: $T = 5 \times 10^{-21}$sec, $\lambda_0 = 30$ sec^{-1}, and $\theta_S = 70$. All the theoretical cross sections have been multiplied by a factor of three to achieve numerical agreement. It can be seen that the theory produces the right general trends in the angular distributions. The scaling that was necessary seems to be an artifact of the saddle point shape parameterization (two touching spheres). Preliminary results using spheres with an hyperboloid neck parameterization not only reproduce the shapes of the angular distribution, but also reproduce the absolute cross sections as well for similar values of the theoretical constants. These results will be published in the near future.

In summary, an attempt at describing the various stages of relaxation of the collective modes excited in heavy-ion reactions has been made using a Master Equation appraoch. The results are seen to be reasonable, and further work on this and other reaction systems is presently being pursued.

Refcrences

1. S. G. Thompson, L.G. Moretto, R. C. Hared, R. P. Babinet, J. Galin, M. M. Fowler, R. C. Gatti and J. B. Hunter, Nobel Symposium on Superheavy Elements, June 1974, Ronneby Brnun, Sweden (Lawrence Berkeley Laboratory Report LBL-2940, June 1974).

2. K. L. Wolf, J.P. Unik, J. R. Huizenga, V. E. Viola, J. Birkelund and H. Freiesleben, Phys. Rev. Lett. 33 1105 (1974).

3. F. Hanappe, M. Lefort, C. Ngo, J. Peter and B. Tamain, Phys. Rev. Lett. 32, 738 (1974).

4. H. H. Gutbrod, F. Plaisil, H. C. Britt, B. H. Erkkila, R. M. Stokes and M. Blann. Third Symposium on the Physics and Chemistry of Fission, August 1973, Rochester, N.Y., U.S.A., IAEA-SM-174/59.

STATISTICAL EMISSION OF LARGE FRAGMENTS – A GENERAL THEORETICAL APPROACH*

L. G. Moretto

A theory for the statistical emission of large fragments has been developed. In analogy with the fission saddle point, a ridge line is defined, which controls the decay width of the system into any given fragment. The normal modes at the ridge are classified into three classes: decay modes, amplifying modes, and non-amplifying modes. The amplification refers to the fact that the thermal fluctuations along an amplifying mode are amplified into a much broader kinetic energy distribution. Analytical expressions for the kinetic energy distributions are developed for various combinations of amplifying and non-amplifying modes. The limit for large amplifications is a Gaussian kinetic energy distribution. The limit for no amplification is a Maxwellian. Thus the formalism comprehends the fission decay on one hand and the neutron evaporation on the other. The angular distributions are evaluated in terms of the ridge-line principal moments of inertia. The analytical expression for the angular distribution predicts, correctly in both limits, the neutron evaporation and the fission angular distribution.

Footnote

*Condensed from LBL-3457.

THERMODYNAMICAL PROPERTIES OF A PAIRED NUCLEUS WITH A FIXED NUMBER OF QUASI-PARTICLES

L. G. Moretto

Introduction

The statistical properties of a system with a fixed number of excitations (quasi-particles) are of interest in the study of relaxation phenomena in nuclei. By far the widest use of these properties has been made in the description of pre-equilibrium emission of nucleons.[1-4] However, one can forecast a multiplicity of cases where the statistical properties of a fixed quasi-particle system may be of interest. For instance, in the description of the width of a doorway state (single particle or collective in nature), the coupling of such a state with a certain class of particle-hole states needs to be considered In systems with unrestricted quasi-particle number of the residual interaction is very important only at low energy.[5-8] In this paper it will oe shown that, at small quasi-particle numbers, the pairing correlation is present even at very high excitation energies and that it plays a dominant role during the relaxation process leading from a small quasi-particle number to its equilibrium value.

The Hamiltonian

In this paper we shall use the simplest form of a pairing Hamiltonian with constant pairing strength:

$$H' = \Sigma(\epsilon_k - \lambda - E_k) + 2\,\Sigma\, n_k E_k + \Delta^2/G,$$

where λ is the Lagrange multiplier introduced to fix the particle number; $n_k = b_k^\dagger b_k$ is the quasi-particle occupation number for the level k; E_k are the quasi-particle energy eigenvalues, and the quantity Δ, called pairing gap, is given by the equation

$$\frac{2}{G} = \Sigma \frac{1 - 2n_k}{E_k}.$$

In order to fix the mean number of quasi-particles we introduce a new auxiliary Hamiltonian:

$$H'' = H' - \xi Q$$

where ξ is the Lagrange multiplier necessary for this particular constraint.

Explicitly, the new Hamiltonian can be written as

$$H'' = \Sigma(\epsilon_k - \lambda - E_k) + \frac{\Delta^2}{G} + 2\,\Sigma\, n_k(E_k - \xi).$$

The Grand Partition Function obtained from the Hamiltonian H'' is:

$$\Omega = -\beta\,\Sigma\,(\epsilon_k - \lambda - E_k) - \beta\frac{\Delta^2}{G}$$

$$2\,\Sigma\,\ln[1 + \exp - \beta(E_k - \xi)]$$

From this expression, all the other thermodynamical functions can be obtained by differentiation.

Application of the Formalism to the Uniform Model

The model is completely described by the single-particle level density g, which defines the independent particle aspect of the problem and by the ground state gap parameter Δ_0, which defines the pairing residual interaction. A great advantage of this model is the fact that the particle

chemical potential λ is a constant due to the symmetry of the single-particle spectrum. Thus one can set $\lambda = 0$ and disregard the particle equation.

In the graphs presented from here on, the gap parameter will be expressed in terms of the ground state gap parameter Δ_0; the energy and free energy in units of the condensation energy

$C = \frac{1}{2} g \Delta_0^2$; the temperature in terms of the critical temperature $T_{cr} = 2\Delta_0/3.5$; the quasi-particle number in terms of the most probable quasi-particle number at the critical temperature $Q_{cr} = 4g\, T_{cr} \ln 2$; the entropy in terms of the entropy at the critical point $S_{cr} = 2(\pi^2/3) g\, T_{cr}$.

Limiting Properties for $T = 0$ $(\beta \to \infty)$

The Gap Equation. The gap equation in the uniform model can be rewritten as follows:

$$2g \int_0^S \frac{\tanh \frac{1}{2}\beta(E - \xi)}{E}\, d\varepsilon = \frac{2}{G} = 2g \int_0^S \frac{\tanh \frac{1}{2}\beta E}{E}\, d\varepsilon .$$

In the limit of $\beta \to \infty$ the following expression for the quasi-particle chemical potential is obtained in terms of Δ:

$$\xi = \frac{1}{2}\sqrt{\frac{\Delta}{\Delta_0}}\ (\Delta + \Delta_0).$$

The Quasi-Particle Equation. Similarly the quasi-particle number equation can be written as:

$$Q = 4g \int \frac{d\varepsilon}{1 + \exp \beta(E - \xi)} .$$

In the limit of $\beta \to \infty$ one obtains the following analytic result:

$$Q = 4g \sqrt{\xi^2 - \Delta^2}$$

or

$$Q = 2g \sqrt{\frac{\Delta}{\Delta_0}}\ (\Delta_0 - \Delta).$$

Discussion on the Phase Stability. Figure 1 shows that Δ is a triple valued function of Q (one trivial and two non-trivial solutions) in the interval $0 \le Q \le Q_{cr}$, where $Q_{cr} = \frac{4}{3\sqrt{3}} g\Delta_0$, and and it is single-valued $(\Delta = 0)$ for $Q > Q_{cr}$.

The larger solution starts at $\Delta = \Delta_0$ when $Q = 0$; it decreases as expected from this value down down to $1/3\ \Delta_0$ at $Q = Q_{cr}$. Similarly the smaller nontrivial solution starts at $\Delta = 0$ for $Q = 0$ and increases with increasing Q until it merges into the larger solution at $Q = Q_{cr}$.

This peculiar state of affairs must be resolved by deciding which of the three solutions is the stable one.

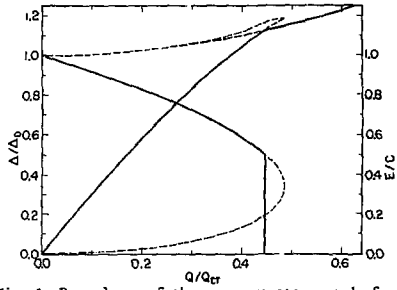

Fig. 1. Dependence of the gap parameter and of the energy E upon quasi-particle number Q at $T = 0$. The dashed lines correspond to the unstable solutions. (XBL 742-2400)

An immediate test on the two nontrivial solutions can be made by checking the sign of $\partial^2 H''/\partial\Delta^2$. If $\partial^2 H''/\partial\Delta^2$ is positive, then one has indeed a minimum, while a negative sign implies that the solution is a maximum.

The second derivative calculated at the equilibrium value of Δ, $\partial H''/\partial\Delta = 0$ is given by the following expression:

$$\frac{\partial^2 H''}{\partial \Delta^2} = 2g \left\{ 1 - 2\, \frac{\Delta_0 - \Delta}{\Delta_0 + \Delta} \right\}.$$

This expression vanishes for $\Delta = \Delta_0/3$, which is the value of Δ to which the larger and the smaller solutions converge. For values of Δ larger than $\Delta_0/3$ the second derivative is positive, thus indicating a stable solution. For values of Δ smaller than $\Delta_0/3$, the second derivative is negative and the solution is unstable.

The Energy Equation. At this point one must decide on which of the two remaining solutions, the paired or the trivial one $(\Delta = 0)$, is the stable solution. In order to determine such a point, one must inspect the energy equation.

In the limit of $\beta \to \infty$ and for the uniform model, the energy equation becomes

$$E^* = \frac{1}{2} g \left(\Delta_0^2 - \Delta^2 \right) \left(1 + \frac{\Delta}{\Delta_0} \right) \quad \text{for } \Delta > 0,$$

$$E^* = \frac{1}{2} g \Delta_0^2 + \frac{Q^2}{8g} \quad \text{for } \Delta = 0.$$

The Existence of a First-Order Phase Transition. In Fig. 1 the excitation energy is plotted as a function of the quasi-particle number. As the gap parameter Δ goes from Δ_0 to 0, the energy follows a loop. The stable solution is the one with the least energy. Therefore the loop must be bypassed. At the bypass point the curves for the paired and the unpaired energies cross. The bypass coordinates are:

$$\frac{\Delta_x}{\Delta_0} = \frac{1}{2}\,; \qquad Q_x = g\,\frac{\Delta_0}{\sqrt{2}}\,.$$

The excitation energy at the crossing is:

$$E_x = \frac{9}{8}\,\frac{1}{2}\,g\Delta_0^2 = \frac{9}{8}\,C,$$

where C is the pairing condensation energy.

In conclusion, for values of $Q < Q_x$ the paired solution is the stable one. At $Q = Q_x$, Δ goes abruptly from the value $\Delta_0/2$ to zero and it remains zero for any value of $Q > Q_x$.

On the Stability of the Aligned Configuration. A simple inspection of the equations indicates that for $T = 0$ the quasi-particles occupy the single-particle levels pairwise with opposite spin projections. One may wonder whether a configuration with one quasi-particle per level, like that occurring in the yrast line (aligned configuration), is more stable than the configuration described above (normal configuration).

The ratio between the number of quasi-particles necessary to give the same gap parameter in the two configurations is:

$$\frac{Q_{aligned}}{Q_{normal}} = \frac{1}{2}\left[\sqrt{\frac{\Delta_0}{\Delta}} + \sqrt{\frac{\Delta}{\Delta_0}}\right].$$

This ratio is always slightly larger than one in the interval $1 > \Delta/\Delta_0 \geq 0.5$, thus indicating that more quasi-particles are needed by the aligned configuration in order to obtain a given value of Δ.

The ratio of the energies for a fixed value of Δ is:

$$\frac{E_{aligned}}{E_{normal}} = \frac{1}{2}\,\frac{3\Delta_0^2 + \Delta^2}{\Delta_0(\Delta_0 + \Delta)}.$$

This ratio is also slightly larger than one for $1 > \Delta/\Delta_0 \geq 0.5$. The ratio of the energies at fixed Q is also larger than one in the same interval, thus proving that the aligned configuration never has the lowest energy at fixed Q.

Properties of the System for $T > 0$

Solution of the Gap Equation. The dependence of the gap parameter Δ upon the quasi-particle number Q at various temperatures can be determined by solving simultaneously the gap equation and the quasi-particle equation numberically. Such a dependence is illustrated graphically in Fig. 2. For temperatures smaller than the critical temperature T_{cr} two paired solutions exist. For temperatures above the critical temperature, only one paired solution exists. An increase in temperature has the effect of pushing the quasi-particles farther and farther away from the particle Fermi surface. The blocking due to the quasi-particles becomes less effective and the pairing corrleation is enhanced.

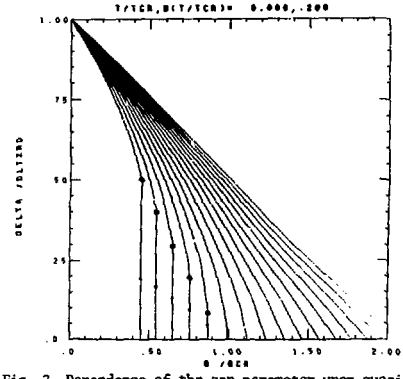

Fig. 2. Dependence of the gap parameter upon quasi-particle number at various temperatures. The inner isotherm corresponds to $T/T_{cr} = 0.00$; the successive isotherms are spaced at intervals of 0.2 T/T_{cr}. The onset of the first order phase transition is indicated by an open circle, the unstable solution at the same temperature is indicated by a solid point. (XBL 7411-8555)

Free Energy and Phase Stability

A general view of Free Energy isotherms is available in Fig. 3. All of these isotherms present a minimum which corresponds to the equilibrium

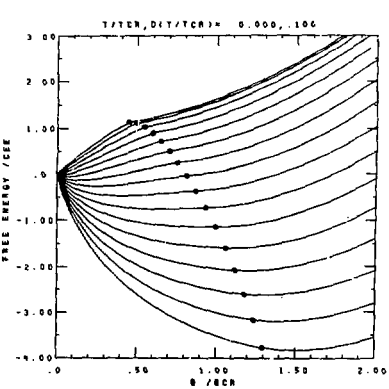

Fig. 3. Dependence of the Free Energy upon quasi-particle number at various temperatures. The upper line corresponds to $T/T_{cr} = 0.00$. The following lines are spaced at intervals of 0.2 T/T_{cr}. The open circles represent the region of the first-order phase transition. The bypassed loops are not shown. (XBL 7411-8557)

value of Q is no restriction is set upon the system. Such a minimum satisfies the condition

$$\frac{\partial F}{\partial Q} = \xi = 0.$$

The T, Q Phase Diagram and the Plots of Various Thermodynamical Functions. In Fig. 4 lines of constant gap parameter Δ are projected in the T, Q plane. It is possible to appreciate two facts already pointed out before, Firstly, the gap parameter at fixed Q actually increases and tends to go to its ground state value as T tends to infinity. Secondly, even for those values of Q for which $\Delta = 0$ at $T = 0$, an increase in temperature eventually leads to the onset of pairing and to its increase towards the ground state value as an asymptotic limit.

In Fig. 5, the lines of constant energies are projected on the same T, Q plane. At high temperatures one observes a nearly hyperbolic behavior typical of the Boltzmann limit. The change in the second derivative visible at low temperature in the unpaired region is due to the onset of the strong degeneracy limit. Similar considerations hold for the entropy plot shown in Fig. 6.

E, Q Diagrams and the Plots of Various Thermodynamical Quantities. The relevance of constant energy processes in nuclei makes it desirable to use the energy itself as an independent variable. The transformation can be done by means of the energy versus quasi-particle number isotherm plot shown in Fig. 7. The first-order phase transition produces a discontinuity responsible for a gap in the E, Q plane.

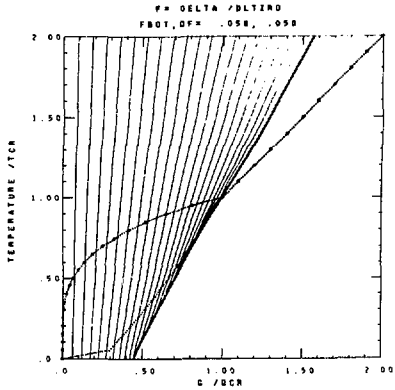

Fig. 4. Lines of constant gap parameter in the T, Q plane. The solid line corresponds to $\Delta = 0$; the lines to the left correspond to increasing values of Δ in steps of 0.05 Δ/Δ_0. (XBL 7411-8559)

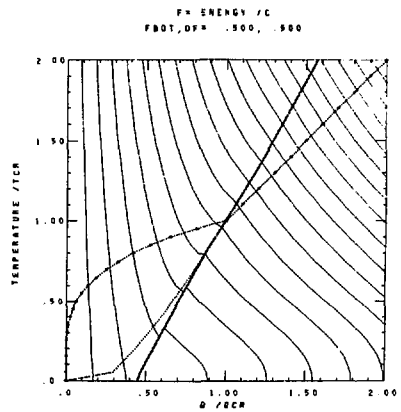

Fig. 5. Lines of constant energy in the T, Q plane. The leftmost line corresponds to E/C = 0.5. The lines to the right are spaced in steps of 0.5 E/C. Notice the mismatch of the lines in the region of the first-order phase transition. (XBL 7411-8560)

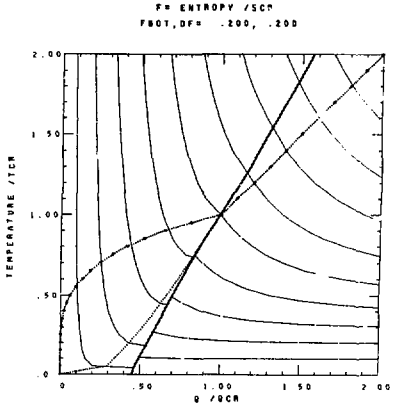

Fig. 6. Lines of constant entropy in the T, Q plane. The leftmost line corresponds to $S/S_{cr} = 0.2$. The lines to the right are spaced in steps of $S/S_{cr} = 0.2$. Notice the mismatch of the lines in the region of the first-order phase transition. (XBL 7411-8561)

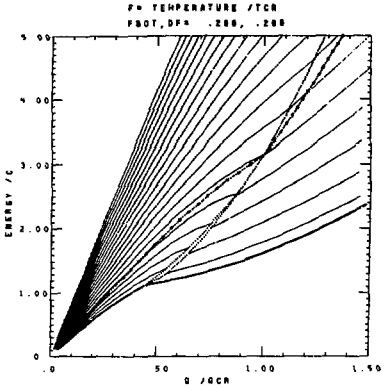

Fig. 7. Energy quasi-particle number isotherms. The lowest line for T = 0 is the same as in Fig. 1. The higher isotherms are spaced in steps of 0.2 T/T_{cr}. The forbidden region, defined by the two dotted lines, originates at the phase transition for T = 0 and terminates at $T = T_{cr}$, $Q = Q_{cr}$. The boundaries of this region converge into a single line for T T_{cr}. The locus of most probable Q is shown by the small and large dot line.
(XBL 7411-8562)

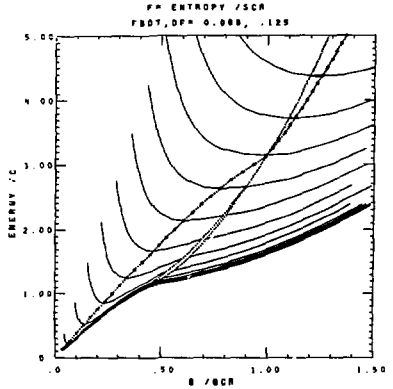

Fig. 8 Lines of constant entropy in the E, Q plane. The thick solid line corresponds to $S/S_{crit} = 0$. The lines above it are plotted in intervals of 0.125 S/S_{crit}. (XBL 7411-8564)

In Fig. 8 the lines of constant entropy are plotted in the E, Q plane This graph is perhaps the most significant insofar as it provides information on the driving force along the path towards equilibrium at constant energy.

The entropy is small at very small quasi-particle numbers; it increases with increasing quasi-particle numbers and reaches a maximum at the $\xi = 0$ line; a further increase in quasi-particle number leads to a decrease in entropy.

The maximum entropy at constant energy obviously represents the equilibrium condition.

The Level Density. In Fig. 9 the constant level density lines for a system characterized by $g = 7\ MeV^{-1}$, $\Delta_0 = 1$ MeV can be seen in an E, Q plot. The pattern is very similar to that of the entropy plot in the E, Q plane and the same comments apply.

A larger gap in the plot is visible due to the failure of the saddle-point method close to the region of phase transition.

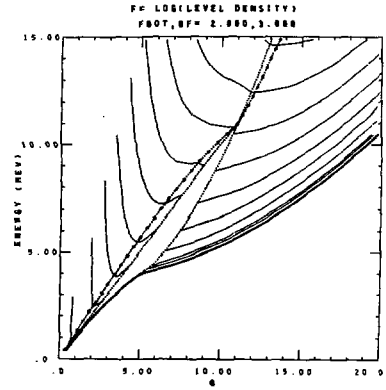

Fig. 9. Lines of constant level densities in the E, Q plane. The calculation refers specifically to a nucleus with $g = 7.0\ MeV^{-1}$ and the $\Delta_0 = 1.0$ MeV. The lowest level density line has a value $\ln\rho = 2.0$. The higher lines are plotted in steps of 3.0 $\ln\rho$. (XBL 7411-8567)

References

1. J. J. Griffin, Phys. Rev. Lett. 17, 478 (1966).

2. C. K. Cline and M. Blann, Nucl. Phys. A172, 225 (1971).

3. M. Blann and A. Mignerey, Nucl. Phys. A186, 245 (1972).

4. C. K. Cline, Nucl. Phys. A193, 417 (1972).

5. M. Sano and S. Yamasaki, Prog. Theor. Phys. 29 397 (1963).

6. P. Decowski, W. Grochulski, A. Marchinkowski, K. Siwek, and Z. Wilhelmi, Nucl. Phys. A110, 129 (1968).

7. L. G. Moretto, Nucl. Phys. A182, 641 (1972).

8. A more complete list of references is available in J. R. Huizenga and L. G. Moretto, Ann. Rev. Nucl. Sci. 22, 427 (1972).

INFLUENCE OF PAIRING AND OF THE SPIN PROJECTION DISTRIBUTION ON THE "CLASSICAL" ISOTHERMAL ROTATIONS OF A NUCLEUS*

L. G. Moretto

The properties of spherical, paired nuclei with finite angular momentum are discussed in terms of "classical" rotations. Rotational quantities like the angular velocity and the moment of inertia are calculated both for the yrast line (T = 0) and for higher temperatures. Particular attention is paid to the superfluid features associated with the pairing correlation. Three different models are considered. The first model is characterized by a constant spacing in the single particle levels and by a constant spin projection, and it is treated analytically in the zero temperature limit. It is shown that this model leads to a very strong back-bending. Calculations accounting for the pairing fluctuations are shown. The second model differs from the first one in the spin projection distribution which, in analogy with a spherical shell model nucleus, is taken to be rectangular. Analytical calculations show that, while strong superfluid properties remain, the back-bending seen in the previous model disappears. The third model used is the shell model. Numerical calculations of the angular velocities and of the moments of inertia are compared with the results obtained from the previous two models. A remarkable agreement is observed between the second model and the shell model.

Footnote

*Abstract of paper; Nucl. Phys. A226, 9 (1974).

STATISTICAL DECAY OF GAMMA RAYS IN (n_{th},γ) REACTIONS*

E. Nard,† L. G. Moretto and S. G. Thompson

Isomer ratios obtained in doubly even targets in the (n_{th},γ) reaction are calculated using realistic level densities and spin cut-off parameters. The calculations were performed using the Monte-Carlo method and the general agreement between the present calculations and experimental data is satisfactory. In one case the shape of the γ-ray spectrum was calculated and good agreement with experimental data was obtained.

Footnotes

*Abstract of paper; Nucl. Phys. A259, 170 (1974).

†Present address: Israel Atomic Energy Commission, Soreq Research Center, Yavne, Israel and Weizmann Institute of Science, Rehovot, Israel.

SEMICLASSICAL CALCULATIONS FOR COULOMB EXCITATION*

J. de Boer,† H. Massmann, and Aa. Winther‡

The Coulomb excitation of a deformed target (index t) by a heavy ion (index p) involves many couplings. A fully quantum mechanical (QM) treatment[1] of, e.g., the excitation of the rotational levels in an even-even target by an inert projectile can therefore presently include only the ground state (level index $N = 1$) and the first five excited states ($N = 2 - 6$). The interpretation of experiments involving more levels must rely on classical[2,3] or semiclassical[4] (SC) computational methods. The relative deviations of the cross sections ($d\sigma_{SC} - d\sigma_{QM})/d\sigma_{SC}$ have been found[5] to increase with transferred angular momentum I_N and to be roughly proportional to the reciprocal Bohr parameter $1/\eta$, where $\eta_N = Z_p Z_t e^2/\hbar v_N$ with v_N being the relative velocity at infinity after exciting level N.

In modern experiments, where spins in excess of 20ħ have been Coulomb-excited (e.g., ^{84}Kr and ^{136}Xe on ^{238}U)[6] the experimental accuracy of the measured cross-sections often matches or exceeds the accuracy with which older SC calculations[4] can be corrected for expected QM effects.[1,5] The accuracy of interpretation may thus be limited by the accuracy of the calculation. The present approximations presented here strive to remedy this situation.

The semiclassical system of coupled differential equations in the amplitudes c_s can be written in the form

$$\frac{dc_r}{dt} = \text{const.} \sum_{\lambda,s} M_{rs}^{(\lambda)} \cdot O_{rs}^{(\lambda)}(t) \times \exp\left\{\frac{i}{\hbar}(E_{Nr}-E_{Ns})\,t\right\} c_s(t) \,.$$

The indices r and s label the nuclear states $|I_r M_r>$ and $|I_s M_s>$ with excitation energies E_{Nr} and E_{Ns}; λ is the multipole order and $M_{rs}^{(\lambda)}$ is the electric multipole matrix-element. By symmetrization one denotes the choice of the orbit, given by $O_{rs}^{(\lambda)}(t)$ which depends on the impact parameter or the initial orbital angular momentum $J\hbar$ and which may depend on the transitions $s \to r$ considered. For a hyperbola, the orbital angular momentum ℓ and the scattering angle θ are connected by $\ell = \eta \operatorname{ctg}(\theta/2)$. The present symmetrization procedure uses a set of hyperbola with the following features:

1) All lie in the same plane (x-y plane),
2) All have the same symmetry axis (x axis),
3) For each transition $s \to r$ the half-distance of closest approach a_{NrNs} and the velocities v_{NrNs} are adjusted to the average excitation energy by choosing

$$v_{NrNs} = \sqrt{v_{Nr} \cdot v_{Ns}}$$

$$a_{rs} = \frac{Z_p Z_t e^2}{v_1^2 A_p} \cdot \frac{A_p + A_t}{A_t} \cdot \left(\frac{v_1}{v_{NrNs}}\right)^2$$

4) For each transition $s \to r$ the scattering angle θ_{rs} is adjusted to the average angular-momentum projection $\hbar M_{rs} = (\hbar/2)(M_r + M_s)$ along a z axis perpendicular to the orbital plane by choosing

$$\left.\begin{aligned} \ell_{rs} &= J - M_{rs} \\ \eta_{N_r N_s} &= \eta_1 \cdot (v_1/v_{NrNs}) \end{aligned}\right\} \theta_{rs} = 2 \cdot \operatorname{arctg} \frac{\ell_{rs}}{\eta_{M_r M_s}}$$

The results of three stages of symmetrization will be considered, namely

		v_{NrNs}	M_{rs}
1	No symmetrization	v_1	0
2	Symmetrization with respect to energy transfer	$\sqrt{v_{Nr} \cdot v_{Ns}}$	0
3	Symmetrization with respect to energy and angular momentum transfer	$\sqrt{v_{Nr} \cdot v_{Ns}}$	$\frac{1}{2}(M_r+M_s)$

The second symmetrization is the one used in Ref. 4. The WKB limit of the QM equations leads to the third one and allows an identification of the SC complex amplitudes c_s with the reaction matrix $r^J_{\ell,I}$ [7-9] given by $c_{Is,Ms}(t = +\infty) = r^J_{\ell=J-Ms,Is}$.

For a projectile with $\eta_1 = 20$ exciting a rotational even-even nucleus the comparisons of the absolute values $|r|$, multiplied with $\sqrt{2J+1}$, and of the phases $\phi(r=|r|e^{i\phi})$ for $J_{min} \le J \le 60$ ($2J_{min} = M + I$) with the QM values are shown for $I = 10$ ($N = 6$) and $M = -10,0,+10$ in the two figures. A marked improvement in $|r|$ is achieved, especially for $M = -I$ ($M = +I$ is the largest summand in $d\sigma_I = \sum_M d\sigma_{IM}$). The main contribution to the cross section arises from channel spins $J \le \eta$; the smooth behaviour of r allows interpolation in large steps. A larger number of comparisons[10] indicates that the $M_{rs}=(1/2)\cdot(M_r+M_s)$ symmetrization diminishes the deviations $\phi_{SC}(N) - \phi_{QM}(N)$.

Investigations tracing the origin of remaining deviations are in progress. There are indications that they stem from the detailed properties of the wave function near the classical turning point[11] rather than from the inaccurate shape of the orbit. Methods similar to the one used here can be used for non-hyperbolic orbits (nuclear plus Coulomb potential) as well as the approximate accounting for the transfer of mass.[12]

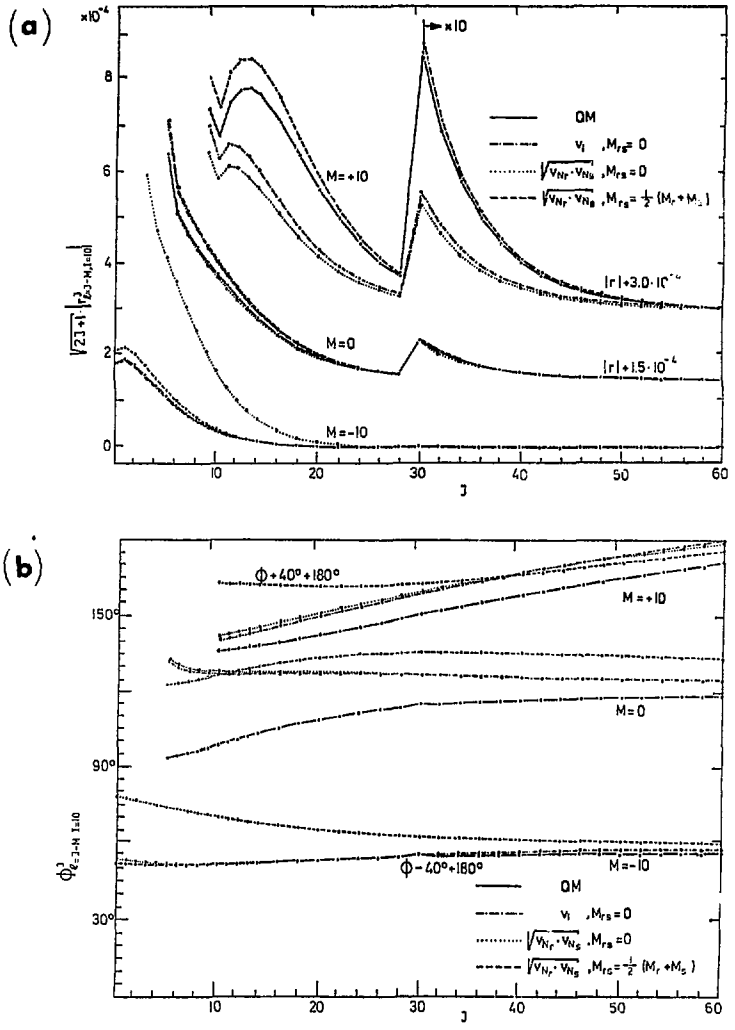

Fig. 1. Reaction matrix for the excitation of a rotational 10^+ state by a projectile with $\eta = 20$, as a function of the channel spin J. Only the values $M = J - \ell = -10, 0,$ and +10 are displayed. The semiclassical results of three types of symmetrization are compared to the quantum mechanical values. The absolute values, multiplied with $\sqrt{2J+1}$, are given in (a), whereas the phases are shown in (b). (XBL 756-1561, XBL756-1562)

Footnotes and References

*Work supported in part by the Ministry of Education and Science of the Federal Republic of Germany. Contribution presented at the International Workshop III on Gross Properties of Nuclei and Nuclear Excitations, Hirschegg, Austria, January 13-18, 1975.

†Sektion Physik, Universität München.

‡Niels Bohr Institute, Copenhagen.

1. F. Roesel, J. X. Saladin, and K. Alder, "Quantum-Mechanical Coupled-Channels Code for Coulomb Excitation", University of Pittsburgh Progress Report, 1973; the code was expanded to include up to six levels (F. Roesel, Berkeley, 1974).

2. H. Massmann and J. O. Rasmussen, Nucl. Phys. A243 (1975), 155.

3. S. Levit, U. Smilansky, and D. Pelte, Phys. Lett. 53B, 39 (1974).

4. Aa. Winther and J. de Boer, in "Coulomb Excitation", Perspectives in Physics, edited by K. Alder and Aa. Winther, Academic Press, 1966, pg. 303.

5. K. Alder, F. Roesel, and J. X. Saladin, Volume 1 of the Proceedings of the Conference on "Reactions Between Complex Nuclei", Nashville, Tennessee, 1974, pg. 28.

6. E. Grosse et al., to be published.

7. K. Alder and H. K. A. Pauli, Nuclear Physics A128, 193 (1969).

8. K. Alder and Aa. Winther, Chapter IX in "Electromagnetic Excitation", to be published by North Holland Publishing Company, 1975.

9. R. A. Broglia et al., Phys. Reports 11C, 1 (1974).

10. J. de Boer, H. Massmann and Aa. Winther, to be published.

11. F. Roesel, private communication.

12. R. A. Broglia and Aa. Winther, Phys. Reports 4C, 153 (1972).

UNIFORM SEMICLASSICAL ORBITAL CALCULATIONS OF HEAVY ION COULOMB EXCITATION*

H. Massmann† and J. O. Rasmussen

In recent years a new semiclassical method, the so called "uniform semiclassical approximation" (USCA) has been developed and applied to molecular scattering and reaction problems.[1-3] Here we wish to report on applications of this method to multiple Coulomb excitation for backward scattering angles.

The equations of the USCA can be derived from Feynman's path integral formulation of quantum mechanics. The semiclassical limit of matrix elements of quantum mechanical operators is found by invoking the stationary phase method to evaluate integrals. By following this procedure one finds the following basic features of this method:

1) The dynamics of the system is completely classical, that is the system follows the classical equations of motion.

2) By evaluating a phase along the classical trajectories one can extract the so called "classical S-matrix" which then by the usual equations yields differential cross sections. In other words the quantum mechanical superposition principle is retained in the USCA since one adds probability amplitudes for indistinguishable processes rather than probabilities.

For the details of the theory we refer to the work of W. H. Miller.[1-3]

We consider here only the scattering of a projectile moving toward an even-even deformed target (initially in its ground state) with zero impact parameter ($\ell_{in} = 0$). In this case since all the motion classicaly takes place in a plane, one can describe the system by using only two variables simplifying the numerical work considerably. However care must be taken to assure that one is solving the backscattering from a three-dimensional rotor and not from a two-dimensional rotor.

In Fig. 1 the excitation probabilities for backscattering ($\theta = 180°$ to the different final angular momenta I are plotted and a comparison is made with results obtained using the conventional de Boer - Winther code for multiple Coulomb excitation.[4] The agreement between the two semiclassical theories is very reasonable.

When writing the equations of motion for the system in terms of dimensionless quantities one finds that the evolution of the system depends only on the following three dimensionless parameters:

1) $\eta = Z_1 Z_2 e^2/\hbar v_0$ (Sommerfeld parameter) being a measure of the monopole-monopole interaction strength.

2) $\xi_{02} = \pi E_2/(2 E_{cm})$ (Adiabaticity parameter) being a measure of how adiabatic the collision is. E_2 is the energy of the first excited rotational state. $\xi_{02} = 0$ would represent a sudden collision.

3) $q_2 = Z_p e^2 Q_0(2)/(4\hbar v_0 a^2)$ (Quadrupole interaction strength parameter) being a measure of the quadrupole-monopole interaction strength.

The ratio η/q_2 gives a measure of how close the trajectory of the projectile corresponds to a hyperbola. For $\eta \to \infty$ the orbit is a pure hyperbola

Table 1. The probabilities for excitation of rotational states in an even-even nucleus in the limit $\xi_{02} = 0$ and $\eta = \infty$. Tabulated are the resuts of the USCA and the conventional semiclassical approximation (Ref. 5).

$\bar{q}_2$	USCA P_0	A-W P_0	USCA P_2	A-W P_2	USCA P_6	A-W P_6	USCA P_{10}	A-W P_{10}	USCA P_{14}	A-W P_{14}	USCA P_{18}	A-W P_{18}
1.0	0.6339	0.6945	0.2518	0.2850	0.0003	0.0006						
1.5	0.3850	0.4300	0.4917	0.4812	0.0039	0.0057						
2.0	0.1940	0.2152	0.5733	0.5597	0.0203	0.0260	0.0000	0.0001				
2.5	0.0988	0.1021	0.4892	0.4842	0.0650	0.0750	0.0004	0.0006				
3.0	0.0842	0.0835	0.3084	0.3098	0.1485	0.1572	0.0022	0.0029				
3.5	0.1067	0.1108	0.1362	0.1389	0.2568	0.2563	0.0084	0.0104		0.0001		
4.0	0.1224	0.1317	0.0509	0.0514	0.3385	0.3354	0.0247	0.0286	0.0003	0.0004		
4.5	0.1115	0.1214	0.0622	0.0600	0.3571	0.3555	0.0581	0.0634	0.0011	0.0014		
5.0	0.0820	0.0881	0.1193	0.1158	0.2999	0.3006	0.1127	0.1171	0.0038	0.0046		
5.5	0.0553	0.0571	0.1569	0.1540	0.1911	0.1932	0.1829	0.1831	0.0107	0.0124		
6.0	0.0461	0.0463	0.1427	0.1412	0.0828	0.0848	0.2451	0.2436	0.0255	0.0283	0.0006	0.0007
6.5	0.0550	0.0547	0.0921	0.0917	0.0242	0.0250	0.2768	0.2757	0.0523	0.0558	0.0018	0.0022
7.0	0.0630	0.0671	0.0462	0.0459	0.0317	0.0312	0.2615	0.2616	0.0933	0.0961	0.0050	0.0058
7.5	0.0637	0.0687	0.0352	0.0343	0.0809	0.0798	0.2004	0.2014	0.1452	0.1455	0.0120	0.0134
8.0	0.0532	0.0570	0.0568	0.0552	0.1251	0.1242	0.1160	0.1174	0.1946	0.1938	0.0253	0.0274
8.5	0.0396	0.0413	0.0936	0.0819	0.1293	0.1292	0.0436	0.0446	0.2266	0.2258	0.0478	0.0503
9.0	0.0324	0.0329	0.0892	0.0879	0.0925	0.0930	0.0124	0.0128	0.2277	0.2275	0.0808	0.0828
9.5	0.0345	0.0355	0.0692	0.0685	0.0442	0.0447	0.0290	0.0286	0.1930	0.1935	0.1221	0.1223
10.0	0.0409	0.0432	0.0412	0.0408	0.0188	0.0189	0.0725	0.0719	0.1316	0.1326	0.1627	0.1622

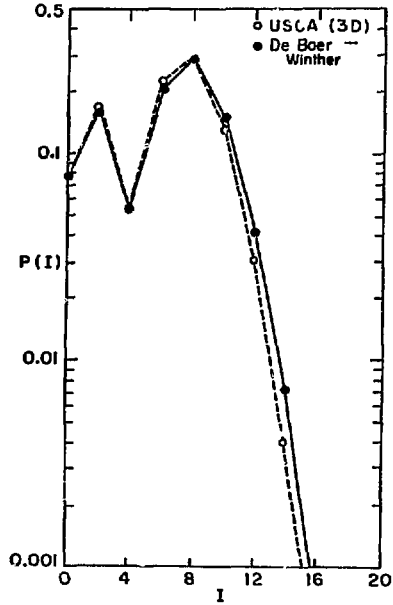

Fig. 1. Calculations of Coulomb Excitation probabilities to excite members of rotational ground band in ^{238}U with the backscattering of ^{40}Ar at E_{lab} = 170. MeV on ^{238}U. For this case: E_2=170.0 MeV, $Q_0^{(2)}$= 10.84 barn, $Q_0^{(4)}$= 0 barn^2, ξ_{02} = 0.0196, η = 127.0 and $\bar{q}_2$ = 5.574. The black triangles correspond to the result obtained if the interference term is neglected. The open squares correspond to the result for the backscattering from a 2 dimensional rotor. (XBL 756-1563)

(as in the de Boer - Winther code).

The $\eta \to \infty$, $\xi_{02} = 0$ limit can be found analytically for our example and this limit is in very good agreement with results published for this case using the conventional semiclassical approach[5] as can be seen from Table 1.

In realistic scattering problems, η is finite and the projectile's orbit will differ from a pure hyperbola. Figure 2 shows the backscattering excitation probability for $\xi_{02} = 0$ and $\bar{q}_2 = 9.0$ vs $1/\eta$. The finite η corrections shown in Fig. 2 come about because of the change in the projectile's orbit due to the angular momentum transfer between the target and the projectile. The angular momentum transfer between target and projectile is not taken into account in the conventional de Boer - Winther code although work is currently being done to include it approximately.[6]

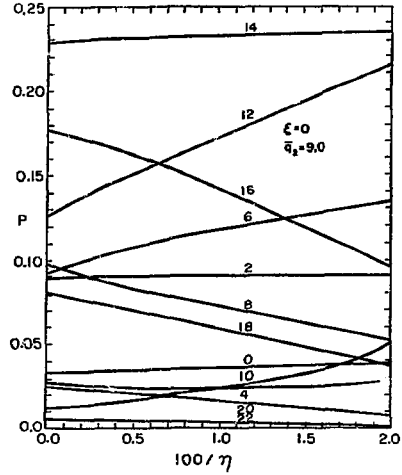

Fig. 2. Backward scattering excitation probabilities to Coulomb Excite members of a ground rotational band of an even-even target. Results are shown vs η for $\xi_{02} = 0$ and $\bar{q}_2 = 9.0$. The $\eta \to \infty$ limit was evaluated analytically. (XBL 756-1564)

Footnotes and References

*Condensed from LBL-3440. Submitted to Nuclear Physics A (November 1974).

†On leave from Facultad de Ciencias, Universidad de Chile, Santiago, Chile, with a fellowship from Convenio Universidad de Chile - University of California.

1. W. H. Miller, J. Chem. Phys. 53, 1949 (1970).

2. W. H. Miller, J. Chem. Phys. 53, 3578 (1970).

3. W. H. Miller, "The classical S-matrix in molecular collisions" in Molecular Beams, ed. K. P. Lawley, Wiley; to be published (1975).

4. J. de Boer and Aa. Winther, in Coulomb Excitation ed. by K. Alder and Aa. Winther, Academic Press (1966).

5. K. Alder and Aa. Winther, Kgl. Danske Videnskab. Selskab, Mat. Fys. Medd. 32 8, (1960).

6. J. de Boer, H. Massmann and Aa. Winther. Proceedings of the International Workshop III on Gross Properties of Nuclei and Nuclear Excitations. Hirschegg, Austria, January 1975.

TWO HYDRODYNAMICAL LIMITS IN THE DESCRIPTION OF HIGH-SPIN YRAST CASCADES

J. Meyer-ter-Vehn*

Experimental work on yrast cascades after heavy-ion reactions[1,2] indicates that these cascades proceed through a smooth band system and are spread over a least five separate bands. Mottelson has pointed out that the spectrum of a triaxial rotor can possibly explain these features.[3] On the other hand, Swiatecki and coworkers have studied the rotating liquid drop and predict oblate equilibrium shapes for angular momenta $I < 60\hbar$[4].

The answer to the question which shape will occur critically depends on which kind of nuclear flow prevails in these strongly rotating nuclei. As long as the shape deformation is not too large ($\beta < 0.5$) so that the nuclear surface can be described by the first-order parameters β and γ, irrotational flow favors shapes of maximum γ-symmetry ($\gamma = 30°$), whereas 'rigid' flow leads to oblate shapes ($\gamma = 60°$). Beyond a certain angular momentum, very elongated shapes are likely to appear for any kind of flow and these will finally lead to fission. In this region, which is expected for $I > 60\hbar$ in medium-mass nuclei, the following arguments do not apply.

The aim of this note is to show that the rotational spectra and the decay properties of the two limiting model cases, (a) the $\gamma = 30°$ rotor with irrotational moments-of-inertia, and (b) the $\gamma = 60°$ rotor with rigid moments-of-inertia, can be treated in an elementary way. Neither of these two models is expected to describe actual yrast cascades quantitatively, but they represent two interesting approximations because they sharply illuminate a characteristic difference between irrotational and rigid flow models that is likely to be also present in more elaborate treatments and that allows one to some extent to distinguish between the two kinds of flow on the basis of the existing experimental data.

The moments-of-inertia corresponding to rigid flow and irrotational flow are given as functions of γ in Fig. 1. Maximum moments-of-inertia are obtained at $\gamma = 60°$ and $\gamma = 30°$, respectively, and

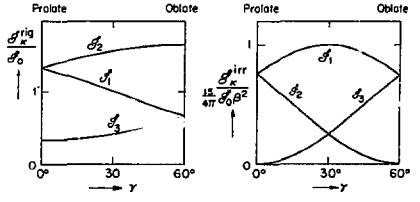

Fig. 1. Rigid (left side) and irrotational (right side) moments-of-inertia as functions of the asymmetry parameter γ. For illustrative reasons, a very large $\beta \approx 1$ has been assumed for the rigid case. (XBL 744-2782)

the two smaller moments-of-inertia are equal at exactly these γ's in both cases. Choosing the axes such that $\mathcal{J}_1 > \mathcal{J}_2 = \mathcal{J}_3$, the rotor Hamiltonian

$$H = AI_1^2 + A_\perp(I_2^2 + I_3^2),$$

with $A = 1/2\mathcal{J}_1$ and $A_\perp = 1/2\mathcal{J}_{2,3}$, is axially symmetric about the 1-axis (though not necessarily the shape!). For this reason, standard rotor formulas are applicable. The energy spectrum is

$$E_{I,\alpha} = A\alpha^2 + A_\perp[I(I+1) - \alpha^2]$$

and the wavefunctions are

$$\psi_{IM,\alpha} = \sqrt{\frac{2I+1}{16\pi^2(1+\delta_{\alpha,0})}}\left[D^{(I)}_{M\alpha} + (-)^I D^{(I)}_{M-\alpha}\right]$$

where α denotes the angular momentum projection on the 1-axis and has to be an even integer ≥ 0. The general expression for the E2 transition probabilities is

$$B(E2;I_1\alpha_1 \to I_2\alpha_2) = \frac{5}{16\pi}\cdot\frac{2I_2+1}{\left(1+\delta_{\alpha_1,0}\right)\left(1+\delta_{\alpha_2,0}\right)}$$

$$\cdot\left\{\begin{pmatrix} I & I_2 & 2 \\ \alpha_1 & -\alpha_2 & 0\end{pmatrix} q^{(1)}_{20} + (-)^{I_1}\begin{pmatrix} I_1 & I_2 & 2 \\ -\alpha_1 & -\alpha_2 & 0\end{pmatrix} q^{(1)}_{20}\right.$$

$$\left. + \left[\begin{pmatrix} I_1 & I_2 & 2 \\ \alpha_1 & -\alpha_2 & 2\end{pmatrix} + \begin{pmatrix} I_1 & I_2 & 2 \\ \alpha_1 & -\alpha_2 & -2\end{pmatrix}(-)^{I_2}\begin{pmatrix} I_1 & I_2 & 2 \\ -\alpha_1 & -\alpha_2 & 2\end{pmatrix}\right] q^{(1)}_{22}\right\}^2.$$

Here, $q^{(1)}_{2\mu}$ is the intrinsic quadrupole tensor related to the 1-axis. For the $\gamma = 30°$ case, it is convenient to introduce the so-called wobbling quantum number[3] $n = I - \alpha$, since, in this case, states with same n are connected by large B(E2)'s. Inserting $\alpha = I - n$, the energy spectrum reads

$$E_{I,n} = AI^2 + A_\perp I + (A_\perp - A)n(2I-n).$$

The quantum number n labels a series of rotational bands parallel to the yrast band (n = 0) as shown in Fig. 2. For a given level (I,n) there are 5 possible ways to decay via E2 transitions. These are also indicated in Fig. 2. For $I \gg 1$, one obtains:

(a) $B(E2;(I,n) \to (I-2,n)) \cong \frac{5}{16\pi} q^{(1)2}_{22} \cdot \left(\frac{2I-n}{2I}\right)^4$,

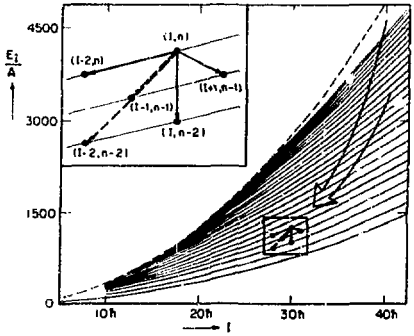

Fig. 2. Band structure of a triaxial rotor at $\gamma = 30^\circ$ assuming irrotational flow. Possible E2-transitions from a given state (I,n) are indicated. (XBL 744-2779)

(c) $B[E2;(I,n) \to (I,n-2)] \cong \frac{5}{16\pi} q_{22}^{(1)2} \cdot \frac{3n(n-1)}{(2I)^2}$,

(c) $B[E2;(I,n) \to (I+1,n-1)] \cong \frac{5}{16\pi} q_{22}^{(1)2} \cdot \frac{n(2I-n)^3}{4I^4}$,

(d) $B[E2;(I,n) \to (I-1,n-1)] \cong \frac{5}{16\pi} q_{20}^{(1)2} \frac{3n(I-n)^2(2I-n)}{2I^4}$,

(e) $B[E2;(I,n) \to (I-2,n-2)] \cong \frac{5}{16\pi} q_{20}^{(1)2} \frac{6n(n-1)(2I-n)^2}{2I^4}$.

From these results, two important conclusions can be drawn:

(1) For triaxial shapes with $\gamma = 30^\circ$, favored by pure irrotational flow, one has $q_{20}^{(1)} = 0$ and a maximum $q_{22}^{(1)} = Q_0/\sqrt{2}$, where $Q_0 = 3/\sqrt{5\pi} \cdot R_0^2 Ze\beta$ is the intrinsic quadrupole moment. In the yrast region $n \ll I$, transitions (a) along the n-bands are dominant, cross-transitions (b) and (c) are reduced by factors $(n/I)^2$ and (n/I), respectively, and transitions (d) and (e) are completely suppressed. The E2-cascade is therefore channeled through a number of bands parallel to the yrast band as needed to explain the experimental results.

(2) For oblate shapes with $\gamma = 60^\circ$, favored by rigid flow, the energy spectrum has the same structure as for the $\gamma = 30^\circ$ case, but the decay properties are decisively different due to the different shape. Since now $q_{20}^{(1)} = Q_0$ has reached its maximum and $q_{22}^{(1)} = 0$, the cascade proceeds through the transitions (d) and (e) and is trapped on the yrast line. Since the yrast states correspond to rotation about the symmetry axis in this case, nuclei in these states do not radiate and form high-spin isomers. Even if the isomers would be relatively short-lived due to small deviations *from pure oblate shapes, most of the population* after a heavy-ion reaction would quickly drop into the yrast band, and individual yrast transitions should be observed up to very high angular momenta. This is in clear contradication to the experimental evidence.

It is concluded that the $\gamma = 30^\circ$ rotor based on irrotational flow is in qualitative agreement with experimental data on yrast cascades, whereas the $\gamma = 60^\circ$ rotor based on rigid flow is not. This might indicate that the nuclear flow corresponding to the yrast region has a strong irrotational component. Due to the large overall values of the empirical moments-of-inertia, however, the flow cannot be completely irrotational. This is known already from groundstate moments-of-inertia that lie between irrotational and rigid values. A two fluid model accounting for a mixture of both kinds of flow is therefore suggested to describe the hydrodynamics of rotating nuclei. An investigation in this direction based on classical work by B. Riemann (1860) is now in progress.

Footnotes and References

*On leave from Technische Universität München, München, West Germany.

1. J. O. Newton, F. S. Stephens, R. M. Diamond, W. H. Kelley, and D. Ward, Nucl. Phys. A141, 361 (1970).

2. P. O. Tjøm, F. S. Stephens, R. M. Diamond, J. de Boer, and W. E. Meyerhof, submitted to Phys. Rev. Letters (1974).

3. B. R. Mottelson, The Nuclear Structure Symposium of the Thousand Lakes, Joutsa, Finland, 1970.

4. S. Cohen, F. Plasil, and W. J. Swiatecki, Annals of Physics 82, 557 (1974).

5. B. Riemann, "Abh. I. Königl. Gesell. der Wis. zu Göttingen, 9, 3-36 (1860).

THE TRIAXIAL-ROTOR-PLUS-QUASIPARTICLE MODEL*

J. Meyer-ter-Vehn†

Calculated energies, moments and transition probabilities of the triaxial-rotor-plus-quasiparticle model are presented in a series of plots (Figs. 1-9) to provide the basis for a systematic study of unique parity spectra in transitional odd-A nuclei in the A = 190 and A = 135 mass regions.

The model Hamiltonian

$$H = \sum_{\kappa=1}^{3} \frac{(I_\kappa - j_\kappa)^2}{2\mathcal{I}_\kappa} + \sum_{\nu=1}^{j+\frac{1}{2}} e_\nu a_\nu^+ a_\nu \qquad (1)$$

describes the core as a rigid triaxial rotor (Davydov approximation) and restricts the configuration space of the odd nucleon to one complete j-shell. The quasiparticle energies

$$e_\nu = \sqrt{(\varepsilon_\nu - \lambda_F)^2 + \Delta^2} \quad (\nu = 1,2,\cdots, j+\tfrac{1}{2})$$

are obtained from the Fermi energy λ_F, the pairing gap Δ, and the single-particle energies ε_ν which result from the diagonalization of the particle-core interaction

$$H_p = -k\beta[\cos\gamma\, Y_{20} + \frac{\sin\gamma}{\sqrt{2}}(Y_{22} + Y_{2-2})] .$$

The coupling strength k is taken as $k \cong 206$ MeV/$A^{1/3}$ consistent with the Nilsson model. The moments-of-inertia are chosen as

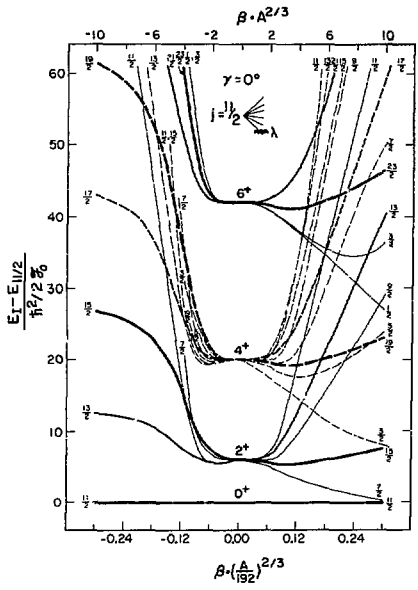

Fig. 1. The odd-A energy spectrum as a function of β for $\gamma = 0°$, $\lambda_F = \varepsilon_{11}$ and $j = 11/2$. The core states underlying the multiplets at $\beta = 0$ are indicated. (XBL 749-4307)

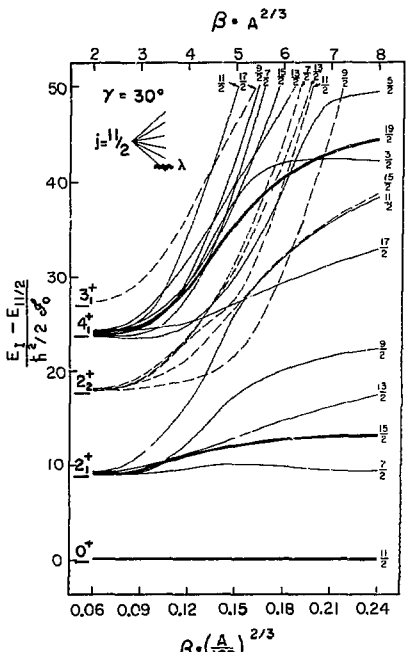

Fig. 2. Same as Fig. 1, but for $\gamma = 30°$ and $\lambda_F = \varepsilon_{11}$. (XBL 747-3731)

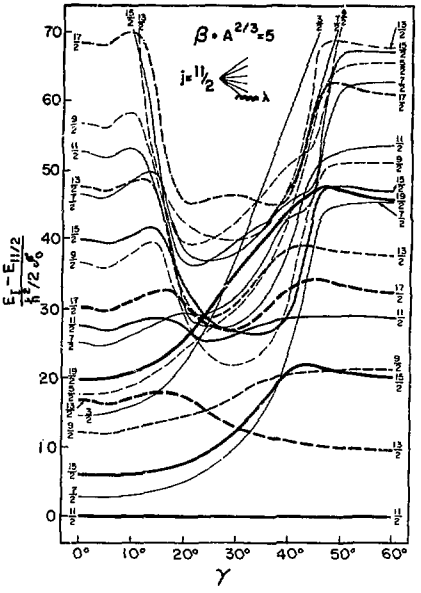

Fig. 4. The odd-A energy spectrum as a function of γ for $\beta \cdot A^{2/3} = 5$, $\lambda_F = \varepsilon_1$, and $j = 11/2$.

(XBL 747-3734)

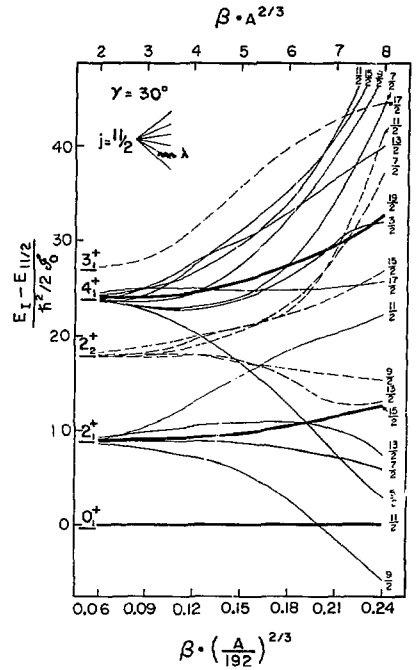

Fig. 3. Same as Fig. 1, but for $\gamma = 30°$ and $\lambda_F = \varepsilon_2$.

(XBL 747-3732)

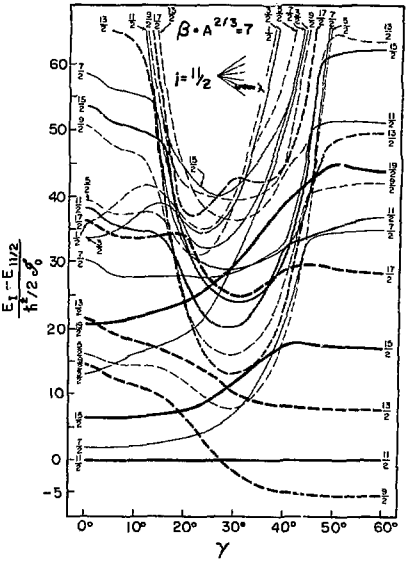

Fig. 5. Same as Fig. 4, but for $\beta \cdot A^{2/3} = 7$ and $\lambda_F = \varepsilon_2$.

(XBL 747-3733)

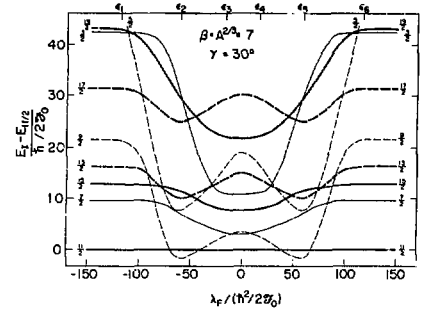

Fig. 6. The odd-A energy spectrum as a function of λ_F for $\beta \cdot A^{2/3}$, $\gamma = 30°$, and $j = 11/2$. (XBL 7410-4395)

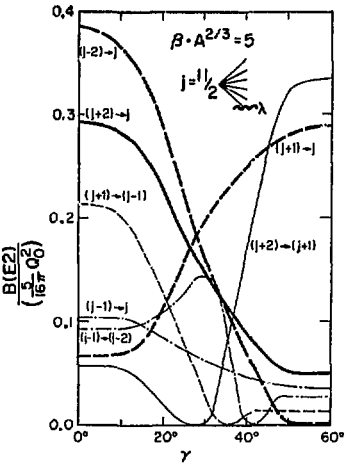

Fig. 8. Reduced E2-transition probabilities for the lowest odd-A states as functions of γ for $\beta \cdot A^{2/3} = 5$, $\lambda_F = \varepsilon_1$, and $j = 11/2$. (XBL 749-4304)

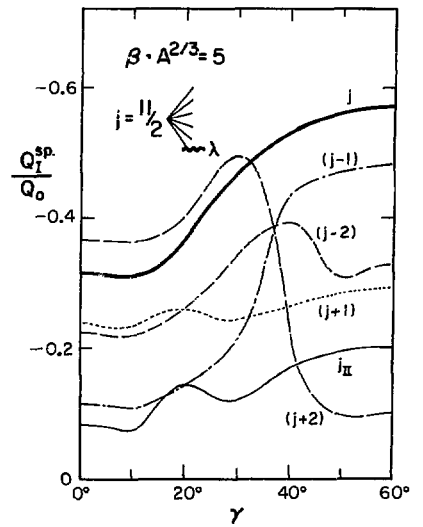

Fig. 7. Spectroscopic quadrupole moments of the lowest odd-A states, including the second j state, as functions of γ for $\beta \cdot A^{2/3} = 5$, $\lambda_F = \varepsilon_1$, and $j = 11/2$, given in units $Q_0 = \frac{3}{\sqrt{5\pi}} \cdot R_0^2 \cdot Z \cdot \beta$. (XBL 749-4306)

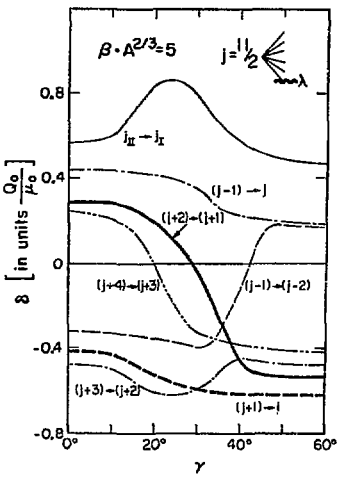

Fig. 9. Ratios $\delta = \langle I_2 || \sqrt{5/16\pi}\, Q || I_1 \rangle \,/\, \langle I_2 || M || I_1 \rangle$ for the lowest odd-A states, including the second j state, as functions of γ for $\beta \cdot A^{2/3} = 5$, $\lambda_F = \varepsilon_1$, and $j = 11/2$. The magnetic unit $\mu_0 = \mu_{s.p.} - g_{R\cdot j}$ with $\mu_{s.p.}$ being the single-particle magnetic moment. (XBL 749-4305)

$$\mathcal{J}_\kappa = \mathcal{J}_0 \cdot \frac{4}{3} \sin^2(\gamma - \frac{2\pi}{3}\kappa)$$

with $\kappa = 1,2,3$ and $\mathcal{J}_0$ determined according to Grodzin's general empirical rule[1] $\hbar^2/(2\mathcal{J}_0) \cong 204\ \mathrm{MeV}/(\beta^2 \cdot A^{7/3})$. Choosing furthermore $\Delta \cong 135$ MeV/A, consistent with even-odd mass differences in the region $100 < A < 200$, and expressing all energies in units $\hbar^2/(2\mathcal{J}_0)$, the only free parameters of the model are $\beta \cdot A^{2/3}$, γ, and λ_R. The final diagonalization of the Hamiltonian (1) involves matrices of dimension $(I+\frac{1}{2})(j+\frac{1}{2})$ where I denotes the total angular momentum. The eigenvalues satisfy the important symmetry $E(\beta,\gamma,\lambda_R) = E(\beta,60^\circ - \gamma, -\lambda_R)$ which relates particle and hole spectra. Earlier work on this model has been done by Pashkevich and Sardanyan.[2]

The FORTRAN program ASQROT which calculates energies, momenta and transition probabilities of this model is available on request.

Footnotes and References

*Condensed from work to be published in Nucl. Physics.

†On leave of absence from Physik-Department, T30, Technische Universität München, München, West Germany.

1. L. Grodzins, Phys. Letters 2, 88 (1962).

2. V. V. Pashkevich and R. A. Sardaryan, Nucl. Phys. 65, 401 (1965).

ON THE YRAST STATES OF γ-UNSTABLE NUCLEI

J. Meyer-ter-Vehn*

Judged from microscopic calculations of potential energy surfaces $V(\beta,\gamma)$, a wide class of nuclei is characterized by potentials which are rather soft in γ-direction. On the basis of these potentials, one obtains collective wave functions which are spread all over the γ-range $0° \leq \gamma \leq 60°$. This result holds for low angular momentum. Going to higher angular momenta, however, one expects the wave functions to localize more and more about $\gamma = 30°$ due to a dynamic stabilization[1] – provided the moments-of-inertia depend on γ as those of irrotational flow

$$\mathcal{J}_\kappa = 4B\beta^2 \sin^2(\gamma - \frac{2\pi}{3}\kappa) \quad \kappa = 1,2,3.$$

In this case, the largest moment-of-inertia occurs for maximum asymmetry at $\gamma = 30°$ and, of course, favors the $\gamma = 30°$ shape at high angular momenta. It should be recalled that the γ-dependence of irrotational moments-of-inertia is well supported empirically by spectra of odd-A nuclei.[2]

The aim of this note is to show that the process of localization can be studied analytically in the limit of γ-unstable potentials (V independent of γ). In this case, Bohr's collective Hamiltonian[3] separates in β and γ, and the total wave function can be written[3] as

$$\Psi_{IM,n\lambda} = f_{n,\lambda}(\beta) \cdot \phi_{\lambda,IM}(\gamma,\Omega). \qquad (1)$$

The γ-dependent part φ does not depend on the potential $V(\beta)$ and is common to all γ-unstable systems, including the harmonic quadrupole oscillator $V \sim \beta^2$. Since the wavefunctions of the latter are known, it is relatively easy to construct φ.[4] For the yrast states with even I, one obtains

$$\phi_{\lambda = \frac{I}{2}, IM=I} = \left[\left(\frac{\alpha_{22}}{\beta}\right)^{\frac{I}{2}}\right]_{IM=I} = \left[\left(\cos\gamma\, D^{(2)}_{20} + \frac{\sin\gamma}{\sqrt{2}}\left(D^{(2)}_{22} + D^{(2)}_{2-2}\right)\right)^{\frac{I}{2}}\right]_{IM=I} . \qquad (2)$$

The easiest way to analyze this expression is to look for the solution in the range $60° < \gamma < 120°$, where the moment-of-inertia has its maximum at $\gamma = 90°$. In fact, from Eq. (2) one expects φ to have the asymptotic form

$$\phi_{\lambda = \frac{I}{2}, IM = I} \propto (\sin\gamma)^{\frac{I}{2}} \frac{1}{\sqrt{2}} \left(D^{(I)}_{II} + D^{(I)}_{I-I}\right) \qquad (3)$$

for $I \to \infty$, since $\cos\gamma \ll 1$ for $60° < \gamma < 120°$. The completely coupled form of φ is

$$\phi_{\lambda = \frac{I}{2}, IM} = \sum_{K=0}^{\lambda} g_{\lambda = \frac{I}{2}, (I-2K)}(\gamma)\ \psi_{IM,2K}(\Omega) \qquad (4)$$

with

$$g_{\lambda,\mu}(\gamma) = N_\lambda \sqrt{\frac{12^\mu}{\binom{4\lambda}{2\mu}}} \sum_{\nu=0}^{[\frac{\mu}{2}]} \frac{\lambda!\, \cos^{\mu-2\nu}\gamma \cdot \sin^{\lambda-\mu+2\nu}\gamma}{12^\nu (\lambda-2\nu)!\, \nu!\, (\lambda-\mu+\nu)!}$$

and

$$\psi_{IM,\,K}(\Omega) = \sqrt{\frac{2I+1}{16\pi^2(1+\delta_{K,0})}}\left[D^{(I)}_{MK}(\Omega) + D^{(I)}_{M-K}(\Omega)\right]$$

N_λ is a normalization constant and $[\frac{I}{2}]$ the largest integer smaller than $\frac{I}{2}$. The γ-density

$$\rho_I(\gamma) = \int d\Omega \left|\phi_{\lambda=\frac{I}{2},IM}(\gamma,\Omega)\right|^2$$

is plotted for different I in Fig. 1. It is seen that the localization about $\gamma = 30°$ sets in rather slowly for $I \gtrsim 6$. For $I = 2$ and 4, the wave function is equally distributed over γ. For $I = 40$,

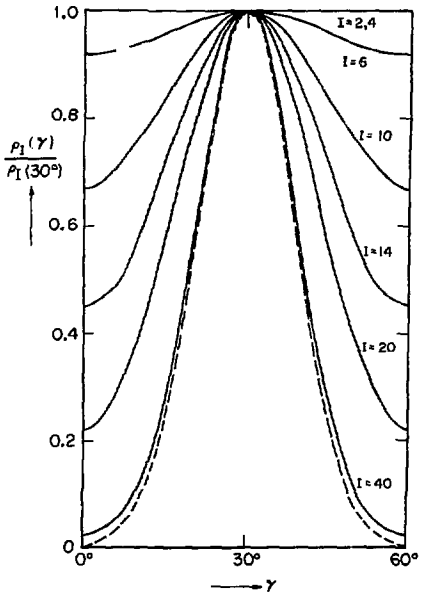

Fig. 1. The distribution of γ- unstable wave functions over the γ-coordinate. With increasing angular momentum the wave functions localize about $\gamma = 30°$ and approach the asymptotic limit (given for I = 40 as broken Line).

(XBL 744-2780)

$\rho_I(\gamma)$ is sharply peaked at $\gamma = 30°$ and has almost reached the asymptotic limit.

The yrast energies corresponding to Eq. (1) depend on $V(\beta)$. If the potential has a sharp β-minimum and localizes the wave function at a definite $\beta = \beta_0$, the spectrum for even I is

$$E_I = \frac{\hbar}{8B\beta_0^2} I(I+6) .$$

But also in the case of an harmonic oscillator, the centrifugal term in the effective potential

$$V^{\text{eff}}(\beta) = \frac{C}{2}\beta^2 + \frac{\hbar^2}{8B\beta^2} I(I+6)$$

tends to localize the wavefunction at

$$\beta_0(I) = \sqrt[4]{\frac{\hbar^2 I(I+6)}{4BC}} .$$

For $I \to \infty$, the minima of V^{eff} are just

$$E_I = \sqrt{\frac{C}{B}} \cdot \frac{\hbar I}{2}$$

the exact yrast energies of the harmonic oscillator.

It is concluded that the moments-of-inertia of irrotational type stabilize triaxial shapes at high angular momenta no matter how γ-soft the collective potential is. This process sets in, however, rather slowly. It cannot be responsible for triaxial shapes in the region $I < 10$.

Footnotes and References

* On leave from Technische Universität München, München, West Germany.

1. This has been realized earlier by B. Mottelson, private communication to F. S. Stephens.

2. J. Meyer-ter-Vehn, F. S. Stephens, and R. M. Diamond, Phys. Rev. Letters 32, 1383 (1974).

3. A. Bohr, K. Danske Vidensk. Selsk. mat.-fys. medd. 26, No. 14 (1952).

4. L. Wilets and M. Jean, Phys. Rev. 102, 788 (1956).

5. D. R. Bes, Nucl. Phys. 10, 373 (1959).

THEORETICAL INVESTIGATION OF UNIQUE PARITY SPECTRA OF ODD-A NUCLEI IN THE A = 135 AND A = 190 MASS REGION*

J. Meyer-ter-Vehn†

Unique parity spectra of transitional odd-A nuclei in the A = 135 and A = 190 mass region have been investigated based on the triaxial-rotor-plus-quasiparticle model.[1] Triaxial shapes are indicated in these mass regions already by the low-lying second 2^+ states in even nuclei. It is shown in this work that the odd-A spectra contain much more detailed evidence for triaxial shapes than the even ones. Here, only a brief summary can be given. The comparison between experiment and theory is given for some representative cases in Figs. 1-10. Features of the spectra which are characteristic for the various triaxial regions are pointed out in the captions. References to the experimental data are given in the main publication.[2]

The calculated spectra represent essentially parameter-free calculations. The parameters β and γ are derived from the lowest excited states in neighbouring even nuclei according to a standard procedure which is described in Ref. 2. In particular, the γ-parameter is derived from the (A-1) even neighbor for particle spectra (λ_F below the unique parity j-shell) and from the (A+1) neighbour for hole spectra (λ_F above the j-shell). The Fermi energy λ_F is estimated from a Nilsson level scheme.

The surprising result of this work is that rather complex families of unique parity states can be reproduced theoretically on the assumption of triaxial shapes with fixed β and γ values. In particular, the odd-A spectra define γ rather sharply, and the values obtained in this way, coincide consistently within a few degrees with those derived from the even neighbors. This result suggests that a number of transitional nuclei are less soft than expected from existing theoretical calculations of potential energy surfaces.

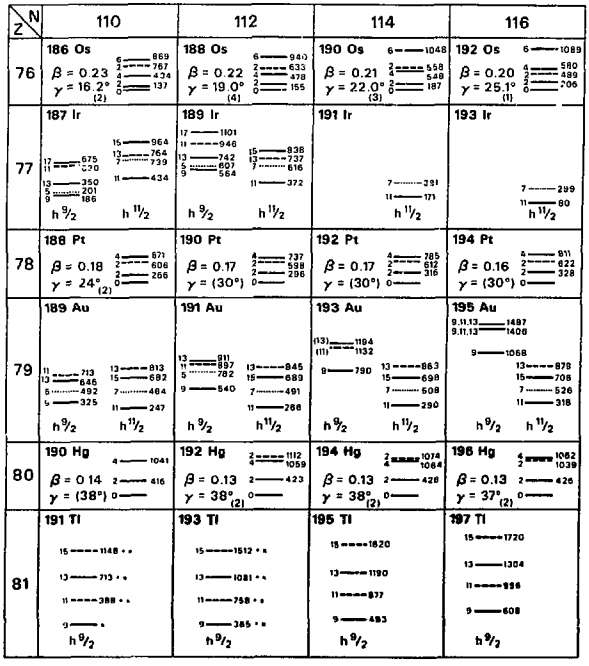

Fig. 1. Systematics of experimental unique parity spectra built on the $h_{9/2}$ and $h_{11/2}$ shell of odd proton nuclei are shown for nuclei in the A = 190 mass region. Lowest energies (in keV) of adjacent even nuclei and values for β and γ, derived from these energies, are also given. The odd-A spectra confirm a gradual transition from prolate to oblate between Os and Hg. In such a transition, the theoretical spectra change from a decoupled type (j + 1) level above the (j + 2) level to a strongly coupled type (j + 1) level below (j + 2) level) for particle spectra and vice versa for hole spectra. This change is observed in the experimental spectra, e.g., those of ^{187}Ir, ^{189}Au, and ^{191}Tl where the $h_{\frac{9}{2}}$ particle spectra are based on the $\gamma = 16°$ ^{186}Os, $\gamma = 24°$ ^{188}Pt, and $\gamma = 38°$ ^{190}Hg cores and the $h_{\frac{11}{2}}$ hole spectra are built on the ^{188}Pt and ^{190}Hg cores, respectively. Both spectra are decoupled in ^{189}Au because the $h_{\frac{9}{2}}$ states are related to the prolate ^{188}Pt core and the $h_{\frac{11}{2}}$ states to the oblate ^{190}Hg core. (XBL 7411-8166)

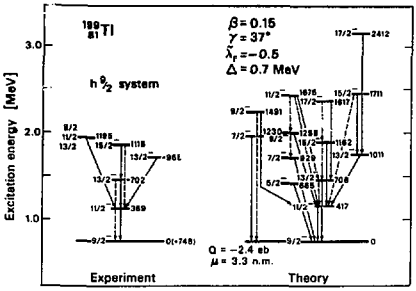

Fig. 2. Negative parity states in ^{199}Tl. Solid lines indicate the strongest observed or calculated decay transitions of each level. The calculation with standard parameters reproduces the experimental states. Strong evidence for a triaxial shape is given by the second $\frac{13}{2}^-$ state. The calculation seems to identify the measured state at 1195 keV as the second $\frac{9}{2}^-$ state. (XBL 7411-8170)

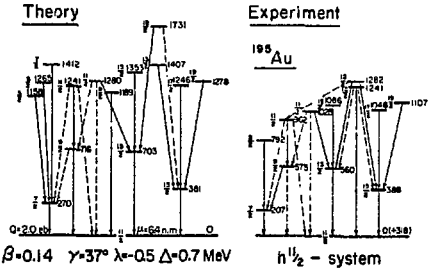

Fig. 3. Negative parity states in ^{195}Au built on the $h_{11/2}$ shell. Solid lines indicate transitions with 80 to 100% of the strongest decay intensity of each level. The level order of the 12 states above the basic $\frac{11}{2}^-$ states is almost completely reproduced by the standard calculation. This agreement depends sensitively on the γ-value γ = 37° derived from the ^{196}Hg core, in particular, for the close positions of the first $\frac{9}{2}^-$ and $\frac{13}{2}^-$ state, the $\frac{17}{2}^-$ and $\frac{19}{2}^-$ state, and the second and third $\frac{11}{2}^-$ states. (XBL 749-4250)

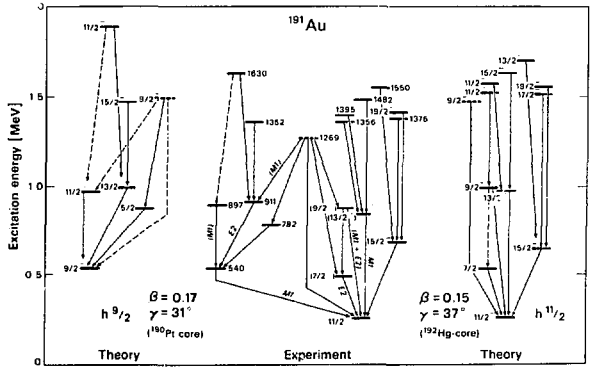

Fig. 4. Negative parity states in ^{191}Au. The decay scheme separates into two systems, the one built on the $h_{\frac{11}{2}}$ shell and the other probably on the $h_{\frac{9}{2}}$ shell. The two standard calculations suggest spin-values for all unassigned levels. The measured state at 1269 keV which decays to both systems is possibly a mixture of the second $\frac{9}{2}^-$ states which appear -- at least in the calculation -- at about the same energy in both systems and could be subject to an accidental resonance coupling. (XBL 7411-8167)

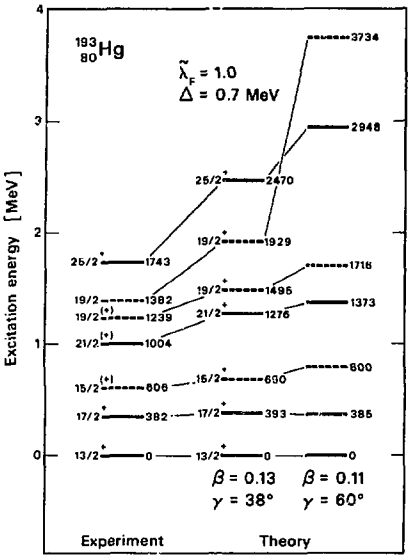

Fig. 5. Positive parity states in ^{193}Hg built on the $i_{13/2}$ shell. Evidence for a triaxial shape is provided by the second 10^+ state which is found in right relative order in the calculation with the standard value $\gamma = 38°$, but not with an $\gamma = 60°$ core. (XBL 7411-8171)

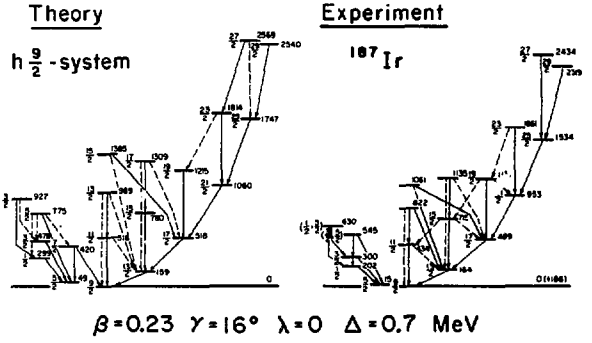

Fig. 6. The $h_{\frac{9}{2}}$ system in ^{187}Ir. The transition lines are defined as in Fig. 3. The large number of yrast states and the 5 non-yrast states which are observed in experiment are almost completely reproduced by the triaxial calculation with $\gamma = 16°$ derived from ^{186}Os. The vertical $\Delta I = 1$ band structures in the calculated spectrum can be classified by approximate K and Ω values. Some higher members of these bands are seen in experiment. (XBL 7410-4390)

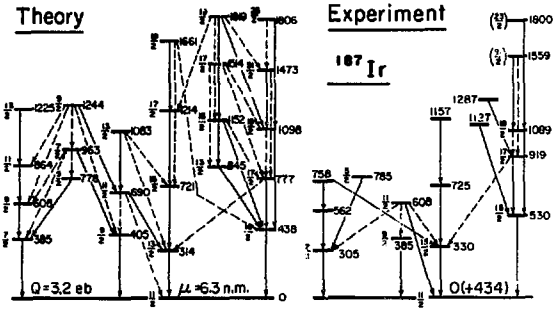

Fig. 7. The $h\frac{11}{2}$ system in ^{187}Ir. The transition lines are defined as in Fig. 3. The standard calculation reproduces the low-lying $\frac{7}{2}^-$ state including its large $B(E2; \frac{7}{2}^- \rightarrow \frac{11}{2}^-) = 0.32$ (eb)^2 which is found = 0.3 (eb)^2 experimentally in ^{189}Ir. At the same time, it yields the strongly-coupled yrast band and the side bands. This result strongly supports a triaxial shape of ^{187}Ir. (XBL 749-9249)

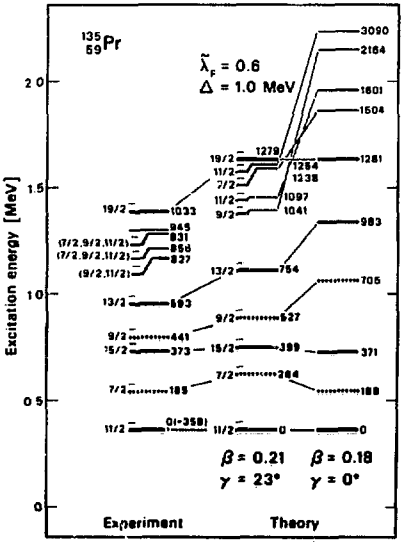

Fig. 8. The $h\frac{11}{2}$ family in ^{135}Pr. This spectrum is characteristic for odd proton nuclei in the A = 135 mass region. Similar spectra have been observed in ^{133,133a}La and ^{129}Cs. The decoupled level structure indicates a prolate-type core deformation. The second and third states of spin $\frac{9}{2}^-$, $\frac{7}{2}^-$, and $\frac{11}{2}^-$ observed for ^{135}Pr change sharply in energy as a function of γ. They appear just below the $\frac{19}{2}^-$ state for the standard value $\gamma=23°$, derived from ^{134}Ce, in agreement with experiment, but lie far too high for a $\gamma=0°$ core. (XBL 7412-8175)

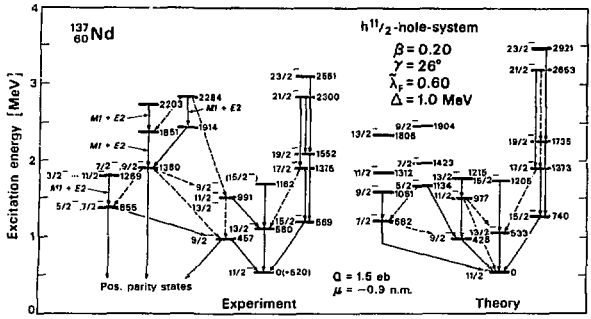

Fig. 9. Negative parity states in ^{137}Nd. Strongly-coupled yrast bands of the ^{137}Nd type have also been observed in ^{135}Nd, ^{133,135}Ce, and ^{131}Ba. These odd-neutron-hole spectra in N = 75, 77 nuclei are very similar to the Z = 77 odd-proton-hole spectra in Ir isotopes. In both mass regions, they indicate strongly triaxial shapes of prolate type. The additional level structure observed in ^{137}Nd, which is shown in the three columns on the right of the experimental spectrum, is probably not based on the $h_{11/2}$ shell, but is tentatively attributed to the $h_{9/2}$ shell and possibly the $f_{7/2}$ shell (levels at 1374 and 1788 keV). (XBL 7411-8159)

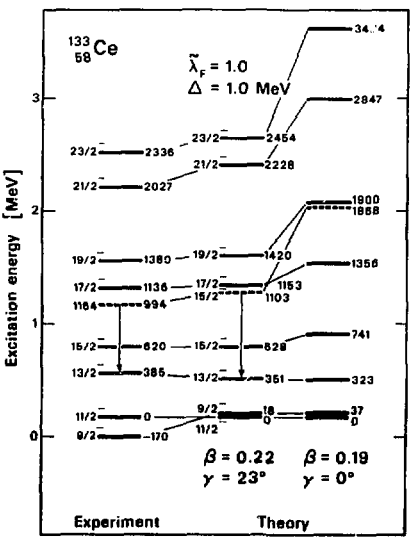

Fig. 10. the $h_{\frac{11}{2}}$ family in ^{133}Ce. Triaxiality of the core is indicated by the position of the second $\frac{15}{2}^-$ state. The model calculation with standard parameters as well as for $\gamma = 0°$ does not reproduce the low positions of the first $\frac{9}{2}^-$ state. This deficiency could be remedied by an attenuation of the Coriolis matrix elements which has not been used in the present calculation. (XBL 7411-8172)

The present work has strong applications in the field of experiment. It provides a general frame for analyzing low-energy spectra of transitional odd-A nuclei. It predicts numerous states, their energies, moments, and transition probabilities. More experimental results are necessary to judge the range of validity of the present model. Certain discrepancies are expected due to shape fluctuations and other effects. But the present work clearly points out that there is a simple general structure behind the odd-A spectra in the transitional regions and that triaxial nuclear deformations are a simple way to understand their systematic behaviour.

Footnotes and References

*Condensed from LBL-3416 and Ref. 2.

+On leave from Techn. Universität München, Munich, West Germany.

1. J. Meyer-ter-Vehn, submitted to Nucl. Physics, see contribution to this report.

2. J. Meyer-ter-Vehn, submitted to Nucl. Physics.

TEST OF MANYBODY METHODS IN AN EXACTLY SOLUBLE BACKBENDING MODEL

S. Y. Chu, E. R. Marshalek,* J. O. Rasmussen, and P. Ring+

Much attention has been focused on the behavior of the nuclear moment of inertia at high spins in the last few years. The sudden increase of the moment of inertia and the occurence of backbending has been studied in a number of exactly soluble models by Krumlinde and Szymanski.[1] For realistic calculations the selfconsistent cranking model (SCC) has proved to be very successful.[2] Some reasons for this success may be that the underlying wave functions are product wave functions and therefore simple enough to be applied for realistic calculations and general enough to contain all the necessary degrees of freedom, such as, changes in shape, pairing correlations and decoupling processes, which seem to be very important for these high-spin states.

There are, however, some serious shortcomings of that method: 1) The cranking wave functions violate symmetries; in particular they are not eigenstates of angular momentum and particle number. 2) There seem to be some regions in the backbending curve where one has great quantum fluctuations which cannot be handled within the cranking model.

One way to overcome some of these difficulties is a particle-number projection which has to be carried out before the variation. Another method is the random phase approximation (RPA) based on the cranking model basis. The RPA allows the inclusion of higher correlations and includes an approximate projection of angular momentum and particle number.

We therefore decided to study the cranking model and these two methods in an exactly soluble case. For this purpose we took the R(8)-model of Krumlinde and Szymanski.[1]

The model consists of 2Ω identical fermions, interacting via a pairing force, distributed among two 2Ω-fold degenerate single particle levels separated by an energy 2ε and coupled to an external rotor with fixed moment of inertia a^{-1}.

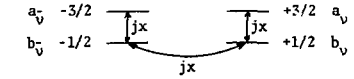

The Hamiltonian is

$$H = \frac{1}{2} a (\vec{I} - \vec{j})^2 + H_{sp} + H_p \qquad (1)$$

with

$$H_{sp} = \varepsilon \sum_\nu^\Omega (a_\nu^+ a_\nu + a_\nu^+ a_\nu^- - b_\nu^+ b_\nu - b_\nu^+ b_\nu^-) \qquad (2)$$

$$H_p = -g \sum_\nu^\Omega (a_\nu^+ a_\nu^+ + b_\nu^+ b_\nu^+) \sum_\nu^\Omega (a_\nu^- a_\nu + b_\nu^- b_\nu) \qquad (3)$$

j_k are the components of the angular momentum of the particles.

For instance,

$$j_x + i j_y = \sqrt{3} \sum_\nu^\Omega (a_\nu^+ b_\nu - b_\nu^+ a_\nu^-) + 2 \sum_\nu^\Omega b_\nu^+ b_\nu^- \qquad (4)$$

As shown in Ref. 1, the Hamiltonian is composed of generators of the group R(8). This makes an exact solution of the model possible.

We study small oscillations about a classically rotating solution: In lowest order

$$\hat{I}_x = I \ , \quad \hat{I}_y = \hat{I}_z = 0 \ .$$

Applying the Hartree-Fock-Bogolyubov factorization for the particle operators gives the cranking model

Hamiltonian H_ω with the selfconsistency relations

$$\omega = a(I - \langle j_x \rangle_\omega) \qquad (5.a)$$

$$\Delta = g \sum_\nu^\Omega (\langle a_\nu a_\nu \rangle_\omega + \langle b_\nu b_\nu \rangle_\omega) \qquad (5.b)$$

The diagonalisation of H_ω corresponds to the solution of the HFB-equations. It can be carried out analytically. Since the levels are half filled, the chemical potential λ is always 0. The four quasiparticle energies are

$$E_i = \pm \frac{\omega}{2} + E_\pm \qquad (6)$$

with

$$E_\pm = \sqrt{\varepsilon^2 + \Delta^2 + \omega^2 \pm \omega\sqrt{\varepsilon^2 + 4\Delta^2}}$$

Obviously one of them can go to 0 for certain values of Δ and ω, which corresponds to a gapless superconductivity. This happens also in realistic calculations (Ref. 2). To get selfconsistency one has to solve the system (5), which can be written as two transcendental equations for the variables ω and Δ. Within some ω-regions there can be two solutions for Δ. Within the cranking model the classical expression I is usually replaced by

$$\sqrt{I(I+1)} \quad .$$

On the basis of the cranking model we studied two methods to improve the results: The first method is a particle number projection before the variation. We used the method of contour integrals proposed in Ref. 3. Since time reversal symmetry is violated by the cranking operator ωj_x one has first to determine the conjugate states of the BCS-theory. This is done by diagonalizing the density matrix which gives the canonical basis. Within this basis the formulas of Ref. 3 are applied. For each pair of (ω,Δ) the projected energy

$$E_{proj} = \langle H_\omega P^N \rangle_{\omega,\Delta} \qquad (7)$$

is calculated and according to the cranking model the stationary points

$$\frac{\partial}{\partial\Delta} E_{proj}\Big|_{\omega fixed} = 0 \qquad (8)$$

are calculated. ω is determined by

$$\omega = a\left(\sqrt{I(I+1)} - \langle j_x P^N \rangle\right) \qquad (9)$$

Figure 1 shows the surface of the projected energy. For $\omega = 0$ there is a minimum at $\Delta = 0.335$ (MeV) and a maximum at $\Delta = 0$. With increasing ω this minimum moves to smaller values of Δ (Coriolis antipairing effect). The solid line connects the stationary points (8). It approaches $\Delta = 0$ for high ω-values. The dots on that line correspond to the integer even I-values. The dashed line represents $\Delta(\omega)$ in the unprojected calculation, which has sharp transition to zero.

The second method is a generalized Holstein Primakoff boson expansion in powers of Ω^{-1} (Refs. 4 and 5) and I^{-1}. Since one has two kinds of degrees of freedom, namely particle degrees of freedom and rotor degrees of freedom, one has two kinds of bosons: The particle bosons B^+ are super-positions of two quasi-particle operators. The rotor boson b defines a wobbling motion of the nucleus around the steady rotation around the x-axis. The rotor wave function is written as

$$|IK\rangle = \frac{e^{iI\Phi}}{\sqrt{2\pi}} \cdot \frac{(b^+)^{I-K}}{\sqrt{(I-K)!}} 10) \qquad (10)$$

where Φ is an azimuth around the x-axis, K is the projection of the angular momentum onto that axis and the boson is defined by

$$\hat{I}_x = \frac{1}{i}\frac{\partial}{\partial\phi} - b^+b \quad ;$$

$$\hat{I}_y + i\hat{I}_z = b^+\sqrt{\frac{2}{i}\frac{\partial}{\partial\phi} - b^+b} \quad . \qquad (11)$$

The expansion of the Hamiltonian yields in zeroth order the selfconsistent cranking model. In the next order one has a bilinear form of bosons. The diagonalization corresponds to the RPA. It

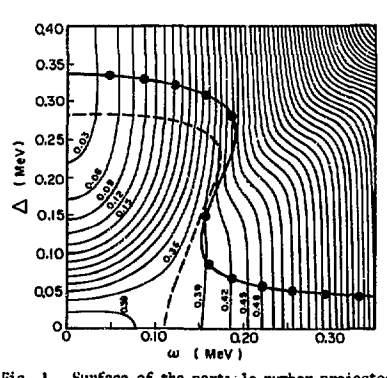

Fig. 1. Surface of the particle number projected energy (7). The contour lines have an energy difference of 0.03 MeV. (XBL 757-3500)

gives us vibrations for each point on the yrast curve. The zero point correction of these vibrations is calculated. On the other hand, this kind of boson expansion has the nice feature that it conserves the particle number approximately. That means as long as $\Delta \neq 0$ one has a zero frequency mode which corresponds to a pairing rotation. The corresponding moment of inertia and its contribution to the energy can be calculated. For $\Delta = 0$ this mode is a pairing vibration and the frequency no longer vanishes.

In Fig. 2 the three methods are compared with the exact solution for $\Omega = 4$, $a = 0.0197$ (MeV), $g = 0.075$ (MeV), $\varepsilon = 0.1$ (MeV). Outside the backbending region all three methods agree quite well with the exact result. One has a transition from the paired ground state to the normal-fluid, high-spin states. Within the backbending region there are differences. Selfconsistent cranking gives a too strong backbending. This can be understood easily. Since the cranking wave functions are product wave functions, they do not contain enough correlations to describe the mixing of the two bands in the right way. Particle number projection gives an improvement. However, for the upper branch ($\Delta \approx 0$) it corresponds nearly to the cranking solution. Obviously the particle number projected wave functions do not have the right type of correlations, which is important there. The best agreement with experiment is shown by the RPA curve. One has, however, to mention that there are points along that curve where the RPA gets unstable.

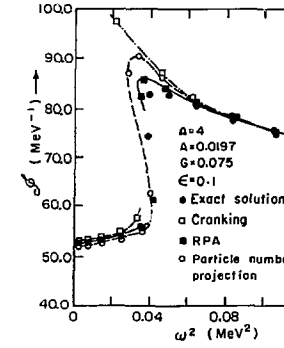

Fig. 2. Moment of inertia $\mathscr{I}$ against the square of the angular velocity ω. The full points are the exact values, the full line corresponds to the RPA, the dashed line is the particle number projection and the dashed-dot line is the selfconsistent cranking model. (XBL 757-3505)

Footnotes and References

*Permanent address: Physics Department, University of Notre Dame, Southbend, Ind.

†Supported by the Deutsche Forschungsgemeinschaft.

1. J. Krumlinde and Z. Szymanski, Ann. of Phys. 79, 201 (1973).

2. B. Banerjee, H.J. Mang and P. Ring, Nucl. Phys. A211, 366 (1973).

3. K. Dietrich, H.J. Mang and J.H. Pradal, Phys. Rev. 135B, 22 (1964).

4. T. Holstein and H. Primakoff, Phys. Rev. 58, 1098 (1940).

5. E.R. Marshalek, Nucl. Phys. A224, 221 (1974).

ATTENUATION OF THE CORIOLIS INTERACTION WITHIN THE CRANKING MODEL*

P. Ring† and H. J. Mang

The description of strongly distorted rotational bands within the cranking model allows an interpretation of the attenuation factors used in the particle plus rotor model. It turns out that they are not very much influenced by the residual interaction, but strongly dependent on the angular momentum. A simple model is proposed to calculate distorted spectra which are in rather good agreement with the experimental data and with the fully self-consistent calculation.

* * *

The description of very distorted rotational bands of odd mass deformed nuclei is possible within the particle plus rotor model[1] (PRM) by the coupling of particles to the collective rotation using a Coriolis interaction. Practical calculations, however, allow a reproduction of the experimental data only by reproducing the strength of this interaction. The attenuation factors R used for this purpose lie between 0.4 and 0.9.[2] There exist attempts to give an interpretation of these factors by taking into account the coupling of the outside particle to collective vibrations of the core.[3] A purely microscopic derivation of the Coriolis interaction is possible by using the method of angular momentum projection after the variation.[4] Recently[5] it has been shown that the application of the cranking model within the framework of the Hartree-Fock-Bogolyubov-Theory (HFB), which can be derived from a projection of the

angular momentum before the variation,[6] allows a quantitative description of these bands without any fit parameter. In particular, no extra attenuation of the Coriolis term has to be introduced.

Within the cranking model the internal wave function ϕ_α of the odd nucleus is calculated by the variational equation

$$\langle \delta\phi_\alpha | \hat{H} - \omega \hat{J}_x - E^\alpha | \phi_\alpha \rangle = 0 \quad . \tag{1}$$

If one restricts ϕ_α to the HFB - functions, it corresponds to the blocked *HFB - Equations*[7] in the rotating frame. One has to look for solutions of this system which have odd particle number parity[8] and which are eignfunctions of a rotation about 180° around the x-axis

$$e^{i\pi J_x} \phi_\alpha = i(-)^{I-1/2} \phi_\alpha \quad . \tag{2}$$

I is the total angular momentum and the cranking frequency ω is determined by the subsidiary condition

$$\langle \phi_\alpha | J_x | \phi_\alpha \rangle^2 + \langle \phi_\alpha | J_z^2 | \phi_\alpha \rangle = I \cdot (I + 1) \quad . \tag{3}$$

Equation 1 is solved directly in Ref. 5 for ^{159}Dy. For comparison with the particle plus rotor model, however, it is useful to decompose ϕ_α

$$\phi_\alpha = \gamma_\alpha^+ | \phi_o \rangle = \sum_K C_K^\alpha \beta_K^+ | \phi_o \rangle \tag{4}$$

where ϕ_o is the underlying HFB - wave function of the even core and β_K^+ are the quasiparticle operators corresponding to this core, which diagonalizes the Hamiltonian (H^{11} diagonal). For $\omega = 0$, K is a good quantum number (it corresponds to the eigenvalue of J_z) because of the axial symmetry of the core. For higher ω this is not exactly true. In the numerical calculation of ^{159}Dy (see Fig. 1) however, it turns out that for a large region of spin values ($I < 21/2$) the core stays nearly axially symmetric and K is a rather good quantum number. The variation (1) is therefore decomposed into a variation of the core function φ_o and a variation of the mixing coefficients C_K^α

$$\langle \delta\phi_o | \gamma_\alpha \, (H - \omega J_x) \gamma_\alpha^+ | \phi_o \rangle = 0 \tag{5}$$

$$\sum_K \left\{ \left(\langle \phi_o | H - \omega J_x | \phi_o \rangle + E_K(\omega) \right) \delta_{KK'} - \omega j_x^{11} \right\} C_K^\alpha = E^\alpha C_{K'}^\alpha \tag{6}$$

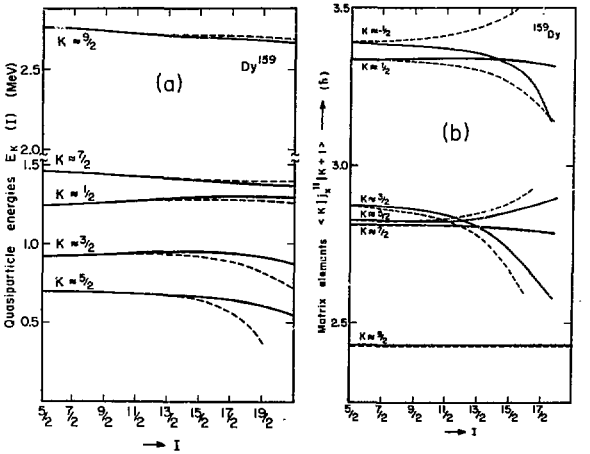

Fig. 1. The dependence of (a) the quasiparticle energies E_K, and (b) the matrix elements j^{11}_{KK+1} of Eq. (6) on the angular momentum I; $K = -1/2$ corresponds to the decoupling parameter. Full lines correspond to the favored solutions, dashed lines to the unfavored solutions (see Ref. 9).

(XBL 745-3201)

j^{11}_X is the one quasiparticle part of J_X corresponding to the operators β^+_K. Equation 5 corresponds to blocked HFB - equations for the determination of the core wave function ϕ_0 with even number parity. It is coupled by the blocking of γ_α to Eq. (6) which determines the mixing amplitudes C^α_K.

The PRM replaces the calculation of ϕ_0 by assuming a rotor with a fixed moment of inertia. Equation (6) corresponds to the diagonalization of the PRM for the calculation of the mixing amplitudes.

Besides the fact that the cranking model gives energies in the rotating frame, there is a close analogy between Eq. (6) and the PRM concerning the amplitudes C^α_K.

a) Neglecting constants the diagonal elements are in both cases essentially the quasiparticle energies E_K. In the cranking model they depend on ω, but only very weakly, as shown in Fig. 1(a).

b) The non-diagonal elements vanish exactly for $K \neq K' \pm 1$ in the PRM and approximately in the cranking model. In the latter model the frequency is $\omega = \langle \phi_\alpha | J_x | \phi_\alpha \rangle / \mathcal{J}_{sc}$. $\mathcal{J}_{sc}$ is the self-consistently determined moment of inertia. Regarding Eq. (3) the elements $K' = K + 1$ are

in the cranking model

$$-\frac{\sqrt{I(I+1) - \langle J_z^2 \rangle}}{\mathcal{J}_{sc}} \cdot j^{11}_{X\,K\,K+1}(\omega) \qquad (7)$$

in the PRM[1]

$$-\frac{\sqrt{(I+1) - K(K+1)}}{\mathcal{J}_{rotor}} \; j^{11}_{X\,K\,K+1}(\omega = 0) \qquad (8)$$

Both expressions are very similar. If one neglects the small ω-dependence of the matrix elements j^{11}_X in the cranking model (see Fig. 1(b)) and the fact that $\sqrt{I(I+1) - K(K+1)}$ is replaced by $\sqrt{I(I+1) - \langle J_z^2 \rangle}$ in the cranking model, there remains only one big difference between both Coriolis interactions explaining why one needs attenuation factors in the PRM but not in the cranking model: the cranking model uses a self-consistently determined moment of inertia $\mathcal{J}_{sc}$, which includes the effect of the decoupling particle and which is strongly I-dependent (see Fig. 2). For small I-values, where the particle is coupled to the core, it is very easy to gain angular momentum in x-direction by decoupling the particle. Therefore, the value of $\mathcal{J}_{sc}$ is large and the Coriolis interaction is strongly attenuated. This effect can also be seen in the simple Inglis formula for the odd nucleus in the state α

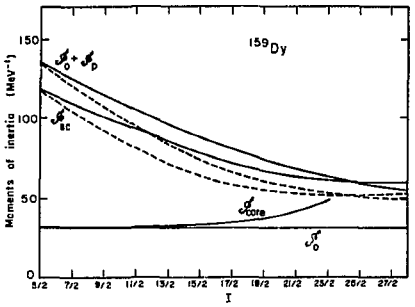

Fig. 1. Moments of inertia dependent on the angular momentum. $\mathcal{J}_{sc} = \langle \phi_\alpha | J_x | \phi_\alpha \rangle / \omega$ and $\mathcal{J}_{core} = \langle \phi_0 | J_x | \phi_0 \rangle$ correspond to the many body wave function (KO_c in Fig. 3). $\mathcal{J}_0$ and $\mathcal{J}_0 + \mathcal{J}$ correspond to the particle plus cranking model (see Eq. (10)). (XBL 747-36...

$$\mathcal{J}^{ing}_\alpha = \sum_{K\,K'\,\alpha} \frac{|J^{20}_{x\,KK'}|^2}{E_K + E_{K'}} + \sum_{K\,\alpha} \frac{|j^{11}_{x\,K\alpha}|^2}{E_K - E_\alpha} \qquad (9)$$

The first part comes from the core. The second part describes the particle. Because of the small energy denominator it can become much larger than the first part. In the case of ^{159}Dy, we found $\mathcal{J}_{sc} = 123.35 = 26.82 + 96.53$ (MeV^{-1}).

However, for higher spin values a perturbation theoretic treatment is no longer possible. The exact solution (see Fig. 2) shows that the particle is more and more aligned and its contribution to the moment of inertia becomes smaller and smaller. Therefore the self-consistent moment of inertia $\mathcal{J}_{sc}$ diminishes with increasing spin. Only for very high spin values should it increase again because of the antipairing and the stretching effect of the core.

Figure 3 shows the experimental spectrum of the positive parity band in ^{159}Dy and different calculations. Kisc is the fully self-consistent solution of Eq. (1) as described in Ref. 5. It uses a pairing plus quadrupole force including the exchange term of the QQ-force, its contribution to the pairing potential and the contributions of the pairing force to the self-consistent field. KI_{sc} uses a similar force, which does not include the latter three terms and which is adjusted to reproduce the same energy gap and the same deformation.

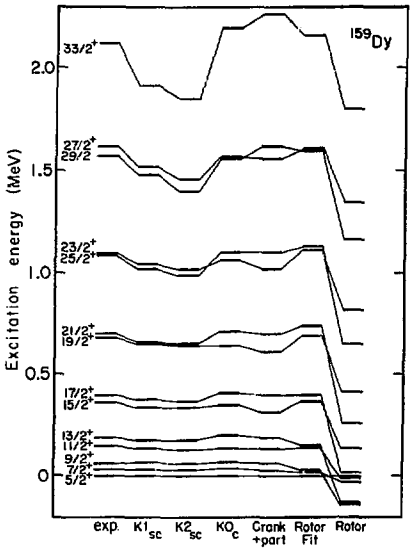

Fig. 3. The positive parity band in ^{159}Dy: Experiment (see Ref. 10) and different calculations as described in the text. (XBL 745-3198)

	K1	K2
$Q_p = Q_n$	-0.034	-0.034
Q_{pn}	-0.089	-0.089
G_p	-0.190	-0.195
G_n	-0.139	-0.148
ΔE_{n+} (MeV)	-0.25	-0.30

Units and details are given in Ref. 5.

In the column $K0_c$ the influence of the residual interaction is neglected, i.e., the calculation is done within constant fields Γ and Δ taken from $K2_{sc}$ at $\omega = 0$. This procedure changes the behavior of the spectrum at very high spin values. However, the attenuation of the Coriolis interaction is only very little influenced by the residual interaction.

We studied it in the following simple model (Column: crank. + part) suggested by Eq. (6). One outside particle is coupled to a rotor with moment of inertia $\mathcal{J}_0$:

$$\langle \phi_0 | H - \omega J_x | \phi_0 \rangle = -\frac{\mathcal{J}_0}{2}\omega^2$$

Neglecting the ω-dependence of E_K and $j^{11}_{KK'}$, one has to diagonalize

$$-\frac{\mathcal{J}_0}{2}\omega^2 + E_K - \omega j^{11}_{x_{KK'}} \qquad (10)$$

The subsidiary condition for ω is

$$\mathcal{J}_0\omega + \langle j_x \rangle = \mathcal{J}_0\omega + \mathcal{J}_p\omega = \sqrt{I(I+1) - \langle j_z^2 \rangle} \qquad (11)$$

Therefore the Coriolis interaction can be written as

$$H_{cor} = -\omega j^{11}_x = -\frac{\sqrt{I(I+1) - \langle j_z^2 \rangle}}{\mathcal{J}_0} j^{11}_x \cdot R \qquad (12)$$

Compared to the PRM it is attenuated by a factor

$$R = \frac{\mathcal{J}_0}{\mathcal{J}_0 + \mathcal{J}_p} = 1 - \frac{\langle j_x \rangle}{\sqrt{I(I+1) - \langle j_z^2 \rangle}} \qquad (13)$$

$\mathcal{J}_p = \langle j_x \rangle / \omega$ is the contribution of the outside particle (see Fig. 2). Taking into account that there was no fit parameter used ($\mathcal{J}_0$ is taken from $K0_c$), the agreement of this simple model with the experiment and with the fully self-consistent calculation is surprisingly good. The last two columns in Fig. 3 are calculations within the PRM, without attenuation (column 7) and with a fit over 4 parameters (see Ref. 5).

Footnotes and References

*Published in Phys. Rev. Lett. 33, 1174 (1974).

†Supported by the Deutsche Forschungsgemeinschaft. Physikdepartment der Technischen Universitaet Muenchen, West Germany.

1. A.K. Kerman, Mat. Fys. Medd. Dan. Selk. 30, 15 (1956).

2. C.W. Reich and M.E. Bunker, Nucl. Structure Dubna Symposium, IAEA, Vienna, 119 (1968); S.A. Hjorth, A. Johnson and G. Ehrling, Nucl. Phys. A181, 113 (1972); G. Lovhoiden et al., Nucl. Phys. A148, 657 (1970); Th. Lindblad, H. Ryde and D. Barneoud, Annual Report 1971 AFI, Stockholm, 43 (1971) and Nucl. Phys. A193, 155 (1972); S.A. Hjorth, H. Ryde, et al., Nucl. Phys. A144, 513 (1970).

3. N.I. Pyatov, M.I. Chernej, M.I. Baznat, JINR, Dubna, E-4-5468 (1970).

4. F.R. May, L. Münchow, and S. Frauendorf, Preprint ZFK Rosendorf.

5. P. Ring, H.J. Mang, and B. Banerjee, Nucl. Phys. A225, 141 (1974)

6. R. Beck, H.J. Mang, and P. Ring, Zs. Phys. 231, 26 (1970).

7. P. Ring, R. Beck, and H.J. Mang, Zs. Phys. 231, 10 (1970).

8. B. Banerjee, P. Ring, and H.J. Mang, Nucl. Phys. A221, 564 (1974).

9. F.S. Stephens, Proc. of the Intern. Conf. on Nucl. Phys., Munich, vol. 2 (1973). Ed. J. deBoer and H.J. Mang, North Holland Amsterdam (1974).

10. J. Boutet and J.P. Torres, Nucl. Phys. A175. 167 (1971).

MICROSCOPIC DESCRIPTION OF "BACKBENDING" IN Yb-NUCLEI*

H. R. Dalafi,† H. J. Mang† and P. Ring

Hartree-Fock-Bogoliubov theory with approximate projection of particle number is used to calculate the nuclear moment of inertia within the framework of the cranking model. In this paper the nuclei ^{166}Yb, ^{168}Yb and ^{170}Yb are studied. The calculation reproduces the experimental data in so far that ^{166}Yb and ^{170}Yb show the "backbending" effect in their ground state bands whereas ^{168}Yb does not. Moreover, we find that "backbending" occurs at higher angular momenta for ^{170}Yb than for ^{166}Yb.

The ground state rotational bands of ^{166}Yb, ^{168}Yb and ^{170}Yb show a rather strange discontinuous behavior as a function of the neutron number.[1,2] While ^{166}Yb and ^{170}Yb show the so called "backbending" effect, ^{168}Yb does not.

In this paper we attempt to reproduce such behavior within the framework of the self-consistent cranking model with inclusion of approximate projection of particle number.[3,4]

The equations of the self-consistent cranking model are most easily obtained from a variation of the energy given by[3]

$$E^N_J = \langle\phi|H - \omega J_x|\phi\rangle - \frac{\langle\phi|(H - \langle\phi|H|\phi\rangle)\Delta\hat{N}^2|\phi\rangle}{2\langle\phi|\Delta\hat{N}^2|\phi\rangle + 4} \qquad (1)$$

with subsidiary conditions

$$\langle\phi|J_x|\phi\rangle = \sqrt{J(J+1)} \qquad (2.a)$$

$$\langle\phi|\hat{N}|\phi\rangle = N \qquad (2.b)$$

where $\hat{N}$ is the number operator and $\Delta\hat{N}$ is defined as

$$\Delta\hat{N} = \hat{N} - \langle\phi|\hat{N}|\phi\rangle \qquad (3)$$

The condition (2.a) on $\langle\phi|J_x|\phi\rangle$ is equivalent to an approximate angular momentum projection.[5] Projection of particle number is treated in a better approximation by not only having the condition (2.b) on $\langle\phi|\hat{N}|\phi\rangle$ but also including the term ΔE^N in Eq. (1). From now on we shall use the short-hand notation ΔE^N for $\frac{(H - \langle H\rangle)\Delta N^2)}{2\langle\Delta N^2\rangle + 4}$.

The moment of inertia θ is directly calculated from

$$\theta = \frac{\sqrt{J(J+1)}}{\omega_J} \qquad (4)$$

where ω_J is obtained from Eq. (2.b). This implies that we can calculate θ as a continuous function of ω.

A completely self-consistent solution of the HFB-equations which arise from a variation of E^N_J (Eq. (1)) is however, very cumbersome. We therefore used the same approximation as in Ref. 3.

We define a single particle Hamiltonian, H_{sp} as

$$H_{sp} = \sum_\alpha E_\alpha C^+_\alpha C_\alpha - \chi \cdot \sum_{\alpha>0} C^+_\alpha C^+_{\bar{\alpha}} - q \sum_{\alpha,\beta} r^2 \cdot Y^{20}_{\alpha\beta} C^+_\alpha C_\beta - \sum_{\alpha\beta} J^{(x)}_{\alpha\beta} C^+_\alpha C_\beta \qquad (5)$$

where the second term is a single-particle pairing potential and the third term is the usual quadrupole potential of Nilsson.[6] The diagonalization of H_{sp} provides wave functions which depend on three parameters κ_p, κ_n and q. A variation of E^N_J with respect to these parameters yields approximate solutions of the HFB-equations for every ω.[3]

The Hamiltonian and the single particle configuration space were the same as used in Ref. 4, with the exception of the strength of the pairing force. The reason for this is that the inclusion of the term ΔE^N effectively increases the pairing interaction.[7] The term ΔE^N depends, however, in a different way on the angular momentum. We therefore used

$$G_N = 0.125 \quad , \quad G_p = 0.165 \quad .$$

Moreover one more approximation was introduced in order to keep the computing time within reasonable limits.[3] The actual variation was only performed with respect to K_n. This approximation was checked for some selected values of the cranking frequency ω and found to be satisfactory, in the sense that all qualitative features were insensitive to this approximation.

Results are presented in Figs. 1 to 3. Figure 1 gives the comparison of experimental and theoretical moments of inertia plotted versus the square of the angular frequency (ω^2). The agreement is qualitative and certainly as good as one can expect from a model like the one we have used. The principal features of the experimental data are well reproduced in particular the differences between the "backbending" nuclei ^{166}Yb and ^{170}Yb.

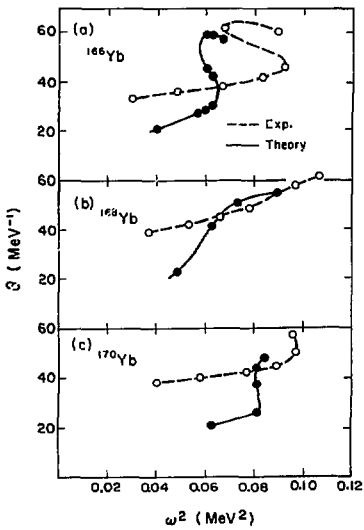

Fig. 1. Moment of inertia as a function of ω^2. (a) ^{166}Yb, (b) ^{168}Yb, (c) ^{170}Yb. (XBL 757-3504)

Figure 2 shows the neutron energy gaps Δ_N for different angular momenta. Δ_N is defined as:

$$\Delta_N = G_N \cdot \sum_K U_K V_K$$

where the sum runs over all neutron states K. This definition of Δ_N amounts to setting Δ_N proportional to the diffuseness of the Fermi surface $D_N = \sum_K U_K V_K$.[8] The energy gap Δ_N defined in such a way does not necessarily coincide with the energy gap $\Delta_{K\bar{K}}$ which occurs in the formula for the occupation probabilities.[9] It is however a good measure for the overall strength of pair correlations. The reason for the difference is that the energy gap $\Delta_{K\bar{K}}$ may be strongly state dependent.[4] Note that up to angular momenta J = 16 the energy gap Δ_N decreases rather slowly with increasing angular momentum.

Figure 3 finally shows the contribution of neutrons of positive parity to the angular momentum ($\langle\phi|J_x^N|\phi\rangle$) as a function of $\langle\phi|J_x|\phi\rangle$. It is interesting to note that from $\langle\phi|J_x|\phi\rangle = 8$ on all curves are straight lines but with slightly different slopes. The slopes are

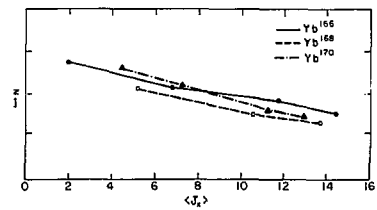

Fig. 2. Neutron energy gap Δ_N as a function of angular momentum $\langle J_x \rangle$. (XBL 757-3511)

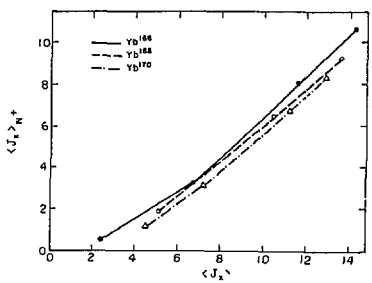

Fig. 3. Angular momentum $\langle J_x^{N+} \rangle$ of neutrons of positive parity as a function of $\langle J_x \rangle$. (XBL 757-3510)

0.98 for ^{166}Yb
0.85 for ^{168}Yb
0.92 for ^{170}Yb

There is clearly a correlation between these slopes and the appearance of the "backbending" effect. The larger the slope the stronger the "backbending". This means that the speed with which the alignment of the neutrons of positive parity occurs, determine whether there is "backbending" or not.

Footnotes and References

*Submitted for publication in Physics Letters.

†Physik-Department der Technischen Universität München, Garching, West Germany.

1. H. Beuscher, W.F. Davidson, R.M. Lieder, C. Mayer-Böricke, Phys. Lett. 40B, 449 (1972).

2. A. Faessler, F. Grümmer, L. Lin and J. Urbano, Phys. Lett. 48B, 87 (1974).

3. H.R. Dalafi, B. Banerjee, H.J. Mang and P. Ring, Phys. Lett. 44B, 327 (1973).

4. B. Banerjee, H.J. Mang and P. Ring, Nucl. Phys. 215, 366 (1973).

5. H.J. Mang, Lectures given at the summer school in Mikolajki, Poland, Sept. 1974. To be published in Nukleonika.

6. S.G. Nilsson, Mat. Fys. Skr. Dan. Vid. Selsk. 29, 16 (1955).

7. H.R. Dalafi, P. Ring, to be published in Z.f. Phys.

8. H.J. Mang, K.J. Poggenburg and J.O. Rasmussen, Nucl. Phys. 64, 353 (1965).

9. B. Banerjee, P. Ring and H.J. Mang, Nucl. Phys. A221, 564 (1974).

APPROXIMATE PROJECTION OF ANGULAR MOMENTUM AND PARTICLE NUMBER IN HEAVY NUCLEI*

H. R. Dalafi,† H. J. Mang† and P. Ring

The problem of symmetry violations in Hartree-Fock-Bogoliubov wave functions is handled by projection techniques. For the cases of strong and weak symmetry violations, approximate formulas of the projected energy are given. They allow an approximate projection before the variation for heavy nuclei. The methods are applied numerically to some model calculations for strong and weak deformations.

Microscopic descriptions of nuclear structure are based on a single particle model. The most general single particle model includes also pairing correlations and is given by the Hartree-Fock-Bogoliubov (HFB) theory.[1] This theory provides a simple tool for the description of many ground state properties in nuclei. Furthermore, it can be used as a basis of a microscopic treatment of collective states.[2,3] The reason for which the theory is working so well in many regions of the periodic table is, that often a very important part of the correlations within such nuclei; can be taken into account by considering symmetry violating single particle wave functions. The symmetries usually violated by the HFB theory are conservation of angular momentum and particle number. The most general HFB wave functions are no eigenstates of the angular momentum operators J^2 and J_z, since they are based on the deformed single particle wave functions, and are a mixture of different particle number components.

The projection before variation, turns out to be the most general extension of the HFB-theory, which handles the symmeteries in the right way. Calculations within this projected HFB-theory have been carried out in the region of light nuclei for small basis spaces.[4] The extension of these methods to deformed heavy nuclei and large configuration spaces, requires further restriction. One of the most commonly used restrictions is that one takes into account only axial symmetric shapes of nuclei.[5] This assumption is rather well justified for the ground state, and many excited states in the well deformed heavy nuclei. In the transitional region, however, the nuclei are usually soft against triaxial deformations, and one should take into account this degree of freedom. For a description of high-spin states, decoupling processes of one and two particles play a very important role and require a mixing of K-values.[6-8]

The aim of this work is to formulate and test approximate methods for handling particle number and angular momentum projection, which are simple enough to be applied for the most general HFB-functions of heavy nuclei. Furthermore, these methods are applied to some interesting nuclear problems.

The HFB solution $|\phi\rangle$ is, in general, not an eigenfunction of the angular momentum J^2, though the Hamiltonian H of the system is rotationally invariant. Wave functions, which are eigenstates of J^2 and J_z, can be obtained by projecting $|\phi\rangle$ onto the eigenstate of angular momentum

$$|\psi^J_M\rangle = P^J_M|\phi\rangle \qquad (1)$$

According to the method of projection, before variation, one has to look for the HFB-wave function $|\phi\rangle$ which minimizes the expectation value of the projected energy

$$E^J_{proj} = \frac{\langle\psi^J|H|\psi^J\rangle}{\langle\psi^J|\psi^J\rangle} \qquad (2)$$

An approximate expression (Ref. 4) that is valid for large deformation is

$$E^J_{proj} = \langle H\rangle - \frac{\langle J_y^2\rangle}{\theta_y} + \frac{\langle J_x\rangle}{\theta_{xc}}\left\{\sqrt{J(J+1)} - \langle J_x\rangle\right\} + \frac{1}{2\theta_y}\left\{\sqrt{J(J+1)} - \langle J_x\rangle\right\}^2 \qquad (3)$$

with

$$\theta_y = \frac{\langle J_x^2\rangle^2}{\langle(H - \langle H\rangle)J_y^2\rangle} \qquad (4.a)$$

and

$$\theta_{xc} = \frac{\langle J_y^2\rangle\langle J_x\rangle}{\langle(H - \langle H\rangle)J_x\rangle} \qquad (4.b)$$

Varying the projected energy[4] with respect to the HFB-wave functions, rather complicated equations are obtained. In the case, however, that the lowering term $-\langle J_y^2\rangle/\theta_y$ varies only slowly with J, it can be neglected in the variation. Then the cranking model, which minimizes

$$\delta\langle H - \omega J_x\rangle = 0 \qquad (5)$$

with the subsidiary condition

$$\langle J_x\rangle = \sqrt{J(J+1)} \qquad (6)$$

provides an approximate solution of the projected HFB equations. This is true as long as one has no big changes of the deformation.

If the lowering term $-\langle J_y^2\rangle/\theta_y$ has to be taken into account in the variation, it is no longer possible to carry out the variation fully self-consistently. One can, however, use a set of trial wave functions, which depend only on a few deformation and pairing parameters. A minimization of the projected energy with respect to these parameters, corresponds to an approximate projection in three dimensions.

In the case of small deformations, we restrict ourselves to I = 0. In this case, it has been shown in Ref. 9 that the overlap $n(\Omega)$ can be approximated by

$$n(\Omega) = \exp\left\{-\frac{1}{2}\langle J_y^2\rangle \sin^2\beta\right\} \qquad (7)$$

An expansion of the energy overlap, analogous to Eq. (3) gives

$$E^{J=0}_{proj} = \langle H\rangle - \frac{\langle(h - \langle H\rangle)J_y^2\rangle}{\langle J_y^2\rangle + 3} \qquad (8)$$

Since the HFB wave functions are a superposition of different particle numbers, one has to carry out a particle number projection

$$P^N = \frac{1}{2\pi}\int e^{i(N-n)\phi}\,d\phi \qquad (9)$$

N is the particle number operator and n is the actual particle number. The corresponding energy is

$$E^N_{proj} = \frac{\int d\phi\,\langle H\,e^{i(N-n)\phi}\rangle}{\int d\phi\,\langle e^{i(N-n)\phi}\rangle} \qquad (10)$$

Since pairing correlations in nuclei are usually very weak, one can use again the limit of weak symmetry violation.[9] Within this limit one can show

$$n(\phi) = \langle e^{i(N-n)\phi}\rangle = \exp\left\{-\frac{1}{2}\langle\Delta N^2\rangle \sin^2\phi\right\} \qquad (11)$$

and

$$E^N_{proj} = \langle H\rangle - \frac{\langle(H - \langle H\rangle)\,\Delta N^2\rangle}{2\langle\Delta N^2\rangle + 4} \qquad (12)$$

The numerical calculations were carried out with a pairing plus quadrupole force.[23,24] With a set of trial wave functions $\phi(g,\chi)$ (g is a quadrupole deformation, χ is a gapparameter) the expectation value of the unprojected and the projected energy is calculated and a minimum of these energy surfaces are determined.

Figure 1 shows the unprojected energy E_{unpro} and the particle number projected energy E^N_{pro} dependent on the pairing parameter χ in the case of ^{164}Er. Particle number projection favors stronger pairing correlations. The third curve in Fig. 1 shows a projection of angular momentum and particle number

$$E^{J,N}_{pro} = \langle H\rangle - \frac{\langle(H - \langle H\rangle)J_y^2\rangle}{\langle J_y^2\rangle} - \frac{\langle(H - \langle H\rangle)\,\Delta N^2\rangle}{2\langle\Delta N^2\rangle + 4} \qquad (13)$$

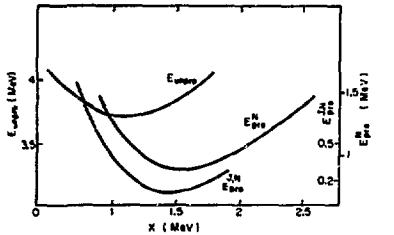

Fig. 1. Unprojected, particle number projected and angular momentum plus particle number projected energy as a function of the pairing parameter χ for the nucleus ^{168}Er.

(XBL 757-3509)

In this approximation, the assumption is made that both projections can be carried out independently. The result is that the angular momentum projection gives a rather constant lowering, and that the projected minimum is not changed very much. The reason for this behavior is, that, the lowering term caused by angular momentum projection, is influenced only very little by changes of the pairing correlations. On the other hand, in the case of the variation of the deformation q (which is not shown in Fig. 1) it turns out, that the lowering due to projection of particle number is a rather slow varying function of q, as compared to the lowering caused by angular momentum projection.

We have carried out calculations on high-spin states in the model nucleus ^{168}Er as described above. Trial wave functions $\phi(q,\chi,\omega)$ were obtained by diagonalizing the single particle Hamiltonian in the rotating frame: $H_0 - \omega J_x$. Using these wave functions the particle number projected energy $E'^N_{pro} = E^N_{pro} - \omega\langle J_x\rangle$ in the rotating frame was calculated. The stationary points of the energy surface $E'^N_{pro}(q,\chi)$ are approximate solutions of the particle number projected HFB-equations before variation. At the end ω is determined by the subsidary condition (6).

Since changes of the deformation and of the proton pairing correlations are less important in this nuclei, we varied for each ω only the pairing parameter of the neutrons χ_n and kept q and χ_p at the optical values of the ground state.

There is, however, a certain ω region ($0.27 \leq \omega \leq 0.33$ MeV) where three stationary points exist (two minima and one maximum). Therefore, one obtains for each ω value within this region; three solutions with different J values. One of these seems to be unstable. However, if one takes into account the other degrees of freedom, it turns out to be a saddle point, and the conservation of angular momentum guarantees the stability of this solution.

Usually, one plots in the back-bending region the moment of inertia

$$\theta = \frac{\langle J_x\rangle}{\omega}$$

against the square of the angular velocity. This is done in Fig. 2 with and without particle number projection. Without projection one has a very steep increase of the moment of inertia; but not back-bending. It corresponds to a breakdown of the neutron gap, which vanishes for $\omega > 0.24$ MeV (Ref. 2), and to a simultaneous de-coupling of one neutron pair in the $i_{13/2}$ shell. With particle number projection, one finds for the ground state a smaller moment of inertia, which corresponds to the stronger pairing correlations. In a certain region, one gets back-bending. An analysis of the internal wave function shows, that it corresponds to a sudden de-coupling of one neutron pair. Because of the blocking effect, the neutron pairing correlations are lowered by a certain amount, but they do not vanish up to $\omega = 0.4$. This behavior agrees qualitatively with the result found in a more realistic calculation of the nucleus ^{162}Er (Ref. 7), without particle number projection. However, particle number projection introduces quantitative changes of the back-bending curve. In particular, the region of back-bending is increased.

For a study of the angular momentum projection at small deformations, we carried out calculations in the nucleus ^{120}Sn.

For the angular momentum projection, the approximation of small deformations is used (Eq. (8)). The results are shown in Fig. 3. The unprojected and the angular momentum projected energy surface, are given depending on the quadrupole deformation Q. The unprojected energy has a minimum at zero deformation. The projected energy shows a qualitatively different behavior.

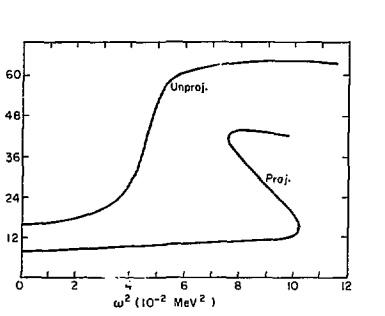

Fig. 2. Moments of inertia depending on the square of the cranking frequency ω^2 with (proj.) and without (unproj.) particle number projection. The nucleus is ^{168}Er. (XBL 757-3508)

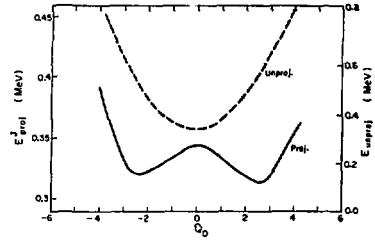

Fig. 3. Unprojected and angular momentum projected (J = 0) energy as a function of the quadrupole moment Q for the nucleus ^{120}Sn.
(XBL (XBL 757-3506)

It has two minima. The prolate one is slightly deeper. However, they are not deep enough to guarantee a stable deformation, therefore, this effect probably will be of very little importance. The situation may be quite different for J ≠ 0 and for nuclei with open proton and neutron shells, cases which are now under investigation.

Footnotes and References

*Submitted for publication in Zeitschrift für Physik.

†Physik-Department der technischen Universität München, Garching, Bundesrepublik Deutschland.

1. M. Baranger, Phys. Rev. 122, 992 (1962).

2. P. Ring, R. Beck, and H.J. Mang, Z. Physik 231, 10 (1970).

3. R. Beck, H.J. Mang, and P. Ring, Z. Physik 231, 26 (1970).

4. K. Goeke, J. Garcia, and A. Faessler, Nucl. Phys. A208, 477 (1973).

5. A. Faessler, F. Grümmer, L. Lin, and J. Urbano, Phys. Lett. 48B, 87 (1974).

6. F.S. Stephens and R.S. Simon, Nucl. Phys. A138, 257 (1972).

7. B. Banerjee, H.J. Mang, and P. Ring, Nucl. Phys. A215, 366 (1973).

8. P. Ring, H.J. Mang, B. Banerjee, Nucl. Phys. A225, 141 (1974).

9. R. Beck, Z. Physik 243, 409 (1971).

CORIOLIS EFFECTS AND ROTATION ALIGNMENT IN NUCLEI

F. S. Stephens

Coriolis effects in nuclei vary from small perturbations in good rotational spectra, to a point where they apparently dominate the low-energy spectrum. The situation for a particular case depends on the relationship of the rotational energy to the energy coupling the particle to the non-spherical part of the potential. If the latter energy is much larger, good rotational spectra exist, whereas if it vanishes, the system is spherically symmetric leading to a spectrum with no energy splitting of the multiplets formed by coupling a particle to a core state. With the assumptions and simplifications outlined in the full report of this work,[1] it is easy to make calculations anywhere between these limits. Adjacent to each limit, one finds regions where a perturbation treatment could apply. This would be a particle-core weak-coupling model near the spherical limit, and a Coriolis perturbation approach near the good rotational region. If the Fermi surface is near high-Ω levels, these two perturbation regions merge into each other, and one changes rather suddenly from a spherical region into one of reasonably good rotors. But if the Fermi surface is near low-Ω states, then there is a broad region where neither of these schemes is very good. Due to a cancellation of terms in this region, the solutions are approximately eigenfunctions of the Coriolis operator and these correspond to a third coupling scheme where the particle angular momentum has sharp values, α, along the rotation axis. Such a rotation-aligned coupling scheme seems to describe rather well the yrast states in many odd-mass nuclei. This coupling scheme probably also applies to non-yrast states, and it is at present a challenge to see how far the model can be extended in this direction.

In the even-even nuclei, the rotation-aligned scheme may also play an important role. It has been suggested[1] that backbending in the light rare-earth region may be just the intersection of the ground band with such a rotation-aligned two-quasiparticle state composed of $i_{13/2}$ neutrons. The observed backbending in odd-mass nuclei suggests that this explanation is correct in the light Er region. Whether this will prove to be the case in other regions is not yet clear.

Reference

1. F.S. Stephens, Rev. Mod. Phys. To be published, Jan. 1975.

ALPHA-DECAY THEORY

T. Fliessbach

Wave Function of Relative Motion and Optical Potential

In the α-decay theory[1] the total wave function is approximated by

$$|\psi\rangle = a|\phi_{A+4}\rangle + \int dE'\, b(E')|\phi_{E'}\rangle \qquad (1)$$

with the open channel state

$$|\phi_E\rangle = |A(U_E(\vec{R}_\alpha)\phi_\alpha\phi_A)\rangle \quad . \qquad (2)$$

Here ϕ_{A+4} describes the parent nucleus which decays into the daughter nucleus ϕ_A and an α-particle. ϕ_α is the internal α wave function. ϕ_{A+4} and ϕ_A are localised shell model states. $\vec{R}_\alpha$ means the center-of-mass coordinate of the α-particle. All states ϕ_{A+4}, ϕ_A and ϕ_α are antisymmetrized and normalized. The antisymmetrization operator $A = [\binom{A}{4}]^{-1/2} \Sigma(-)^P P$ contains the trivial normalization constants. This sum includes all permutations which exchange nucleons between the α-particle and the A-particle core.

The function of relative motion U_E is determined by the contitions

$$\langle\phi_E|\phi_{E'}\rangle = \delta(E - E') \qquad (3)$$

and

$$\langle\phi_E|H|\phi_{E'}\rangle = E\delta(E - E') \quad . \qquad (4)$$

Physically, this means that ϕ_E and U_E, respectively, describe the elastic scattering (without the presence of other open channels). Therefore, in actual applications the difficult Eqs. (3) and (4) are replaced by the assumption that U_E may be approximated by the solution of a Schrödinger equation with a real optical potential. This α-nucleus potential is extracted from experimental data. Similar assumptions are made in the Distorted Wave Born Approximation (DWBA).

In the α-decay theory this approximation for U_E is wrong by orders of magnitude. The reason for this is the normalization of the basis states $|A\delta(\vec{R} - \vec{R}_\alpha)\phi_\alpha\phi_A\rangle$ in (2):

$$\langle A\delta(\vec{R} - \vec{R}_\alpha)\phi_\alpha\phi_A|A\delta(\vec{R}' - \vec{R}_\alpha)\phi_\alpha\phi_A\rangle$$

$$= \delta(\vec{R} - \vec{R}') - K(\vec{R},\vec{R}') \quad . \qquad (5)$$

This equation defines the operator $K(\vec{R},\vec{R}')$. The properties of $K(\vec{R},\vec{R}')$ are discussed by Feshbach[2] for the nucleon-nucleus case: $\hat{K}$ is Hermitian and has eigenvalues between 0 and 1. If we use realistic wave functions for the α-decay in the lead region it turns out that $\hat{K}$ has relevant eigenvalues which differ from 1 only by 10^{-2} or 10^{-3}. $\hat{K}$ has no eigenvalues equal to 1 and therefore we may introduce normalized basis states

$$|A\frac{1}{\sqrt{1 - \hat{K}}}\,\delta(\vec{R} - \vec{R}_\alpha)\phi_\alpha\phi_A\rangle \quad :$$

$$\langle A\frac{1}{\sqrt{1 - \hat{K}}}\,\delta(\vec{R} - \vec{R}_\alpha)\phi_\alpha\phi_A|A\frac{1}{\sqrt{1 - \hat{K}}}\,\delta(\vec{R}' - \vec{R}_\alpha)\phi_\alpha\phi_A\rangle$$

$$= \delta(\vec{R} - \vec{R}') \quad . \qquad (6)$$

Then the open channel wave function can be written in various ways:

$$|\phi_E\rangle = \int d^3R\, U_E(\vec{R})\,|A\delta(\vec{R} - \vec{R}_\alpha)\phi_\alpha\phi_A\rangle$$

$$= \int d^3R\, \Omega_E(\vec{R})\,|A\frac{1}{\sqrt{1 - \hat{K}}}\,\delta(\vec{R} - \vec{R}_\alpha)\phi_\alpha\phi_A\rangle \qquad (7)$$

with

$$\Omega_E = \sqrt{1 - \hat{K}}\; U_E \quad .[2]$$

We introduce the Hermitian operator $\hat{H}$ by $H(\vec{R},\vec{R}') = \langle\vec{R}|\hat{H}|\vec{R}'\rangle = \langle A\delta(\vec{R} - \vec{R}_\alpha)\phi_\alpha\phi_A|H|A\delta(\vec{R} - \vec{R}_\alpha)\phi_\alpha\phi_A\rangle$ where H is the total Hamiltonian. Then the exact equations (3) and (4) for U_E and Ω_E, respectively, read:

$$EU_E = (1 - \hat{K})^{-1}\,\hat{H}U_E \qquad (8)$$

$$E\Omega_E = (1 - \hat{K})^{-1/2}\,\hat{H}(1 - \hat{K})^{-1/2}\,\Omega_E \qquad (9)$$

The approximation of U_E by a real local α-nucleus potential is inconsistent since it means the approximation of a non-Hermitian Hamiltonian $(1 - \hat{K})^{-1}\hat{H}$ by a Hermitian one. The inconsistency is easily seen in the normalization:

$\langle U_E|U_{E'}\rangle = \delta(E - E')$ is contradictory to $\langle \phi_E|\phi_{E'}\rangle = \delta(E - E')$.

Only the approximation of the new wave function Ω_E by an optical potential leads to a consistent theory: The effective Hamiltonian $(1 - \hat{K})^{-1/2}\hat{H}(1 - \hat{K})^{-1/2}$ is Hermitian, and the conditions $\langle \Omega_E|\Omega_{E'}\rangle = \delta(E - E')$ and $\langle \phi_E|\phi_{E'}\rangle = \delta(E - E')$ are equivalent.

The Reduced Width Amplitude (RWA)

The usual α-decay theory[1] leads to a RWA

$$G(\vec{R}) = \langle A \delta(\vec{R} - \vec{R}_\alpha)\phi_\alpha\phi_A|\phi_{A+4}\rangle \qquad (10)$$

which may be interpreted as the amplitude for finding the α-particle in ϕ_{A+4} at $\vec{R}$ with respect to a residual nucleus ϕ_A. The α-decay width is proportional to $|G|^2$.

Constructing a consistent theory[3] which approximates Ω_E but not U_E by an optical potential, one has to replace G by

$$G_N(R) = \langle A \frac{1}{\sqrt{1 - \hat{K}}} \delta(\vec{R} - \vec{R}_\alpha)\phi_\alpha\phi_A|\phi_{A+4}\rangle = \frac{1}{\sqrt{1-\hat{R}}} G \qquad (11)$$

The RWA means something like the projection of ϕ_{A+4} into the space of an α-particle plus ϕ_A. An immediate way to derive the new formula (11) is provided by the easy verification (see (6)) that

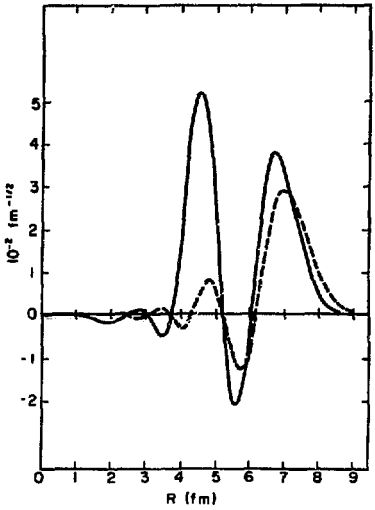

Fig. 1. The RWA's for $^{210}Po \to {}^{206}Pb + \alpha$ versus the radius R. The solid line is $R \cdot G_N$, the broken line is $10 \cdot R \cdot G$. The shell model configuration of the four nucleons is $(1h\ 9/2)^2_0(3p\ 1/2)^2_0$.

(XBL 757-3498)

$$\hat{P} = \int d^3R|A \frac{1}{\sqrt{1 - \hat{R}}} \delta(\vec{R} - \vec{R}_\alpha)\phi_\alpha\phi_A\rangle\langle A \frac{1}{\sqrt{1 - \hat{K}}} \delta(\vec{R} - \vec{R}_\alpha)\phi_\alpha\phi_A| \qquad (12)$$

is a projection operator, which is not true for

$$\int d^3R|A\delta(\vec{R} - \vec{R}_\alpha)\phi_\alpha\phi_A\rangle\langle A\delta(\vec{R} - \vec{R}_\alpha)\phi_\alpha\phi_A| \quad .$$

We calculated G_N for $^{210}Po \to {}^{206}Pb + \alpha$. We used pure shell model configurations and oscillator states (oscillator constants 0.17 fm^{-2} for Po and Pb, and 0.47 fm^{-2} for α). The results are shown in Fig. 1. The shell model state ϕ_{A+4} cannot describe the α-particle when it is outside the nucleus. Therefore a quantitatively reliable result can only be expected for radii $\lesssim 7$ fm. Here $|G_N|^2$ is about 100 times larger than $|G|^2$. This leads to a quantitative agreement with the experiment for the considered decay.

We feel that Eq. (11) is the key to the long-standing problem of the quantitative description of the α-decay. At large radii, where the α-particle and the A-particle core are well separated, there is of course no difference between U_E and Ω_E. Here it is in principle possible to describe the tail of the α-particle wave function by including sufficient configuration mixing. A shell model basis is, however, not well suited for the description of an α-particle separated from the core.

Other Reactions

One of the most widely used approaches for direct reactions is the DWBA. The antisymmetrization is usually not included in these calculations, that means the states

$$|U_\gamma(\vec{R}_\gamma)\phi_{\gamma_1}\phi_{\gamma_2}\rangle = \int d^3R\ U_\gamma(R)|\delta(R - R_\gamma)\phi_{\gamma_1}\phi_{\gamma_2}\rangle$$

are used for the open channels $\alpha,\beta,\gamma,\ldots$. Here the $\phi_{\gamma_1},\phi_{\gamma_2}$ are internal wave functions. Similarly as in the α-decay theory, the DWBA approximates the wave functions of relative motion U_γ by the optical potential solutions χ_γ. This leads to the transition amplitude

$$T_{\alpha\beta} \propto \int d^3R\, d^3R'\, \chi_\alpha^{+}(\vec{R})\chi_\beta^{-}(\vec{R}')\langle \delta(\vec{R}'-\vec{R}_\beta)\phi_{\beta_1}\phi_{\beta_2}|V|\delta(\vec{R}-\vec{R}_\alpha)\phi_{\alpha_1}\phi_{\alpha_2}\rangle \tag{13}$$

with a suitable interaction V.
In the light of the above discussion it is clear that the introduction of the antisymmetrization cannot be done by simply inserting the operator A in the bra and ket of (13). The proper expression with antisymmetrization would be

$$T_{\alpha\beta} \propto \int d^3R\, d^3R'\, \chi_\alpha^{+}(\vec{R})\chi_\beta^{-}(\vec{R}')\left\langle A\frac{1}{\sqrt{1-\hat{K}_\beta}}\delta(\vec{R}'-\vec{R}_\beta)\phi_{\beta_1}\phi_{\beta_2}|A\frac{1}{\sqrt{1-\hat{K}_\alpha}}\delta(\vec{R}-\vec{R}_\alpha)\phi_{\alpha_1}\phi_{\alpha_2}\right\rangle \tag{14}$$

For shell model states $\phi_{sm,\gamma}$ rather than internal states ϕ_γ, and for slow velocities (energy per nucleon much smaller than the Fermi energy) the last expression is approximately

$$T_{\alpha\beta} \propto \int d^3R\, d^3R'\, \chi_\alpha^{+}(\vec{R})\chi_\beta^{-}(\vec{R}')\langle AN_\beta(\vec{R})\phi_{sm,\beta_1}\phi_{sm,\beta_2}|V|\,AN_\alpha(\vec{R})\phi_{sm,\alpha_1}\phi_{sm,\alpha_2}\rangle \tag{15}$$

with the normalization constants

$$N_\gamma(\vec{R}) = \langle A\,\phi_{sm,\gamma_1}\phi_{sm,\gamma_2}|A\,\phi_{sm,\gamma_1}\phi_{sm,\gamma_2}\rangle^{-1}.$$

For product wave functions the form factor in (15) is easy to calculate.

References

1. H.J. Mang, Phys. Rev. 119, 1063 (1960); H.J. Mang, LBL report UCRL-8931.

2. H. Feshbach, Document on Modern Physics, Reaction Dynamics (Gordon and Breach, New York, 1973).

3. T. Fliessbach, Z. Phys., A272,39 (1975).

GRAPHICAL REPRESENTATION IN ALPHA DECAY RATE THEORY OF SPHERICAL ODD-ODD NUCLEI – APPLICATION TO ^{218}At AND ^{212}At*

A. A. Shihab-Eldin, L. J. Jardine† and J. O. Rasmussen

Theoretical calculations of relative alpha decay rates for even-even and even-odd nuclei in the lead region have successfully been carried out[1-3] using the one-level R-matrix alpha decay rate theory[4] with shell-model wave functions. Using a simple delta-function approximation for the alpha particle internal wave function[3] gave greatly simplified formulas and essential agreement with sophisticated theories, though it overestimates rate contributions from higher-j orbitals. The application of these formulas to the alpha decay of odd-odd nuclei requires, in general, carrying out the rather more involved angular momenta recoupling and fractional parentage expansion. However, by making use of the simple and elegant graphical representation techniques of Macfarlane et al.,[5] one can reduce the complexity of the calculation procedure. In addition, this technique helps one to gain more insight into the particular alpha decay case under study.

In the one-level R-matrix alpha decay theory, the L^{th} partial decay constant, λ_L, is usually written as:

$$\lambda_L = \frac{2\gamma_L^2}{\hbar} \times P_L \quad , \tag{1}$$

where P_L is the alpha particle penetration factor through the Coulomb barrier (calculated from the nuclear surface, R_0, to infinity) and γ_L is the partial reduced alpha width, which gives the probability of finding an alpha particle at the nuclear surface. γ_L is given by:[6]

$$\gamma_L = \int d\xi\, d\eta\, d\Omega_{rel} \left(\phi^{M*}_{J_i} \chi_\alpha(\xi) \right) \left\{ Y^{M'}_L(\underline{R}/R)\, \psi^{M-M'}_{J_d}(\eta) \right\}^M_J \times \left[\binom{N}{2} \binom{Z}{2} \right]^{1/2} \quad , \tag{2}$$

where $\phi^M_{J_i}$, ψ_{J_d} and χ_α are the antisymmetrized wave functions of the parent, daughter and α-particle, respectively. The overlap integral in Eq. (2) can be evaluated by expanding the parent-nucleus state vector (wave function) in terms of those for the daughter nucleus and the four nucleons that form the alpha particle.

In the shell model, the parent-nucleus state vector can be thought of as consisting of an inert core of nucleons that is common with daughter-nucleus state vector plus N neutrons and Z protons distributed among the active neutron orbitals $\rho_1, \rho_2, \cdots \rho_m$ and the active proton orbitals $\rho_{m+1}, \rho_{m+2}, \cdots \rho_k$. It will be sufficient here to limit the neutron and proton active orbitals to two each, i.e., ρ_1, ρ_2 (for neutrons), ρ_3 and ρ_4 (for protons). In the general case there will be n_1 neutrons in orbital ρ_1 (denoted $\rho_1^{n_1}$), n_2 in orbital ρ_2, and similarly n_3 and n_4 protons in orbital ρ_3 and ρ_4 respectively. β_1, β_2, etc. will designate a certain coupling scheme with all needed quantum numbers implicitly contained for simplicity. The β_1 and β_2 state vectors are coupled to a vector with J^i_N (angular momentum), and β_3 and β_4 coupled to J^i_P; and finally J^i_N and J^i_P are coupled to give the parent-nucleus state vector, referred to as $|J^M\rangle$. The neutron and proton state vectors, J^i_N and J^i_P are antisymmetric under exchange among all the neutrons and protons, respectively. In the graphical representation this antisymmetry is denoted by a semicircle surrounding the state vector for the nucleons involved. Thus $|J^M\rangle$ is represented by Fig. 1. The daughter state vector will be assumed to consist of an identical inert core plus N-2 neutrons and Z-2 protons distributed in some manner among the active neutron and proton orbitals. We will consider first the case of favored α-decay involving removal of two neutrons from one orbital, say ρ_2, and two protons from orbital ρ_4. The daughter-nucleus state vector $|\psi_{J_d}\rangle$ can then be represented by Fig. 2. where J^d_N and J^d_P are the neutron and proton intermediate

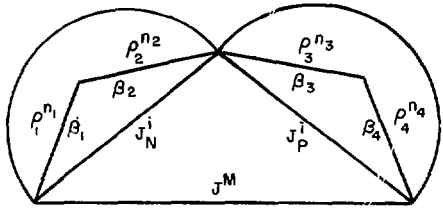

Fig. 1. (XBL 7410-4467)

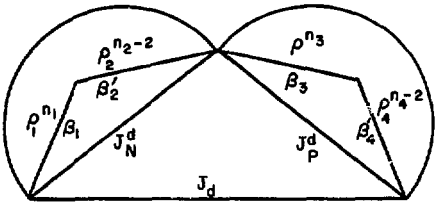

Fig. 2. (XBL 7410-4466)

state vectors, respectively. We can now project the parent-nucleus state vector onto a product subspace of the daughter-nucleus state vector and the shell-model state vectors of the four nucleons that form the α-particle. A typical basis vector of such a subspace appears as shown in Fig. 3. Thus the projection amplitude of the parent-nucleus state vector onto such a basis state vector can be represented by Fig. 4. According to Towner and Hardy,[7] such a term (Fig. 5) is equal to:

$$\binom{n_2}{2}^{\frac{1}{2}}\binom{n_1+n_2}{2}^{-\frac{1}{2}}\binom{n_4}{2}^{\frac{1}{2}}\binom{n_3+n_4}{2}^{\frac{1}{2}}$$

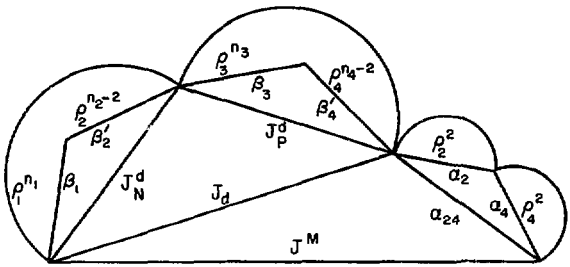

Fig. 3. (XBL 7410-4469)

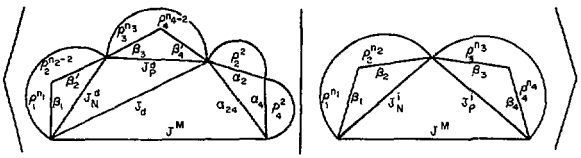

Fig. 4. (XBL 7410-4471)

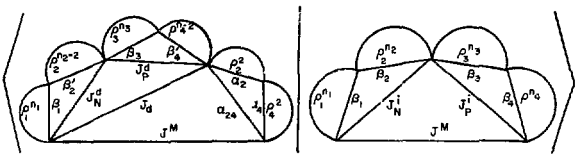

Fig. 5. (XBL 7410-4472)

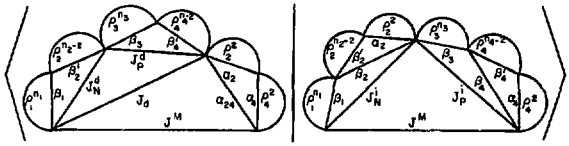

Fig. 6. (XBL 7410-4468)

We now expand $|\rho_2^{n_2}(\beta_2)\rangle$ and $|\rho_4^{n_4}(\beta_4)\rangle$ in the parent-nucleus state vector in terms of $|\rho_2^{n_2-2}(\beta_2')\rangle \otimes |\rho_2^2(\alpha_2)\rangle$ and $|\rho_4^{n_4-2}(\beta_4')\rangle \otimes |\rho_4^2(\alpha_4)\rangle$ using two-particle cfp's (coefficient of fractional parentage). The projection amplitude will become equal to (Fig. 6):

$$\sum_{\beta_2',\beta_4'} b^{n_2}_{\beta_2\beta_2'\alpha_2}\; b^{n_4}_{\beta_4\beta_4'\alpha_4} \binom{n_2}{2}^{1/2} \left[\binom{n_4}{2}^{1/2} \times \binom{n_1+n_2}{2}^{-1/2} \binom{n_3+n_4}{2}^{-1/2}\right.$$

where $b^{n_i}_{\beta_i\beta'_i\alpha_i}$ represents the two-particle cfp:[8]

$$b^{n_i}_{\beta_i\beta_i'\alpha_i} = \left\langle {}^{n_i}_{\rho_i}(\beta_i) \left\{ |\rho_i^{n_i-2}(\beta_i'), \rho_i^2(\alpha_i)\right\rangle \right. . \tag{3}$$

The overlap bracket in Fig. 6 represents a {15 - j}-symbol recoupling coefficient involving six basic angular momentum vectors, β_1, β_2', α_2, β_3, β_4' and α_4.

This expansion can now be made back in Eq. (2). If integration is then carried out, first over the relative coordinates of the four nucleons of the alpha particle, using the delta-function approximation for the spatial part of the α-particle wave function, followed by integration over the internal coordinates of the daughter nucleus and the alpha particle and over the angular coordinates of the relative motion (see Ref. 3 for details, definitions and notations), we get the following expression:

$$\gamma_L = \sum_{\beta_2',\beta_4'} C\{15 - j\} \binom{n_2}{2}^{1/2} \binom{n_4}{4}^{1/2} b^{n_2}_{\beta_2\,\beta_2'\,\alpha_2}\; b^{n_4}_{\beta_4\,\beta_4'\,\alpha_4} \times$$

$$R_1R_2R_3R_4 \times F_N(j_1,j_2,j_N)\, F_P(j_3,j_4,j_P)\, G(J_P\, J_N\, J_L)\ , \tag{4}$$

where we have used j_1, j_2, j_3 and j_4 to indicate the angular momentum of the two neutrons and two protons involved in α decay (in the previous notation $j_1 = j_2 = j(\rho_2)$ and $j_3 = j_4 = j(\rho_4)$), and expressions for C, F and G are given in Ref. 3.

For the most general unfavored alpha decay, we would have to extract one neutron each from the ρ_1 and ρ_2 orbitals and one proton each from the ρ_3 and ρ_4 orbitals. The derivation is basically the same and the results are similar to that of Eq. (4). However, we would end up with four one-particle cfp's, a {21 - j}-symbol recoupling coefficient, and different binomial coefficients, i.e.,

$$\gamma_L = \sum_{\beta_1',\beta_2',\beta_3',\beta_4'} C\{21 - j\} \binom{n_1}{1}^{1/2} \binom{n_2}{1}^{1/2} \binom{n_3}{1}^{1/2} \binom{n_4}{1}^{1/2} b^{n_1}_{\beta_1\,\beta_1'\,\alpha_1}\; b^{n_2}_{\beta_2\,\beta_2'\,\alpha_2}\; b^{n_3}_{\beta_3\,\beta_3'\,\alpha_3} \times$$

$$b^{n_4}_{\beta_4\,\beta_4'\,\alpha_4} \times R_1R_2R_3R_4 \times F_NF_PG\ , \tag{5}$$

where $b^{n_i}_{\beta_i\,\beta_i'\,\alpha_i}$ represents the one-particle cfp:[8]

$$b^{n_i}_{\beta_i\,\beta_i'\,\alpha_i} = \left\langle \rho_i^{n_i}(\beta_i) \left| \rho_i^{n_i-1}(\beta_i'),\ \rho_i(\alpha_i) \right| \right\rangle . \qquad (6)$$

Application to the Alpha Decay of ^{210}At and ^{212}At

Using the above formulation, we have calculated the relative alpha decay rates from ^{210}At 5^+ ground state to the lowest 4_1^+, 3_1^+, 5_1^+, 7_1^+, and 2_1^+ states in ^{206}Bi (unfavored decay). These states were assumed to consist of a pure $[\pi(h_{9/2})\nu(f_{5/2})^{-1}\nu(p_{1/2})_0^{-2}]$ configuration (hereafter denoted configuration {1}). ^{210}At ground state was assumed to consist of a pure $[\pi(h_{9/2})^3_{9/2}(v=1)\nu(p_{1/2})^{-1}]_{5^+}$ configuration. We have also calculated the relative alpha decay rates to the second 5_2^+ and 4_2^+ states in ^{206}Bi (favored decay), assuming they consist of a pure $[\pi(h_{9/2})\nu(f_{5/2})_0^{-2}\nu(p_{1/2})^{-1}]$ configuration (hereafter denoted configuration {2}). The {15 - j}- and {21 - j}-symbol recoupling coefficients that appear in Eqs. (4) and (5) reduce in this case to a {6 - j}-symbol recoupling coefficient (favored decay) and a product of {6 - j}- and {9 - j}-symbol recoupling coefficients (unfavored decay), respectively. The calculated relative alpha decay rates were compared to the experimental relative intensities of the alpha groups measured by Golovkov et al.,[9] and were found to be in fair agreement with them. The agreement is exceptionally good for the relative alpha group intensities to the 6_1^+, and 7_1^+ states, supporting the assumption of a pure configuration for the wave functions of these two states and of the ^{210}At ground state. Also impressive is the fact that the theory predicts small relative alpha group intensities to the 3_1^+, 2_1^+, and 4_2^+ states that are below the intensity limits set from experiment for such possible alpha groups. However, with the present pure configuration assumption, the theory fails to reproduce the experimental relative alpha group intensities leading to the 4_1^+ and 5_1^+ states and slightly overestimates the intensity to the second 5_2^+ state. This suggests that the pure configuration assumption for the 4_1^+, 5_1^+, and 5_2^+ and 4_2^+ states in ^{206}Bi is not valid. No detailed shell-model wave functions, with configuration mixing, are yet available for states of ^{206}Bi. However, we have attempted to use some simple trial wave functions for the 4_1^+, 5_1^+, 5_2^+, and 4_2^+, states with configuration mixing first limited to the two configurations, {1} and {2}, mentioned earlier.

By solving for the mixing parameters that reproduce the experimental results, we were able to arrive at two sets of wave functions for the 5_1^+ and 5_2^+ states that gave improved agreement between calculated alpha decay rates and those experimentally measured for these two states (see Table 1). However, using this limited configuration space, it was not possible to generate a wave function for the 4_1^+ state that yield agreement with experiment. This is due to the relatively small value for $\gamma_2(\{2\}_{4^+})$ which is illustrated in Table 2. In it we show the relative partial

Table 1. Comparison of theoretical and experimental relative alpha intensities using mixed-configuration wave functions for the 5_1^+ and 5_2^+ states.

State	Wave Function		Relative α Intensity[a]		
			Calc.		Expt.
	Set I	Set II	Set I	Set II	
$\|5_1^+\rangle$	$\sqrt{0.78}\{1\} + \sqrt{0.22}\{2\}$	$\sqrt{0.67}\{1\} - \sqrt{0.33}\{2\}$	83	83	95 ± 6
$\|5_2^+\rangle$	$\sqrt{0.22}\{1\} - \sqrt{0.78}\{2\}$	$\sqrt{0.33}\{1\} + \sqrt{0.67}\{2\}$	74	76	83 ± 6

[a] Calculated and experimental alpha-group intensities are relative to that of the ground state (6_1^+) group.

Table 2. The relative reduced α-widths, γ_L.

State		Configuration		
J^π	L	{1}	{2}	{3}
4^+	2	+0.65	+0.154	-0.88
5^+	0	+0.24	-2.39	-0.145
	2	-0.64	+0.64	-0.73

reduced widths to the 4^+ and 5^+ components for configurations {1}, {2} and the $[\pi(h_{9/2})\nu(p_{3/2})^{-1}\nu(p_{1/2})^{-2}]$ configuration (the latter will be denoted configuration {3} hereafter). The large value of $\gamma_2(\{3\}_{4^+})$ immediately suggests the possibility of improving the agreement with experiment for the 4_1^+ state by including some admixture of configuration {3} in the 4_1^+ wave function. Indeed we can achieve exact agreement with experiment if we choose the following mixture for the 4_1^+ wave functions:

$$|4_1^+\rangle = \sqrt{0.92}\ |\{1\}_{4^+}\rangle - \sqrt{0.08}\ |\{3\}_{4^+}\rangle \quad . \tag{7}$$

Of course such a simple description for the 4_1^+ is not realistic, as some mixture from the $|\{2\}_{4^+}\rangle$ has to be included, but this will not alter things by much as $\gamma_2(\{2\}_{4^+})$ is small compared to $\gamma_2(\{1\}_{4^+})$ and $\gamma_2(\{3\}_{4^+})$. Relative intensities for the 5_1^+ and 5_2^+ states can also be brought into a better agreement with experimental values if admixtures from $|\{3\}_{5^+}\rangle$ are included in the description for 5_1^+ and 5_2^+ state vectors. Thus we conclude that matching of the relative alpha decay rates to the 4_1^+, 5_1^+, and 5_2^+ in ^{206}Bi must require wave functions with appreciable admixture from configuration {3}, which has a center of gravity of about 400 keV above the configuration {1}, in addition to admixtures from configurations {1} and {2}.

Both the ^{212}At ground state ($t_{1/2}$ = 0.305 s) and the ^{212m}At isomer ($t_{1/2}$ = 0.1205 s) have a 100% alpha decay mode, and both have large Q_α values[10] (7.827 and 8.952 MeV, respectively). Alpha groups from decay of both states populate many states in ^{208}Bi up to 1.096 MeV.[11] These states can be assumed to belong mainly to the

$$[\pi(h_{9/2})\nu(p_{1/2})^{-1}]_{4,5^+} \quad ,$$

$$[\pi(h_{9/2})\nu(f_{5/2})^{-1}]_{2,3,4,5,6,7^+}$$

and

$$[\pi(h_{9/2})\nu(p_{3/2})^{-1}]_{3,4,5,6^+}$$

configurations, thereafter denoted as configuration {1}, {2} and {3}, respectively. The 5_1^+ ground state and the 4_1^+ first excited state can be assumed to consist, in zeroth order, of a pure configuration {1} . The higher 6_1^+, 4_2^+ , 5_2^+, 3_1^+, 7_1^+ and 2_1^+ states can also be assumed to consist of a pure configuration {2} .The ^{212}At ground state and the ^{212m}At isomer are presumably members of the $[\pi(h_{9/2})^3_{9/2}(\nu = 1)\nu(g_{9/2})]$ configuration multiplet.

From comparison with ^{208}Bi level structure, which has two protons less, 1^- and 9^- spin and parity assignments are most probable for ^{212}At ground state and ^{212m}At isomer, respectively.

With these assumptions, we have calculated the relative alpha decay rates from these two states to the low-lying 5_1^+, 4_1^+, 6_1^+, 4_2^+, 5_2^+, 3_1^+, 7_1^+, and 2_1^+ states in ^{208}Bi. The results are shown in Table 3 which also shows the experimentally measured values[11] for comparison. One notes that there is generally good agreement between calculations and experiment for the 9^- isomer decay, particularly for the 6_1^+ to 7_1^+ alpha decay rate ratio and to a lesser extent for the 4_1^+ to 5_1^+ ratio. In contrast to this, the calculation for the 1^- g.s. decay shows very poor agreement with experiment. These results imply that the pure configuration assumption made for the parent and daughter states is valid for the 9^- ^{212m}At and the 6_1^+ and 7_1^+ ^{208}Bi states and to a lesser extent for the 5_1^+ and 4_1^+ states in ^{208}Bi. All other states, however, must have appreciable configuration admixtures.

Conventional shell-model calculations for ^{208}Bi level strusture have been carried out by numerous authors.[12] No such calculations exist for ^{212}At. However, its low-lying level structure is expected to be similar to that of ^{210}Bi, except for two extra protons coupled to zero. Thus the available shell-model calculations for ^{210}Bi can be used to generate ^{212}At wave functions by extrapolation. The last column of Table 3 shows the percentage of the dominant configuration present in the wave functions of ^{208}Bi and ^{212}At (i.e., ^{210}Bi) states as calculated by Ma and True.[12] Their results are strikingly in full agreement with the conclusions of the comparison between the calculated relative alpha decay rates and experiment. Here again the 9^- ^{212}At isomeric state is shown to have high configuration purity, similarly the 6_1^+ and 7_1^+ ^{208}Bi states are shown to be relatively pure, and so are the 4_1^+ and 5_1^+ ^{208}Bi states, though to a lesser degree. Other ^{212}At and ^{208}Bi states are shown to have appreciable configuration admixtures (> 10%). In particular the 1^- ^{212}At ground state is shown to have about 40% admixtures from other configurations. This is probably the main reason for the above disagreement between calculation and experiment for its relative alpha decay rates. Calculations of relative alpha decay rates for the 1^- and 9^- ^{212}At states, using Ma and True[12] configuration-mixed shell-model function are currently in progress.

Thus, alpha decay rate theory provides a sensitive probe of the sparsely known question of configuration mixing in odd-odd nuclei. We would hope that this work can serve to stimulate further shell-model theoretical work and expanded knowledge of the effective shell model n-p force.

Table 3. Relative alpha decay rates for 1^- and 9^- ^{212}At.

Dominant Configuration	^{208}Bi Levels		$[\pi(h_{9/2})^3_{9/2}\nu(g_{9/2})]$ ^{212}At States				Percentage of Shell-Model Configuration[d]
			1^-		9^-		60% for 1^- 99% for 9^-
	J^{π}[a]	Energy[a]	Theory[b]	Exp.[c]	Theory[b]	Exp.[c]	
$[\pi(h_{9/2})\nu(p_{1/2})^{-1}]$	5^+_1	0.0	100	100	58	44 ± 1	95 %
	4^+_1	0.0635	286	21 ± 6	100	100	92 %
$[\pi(h_{9/2})\nu(f_{5/2})^{-1}]$	6^+_1	0.5103	31	41 ± 10	100	100	96 %
	4^+_1	0.6028	100	100	5.3	17 ± 5	85 %
	5^+_1	0.629	10.5	< 63	37	82 ± 10	89 %
	3^+_1	0.6344	2.2	79 ± 15	8.4	< 62	88 %
	7^+_1	0.6501	2.2	< 16	119	94 ± 19	99 %
	2^+_1	0.9256	23	6 ± 5	0.21	< 3	28 %

[a] Level energies and spin and parity assignments are taken from Ref. 11.

[b] Calculated relative alpha decay rates assuming pure configuration for parent and daughter states, normalized as in (c).

[c] Relative alpha group intensities of Ref.11 , normalized to 100 for strongest transition in each multiplet.

[d] Taken from Ma and True[12] shell-model calculations.

Footnotes and References

*Based mainly on LBL-3409; Nucl. Phys. A244,435 (1975).

†Present address: Argonne National Laboratory, Argonne, Illinois.

1. H.J. Mang, Z. Phys. 148, 582 (1957).

2. K. Harada, Progr. Theoret. Phys. 26, 667 (1961).

3. J.O. Rasmussen, Nucl. Phys. 44, 93 (1963).

4. R.G. Thomas, Progr. Theoret. Phys. 12, 253 (1954).

5. M.H. Macfarlane and J.B. French, Rev. Mod. Phys. 32, 567 (1960).

6. E.A. Rauscher, J.O. Rasmussen, and K. Harada, Nucl. Phys. A94, 33 (1967).

7. I.S. Towner and J.C. Hardy, Adv. Phys. 18, No. 74, 401 (1969).

8. A. de-Shalit and I. Talmi, "Nuclear Shell Theory" (Academic Press, New York, (1963)).

9. N.A. Golovkov, Sh. Guetkh, B.S. Dzhelepov, Yu. V. Norseev, V.A. Khalkin, and V.G. Chumin, Izv. Akad. Nauk. (Fiz. Ser.) 33, 1622 (1969) (translated page 1489).

10. S.C. Pancholi and M.J. Martin, Nucl. Data Sheets B8, 123 (1972).

11. Paul L. Reeder, Phys. Rev. C1, 721 (1970).

12. Chin W. Ma and William W. True, Phys. Rev. C8, 2313 (1973); see also references therein.

KINETIC ENERGY DENSITY OF A DEGENERATE FERMI GAS

H. Gräf*

The simple statistical relation stating the proportionality between the density and the 3/2 power of the maximum kinetic energy for a completely degenerate gas obeying the Pauli principle has been of great value in atomic and nuclear problems. Unfortunately this approach fails completely at the surface region of any system and also the Weizsäcker correction term associated with the presence of density gradients turns out to be no improvement in that region. We found that this correction term and later modifications of it by Wilets[1] and Kirznits[2] have the wrong sign in some common applications.

Swiatecki[3] has given a new generalization of the Thomas-Fermi method, particularly suitable in the surface region. It can be stated in this way: Using the T.F. model in a problem where the potential is given, we approximate to the true density it would have, if the potential were everywhere constant and equal to the actual potential at the point in question, except for a final rise at infinity, necessary to keep the particles from dispersing. We generalize this now by replacing the actual potential at the point in question by a polynomial of the order n such that the actual value and the n first derivatives coincide. For $n = 1$ and $n = 2$ the solutions of the Schroedinger equation are well known and therefore we restrict ourselves to these two cases.

Linear Approximation

The calculations for the density were already done by Swiatecki. For a potential $V(x) = -|V'|x$, the Fermi energy equal to zero and counting only the spin degeneracy we get for the density ρ and for the kinetic energy density τ

$$\rho(\xi) = \left(\frac{3}{2\ell}\right)^3 \frac{18^{-1/3}}{\pi} \left[\xi^2 \mathrm{Ai}^2(-\lambda\xi) + \frac{\xi}{\lambda}\mathrm{Ai}^2(-\lambda\xi) - \frac{1}{2\lambda^2}\mathrm{Ai}(-\lambda\xi)\mathrm{Ai}'(-\lambda\xi)\right] ,$$

$$\tau(\xi) = \frac{\hbar^2}{2m}\left(\frac{3}{2\ell}\right)^5 \frac{12^{1/3}}{10\pi} \left[(\xi^3 - \tfrac{1}{8})\mathrm{Ai}^2(-\lambda\xi) + \frac{\xi^2}{\lambda}\mathrm{Ai}^2(-\lambda\xi) - \frac{\xi}{2\lambda^2}\mathrm{Ai}(-\lambda\xi)\mathrm{Ai}'(-\lambda\xi)\right] ,$$

where $\ell^3 = 9\hbar^2/8m|V'|$, $\xi = x/\ell$, $\lambda = (\frac{3}{2})^{2/3}$ and Ai is the Airy function in the normalisation of Abramowitz.[4]

For a better understanding of these equations it is helpful to make expansions for $|\xi| \gg 1$. So in the limit $\xi \gg 1$ we have

$$\rho(\xi) \sim \left(\frac{3}{2\ell}\right)^3 \frac{\xi^{3/2}}{3\pi^2}\left\{1 - \frac{\xi^{-3}}{72}(1 + 6\sin 2\xi^{3/2})\right\} ,$$

$$\tau(\xi) \sim \frac{\hbar^2}{2m}\left(\frac{3}{2\ell}\right)^3 \frac{\xi^{5/2}}{5\pi^2}\left\{1 - \frac{5\xi^{-3}}{72}(1 + 2\sin 2\xi^{3/2})\right\} .$$

Neglecting the curled brackets, one has the old Thomas-Fermi model. However in this region we have additional tiny rapidly oscillating wiggles. If the actual potential is not a constant slope potential and the point of consideration is far from the turning point there may be no improvement at all, compared with the Thomas-Fermi results.

To make a connection to the Weizsäcker term we rewrite τ in this region by

$$\tau \approx \frac{\hbar^2}{2m}\left\{\frac{3}{5}(3\pi^2)^{2/3}\rho^{5/3} - \frac{1}{8}\cdot\frac{1}{4}\frac{\rho'^2}{\rho}\right\} ,$$

where $\rho' = \frac{d\rho}{dx}$.

Beyond the turning point, where the Thomas-Fermi solution is identical to zero, one expects to get better results from this form of approximation. Expanding for $\xi \gg -1$ we find

$$\rho(\xi) \sim \left(\frac{3}{2\ell}\right)^3 \frac{|\xi|^{-3/2}}{72\pi^2}\exp\left(-2|\xi|^{3/2}\right)\cdot\left(1 - \frac{35}{36}|\xi|^{-3/2}\right) ,$$

$$\tau(\xi) \sim \frac{\hbar^2}{2m}\left(\frac{3}{2\ell}\right)^5 \frac{|\xi|^{-1/2}}{72\pi^2}\exp\left(-2|\xi|^{3/2}\right)\cdot\left(1 - \frac{23}{36}|\xi|^{-3/2}\right) .$$

Again we rewrite τ,

$$\tau \approx \frac{\hbar^2}{2m}\left\{\frac{3}{5}(3\pi^2)^{2/3}\rho^{5/3} - \frac{1}{4}\frac{\rho'^2}{\rho}\right\} .$$

Wilets,[1] Kirznits[2] and others have shown, that one should multiply the Weizsäcker correction term $\frac{\hbar^2}{8m}\frac{\rho'^2}{\rho}$ by a constant factor 1/9. This is in disagreement with our results. At least for the simple constant slope potential this factor must be negative and it should vary between -1/9 and -1.

Quadratic Approximation

Replacing a potential in a certain point by a parabola, we have to distinguish between two cases:

1) The parabola has a minima, that is the potential would be a harmonic oscillator potential. For semi-infinite distributions, we simply replace one branch of the parabola by a constant line.

2) The parabola has a maxima. Again we replace one branch by a constant line, since we are interested in the tail region, where we assume a constant potential.

Let us assume a potential of the form $V(x) = V''x^2$ for $x \geq 0$ and $V(x) = 0$ otherwise and a Fermi energy $\frac{p_0^2}{2m}$. In case 1) we find then the solutions for $x \geq 0$

$$\rho(x) = \frac{\Lambda^3}{2\pi^3}\int_0^P (P - a)\,\frac{\Gamma^2(\frac{1}{4} - \frac{a}{2})\,\Gamma^2(\frac{3}{4} - \frac{a}{2})}{2\Gamma^2(\frac{3}{4} - \frac{a}{2}) + a\Gamma^2(\frac{1}{4} - \frac{a}{2})}\,\sqrt{2a}\;2^a U^2(a, \Lambda x)\,da \quad ,$$

$$\tau(x) = \frac{\hbar^2}{2m}\frac{\Lambda^5}{2\pi^3}\int_0^P (P - a)\left[\frac{1}{2}(P - a) - \frac{\Lambda^2 x^2}{4} + a\right]\frac{\Gamma^2(\frac{1}{4} - \frac{a}{2})\,\Gamma^2(\frac{3}{4} - \frac{a}{2})}{2\Gamma^2(\frac{3}{4} - \frac{a}{2}) + a\Gamma^2(\frac{1}{4} - \frac{a}{2})}\,\sqrt{2a}\;2^a U^2(a, \Lambda x)\,da$$

where $\Lambda = \sqrt[4]{8m|V''|\,/\,\hbar^2}$, $P = \frac{p_0^2}{\hbar^2\Lambda^2}$ and $U(a, x)$ is a parabolic cylinder-function in the normalisation of Abramowitz.[4] In the second case we find

$$\rho(x) = \frac{\Lambda^3}{2\pi^2}\int_P^\infty (a - P)\,\frac{k}{k^2\ell^2 + 1}\,w^2(a, \Lambda x)\,da \quad ,$$

$$\tau(x) = \frac{\hbar^2}{2m}\frac{\Lambda^5}{2\pi^2}\int_P^\infty (a - P\left[\frac{1}{2}(a - P) + \frac{\Lambda^2 x^2}{4} + a\right]\frac{k}{k^2\ell^2 + 1}\,w^2(a, \Lambda x)\,da$$

is the other parabolic cylinder function. k is determined by $1/k = \sqrt{1 + e^{2\pi a}} + e^{\pi a}$,

$$b = \frac{-\sqrt{a}\,\gamma^2 + \sqrt{2}}{\sqrt{a}\,\gamma^2 + \sqrt{2}} \quad , \quad \gamma^2 = \left|\frac{\Gamma(\frac{1}{4} + \frac{1}{2}ia)}{\Gamma(\frac{3}{4} + \frac{1}{2}ia)}\right| \quad \text{and}$$

$w = bW(a, \Lambda x) + W(a, -\Lambda x)$.

Footnotes and References

*On leave from Inst. f. Kernphysik TH Darmstadt, F.R. Germany.

1. R.A. Berg and L. Wilets, Phys. Rev. 101, 201 (1956).

2. D.A. Kirznits, JETP (Sov. Phys.) 5, 64 (1957).

3. W.G. Swiatecki, Proc. Phys. Soc. A68, 285 (1955).

4. Handbook of Mathematical Functions, Ed. M. Abramowitz and I.A. Stegun, NBS Appl. Math. Serie 55 (1969), chapter 19.

PARABOLIC CYLINDER FUNCTIONS W(A > 0, ± X): EXPANSIONS FOR ALL ARGUMENTS*

H. Grät†

The two parabolic cylinder functions W(a,x), W(a,-x), with $x \geq 0$ are the two symmetric solutions of the differential equation

$$d_{xx}y + (1/4\ x^2 - a)y = 0 \quad .$$

Expansions of W(a,±x) which might be used for numerical calculations are e.g. given in Ref. 1.

In Fig. 1 the areas are shown in which all these expansions approximate the parabolic cylinder functions better than a relative 10^{-6} deviation. To cover the whole (x,a 0)-plane one has to include the asymptotic expansions in terms of Airy functions.[2] Unfortunately its first correction term includes the derivative of Airy functions, which are elaborate to calculate. But, making a Taylor expansion, one is able to drop these derivatives completely. The results up to the order of $a^{-10/3}$ are

$$W(a,x) \sim \sqrt{\pi}\,(4a)^{-1/4}\, e^{-1/2\,\pi a}\left(1 - \frac{1}{4608 \cdot a^2}\right)\left(\frac{t}{\xi^2 - 1}\right)^{1/4} \mathrm{Bi}(-\tilde{T})\left(1 - \frac{\tilde{A}_1}{4a^2}\right)$$

and

$$W(a,-x) \sim 2\sqrt{\pi}\,(4a)^{-1/4}\, e^{1/2\,\pi a}\left(1 - \frac{1}{4608 \cdot a^2}\right)\left(\frac{t}{\xi^2 - 1}\right)^{1/4} \mathrm{Ai}(-\tilde{T})\left(1 - \frac{\tilde{A}_1}{4a^2}\right)$$

where

$$\xi = \frac{x}{2\sqrt{a}} \quad ,$$

$$t = (2a)^{2/3}\tau \quad ,$$

$$\tau = (3/4)^{2/3}\begin{cases} -[\arccos\xi - \xi\sqrt{1-\xi^2}\,]^{2/3} & \text{for } \xi \leq 1 \\ [\xi\sqrt{\xi^2 - 1} - \ln(\xi + \sqrt{\xi^2 - 1})]^{2/3} & \text{for } \xi > 1 \end{cases} \quad ,$$

$$\tilde{T} = t - (2a)^{-4/3}\left\{B_0 + \frac{1}{4a^2}\left[-B_1 + B_0\left(\tilde{A}_1 + \tau\frac{B_0^2}{6}\right) + \frac{1}{1152}\right]\right\} \quad ,$$

and

$$B_0 = -|\tau|^{-1/2}\left(\frac{\xi^3 - 6\xi}{24\sqrt{|\xi^2 - 1|^3}} + 5/48\,|\tau|^{-3/2}\right) \quad ,$$

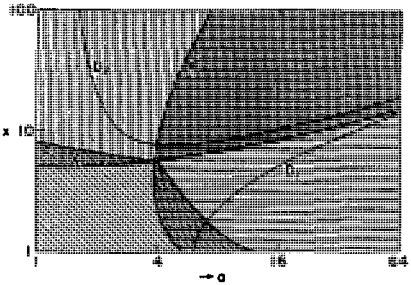

Fig. 1. The region where various expansions of the parabolic cylinder functions have at least a relative accuracy of 10^{-6} (as computed on a CDC 6600).

- P: Power series solution.
- D_1: Darwin's expansion for $x^2 \ll 4a$.
- D_2: Darwin's expansion for $x^2 \gg 4a$.
- x: Expansion for $x \gg 1$ in Ref. 3, the 10^{-6} area is actually much larger than $x \gg a$, as assumed by Ref. 3.
- A: Uniform asymptotic expansion to the order $a^{-10/3}$. (XBL 748-3894)

$$B_1 = -|\tau|^{-1/2}\left(\frac{-4042\xi^9 + 18189\xi^7 - 28287\xi^5 - 151995\xi^3 - 259290\xi}{414720\sqrt{|\xi^2-1|^9}}\right.$$

$$\left. + 5/48\,|\tau|^{-3/2}\,\frac{-9\xi^4 + 249\xi^2 + 145}{1152|\xi^2-1|^3} + \frac{345}{4608}|\tau|^{-3}\,\frac{\xi^3 - 6\xi}{24\sqrt{|\xi^2-1|^3}} + \frac{85085}{663552}|\tau|^{-9/2}\right).$$

$$\tilde{A}_1 = \left(\frac{-9\xi^2 + 249\xi^2 + 145}{1152|\xi^2-1|^3} - 7/48\,|\tau|^{-3/2}\,\frac{\xi^3 - 6\xi}{24\sqrt{|\xi^2-1|^3}} - \frac{455}{4608}|\tau|^{-3}\right) \times \begin{Bmatrix} 1 & \xi > 1 \\ -1 & \xi < 1 \end{Bmatrix} - \frac{\tau B_0^2}{2} .$$

For $\xi \to 1$ these expressions become undefined, since both τ and $\xi^2 - 1$ tend to zero. But the coefficients can be analytically approximated when $(\xi - 1)$ is in the interval -0.003 to 0.004, by

$$B_0 \approx -0.0404974\,(1.484193 - 0.484193\cdot\xi) ,$$

and

$$A_1 \approx -0.008646 ,$$

while t is to second order

$$t \approx 0.2a^{2/3}(\xi - 1)(3 + \xi)$$

and $t/(\xi^2 - 1)$ may be written as

$$\frac{t}{\xi^2 - 1} \approx a^{2/3}(7/5 - 2/5\xi) .$$

Furthermore B_1 can be replaced for all arguments by the much simpler expression

$$B_1 \approx -B_0\,\frac{0.43 + 0.2992\cdot\xi}{0.44 + 1.23\cdot\xi}$$

without any significant loss of accuracy.

Footnotes and References

*Condensed from LBL-2969.

†On leave from Inst. f. Kernphysik, TH Darmstadt, F. R. Germany.

1. Handbook of Mathematical Functions, Ed. M. Abramowitz and I.A. Stegun, NBS Appl. Math. Series 55 (1969), 692, chapter 19.16.

2. F.W.J. Olver, Uniform asymptotic expansions for Weber parabolic cylinder functions of large order, J. Research NBS 63B, 2, 131-169 (1959).

3. Ref. 1, p. 693, chapter 19.19.

THE DYNAMIC r-PROCESS NUCLEOSYNTHESIS OF HEAVY AND SUPERHEAVY ELEMENTS*

O. Johns†

The r-process of nucleosynthesis produces neutron-rich nuclides of constantly increasing nuclear charge until it is cut-off at some maximum proton number by neutron-induced fission. Discussion of this cut-off, and in particular the question of the formation or non-formation of superheavy elements by the r-process, less largely been based on the assumptions that the proton number at cut-off is the same for all r-process *events*, and that it *is* independent of time during any single event. Since Seeger, Fowler, and Clayton[1] showed that there is a single r-process path in the N-Z plane which best reproduces the peaks of element abundance at nucleon numbers 130 and 195, later workers have taken the proton number at which this "best" path first intersects a region of rapid neutron-induced fission to be the cut-off value.[2-5] For example in Fig. 1, which shows several possible r-process paths, the "best" path would have $\gamma \approx 2.5$ MeV.

Recently, however, some attempts have been made[6-8] to place the r-process in a more realistic setting by including a time dependence of mass density, neutron density, temperature, etc., during the r-process phase of a stellar explosion. In particular, Sato[9] has extended the analysis to include the effect of beta decay energy and fission energy depositions on the entropy.

The purpose of this paper is to examine critically the cut-off of the r-process in the light of these dynamic calculations. We use the formalism developed in Johns and Reeves.[10] Two main conclusions result from this examination:

(1) It is found that the maximum atomic number reached before neutron induced fission cuts-off the r-process varies with the instantaneous values of neutron density and temperature, as shown in Fig. 2. It thus varies with the time in dynamic r-process calculations, Fig. 3. This

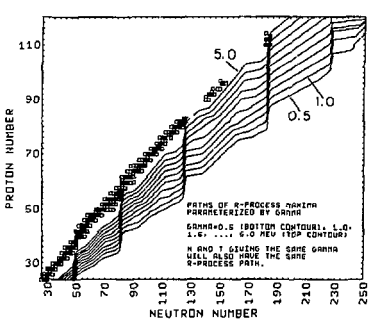

Fig. 1. The r-process paths in the N-Z plane are shown for different γ values. (The paths are contours $\gamma = 1/2\ S_{2n}(Z,N)$; see ref. 10. The Myers and Swiatecki 1967 mass law is used.[15] A path with $\gamma > 5$ MeV (top contour) would have unreasonably long beta decay lifetimes, but paths with $\gamma < 0.5$ MeV are possible. (XBL 7410-1855)

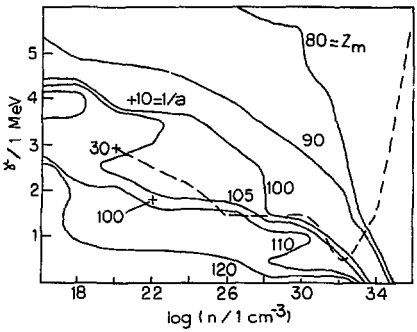

Fig. 2. The solid lines are contours of constant cut-off proton number Z_{max}. The γ is the parameter labeling the r-process paths, and n is the neutron density. The dotted line is the dynamic r-process trajectory of Sato[9] for 1/a - 30 times the free-fall expansion rate, and initial neutron-proton ratio of 20. The crosses are freeze-out points of Sato's calculation for n/p = 20 and 1/a = 10, 30, and 100. (XBL 7410-1856)

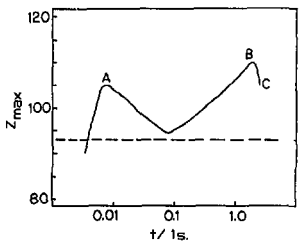

Fig. 3. The cut-off proton number Z_{max} is plotted as a function of time for the Sato[9] dynamic r-process trajectory n/p = 20, 1/a = 30. The dotted line is the constant Z_{max} = 93 cut-off assumed by Sato. (XBL 7410-1860)

time variation of Z_{max} may have significant effects on the rate of deposition of fission energy in calculations such as Sato[9] which treat explicitly the thermodynamics of the r-process environment.

(2) Any discussion of the r-process formation of superheavy elements must consider the possibility of their production by any of a range of different supernova events. The eventual maximum nuclear charge produced in an r-process event depends on the neutron density and temperature at freeze-out (i.e., termination of the r-process). These freeze-out parameters in turn depend on the expansion time scale and on the initial mass density.[9] Three different possible freeze-out points are marked by crosses in Fig. 2. The same points are marked in Fig. 4, which shows that superheavy element production is predicted for this mass law for those events with $1/a > 10$.

Taking the circum-core regions of gravitational collapse supernovae as a possible site of the r-process,[6] it is unlikely that all collapsing cores reach the same maximum density or that all of them explode with the same velocity. This diversity of r-process events is important because the detection threshold of current experimental searches for natural superheavy elements is very low, on the order of 10^{-15} grams per gram of sample.[11,12] At this level, superheavy elements of cosmological lifetime (if any) should be detectable if only a small fraction of r-process events actually have produced elements in the superheavy mass range.

Recently, Howard and Nix,[5] using a new mass and fission barrier determination which combines the Myers and Swiatecki[13] droplet model with the Strutinsky[14] shell-correction method, concluded that the static r-process cannot produce superheavy elements. Fig. 5, taken from Howard and Nix,[5] shows the contours of neutron induced fission threshold E_t calculated by these authors. The superimposed dotted contours are contours of constant neutron separation energy S_n also calculated by Howard and Nix but labeled by us with their equivalent γ values. (Over this restricted region of the N-Z plane, the contours of constant S_n are not much different from the r-process paths.) We note that all r-process paths with $\gamma < 1.4$ MeV fall outside of the region treated by Howard and Nix. However, our analysis suggests that a supernova event could very easily freeze-out near $\gamma = 1.0$ or even 0.5 MeV. The chance that an extremely neutron rich r-process path will reach the superheavy mass range thus cannot be ruled out. To investigate this possibility, it would be necessary to survey the $Z = 80$ to 120 region of the N-Z plane from $N = 184$ all the way out to the neutron drip line (in fact, to the line $S_{2n} = 0$), which may be beyond the $N = 228$ magic number. On the basis of the surveys so far published, it seems that the r-process production of superheavy elements remains a possibility. It seems possible for nuclei with $A \cong 310$ to be produced, at least temporarily. Their subsequent survival depends on the details of the final, ejection phase of the r-process which is not considered here.

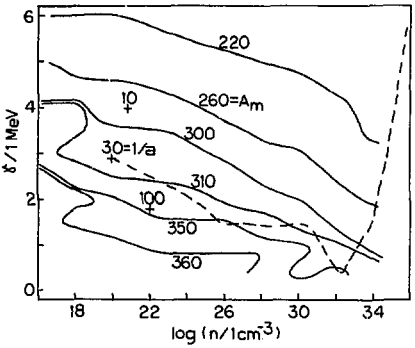

Fig. 4. The same as Fig. 2 except that the solid lines are contours of A_{max} at cut-off. These values are taken as $A_{max} = Z_{max} + N_Z$ and so do not include the effects of spread of the r-process path about its maximum N_Z which could increase the A_{max} by a few units. The solid curves here and in Fig. 2 were calculated using an earlier mass law[15] and hence overestimate the Z_{max} and A_{max} compared to more recent mass and fission barrier determinations. (XBL 7410-1858)

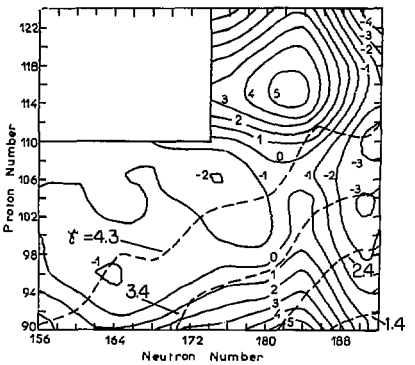

Fig. 5. This figure is a composite of two figures from Howard and Nix[5]. The solid lines are contours of neutron-induced fission threshold E_t. The dotted lines are contours of one neutron separation energy S_n labeled by γ. (XBL 7410-1861)

Footnotes and References

* Brief summary of Laboratoire René Bernas report LRB 74/3, to be published.

†Laboratoire René Bernas, Orsay, France, and Lawrence Berkeley Laboratory, Berkeley, CA .

1. P.A. Seeger, W.A. Fowler, and D.D. Clayton, Ap. J. Suppl. 11, 131 (1965).

2. D.N. Schram and W.P. Fowler, Nature 231, 103 (1971).

3. R. Boleu, S.G. Nilsson, R.K. Sheline, and K. Takahashi, Phys. Lett. 40B, 517 (1972).

4. D.N. Schramm and E.O. Fiset, Ap. J. 180, 551 (1973).

5. W.M. Howard and J.R. Nix, Nature 247, 17 (1974).

6. M. Delano and A.G.W. Cameron, Astro. and Space Sci. 10, 203 (1971).

7. K. Sato, K. Nakazawa, and S. Ikeuchi, Prog. of Theor. Phys. 49, 1166 (1973).

8. D.N. Schramm, Ap. J. 185, 293 (1973).

9. K. Sato, Prog. of Theor. Phys. 51, 726 (1974).

10. O. Johns and H. Reeves, Ap. J. 186, 233 (1973).

11. C. Stephan, J. Tys, M. Sowinski, E. Cieslak, M. Meunier, report of Institut de Physique Nucleaire, Orsay, France (1973).

12. M. Epherre, O. Johns, and C. Stephan, Remarks concerning the experimental search for superheavy elements in nature, Orsay report LRB 74/2 (1974).

13. W. Myers and W. Swiatecki, Lawrence Berkeley Laboratory report LBL-1957 (1973).

14. V.M. Strutinsky, Nucl. Phys. A95, 420 (1967).

15. W. Myers and W. Swiatecki, Arkiv for Fysik 36, 343 (1967).

THE LONG-LIVED RADIOISOTOPES AS MONITORS OF STELLAR, GALACTIC AND COSMOLOGICAL PHENOMENA*

H. Reeves† and O. Johns‡

The possibility of time variation of the characteristic parameters of stellar evolution has been much discussed recently. In particular, in order to account for the paucity of low metal stars, important variations in the Initial Mass Function, the fractional amount of mass going into new stars of mass M,[1] has been suggested by Schmidt,[2] Truran and Cameron.[3] (See the discussions by Pagel,[4] Searle,[5] Tinsley,[6] etc.)

In this paper, we want to illustrate in a simple way, how the study of long-lived radioisotopes can shed some light on this question.

In the present approach we neglect the possibility of infall of extra-galactic matter into the galaxy after the birth of the first stars. We define $S^*(t)$ to be the total mass of stars at time t , and $U(t)$ the total mass of gas and dust. Then $U(t) + S^*(t) = M_G$, the galactic mass and $dU/dt = -dS^*/dt$.

The lifetime τ^* for depletion of the interstellar gas is given by

$$\frac{dS^*}{dt} = \frac{U(t)}{\tau^*(t)} = -\frac{dU}{dt} \qquad (1)$$

Next, we define $M_i(t)$ as the mass of nuclide i in gas and dust, hence $Z_i(t) = M_i(t)/U(t)$ is the mass fraction of i and $Z(t) = \sum_i Z_i$ is the mass of "metals" ($A > 4$) in gas and dust.

The elementary act of astration consists in the following: an interstellar cloud, of metal abundance Z_i, collapses and forms stars. These stars live for a time $t(M)$ during which they produce some new metals by nuclear cooking. Part of this matter is then rejected back into interstellar space. The "instant recycling approximation" can be made, which states that, as far as nucleosynthesis is concerned, we may consider that all the big stars ($M > 2 - 3\ M_\odot$) live instantaneously and immediately reject most of their matter in space while all the small stars live eternally. In other words, a fraction f of the cloud is immediately returned to space while a fraction $(1 - f)$ remains locked in stars. The fraction f is in turn composed of fractions f^p and f^u in which new metals are produced or not produced respectively. Thus $f = f^p + f^u$. The mass fraction of isotope i in the fraction f_p will be denoted z_i.

The isotopes to be considered here are $^{129}I(2.3 \times 10^7 yr)$, $^{244}Pu(1.2 \times 10^8 yr)$, $^{235}U(10^9 yr)$, $^{238}U(6.5 \times 10^9 yr)$, $^{232}Th(2 \times 10^{10} yr)$. They are all generated by the r-process. The time variation of the total mass $[UZ_i]$ of isotope i with radioactive life time τ_i is given by:

$$\frac{d}{dt}(UZ_i) = -Z_i \frac{dS^*}{dt} + y_i \frac{dS^*}{dt} - \frac{1}{\tau_i}(UZ_i)$$

where $y_i = \frac{z_i f^p}{1-f}$ is the "yield"[5] of isotope i per unit increase of the total stellar mass S^*. The solution to this equation at time T , the time of formation of the solar system, can be written

$$Z_i = \left\langle \frac{y_i}{\tau^*} \right\rangle \tau_i (1 - e^{-T/\tau_i})$$

where the brackets indicate an average of y_i/τ^* over a period τ_i before the formation of the solar system (i.e., from $T - \tau_i$ to T).

Information is best obtained by defining the following ratios pertaining to two isotopes i and j, to be called the astration probe parameter.

$$\eta_{ji} \equiv \frac{\frac{1}{Z_j}\left\langle \frac{y_j}{\tau^*} \right\rangle \tau_j}{\frac{1}{Z_i}\left\langle \frac{y_i}{\tau^*} \right\rangle \tau_i} = \frac{Z_j \tau_i z_i (1 - e^{-T/\tau_i})}{Z_i \tau_j z_j (1 - e^{-T/\tau_j})}$$

where T is the period of galactic nucleosynthesis of the solar system material, presumably extending from the birth of the galaxy till the birth of the sun. From data pertaining to the oldest clusters[7] we estimate T to be $6 \pm 2 \times 10^9$y. Clearly from the definition of η_{ji}, if the IMF (and hence the f's) and also the life time τ^* were constant throughout the life of the galaxy, we should get $\eta_{ji} = 1$ for all pairs. Conversely, any strong departure from one (outside of the uncertainties -- which are of the order of two on each side --) should indicate the time variation of at least one of these parameters. Hence the name of astration probe parameter.

Previous studies of the same data[8-10] have tacitely assumed that constancy of these astration parameters and have obtained an age of the galaxy (from the so-called cosmochronology) which turns out to coincide moderately well with the age of the oldest clusters. Here we have taken a different point of view; we use the cluster age to evaluate η_{ji} and test the time constancy of the astration parameters. It is quite remarkable that in Table 1 the only strong departure from $\eta_{ji} = 1$ is found for the shortest time scale of $\sim 2 \times 10^7$ related to ^{129}I. The decrease of η_{ji}

Table 1. Parameters for the interpretation of the data on the long-lived radioisotopes.[(a)]

j/i	τ_j/τ_i (years)	Z_j/Z_i	z_j/z_i	$\frac{(1 - e^{-T/\tau_j})}{(1 - e^{-T/\tau_i})}$	η_{ji}
$^{224}Pu/^{235}U$	$\frac{1.2 \times 10^8}{1.0 \times 10^9}$	0.048	0.48 ± 0.14	$\frac{1}{0.99}$	$0.83^{1.17}_{0.64}$
$^{235}U/^{238}U$	$\frac{1.0 \times 10^9}{6.5 \times 10^9}$	0.32	1.94 ± 0.56	$\frac{0.99}{0.60}$	$0.65^{0.91}_{0.50}$
$^{238}U/^{232}Th$	$\frac{6.5 \times 10^9}{2.0 \times 10^{10}}$	0.44	0.53 ± 0.11	$\frac{0.60}{0.26}$	$1.11^{1.40}_{0.92}$
$^{244}Pu/^{232}Th$	$\frac{1.2 \times 10^8}{2.0 \times 10^{10}}$	0.007	0.49 ± 0.06	$\frac{1}{0.26}$	$0.62^{0.71}_{0.55}$
$^{129}I/^{127}I$	$\frac{2.3 \times 10^7}{\infty}$	10^{-4}	$1.4^{+1.4}_{-0.7}$	$\frac{1}{0}$	$0.019^{0.038}_{0.010}$

(a) Z_j/Z_i is the relative abundance of isotope i and j at the birth of the meteorites (4.7×10^9yr ago) assuming that, in spite of chemical fractionation, one may reconstitute the true cosmic abundance through meteoritic studies. For Pu, U and Th this assumption may be hazardous. The ratios z_j/z_i are the ratios of formation in r-process synthesis. These ratios and their uncertainties are reviewed in a companion paper.[12] The next to last column is a correction term for the finite duration of solar system nucleosynthesis ($T \simeq 6 \times 10^9$yr). The last column gives η_{ji} the astration probe parameter discussed in the text.

The shorter-lived radioisotope is always placed in the numerator. Thus if τ is smaller at earlier galactic times (decreasing rate of star formation), the η_{ji} would be less than unity. The same effect would be produced if f_p^r (and hence all y_i^r) were larger at earlier times.

The η_{ji} values are calculated for $T \cong 6 \times 10^9$ yr. If $T \cong 10 \times 10^9$yr is used,[13] $\eta_{ji} = 1$ is then within the calculated error range for all pairs except $^{129}I/^{127}I$.

to ≈ 0.01 is most likely due not to a variation of the IMF during this short period, but to an increase in τ^* implying a decrease of the nucleosynthesis activity some 2×10^7 y before the formation of the meteorites. The reason why the n_{ji} value for Iodine is low could be due to the fact that, in the last $\sim 10^8$ y before the birth of sun, the protosolar cloud (or clouds) was cruising between two arms of the galaxy where very little astration takes place. The last contribution to solar system ^{129}I was incorporated to the protosolar cloud when it crossed the last are before its arrival in the arm where the sun was born.[10]

Analysis of the data on long-lived radioisotopes, together with the data on the metal abundances in stars, brings us to the following tentative conclusions.

(A) The data is consistent with no great variations (less than a factor of two) of the values of the partial rate of yields of r-process elements averaged over periods of 10^8y, 10^9y and 6×10^9y before the birth of the sun. This result is consistent with a constant initial mass function and a constant for stellar formation throughout the life of the galaxy.

(B) The uncertainty in the data is large enough not to preclude the hypothesis of a large -- but brief -- increase of the rates of yields during the early days of the galactic life. Such an increase, lasting until the interstellar metal abundance reached ≈ 20% of the solar value, could account for the paucity of low-metal stars.

(C) The low iodine isotopic ratio suggest that, when considering periods of less than 10^8 years before the birth of the sun, we should consider the effect of galactic rotation on the rate of yield of nucleosynthesis, as expected for instance in the density wave theory.

(D) The fraction of unastrated gas consistent with these data and analysis is about fifty percent. Hence, accepting the view that Deuterium originates in the Big Bang, we obtain from the calculation of Wagoner[11] that the present universal density is $\approx 5 \times 10^{-31}$ g cm^{-3}.

Footnotes and References

*Condensation of a paper to be submitted for publication in The Astrophysical Journal.

†Centre d'Etudes Nucleaires de Saclay, Institut d'Astrophysique de Paris.

‡Laboratoire René BERNAS - ORSAY and LBL.

1. E.E. Salpeter, The Rate of Star Formation in the Galaxy, Ap. J. 129, 608 (1959).

2. M. Schmidt, The Rate of Star Formation, Ap. J. 137, 758 (1963).

3. J.W. Truran and A.G.W. Cameron, Ap. and Space Sci. 14, 179 (TC) (1971).

4. B. Pagel, unpublished (1973).

5. B. Searle, in "L Age des Etoiles", Meudon I. A.U. Symposium N°34 (ed G. Cayrel and A. Delplace) (1973).

6. B. Tinsley, Lecture notes, Erice, May 1974.

7. A. Sandage, Ap. J. 162, 841 (1970).

8. W.A. Fowler, in Cosmology Fission and Other Matters. A Memorial to George Gamow, ed. F. Reines (Colorado Assoc. Univ. Press, Boulder, CO, 1972).

9. D.N. Schramm, and G.J. Wasserburg, Ap. J. 162, 57 (1970).

10. H. Reeves, Astron. Astrophys. 19, 215 (1972).

11. R.V. Wagoner, Ap. J. 179, 343 (1973).

12. O. Johns and H. Reeves, The r-process production ratios of long-lived radionuclides, to be published in The Astrophysical Journal, 15 November 1975.

13. A Sandage, Quarterly Journal of the Royal Astronomical Society 13, 282 (1972).

2. Chemical and Atomic Physics

Heavy Ion Induced Atomic Reactions

Atomic and Molecular Spectroscopy

Photoelectron Spectroscopy and Hyperfine Interactions

ATOMIC PROCESSES IN HEAVY ION COLLISIONS

W. E. Meyerhof,*† T. K. Saylor,† S. M. Lazarus,† W. A. Little,†
B. B. Triplett,† L. Γ. Chase, Jr.‡, R. Anholt,§ and P. D. Bond‖

Work has been done at the Stanford University tandem accelerator, the Brookhaven National Laboratory tandem accelerator, and the Berkeley SuperHILAC. Kr, Br, I, and Pb beams were used with a variety of targets and separated atom (SA) K x rays of the target and projectile were measured. Continuum radiation due to molecular orbital (MO) x rays was observed in many cases. The focus of our work is to explain the observed cross sections for SA K x ray production and the thick target yields of MO x rays. Through theories exist for proton and alpha particle excitation of SA x rays, none exist that quantitatively explains the cross sections for asymmetric collisions where the atomic number of the projectile is comparable to that of the target atom. Universal curves have been developed that semi-empricaly fit the observed data with a fair reliability. In addition, theories of the one and two collision yield have been applied successfully to cases where Br and I were used as projectiles.

This work has been described in the Annual Report of the Tandem Laboratory at Stanford under the following headings.

A. K Vacancy Production in Symmetric Heavy Ion Collisions.
B. Electron Promotion Contribution to Symmetric K X-ray Production for Z > 10 by Two Collision Processes in a Solid.
C. Measurement of K X-ray Yield in 100 MeV Pb + Pb Collisions and Approximate Scaling Law for K Vacancy Production in Heavy Ion Collisions with Z > 10.
D. Theory of Molecular Orbital X-ray Formation in Heavy Ion Collisions.
E. Approximate Interpolation Procedure for the 1sσ Molecular Orbital Level in Asymmetric Heavy Ion Collisions.
F. Impact Parameter Dependence of K-Vacancy Production in Heavy Ion Collisions.
G. Observation of Molecular Orbital K X-ray in Heavy Ion Collisions.

Of these topics, C and G above are reproduced in the following articles of this annual report.

Footnotes and References

*On partial leave at Lawrence Berkeley Laboratory.

†Department of Physics, Stanford University, Stanford, Ca 94305.

‡Lockheed Palo Alto Research Laboratory, Palo Alto, Ca.

§Department of Chemistry, University of California and Lawrence Berkeley Laboratory.

‖Physics Division, Brookhaven National Laboratory, Upton, New York.

1. Abstracts from Stanford Annual Report of the Tandem Laboratory 3/1/73-2/28/74, "Nuclear Structure Investigations with an FN Tandem Accelerator-Atomic Processes in Heavy Ion Collisions" August, 1974.

MEASUREMENT OF K X-RAY YIELD IN 100 MeV Pb + Pb COLLISIONS AND AN APPROXIMATE SCALING LAW FOR K VACANCY PRODUCTION IN HEAVY-ION COLLISIONS WITH Z > 10

W. E. Meyerhof, R. Anholt,* T. K. Saylor and P. D. Bond†

In order to examine the scaling law proposed in Section IX.A of ref. 2 for higher Z collisions, we have measured the Pb K x ray yield from 88- and 107-MeV Pb + Pb collisions using the Brookhaven Tandem Van de Graaff accelerator. We have also determined an upper limit for Pb K x ray production in 107-MeV Pb + Ta collisions. Table 1 gives our results. Cross sections were determined from thick target yields by assuming that the yield y_K varies exponentially with the bombarding energy E_1 ($y_K \propto E_1^s$) and then using a well known formula[1] to extract the cross section. This gives, for a target of 45° to the beam direction and a detector placed at 90°, viewing the front of the target

$$\sigma = \frac{A_2}{N_0} s \frac{y_K}{E_1} \frac{dE_1}{d\rho x} + \frac{\mu}{\rho} , \qquad (1)$$

where A_2 = target atomic number, N_0 = Avogadro's number, ρ = target density, μ = K x-ray absorption coefficient. Table 1 gives the experimental yields and derived cross sections (s = 6.5).

Since, in accordance with the ideas presented in Section IX.A Pb K vacancies in Pb + Pb collisions should be produced by 2pσ excitation and ionization [process (b)], we scaled the experimental cross sections according to Eq. (1) of Ref. 2. We found that the scaled cross sections are approximately two orders of magnitude below the points associated with 2pσ excitation.

It turns out that for Pb + Pb the relativistic 2pσ MO binding energy is much larger[3] than one would expect from non-relativistic scaling of the MO energy levels. Furthermore, with the available

TABLE 1.

E_1 (MeV)	y_x [a]	σ_x (cm²)	$E_1/\lambda U$	$Z^2\sigma_K$ (a.u.) [b]	$E_1/\lambda G$
107.2	5.6×10^{-9}	1.9×10^{-27}	3.22×10^{-3}	4.8×10^{-7}	1.47×10^{-3}
87.7	1.5×10^{-9}	5.5×10^{-28}	2.64×10^{-3}	1.4×10^{-7}	1.25×10^{-3}

[a] Thick target K x-ray yield per projectile. Error ≈ ±20%.

[b] Corrected for neutral atom fluorescence yield (0.96).

(1 a.u. = 2.80×10^{-17} cm²)

bombarding energy the distance of closest approach D of the nuclei is much larger than that required to bring the MO levels to their united-atom values. Hence it occurred to us to replace the atomic binding energy U in Eq. (1) of Ref. 2 by the MO binding energy G at the distance of closest approach. This changes the scaling law to read

$$Z^2\sigma_K = F(E_1 m/GM_1) \quad , \qquad (2)$$

where G = G(D) with $D = Z^2e^2/(1/2)E_1$.

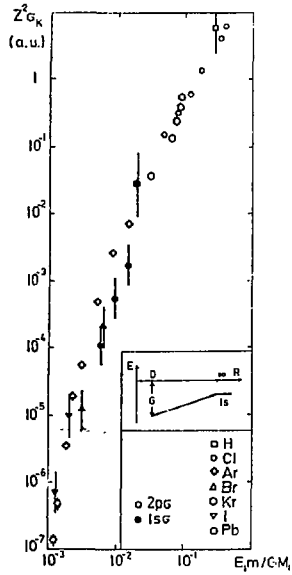

Fig. 1. K vacancy yield for symmetric collisions scaled according to Eq. (2). Open symbols - 2pσ excitation cross sections, closed symbols - 1sσ excitation cross sections. (XBL 756-1554)

Values of G were looked up or interpolated from relativistic and non-relativistic MO level calculations[3,4] for all cases where the bombarding energy was insufficient to bring G to its united atom limit. The Pb + Pb cross sections, as well as all cross sections assigned to 2pσ [process (b)] and 1sσ excitation [process (c)] were scaled according to Eq. (2). The resulting points are shown in Fig. 1. Two facts can be noted. (1) The Pb + Pb cross sections fall nicely into the band of points representing 2pσ excitation. (2) Within an order of magnitude the cross sections assigned to 2pσ and to 1sσ excitation fall on a universal curve, extending from H to Pb.

The theoretical basis of Eq. (3) has yet to be examined. It appears, though, that the energy gap G between the MO and the continuum is the important physical quantity which determines K vacancy production in heavy-ion collisions with Z > 10. The type of coupling (radial or rotational) appears to play a less important role.[5]

We thank Dr. Thieberger for producing the Pb beam at the Brookhaven Tandem.

Footnotes and References

*Nuclear Chemistry Department, Lawrence Berkeley Laboratory, University of California, Berkeley, California 94720.

†Physics Division, Brookhaven National Laboratory, Upton, New York.

‡Department of Physics, Stanford University, Stanford, California 94305.

1. E. Merzbacher and H. W. Lewis, Handbuch der Physik, Vol. 34 (Springer Verlag, 1958) p. 166.

2. Stanford Annual Report of the Tandem Laboratory, March 1, 1973 to February 28, 1974 (August 1974), Section IX.A.

3. B. Müller, J. Rafelski and W. Greiner, Phys. Lett. 47B, 5 (1973).

4. F. P. Larkins, J. Phys. B5, 571 (1972).

5. V. SethuRaman, W. R. Thorson and C. F. Lebeda, Phys. Rev. A8, 1316 (1973).

OBSERVATION OF MOLECULAR ORBITAL K X-RAYS IN HEAVY ION COLLISIONS

W. E. Meyerhof, T. K. Saylor, S. M. Lazarus, W. A. Little,
B. B. Triplett, L. F. Chase, Jr.,* and R. Anholt†

Following up our earlier work[1] we have made extensive measurements, partially published,[2] of continuum x ray spectra from heavy-ion collisions using 30- and 60-MeV Br beams and a 82-MeV I beam. We compared our results with the theory of molecular-orbital (MO) K x ray formation as outlined in the preceding three sections. We showed that the most significant backgrounds in the region of the MO K x-ray continuum in our measurements are nucleus-nucleus bremsstrahlung[3] and, at bombarding energies above 30 MeV, Coulomb-excited nuclear gamma rays. Also, close to the atomic K x ray lines radiative electron capture produces an important continuum.[4] The continuum in excess of these backgrounds is in quantitative agreement with the predictions of Eqs. (2) and (4) of Ref. 5.

For very asymmetric collisions at low bombarding energies the two-collision spectrum should be very small, the one-collision spectrum is important only at low x ray energies, and nuclear Coulomb excitation is very small so that here the continuum spectrum well above the atomic K x-ray lines should consist only of nucleus-nucleus bremsstrahlung. Figure 1 shows the continuum spectrum from 30 MeV ^{79}Br + Al. Only room background has been subtracted from the experimental spectrum. The spectrum has been corrected for absorption and detection efficiency effects and has been unfolded using experimental line shapes[6] (a 17-cc GeLi detector was used in this work). Curves T and O are the computed two- and one-collision spectral yields, B is the computed nucleus-nucleus bremsstrahlung spectrum. Since the latter depends on the square of the difference between the target and projectile charge to mass ratio[7] it turns out that the computed bremsstrahlung spectrum for ^{79}Br + Al is 1.65 times more intense than for ^{81}Br + Al. It is pleasing to note that the experimental spectrum agrees with the appropriate computer spectrum. This is a good check on our current integration and absorber and efficiency corrections. The excess counts at the upper end of the spectrum could be caused by weak nuclear Coulomb-excited gamma rays.

Figure 2 gives an example of appreciable nuclear Coulomb excitation typical of a higher bombarding energy. Fortunately the spectrum associated with MO K x ray production rises sharply at lower x-ray energies (note the log scale), so that the "flat" Compton background can be subtracted with reasonable certainty. The major uncertainty occurs at the upper end of the MO spectrum. A detailed comparison of the 60-MeV Br + Ti spectrum with the theory is shown in Fig. 1 of the preceding section. In agreement with Table 1 of Ref. 5 the one-collision process dominates here since the collision is sufficiently asymmetric. The absolute fit is about as good as can be expected.

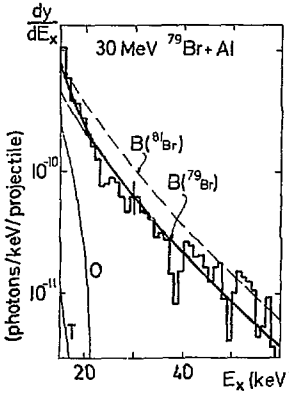

Fig. 1. Continuum x ray spectrum from 30-MeV ^{79}Br + Al (room background subtracted). T, O and B are the computed two-collision, one-collision and bremsstrahlung spectra, respectively. The dark line is the sum T + O + B (^{79}Br). (XBL 756-1545)

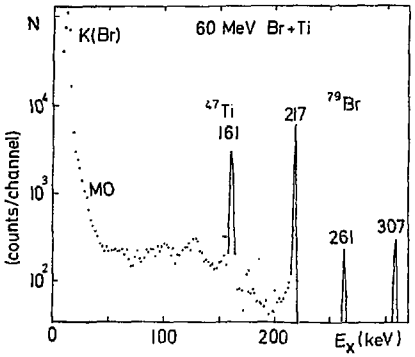

Fig. 2. Detected pulse height spectrum from 60-MeV ^{79}Br + Ti (room background subtracted). Coulomb excited gamma rays from ^{47}Ti and ^{79}Br are seen. The region of the molecular orbital spectrum (MO) is indicated, as well as the unresolved K x-ray peak of Br. A 17 cc GeLi detector was used. For the interpretation of the MO spectrum see Fig. IX.F.1. of Ref. 5., Section IX.F. (XBL 756-1546)

Figure 3 shows that for a symmetric collision with relatively low Z the two-collision mechanism is dominant, in agreement with the Table 1 of *Ref. 5. The dominance of the two-collision process* in this case can be tested directly by varying the target-atom density n. The test can be made with solid targets,[8] provided the other target atoms do not contribute to the MO yield. We have found that if K or Cl are bombarded with 30 MeV Br, the projectile K vacancy yield, which is due to direct 1sσ MO excitation in that case,[9] is only 10^{-3} of the 30-MeV Br + Br K vacancy yield. Hence we bombarded targets of solid Br (on a refrigerated Al backing) and of KBr + KCl mixtures (evaporated onto Al backings) with 30-MeV Br. After correction for absorber and efficiency effects the spectra shown in Fig. 4a are obtained. Subtracting the expected nucleus-nucleus bremsstrahlung background [curves B, computed from Eq. (II.E.13) of Ref. 7] one can deduce the net integrated MO K x-ray yields y_{MO}. Figure 4b shows that the ratio $y_{MO}(E_x = 27$ to 50 KeV)/y_K is approximately proportional to n (normalized relative to pure solid Br). A better proportionality is obtained if the one-collision yield (O) is also subtracted. Figure 4b indicates a dominant two-collision mechanism for 30-MeV Br + Br collisions confirming the direct spectral fits shown in Fig. 4a. These fits used a MO level calculation of Müller et al.[10] for the Br + Br system. To estimate τ_K we used the empirical relation[11] between the radiative K vacancy lifetime for atoms and the K_α x-ray energy. This yields the correct τ_K at the separate and united atom limits, but is only approximate between. The calculated curves T in Fig. 4a show that in situations in which the two collision process should dominate this prescription is reasonably successful in fitting the experimental results.

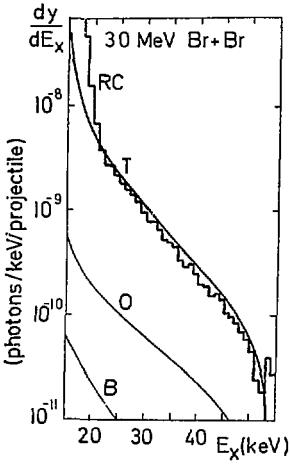

Fig. 3. Continuum x ray spectrum from 30-MeV ^{79}Br + Br. Notation as for Fig. 1. RC indicates the continuum spectrum from radiative electron capture. (XBL 756-1547)

Table 1 of Ref. 5 indicates that at higher Z the one-collision process should dominate MO K x-

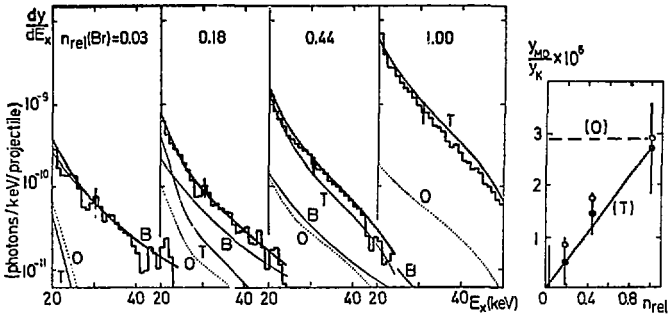

Fig. 4. (a) Corrected x-ray spectra from 30-MeV Br bombardment of various Br targets. Room background subtracted. Typical systematic errors are ±30%. The relative Br density corresponds to the following targets: 1.00: pure Br, 0.44: pure KBr, 0.18: 50% KBr + 50% KCl, 0.03: 10% KBr + 90% KCl. In each case, B, O, and T are the computed bremsstrahlung, one-two-collision MO spectra, respectively. The darker curves give B + O + T. (b) Ratio of integrated MO K x-ray yield (E_x = 27 to 50 keV) to beam K vacancy yield versus relative Br density. Lines (O) and (T) give the relationships expected for one- and two-collision mechanisms; respectively. Open symbols - total MO yield minus estimated one-collision contribution. (XBL 756-1548)

ray formation even in symmetric collisions. To check this, we bombarded thick, evaporated NaI targets with 82-MeV I (Fig. 5a). Unfortunately nuclear gamma rays from ^{127}I (58, 145, 230 keV) are strongly Coulomb excited. After convincing ourselves that the continuum between the 58- and 145-keV gamma rays is not due to pileup, we have extracted an x-ray band which we believe to be due to the I + I MO K x-rays (Fig. 5b). Theoretical curves were computed using an R, E_x relation from Ref. 10. The fit to experiment is reasonable and suggests the dominance of one-collision 1sσ excitation in MO K x-ray production in higher Z (Z ≳ 50) collisions.

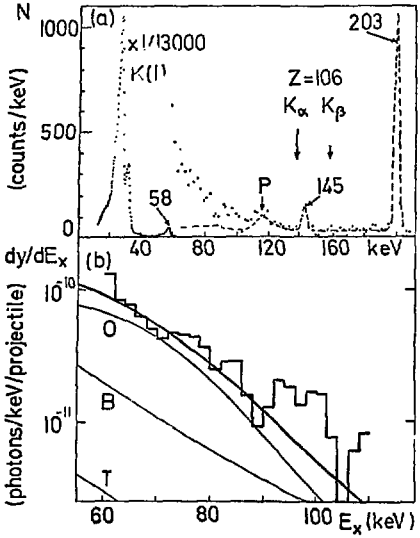

Fig. 5. X-ray spectra from NaI bombarded by 82-MeV I. (a) Room-background subtracted data, 17-cc Ge(Li) detector, 0.3-mm stainless steel absorber. Iodine K lines and Coulomb excited gamma rays are indicated. Dashed line is assumed background under continuum; P is a backscattering peak. Arrows give UA K x-ray limits. (b) Corrected x-ray spectrum. Above 100 keV the spectral shape is unreliable. Notation as for Fig. IX.G.1. The dark curve gives B + O + T. (XBL 756-1549)

Although, overall, the fit of the theory outlined in Section IX.D to the experimental spectra is satisfactory, further theoretical and experimental studies are needed. In the former one must investigate the dynamic effects due to the nuclear motion,[12] in the latter better investigations of the various continuum backgrounds are important.

Footnotes and References

*Lockheed Palo Alto Research Laboratory, Palo Alto, California.

†Nuclear Chemistry Department, Lawrence Berkeley Laboratory, University of California, Berkeley, California 94720.

‡Department of Physics, Stanford University, Stanford, California 94305.

1. W. E. Meyerhof, T. K. Saylor, S. M. Lazarus, W. A. Little, B. B. Triplet and L. F. Chase, Jr., Phys. Rev. Lett. 30, 1279 (1973); 32, 502 (1974).

2. W. E. Meyerhof, T. K. Saylor, S. M. Lazarus, W. A. Little, B. B. Triplett, L. F. Chase, Jr. and R. Anholt, Phys. Rev. Lett. 32, 1279 (1974).

3. T. K. Saylor, unpublished (June 1973); W. E. Meyerhof, Third Int. Sem. on Ion-Atom Collisions, Gif-sur-Yvette, France (July 1973), unpublished; C. K. Davis et al., Bull. Am. Phys. Soc. 18, 1406 (1973).

4. P. Kienle et al., Phys. Rev. Lett. 31, 1099 (1973).

5. Stanford Annual Report of the Tandem Laboratory, March 1, 1973 to February 28, 1974 (August 1974), Section IX.D.

6. T. K. Saylor, unpublished. See also Section IX.B of Ref. 5.

7. K. Alder et al., Rev. Mod. Phys. 28, 432 (1956).

8. Jacob A. Aten, F.O.M. Institute, Amsterdam, private communication.

9. W. E. Meyerhof, Phys. Rev. Lett. 31, 1314 (1973).

10. B. Müller, J. Rafelski and W. Greiner, Phys. Lett. 47B, 5 (1973).

11. W. Bambynek et al., Rev. Mod. Phys. 44, 716 (1972).

12. W. Lichten, Phys. Rev. A9, 1458 (1974); K. Smith, B. Müller and W. Greiner, to be published; J. S. Briggs and J. Macek, J. Phys. B, to be published.

DESCRIPTION OF THE ONE AND TWO COLLISION MOLECULAR ORBITAL X-RAY YIELD

R. Anholt

The purpose of this note is to present semi-empirical calculations of the one and two collision molecular orbital (MO) K X-ray yield. As opposed to discrete Kα or Kβ transitions in separated atoms (SA), MO K X-rays are observed in collisions as a continuum stretching from the K X-ray peaks of the SA down to the Kβ transition energy in the united atom (UA). The theory of the two collision MO X-ray yield was given by Briggs and Macek and Meyerhof et al.[2] and the one collision yield by Meyerhof et al.[2] Although the Meyerhof group has presented calculations which fit the experimental observations very well, their calculation only includes the $2p\pi$-$1s\sigma$ transition rate adjusted to the inverse of the total lifetime of a vacancy in the $1s\sigma$ orbital, and the transition energy was the $2p\pi \rightarrow 1s\sigma$ energy interpolated from one-electron, non-relativistic[3] and relativistic calculations.[4] Other transitions from the $2p\sigma$, $3p\sigma$, $3p\pi$, $4p\pi$, etc. molecular orbitals are also important, and since the yields from these orbitals are expected to have a different shape from the $2p\pi \rightarrow 1s\sigma$, it is not clear if Meyerhof's procedure is entirely valid.

To check this, we have calculated transition rates as a function of the internuclear distance, R, using exact, one-electron H_2^+ and HeH^{+2} type wave functions.[5] Though one-electron calculations give fairly accurate values for transition rates and transition energies for intermediate atomic numbers $20 < Z < 100$, there is nevertheless a tendency for the transition energies to be lower (for $Z < 50$) and higher for $Z > 50$) than experiment and the transition rates to be higher than experiment. To correct for these deficiencies, we have adopted a semi-empirical procedure which is described below. In the following section we present theoretical expressions for the MO K X-ray yield and calculations using these expressions. Following this we describe our semi-empirical procedure and use it to calculate thick target yields for 30 MeV Br + Br_2 and 60 MeV Br + Ti. These are compared with Meyerhof's method and with experiment.

The theoretical expressions for the one and two collision MO K X-ray thick target yields are given in Table 1. This is for two states 1 and 2 only; for many states orbital 2 is replaced by j and the yield is summed X-ray energy-wise over many other transitions. The form of P(b, E) which we used is:

$$P(b, E) = .2\frac{\sigma_{1s}(E)}{a^2}\{1 + e^{b/a}\}^{-1}$$

where $a = 2a_0[Z_1 + Z_2]^{-1}$ with a_0 equal to the Bohr radius and $\sigma_{1s}(E)$ is the cross section for making vacancies in the $1s\sigma$ orbital. The transition energies $E_X(R)$ and rates $\lambda_{12}(R)$ are calculated using one-electron wave functions and experimental values for the cross sections (or thick target yields) are used. The Demkov theory allows us to calculate W(2p - 1s) etc.

Yields for 30 MeV Br + Br_2 and 60 MeV Br + Ti are shown in Figs. 1 and 2. It should be noted that for the $3p\sigma$ and $4p\sigma$ orbitals the radiative dipole matrix element changes sign at ∿.03A which is where the transition energy is approximately 25 keV (for Br + Br), which explains the behavior of the X-ray yield as a function of $E_X(R)$ in those cases. Note that the quite different behavior of the orbital transitions makes a sort of bulge in the total two-collision yield which is not seen in the $2p\pi$ yield.

To correct these intensities for relativistic and many-electron effects, we have adopted the following procedure: At each internuclear distance the $2p\pi$ transition energy and rate is calculated using one-electron wave functions. The energy is compared to $2p \rightarrow 1s$ energies in hydrogenic atoms which is then compared to experimental $2p_{3/2} \rightarrow 1s$ energies in atoms. A simple interpolation is performed to find a semi-empirical value for the $2p\pi$ or $2p_{3/2}$ molecular orbital energy. For $2p\sigma$ transitions, $2p_{1/2}$ energies for atoms are used, for $3s\sigma$, $3p\sigma$, $3p\pi$, $4s\sigma$, etc. $3s_{1/2}$, $3p_{1/2}$,

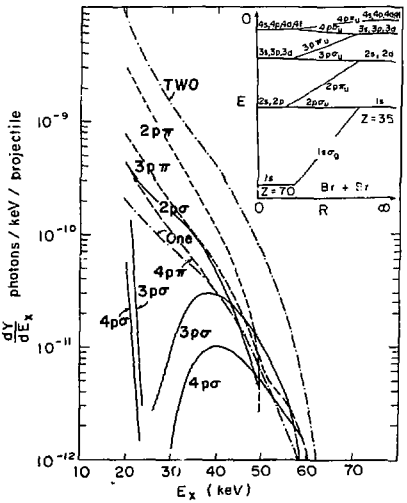

Fig. 1. Thick target yields for 30 MeV Br + Br_2. Component two collision yields from π transition (dash lines) and σ transition (solid lines) are shown. Total one and two collision yields are shown as dash-dot-dash line. (XBL 757-3572)

TABLE 1.

One Collision Yield

$$\frac{dY_{12}}{dE_X} = \int_0^{E_1} dE\ S(E)^{-1} n_2 \int_0^{\rho} 2\pi b\,db\ P(b,E)\ \frac{\lambda_{12}(R)}{v_R}\ \frac{dR}{dE_X}$$

Two Collision Yield

$$\frac{dY_{12}(E_X)}{dE_X} = \int_0^{E_1} dE\ S(E)^{-1} n_2 \sigma(E) f(\omega) \omega_K\ 4\pi m_2 R^2\ \frac{dR}{dE_X}\ \frac{\lambda_{12}(R)}{\lambda_1}\ \left[1 - \frac{d_o}{R}\right]^{\frac{1}{2}}$$

dY/dE_X: Yield per projectile per unit energy.

$E_X^{12}(R)$: X ray transition energy between 1sσ = 1 and molecular orbital 2 at internuclear distance R.

$S(E)$: Stopping power of the ion in the target with projectile energy E.

n_2: Target atom density.

$\sigma(E)f(\omega) = \sigma 2_{p\sigma}(E) \times \omega(2p\sigma - 1s) \times \omega(1s\sigma - 1s) + \sigma_{1s}(E) \times \omega(1s\sigma - 1s) \times \omega(1s - 1s\sigma)$

$\sigma_{2p\sigma}$, $\sigma_{1s\sigma}$: Is the cross section for making vacancies in the 2pσ and 1sσ orbital,

$\omega(2p\sigma - 1s)$, $\omega(1s\sigma - 1s)$ is the probability of transferring the vacancy from the 2pσ, 1sσ MO to the projectile 1s orbital.

b: The impact parameter.

d_o: The distance of closest approach at $b = 0$.

$\rho = (R^2 - d_o R)^{\frac{1}{2}}$, $V_R = v_1(1 - d_o/R - b^2/R^2)^{\frac{1}{2}}$, where v_1 is the projectile velocity.

$\lambda_{12}(R)$: The radiative transition rate from orbital 1 to 2.

λ_1: The total radiative transition rate into the 1s orbital of the projectile.

dR/dE_X: The change in nuclear distance with respect to the transition energy.

$P(b,E)$: The probability of creating a 1sσ vacancy at impact parameter b and projectile energy E.

E_1: The initial energy of the projectile.

ω_K: The neutral atom fluorescent yield for projectile K vacancies.

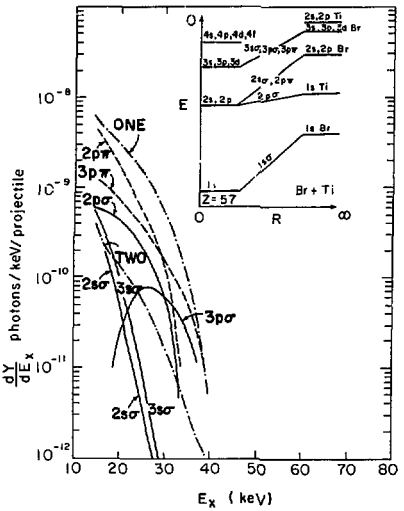

Fig. 2. Thick target yields for 60 MeV Br + Ti. Since the one collision yield is dominant here, only the component one collision yields from the σ (solid line) and π (dashed) transitions are shown. Total one and two collision yields dash-dot-dash line. (XBL 757-3574)

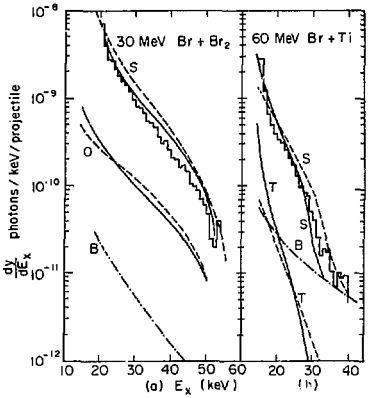

Fig. 3. Semi-empirically calculated (dash line) thick target yields for 30 MeV Br + Br_2 and 60 MeV Br + Ti. Meyerhof's calculations are shown by a solid line. O = one collision, T = two collision, B = nucleus-nucleus bremsstrahlung, S = T+O+B. T or O not shown when T ≈ S or O ≈ S. (XBL 757-3573)

$3p_{3/2}$, $4s_{1/2}$, values are used. Since the ratio of the transition rates calculated using one-electron and many electron wave functions[6] doesn't vary much over $20 < Z < 100$, we do not correct for this many-electron effect for the two-collision yield (since only the ratio of $\lambda(R)/\lambda$ is used anyway). In the one-collision formula, we multiply by $\lambda(M.E.,UA)/\lambda(O.E.,UA)$ which is the ratio of the total 1s transition rate in the united atom calculated using many-electron wave functions to that using one-electron wave functions.

Using these semi-empirical values, we calculate the thick target yield for Br + Br_2 and Br + Ti and compare these with experiment and with Meyerhof's approximate calculations in Fig. 3. Both methods fit the experimental data fairly well, though there is a tendency for our calculations to overestimate the yield. This overestimation is not serious, however, and within the accuracy of the experimental data and the theory, it is probably impossible to say whether our calculations or Meyerhof's much simpler ones are better.

References

1. J. H. Macek and J. S. Briggs, J. Phys. B7, 1312 (1974).

2. W. E. Meyerhof, T. K. Saylor, S. M. Lazarus, A. Little, L. F. Chase, Jr., R. Anholt, Phys. Rev. Lett. 32, 1279 (1974)

3. K. Helfrich and H. Hartmann, Theor. Chim. Acta. 16, 263 (1970).

4. B. Müller, J. Rafelski, and W. Greiner, Phys. Lett. 47B, 5 (1973).

5. W. E. Meyerhof, Phys. Rev. Lett. 31, 134 (1973).

6. J. H. Scofield, Phys. Rev. 179, 9 (1969).

SECONDARY ELECTRON BREMSSTRAHLUNG YIELD IN SYMMETRIC HEAVY ION COLLISIONS

R. Anholt and J. O. Rasmussen

X-ray continua in 30-200 MeV Br, Nb, Ni, and I bombardments of thick targets of the same atomic number have recently been observed by several groups.[1,2,3] These continua are thought to be due to molecular orbital (MO) x-rays. The major background in these experiments is electron-nucleus and nucleus-nucleus bremsstrahlung. Although nucleus-nucleus bremsstrahlung can be calculated quite simply,[4] the calculation of electron-nucleus bremsstrahlung yields is more difficult because the yield of secondary electrons in the region above 10 keV must first be calculated.

Recently a calculation by Folkmann et. al.[5] has been used to estimate the yield of secondary electrons and the bremsstrahlung yield in symmetric[2] and nearly symmetric[6] collisions. Folkmann's code uses the binary encounter approximation (BEA) to calculate the yield of secondary electrons and while this approximation gives good results for very asymmetric encounters where alpha particles and protons are the projectiles, there is less evidence of its applicability in the present cases.[7]

In the collisions of interest, the ratio of the projectile velocity to the velocity of the K electron of the lower-Z collision partner is much less than unity, hence the electrons may readjust themselves to the presence of the added charge of the projectile, thereby forming molecular orbitals. The velocity distribution used in the BEA calculations is no longer atomic, but is a molecular distribution; hence, this theory should not be applicable in these cases. Clearly there is more fundamental justification to use the method of Perturbed Stationary States (PSS) rather than the BEA theory to calculate secondary electron yields.

The most extensive PSS calculation has been made for 100-500 eV proton + hydrogen collisions by Thorson and co-workers.[8,9] The electron production cross sections obtained in their calculations for the dominant 2pσ → continuum process are shown in Fig. 1 along with BEA calculations for the same system. Except for the results at lower bombarding energy, these is remarkable agreement in absolute magnitude between the BEA and PSS results, which suggests that despite doubts about the validity of the BEA theory, the theory nevertheless provides a fairly good estimate of electron production cross sections at least for the proton + hydrogen system at these energies.

To extend this comparison to the systems of interest, we first discuss the way in which these cross sections scale with bombarding energy, electron energy, and atomic number. The BEA theory scales in the following manner:

$$\frac{d\sigma_e}{dE_e}\left(Z_2^{*2}E_e,\ A_1 Z_2^{*2}E_1\right) = \frac{Z_1^2}{Z_2^{*6}}\frac{d\sigma_e}{dE_e}\left(E_e,E_1\right) \quad (1)$$

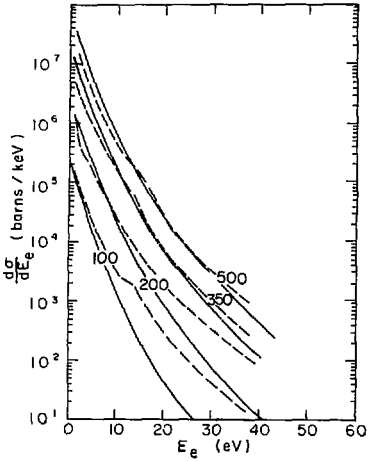

Fig. 1. Differential cross section for the production of secondary electrons in 100, 200, 350, and 500 eV proton + hydrogen collisions. Perturbed Stationary State calculation (dashed line) compared to binary encounter theory (solid line).
(XBL 757-3575)

where E_e and E_1 are the electron and projectile energies in the proton + hydrogen calculation, A_1 and Z_1 are the mass (in a.m.u.) and atomic number of the projectile, and $Z_2^{*2} = U_{K2}/0.0136$ where U_{K2} is the binding energy of the target K electron in keV.

The work of Briggs and Macek,[10] Meyerhof,[11] and Thorson[8,9] suggests that the PSS calculations may be scaled according to:

$$\frac{d\sigma_e}{dE_e}\left(Z_2^{*2}E_e,\ A_1 Z_2^{*2}E_1\right) = \frac{1}{Z_2^{*4}}\frac{d\sigma_e}{dE_e}\left(E_e,E_1\right) \quad (2)$$

which differs from the BEA scaling by an amount $(Z_1/Z_2^*)^2$. For symmetric encounters this ratio is of the order of unity (1.23 for Br, 1.15 for I). The greatest deviations occur for very low atomic numbers ($Z < 20$) and very high atomic numbers ($Z > 100$).

Using Eq. (1) and (2), the electron cross sections in Fig. 1 may be scaled up to Br + Br encounters. Then, given the yield of electrons of

energy E_e, standard bremsstrahlung formulas[12] may be used in order to calculate the secondary electron bremsstrahlung yields. We shall not describe this herein but will refer to Folkmann's paper,[5] which we have closely followed.

Bremsstrahlung cross sections for 39.6 MeV Br + Br (Scaled from 500 eV p + H) are shown in Fig. 2. The calculation was made considering only one K electron as in p + H. The agreement, like that for the electron cross section is very good and shows that the BEA theory can be used with a fair reliability for calculationg secondary electron bremsstrahlung cross sections over the range $20 < Z < 100$ and for bombarding energies $100 < E/A_1 Z_2^{*2} < 500$ eV.

For the many electron systems involved in the cases of interest we have still not shown that the BEA theory is reliable for predicting cross sections for excitation of electrons out of the L, M, and N orbitals. Calculations using the BEA theory however, show that the addition of the bremsstrahlung yield caused by electrons excited out of the L, M, and N orbitals increases the total cross section by a factor of 2 to 4 as is shown in Fig. 2. Because of the very good agreement with the K electron cross sections, it is unlikely that the L,M, and N cross sections differ from what is predicted by the BEA theory by more than a factor of two.

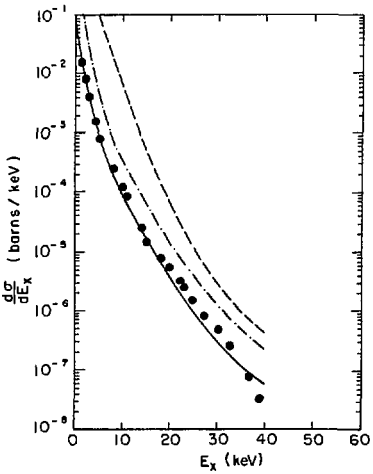

Fig. 2. Differential cross section for the production of secondary electron bremsstrahlung in 39.6 MeV Br + Br collisions. One-electron BEA calculations (solid line) compared to PSS calculations (points). Dashed line is for many-electron Br+Br. Dash-dot-dash line is for 4 K electron Br + Br. (XBL 757-3571)

In conclusion, the BEA theory provides a fairly reliable way of estimating the secondary electron bremsstrahlung yeild in symmetric heavy-ion collisions. We have calculated many electron thick target yields in a number of cases and find that it makes a negligible contribution to the total continuum yield for 30-200 MeV Br, I, Nb, and Ni collisions. For 30-MeV Br + Br_2, the bremsstrahlung yield lies two and a half to three orders of magnitude lower than the experimental yield.[1] For 60-MeV Nb + Nb, Gippner et. al.[2] report a yield of 6.2×10^{-5} photons/projectile integrated between 16 and 30 keV x-ray energy. We disagree with their suggestion that this yield could be due to secondary electron bremsstrahlung for we calculate that this contributes only 9.4×10^{-9} photons/projectile to the total yield in that region.

References

1. W. E. Meyerhof, T. K. Saylor, S. M. Lazarus, A. Little, B. B. Triplett, L. F. Chase, Jr., Phys. Rev. Letters, 30, 1279 (1973) and 32, 502 (1974).

2. P. Gippner, K. H. Kaun, H. Sodan, F. Stary, W. Schulze and Yu. P. Tretyakov, Physics Letters, 52B, 183 (1974).

3. J. S. Greenberg, C. K. Davis, P. Vincent, Phys. Rev. Lett., 33, 473 (1974).

4. K. Alder, A. Bohr, T. Huus, B. Mottleson, and A. Winther, Review Modern Physics, 28, 432 (1956).

5. F. Folkmann, C. Gaarde, T. Huus, and K. Kemp, Nuc. Inst. Methods, 116, 487 (1974).

6. F. C. Jundt, H. Kubo, and H. E. Gove, Phys. Rev. A10, 1053 (1974).

7. M. E. Rudd, J. H. Macek, Case Studies in Atomic Physics, 3, 47 (1972). The authors show that the BEA theory gives good agreement with experimental measurements of electron production cross-sections in 20-300 keV proton + He collisions.

8. W. R. Thorson, Phys. Rev. A to be published.

9. V. SethuRaman, W. R. Thorson, and C. F. Lebeda, Phys. Rev. A8, 1316 (1973).

10. J. S. Briggs, J. H. Macek, J. Phys. B6, 982 (1973).

11. W. E. Meyerhof, Phys. Rev. A10, 1005 (1974) and to be published.

12. H. W. Koch, J. W. Motz, Reviews of Modern Physics, 31, 920 (1959).

X-RAY CONTINUA IN 60 MeV Br AND 202 MeV Kr BOMBARDMENTS OF Au, Pb, AND U

R. Anholt, J. O. Rasmussen, H. Bakhru,* N. Cue,*
T. K. Saylor,† S. M. Lazarus,† and A. Little†

The discovery of molecular orbital (MO) x rays by Saris et al.,[1] Armbruster et al.,[2] and MacDonald et al.[3] suggested the possibility that binding energies and x-ray transition energies in as yet undiscovered superheavy elements could be measured by finding the endpoints in the MO x-ray spectra. To this end, we examined 10-80 keV x-ray continua in Kr and Br ion bombardments of Au, Pb, and U targets. In this region, MO L x-rays corresponding to transitions to the 2sσ, 2pσ, and 2pπ molecular orbitals are expected (see Fig. 1 for notation). In previous work the yield of MO x-rays was observed to be greatly enhanced around the matching of the K-K and L-M binding energies. We would expect a similar enhancement in the present cases since the target L shell binding energy approximately matches that of the projectile K shell.

A 60-MeV ^{79}Br beam from the Stanford tandem accelerator and a 202-MeV ^{84}Kr beam from the Berkeley SuperHILAC were used to bombard thick targets of gold, lead, and uranium. The target faced 45° to the beam and 17 cc Ge(Li) (at Stanford) and a 1 cc intrinsic Ge (at Berkeley and Stanford) viewed the front of the target through a 0.0025 cm beryllium window. Various absorbers were used to attenuate the separated atom (SA) x-rays. The beam current was measured by integrating the charge from the entire target chamber which was electrically insulated from the beam line. An electron suppressor located between the collimator and the target was used to prevent electrons from streaming into or out of the chamber.

In Fig. 2 we show the absolute yield of these continuum x-rays for 60-MeV Br + Au, Pb, and U. The 202-MeV Kr data are similar to the Br data and are not shown here. These spectra appear to be due to MO L x-rays. The x-ray energy is about right, stretching from the L x-ray transitions in the SA down to approximately the L transition energy in the united atom (UA). The endpoints are not quite right as will be discussed below. To establish that these are MO x-rays we have shown in a number of additional experiments and calculations that this yield can not be due to other processes also giving x-ray continua: 1) electron-nucleus or nucleus-nucleus bremsstrahlung, 2) Compton tails from strongly excited K x-rays and γ-rays of the target, and 3) electronic pileup.

1) Bremsstrahlung yields are shown in the figure; they have been calculated using the nucleus-nucleus dipole bremsstrahlung formula of Adler et al.[4] and the secondary electron bremsstrahlung code of Folkmann et.al.[5] The applicability of the Folkmann code was recently examined by Anholt and Rasmussen.[6] In both cases, bremsstrahlung make a negligible contribution to the continuum yield.

2) By semi-empirically estimating the response function of the detector to high energy x-rays and γ-rays, we have shown that Compton tails from the K x-rays and Coulomb excited γ-rays of the target could not account for this yield either.

3) Lastly, in one run, we used 62-, 82-, and 125-mil aluminum absorbers to attenuate the SA x-rays. When the observed counts were corrected for these differing absorbers, the same absolute

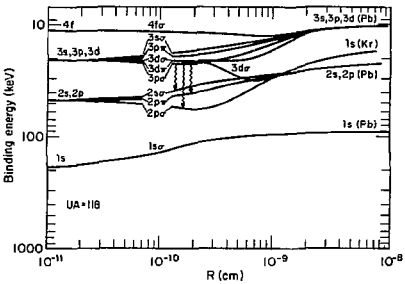

Fig. 1. Molecular Orbital correlation diagram calculated using one-electron non-relativistic wavefunctions. For these high atomic numbers, j-j coupling is more appropriate and we would denote 1sσ by $1s_{1/2}$, 2pπ by $2p_{3/2}$ etc. (XBL 7410-4565)

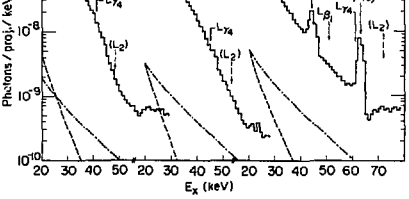

Fig. 2. Absolute yields for 60 MeV Br + Au, Pb, and U. Jagged solid line is experimental yield. Nucleus-nucleus and secondary electron bremsstrahlung yield shown as dash-dot and dashed lines respectively. Lα, Lβ, and Lγ arrows show transition energies in the united atom. (L_2) arrow explained in text. The target L x ray transitions are too intense to show on these plots and lie between 10 and 20 keV. (XBL 7410-4562)

yield was obtained to within 20%. Since the addition of more attenuation decreased the counting rate and thus the pileup of the intense L x-rays of the target by more than a factor of 1000 here, this experiment shows that pileup could not account for this continuum yield.

Lastly, we discuss the endpoints in the MO x-ray spectra. In the cases of MO K x-rays the largest possible transition energy occurs at the UA limit ($R \sim 0$) on the MO correlation diagram. In the early experiments,[7] the MO x-ray yield was observed to approach zero around the Kα and Kβ x-ray energies of the UA and this not only confirmed the assignment of this continuum being due to MO x-rays, but suggested that at least the Kβ transition energy in the UA could be found even in cases where the UA atomic number exceeds 110. Later experimental work and theoretical work by Briggs and Macek[8] showed that due to dynamical line broadening considerations, the endpoint is not expected to be very sharp and in fact may not be distinct at all in some cases. MacDonald et.al.[3] saw that the MO yield in carbon + carbon collisions overshoots the UA transition energy with no visible break around the expected endpoint. Greenberg[9] and Davis observed the same in Ni - Ni collisions.[9]

For these reasons, it is not surprising that the L MO yield in Fig. 2 overshoots the maximum UA transition energy ($L\gamma_4$ arrows in the figure). However, for these L MO x rays, there is the added complication that the transition energy at the UA is not the highest possible transition energy; there is a minimum on the 2pσ curve in Fig. 1 occuring at $R \sim 0.03$A and hence the endpoint should be at approximately the binding energy of the 2pσ orbital at that distance. In Fig. 2 that energy is shown as dotted L_2 arrows and for probably the reasons we discussed earlier, the yield overshoots these points also.

Despite these anomalies, we conclude that the spectra observed in our experiments are due to MO L x-rays. We have ruled out the possibility that bremsstrahlung, Compton tails, or electronic pileup could account for the yield of continuum x rays. The endpoints in these spectra are not well explained. Evidently, the effects that cause the continuum endpoints to lie beyond the united atom L binding energies preclude any precise measurements of electron binding energies of superheavy elements by this technique.

Footnotes and References

*Department of Physics, State University of New York, Albany, N.Y. 12222.

†Department of Physics, Stanford University, Stanford, Ca. 94305.

1. F. W. Saris, W. F. van der Weg, H. Tawara and R. Laubert, Phys. Rev. Lett. 28, 717 (1972).

2. P. H. Mokler, H. J. Stein, and P. Armbruster, Phys. Rev. Lett. 29, 827 (1972).

3. J. R. MacDonald, M. D. Brown and T. Chiao, Phys. Rev. Lett. 30, 471 (1973).

4. K. Alder, A. Bohr, T. Huus, B. Mottleson, and A. Winther, Rev. Mod. Phys. 28, 432 (1956).

5. F. Folkmann, G. Gaarde, T. Huus, and K. Kemp, Nuc. Inst. Methods to be published.

6. R. Anholt, J. O. Rasmussen, to be published and herein.

7. W. E. Meyerhof, T. K. Saylor, S. M. Lazarus, A. Little, B. B. Triplett, L. F. Chase, Jr., and R. Anholt, Phys. Rev. Lett. 32, 1279 (1974).

8. J. H. Macek and J. S. Briggs, to be published Journal of Physics B.

9. C. K. Davis and J. S. Greenberg, private communication.

RADIATIVE DECAY OF THE 2^3S_1 AND 2^3P_2 STATES OF HELIUM-LIKE VANADIUM (Z = 23) AND IRON (Z = 26)*

H. Gould, R. Marrus, and P. J. Mohr

The study of radiative decay from the 2^3S_1 and 2^3P_2 levels of the two-electron system offers an opportunity to test the theory of forbidden decay in a system where precise, unambiguous calculations of decay rates can be made. In this report, we describe some measurements designed to extend existing experimental information on the rates of these decays to the two-electron atoms V^{+21} and Fe^{+24}. We develop a theory for the 2^3P_2 rates which take into account leading order relativistic corrections and hyperfine effects. Our results on vanadium show the first evidence for the influence of the hyperfine interaction on the radiative decay of an energy level belonging to the two-electron system.

Experimental work on the 2^3S_1 levels of the two-electron system has established the single-photon nature of the decay in Ar^{+16} (Ref. 1) and ordinary helium.[2] The theory of this decay has been examined by several authors[3] and detailed calculations of the rates have been made by Drake[4] and by Johnson and Lin[5] using somewhat different starting points. Measurements of this decay rate have been made on Ar^{+16}, Ti^{+20} (Ref. 6) and Cl^{+15} (Ref. 7). The measured rates in Cl and Ar differ from theory by several times the quoted error, whereas the result in Ti is in agreement. In order to establish the Z dependence of this discrepancy we report here measurements on V^{+21} and Fe^{+24}.

Interest in the 2^3P_2 levels centers mainly on the M2 decay mode to the 1^1S_0 ground level which has a rate comparable with the E1 rate to 2^3S_1 for ions with $Z \approx 20$. The M2 decay was first observed in Ar^{+16} (Ref. 8) and rates have now been measured in S^{+14} (Ref. 9), Cl^{+15} (Ref. 10) and Ar^{+16} (Ref. 11). In this report we present evidence indicating that the decay of this level is strongly influenced by the hyperfine interaction in V^{+21} and give results for Fe^{+24}.

The lifetimes were measured by the beam-foil time-of-flight method. Our apparatus has been described previously[6] and the details are not repeated here. The vanadium (Z = 23) and iron (Z = 26) ions were obtained from the SuperHILAC at an energy of 7.2 MeV/AMU. Excitation of the beams into the metastable states was done with a 50 μgm/cm^2 carbon foil. Decay curves are taken by varying the foil-detector separation. The total number of counts under the peak is integrated and normalized to the integrated beam current collected in a Faraday cup. This quantity is plotted vs. foil-detector separation. A sample decay curve is shown in Fig. 1.

Since the 2^3P_2 and 2^3S_1 energy separations are small compared with the detector resolution, the decay curves are composites, exhibiting fast components and slow components. The slow components are ascribed to the 2^3S_1 decay and the fast components to decay from 2^3P_2. As discussed below, the slow and fast components are probably composites of two or more exponentials as the result of hyperfine effects in V^{+21} and cascading effects in Fe^{+24}.

The isotope ^{51}V has a nuclear spin I = 7/2 and magnetic moment μ = 5.15 nm.[12] The resulting hyperfine structure (HFS) influences our decay curves by admixing 2^3P_2 with 2^3P_1 and 2^1P_1. The 2^3P_2 level is split into five components with total angular momentum between F = 3/2 and F = 11/2 (Fig. 1). Because the hyperfine interaction is diagonal in F, the rates from both F = 3/2 and F = 11/2 are unaffected by hyperfine structure. However, the rates from F = 5/2, 7/2 and 9/2 will all be altered. Hence, the observed decay curve will be a composite of four exponentials weighted according to the initial populations of each of the hyperfine levels.

The most abundant stable iron isotope has zero spin and hyperfine effects are not present. Hence the decay of 2^3P_2 is exclusively by E1 decay to 2^3S_1 and M2 to 1^1S_0.

A problem arises in the interpretation of the 2^3S_1 decay due to cascading from 2^3P_0. The lifetime of 2^3P_0 is calculated to be $\tau = 2.7$ nsec which is close to that of 2^3S_1. Hence cascading effects from this level may be important. The shape of the resultant curve will depend upon the relative population

$$R \equiv \frac{N_0(2^3P_0)}{N_0(2^3S_1)}$$

of the two states and decay rates. It was found that the data could be fit to two exponentials for $0 \leq R \leq 0.8$. Varying the lifetimes of the two exponentials, we find that the "best fit" values for $\tau(2^3S_1)$ varied between 4.2 ns and 5.3 ns, where 5.3 ns results from a single exponential fit (R = 0) and, hence, is an upper limit to the 2^3S_1 lifetime. Similarly, the values for $\tau(2^3P_0)$ varied between 1.3 ns and 3.3 ns. We note that the theoretical value of $\tau(2^3P_0) = 2.7$ nsec corresponds to $\tau(2^3S_1) = 4.8$ nsec. We have chosen to take the mean value

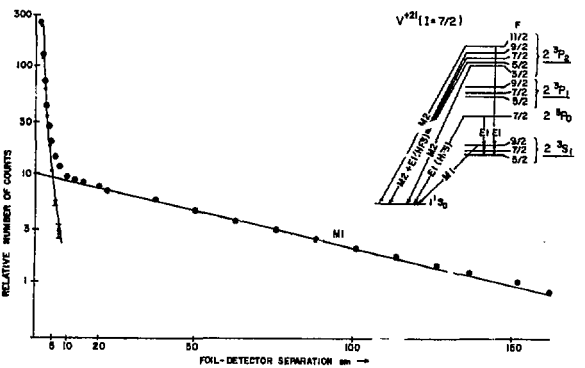

Fig. 1. Sample decay curve obtained with V^+ beam. The points beyond 22 cm are fit to a single exponential and ascribed to decay of the 2^3S_1 level. The near points are fit to a composite of four exponentials as described in the text and are ascribed to decay of the 2^3P_2 level.
(XBL 746-1022)

as the experimental value and to take cascading into account by using an increased error.

In Fig. 1, an experimental decay curve is shown for the V^{+21} beam. The decay curve is fit by identifying the data points beyond 22 cm with the 2^3S_1 decay. These yield a lifetime $\tau(2^3S_1) = 16.9(7)$ nsec. When this decay is subtracted from the experimental curve it yields the points shown. These are fit to a composite decay curve constructed by assuming that each of the F states associated with 2^3P_2 has the theoretical lifetime shown in Table I. These lifetimes include effects due to hyperfine quenching. Moreover, the initial populations of the F states are taken as proportional to $(2F+1)$. The resultant fit to the experimental points is as shown and is seen to be quite good.

To calculate accurate theoretical rates for the 2^3P_2 level, the transition matrix elements are evaluated to zeroth and first order in the quantities Z^{-1} and $(Z\alpha)^2$. The zeroth order term is the non-relativistic hydrogenic approximation. The term of order Z^{-1} is the first correction in the nonrelativistic Z-expansion of the matrix element. The leading relativistic correction, of order $(Z\alpha)^2$, is obtained by evaluating the relativistic transition operator between states formed from properly symmetrized products by hydrogenic Dirac wave functions.

For the M2 transition, the coefficient of Z^{-1} has been determined by Drake[15] from the Z-expansion of Dalgarno and Parkinson.[14] Taking his result together with the leading relativistic and finite wavelength (retardation) correction yields

$$A_{M2}(2^3P_2) = \alpha k^5 \frac{2^{15}}{5\cdot 3^{10}} (Z\alpha)^{-2}[1 + .147\, Z^{-1} - .640(Z\alpha)^2]^2 \tag{1}$$

(in units where $m_e = c = \hbar = 1$) where k is the transition energy.

Because the nonrelativistic velocity form of the matrix element for $n \to n$ E1 transitions vanishes to lowest order in Z^{-1}, the evaluation of the E1 transition rate $2^3P_2 \to 2^3S_1$ is simplified by making the dipole approximation and converting the matrix element to the length form. The error in making this approximation is negligible due to the smallness of the transition energy: $\langle \vec{k} \cdot \vec{r} \rangle = O(\alpha)$. The conversion to length form is valid relativistically and so relativistic corrections may be obtained as described above. For this transition matrix element, the coefficient of Z^{-1} has been obtained by Cohen and Dalgarno. We thus have

$$A_{E1}(2^3P_2) = \alpha k^3\, 12(Z\alpha)^{-2}[1 + .759\, Z^{-1} - .167(Z\alpha)^2]^2 \tag{2}$$

The transition probability for the E1 decay $2\ ^3P \to 2\ ^3S$, obtained as for the $2\ ^3P$ decay, is given by

$$A_{E1}(2^3P_0) = \alpha k^3\, 12(Z\alpha)^{-2}[1 + .759\, Z^{-1} - .417(Z\alpha)^2]^2 \tag{3}$$

We note that the theoretical uncertainty in the expressions for the transition rates listed above is expected to be of the order of 1% or less for Z in the range 10 - 40.

In the case of vanadium, which has a non-zero nuclear spin, the 2^3P_2 and 2^3P_0 states undergo an E1 transition to the 1^1S_0 state due to hyperfine mixing.[16] An estimate of the transition rate is obtained in the following way. Nonrelativistic intermediate coupling wave functions are taken as the unperturbed basis. The hyperfine interaction which is diagonal in $\vec{F} = \vec{J} + \vec{I}$, is treated in first-order perturbation theory. Only the effect of mixing of the 2^3P_2 and 2^3P_0 states with the nearby 2^3P_1 and 2^1P_1 states is included. The dipole transition operator has then a non-vanishing matrix element between the perturbed 2^3P_2 and 2^3P_0 states and the 1^1S_0 state which is proportional to the dipole matrix element between the LS coupled 2^1P_1 state and the 1^1S_0 state. The latter is evaluated with the aid of the Z-expansion of Dalgarno and Parkinson.[14] The hyperfine matrix elements are approximated by evaluating the contact interaction term between hydrogenic product wave functions. Energy differences are evaluated by means of the Z expansion of the nonrelativistic energies,[17] together with the Z expansion of the order α^4 corrections.[18] The transition rates thus obtained are added to the rates discussed above and the resulting values for the lifetime of the 2^3P_2 state are listed in Table I.

TABLE I. Theoretical transition rates and lifetime of the 2^3P_2 state in helium-like ions.

Z	A_{E1} (nsec^{-1})	A_{M2} (nsec^{-1})	F	A_{E1}^{HFS} (nsec^{-1})	τ (nsec)
16	.259	.117			2.66
17	.301	.194	All	<.007	≈2.01
18	.352	.312			1.51
22	.687	1.64			.429
			3/2	0	.313
			5/2	.99	.239
23	.820	2.37	7/2	1.75	.202
			9/2	1.69	.205
			11/2	0	.313
26	1.43	6.50			.126

In Fig. 2 we compare all of the measured decay rates of 2^3P_2 with the corresponding theoretical rates. Agreement is seen to be very good over a wide range of Z. For vanadium, the theoretical rate includes the contribution from hyperfine quenching. It is seen that the experimental and theoretical rates would be in serious disagreement without contributions from this mechanism. We take this as very strong evidence that hyperfine quenching is indeed present.

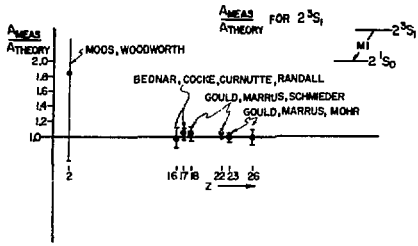

Fig. 2. Comparison between measured and calculated decay rates for the 2^3S_1 level. (XBL 742-295)

In Fig. 3 we compare the measured 2^3S_1 decay rates with the calculated rates. Agreement between theory and experiment is satisfactory for Z = 22, 23, 26, but puzzling discrepancies exist at Z = 17 and 18.

We are indebted to Al Ghiorso and the staff of the SuperHILAC for their enthusiastic support of this work. The development of the vanadium and iron beams was a vital product of this support. Doug MacDonald gave valuable engineering support. One of us (P.J.M.) gratefully acknowledges helpful conversations with Professors Charles Schwartz and Eyvind H. Wichmann.

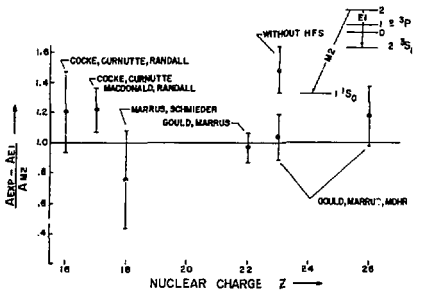

Fig. 3. Comparison between measured and calculated M2 rates for decay from the 2^3P_2 level. The point at Z = 23 labeled "without HFS" is obtained by making a best fit to our vanadium data using a single exponential. (XBL 746-1021)

Footnotes and References

*Submitted to Phys. Rev. Letters (LBL preprint LBL-2906).

1. R. Marrus and R. W. Schmieder, Phys. Lett., 32A, 431 (1970).

2. H. W. Moos and J. R. Woodworth, Phys. Rev. Lett. 30, 775 (1973).

3. G. Feinberg and J. Sucher, Phys. Rev. Lett. 26, 681 (1971); H. R. Griem, Astrophys. J. 156, 1103 (1969); I. L. Beigman and V. I. Safronova, Zh. Eksp. Teor. Phys. 60, 2045 (1971) [Sov. Phys. JETP 33, 1102 (1971)]; S. Feneuille and E. Koenig, Comptes Renues Acad. Sc. Paris 274, 46 (1972); G. W. F. Drake, Phys. Rev. A 5, 1979 (1972).

4. G. W. F. Drake, Phys. Rev. A3, 908 (1971).

5. W. R. Johnson and C. Lin, Phys. Rev. A 9, 1486 (1974).

6. H. Gould, R. Marrus and R. W. Schmieder, Phys. Rev. Lett. 31, 504 (1973).

7. C. L. Cocke, B. Curnutte and R. Randall, Phys. Rev. Lett. 31, 508 (1973).

8. R. Marrus and R. W. Schmieder, Phys. Rev. Lett. 25, 1689 (1970).

9. C. L. Cocke, B. Curnutte and R. Randall, Phys. Rev. A 9, 1823 (1974).

10. C. L. Cocke, B. Curnutte, J. R. MacDonald and R. Randall, Phys. Rev. A 9, 57 (1974).

11. R. Marrus and R. W. Schmieder, Phys. Rev. A 5, 1160 (1972).

12. W. F. Ramsey, Molecular Beams, Oxford University Press, p. 173 (1963).

13. G. W. F. Drake, Astrophys. J. 158, 1199 (1969).

14. A. Dalgarno and E. M. Parkinson, Proc. Roy. Soc. A 301, 253 (1967).

15. M. Cohen and A. Dalgarno, Proc. Roy. Soc. A 293, 359 (1966).

16. A discussion of the history and calculations of this effect is given in R. H. Garstang, J. Opt. Soc. Am. 52, 845 (1962).

17. R. E. Knight and C. W. Sherr, Rev. Mod. Phys. 35, 431 (1963).

18. H. T. Doyle, Adv. At. Mol. Phys. 5, 337 (1969).

COHERENT ORIENTATION AND ALIGNMENT OF ION LEVELS BY A BEAM-TILTED-FOIL COLLISION

D. A. Church, W. Kolbe, and M. C. Michel

Based on symmetry considerations, novel coherence effects were recently predicted[1] and observed[2] when ions are charge-changed and excited by passage through a thin, tilted foil. To investigate these predictions, we used a "quantum-beat" technique, which preserves such coherence, to study the light emitted from the levels of fast, excited He atoms and ions.[3]

A beam of He ions, accelerated to tens of keV energy and e/m analyzed by means of the Cascade Isotope Separator, was passed through thin (≈ 6 μg/cm²) carbon foils tilted at an angle β with respect to the beam direction (see Fig. 1). The ions were neutralized by the collision, which left many atoms in excited levels. Light emitted downstream was collected from a narrow spatial region parallel to the foil surface. A uniform magnetic field was applied either parallel or perpendicular to the beam direction. Any moments present in the excited states precess in the field, producing intensity variations in the emitted light at multiples of the Larmor frequency ω. Intensity variations at 2ω are observed in linearly polarized light when the foil surface is perpendicular to the beam direction, arising from partial excited state alignment. With a tilted foil, we observed quantum beats at ω in both circularly and linearly polarized light, indicative of the predicted excited level orientation, and of new alignment components.[3] These effects appear in ion and atom levels with $L > 0$. The observations in linearly polarized light were not initially in agreement with the theoretical predictions,[1] but after publishing our results we have learned that the published equations were in error.[4] The corrected equations are in agreement with our measurements (see Fig. 2), and with them we can analyze our data to obtain a complete description of the moments of the excited level.[5]

To understand the interaction responsible for the orientation, we have investigated the dependence of the magnitude of the new coherence effects on the foil tilt angle, the incident ion velocity, and the foil surface material. We find that the orientation is reduced by 30% when a thin layer of gold is applied to the final carbon foil surface, but little change is produced by aluminum.[3] A definite energy dependence of the orientation is observed in the energy range 15 - 80 keV.[6] The orientation magnitude is proportional to $\sin^2\beta$, where β is the foil tilt angle, while specific alignment components vary as $\sin\beta$ or $\sin^2\beta$.

The interaction is almost certainly electrostatic in nature. We have proposed[3] either a moment precession due to electric field gradients,[7] or to static electric fields, as a source of the orientation. The latter effect has been proposed independently,[8] but recent measurement results are not in agreement with the predictions. When better understood, the experimental observations may serve as a novel and useful probe of certain surface effects in amorphous or crystalline materials.

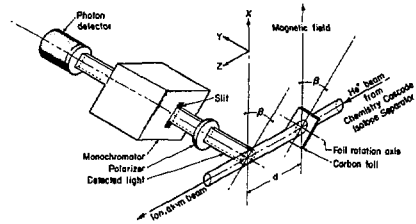

Fig. 1. Apparatus configuration used in tilted-foil quantum-beat measurements. A circular polarizer and a linear polarizer with axis at various angles ψ with respect to the beam direction are used to analyze the light emitted by the beam particles. (XBL 746-3488)

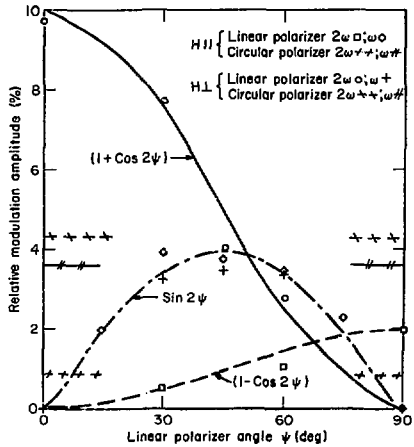

Fig. 2. Theoretical curves and experimental points measured from quantum beats at various frequencies. ψ is measured relative to the beam direction. The angle-independent circular polarization data are shown by broken horizontal lines. (XBL 751-2020)

Another use of these coherence effects is in the study of fine- and hyperfine-structure of atom and ion levels by level-crossing and rf resonance methods. We have studied the hyperfine interaction

in the $4d^1D_2$ (F = 3/2, 5/2) state of ^3He by applying magnetic fields sufficiently large to partially decouple the nuclear and electronic moments. We observe a change in the magnitude of the hyperfine g-values as a function of relative time after excitation, when quantum beats are observed as a function of magnetic field strength.[9] Level-crossing measurements in more complex states should be generally applicable, and should provide more precise results than those of other techniques.

References

1. U. Fano and J. H. Macek, Rev. Mod. Phys. 45, 553 (1973).

2. H. G. Berry, L. J. Curtis, D. G. Ellis, and R. M. Schectman, Phys. Rev. Lett. 32, 751 (1974).

3. D. A. Church, W. Kolbe, M. C. Michel, and T. Hadeishi, Phys. Rev. Lett. 33, 565 (1974).

4. J. H. Macek (private communication).

5. D. A. Church, M. C. Michel, and W. Kolbe, Phys. Rev. Letters 34, 1140 (1975).

6. D. A. Church, M. C. Michel, W. Kolbe, and T. Hadeishi, Bull. Am. Phys. Soc. II 20, 74 (1975).

7. U. Fano, Phys. Rev. 133, B828 (1964).

8. T. G. Eck, Phys. Rev. Lett. 33, 1055 (1974).

9. D. A. Church, W. Kolbe, M. C. Michel, and T. Hadeishi, Bull. Am. Phys. Soc. II 19, 1761 (1974).

THE INFRARED EMISSION SPECTRA OF CURIUM, BERKELIUM AND CALIFORNIUM

J. G. Conway

The emission spectra of curium, berkelium and californium have been run on the high resolution Fourier transformance spectrometer at Laboratoire Amié Cotton in Orsay France. The elements were run as the iodide sealed in a quartz tube to form an electrodeless lamp. The lamps were 25 mm long and 6 mm inside diameter and operated in a cavity at 2450 M Hz with approximately 80 watts of input power.

For curium the isotope was 244 with about 3% 246. The spectrum was recorded between 3700-11800 cm^{-1} and the run took 12 hours and 800,000 data points were recorded. Figure 1 is a tracing of the curium line at 9482.390 cm^{-1} showing reversal of the strong line on the left and isotope shift, the weak line on the right. A total of 1743 lines have been ascribed to curium and 87% of the lines have been assigned to transitions between known energy levels. At one point in the analysis a check was made between observed and calculated energies. The root-mean square deviation was 1.8×10^{-3} cm^{-1}. However, from a check of impurities common to several runs we found a difference of over 5×10^{-3} cm^{-1}. A complete report will appear as LBL-3401.

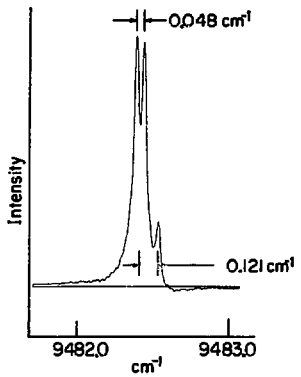

Fig. 1. Curium line at 9482.390 cm^{-1}.

The berkelium and californium were run with extra coverage in the higher wave number range. There are a great number of lines exhibiting hyperfine structure and many are fully resolved. Only two californium lines were fully resolved into 10 components. These two spectra, Bk and Cf, must be worked on together since the Bk decays into Cf and there are a number of Cf lines observed in the Bk spectrum. Also, the Cf was not sufficiently pure so we see Bk lines in the Cf spectrum.

An interesting feature of both the Cm and Cf spectra is that each contains a forbidden line which is a transition within the same multiplet of the same configuration. In Cm the line at 3922.316 cm^{-1} is a transition between the level at 1214.200 a $^7F_6$ and 5136.522 a $^7F_5$ both belonging to $5f^8\ 7s^2$ configuration. In Cf a similar transition occurs between $^5I_8$ and $^5I_7$ of the $5f^{10}\ 7s^2$ configuration at 9078.149 cm^{-1}.

HIGH IONIZATION SPECTRA EXPERIMENTS

G. V. Shalimoff and S. P. Davis*

We have investigated source conditions necessary to produce highly ionized spectra of some metallic elements.[1,2] A sliding-spark source capable of producing V V, Mn VI, and Th IV yields rich spectra in the vacuum ultraviolet region, that is, below 2000 Å. However, the normal incidence vacuum spectrograph at LBL is only able to photograph spectra down to around 500 Å, thereby cutting off much of the wavelength region of interest. Although lines of lower wavelength can be observed in higher orders with this instrument, they are frequently intermingled with other lines and are difficult to isolate and identify. Ideally a grazing incidence vacuum spectrograph capable of photographing the wavelength region below 500 Å is required.

The National Bureau of Standards kindly permitted us to use their 10-meter grazing incidence spectrograph to take spectrograms in the region of 200 to 600 Å. We also used their 10-meter normal incidence vacuum spectrograph for the 540 to 2100 Å region which corresponds to the useful region of the LBL instrument but with a three times gain in dispersion. With the vacuum sliding-spark source we photographed the spectra of V, Mn, Th, and U. Reference spectrum of Y IV and V also from a sliding-spark source was used in the grazing incidence region and Cu II from a copper hollow cathode was used for the normal incidence region.

The spectrum of V V obtained at 1225 A peak current allows better measurement of the low wavelength lines reported by Van Deurzen[1] and subsequent better energy level assignment.

The sliding-spark source at the NBS produced a greater peak current (2500 A) in the excitation of Mn than we have been able to produce at LBL. Consequently we were able to obtain Mn VI readily although isolation is still difficult. Even some predicted lines of Mn VIII were observed.

The Th and U plates of the grazing incidence region continue to show many lines which complicates the identification of the ionization states.

We are grateful for the hospitality and assistance given us by the members of the Spectroscopy Section of NBS, especially V. Kaufmann and J. Reader.

Footnotes and References

*Physics Department, University of California, Berkeley.

1. C. H. H. Van Deurzen, J. G. Conway, and S. P. Davis, J. Opt. Soc. Am. 64, 498 (1974).

2. See following article by W. H. King, S. P. Davis, and G. V. Shalimoff in this annual report.

SPECTRUM OF QUINTUPLY IONIZED MANGANESE (Mn VI)*

W. H. King,† S. P. Davis,‡ and G. V. Shalimoff

The spectrum of Mn VI from 800 to 1600 Å has been observed in a vacuum sliding-spark source. Although this work started out as an attempt to obtain the spectrum of Mn VII, in the isoelectronic sequence with Sc III and V V as reported by Van Deurzen,[1,2] and Cr VI as reported by Ekberg,[3] it was not possible to excite and isolate Mn VII with our source conditions. Only Mn III, IV, V and VI were easily isolated by observing their common intensity behavior with variations in current and source parameters.

Some 50 lines ascribed to Mn VI were observed on spectra photographed with the LBL 3-meter normal incidence vacuum spectrograph having a plate factor of 2.78 Å/mm. By taking many exposures with variations in the inductance and capacitance of the spark circuit and by studying the variations of line intensities of known lower states of ionization and unknown lines, it was possible to isolate and designate lines belonging to Mn VI.

Supplementary lines were obtained on spectrograms taken at the National Bureau of Standards with the 10-meter normal incidence vacuum spectrograph having a plate factor of 0.78 Å/mm. The sliding-spark source at the NBS was operated at higher current than was possible at LBL. Though many of the spectrograms show broad lines, the wavelengths from plates made at the two sites agree well.

The sliding-spark circuit used was described by Van Deurzen and Conway.[4] For the Mn VI spectrum, a peak current of 1600 A was obtained at LBL using 34 μF capacitance and no added inductance in the circuit. At the NBS a peak current of 2500 A was achieved using 64 μF capacitance and no added inductance. The circuit is critically damped. The manganese electrodes were 1/4-inch diameter rods of hot pressed powder and withstood the spark discharge quite well.

In the sliding-spark source the electrodes are separated with spacers made of silica and boron nitride. The elements of the spacer material are also excited during the spark discharge and provide useful internal wavelength standards for wavelength

measurements. The B, N, O, Si, and C lines were particularly useful below 1000 Å.

The spectra were photographed on Kodak short-wave radiation (SWR) plates. In addition to the internal wavelength standards, reference spectra of Cu II from a copper hollow cathode source were photographed with the manganese spectra. The spectral lines were measured on a Grant comparator and computed with a sixth degree polynomial. For most lines the error limits in the manganese wavelengths are estimated to be 0.007 Å with a fraction of them having twice this error.

Intensities were estimated visually from the plates on a scale of 1 - 1000.

The level analysis of Mn VI was begun by Cady[5] in 1933 who established the ground configuration of $3d^2$ and some levels of 3d4p. The level values that we developed are given in Table 1.

TABLE 1.

Even Levels		Odd Levels	
Symbol	Energy (cm^{-1})	Symbol	Energy (cm^{-1})
$3d4s\,^3D_1$	250097.5	$3d4p\,^1D_2$	319819
$^3D_2$	250527.8		
$^3D_3$	251402.8	$^3D_1$	321694.7
		$^3D_2$	322409.9
$^1D_2$	255238.8	$^3D_3$	323282.5
$3d4d\,^3G_3$	432093	$^3F_2$	323798.0
$^3G_4$	432654	$^3F_3$	324850.1
$^3G_5$	433464	$^3F_4$	326372.6
		$^3P_0$	329730.7
		$^3P_1$	329635.6
		$^3P_2$	329992.0
		$^1F_3$	333052
		$^1P_1$	336129

Table 2 lists the 26 classified lines of Mn VI which we were able to assign from our line list at present. Additional lines fit into the level scheme but they have not yet been checked in detail to verify their assignment.

The main difficulty in the work thus far has been the positive identification of the Mn VI lines in the midst of lines of other states. Only after intensive examination of line intensity behavior can lines be added to the list and attempts made to fit them into a level scheme.

TABLE 2.

Level Combination		Wavenumber	Wavelength	
Odd	Even	(cm^{-1})	(Å)	Intensity
$3s4p\,^3F_2$ -	$3d4d\,^3G_3$	108295.4	923.400	55
$^3F_3$ -	$^3G_4$	107803.5	927.614	60
$^3F_3$ -	$^3G_3$	107241.4	932.476	5
$^3F_4$ -	$^3G_5$	107091.0	933.785	90
$^3F_4$ -	$^3G_4$	106278.5	940.924	50
$^3F_4$ -	$^3G_3$	105721.8	945.879	10
$^1P_1$ -	$3d4s\,^1D_2$	80891.1	1236.230	230
$^3P_0$ -	$^3D_1$	79632.7	1255.766	90
$^3P_1$ -	$^3D_1$	79537.6	1257.267	
$^3P_2$ -	$^3D_2$	79465.2	1258.413	100
$^3P_1$ -	$^3D_2$	79107.6	1264.101	200
$^3P_2$ -	$^3D_3$	78588.9	1272.444	500
$^1F_3$ -	$^1D_2$	77814.8	1285.102	700
$^3F_4$ -	$^3D_3$	74969.6	1333.874	1000
$^3F_3$ -	$^3D_2$	74322.1	1345.494	800
$^3F_2$ -	$^3D_1$	73700.0	1356.852	600
$^3F_2$ -	$^3D_2$	73269.2	1364.829	150
$^3D_2$ -	$^3D_1$	72312.6	1382.885	
$^3D_2$ -	$^3D_2$	71881.8	1391.173	500
$^3D_3$ -	$^3D_3$	71879.5	1391.218	750
$^3D_1$ -	$^3D_1$	71596.9	1396.708	180
$^3D_1$ -	$^3D_2$	71166.5	1405.156	55
$^3D_2$ -	$^3D_3$	71007.0	1408.312	120
$^3F_2$ -	$^1D_2$	68556.1	1458.660	30
$^3D_2$ -	$^1D_2$	67170.2	1488.755	25
$^1D_2$ -	$^1D_2$	64581.5	1548.430	1000

Footnotes and References

*Reported at the Optical Society of America meeting at Houston, Texas, October 1974.

†School of Physics, University of Newcastle upon Tyne, England.

‡Physics Department, University of California, Berkeley.

1. C. H. H. Van Deurzen, J. G. Conway, and S. P. Davis, J. Opt. Soc. Am. 63, 158 (1973).

2. C. H. H. Van Deurzen, J. G. Conway, and S. P. Davis, J. Opt. Soc. Am. 64, 498 (1974).

3. J. O. Ekberg, Physica Scripta 8, 35 (1973).

4. C. H. H. Van Deurzen and J. G. Conway, Appl. Spectrosc. 28, 223 (1974).

5. W. M. Cady, Phys. Rev. 43, 322 (1933).

SOME PROPERTIES OF H_2CN^+: A POTENTIALLY IMPORTANT INTERSTELLAR SPECIES*

P. K. Pearson† and H. F. Schaefer III

Ab initio quantum-mechanical electronic-structure calculations have been performed on the molecular ion H_2CN^+. Geometries have been predicted for both the acetylene-like ($C_{\infty v}$) and formaldehyde-like (C_{2v}) isomers. The linear structure H-C-N-H$^+$ is predicted to lie lower by 3.0 eV. Thus the properties of the H_2CN^+ ion are expected to be rather similar to those of acetylene. For the vibrational frequencies, this similarity is demonstrated theoretically as is seen in Table 1.

The implications of these results for interstellar chemistry are discussed, including the intriguing possibility that H_2CN^+ may be the precursor of the tentatively identified (90.665 GHz) HNC model. The surprisingly high observed DCN/HCN ratio is also discussed in terms of the interstellar D/H ratio (see Table 2). The $J = 0 \rightarrow J = 1$ rotational transition is predicted to occur at 74.8 GHz, with an expected reliability of 1.1 GHz.

TABLE 1. Theoretical vibrational frequencies (in cm^{-1}) of HC≡CH, DC≡CH, H_2CN^+, and $HDCN^+$.

Parameter	HCCH	DCCH	$HCNH^+$	$CDNH^+$
ν_1	3675(3374)	3641(3336)	4300	4232
ν_2	2139(1974)	1996(1854)	2354	2082
ν_3	3600(3289)	2806(2584)	3507	2902
ν_4	847(612)	865(683)	1023	962
ν_5	889(730)	683(519)	922	774
Zero-point energy ...	6443(5661)	5769(5089)	7025	6344
Difference.....	673(572)		681	

TABLE 2. Dependence of predicted interstellar D/H ratio on temperature and ΔE for the reaction $H_2CN^+ + HD \rightarrow HDCN^+ + H_2$

	T(°K)			
ΔE(cm^{-1})	40	60	80	100
263	4.7×10^{-7}	1.1×10^{-5}	5.3×10^{-5}	1.4×10^{-4}
283	2.3×10^{-7}	6.8×10^{-6}	3.7×10^{-5}	1.0×10^{-4}
303	1.1×10^{-7}	4.2×10^{-6}	2.6×10^{-5}	7.7×10^{-5}

Footnotes

*Published in The Astrophysical Journal 192, 33 (1974).

†Present address: Centre European de Calcul Atomique et Moleculaire, Batiment 506, Faculte de Sciences, 91-Orsay, France.

POTENTIAL ENERGY SURFACE FOR THE MODEL UNIMOLECULAR REACTION HNC → HCN*

P. K. Pearson† and H. F. Schaefer III

Ab initio electronic structure theory has been used to determine the more important features of the potential energy surface for the simple isomerization reaction HNC → HCN. A qualitative view of the surface is seen in Fig. 1. Extended basis sets were used in conjunction with both self-consistent-field (SCF) and configuration interaction (CI) wave functions. For nonlinear or C_s geometrical arrangements of the three atoms, the CI included 11,735 configurations, i.e., all single and double excitations. This large scale CI reproduces the HCN ground state geometry quite accurately and has been used to tentatively identify HNC in the interstellar medium. The SCF calculations predict HNC to lie 9.5 kcal/mole above HCN, while CI yields 14.6 kcal/mole. Similarly, barrier heights of 40.2 and 34.9 kcal/mole are predicted by SCF and CI.

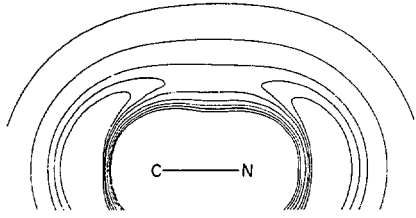

Fig. 1. (XBL 7310-4158)

Thus the SCF approximation is qualitatively reasonable for HNC→HCN. If HNC is designated by a reaction angle of 180° and HCN by 0°, then the saddle point or transition state is predicted to lie at 73.7°, significantly closer to HCN. A reaction path is determined from the SCF potential surface. The surface will be used in RRKM and classical trajectory studies of the dynamics of this reaction.

Footnotes

*Published in J. Chem. Phys. 62, 350 (1975).

†Present address: Centre Europeen de Calcul Atomique et Moleculaire, Batiment 506, Faculte des Sciences, 91-Orsay, France.

POTENTIAL ENERGY SURFACES FOR H + Li_2 → LiH + Li GROUND STATE SURFACE FROM LARGE SCALE CONFIGURATION INTERACTION*

P. Siegbahn and H. F. Schaefer III

Lee, Gordon and Herschbach[1] have reported crossed molecular beam studies of the reactions of H and D atoms with K_2, Rb_2, and Cs_2. From their results a number of important qualitative conclusions were drawn. For example, only a small fraction of the available energy appeared in product translation. Thus it seems likely that either the alkali hydride product MH is vibrationally and/or rotationally excited or the alkali atom M must be electronically excited. In addition, Lee, Gordon, and Herschbach[1] concluded that there is an anisotropic reaction probability for H+M, with $M\text{—}H$ configurations more likely to lead to reaction.

The hydrogen atom plus alkali dimer reactions are of interest to theoreticians first because of the opportunity for fruitful interaction with experiment and second because these systems are among the simplest for which the dynamics frequently must be described in terms of more than a single potential energy surface.[2,3] For the simplest such reaction at thermal energies only a single channel is energetically open:[4]

$$H + Li_2 \rightarrow LiH(^1\Sigma^+) + Li(^2S) \qquad (1)$$

$$\Delta H = -30 \text{ kcal/mole}$$

However, under the conditions utilized by Lee et al, namely 10 kcal/mole of H or D atom translational energy and 6 3 kcal/mole of alkali dimer vibrational excitation, a second pathway is possible:[5]

$$H + Li_2 \rightarrow LiH(^1\Sigma^+) + Li(^2P) \qquad (2)$$

$$\Delta H = +12 \text{ kcal/mole}$$

From either an experimental or theoretical viewpoint then, it will be of great interest to determine the relative importance of these two competing reaction pathways. Herschbach's work, though not definitive, suggested the former path (1) to be the dominant one.

The potential beauty of a theoretical treatment of this reaction lies in the opportunity to study the product energy distribution as a function of initial conditions. While the molecular beam experimentalist will do splendidly to study this reaction under one particular set of circumstances, we are free to study it under whichever circumstances appear most interesting. For example, the ratio of LiH+Li to LiH+Li* can be studied as a function of H atom translational energy or as a function of Li_2 vibrational energy. Even if the LiH+Li* pathway is shown to be unimportant, the partitioning[6] of the available energy into translation, vibration, and rotation of LiH+Li should be interesting.

Ab initio electronic structure calculations have been performed to determine the HLi_2 potential energy surface. A contracted Gaussian basis set was employed: H(5s 1p/3s 1p), Li(8s 3p/4s 3p). In addition to self-consistent-field (SCF) wave functions, full configuration interaction (CI) was carried out for the three valence electrons. For general geometry (point group C_s) the CI included 5,175 configurations. For the diatomic molecules Li_2 and LiH, these methods yield dissociation energies within 5 kcal/mole of experiment, and accurate spectroscopic constants are also predicted. The minimum on the HLi_2 CI potential surface occurs for an isosceles triangle structure with r(H-Li) = 1.72 Å and an LiHLi bond angle of 95°. This minimum lies 22.4 kcal/mole below the separated products LiH+Li. The linear HLiLi minimum is much shallower, lying only 4.2 kcal/mole below the products. The much simpler single configuration SCF calculations yield qualitatively similar results (see Figs. 1 and 2). Furthermore, these features of the surface are quite analogous to those predicted for F + Li_2 by Pearson and coworkers. The angular dependence of the surface between the C_{2v} and $C_{\infty v}$ extremes is discussed. The "electron jump" from covalent HLi_2 to ionic $H^-Li_2^+$ is seen to be much more gradual than was the case for FLi_2. The electronic structure is described using a natural orbital analysis of the most important configurations in the wave function.

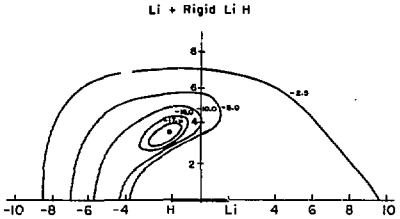

Fig. 1. Contour map of one part [r(Li-Li) fixed at 5.27 bohrs] of the SCF potential surface for HLi_2. Distances from the Li_2 bond midpoint are given in bohrs. The contours are labeled in kcal/mole relative to separated $H+Li_2$. (XBL 7410-4436)

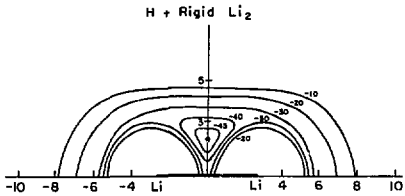

Fig. 2. Contour map for the part of HLi_2 potential surface with r(LiH) held fixed at 3.04 bohrs. Distances relative to the midpoint of the LiH bond are given in bohrs. Contours are labeled in kcal/mole relative to separated LiH+Li. (XBL 7410-4437)

Footnotes and References

*Published in J. Chem. Phys. 62, 3488 (1975).

1. Y. T. Lee, R. J. Gordon, and D. R. Herschbach, J. Chem. Phys. 54, 2410 (1971).

2. R. K. Preston and J. C. Tully, J. Chem. Phys. 54, 4297 (1971); J. Chem. Phys. 55, 562 (1971).

3. C. W. Bauschlicher, S. V. O'Neil, R. K. Preston, H. F. Schaefer, and C. F. Bender, J. Chem. Phys. 59, 1286 (1973).

4. We take the dissociation energies $D_0(^7Li_2)$ = 25.8 ± 0.7 kcal/mole and $D_0(^7Li^1H)$ = 56.0 kcal/mole from A. G. Gaydon, Dissociation Energies and Spectra of Diatomic Molecules (Chapman & Hall, London, 1968). The zero point energies of 0.5 kcal/mole (Li_2) and 2.0 kcal/mole (LiH) may be found in B. Rosen, Spectroscopic Data Relative to Diatomic Molecules (Pergamon Press, Oxford, 1970). Thus the exothermicity based on D_0's is 30.2 ± 0.7 kcal/mole, while the classical exothermicity (obtained from the D_e values) is 31.7 ± 0.7 kcal/mole.

5. The $^2S-{}^2P$ excitation energy for the Li atom is 42.6 kcal/mole. See C. E. Moore, "Atomic Energy Levels", Nat. Bur. Std. (U.S.) Cir. No. 467 (1949).

6. R. D. Levine and R. B. Bernstein, Disc. Faraday Soc. 55, 100 (1973).

SADDLE POINT GEOMETRY AND BARRIER HEIGHT FOR H + F_2 → HF + F*

C. F. Bender,† C. W. Bauschlicher, Jr., and H. F. Schaefer III

This communication concludes a series of theoretical papers[1-4] concerning the potential surfaces for the laser-related family of reactions

$$F + H_2 \rightarrow FH + H$$
$$H + F_2 \rightarrow HF + F$$
$$F + HF \rightarrow FH + F$$

For each of these three reactions, *ab initio* calculations have now been completed at four levels:

a) Single configuration self-consistent-field (SCF)[5] employing a double zeta (DZ) basis set. The basis set used is designated[6,7] F(9s 5p)/(4s 2p), H(4s/2s).

b) SCF employing a double zeta plus polarization (DZ + P) basis set. Here a set of d functions on the F atoms and a set of p functions on the H atoms are added.

c) First-order configuration interaction (CI) wave functions[8] employing a DZ basis set.

d) First-order CI wave functions employing a DZ + P basis set.

The purpose of this research has been twofold: 1) to ascertain features of the surfaces not obtainable from experiment (e.g., saddle point geometries[1-4] and the barrier height[4] for F + HF → FH + F and, 2) to begin to gain an understanding of the effects of basis set and electron correlation in the theoretical description of reactive potential energy surfaces.

In a previous paper[3] the results of methods a) and c) were reported for the H + F_2 reaction. Those calculations indicated that the minimum energy path occurs for a linear H-F-F arrangement. Here we present the results of methods b) and d) for the linear H + F_2 surface. Since the present calculations, which employ the larter DZ + P basis set, are completely analogous to those reported recently[4] for F + HF, very little need be said about the methods used. Let it suffice to note that the orbitals of our 670 configuration first-order wave

TABLE 1. Comparison of theoretical methods for the $H + F_2 \rightarrow HF + F$ reaction. Bond distances are given in Å and energies in kcal/mole.

		Saddle Point Geometry			
Basis set	Wave function	r(HF)	r(FF)	Barrier height	Exothermicity
Double zeta	Self-Consistent-Field	1.56	1.49	12.2	132.4
Double zeta	First-Order CI	2.05	1.57	1.0	88.3
Double zeta plus polarization	Self-Consistent Field	1.61	1.41	13.9	130.1
Double zeta plus polarization	First-Order CI	1.68	1.50	4.1	99.0
Experiment		--	--	2.4 0.2[a]	102.5 2.8[b]

[a] Experimental activation energy. R. G. Albright, A. F. Dodonov, G. K. Lavrovskaya, I. I. Morosov, and V. L. Tal'rose, J. Chem. Phys. 50, 3632 (1969).

[b] We consider the exothermicity to be $[D_e(F_2) - D_e(HF)]$. For F_2, D_e is 38.8 ± 2.3 kcal/mole; see J. J. DeCorpo, R. P. Steiger, J. L. Franklin, and J. L. Margrave, J. Chem. Phys. 53, 936 (1970). For HF, D_e is 141.3 ± 0.5 kcal; see W. A. Chupka and J. Berkowitz, J. Chem. Phys. 54, 5126 (1971).

functions were optimized via the iterative natural orbital method.[9]

Table 1 summarizes the results for $H + F_2$ and compares them with the earlier work[3] using a double zeta basis set. The most discouraging aspect of the calculations is the barrier height, 4.1 kcal/mole, which differs by nearly 2 kcal/mole from the experimental activation energy. In fact, the DZ CI calculation yielded a barrier closer to experiment. Hence we must conclude that our result[2] for $F + H_2$ (predicted barrier 1.66 kcal/mole; experimental activation energy 1.7 kcal/mole) was somewhat fortuitous and that our most reliable method [method d) above] yields barrier heights which are subject to errors as large as 2 kcal/mole. Note, however, that an error of this magnitude does not affect our conclusions for the F + HF system,[4] where the experimental situation is uncertain and an uncertainty of 6 kcal/mole would not affect the essential prediction.

The exothermicity obtained in our DZ + P CI calculation is in distinctly better agreement with experiment than the other calculations. In fact the value of 99.0 nearly falls in the experimental range 99.7 - 105.3 kcal/mole.

Another significant improvement over surface b) is in the predicted bond distances of F_2 and HF. Surface b), the DZ CI, predicted r(F - F) = 1.537 Å, r(H - F) = 0.947 Å, as opposed to experiment r(F - F) = 1.417 Å, r(H - F) = 0.917 Å. Surface d) yields much more accurate bond distances, r(F - F) = 1.441 Å, r(H - F) = 0.925 Å. Hence we expect the saddle point geometry predicted by surface d) to be fairly reliable. Comparison with the semiempirical LEPS surface of Wilkens[10] shows the F-F saddle point separations to agree well, but our HF separation is 0.43 Å shorter.

One of the most obvious features of Table 1 is the unrealistically high barrier predicted at the SCF level of theory. This same characteristic was observed[1-3] to an even greater degree for $F + H_2$ and F + HF. We are led to the conclusion that explicit consideration of electron correlation is required for realistic barrier height predictions on repulsive[11] potential surfaces.

Finally, several points on the minimum energy path, in the vicinity of the saddle point, are shown in Table 2. Starting from the saddle point, the minimum energy path was found by following the gradient of the energy in the direction of most negative curvature. From Table 2 it is apparent that the saddle point occurs quite near the reactants, in keeping with Hammond's postulate.[12]

TABLE 2. A few points on the minimum energy path for $H+F_2 \rightarrow HF+F$. Bond distances are given in bohrs and energies in kcal/mole relative to separated $H+F_2$.

R(HF)	R(FF)	Energy	
100	2.724	0.00	Reactants
3.55	2.77	2.93	Saddle point
3.45	2.78	3.30	
3.35	2.79	3.67	
3.175	2.842	4.11	
3.10	2.90	3.82	
3.00	2.96	2.19	
2.90	2.97	0.01	
2.75	3.00	-4.79	
1.747	100	-99.04	Products

Footnotes and References

*Published in J. Chem. Phys. 60, 3707 (1974).

†Lawrence Livermore Laboratory, University of California, Livermore, CA 94550.

1. C. F. Bender, P. K. Pearson, S. V. O'Neil, and H. F. Schaefer, J. Chem. Phys. 56, 4626 (1972).

2. C. F. Bender, S. V. O'Neil, P. K. Pearson, and H. F. Schaefer, Science 176, 1412 (1972).

3. S. V. O'Neil, P. K. Pearson, H. F. Schaefer, and C. F. Bender, J. Chem. Phys. 58, 1126 (1973).

4. S. V. O'Neil, H. F. Schaefer, and C. F. Bender, Proc. Natl. Acad. Sci. (USA) 71, 000 (1974).

5. C. C. J. Roothaem, Rev. Mod. Phys. 32, 179 (1960).

6. S. Huzinaga, J. Chem. Phys. 43, 1293 (1965).

7. T. H. Dunning, J. Chem. Phys. 53, 2823 (1970).

8. H. F. Schaefer, The Electronic Structure of Atoms and Molecules: A Survey of Rigorous Quantum Mechanical Results (Addison-Wesley, Reading, Massachusetts, 1972).

9. C. F. Bender and E. R. Davidson, J. Phys. Chem. 70. 2675 (1966).

10. R. L. Wilkens, J. Chem. Phys. 58, 2326 (1973).

11. J. C. Polanyi, in Proceedings of the Conference on Potential Energy Surfaces in Chemistry, edited by W. A. Lester (IBM Research, San Jose, 1971).

12. G. S. Hammond, J. Amer. Chem. Soc. 77, 334 (1955).

POTENTIAL ENERGY SURFACES AND METHYLENE REACTIONS*

H. F. Schaefer III

One of the goals of modern chemistry is to understand, on the molecular level, how chemical reactions occur. One can tackle this problem at various levels. For a complicated organic reaction we may be extremely successful if we are able to learn something about the reaction mechanism, i.e., obtain some information about an intermediate along the most favorable reaction pathway. For the simplest reactions, e.g., $H+H_2$, we may be much more demanding and desire a quantitative knowledge of the importance of quantum mechanical tunneling.

From a theoretical viewpoint, our problem may be separated into two parts:

a) the potential energy surface of surfaces,

b) the molecular dynamics which occur given the surface.

Although no theoretical study will be complete without consideration of both areas, the two parts take on different degrees of importance depending on the observer. The organic chemist in search of a mechanism probably wants to know only the gross features of the potential surface. On the other hand, the physical chemist interested in $H+H_2$ tunneling can use any of several available potential surfaces and is really only interested in the dynamics.

The thrust of the present review article is that potential energy surfaces may now be predicted *ab initio* from quantum mechanical electronic structure calculations. The reactions of triplet and singlet methylene with molecular hydrogen provide particularly fascinating examples.

Footnote

*Published in Chemistry in Britain 11, 227 (1975).

A CRITICAL TEST OF SEMI-EMPIRICAL FH_2 POTENTIAL ENERGY SURFACES: THE BARRIER HEIGHT FOR H + HF → HF + H*

C. F. Bender,† B. J. Garrison and H. F. Schaefer III

One of the fundamental goals of modern chemical physics is to determine the forces which govern atomic and molecular interactions. The most successful approach has traditionally been to work back from experimental observations to the hypothesized potential energy surface. This approach is perhaps best epitomized by the recent work of Lee, Barker, and colleagues,[1] in which experimental differential cross sections, second virial coefficients, and diffusion coefficients have been used to deduce interatomic potentials for noble gas pairs.

For polyatomic systems the procedures for deducing interaction potentials from experiment are at a much earlier stage of development. These procedures often rely heavily on data gleaned from infrared chemiluminescence,[2] chemical laser,[3] and crossed molecular beam[4] experiments. The system which has been studied most thoroughly to date is the F + H_2 → FH + H reaction. At least eleven semi-empirical potential energy surfaces have been proposed[5-13] for FH_2. Several[12,13] of these have been calibrated with experiment via an iterative method, which begins with an assumed potential surface. Using this surface the dynamics are treated using classical trajectories and comparison made with experiment. Then the surface is adjusted and the

TABLE 1. Barrier height and saddle point geometry for H + FH → HF + H. The saddle point occurs for a linear symmetric H-F-H geometry.

Type of potential energy surface	Authors	r(H-F) Å	Barrier (kcal/mole)
Bond-energy Bond-order (BEBO)	Johnston[a]	1.10	6.8
London-Eyring-Polanyi-Sato (LEPS)	Muckerman[5] I	1.04	1.0
LEPS	Jaffe and Anderson	1.05	3.1
LEPS	Muckerman[7] II	1.04	1.0
	Muckerman III	1.05	1.7
	Muckerman IV	1.05	2.3
LEPS	Wilkins[8]	1.04	1.4
LEPS	Thompson[9]	1.12	28.6
Semi-empirical valence bond	Blais and Truhlar[10]	1.10	14.0
Diatomics-in-molecules	Tully[11] I	1.05	14.4
	Tully II	1.09	13.1
LEPS	Muckerman[12] V	1.04	1.2
LEPS	Polanyi and Schreiber[13]	1.05	3.5
A Priori methods	This work		
Self-consistent-field		1.12	67.8
Configuration Interaction		1.14	49.0

[a] H. S. Johnston, Gas Phase Reaction Rate Theory (Ronald Press, New York, 1966).

process repeated until satisfactory agreement with the experimental findings is achieved.

Although most of the proposed FH_2 surfaces appear to reproduce the qualitative features of the vibrational energy distribution for $F+H_2 \rightarrow FH+H$, additional tests of these surfaces are needed before one can assume that a fundamentally correct description of the interaction between these three atoms has been obtained. Although all of the semi-empirical surfaces yield essentially the correct barrier height (activation energy) for the $F+H_2$ reaction, there is a second barrier height which any FH_2 potential should reproduce. This is the barrier for the exchange reaction $H+FH \rightarrow HF+H$. Furthermore, this barrier is of considerable importance in its own right, due to its role in the vibrational relaxation of HF by hydrogen atoms, a process which has already been the subject of two classical trajectory studies.[9,14]

The same sort of internal consistency test has already been completed for a related triatomic system, HF_2. There it has been found that two LEPS surfaces specifically tailored to describe $H+F_2 \rightarrow HF+F$ also yield reasonable values for the $F+HF$ exchange reaction barrier.[15-18] The F+HF barriers of the Thompson[15] and Wilkens[16] surfaces are 27.8 and 22.4 kcal/mole, compared to theoretical results,[17] 21.8 and 23.9 kcal/mole. Thus there is ample reason to believe that semi-empirical surfaces for $F+H_2$ might do an adequate job of describing H+FH.

In the present paper, we report the H+FH barrier as obtained from *a priori* electronic structure theory. The theoretical method used was similar, but more exhaustive than that adopted in earlier studies[17,19,20] of $F+H_2$, $H+F_2$ and F+HF. A contracted Gaussian basis set of size H(5s 1p/3s 1p), F(9s 5p 2d/5s 3p 1d) was employed. Thus we have added s and p functions on fluorine and an s function on hydrogen to the basis used in the study of the other fluorine-hydrogen systems. Furthermore, a more complete configuration interaction (CI) was decided upon, including all interacting single and double excitations relative to the SCF or reference configuration. A total of 1583 configurations were included in the CI calculations.

The barrier occurs for a linear symmetric H-F-H structure, and our results are compared with the various semi-empirical surfaces in Table 1. Although the *a priori* barrier height is likely to be somewhat higher than the exact (unknown) barrier, this difference is unlikely to be more than 5 kcal/mole. In any case we conclude that the true barrier height for H+FH is no less than 40 kcal/mole. As in previous studies of this type, we find electron correlation to be much more important (18.8 kcal/mole here) at the saddle point than for the reactants. The large barrier also rules out the possibility that F atom exchange is a significant contributor to the vibrational relaxation of HF by H atoms.

Most important, however, is the fact that all available semi-empirical potential surfaces for FH_2 fail to predict this large barrier for H+FH. Only Thompson's LEPS surface yields a qualitatively reasonable value for the barrier.[21] This of course does not necessarily mean that these surfaces are inappropriate for the study of the $F+H_2$ dynamics, for which most of them were designed. It does, however, raise serious questions about the fundamental ability of these semi-empirical forms to predict features of the true surface not known in advance.

Footnotes and References

*Published in J. Chem. Phys. 62, 1188 (1974).

†Lawrence Livermore Laboratory, University of California, Livermore, CA 94550.

1. See, for example, C. Y. Ng, Y. T. Lee, and J. A. Barker, J. Chem. Phys. 61, 1996 (1974).

2. A. M. G. Ding, L. J. Kirsch, D. S. Perry, J. C. Polanyi, and J. L. Schreiber, Faraday Disc. Chem. Soc. 55, 252 (1973).

3. R. D. Coombe and G. C. Pimentel, J. Chem. Phys. 59, 1535 (1973).

4. T. P. Schaefer, P. E. Siska, J. M. Parson, F. P. Tully, Y. C. Wong, and Y. T. Lee, J. Chem. Phys. 53, 3755 (1970).

5. J. T. Muckerman, J. Chem. Phys. 54, 1155 (1971).

6. R. L. Jaffe and J. B. Anderson, J. Chem. Phys. 54, 2224 (1971).

7. J. T. Muckerman, J. Chem. Phys. 56, 2997 (1972).

8. R. L. Wilkins, J. Chem. Phys. 57, 912 (1972).

9. D. L. Thompson, J. Chem. Phys. 57, 4170 (1972).

10. N. C. Blais and D. G. Truhlar, J. Chem. Phys. 58, 1090 (1973).

11. J. C. Tully, J. Chem. Phys. 58, 1396 (1973).

12. J. T. Muckerman, unpublished "Surface V" for the FH_2 system. Despite the fact that this surface has not been published, it has been used in a number of dynamical studies, e.g., G. C. Schatz, J. M. Bowman, and A. Kuppermann, J. Chem. Phys. 58, 4023 (1973).

13. J. C. Polanyi and J. L. Schreiber, Chem. Phys. Letters, to be published.

14. R. L. Wilkins, J. Chem. Phys. 58, 3038 (1973).

15. D. L. Thompson, J. Chem. Phys. 57, 4164 (1972).

16. R. L. Wilkins, J. Chem. Phys. 59, 698 (1973).

17. S. V. O'Neil, H. F. Schaefer, and C. F. Bender, Proc. Nat. Acad. Sci. (USA) 71, 104 (1974).

18. R. L. Thommarson and G. C. Berend, Int. J. Chem. Kinet. 6, 597 (1974).

19. C. F. Bender, S. V. O'Neil, P. K. Pearson, and H. F. Schaefer, Science 176, 1412 (1972).

20. C. F. Bender, C. W. Bauschlicher, and H. F. Schaefer, J. Chem. Phys. 60, 3707 (1974).

21. Note, however, that Thompson's surface predicts a barrier of 10.9 kcal/mole for $F + H_2 \rightarrow FH + H$.

A PRIORI PREDICTION OF THE COHESIVE ENERGY OF ONE-DIMENSIONAL METALLIC HYDROGEN*

D. H. Liskow, J. M. McKelvey, C. F. Bender, and H. F. Schaefer III

For more than forty years, the hydrogen molecule has served as a prototype for theoretical studies of the electronic structure of molecules. Since the work of James and Coolidge,[1] who in essence solved the problem *ab initio*, most of the calculations carried out on H_2 have had as their purpose the testing of some particular method for the description of electronic structure. Unfortunately, there has been no comparable prototype for studies of the electronic structure of solids. This problem is of course due to the fact that, prior to the very recent work of Harris and coworkers,[2,3] there has been no truly *ab initio* calculations carried out on solids. It has been suggested many times[4] that the most logical prototype for the electronic structure of solids would be a one-dimensional array of hydrogen atoms. It seems clear that accurate *ab initio* calculations on one-dimensional hydrogen would fill the need for a benchmark, with which to compare approximate methods for the calculation of energy bands and other electronic properties of solids. In addition it should be pointed out that in recent years a significant amount of interest[5-7] has developed in the properties of the thus-far hypothetical substance, metallic hydrogen.

In the present research we have attempted to treat one-dimensional hydrogen as a large molecule. It is clear[4] that if one takes a finite chain of hydrogen atoms and increases n in H_n, the behavior of the system will ultimately approach that of one-dimensional hydrogen to within any specified tolerance. However, the very important question of "at what point" does this large molecule take on the properties of an infinite chain has never, to our knowledge, been investigated *ab initio*. In addition to completing self-consistent-field (SCF) calculations on systems as large as H_{62}, we are able to report a detailed calculation taking account of electron correlation for H_{14}.

Our first step was to carry out SCF computations on successively larger rings of hydrogen atoms. The spacings between each adjacent pair of atoms were constrained to be equal. A single 1s Slater function, $(\zeta^3/\pi)^{1/2} \exp(-\zeta r)$, where ζ is the orbital exponent or scale factor, centered on each H atom. Further, each Slater function was approximated as a linear combination of four Gaussian functions.[8] For the hydrogen atom in its ground state, this approximation yields a total energy of -0.49928 hartrees, while the exact result in these units is -0.5 hartrees. In general one does not expect such a "minimum basis set" to yield particularly reliable *ab initio* results.[9] However, for H_n systems, such a basis yields surprisingly low total energies, especially if the energy is minimized at each geometry with respect to the orbital exponent ζ.

Table 1 summarizes these initial calculations on the closed shell singlet ($^1\Sigma_g^+$ in the limit of linearity) systems H_{14}, H_{26}, H_{38}, H_{50}, and H_{62}. It should be emphasized that the orbital exponent ζ and the H-H bond distance were simultaneously optimized to yield the lowest possible variational energy. In addition, Fig. 1 displays the orbital energies as a function of the number of atoms

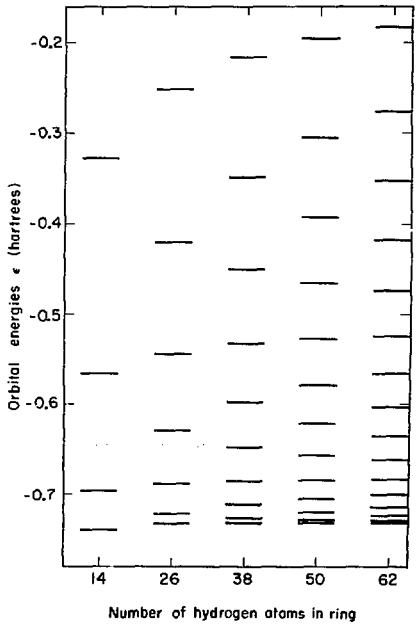

Fig. 1. *Ab initio* orbital energies for rings of hydrogen atoms. (XBL 741-2173)

comprising the ring. Table 1 indicates that a decidedly finite ring of hydrogen atoms can effectively simulate one-dimensional metallic hydrogen. "How many" atoms are required depends on the accuracy one demands for the predicted properties. The two most important properties illustrated in Table 1 are the bond distance and the cohesive energy. If the accuracy demanded is 0.002 bohrs (= 0.001 Å) in the bond distance and 0.07 eV in the cohesive energy, then H_{14} seems to be an adequate representation of H_∞. The difference in bond distance between H_{26} and H_∞ is less than 0.0005 Å and hence not observable by conventional experimental methods, even if our hypothetical metal could be made. The binding energy converges somewhat more slowly, with a ring of 38 atoms required to approach within 0.01 eV/atom of the result expected for H_∞.

TABLE 1. Summary of self-consistent-field calculations on rings of hydrogen atoms.

	Predicted bond distance (bohrs)	Optimized orbital exponent	Total energy (hartrees)	Binding energy per H atom (eV)
H_{14}	1.888	1.129	- 7.45248	0.879
H_{26}	1.886	1.130	-13.79617	0.833
H_{38}	1.886	1.130	-20.14432	0.819
H_{50}	1.886[a]	1.130[a]	-26.49482	0.813
H_{62}	1.886[a]	1.130[a]	-32.84656	0.810

[a]Bond distance and orbital exponents assumed, not optimized.

Our results should not be directly compared with those of Harris, Monkhorst, and Kumar,[2,3] since the latter computations are in three dimensions. However, such a comparison is illustrative since it may enhance our understanding of the differences between one- and three-dimensional systems. The most surprising result of the Harris calculations is the prediction that metallic hydrogen is unbound in the SCF approximation by ~ 0.8 eV/atom with respect to separated hydrogen atoms. Even with our limited basis set, the present SCF calculations predict the one-dimensional structure to be bound by 0.81 eV per H atom. Harris's predicted bond distances for simple cubic, bcc, and fcc lattices are 2.83, 2.85, and 2.99 bohrs, all much larger than the 1.89 bohrs we predict for one-dimensional metallic hydrogen.

The goal of the present research was to make an *a priori* (i.e., without reference to experiment) prediction of the cohesive energy of one-dimensional metallic hydrogen. To do this we must evaluate a) the difference between the SCF energies shown in Table 1 and the true Hartree-Fock energies, and b) the importance of electron correlation in rings of hydrogen atoms. We have carried out more extensive calculations on H_{14} to investigate both of these points.

First, a self-consistent-field calculation was carried out for H_{14} using a much larger basis set of three s (with optimized scale factor ζ = 1.156) and one set (p_x, p_y, p_z) of p functions on each atom. At a nearest neighbor separation of 1.888 bohrs (the optimum for H_{14} from the earlier calculations), the SCF energy obtained was -7.54085 hartrees. This extended basis SCF calculation suggests that we should add 0.17 eV/atom to the SCF binding energies shown in Table 1. Comparison of H_2 SCF results with this extended basis (-1.13262 hartrees) to the exact Hartree-Fock energy[10] (-1.13364 hartrees) of H_2 suggests that an additional 0.014 eV/atom should be added if we are to estimate the true Hartree-Fock energy. Thus we arrive at a prediction of 1.00 eV for the Hartree-Fock cohesive energy of one-dimensional metallic hydrogen.

As a first step in evaluating the correlation energy of H_{14}, we carried out 8-configuration SCF calcualtions using the method developed by Hunt, Dunning, and Goddard.[11] The orbitals resulting from these seven configuration calculations are automatically localized[12] and are best discussed with reference to Fig. 1. There it is seen that a localized description of the H_{14} Hartree-Fock wave function involves seven equivalent orbitals 1b, 2b, 3b, 4b, 5b, 6b, 7b, where "b" signifies a bonding orbital with amplitude predominantly centered on a pair of adjacent hydrogen atoms. A minimum basis set also yields six equivalent antibonding orbitals 1a, 2a, 3a, 4a, 5a, 6a, and 7a. The eight configurations included in the multiconfiguration (MC) SCF calculations are

$$1b^2\ 2b^2\ 3b^2\ 4b^2\ 5b^2\ 6b^2\ 7b^2$$
$$1a^2\ 2b^2\ 3b^2\ 4b^2\ 5b^2\ 6b^2\ 7b^2$$
$$1b^2\ 2a^2\ 3b^2\ 4b^2\ 5b^2\ 6b^2\ 7b^2$$
$$1b^2\ 2b^2\ 3a^2\ 4b^2\ 5b^2\ 6b^2\ 7b^2$$
$$1b^2\ 2b^2\ 3b^2\ 4a^2\ 5b^2\ 6b^2\ 7b^2$$
$$1b^2\ 2b^2\ 3b^2\ 4b^2\ 5a^2\ 6b^2\ 7b^2$$
$$1b^2\ 2b^2\ 3b^2\ 4b^2\ 5b^2\ 6a^2\ 7b^2$$
$$1b^2\ 2b^2\ 3b^2\ 4b^2\ 5b^2\ 6b^2\ 7a^2$$

That is, each localized pair of electrons in H_{14} is treated in a manner equivalent to using the $1\sigma_g^2$ and $1\sigma_u^2$ configurations to describe H_2.

Given the 1b - 7b and 1a - 7a orbitals from the MCSCF calculations, CI calculations were then carried out including all configurations differing by one or two orbitals (i.e., single and double excitations[9]) from the Hartree-Fock configuration. At R(H-H) = 1.888 bohrs, this 1275 configuration wave function yields a total energy of -7.61657 hartrees, implying a correlation energy of 0.16409

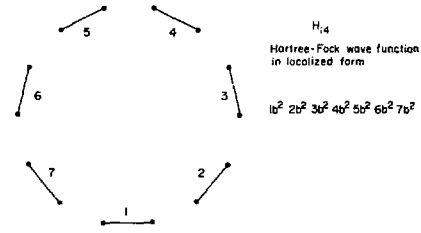

Fig. 2. Graphical representation of the localized orbitals of H_{14}. (XBL 741-2172)

hartrees or 0.32 eV/atom. Comparison with analogous calculations for H_2 suggests the minimum basis set is deficient by 0.41 eV/atom of correlation energy. In this way we predict the correlation energy of one-dimensional metallic hydrogen to be 0.73 eV/atom and thus the cohesive energy to be 1.73 eV/atom. For comparison the binding energy of the hydrogen molecule is 2.38 eV per H atom. Consideration of possible errors in the above extrapolation procedure leads to an estimate of 0.2 eV for the reliability of our prediction.

Footnote and References

*Published in Phys. Rev. Letters 32, 933 (1974).

1. H. M. James and A. S. Coolidge, J. Chem. Phys. 1, 825 (1933).

2. F. E. Harris and H. J. Monkhorst, Phys. Rev. Letters 23, 1026 (1969).

3. F. E. Harris and H. J. Monkhorst, Solid State Commun. 9, 1449 (1971); F. E. Harris, L. Kumar, and H. J. Monkhorst, Intern. J. Quantum Chem. 55, 527 (1971); Phys. Rev. B 7, 2850 (1973).

4. See, for example, Chapter 26 of J. C. Slater, Quantum Theory of Matter (McGraw-Hill, New York, 1968).

5. N. W. Ashcroft, Phys. Rev. Letters 21, 1748 (1968).

6. G. A. Neece, F. J. Rogers, and W. G. Hoover, J. Comput. Phys. 7, 621 (1971).

7. E. E. Salpeter, Phys. Rev. Letters 28, 560 (1972).

8. S. Huzinaga, J. Chem. Phys. 42, 1293 (1965).

9. H. F. Schaefer, The Electronic Structure of Atoms and Molecules: A Survey of Rigorous Quantum Mechanical Results (Addison-Wesley, Reading, Massachusetts, 1972).

10. W. Kolos and C. C. J. Roothaan, Rev. Mod. Phys. 32, 219 (1960).

11. W. J. Hunt, T. H. Dunning, and W. A. Goddard, Chem. Phys. Letters 3, 606 (1969); 4, 231 (1969); 6, 147 (1970).

12. W. England, L. S. Salmon, and K. Ruedenberg, Topics in Current Chemistry 23, 31 (1971).

THE WEAK ATTRACTION BETWEEN WATER AND METHANE*

S. R. Ungemach and H. F. Schaefer III

The present research concerns the simplest hydrophobic[1] interaction, the interaction between a single water molecule and a single methane molecule. One's first inclination might be to assume that biological systems are so much more complex than the H_2O-CH_4 model that such a model is not relevant to an understanding of the hydrophobic effect. However, in his review, Tanford[1] concludes that the hydrocarbon tail of an amphiphile should have thermodynamic properties similar to those of a hydrocarbon molecule in water solution. Since it is clear that the water-methane interaction potential plays a crucial role in determining the latter thermodynamic properties, the relation between the present study and the hydrophobic effect is indirectly established. For physical chemists, of course, the H_2O-CH_4 interaction is of inherent interest, and would probably be estimated to be intermediate between a van der Waals attraction (e.g., Ne-Ne, $\sim$ 0.09 kcal/mole[2]) and a true hydrogen bond (e.g., H_2O-H_2O, $\sim$ 5 kcal/mole[3]).

A series of *ab initio* self-consistent-field calculations have been performed to discern some features of the H_2O-CH_4 potential energy surface. The equilibrium configuration corresponds to a linear O-H-C arrangement, with r(C-O) = 3.85 Å, and a binding energy of 0.5 kcal/mole. Potential curves are presented for a number of other approaches. Using a double zeta basis set, several calculations were also carried out for CH_4-$(H_2O)_2$. With one water fixed at its equilibrium separation with respect to methane, the approach of a second H_2O in an analogous manner yields a repulsive interaction energy. This result is qualitatively explained by a pairwise additive model of the three molecule potential surface. Finally, a qualitative discussion is given in terms of Mulliken atomic populations.

Footnote and References

*Published in J. Amer. Chem. Soc. 96, 7898 (1974).

1. C. Tanford, The Hydrophobic Effect (Wiley-Interscience, New York, 1973).

2. P. E. Siska, J. M. Parson, T. P. Schafer, and Y. T. Lee, J. Chem. Phys. 55, 5762 (1971).

3. H. Popkie, H. Kistenmacher, and E. Clementi, J. Chem. Phys. 59, 1325 (1973).

TRIPLET ELECTRONIC GROUND STATE OF TRIMETHYLENEMETHANE*

D. R. Yarkony and H. F. Schaefer III

A nonempirical quantum mechanical study of the electronic structure of $C(CH_2)_3$ has been carried out. A double ζ basis set of contracted Gaussian functions was employed, and self-consistent-field wave functions were obtained for the triplet ground state. The planar (D_{3h}) configuration is predicted to lie 17 kcal/mole below the orthogonal (C_{2v}) form. The electronic structure is discussed in terms of Mulliken populations (see Table 1) and orbital perspective plots. Some preliminary results for the lowest singlet states are reported.

TABLE 1. Orbital energies and Mulliken populations for the triplet ground state of planar trimethylenemethane[a]

Orbital	hartrees	Central C		Terminal C		Hydrogen s
		s	p	s	p	
$1a_1'$	-11.2690	2.00	0.00	0.00	0.00	0.00
1e'	-11.2447	0.00	0.00	4.00	0.00	0.00
$2a_1'$	-11.2446	0.00	0.00	2.00	0.00	0.00
3a'	-1.0956	0.84	0.00	0.96	0.13	0.08
2e'	-0.9082	0.00	0.09	3.00	0.09	0.72
$4a_1'$	-0.7189	0.29	0.00	0.35	0.71	0.65
3e'	-0.6327	0.00	0.41	0.05	2.35	1.19
$1a_2'$	-0.5437	0.00	0.00	0.00	1.03	0.97
4e'	-0.5236	0.00	0.77	-0.01	1.99	1.25
$1a_2''$	-0.4383	0.00	0.99	0.00	1.01	0.00
1e''	-0.3211	0.00	0.00	0.00	2.00	0.00
Totals		3.12	2.26	3.45	3.13	0.81
Atom Totals		5.38		6.58		0.81

[a]The totals take into account the equivalence of the terminal carbon atoms and of the hydrogens.

Footnote

*Published in J. Amer. Chem. Soc. 96, 3754 (1974).

THREE ISOMERS OF THE NO_2^- ION*

P. K. Pearson,† H. F. Schaefer III, J. H. Richardson,‡
L. M. Stephenson,§ and J. I. Brauman§

Charge transfer experiments[1] have resulted in a value of (2.36 ± 0.06) eV as the best estimate of the electron affinity of NO_2. Photodetachment experiments using conventional light sources determined a vertical detachment energy of ≤ 2.8 eV.[2] The large difference between the electron affinity and vertical detachment energy is readily explained by the significant geometry change and hence poor Franck-Condon factors between NO_2^- and NO_2. The transition $NO_2^-(0,0,0) \rightarrow NO_2(0,0,0)$ has a Franck-Condon factor of 0.003.[3]

Photodetachment experiments with both a conventional light source-ion cyclotron resonance apparatus and a tunable dye laser have detected an anomalous NO_2^- which photodetaches at energies below the electron affinity of NO_2.[2,3] The apparent photodetachment threshold for this unusual

ion is 1.8 eV. It is unlikely that this long wavelength photodetachment is the result of either 1) vibrationally excited $\tilde{X}\ ^1A_1\ NO_2^-$, or 2) an excited electronic state of NO_2^-; considerations of effective temperature, energy separation, method of formation, and long trapping times in the ICR discount possibilities 1) and 2).

A third and more likely possibility would be an isomer of NO_2^-. This possibility is consistent with an anomalous NO_2^-, formed by the reaction of NO with a cluster ion of O^-, $CO_3^- + NO \rightarrow NO_2^- + CO_2$, which has been reported[4] and is expected to be several electron volts less stable than the symmetric, normal NO_2^-. It is quite conceivable that the anomalous NO_2^- could be a peroxy isomer. A peroxy form of NO_3^-, formed by a similar reaction of NO with a cluster ion of O_2^-, has also been suggested.[4] A peroxy form of NO_2^- would also be isoelectronic with the recently reported NOF.[5] It has been suggested[5] that the anomalous NO_2^- is the result of a weak electrostatic interaction between NO and O^-; hence the close resemblance of the long wavelength photodetachment cross section and threshold to that of O^-.[6]

There is at least one other plausible isomer of NO_2^-. We draw this conclusion from the simple observation that NO_2^- is isoelectronic with ozone, a molecule which has been the subject of several *ab initio* theoretical electronic structure studies.[7-10] The work of Peyerimhoff and Buenker[7] was the first to suggest that the equilateral triangle form of O_3 lies quite close energetically to the accepted geometry,[12] $\theta = 116.8°$, $r(O\text{-}O) = 1.278$ Å. More recently, Hay, Dunning, and Goddard[11] have reported extensive configuration interaction calculations which predict this "ring state" to lie 1.57 eV above the accepted ground state. We note that the ring state does represent a well-defined minimum in the potential energy surface and is the lowest electronic state of ozone at $\theta = 60°$, $r(O\text{-}O) = 1.45$ Å.

We have carried out *ab initio* self-consistent-field calculations to investigate the relative energies of the various NO_2^- isomers. Atom-optimized primitive Gaussian basis sets[13] of size (9s 5p) were centered on the N and O nuclei. Although we usually contract this size basis to (4s 2p), in the present study a more flexible (5s 3p) contraction was chosen,[14] to allow for some of the distortion inherent in molecular negative ions. The electron configuration for the expected (bond angle ≈ 116° in analogy with ozone) ground state is[8]

$$1a_1^2 1b_2^2 2a_1^2 3a_1^2 2b_2^2 4a_1^2 5a_1^2 3b_2^2 1b_1^2 4b_2^2 6a_1^2 1a_2^2 \qquad (1)$$

The peroxy form of NO_2^- has only a plane of symmetry (point group C_s), with resulting electron configuration

$$1a'^2 2a'^2 3a'^2 4a'^2 5a'^2 6a'^2 7a'^2 8a'^2 1a''^2 9a'^2 10a'^2 2a''^2 \qquad (2)$$

The ring state is again of C_{2v} symmetry, with configuration

$$1a_1^2 1b_2^2 2a_1^2 3a_1^2 2b_2^2 4a_1^2 5a_1^2 3b_2^2 1b_1^2 6a_1^2 1a_2^2 2b_1^2 \qquad (3)$$

The present study, then, centered about a series of nonempirical self-consistent-field computations, with electron configurations (1), (2), and (3) representing the three expected isomers. A helpful qualitative discussion of the analogous states of ozone has been given by Goddard and co-workers.[15]

One important qualitative conclusion may be drawn prior to the calculations. This concerns the possible interconversion of the "normal" and peroxy forms of NO_2^-. The most likely pathway for this conversion would be (schematically)

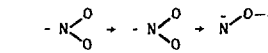

In fact, such a path is highly improbable, since the ring state has three occupied π (or a") orbitals ($1b_1$, $2b_1$, and $1a_2$) while the normal and peroxy forms have only two occupied π orbitals. Thus, orbital symmetry suggests that there should be a substantial barrier preventing access to the ring state from either direction.

The structure of each isomer has been predicted by minimizing the total energy with respect to the various geometrical parameters. The results are summarized in Table 1. Note first that the expected ground state geometry is indeed remarkably close to that of ozone, the difference in bond angles being less than 1°. The difference in bond distances is less than 0.02 Å, another indication of the validity of isoelectronic arguments.[16] Finally, this geometry agrees quite well with the experimental structure of the NO_2^- ion in crystalline sodium nitrite.[17] The peroxy form has a similar bond angle, 118° and NO bond distance, 1.25 Å. However, the O-O bond distance is much longer than in ozone. In fact, the O-O distance is slightly greater than in hydrogen peroxide,[18] 1.475 Å. Thus the labeling of this second isomer

TABLE 1. Geometries, energies, and Mulliken populations for three isomers of NO_2^-. Bond distances are in Å. O_1 is the central atom in the peroxy isomer.

Property	Isomer: Normal	Peroxy	Ring
r(N-O)	1.264	1.245	1.502
r(O-O)	--	1.493	--
θ	117.0°	118.5°	58.5°
E(hartrees)	-204.0336	-203.9161	-203.8736
E(eV)	0.00	3.20	4.35
Atomic Populations			
N	6.83	7.21	7.24
O_1	8.58	8.22	8.38
O_2	8.58	8.57	8.38

as the peroxy form is quite appropriate. The peroxy form lies 3.20 eV above the normal isomer. The ring isomer is indeed very nearly an equilateral triangle, the ONO bond angle being 58°. The NO bond distance is 1.50 Å, or 0.05 Å longer than the predicted bond distance[11] for the comparable isomer of O_3. However, the ring isomer is seen to lie much higher (4.4 eV) for the NO^- system than for O_3 (1.6 eV). Thus our isoelectronic analogy is not very accurate in this particular regard.

Since it has been suggested[3] that the anomalous NO_2^- is the result of a weak electrostatic interaction between NO and O^-, we report in the Table Mulliken populations for the three isomers. There it is seen that the terminal oxygen is indeed the most negatively "charged", in a simple picture. However, the other two atoms account for nearly half of the ion's -1 charge.

In conclusion, the peroxy form of NO_2^- corresponds to a well-defined minimum in the potential energy surface. Consequently, its postulation by experimentalists is given substantive theoretical support. Moreover, the fact that the peroxy and normal forms of NO_2^- do not appear[2-4] to interconvert can be understood in terms of the relatively high energy of the ring state, the superficially logical intermediate for such an interconversion.

Footnotes and References

*Published in J. Amer. Chem. Soc. 96, 6778 (1974).

†Present address: Centre Européen de Calcul Atomique et Moleculaire, Batiment 506, Faculté des Sciences, 91-Orsay, France.

‡Present address: Lawrence Livermore Laboratory, University of California, Livermore CA 94550.

§Department of Chemistry, Stanford University, Stanford, CA 94305.

1. D. B. Dunkin, F. C. Fehsenfeld, and E. E. Ferguson, Chem. Phys. Letters 15, 257 (1972); see also B. M. Hughes, C. Lifshitz, and T. O. Tiernan, J. Chem. Phys. 59, 3162 (1973).

2. J. H. Richardson, L. M. Stephenson, and J. I. Brauman, Chem. Phys. Letters 3, 313 (1974).

3. E. Herbst, T. A. Patterson, and W. C. Lineberger, J. Chem. Phys. (August 1974).

4. a) N. G. Adams, D. K. Bohme, D. B. Dunkin, F. C. Fehsenfeld, and E. E. Ferguson, J. Chem. Phys. 52, 3133 (1970); b) E. E. Ferguson, D. B. Dunkin, and F. C. Fehsenfeld, J. Chem. Phys. 57, 1459 (1972); see also E. E. Ferguson, F. C. Fehsenfeld, and A. V. Phelps, J. Chem. Phys. 59, 1565 (1973).

5. R. R. Smardzewski and W. B. Fox, J. Amer. Chem. Soc. 96, 304 (1974).

6. L. M. Branscomb, D. S. Burch, S. J. Smith, and S. Geltman, Phys. Rev. 111, 504 (1958).

7. S. D. Peyerimhoff and R. J. Buenker, J. Chem. Phys. 47, 1953 (1967).

8. S. Rothenberg and H. F. Schaefer, Mol. Phys. 21, 317 (1971).

9. P. J. Hay and W. A. Goddard, Chem. Phys. Lett. 14, 46 (1972).

10. J. S. Wright, Can. J. Chem. 51, 139 (1973).

11. P. J. Hay, T. H. Dunning, and W. A. Goddard, Chem. Phys. Lett. 23, 457 (1973).

12. R. H. Hughes, J. Chem. Phys. 24, 131 (1956).

13. S. Huzinaga, J. Chem. Phys. 42, 1293 (1965).

14. T. H. Dunning, J. Chem. Phys. 53, 2823 (1970).

15. W. A. Goddard, T. H. Dunning, W. J. Hunt, and P. J. Hay, Accounts of Chemical Research 6, 368 (1973).

16. A. D. Walsh, J. Chem. Soc. 00, 2266 (1953).

17. In the solid state, the ion has the geometry r(N-O) = 1.236 Å, θ = 115.4°; see M. R. Truter, Acta. Cryst. 7, 73 (1954). The gas phase NO radical has a rather different structure r(N-O) = 1.197 Å, θ = 134.3°; see G. R. Bird, J. Chem. Phys. 25, 1040 (1956).

18. R. H. Hunt, R. A. Leacock, C. W. Peters, and K. T. Hecht, J. Chem. Phys. 42, 1931 (1965).

ELECTRONIC STRUCTURE ON NITRENES: LiN, THE SIMPLEST IONIC SPECIES*

C. E. Dykstra, P. K. Pearson,† and H. F. Schaefer III

From qualitative molecular orbital arguments, it is predicted that the $^3\Sigma^- - {}^3\Pi$ separation in the ionic LiN molecule should be significantly less than the 3.69 eV found spectroscopically for the analogous covalent molecule NH. To test this prediction, an *ab initio* theoretical study of the electronic structure of LiN has been carried out. A Slater basis set was employed, of size Li(4s 2p), N(4s 3p 1d). Both self-consistent-field and configuration interaction (CI) methods were used. For both $^3\Sigma^-$ (335 configurations) and $^3\Pi$ (546 configurations) states, the CI included all interacting single and double excitations with respect to the two-configuration wave functions required to insure dissociation to Hartree-Fock atomic wave functions. Consistent with the ionic model, the two states are predicted to be very close in energy, the $^3\Sigma^-$ state being the lower by 0.34 eV. Potential energy curves are seen in Fig. 1. An important aspect of the study is the prediction of electronic transition probabilities. It is shown that the use of natural orbitals greatly facilitates the calculation of transition moments, and the "length" form is seen to be less sensitive to details of the correlated wave function than is the "velocity" form. The $^3\Sigma^- - {}^3\Pi$ oscillator strength, consistent with the ionic model, increases rapidly as a function of bond distance.

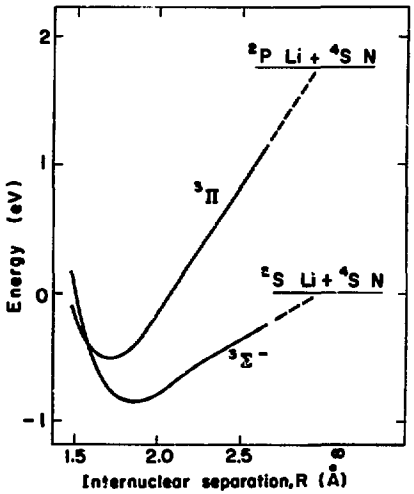

Fig. 1 (XBL 747-3751)

Footnotes

*Published in J. Amer. Chem. Soc. 97, 0000 (1975).

†Present address: Centre Europeen de Calcul Atomique et Moleculaire, Batiment 506, Faculte des Sciences, 91-Orsay, France.

X^3A_2, a^1E, AND b^1A_1 ELECTRONIC STATES OF METHYL NITRENE*

D. R. Yarkony, H. F. Schaefer III, and S. Rothenberg

An *a priori* theoretical study of the electronic structure of methyl nitrene has been carried out. Using a double zeta basis set, the geometries of the lowest $^3A_2$, ^1E, and $^1A_1$ states have been predicted at the self-consistent-field level of theory. The three states, all of which arise from the same electron configuration $1a_1^2 2a_1^2 3a_1^2 4a_1^2 1e^4 5a_1^2 2e^2$, are predicted to have very similar geometries. For the ground $^3A_2$ state, we predict r(CH) = 1.09 Å, R(CN) = 1.47 Å, ∠(NCH) = 110°. At the predicted $^3A_2$ equilibrium geometry, several molecular properties were calculated using a larger basis set including d functions on C and N and p functions on hydrogen. These results are summarized in Table 1. The predicted dipole moments are substantial: 2.11 debye ($^3A_2$), 2.23 debye (^1E), and 2.36 debye ($^1A_1$). The ^1E and $^1A_1$ states are predicted to lie 14,200 and 27,700 cm^{-1} above the $^3A_2$ ground state. Comparisons are made with the properties of the simplest nitrene, NH.

TABLE 1. Molecular properties of methyl nitrene, obtained with a double zeta plus polarization basis set. The z coordinate lies along the C_3 axis of the molecule, and one of the H atoms has been placed at $y = 0$. Atomic units are used throughout.

Moments (with respect to the center of mass) of the electronic charge distribution	$^3A_2$	^1E	$^1A_1$
$\langle z \rangle$	2.13	2.08	2.03
$\langle x^3 \rangle = \langle y^3 \rangle$	−14.75	−14.82	−14.90
$\langle z^3 \rangle$	−48.18	−48.16	−48.13
$\langle x^2 y \rangle = -\langle xy^2 \rangle$	−4.47	−4.44	−4.41
$\langle z^2 y \rangle$	11.21	10.86	10.50
$\langle x^2 z \rangle = \langle y^2 z \rangle$	11.79	11.53	11.27
Multipole moments			
μ_z (+CN−)	0.831	0.876	0.93
$\Theta_{zz} = \Theta_{yy}$	0.86	0.81	0.76
Θ_{xy}	−1.71	−1.62	−1.51
$\Omega_{zzz} = -\Omega_{zyy}$	2.32	2.38	2.46
Ω_{xxz}	−2.23	−1.81	−1.37
$\Omega_{xxx} - \Omega_{xyy}$	1.11	0.91	0.69
Potential at nucleus			
Φ(H)	−1.095	−1.091	−1.085
Φ(C)	−14.70	−14.69	−14.69
Φ(N)	−18.36	−18.34	−18.32
Electric field at nucleus			
E_z(H)	0.010	0.011	0.012
E_z(H)	−0.002	−0.002	−0.003
E_z(C)	−0.008	−0.007	−0.005
E_z(N)	0.072	0.071	0.070
Diamagnetic susceptibility tensor			
$\chi_{zz}^d = \chi_{xx}^d$	−62.92	−62.98	−63.03
χ_{yy}^d	−29.49	−29.65	−29.80
χ_{xx}^d	−51.78	−51.87	−51.96

TABLE 1. (Continued)

Moments (with respect to the center of mass) of the electronic charge distribution	$^3A_2$	^1E	$^1A_1$
Diamagnetic shielding tensor			
σ_{zz}(H)	−3.19	−3.19	−3.19
σ_{yy}(H)	−0.94	−0.93	−0.93
σ_{xy}(H)	−2.25	−2.24	−2.24
σ_{zy}(H)	1.27	1.27	1.27
σ_{xx}(H)	−2.12	−2.12	−2.12
σ_{xx}(C) = σ_{yy}(C)	−5.65	−5.65	−5.65
σ_{zz}(C)	−7.37	−7.37	−7.36
σ_{xx}(C)	−6.22	−6.22	−6.22
σ_{zz}(N) = σ_{yy}(N)	−6.36	−6.35	−6.34
σ_{xx}(N)	−8.56	−8.56	−8.56
σ_{xx}(N)	−7.09	−7.08	−7.08
Electric field gradient tensor			
q_{zz}(H)	−0.259	−0.259	0.260
q_{yy}(H)	0.163	0.164	0.163
q_{xx}(H)	0.095	0.096	0.096
q_{zy}(H)	0.149	0.149	0.150
q_{xx}(C) = q_{yy}(C)	0.086	0.090	0.091
q_{zz}(C)	−0.172	−0.179	−0.181
q_{xx}(N) = q_{yy}(N)	−0.195	−0.272	−0.340
q_{zz}(N)	0.389	0.543	0.681

[a] The z coordinate lies along the C axis of the molecule, and one of the H atoms has been placed at $y = 0$. Atomic units are used throughout.

Footnote

[a] Published in J. Amer. Chem. Soc. 96, 5974 (1974).

EXCITED ELECTRONIC STATE OF HNC, HYDROGEN ISOCYANIDE[a]

G. M. Schwenzer and H. F. Schaefer III

Walsh's rules suggest that the excited states of HNC should have bond angles similar to the analogous states of HCN. To test this hypothesis, *ab initio* calculations have been carried out and compared to earlier calculations on HCN. Our results are summarized in Table 1. The most surprising result is the prediction that several of the excited electronic states of HNC lie below the corresponding states of HCN. Also unanticipated are the unusually long CN bond lengths found for several of the lower excited states of HNC. The excited singlet states have bond angles qualitatively similar, although somewhat smaller, than those of HCN. For the triplet states, Walsh's

TABLE 1. Summary of theoretical predictions for the singlet states of HNC. Excitation energies and bond angles given in parentheses are those predicted by analogous calculations on HCN. Bond distances are in Å.

Symmetry	T_e (eV)	r_e(HN)	r_e(NC)	θ_e (HNC)	Most important configurations	Coefficients
$1\ ^1A'(^1\Sigma^+)$	0.00 (0.00)	0.987	1.204	180° (180°)	$5a'^2 6a'^2 1a''^2$	0.968
$1\ ^1A''$	4.95 (6.48)	1.022	1.461	112.8°(127.2°)	$5a'^2 6a'^2 1a'' 7a'$	0.939
$2\ ^1A'$	5.51 (6.78)	1.015	1.417	119.7°(124.9°)	$5a'^2 6a' 7a' 1a''^2$	0.819
					$5a'^2 6a'^2 1a'' 2a''$	0.444
$2\ ^1A''$	6.22 (7.52)	0.996	1.418	156.8°(164.4°)	$5a'^2 6a' 1a''^2 2a''$	0.910
$3\ ^1A'$	7.34 (7.85)	1.021	1.266	142.0°(141.2°)	$5a' 6a'^2 1a''^2 7a'$	0.771
					$5a'^2 6a' 7a' 1a''^2$	0.365
					$5a'^2 6a'^2 1a'' 2a''$	0.358
$3\ ^1A''$	8.17 (8.97)	0.979	1.220	180° (180°)	$5a'^2 6a' 1a''^2 2a''$	0.944
$4\ ^1A'$	8.50 (9.54)	1.150	1.198	180° (180°)	$5a'^2 6a' 8a' 1a''^2$	0.813

concept appears less successful, primarily due to strong mixing between several different electronic configurations. Mulliken populations are used in the discussion of these results.

Footnote

*Published in J. Chem. Phys. 63, 0000 (1975).

CORRELATION DIAGRAM FOR He + He → Be*

D. R. Yarkony and H. F. Schaefer III

An electronic correlation diagram has been calculated *a priori* for the model system He + He → Be. The suitability of different types of basis sets and of the Hartree-Fock approximation is discussed. The relation of this diagram to experimental inner shell collision chemistry is discussed briefly. The figure shows the adiabatic total energies and orbital energies. Note especially the avoided crossing at R = 0.56 bohrs. This crossing corresponds, in a single configuration picture, to a jump from $1\sigma_g^2\,1\sigma_u^2$ to $1\sigma_g^2\,2\sigma_g^2$.

Footnote

*Published in J. Chem. Phys. 61, 4921 (1975).

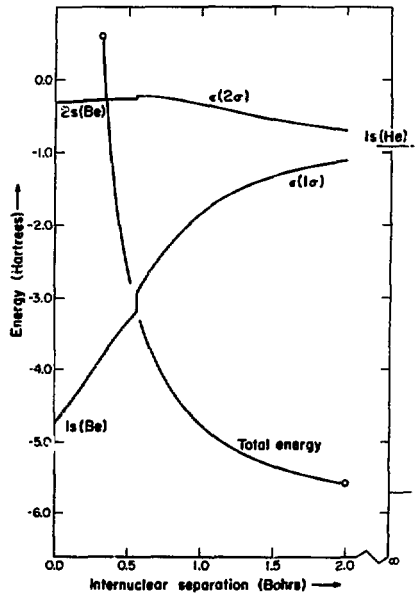

Fig. 1. (XBL 745-3037)

THE HYPERVALENT MOLECULES SULFURANT (SH_4) AND PERSULFURANE (SH_6)*

G. M. Schwenzer and H. F. Schaefer III

The electronic structures of SH_2, SH_4, and SH_6 have been investigated by *ab initio* theoretical methods. The geometry of each species has been predicted using self-consistent-field wave functions employing a S(12s 9p/7s 5p), H(5s/3s) basis set of contracted Gaussian functions. These results are summarized in Table 1. Using these geometries, the effects of hydrogen scale factor, d functions on sulfur, and p functions on hydrogen have been explored. It is concluded that SH_4 lies energetically above $SH_2 + H_2$, and that SH_6 lies at least 36 kcal/mole above $SH_2 + 2H_2$. Thus SH_4 and SH_6 at best represent local minima on their respective potential energy surfaces. The structure predicted for SH_4 is quite reminiscent of the known geometry of SF_4 seen in Fig. 1. The bonding in these two model systems is discussed making use of population analyses. A number of molecular properties are predicted.

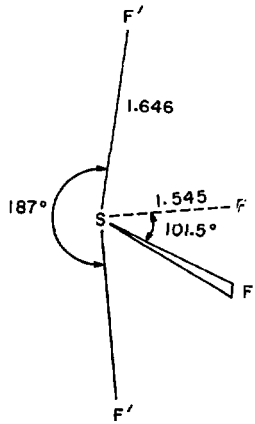

Fig. 1. (XBL 748-4143)

Table 1. Predicted geometries of SH_2, SH_4, SH_6[a] The experimental H_2S geometry[b] is given in parentheses.

	SH_2	SH_4	SH_4	SH_6
r(S–H)	1.357 (1.328)	1.489	1.70	1.461
r(S–H′)		1.489	1.35	1.461
θ(HSH), deg	96.2 (92.2)	90	105.6	90
θ(H′SH′), deg		180	191.8	180
Hydrogen scale factor	1.19	1.19[c]	1.00	1.02
Energy, hartrees	−398.6469	−399.5308	−399.5753	−400.5351

[a] Bond distances (Å) and bond angles are specified in a manner analogous to Figure 1.
[b] Geometry recalculated by L. E. Sutton and D. H. Whiffen, *Chem. Soc., Spec. Publ.*, No. 18 (1965), using moments of inertia from H. C. Allen and E. K. Plyer, *J. Chem. Phys.*, 25, 1132 (1956).
[c] Not optimized.

Footnote

*Published in J. Amer. Chem. Soc. 97, 1393 (1975).

MOLECULAR PROPERTIES OF EXCITED ELECTRONIC STATES: THE $\tilde{a}^3A''$ AND $\tilde{A}^1A''$ STATES OF FORMALDEHYDE*

B. J. Garrison, H. F. Schaefer III, and W. A. Lester†

One of the most important recent trends in chemical physics has been the development of new experimental and theoretical methods for studying the excited electronic states of molecules.[1] Since excited state properties are often strikingly different from their ground state counterparts, the results of experiments on excited states sometimes force us to reevaluate our thoughts concerning the nature of molecular structure and properties.

As one of the earliest studied examples, consider the lowest two excited states of formaldehyde. For reference, we note the planar C_{2v} structure[2] of the ground state,

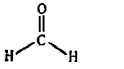

with r(CO) = 1.208 Å, r(CH) = 1.116 Å, θ(HCH) = 116° 31'. The electron configuration for the $^1A_1$ ground state may be written[3]

$$1a_1^2 2a_1^2 3a_1^2 4a_1^2 1b_2^2 5a_1^2 1b_1^2 2b_2^2 \qquad (1)$$

In both excited states, the geometries are quite different;[3-5] in fact both are nonplanar, with the methylene group tilted out of the plane defined by the ground state molecular structure. For the lowest triplet state, this out of plane angle is ∿ 34°, while it is ∿ 31° for the first excited singlet state.[5] Although these two states would be labeled $^3A_2$ and $^1A_2$ if they retained the ground state's C_{2v} equilibrium geometry, these labels are not appropriate since only a plane of symmetry is required. Hence the states are properly designated $\tilde{a}^3A''$ and $\tilde{A}^1A''$ and both arise from the electron configuration.

$$1a'^2 2a'^2 3a'^2 4a'^2 1a''^2 5a'^2 6a'^2 2a'' 7a' \qquad (2)$$

Note that the half-filled 2a" and 7a' orbitals correlate with the C_{2v} orbitals $2b_2$ and $2b_1$, the latter being unoccupied in the ground state. Finally, it should be mentioned that the CO distance in the two excited states is more than 0.1 Å longer than for the ground state: $\tilde{a}$ 1.312 Å, $\tilde{A}$ 1.323 Å.

The above illustrates some of the interesting relationships that have been established between ground and excited state molecular geometries. For other properties, however, less is known about excited states. For example, there are only a small number of polyatomic molecules for which excited state electric dipole moments have been measured. Again, one of the systems for which experiments have been possible is the $\tilde{A}^1A''$ state of H_2CO. There Freeman and Klemperer[6a] have obtained $\mu_z = 1.56 \pm 0.07$ debyes from the Stark effect of the near-ultraviolet absorption spectrum. For comparison, the $^1A_1$ ground state dipole moment[7] is 2.323 ± 0.015 debye, or 0.76 ± 0.09 debye larger than the excited state value. In addition Buckingham, Ramsay, and Tyrrell[6b] have measured μ_z for the $\tilde{a}$ state and obtained 1.29 ± 0.03 debye.

The purpose of the present research was to report near Hartree-Fock values of several molecular properties of the $\tilde{a}$ and $\tilde{A}$ states of formaldehyde. In addition to the dipole moment, known experimentally for both states, we report a number of properties (e.g. molecular quadrupole moments and electric field gradients) which are of interest but very difficult to measure for excited electronic states. To evaluate the reliability of the predicted properties, the ground state H_2CO properties have also been calculated using a variety of basis sets.

Footnotes and References

*Published in J. Chem. Phys. 61, 3039 (1974).

†Present address: IBM Research Laboratory, Monterey and Cottle Roads, San Jose, CA 95193.

1. See, for example, Vol. 1, Excited States, edited by E. C. Lim (Academic Press, New York, 1974).

2. T. Oka, J. Phys. Soc. Japan 15, 2274 (1960); K. Tagaki and T. Oka, J. Phys. Soc. Japan 18, 1174 (1963).

3. G. Herzberg, Electronic Spectra of Polyatomic Molecules (Van Nostrand Reinhold, New York, 1966).

4. J. C. D. Brand, J. Chem. Soc. (London) 858 (1956).

5. V. E. DiGiorgio and G. W. Robinson, J. Chem. Phys. 31, 1678 (1959).

6. a) D. E. Freeman and W. Klemperer, J. Chem. Phys. 45, 52 (1966); b) A. D. Buckingham, D. A. Ramsay, and J. Tyrrell, Can. J. Phys. 48, 1242 (1970).

7. K. Kondo and T. Oka, J. Phys. Soc. (Japan) 15, 307 (1960).

SUPERTRANSFERRED HYPERFINE INTERACTION: PERTURBED ANGULAR CORRELATION OF ^{111m}Cd IN ANTIFERROMAGNETIC NiO, CoO, AND MnO

H. H. Rinneberg and D. A. Shirley

The time differential perturbed angular correlation (PAC) of ^{111m}Cd substituted as a dilute impurity into antiferromagnetic NiO, CoO, and MnO has been observed. (Fig. 1). Above their Néel temperatures the divalent oxides NiO ($T_N \approx 520°K$), CoO ($T_N \approx 293°K$) and MnO ($T_N \approx 118°K$) have the rock salt structure. Cd^{2+} is assumed to enter substitutionally for a transition metal ion. It is surrounded by a regular octahedron of O^{2-} anions. Because of symmetry, in the antiferromagnetic state the 12 nearest magnetic ions do not contribute to the observed isotropic supertransferred hyperfine interaction. This can be seen very easily by considering one of the O^{2-} anions next to the dopant (Cd^{2+}). It is octahedrally surrounded by 6 cations, where transition metal ions on opposite corners, have antiparallel spins. Thus only the effect of the magnetic ion which is linked to the Cd^{2+} by a 180° Me^{2+} - O^{2-} - Cd^{2+} bond does not vanish by symmetry. There are six such next-nearest magnetic ions--all belonging to the same sublattice--which octahedrally surround the dopant. Thus for the supertransferred hyperfine interaction the divalent oxides NiO, CoO, MnO constitute the same local environment around the dopant (Cd^{2+}) as the perovskites $KNiF_3$, $KCoF_3$, and $RbMnF_3$. Whereas the 12 nearest cations do not contribute to the unpaired spin density in Cd^{2+} s-orbitals, they give rise to a dipolar field at the Cd nucleus. In Table 1 the experimental internal fields H_{int} (4.2°K) and the hyperfine fields H_{hf}(4.2°K) corrected for the dipolar contribution are given for the divalent oxides NiO, CoO, and MnO. For comparison the perovskites $KNiF_3$, $KCoF_3$, and $RbMnF_3$ are included. It is seen, that the hyperfine fields observed in the oxides are about twice as large as in the corresponding fluorides. Qualitatively, if we assume the transfer of spin density through the intervening anion to be the dominant mechanism, then from the larger unpaired spin density at the Cd impurity in the oxides we expect a larger unpaired spin density at the O^{2-} ion provided the transfer of spin density from the anion into the Cd s-shells is not too different for the Cd-O and Cd-F bonds. This is consistent with recent results obtained by Freund, who measured the ^{17}O ENDOR in $Mg(^{61}Ni^{2+})^{17}O$. He obtained for the amount of unpaired spin density f_σ(Ni-O) = 8.5%, whereas f_σ(Ni-F) = 3.9% is known from the ^{19}F NMR in $KNiF_3$.

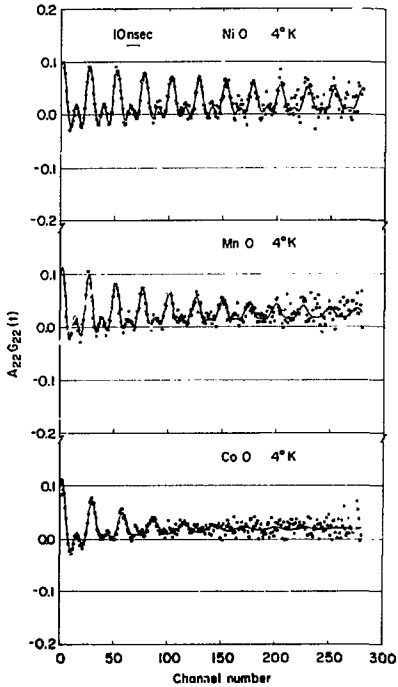

Fig. 1. Time differential PAC spectra of ^{111m}Cd doped into antiferromagnetic NiO, MnO, and CoO. (XBL 742-2362)

Table 1. Experimental values for the internal fields H_{int} (4 K) and hyperfine fields H_{hf}, corrected for a dipolar contribution, at Cd in various antiferromagnetic fluorides[1] and oxides.

	NiO	CoO	MnO	$KNiF_3$	$KCoF_3$	$RbMnF_3$
H_{int}(kOe)	191.1±2.5	170.8±3.0	194.7±2.5	105.7±1.5	74.1±1.5	113.8±1.5
H_{hf} (kOe)	196.0±3.5	176.9±4.0	202.4±3.0	105.7±1.5	74.1±1.5	113.8±1.5

A closer analysis of the hyperfine fields has been performed following the configuration interaction calculation of Taylor et al.[1] Because of uncertainties in the wavefunctions used to calculate overlap integrals and since the impurity-ligand distance is not known, these calculations predict the observed fields with an uncertainty of better than a factor of two. From the ratio of the hyperfine fields H(MnO)/H(NiO) a new estimate for the spin density parameter f_σ(Mn-O) = 8.1% has been obtained, which is considerably larger than the value inferred from neutron diffraction.

PERTURBED ANGULAR CORRELATION OF ^{111}Cd IN ANTIFERROMAGNETIC MnF_2, FeF_2, CoF_2, AND NiF_2[†]

H. H. Rinneberg and D. A. Shirley

The time differential perturbed angular correlation (PAC) of ^{111m}Cd doped into antiferromagnetic MnF_2, FeF_2, CoF_2 and NiF_2 has been observed. The perturbation is caused by a combined electric quadrupole and magnetic dipole interaction.

The divalent fluorides MnF_2 (T_N = 67.4°K), FeF_2 (T_N = 78.1°K), CoF_2 (T_N = 37.7°K) and NiF_2 (T_N = 73.2°K) have the rutile structure (D_{4h}^{14}). Cd^{2+} enters substitutionally for a transition metal ion. Because of the point symmetry at the metal site (D_{2h}) the orientation of the field gradient tensor, produced by the crystalline surroundings at the Cd nucleus, is fixed with the principal axes pointing along [110], [$\bar{1}$10], and [001]. In the antiferromagnetic state there are two interpenetrating sublattices. For MnF_2, FeF_2 and CoF_2 the spins point along the c-axis. Hence the hyperfine field at the Cd nucleus is parallel to [001], that is, one of the axes of the field gradient tensor.

The spin structure of NiF_2 is more complicated. The spins are perpendicular to the c-axis, with the spin axis along [100] or [010]. The hyperfine field is therefore perpendicular to one of the field gradient axes. The time differential perturbed angular correlation spectra of ^{111}Cd doped into MnF_2, FeF_2, CoF_2, and NiF_2 are shown in Figs. 1 and 2 for temperatures below and above their Néel points. The spectrum obtained for MnF_2 in the paramagnetic state (77°K) shows almost exactly the periodic variation expected for axially symmetric quadrupole interaction. Therefore approximate values for ν_Q and η ($\eta \approx 0$) are easily obtained, which can be improved by a least-squares fit. For paramagnetic FeF_2 (T = 90 K, H_{int} = 0) the observed PAC spectrum is no longer periodic. Since ν_Q essentially determines the time scale, the specific form of $G_{22}(t)$ depends only on the asymmetry parameter $0 \leq \eta \leq 1$, which is easily found by trial and error. However in the antiferromagnetic state, where more parameters have to be determined, this method becomes increasingly difficult and tedious. Clearly, the Fourier coefficients $F(\omega)$ of the perturbation factor $G_{22}(t)$ are needed to estimate these parameters. Since we are only interested in frequencies, the power spectral density $P(\omega) = |F(\omega)|^2$ can be used instead.

In order to improve the signal/noise ratio, the power spectral density is calculated, after the experimental values of the perturbation factor have been weighed according to their statistical accuracy. Since the statistical error increases significantly for times $t > t_{max}$, for which the

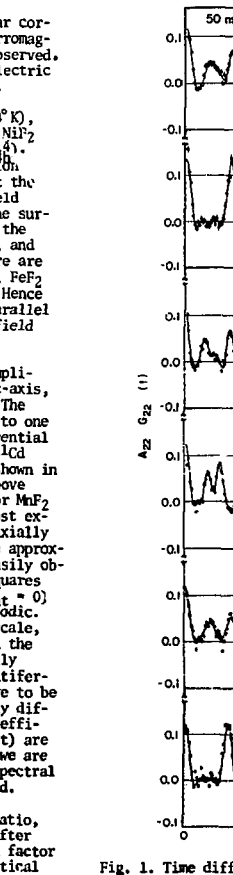

Fig. 1. Time differential PAC spectra of ^{111m}Cd doped into paramagnetic and antiferromagnetic MnF_2, FeF_2, and CoF_2. (XBL 744-2785)

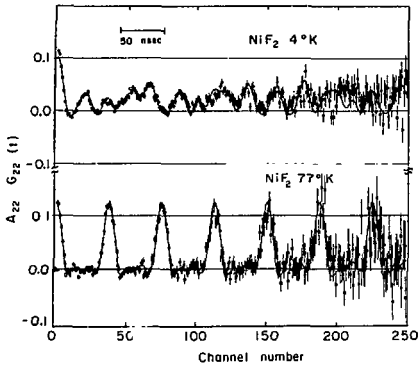

Fig. 2. Time differential PAC spectra of ^{111m}Cd in paramagnetic and weakly ferromagnetic NiF_2. (XBL 745-2998)

number of true coincidences is smaller or equal to the number of random events, the perturbation factor $G^{u}_{22}(t)$ thus obtained is essentially zero for $t \geq t_{max}$. Since the multiplication by a weighing factor corresponds to a convolution in the frequency domain using $G^{u}_{22}(t)$ an averaged power spectral density $W(\omega)$ is obtained. The increase in signal/noise ratio corresponds to a decrease in frequency resolution. The power spectral density $W(\omega)$ can be obtained directly from the Fourier coefficients of $G^{u}_{22}(t)$. Equivalently it can be calculated as the Fourier transform of the autocorrelation function $C(\tau)$ of $G^{u}_{22}(t)$ if the maximum time lag τ_{max} for which $C(\tau)$ is calculated is equal to the time interval, in which $G^{u}_{22}(t)$ is essentially different from zero ($\tau_{max} = t_{max}$).

In this way we obtain from the experimental time differential PAC spectra (Figs. 1 and 2) the experimental average power spectral density functions W^{exp} shown in Figs. 3 and 4 for MnF_2, FeF_2, CoF_2, and NiF_2 (dotted lines). Since the natural line width associated with the γ-γ cascade of ^{111m}Cd, $\Delta\nu = (\pi\tau_N)^{-1}$, is about 2.5 MHz, the individual Fourier components overlap heavily. Assuming certain values for ν_Q, η, and H_{int}, the perturbation factor $G^{u}_{22}(t)$ is calculated. Using these theoretical estimates instead of the measured values for $G^{u}_{22}(t)$, a theoretical estimate of the average power spectral density W^{calc} and W^{exp} in the frequency or by a fit of G^{calc}_{22} and G^{exp}_{22} in the time domain. Good agreement was obtained between the results of a minimization in frequency space and time space. The solid curves in Figs. 3,4 and 1,2 represent the calculated average power spectral density W^{calc} and perturbation factor G^{calc}_{22} respectively.

The internal fields (Table 1) found in MnF_2/Cd, FeF_2/Cd, CoF_2/Cd, and NiF_2/Cd at 4°K

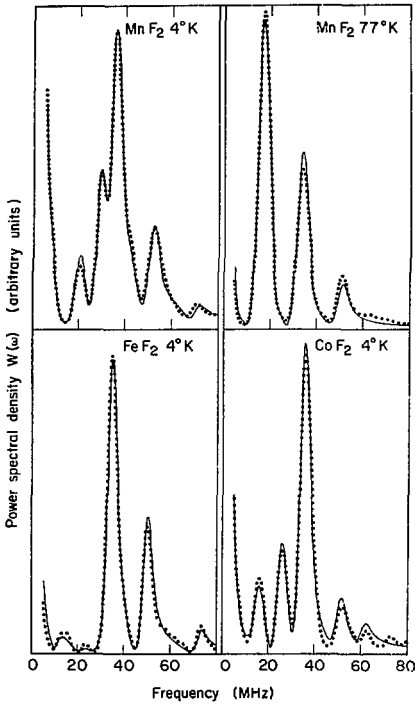

Fig. 3. Average power spectral density of the time differential PAC spectra (dotted line) for MnF_2/Cd, FeF_2Cd, and CoF_2/Cd. The solid curves represent a least squares fit. (XBL 744-2786)

are rather similar. For comparison we include in Table 1 the hyperfine fields at the Cd nucleus doped into the antiferromagnetic perovskites $RbMnF_3$, $KFeF_3$, $KCoF_3$, and $KNiF_3$. The hyperfine fields at the impurity are caused by unpaired spin densities transferred from the magnetic neighbors into the Cd s-shells. In the perovskites, e.g., $KNiF_3$, the six nearest magnetic neighbors belonging to the same sublattice contribute to the hyperfine field. For the difluorides, two nearest magnetic ions of one sublattice and eight next nearest magnetic neighbors belonging to the other sublattice have to be considered. Because of symmetry arguments, the influence of the latter is expected to be dominating. The smaller fields found in the difluorides compared to the perovskites are due to the transfer of spin density along angular exchange paths $M^{2+} - F^- - Cd^{2+}$, resulting in smaller overlaps of the orbitals involved.

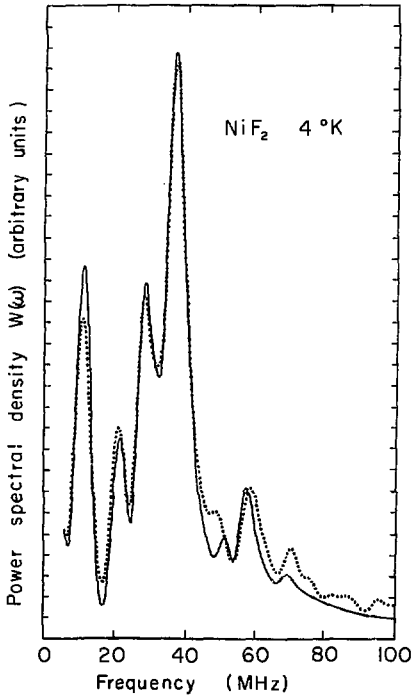

Fig. 4. Average power spectra density of the time differential PAC spectrum of NiF_2/Cd at 4° K (dotted line). The solid curve represents a least squares fit. (XBL 745-2997)

Table 1. Quadrupole coupling parameters and hyperfine fields in various antiferromagnetic fluorides at 4°K.

	ν_Q(MHz)	η	H_{int}(kOe)	
MnF_2	16.7±0.2	0.05±0.02	34.4±0.8	$\vec{H}_{int} \parallel \vec{y}_{FG}$
FeF_2	21.6±0.3	0.49±0.02	40.2±0.8	$\vec{H}_{int} \parallel \vec{x}_{FG}$
CoF_2	17.7±0.3	0.0 ±0.02	16.4±0.8	$\vec{H}_{int} \perp \vec{z}_{FG}$
NiF_2	16.5±0.5	0.1 ±0.08	24.4±0.8	$\vec{H}_{int} \parallel$ in x_{FG},z_{FG} plane
				$\measuredangle \vec{H}_{int}, \vec{z}_{FG} = 48\pm5°$
$RbMnF_3$	--	--	113.8±1.5	--
$KFeF_3$	--	--	~ 100	--
$KCoF_3$	--	--	74.1±1.5	--
$KNiF_3$	--	--	105.7±1.5	--

A NUCLEAR ORIENTATION MEASUREMENT OF PARITY ADMIXTURE IN THE 501-keV GAMMA TRANSITION IN $^{180}Hf^{m}$

T. S. Chou, K. S. Krane, and D. A. Shirley

The current-current theory of weak interactions of Feynman and Gell-Mann[1,2] suggests that the strangeness-conserving, non-leptonic weak interaction will contribute to the internucleon potential and will result in small parity impurities in nuclear states. The ratio F of the strength of the parity non-conserving force to that of the parity-conserving force was estimated by Blin-Stoyle[3] to be of the order of 10^{-7}; thus these parity admixtures are expected to be quite small. However, in the event that nuclear observables resulting from the parity-conserving component are strongly hindered, effects of the parity impurity may compete more successfully. The case of ^{180}Hf provides a particularly striking example of this relative enhancement. We have undertaken a measurement of the asymmetry in the angular distribution of the 501-keV gamma ray following the decay of polarized ^{180m}Hf. Earlier measurements of parity nonconserving effects in this transition had been reported in three previous studies of the circular polarization of radiation from an unpolarized sample,[4-6] as well as in one previous study of the angular distribution asymmetry from a polarized sample.[7] Nevertheless, we felt that the size of the effect in this transition and its significance for comparisons with theoretical calculations warranted an independent remeasurement under somewhat varied conditions.

The parity-nonconserving weak interaction introduces a small parity admixture into the nuclear levels, such that the nuclear wave function may be written as

$$\psi = \psi^{(\pi)} + \zeta \psi^{(\pi')} , \qquad (1)$$

where $\pi \neq \pi'$. Parity mixing gives rise to irregular electromagnetic transitions $\pi_i \rightarrow \pi_f$' and $\pi_i' \rightarrow \pi_f$, in addition to the regular transition $\pi_i \rightarrow \pi_f$. The interference term is proportional to the ratio of the amplitudes of the irregular and regular transitions

$$\frac{\text{irregular}}{\text{regular}} = \frac{\zeta \langle \psi_f^{(\pi_f)} | H | \psi_i^{(\pi_i')} \rangle + \langle \psi_f^{(\pi_f')} | H | \psi_i^{(\pi_i)} \rangle}{\langle \psi_f^{(\pi_f)} | H | \psi_i^{(\pi_i)} \rangle} = \zeta R.$$

The ^{180}Hf level scheme is illustrated in Fig. 1.[8] The 8^- isomeric level is characterized as K = 8. The 501-keV transition to the 6^+ level of the K = 0 ground-state rotational band is of mixed E3/M2 multipolarity, with $\langle E3 \rangle / \langle M2 \rangle = +5.3 \pm 0.3$.[7] The parity nonconserving interaction is expected to admix a small 8^+ component into the 1.142 MeV 8^- level. The close spacing between the 8^- level and the 8^+ level at 1.084 MeV tends to magnify the admixture; in addition, the regular (parity conserving) E3 and M2 components of the 501-keV radiation field are strongly hindered, resulting in a relative enhancement of any possible irregular component.

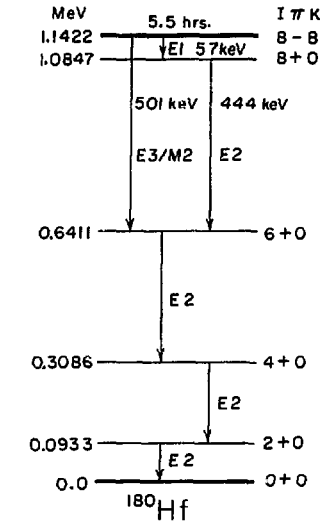

Fig. 1. Decay scheme of $^{180}Hf^{m}$. (XBL 741-2204)

The angular distribution of gamma radiation from an oriented nucleus is described by

$$W(\theta) = \sum_k Q_k B_k U_k A_k P_k(\cos\theta). \qquad (3)$$

For odd k,

$$A_k = \frac{2\varepsilon}{1+\delta^2} [F_k(LLI_fI_i) + \delta F_k(LL'I_fI_i)],$$

where the F_k are the F-coefficients. Here ε is the ratio of the irregular to regular matrix elements, in this case $\langle E2 \rangle / \langle M2 \rangle$, and δ is the $\langle E3 \rangle / \langle M2 \rangle$ mixing ratio. The asymmetry α is defined as

$$\epsilon = 2\,\frac{W(180°) - W(0°)}{W(180) + W(0)}$$

$$= -\,2\,\frac{Q_1 B_1 A_1 + Q_3 B_3 A_3}{1 + Q_2 B_2 A_2 + Q_4 B_4 A_4}\,. \qquad (5)$$

In the present experiment the asymmetry ϵ of the 501 keV gamma ray has been determined and the irregular-to-regular mixing ratio δ has been deduced.

The low temperatures necessary to polarize the nuclei were produced by the demagnetization of chromium potassium sulfate (chrome alum) salt prepared in a glycerin slurry. Thermal contact to the salt slurry was achieved by means of 16 sheets of 0.13 mm (5 mil) copper foil. A schematic view of the apparatus is shown in Fig. 2. The sample temperature was monitored using a ^{60}Co(Fe) thermometer; the anisotropy of the angular distribution of the gamma rays following the ^{60}Co decay was used to deduce the temperature. The data were written onto magnetic tape in the form of 1024-channel gamma-ray spectra. Each spectrum corresponds to the results of counting with a single detector at a given position of the applied field for a period of approximately 10 minutes. Also written onto the magnetic tape were markers defining the positions of the 444-keV and 501-keV peaks along with the positions of appropriate regions of background.

The results of this experiment represent data from 4 different samples, each of which was counted during two half-lives. Representative temperatures

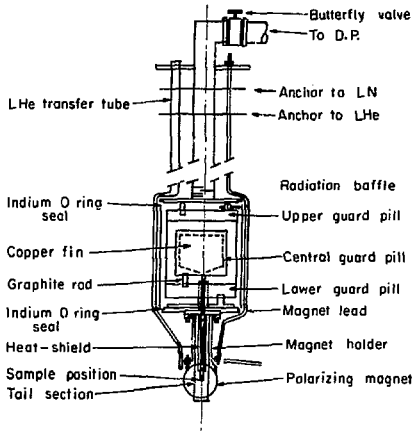

Fig. 2. The low-temperature cryostat and dewar system. (XBL 741-2063)

at which three of the four samples were run were 16 mK, 17 mK, and 22 mK; a fourth sample was observed at temperatures in the range 16-28 mK. The results are summarized in Table 1.

Table 1. Parity nonconserving asymmetry of the ^{180}Hf 501-keV gamma-ray.

Sample No.	Temperature	Detector No.	Source-to-Detector Distance(cm)	Detector Orientation	Asymmetry[a]	$\lvert\epsilon\rvert$[a]
1	16-28 mK	A	22	270°		0.0464 (59)
		B	20	0°		0.0378 (68)
		C	10	90°		0.0464 (64)
		D	11	180°		0.0252 (63)
2	16 mK	A	30	180°	0.0160 (40)	0.0293 (75)
		B	11	270°	0.0100 (28)	0.0184 (52)
		C	12	90°	0.0138 (27)	0.0252 (50)
		D	13	0°	0.0167 (44)	0.0296 (81)
3	22 mK	A	27	270°	0.0111 (30)	0.0244 (67)
		B	10	180°	0.0068 (25)	0.0151 (55)
		C	12	0°	0.0131 (23)	0.0290 (52)
		D	13	90°	0.0111 (33)	0.0244 (73)
4	17 mk	A	17	270°	0.0127 (47)	0.0281 (89)
		B	9	90°	0.0129 (49)	0.0283 (92)

[a]The statistical uncertainties of the last two digits are indicated in parenthesis.

The weighted average value of ε based on the data of Table 1 is ε = - 0.029±0.002. Computing the normalized chi-squared value of the 14 individual measurements of ε, we obtain $\chi^2 = 2.3$. This value is somewhat large, and perhaps suggests a systematic source of error in the data. We allow for the possibility of some as yet unknown source of systematic error by increasing the individual statistical uncertainties by a factor of 1.5 The final result of the present experiment is compared with those of previous studies in Table 2. In doing the comparison, all results have been evaluated using δ = + 5.3. The weighted average of the six results to date is ε = - 0.032±0.002 ($\chi^2 = 1.0$).

Table 2. Comparison of results on parity nonconservation in the 501-keV transition of ^{180}Hf.

Method[a]	ε = ⟨E2⟩ / ⟨M2⟩	Reference
P_γ	-0.041±0.007	Jenschke and Bock, ref.4
P_γ	-0.033±0.009	Lipson, Vanderleeden, and Boehm, ref. 5
P_γ	-0.029±0.006	Kuphal, ref. 6
γ(θ)	-0.038±0.004	Krane, Olsen, Sites, and Steyert, ref. 7
γ(θ)	-0.031±0.003	Krane, Olsen, and Steyert,[b]
γ(θ)	-0.029±0.003	present work

[a] P_γ = circular polarization of *gamma* radiation from a randomly source; γ(θ) = angular distribution asymmetry from a polarized source.

[b] K. S. Krane, C. E. Olsen, and W. A. Steyert, Phys. Rev. C5, 1663 (1972).

The case of ^{180}Hf thus represents the only nucleus for which consistent evidence of parity nonconservation has been obtained from different methods and from independent investigations. Possible evidence has been found in other cases, but there is in general a lack of agreement among the various results. The present results are entirely consistent with the other published results for ^{180}Hf and support the evidence for parity nonconserving effects in this nucleus.

Footnotes and References

1. R. P. Feynman and M. Gell-Mann, Phys. Rev. 109, 193 (1958).

2. M. Gell-Mann, Rev. Mod. Phys. 31, 834 (1959).

3. R. J. Blin-Stoyle, Phys. Rev. 118, 1603 (1960).

4. P. Jenschke and P. Bock, Phys. Letters 31B, 65 (1970).

5. E. D. Lipson, F. Boehm, and J. C. Vanderleeden, Phys. Letters 34B, 307 (1971).

6. E. Kuphal, Z. Phys. 253, 314 (1972).

7. K. S. Krane, C. E. Olsen, J. R. Sites, and W. A. Steyert, Phys. Rev. C4, 1906 (1971).

8. C. M. Lederer, J. M. Hollander, and I. Perlman, Table of Isotopes (New York, Wiley, 1967).

NUCLEAR ORIENTATION STUDIES OF ^{241}Am AND ^{255}Fm

A. J. Soinski and D. A. Shirley

Nuclear orientation results for ^{253}Es substituted into a single crystal of neodymium ethylsulfate (NES) were reported earlier.[1] The expected similarity between the electronic ground states of the analogous lanthanide and actinide trivalent ions, as exemplified by similar hyperfine interaction parameters, was confirmed for the pair Ho^{3+} - Es^{3+}. Nuclei of trivalent Eu ions have also been aligned in NES by means of the electric hyperfine ineraction between the nuclear quadrupole moment and the electric field gradient arising from both the open f-electron shell and the lattice charges.[3] *Judd et al.*[2] proposed that distortion of the closed electronic shells by the lattice charges increased or antishielded the crystal field gradient at the nucleus. This unexpected result suggested that americium should also be studied. *Sternheimer*[3] and later *Gupta and Sen*[4] predicted that the lattice antishielding factor, γ_∞, is larger for Am^{3+} than for Eu^{3+}; therefore appreciable alignment of Am^{3+} would be expected. In this paper we report nuclear orientation experiments on ^{241}Am. The data are interpreted in terms of both the crystal field parameters and the relative amplitudes and phases of the alpha waves in the favored decay to ^{237}Np. As in ^{253}Es, the relative s-d phase in ^{241}Am favored decay is positive. We also report results for ^{255}Fm in NES. We find that the s and d waves are also in phase in this case. Because of the short half-life (20.1 *h*) and the limited mass available, the statistical accuracy was not high enough to permit the extraction of the sign of the relative s-g wave phase. The similar electronic ground state of the pair Er^{3+} - Fm^{3+} confirmed.

The experimental ^{241}Am alpha particle angular distribution measured at 0° and 90° with respect to the NES c-axis as a function of the inverse temperature is shown in Fig. 1. Details of the experimental technique have been given in Ref. 1. The linear temperature dependence of W(θ) at higher temperatures is characteristic of electric quadrupole alignment. The angular distribution function has the form

$$W(\theta) = 1 + A_2(\ell\ell' I_f I_i) Q_2 B_2(I_i,T)\ (3\cos^2\theta - 1)/2. \qquad (1)$$

and $B_2(I_i,T) \propto 1/T$ at high temperatures for quadrupole alignment.

In order to determine accurately the value of the quadrupole coupling constant, P, it is necessary that the temperature be low enough such the $P \gg KT$, where k is Boltzmann's constant. Then curvature develops in the W(θ) vs. 1/T curve. Since sufficiently low temperatures were not possible using NES as a host, our value for P of -0.0033(6) cm^{-1} (P/k = - 0.0048(8)K) lacks precision. The negative sign implies that the nuclear magnetic substates $I_z = \pm 5/2$ lie lowest in energy. Detailed analysis of this result indicates that $\gamma_\infty \approx -100$ and that the shielding constant $\sigma_2(Am^{3+}) = 0.7$, in agreement both with theoretical estimates and with the Eu^{3+} value of 0.72.[5]

The α phase shifts are the sum of the intrinsic phases on the nuclear surface plus the phase shifts that occur upon transmission through the combined Coulomb and quadrupole barriers. The intrinsic phases are taken from the microscopic shell model theory;[6] namely, the s, d, and g waves are all in phase but the i wave is out of phase. The

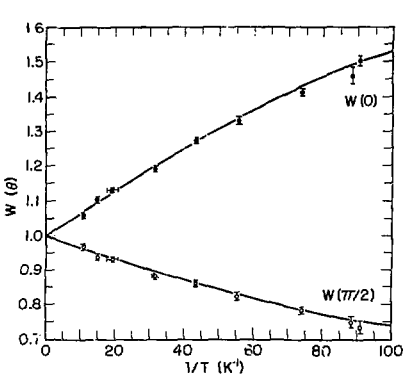

Fig. 1. ^{241}Am in neodymium ethylsulfate (NES) alpha particle angular distribution at 0° and 90° with respect to the crystalline c-axis as a function of the inverse temperature. (XBL 745-3063)

Coulomb barrier phase shift difference for alpha decay is

$$\sigma_{\ell+2} - \sigma_\ell = \tan^{-1}\frac{\eta}{\ell+1} + \tan^{-1}\frac{\eta}{\ell+2}$$

where η is the argument of the Coulomb functions. For ^{241}Am the d wave lags the s wave by approximately 7° and the g wave lags the s wave by approximately 23.5°. The quadrupole phase shifts for ^{241}Am would be additive to the Coulomb phase shifts except for the i wave.

In order to compare theory with experiemnt we write

$$W(\theta)_{expt.} = 1 + R[Q_2A_2B_2P_2(\cos\theta) + Q_4A_4B_4P_4(\cos\theta)].$$

Higher-order Legendre polynomials are excluded for the decay of a spin 5/2 state. The factor R is an anisotropy reduction factor accounting for the fact that not all ^{241}Am nuclei are at rare-earth sites in the NES lattice. The solid curve in Fig. 1 was obtained using P = - 0.0033 cm^{-1}, $RA_2 = 0.54$ and $RA_4 = 0.05$.

Three different estimates are available for the partial wave amplitudes.[6-8] The resulting A_2 and A_4 coefficients are tabulated in Table 1. The fact that W(0) > 1 means that the s and d waves are in phase for ^{241}Am, in confirmation of the shell model calculations. Our experimental results do not

Table 1. Coefficients A_2 and A_4 for the ^{241}Am in NES angular distribution function $W(\theta) = 1 + R[A_2Q_2B_2P_2(\cos\theta) + A_4Q_4B_4P_4(\cos\theta)]$.

BFM theory,[a] s and g waves in phase	0.7747	0.0756
BFM theory, s and g waves out of phase	0.7477	0.0483
BFM theory, Chasman and Rasmussen correction,[b] s and g waves in phase	0.8668	0.1032
BFM theory, Chasman and Rasmussen correction, s and g waves out of phase	0.8390	0.0770
Mang theory,[c] s and g waves predicted to be in phase	0.7838	0.0847
Mang theory but with s and g waves out of phase	0.7598	0.0597

[a] Ref. 7.
[b] Ref. 8.
[c] Ref. 6.

establish the relative s-g wave phase (predicted to be positive), primarily because of the weakness of the g wave. Therefore Table 1 includes the A_2 and A_4 values for both relative g wave phases.

We now briefly discuss the ^{255}Fm NO results. Paramagnetic resonance studies[9] of Er^{3+}, the lanthanide analogue of Fm^{3+}, diluted in lanthanum ethylsulfate, yielded the hf interaction parameters $|A| = 0.0052(1)$ cm^{-1}, $|B| = 0.0314(1)$ cm^{-1} and $|P| = 0.0030(3)$ cm^{-1}. For $|B| > |A|$ the nuclear magnetic substates are admixed except when $|k| = I + 1/2$ where $k = I_z + S_z$ where $S_z = \pm 1/2$. The levels labeled by $+k$ and $-k$ are degenerate except when $k = 0$. The ground state for a half integral nuclear spin is a singlet $(|1/2, -1/2\rangle - |-1/2, 1/2\rangle)/\sqrt{2}$, and a doublet lies closely above. The alignment may be regarded as being in a plane perpendicular to the crystalline c-axis, and the degree of alignment is relatively small.

The experimental α-particle angular distribution from ^{255}Fm nuclei aligned in NES is shown in Fig. 2. The statistical accuracy of the results is limited by the low degree of alignment, the mass of ^{255}Fm available (~ 200 disintegrations/m), and the short half-life. The shape of the anisotropy curve yields a value for $|B|$ of 0.035(7) cm^{-1} or $|B|/k = 0.05(1)$ K. We could not determine the value of $|B| / |A|$, but as for Er^{3+}, the temperature dependence of W(0) establishes that the magnitude of B is greater than that of either A or P.

For non-axial alignment the counting rate along the c-axis decreases for a positive s-d phase. From Fig. 2 it is seen that this is the case. The solid curve in Fig. 2 was obtained using our value for $|B|$ with $|A| = 0$ and the relative amplitudes and phases given by Poggenburg[6] for the favored decay to the 7/2+[613] rotational band in ^{251}Cf. On the basis of NO experiments on ^{253}Es,[1] the negative relative phase should be correct.

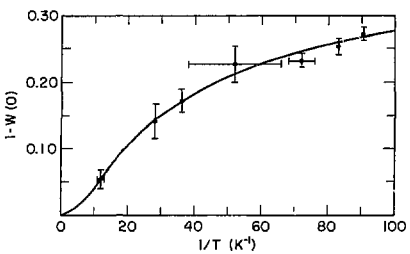

Fig. 2. ^{255}Fm in NES alpha particle angular distribution at 0° with respect to the crystalline c-axis as a function of the inverse temperature.
(XBL 745-3064)

In summary, the orientation of trivalent actinide elements in the neodymium ethylsulfate lattice is straighforward. The four elements Am, Cf, Es and Fm have been oriented in this way. It is difficult, however, to study α-particle angular distributions with precision. The results reported here for ^{241}Am and ^{255}Fm are sufficiently quantitative to establish that the s and d waves in the favored transitions are in phase, but they do not permit the determination of the relative s-g wave phase. The orientation data yielded definitive information about the electronic ground states of both Am^{3+} and Fm^{3+}. In $Am^{3+}(5f^6)$ as in $Eu^{3+}(4f^6)$, quadrupole coupling dominated the nuclear orientation, and the antishielded crystal field term A_0^2 was the main contributor to the electric field gradient. The data strongly support a large negative Sternheimer antishielding factor, $\gamma_\infty \approx -10^2$, and they also indicate a shielding constant $\sigma_2 \approx 0.7$, in good agreement with an earlier value for Eu^{3+}. In $Fm^{3+}(5f^{12})$, as in $Er^{3+}(4f^{11})$, the electronic ground-state in the ethylsulfate lattice has $|B| > |A|$.

References

1. A. J. Soinski, R. B. Frankel, W. O. Navarro and D. A. Shirley, Phys. Rev. C2, 2379 (1970).

2. B. R. Judd, C. A. Lovejoy and D. A. Shirley, Phys. Rev. 128, 1733 (1962).

3. R. M. Sternheimer, Phys. Rev. 159, 266 (1967).

4. R. P. Gupta and S. K. Sen, Phys. Rev. A7 850 (1973) and S. K. Sen, private communication, 1973.

5. J. Blok and D. A. Shirley, Phys. Rev. 143, 278 (1966).

6. J. K. Poggenburg, H. J. Mang and J. O. Rasmussen, Phys. Rev. 181, 1697 (1969) and J. K. Poggenburg, Jr., Lawrence Radiation Laboratory Report UCRL-16187 (1965) (unpublished).

7. A. Bohr, P. O. Fröman and B. R. Mottelson, Dan. Mat. Fys. Medd. 29 no.10 (1955).

8. R. R. Chasman and J. O. Rasmussen, Phys. Rev. 115, 1257 (1959).

9. G. S. Bogle, H. F. Dufus and H. E. D. Scovill, Proc. Phys. Soc. (London) A 65, 760 (1952).

PARAMAGNETIC SHIFTS AND SPIN-FLOP IN SUPERTRANSFERRED HYPERFINE STRUCTURE OF ^{111m}Cd IN $RbMnF_3$

H. H. Rinneberg, G. P. Schwartz, and D. A. Shirley

We have measured the time differential PAC of ^{111m}Cd doped into paramagnetic, polycrystalline $RbMnF_3$, $KFeF_3$, $KCoF_3$, and $KNiF_3$ in order to obtain the sign of the supertransferred hyperfine field at the Cd nucleus. Shown in Fig. 1 are the spectra for $RbMnF_3$ that were observed at 300 K and 87 K (close to the Néel point T_N = 83 K), with an external field H_{ext} = 31.3 kOe applied perpendicular to the detector axis. In Fig. 1 the perturbation factor [1] , $A_{22}G_{22}(t) = A_{22}(0.25 + 0.75\cos(4\pi\nu_L t)$ is shown for ^{111m}Cd in $RbMnF_3$ and for a diamagnetic standard ($CdCl_2$ solution) in the same external field. The higher frequency of ^{111m}Cd in $RbMnF_3$ corresponds to a higher effective field $H_{eff} = H_{ext} + H_{ex} + \Delta H$. This paramagnetic shift arises from a supertransferred contact field at the Cd nucleus created by polarization of the Mn^{2+} electron spin S = 5/2. Since the electronic spin fluctuations are fast compared to the characteristic time of the PAC experiment, only the effect of the time average $\langle S_z \rangle$ is seen. Therefore, $\Delta H = H_{hf}(4°\text{ K})\ \langle S_z \rangle / S$, where $H_{hf}(4°\text{ K})$ = 116 kOe is taken as the low-temperature limit of the hyperfine field at the Cd nucleus in the antiferromagnetic state and $\langle S_z \rangle = 2.5$ has been used as the local value of $\langle S_z \rangle$ for T = 4° K. The spin expectation value $\langle S_z \rangle = (-\chi_m H_{ext})/(g\beta N_1)$ in the paramagnetic state can be estimated using the molar susceptibility $\chi_m = C/(T+\theta)$. In this way we estimate for ^{111m}Cd in $RbMnF_3$, at 87° K, ΔH_{est} = + 2.0 kOe compared to ΔH_{obs} = + 3.0±0.5 kOe. The lower susceptibility at room temperature corresponds to a smaller paramagnetic shift (Fig. 1). The following relative shifts $\Delta H/H_{ext}$ were observed; $RbMnF_3$: +9.6±1.6% (87°K), +5.1±1.6% (300°K); $KFeF_3$: +5.4±2.2% (120°K); $KCoF_3$: + 4.5±1.6% (120°K) and $KNiF_3$: + 1.3±1.6% (265°K). Because of lower susceptibilities, smaller paramagnetic shifts were observed in $KFeF_3$, $KCoF_3$ and $KNiF_3$ compared to $RbMnF_3$/Cd. For $KniF_3$ the large values of θ and T_N led to a paramagnetic shift that lay within our experimental error. The experiments reported here are analogous to paramagnetic shift measurements that have been made on F nuclei in these lattices using NMR.

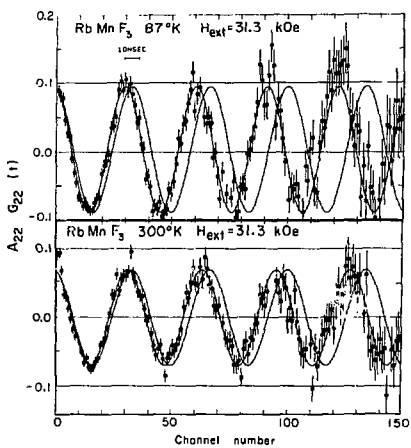

Fig. 1. PAC of ^{111m}Cd in paramagnetic $RbMnF_3$, compared to a diamagnetic standard ($CdCl_2$ solution) in the same external field H_{ext} = 31.3 kOe.
(XBL 748-3990)

$RbMnF_3$ has an exceptionally low critical field H_c = 2.45 kOe for the spin-flop transition. Above this value the spin axis lies perpendicular to the external field. In polycrystalline $RbMnF_3$/Cd (4° K)

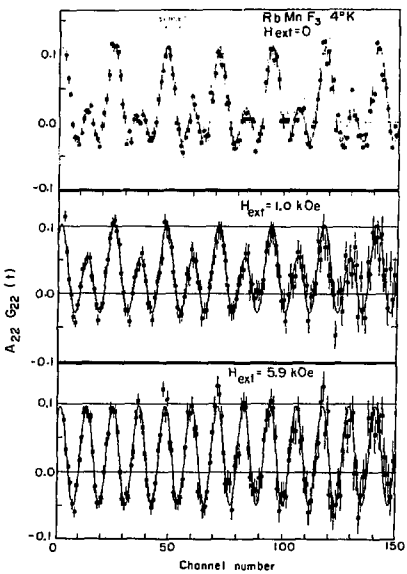

Fig. 2. Spin-flop transition in $RbMnF_3$ detected by PAC of ^{111m}Cd.
(XBL 748-3991)

the hyperfine fields at the Cd are randomly oriented for $H_{ext} = 0$, whereas they are confined in a plane perpendicular to the external field for $H_{ext} > H_c$. Since PAC is sensitive to the orientation of the hyperfine fields relative to the detector axis, this method lends itself to the observation of the spin-flop transition, as shown (Fig. 2). The time spectra were taken with the detectors at 180° parallel to H_{ext}. In this case the perturbation factor can be written as $A_{22}G_{22}(t) = A_{22}(1-b_1-b_2 + b_1\cos(2\pi\nu_L t) + b_2\cos(4\pi\nu_L t))$. The Fourier coefficients b_1, b_2 are equal for the random distribution $b_1 = b_2 = 0.4$ ($H_{ext} = 0$) and $b_1 = 0$, $b_2 = 0.75$ if the hyperfine fields are in a plane perpendicular to H_{ext}. The spin-flop transition was observed as a change in the ratio b_1/b_2 of the Fourier coefficients (Fig. 2). Since a polycrystalline sample was used, the transition is fairly smeared out; for a precise determination of H_c a single crystal should be used.

Footnotes and References

*Condensed version of a paper submitted to Journal of Physics Letters A.

1. H. Frauenfelder and R. M. Steffen, In Alpha-, Beta-, and Gamma-Ray Spectroscopy, ed. by K. Siegbahn (North-Holland, 1965), Vol. 2.

PERTURBED ANGULAR CORRELATION OF ^{111m}Cd IN ANTIFERROMAGNETIC MnS UNDER EXTERNAL PRESSURE*

H. H. Rinneberg, G. P. Schwartz, and D. A. Shirley

We have recently extended our program of PAC studies in insulating antiferromagnets by building a clamping type pressure cell with partially scooped out windows for easy gamma-ray exit. The spin density transferred by covalency and overlap effects from the metal ions into the cadmium impurity is sensitive to the bond distance and hence to the external pressure. One can qualitatively estimate the fractional shift in the observed hyperfine field using $\Delta H/H_{4.2°K} = \frac{1}{3}\gamma_m \Delta p K_T = 4.2$, where γ_m is the magnetic Gruneisen parameter, p the pressure, and K_T the isothermal compressibility. Because the isothermal compressibility at 4.2°K is not available for MnS, our estimate for the relative field enhancement using the room temperature value will represent an upper limit. At a pressure of 20 kbar this estimate gives an 8% effect, while the measured shift shown in Fig. 1 at 4.2°K is 3.8%. The spectrum for polycrystalline MnS at zero pressure and 4.2°K is shown for comparison, and the shift to a higher frequency is readily apparent.

We would like to thank Duane Newhart for valuable assistance in both the design and construction of the pressure cell. We would also like to acknowledge Drs. S. D. Bader, G. Kaindl, and R. Schock for many helpful discussions concerning pressure effects.

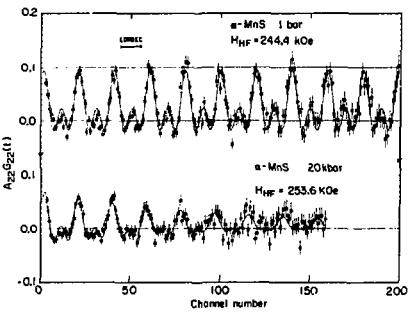

Fig. 1. (XBL 751-2078)

Footnote

*Condensed version of a paper submitted to Physics Letters A.

PERTURBED ANGULAR CORRELATION OF ^{111m}Cd IN ANTIFERROMAGNETIC INSULATORS*

H. H. Rinneberg, G. P. Schwartz, and D. A. Shirley

The time differential perturbed angular correlation of ^{111m}Cd doped into various antiferromagnetic insulators has been observed. From the experimentally determined perturbation factors the internal magnetic fields and electric field gradients at the cadmium nucleus are deduced (Table 1). Most of the observed magnetic fields, ranging from approximately zero kOe in $KCuF_3$ to 245 kOe in MnS can be understood at least qualitatively. A low field is to be expected for $KCuF_3$ because of the spin structure and the ground state wavefunction of Cu^{2+} in this lattice. The effective local environment of the cadmium impurity is the same for $RbMnF_3$, MnO, and MnS. From a comparison of the deduced hyperfine fields 114 kOe ($RbMnF_3$), 202 kOe (MnO), and 250 kOe (MnS), the covalency of the intervening anion is seen to affect the transfer of unpaired spin density from the magnetic ions into the s shells of the cadmium impurity. Similarly in the isomorphic compounds Rb_2MnF_4 (H_{int}=69.6 kOe) and Rb_2MnCl_4 (H_{int}=98.4 kOe) the more covalent chloride shows the larger field. Contrary to Rb_2MnCl_4, where the spin density is transferred along linear Mn^{2+}-Cl^--Cd^{2+} exchange paths, in $FeCl_2$ and $CoCl_2$ the impurity is connected to the nearest magnetic neighbors by angular Mn^{2+}-Cl^--Cd^{2+} bonds with a bond angle close to 90°. Because of the reduced overlaps of the orbitals involved in the spin transfer, internal fields close to zero are observed in $FeCl_2$ and $CoCl_2$.

Table 1. Hyperfine fields and quadrupole interactions of ^{111m}Cd in various antiferromagnets.

	T_n °K	H_{exp} kOe	H_{Hf} kOe	ν_Q mHz	η
$KCuF_3$	20,38	4		19.0	0.72
$KNiF_3$	253	104.8±1.5	104.8	0	0
$KCoF_3$	114	74.1±1.5	74.1	0	0
$RbCoF_3$	~ 101	67.8±1.5	67.8	0	0
$TlCoF_3$	94	67.9±1.5	67.9	0	0
$KFeF_3$	112.5	100.1±1.5		0	0
$KMnF_3$	~ 95	102.6±1.5		0	0
$RbMnF_3$	83	113.8±1.5	113.8	0	0
$TlMnF_3$	76	118.7±1.5	118.7	0	0
K_2NiF_4	97	54.9±1.5	55.8	3.7	0
Rb_2NiF_4	~ 95	51.3±2.5	52.1	7.4	0
K_2CoF_4	107	51.5±2.5	52.7	5.5	0
Rb_2CoF_4	101	48.9±2.5	50.0	8.2	0
K_2MnF_4	~ 45	71.6±2.5	73.3	3.4	0
Rb_2MnF_4	38.5	67.9±2.5	69.6	4.7	0
$FeCl_2$	23.5	4.8±2.0			
$CoCl_2$	25	~ 0 ±2.0			
Rb_2MnCl_4	57	97.4±2.5	98.4	8.1	0
NiO	~ 520	191±2.5	196	0	0
CoO	~ 293	171±2.5	177	0	0
MnO	~ 118	195±2.5	202	0	0
K-MnS	156	245.2±1.5	250	0	0

It is interesting to compare the hyperfine fields in the perovskites and the corresponding quadratic layered fluorides, especially $KNiF_3$ and K_2NiF_4 or $RbMnF_3$ and Rb_2MnF_4. In $KNiF_3$ and $RbMnF_3$ the impurity is octahedrally surrounded by six nearest magnetic neighbors belonging to the same magnetic sublattice in the antiferromagnetic state. In the layered fluorides K_2NiF_4 and Rb_2MnF_4 however, only the four nearest magnetic neighbors in the (001) plane contribute to the hyperfine field. Therefore, without taking the zero point spin deviations of the two and three dimensional antiferromagnets into account, the hyperfine field in K_2NiF_4 should be approximately 2/3 of the value found in $KNiF_3$, yielding 75.8 kOe compared to the experimental value of 55.8 kOe. The theoretical value for the zero point spin deviation in a pure three dimensional antiferromagnet is $\langle S_z \rangle = S - \Delta_0$ where $\Delta_0 = 0.0788$. A larger deviation is expected in two dimensional antiferromagnets, where a value of $\Delta_0 = 0.20 \pm 0.03$ has been observed for K_2NiF_4. Since the hyperfine field at the cadmium impurity is proportional to $\langle S \rangle / S$, the larger spin deviation for the layered fluoride K_2NiF_4 compared to the perovskite $KNiF_3$ will result in a lower hyperfine field for K_2NiF_4 compared to the value of 75.8 kOe which considers the number of nearest magnetic neighbors only. Assuming for the magnetic ions next to the impurity the spin reductions known for the pure antiferromagnets, a field of 60.6 kOe is expected in K_2NiF_4. In this way most of the experimentally observed reduction (75.8-55.8=20 kOe) can be explained. Similar effects were found for $RbMnF_3$ and Rb_2MnF_4. However, because of the larger spin S = 5/2 of manganese, the reductions are considerably smaller.

The temperature dependence of the hyperfine field in $RbMnF_3$ and the internal field in MnF_2 is shown in Fig. 1. For comparison we include the MFA Brillouin function for S = 5/2 and the temperature dependence of the sublattice magnetization for MnF_2. In MnF_2 the internal field at the impurity has to be corrected for a dipolar contribution to obtain the supertransferred hyperfine field. The unpaired spin density in Cd s shells is caused by two nearest magnetic neighbors of one sublattice and eight next nearest magnetic neighbors belonging to the other sublattice, with the latter most likely dominating. Although the relative sign of the dipolar and hyperfine fields is not known, the dipolar field is at most a 20% correction and is expected to have the same temperature dependence as the hyperfine field. Therefore the ratio

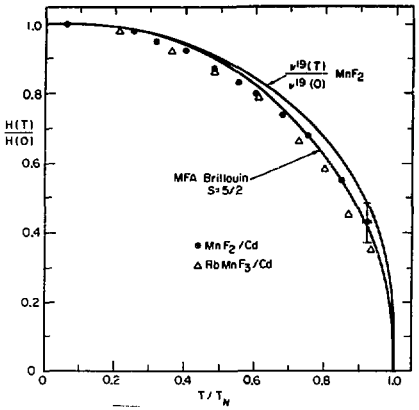

Fig. 1. (XBL 751-2075)

$H_{int}(T)/H_{int}(0)$ reflects to a good approximation the temperature dependence of the supertransferred hyperfine field. Since for MnF_2 $|J_{nnn}| >> |J_{nn}|$, the replacement of a Mn ion by the diamagnetic impurity demagnetizes the second nearest neighbors and the internal field is expected to decrease faster with increasing temperature than the host magnetization. Although the error of the experimentally determined internal field is rather large due to the presence of a combined ineraction, the ratio $H_{int}(T)/H_{int}(0)$ is seen to lie systematically below the corresponding ratio for the host magnetization.

Footnote

*Condensed version of a paper submitted to Journal of Chemical Physics

INITIAL-STATE CONFIGURATION-INTERACTION SATELLITES IN THE PHOTOEMISSION SPECTRUM OF Cd*

S. Süzer and D. A. Shirley

The photoemission spectrum of atomic cadmium ($4d^{10}5s^2;{}^1S$) should show three peaks below 20 eV, at binding energies[1] of 8.99, 17.58, and 18.28 eV, arising repsectively from transitions to the ($d^{10}s;{}^2S$), ($d^9s^2;{}^2D_{5/2}$)and ($d^9s^2;{}^2D_{3/2}$) final states in Cd^+. In addition to these three lines, we have also observed two weaker peaks at 14.44(3) and 14.79(3) eV in high-temperature ultraviolet photoemission studies on atomic Cd. These latter peaks are assigned to the ($d^{10}p;{}^2P_{1/2}$) and ($d^{10}p;{}^2P_{3/2}$) states, respectively. Their presence in the spectrum is attributed to photoemission of an np($n \geq 5$) electron from ($d^{10}5pnp;{}^1S$) components that are mixed into the nominal ($d^{10}s^2;{}^1S$) ground state by configuration interaction, forming the eigenstate

$$\Psi({}^1S) = a\,|\,d^{10}s^2;{}^1S\rangle + \sum_{n\geq 5} |d^{10}5pnp;{}^1S\rangle + \cdots .$$

The experiments were carried out with 21.2 eV HeI radiation at 663 °K, using the high-temperature probe in a Perkin-Elmer P.S. 18 Ultraviolet Photoelectron Spectrometer. A typical spectrum is shown in Fig. 1. Derived parameters, based on average values from three separate runs, are given in Table 1.

Configuration-interaction satellite lines in photoemission spectra have been observed as "shake-up" peaks in gases[2] and solids[3] and as satellites in multiplet spectra.[4] Such satellites are usually interpreted as arising from final-state configuration interaction. They therefore have the same

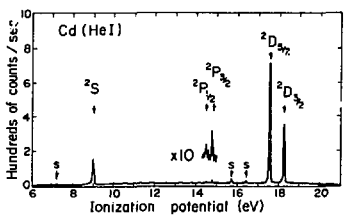

Fig. 1. Photoemission spectrum of Cd vapor at 633°K using 21.2 eV HeI radiation. The whole spectrum took 2.5 h to scan. Lines marked "s" arise from the HeI 23.08 eV radiation (i.e., $1s3p(^1P) \rightarrow 1s^2$). (XBL 742-2470)

Table 1. States of Cd^+ observed in photoemission from Cd vapor.

Final state	Apparent relative intensity[a]	Binding energy, eV[a]	Energy from optical data[b]
$4d^{10}5s\ {}^2S$	(1)	8.96(2)	8.991
$4d^{10}6p\ {}^2P_{1/2}$	0.03(1)	14.44(3)	14.463
$4d^{10}6p\ {}^2P_{3/2}$	0.06(1)	14.79(3)	14.771
$4d^{9}5s^2\ {}^2D_{5/2}$	2.5(2)	17.57(2)	17.578
$^2D_{3/2}$	1.3(2)	18.28(2)	18.276

[a]This work. Values given are averages of three runs. Errors in last place are given parenthetically. The Xe lines at 12.130 and 13.436 eV and the argon lines at 15.759 and 15.937 eV were used for calibration.
[b]Ref. 1.

symmetry as the main final-state peak (this result is also discussed as an "E0" selection rule for shake-up "transitions"). The Cd^+ satellites are strictly forbidden by this selection rule.[5] They arise instead from initial-state configuration interaction.

Footnotes and References

*Condensed from LBL-Publication J. Chem. Phys. 61, 2481 (1974).

1. C. E. Moore, Natl. Bur. Std. (U.S.) Circ. 467, Vol. 3 (1962).

2. M. O. Krause, T. A. Carlson, and R. D. Dismukes, Phys. Rev. 170, 37 (1968).

3. T. Novakov, Phys. Rev. B3, 2693 (1971); A. Rosencwaig, G. K. Wertheim, and H. J. Guggenheim, Phys. Rev. Lett. 27, 479 (1971).

4. C. S. Fadley, D. A. Shirley, A. J. Freeman, P. S. Bagus, and J. R. Mallow, Phys. Rev. Letters 23, 1397 (1969); S. P. Kowalczyk, L. Ley, R. A. Pollak, F. R. McFeely, and D. A. Shirley, Phys. Rev. B7, 4009 (1973).

5. This statement is rigorously true only if the "final state" is that of the Cd^+ ion alone. If the system (ion plus outgoing electron) is considered, the $Cd^+ {}^2P_{1/2}$ and $^2P_{3/2}$ states are accessible if the photoelectron leaves in a continuum s state ("conjugate skae-up"). Earlier work indicated that the cross section for this process would be very small in He (R. L. Brown, Phys. Rev. A1, 341 (1970) and Ne (F. Wuilleumier and M. O. Krause, In "Electron Spectroscopy," edited by D. A. Shirley (North-Holland, 1972), p. 259). Recently, however, J. Berkowitz et al. (private communication) have found that this process is more important in Hg. If its importance in Cd is intermediate, conjugate shake-up would account for several percent of the intensity of the $^2P_{1/2}$ and $^2P_{3/2}$ lines.

X-RAY PHOTOEMISSION MOLECULAR ORBITALS OF HYDROGEN FLUORIDE AND THE FLUORINATED METHANES*

M. S. Banna, B. E. Mills, D. W. Davis, and D. A. Shirley

The development of molecular photoelectron spectroscopy[1,2] has made it possible to establish the binding energies of individual molecular orbitals (MO's). Detailed analyses of spectra can yield further information concerning the electronic structure of the molecule. For example, Gelius[3] has proposed that x-ray photoemission (XPS) cross sections of MO's should be given approximately by a sum of atomic orbital (AO) cross sections, weighted according to the electronic contribution of each AO to the MO in question. This is reasonable since, for x-ray energies, the major contribution to the cross-section comes from electrons in the region near the nuclei where there is substantial overlap between the photoelectron and orbital wave functions. The work reported below was undertaken to acquire some insight into the usefulness of the Gelius model. The fluorinated methanes were chosen as the model system because they have already been studied by UPS and are large enough to be challenging but small enough to be tractable, both spectroscopically and theoretically.

Samples were obtained from Matheson Gas Co. and studied in the gas phase with the Berkeley Iron-Free Spectrometer.[4] They were irradiated with Mg $K\alpha_{1,2}$ (1.2536 keV) or Al $K\alpha_{1,2}$ (1.4866 keV) x-rays using sample pressures of 50 to 100 microns. The binding energies were referenced by bleeding in neon simultaneously with the gas under study.

Orbital Binding Energies

The XPS molecular orbital spectra of HF and the five gases $CH_{4-n}F_n$ ($0 \leq n \leq 4$) are shown in Fig. 1. The measured binding energies, $E_B(MO)$ are given in Table 1 and compared to the vertical binding energies measured by UPS.[5,6] The agreement between the two sets of values is generally excellent, in most cases within 0.1 or 0.2 eV.

Comparison of experimental $E_B(MO)$ values with theory is less straightforward, because self-consistent field calculations of the molecular ground states yield only the orbital energies, $\epsilon(MO)$, rather than actual binding energies, $E_B(MO)$, of the molecular orbitals. Table 1 lists the results of *ab initio* calculations by Snyder and Basch,[7] as well as orbital energies obtained from our CNDO/2 program. For each MO, comparison of the figures in Table 1 establishes the order

$$E_B(MO) < -\epsilon(MO)_{ab\ initio} < -\epsilon(MO)_{CNDO/2}\ .$$

The CNDO/2 approach is known to give unreliable energies, and little further discussion seems warranted here. However, in comparing $E_B(MO)$ and $-\epsilon(MO)_{ab\ initio}$, the accuracy of the latter is high enough that most of the difference can realistically be attributed to physical effects. The binding energy and orbital energy are related by

$$E_B(MO) = -\epsilon(MO) - E_R(MO) + \Delta E(MO)_{corr} + \Delta E(MO)_{rel}. \quad (1)$$

Here $E_R(MO)$ is the relaxation energy of the final state with a hole in the molecular orbital under study, and $\Delta E(MO)_{corr}$ and $\Delta E(MO)_{rel}$, which may

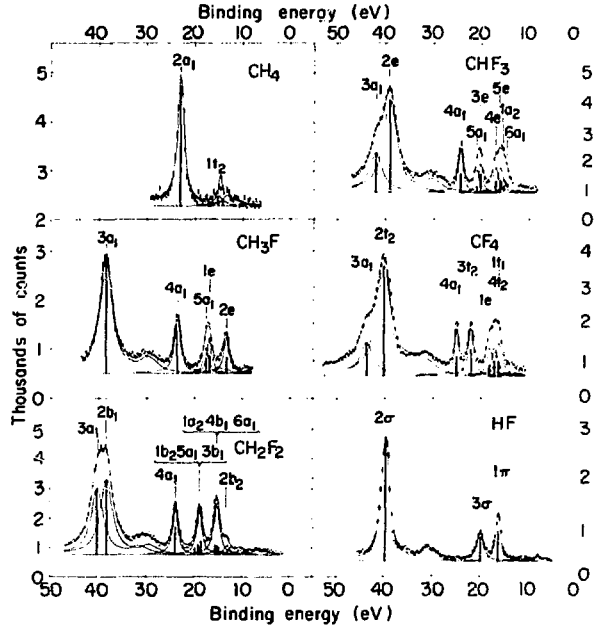

Fig. 1. X-ray photoelectron spectra of HF and the fluoromethane series $CH_{4-n}F_n (0 \leq n \leq 4)$ taken at increments of ~ 0.33 eV. Vertical bars correspond to intensity ratios computed using POLYATOM net populations.[7] They are not corrected for the considerable variation in line width. In some cases, noted in Table 1, separations from UPS and/or intensity ratios from CNDO/2 were used. For CH_2F_2 two groups of levels were fit as two peaks. (XBL 746-3464)

have either sign, are the excess correlation and relativistic energies in the final state over those in the initial state. We shall neglect these last two terms for lack of a good approximate method of dealing with them, noting that they are usually relatively small(i.e., 1 eV or less) in the cases studied here.

The E_R term is often larger and always positive. It arises because the wavefunctions of the passive electrons relax during photoemission from an N-electron system, lowering the energy of the hole state. This phenomenon is usually discussed in connection with Koopmans' Theorem,[8] which states the approximate equality $E_B(MO) \cong -\varepsilon(MO)$. Since E_R tends to increase with E_B, it has become customary to correct for E_R empirically by reducing $-\varepsilon$ by some fixed percentage. Thus, Brundle et al.[7] found that the approximate relation $E_B(\text{theo}) \cong 0.92(-\varepsilon)$ gave a rather good estimate of binding energies in the fluorinated methanes.

With the increased understanding of atomic and extra-atomic relaxation energies accompanying photoemission that has emerged recently, it appears possible to improve our estimates of $E_B(MO)$ from $\varepsilon(MO)$. Relaxation energies can be somewhat arbitrarily separated into atomic and extra-atomic contributions,

$$E_R = E_R^a + E_R^{ea} . \qquad (2)$$

We propose a three-parameter model for estimating the relaxation energies of all the MO's of the fluorinated methanes. We assume, for simplicity, that all "F 2s-like" orbitals have one mean value of E_R, that all other orbitals have another, and that E_R^a is the same for all orbitals within a given molecule, but that it rises linearly with the number of fluorines (this crudly expresses the molecular size dependence). After the $\Delta\varepsilon_{ai} = -t_{ab\ initio} - E_B(XPS)$ values have been used to adjust parameters, the expressions for E_R are

Table 1. Molecular Orbital Binding Energies in Fluorinated Methanes (in eV).

Molecule	Orbital	E_B(XPS)[a]	E_B(UPS)[b]	$-\epsilon_{ab\ initio}$	$-\epsilon_{CNDO/2}$	E_B(theo)
CH_4	$1t_2$	14.2(2)[c]	14.0	14.74	19.79	13.74
	$2a_1$	23.05(2)	23.0	25.68	34.58	24.68
CH_3F	2e	13.31(4)	13.05	14.43	17.57	12.93
	1e	16.85(7)	~ 17.0	18.00	21.28	16.50
	$5a_1$	17.56(9)		18.89	24.12	17.39
	$4a_1$	23.48(3)	23.4	26.13	32.06	24.63
	$3a_1$	38.41(3)	-	43.17	47.10	38.17
CH_2F_2	$2b_2$	13.17[d,e] (2)	13.27	14.89	17.11	12.89
	$6a_1$	14.91[e]		16.94	18.88	14.94
	$4b_1$	15.29[d,e]	15.3	17.23	19.82	15.23
	$1a_2$	15.61[d,e]	15.71	18.22	21.38	16.22
	$3b_1$	18.51(4)[e]		20.38	23.96	18.38
	$5a_1$	19.07(3)[e]	18.9	21.13	25.23	19.13
	$1b_2$	19.76(7)		21.54	26.97	19.54
	$4a_1$	23.86(3)	23.9	26.77	31.15	24.77
	$2b_1$	38.20(7)	-	43.79	45.82	38.29
	$3a_1$	40.13(7)	-	45.63	50.15	40.13
CHF_3	$6a_1$	14.67[d,e] (4)	14.80	16.53	17.77	14.03
	$1a_2$	15.29[d,e]	15.5	18.33	21.52	15.83
	5e	15.99[d,e]	16.2	18.54	19.94	16.04
	4e	17.03[d,e]	17.24	19.71	22.24	17.21
	3e	20.25(3)	20.6[f]	22.87	26.35	20.37
	$5a_1$	20.89(3)		23.78	27.86	21.28
	$4a_1$	24.38(3)	24.44	27.49	30.88	24.99
	2e	39.15(4)	-	45.34	47.20	39.34
	$3a_1$	42.03(9)	-	48.22	52.78	42.22
CF_4	$1t_1$	16.23(3)	16.20	19.40	22.24	16.40
	$4t_2$	17.41(4)	17.40	19.65	20.20	16.65
	1e	18.43(4)	18.50	21.34	23.30	18.34
	$3t_2$	22.14(2)	22.12	24.89	28.18	21.89
	$4a_1$	25.11(2)	25.12	28.15	29.48	25.15
	$2t_2$	40.30(4)	-	46.65	48.22	40.15
	$3a_1$	43.81(10)	-	50.50	54.63	44.00
HF	1π	16.12(4)	16.04	17.50	21.28	
	3σ	19.89(7)	19.90	20.50	23.14	
	2σ	39.65(2)	-	43.61	45.55	

[a] Binding energies using Mg Kα x-rays except with CH_4 where Al Kα x-rays were used.

[b] Vertical binding energies from Refs. 5 and 6.

[c] Weighted average of Jahn-Teller levels

[d] Separations from UPS used.

[e] Area ratios from CNDO/2 used.

[f] This value is probably correct. The value given in Ref. 6 is 19.84 eV for the vertical IP and 20.6 eV for the adiabatic IP.

$$E_R = (4.5 + 0.5\ n)\ eV \qquad (3)$$

for F 2s-like orbitals, and

$$E_R = (1.0 + 0.5\ n)\ eV \qquad (4)$$

for all other orbitals, where n is the number of fluorines. With this approach we have estimated the "theoretical" values $E_B(theo) = -\varepsilon - E_R$ given in Table 1. The agreement between $E_B(theo)$ estimated this way and $E_B(expt)$ is on the whole excellent, as Fig. 2 shows. For the 33 orbitals studied the standard and mean deviations between $E_B(theo)$ and $E_B(expt)$ are 0.48 eV and 0.27 eV, respectively. This figure also shows the marked separation between E_B values of the F 2s-like orbitals and those of the other molecular orbitals in these molecules. We conclude that relaxation corrections for the type described here are both conceptually and pragmatically superior to simply reducing the orbital energies by a constant factor.

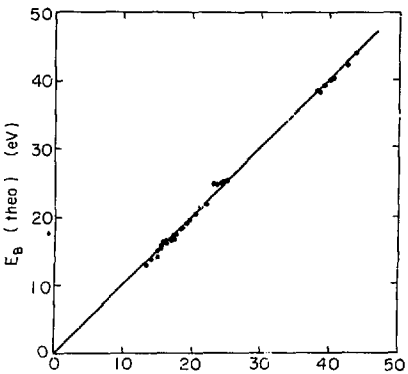

Fig. 2. Plot of binding energies calculated from a three-parameter model versus experimental values. (XBL 745-3290)

Intensities and Spectroscopic Assignments

In order to apply the intensity model outlined above, a knowledge of the relative atomic cross section is needed. Thus, to interpret the fluoromethane data the ratios

$$\sigma(C2s)/\sigma(C2p)\ ,\ \sigma(F2s)/\sigma(F2p)$$

and

$$\sigma(F2s)/\sigma(C2s)$$

are required. Gelius obtained the first of these three quantities from the experimental XPS area ratios of methane ($2a_1$ and $1t_2$) and an *ab initio* calculation. Similarly, the last ratio was obtained from the $4a_1$ and $3t_2$ levels of CF_4. The $\sigma(F2s)/\sigma(F2p)$ ratio was interpolated due to the unavailability of a spectrum of either HF or F_2. In our case, the $\sigma(C2s)/\sigma(C2p)$ was similarly calculated from the $2a_1$ and $1t_2$ of methane. However, we chose instead to use the $3a_1$ and $4a_1$ levels of CH_3F for the $\sigma(F2s)/\sigma(C2s)$. The $\sigma(F2s)/\sigma(F2p)$ ratio was obtained from 2σ and $1\Pi_x$, $1\Pi_y$ orbitals of HF (Fig. 1). Gelius used gross populations in calculating his ratios. Since his model neglects the contributions to the cross section from electrons far from the nuclei, it seems more appropriate to employ net populations instead. We have computed ratios using both types of populations. The results are shown in Table 2.

The relative molecular orbital intensities calculated from POLYATOM and CNDO/2 populations (using the cross section ratios from Table 2) are compared with experiment in Table 3 and are shown as vertical bars (using POLYATOM net populations) in Fig. 1. Their positions have been adjusted to match those of the experimental peaks. Some fitting

Table 2. Calculated Relative Atomic Photoelectric Cross Sections.

Ratio	CNDO	POLYATOM (Net)[b]	POLYATOM (Gross)[b]	Gelius[a]
$\sigma(C2s)/\sigma(C2p)$	23.3[c]	19.9	19.2[c]	13
$\sigma(F2s)/\sigma(F2p)$	9.5[d]	10.3[d]	9.1[d]	10
$\sigma(F2s)/\sigma(C2s)$	8.0[e]	5.8[e]	4.1[e]	2

[a] Ref. 3.

[b] Wavefunctions and overlaps obtained from Ref. 7.

[c] Using relative areas of $2a_1$ and $1t_2$ orbitals of methane.

[d] Using relative areas of 2σ and 1Π orbitals of hydrogen fluoride.

[e] Using relative areas of $3a_1$ and $4a_1$ orbitals of methyl fluoride.

Table 3. Computed Molecular Orbital Intensity Ratios from CNDO and POLYATOM Calculations.

Molecule	Molecular Orbital	I^a_{CNDO}	I^b_{NP}	I_{exp}
HF	1π	0.24	0.24	0.24(2)
	3σ	0.14	0.20	0.19(3)
	2σ	1.00	1.00	1.00(2)
CH_4	$1t_2$	0.12	0.12	0.12[c](2)
	$2a_1$	1.00	1.00	1.00(3)
CH_3F	2e	0.14	0.12	0.13(1)
	1e	0.14	0.14	0.11(2)
	$5a_1$	0.12	0.11	0.08(2)
	$4a_1$	0.24	0.23	0.23(1)
	$3a_1$	1.00	1.00	1.00(3)
CH_2F_2	$2b_2$	0.058	0.064	0.05[d,e] (1)
	$6a_1$	0.089	0.10	0.07[d] (1)
	$4b_1$	0.11	0.12	0.09[d,e] (1)
	$1a_2$	0.12	0.12	0.09[d,e] (1)
	$3b_1$	0.14	0.16	0.08[d] (1)
	$5a_1$	0.14	0.10	0.08[d] (1)
	$1b_2$	0.062	0.055	0.04[d] (1)
	$4a_1$	0.24	0.32	0.28(1)
	$2b_1$	1.00	1.00	1.00(6)
	$3a_1$	0.84	0.85	0.89(5)
CHF_3	$6a_1$	0.058	0.049	0.03[d,c] (1)
	$1a_2$	0.062	0.064	0.05[d,e] (1)
	5e	0.12	0.12	0.09[d,e] (1)
	4e	0.12	0.12	0.09[d,e] (1)
	3e	0.18	0.19	0.09(1)
	$5a_1$	0.12	0.048	0.06(1)
	$4a_1$	0.10	0.20	0.18(1)
	2e	1.00	1.00	1.00(3)
	$3a_1$	0.45	0.40	0.42(2)
CF_4	$1t_1$	0.13	0.14	0.12(1)
	$4t_2$	0.12	0.13	0.11(1)
	1e	0.083	0.080	0.08(1)
	$3t_2$	0.20	0.23	0.17(1)
	$4a_1$	0.11	0.16	0.16(1)
	$2t_2$	1.00	1.00	1.00(3)
	$3a_1$	0.28	0.26	0.29(2)

[a] Relative intensity using CNDO populations.

[b] Relative area intensity using POLYATOM net population calculated from [illegible].

[c] Assuming one level, not Jahn-Teller split.

[d] Area ratios taken from CNDO.

[e] Separations taken from UPS.

of the spectra is shown in Fig. 1. Expanded spectra of the low binding-energy regions of the fluorinated methanes are shown in Fig. 3 (with relative intensity calculated using CNDO/2 populations). Individual spectroscopic assignments are discussed below.

CH_4

It is unfortunate that the $K\alpha_3$ and $K\alpha_4$ satellites of the exciting Mg radiation obscure the $1t_2$ peak in methane. The situation is not quite so bad with Al x-rays because the satellites are farther from the $K\alpha_{1,2}$ line. Nonetheless, this has resulted in a large uncertainty in the $2a_1/1t_2$ area ratio. In Fig. 1 the $1t_2$ region of the Al $K\alpha_{1,2}$ XPS spectrum is reproduced using a Jahn-Teller splitting of 0.8 eV and a 2 to 1 intensity ratio of the Jahn-Teller components.[9] These are the values seen in UPS studies.[6]

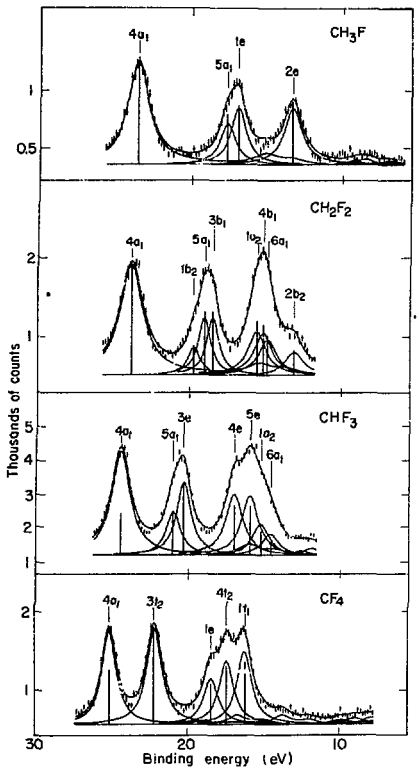

Fig. 3. X-ray photoelectron spectra of the fluoromethanes in the region up to approximately 30 eV binding energy taken at increments of ~ 0.16 eV. Vertical bars correspond to computed intensity ratios using CNDO/2 populations. In some cases separations and intensity ratios were used as explained for Fig. 1. (XBL 746-3465)

CH_3F

The ordering of $5a_1$ and 1e has been uncertain. Both CNDO and POLYATOM yield a lower binding energy for $5a_1$. The calculated intensities all agree that 1e is somewhat more intense. The experimental peak is asymmetric on the high binding energy side, indicating the location of the smaller peak. This is seen most clearly in Fig. 3. Thus, the Gelius model seems to favor placing 1e at a lower binding energy than $5a_1$.

CH_2F_2

The $2b_1$ and $3a_1$ orbitals are reported here for the first time. The level ordering indicated by orbital energies is supported by the intensity ratios. The remaining peaks are shown in more detail in Fig. 3. In the case of the two lowest binding energy groups of peaks, our analysis of the peaks in Fig. 3 is based on the calculated CNDO intensities which give a good overall fit of the experimental data. The experimental ratio of the $1a_2$, $4b_1$, $6a_1$ peak area to that of the $2b_2$ peak is approximately 5:1. This is to be compared to a ratio of 3:1 in the He II spectrum.[6] The increase in the relative intensities over the statistical value can be understood in terms of our model as follows: the orbitals $1a_2$ and $4b_1$ do not have any hydrogen character by symmetry. The $6a_1$ has less contribution from hydrogen than does $2b_2$.[7] Thus, in all four orbitals most of the electron density is on the fluorines, mainly in the 2p levels; and the ($1a_2$ + $4b_1$ + $6a_1$) peak has a larger percentage of electrons on the fluorines than does $2b_2$.

In the next peak, at ~ 19 eV, there are three orbitals. The ordering of $3b_1$ and $5a_1$ may be reversed without disagreeing with our spectrum. However, it seems quite likely that $1b_2$ has a higher binding energy than both of them, as shown, because its low intensity is consistent with the asymmetry of this peak on the high-energy side.

CHF_3

The *ab initio* and CNDO calculations, together with the Gelius model place $3a_1$ unambiguously as the most tightly bound MO. The model also seems to indicate that 3e is less tightly bound than $5a_1$ (Fig. 3). This is in agreement with Brundle et al.[6] who relied on the Koopmans' theorem energies. We also propose in Fig. 3 an ordering for the four outer orbitals which is predicted by POLYATOM.[7] This fit was obtained using the reported UPS vertical ionization potentials and the area ratios calculated from CNDO. The ordering of $5e_1$ and $1a_2$ is reversed by CNDO. On the basis of intensity ratios our spectra establish the ordering of these four levels as shown in Fig. 3.

CF_4

Siegbahn[10] has studied the CF_4 spectrum with monochromatized x-rays. His results as well as ours show that the least-bound orbital is more intense than the next one. According to the cross-section ratios obtained from both POLYATOM and CNDO/2 populations $1t_1$ should be the least-bound orbital (see Table 3) as predicted by *ab initio* calculations. Thus comparison with our experimental intensities very slightly favors $1t_1$ as the most weakly bound orbital.

Footnotes and References

*Condensed from LBL-2930.

1. D. W. Turner, C. Baker, A.D.Baker and C. R. Brundle, Molecular Photoelectron Spectroscopy (Wiley-Interscience, London, 1970).

2. K. Siegbahn, C. Nordling, G. Johansson, J. Hedman, P. F. Heden, K. Hamrin, U. Gelius, T. Bergmark, L. O. Werme, R. Manne and Y. Baer, ESCA Applied to Free Molecules (North Holland, Amsterdam, 1969).

3. U. Gelius in Electron Spectroscopy, D. A. Shirley, ed. (North Holland, Amsterdam, 1972).

4. D. W. Davis, D. A. Shirley, and T. D. Thomas, J. Amer. Chem. Soc. 94, 6565 (1972).

5. C. R. Brundle, Chem. Phys. Letters 7, 317 (1970).

6. C. R. Brundle, M. B. Robin and H. Basch, J. Chem. Phys. 53, 2196 (1970).

7. J. C. Snyder and H. Basch, Molecular Wave Functions and Properties (John Wiley and Sons, New York, 1972).

8. T. Koopmans, Physica 1, 104 (1933).

9. See for example C. A. Coulson and H. L. Strauss, Proc. Roy. Soc. (London) A 269, 443 (1962), and ref. 6.

10. K. Siegbahn, in Atomic Physics 3, Proceedings of the Third International Conference on Atomic Physics, Boulder, Colorado, 1972, edited by S.J. Smith and G. K. Walters, p. 493. Also K. Siegbahn, University of Upsala, Report No. UUIP-793.

THE RELATION OF CORE-LEVEL BINDING ENERGY SHIFTS TO PROTON AFFINITY AND LEWIS BASICITY*

R. L. Martin and D. A. Shirley

The relationship between molecular structure and reactivity is one of the central problems of chemistry. It may be divided into two parts. *Qualitative* questions about reactivity tend to focus on whether a reaction path exists that can take reactant R to product P. Principles such as orbital symmetry[1] can be applied to answer these questions. If a path exists for a given type of reaction, we may then be interested in its *quantitative* aspects, e.g., the extent to which the reaction proceeds. An important component of this second part is the relationship between the structures of the reactant and the product and the equilibrium constant for the rapid reversible reaction

$$R \rightleftharpoons P \,. \qquad (1)$$

In this paper we shall investigate the way in which a relatively new experimental parameter, the shift in core-level binding energy, can be related to certain reactions of the above type, particularly those involving the gain of a hydrogen ion. In making the analogy between the core-level ionization reaction

$$A \rightarrow A^+ \text{ (core-level hole + } e^-) \qquad (2)$$

and the ionization process

$$A + H^+ \rightleftharpoons AH^+ \,. \qquad (3)$$

we shall find it useful to generalize further the Lewis concept[2] of an acid as an electron acceptor and a base as an electron donor to include core orbitals. By applying principles that have emerged from the theory of core-level shifts, we shall attempt to show how insight can be gained into the relative importance for acid-base reactions of inductive (initial-state) effects and polarization (final-state) effects.

Relative core-level binding energies of the oxygen 1s orbital were measured for isopropyl and *tert*-butyl alcohols in the gas phase, using the Berkeley iron-free spectrometer. These were combined with previously reported values for methanol[3a] and ethanol.[3b] The experimental techniques have been described earlier.[4] This series was chosen to determine the effect on the O(1s) binding energy of successive methyl substitution on the adjoining carbon. An internal standard of water was used to enhance the accuracy of the measured shifts. The alcohol O(1s) shifts are given in Table 1.

In photoemission from the oxygen 1s orbital of an alcohol

$$(RR'R'')COH \rightarrow [(RR'R'')CO^*H]^+ + e^- \qquad (4)$$
$$\Delta H = E_B(1s)$$

the O(1s) binding energy E_B(O 1s) is given by the difference between initial- and final-state energies

$$E_B(O\ 1s) = E_f(RO^*H) - E_i(ROH). \qquad (5)$$

Table 1. O(1s) Binding Energy Shifts (eV)

Alcohol	Exptl.Shift
H_2O	(0.0)
CH_3OH	-0.8[a]
CH_3CH_2OH	-1.16(6)[b]
$(CH_3)_2CHOH$	-1.24(1)[c]
$(CH_3)_3COH$	-1.62(1)[c]
CF_3CH_2OH	-0.04(4)[b]

[a]Reference 2a. [b]Reference 3b. [c]This work.

An approximate value of E_B(O 1s) is given by (minus) the O(1s) orbital energy, $-\varepsilon$(O 1s), which may be obtained directly from a Hartree-Fock calculation on the ground state of ROH. In approximate discussions of core-level binding-energy shifts, it is common to approximate E_B by $-\Delta\varepsilon$.[5] Now ε and E_B are related by

$$E_B^i = -\varepsilon^i - E_R^i \qquad (6a)$$

$$E_B^i = -\Delta\varepsilon^i - \Delta E_R^i \qquad (6b)$$

where E_R^i is the "relaxation energy" accompanying loss of an electron from core level i and Δ implies the comparison of a given core level (such as O(1s)) between two molecules. The use of $\Delta\varepsilon$ for ΔE_B is *equivalent* to considering only the differences between ground-state properties, i.e., inductive effects. This approach is quite useful when inductive effects are dominant. Thus the higher carbon 1s binding energy in CF_4 than in CH_4 is quite properly attributed to the widthdrawal of electronic charge from carbon by the four fluorines, leaving a more positive environment at the carbon atom.

In considering only ground-state, or inductive, effects above we have neglected a crucial parameter of great chemical importance, the internal polarizability of the molecule. As an electron is removed from the O(1s) orbital in an alcohol, other electrons in the molecule are polarized toward the resultant positive hole. Since this polarization occurs adiabatically as part of the photoemission process, it is manifest as a reduction of the binding energy by an amount E_R, the "relaxation" energy. Thus ΔE_B^i in Eq. 6b will follow $\Delta\varepsilon^i$ only to the extent that ΔE_R^i can be neglected. Now it happens that E_R has a tendency to increase with molecular size. This can perhaps be best understood if the molecule in its final state is regarded as the neutral molecule plus an electron hole of charge +e.[6] The electronic charge distribution of the molecule will relax to "screen" the hole charge. In effect the hole charge is almost totally screened locally by polarization of charge ~ -e to the oxygen atom. The molecule's excess positive charge thus moves to the outside of the molecule to minimize the Coulombic repulsion. Larger molecules can therefore minimize this repulsion most effectively.

To express the above in chemical terms, the *O(1s) photoemission process in Eq. 4 can be split* into two *hypothetical* reactions. In the first an O(1s) electron is removed bu the orbitals do not relax and the alcohol goes to an imaginary unrelaxed intermediate state in which the oxygen atom has an additional charge of +1.

$$(RR'R'')COH \rightarrow (RR'R'')CO^{*+}H + e^- \qquad (7)$$
$$\Delta H = -\varepsilon(O\ 1s)\ .$$

Shifts in the energy of this "reaction" are determined by differences in the electron density about the oxygen in the ground state of the alcohol and are *inductive* shifts. In the second step the remaining electronic charge distribution relaxes to screen the positive hole, carrying the molecule into its actual final state.

$$(RR'R'')CO^{*+}H \rightarrow [(RR'R'')CO^{*}H]^+ \qquad (8)$$
$$\Delta H = -E_R(O\ 1s)\ .$$

Shifts in the energy of this "reaction" are *polarization* shifts. The two types of shifts are not separately observable because the unrelaxed intermediate state does not really exist. The "reactions" in Eqs. 7 and 8 sum to the real process, in Eq. 4, for which the energy change $E_B = -\varepsilon - E_R$ is observed.

Turning now to the relative basicities of these alcohols, we will argue that the effects which are important in determing the gas-phase proton affinity (PA) of an alcohol are analogous to those which determine the oxygen core-level binding energy. Thus the reaction

$$(RR'R'')COH + H^+ \rightarrow [(RR'R'')COH_2]^+ \qquad (9)$$
$$\Delta H = -PA$$

is very similar to Eq. 4. In both cases the alcohol must accommodate to the appearance of a highly localized positive charge on or near the oxygen: an electron hole in the 1s orbital in Eq. 4 or a proton in Eq. 9. The proton attachment reactions can also be broken up into two *hypothetical* steps. In the first, the analog of Eq. 7, the proton would attach to the oxygen without flow of charge in the molecular framework.

$$(RR'R'')COH + H^+ \rightarrow (RR'R'')COH_2^+ \qquad (10)$$
$$H = -E(H^+).$$

Here the product is written to indicate that the excess positive charge is localized on the proton, and $E(H^+)$ would be a "rigid-molecule" proton dissociation energy. In the second hypothetical step the electronic charge in the alcohol relaxes to shield the added positive charge, and the excess charge is effectively distributed over the whole molecule. This step, the analog of Eq. 8, can be written

$$(RR'R")COH_2^+ \rightarrow [(RR'R")COH_2]^+ \qquad (11)$$
$$\Delta H^\circ = -E_R(PA)$$

where $E_R(PA)$ is a relaxation energy analogous to $E_R(O\ 1s)$ for the photoemission process. For a series of simple alcohols in which the charge on oxygen stays essentially constant from one member of the series to the next, the inductive term, $E(H^+)$ in Eq. 10, should remain essentially constant. Differences in the inductive effect throughout the series would be expressed as a variation in the O-H bond strength. As Brauman and Blair have pointed out, however,[7,8] the O-H bond strength is essentially constant at 104 kcal/mol for all the simple alcohols; thus variations in the proton affinity arise mainly from variations in the "relaxation" term. We then have

$$\Delta(PA) \cong \Delta E_R(PA) \ . \qquad (12)$$

For these same alcohols the variations in the O(1s) orbital energy should be small, for the same reasons. Thus from Eq. 6b

$$E_B(O\ 1s) \cong -\Delta E_R(O\ 1s) \ . \qquad (13)$$

Now Eqs. 8 and 11 are very similar to one another in their overall effect, namely, the relaxation of electronic charge to shield an excess positive charge on or near the oxygen. The incremental relaxation energies ΔE_R should therefore be nearly the same, and from Eqs. 12 and 13 one would expect

$$\Delta(PA) \cong -\Delta E_B(O\ 1s) \qquad (14)$$

That is, *the variation in proton affinity of an alcohol should be nearly equal to the variation in the O(1s) binding energy*. The negative sign in Eq. 14 is a consequence of the sign conventions for binding energy and proton affinity.

That Eq. 14 is rather accurately obeyed by the simple alcohols is illustrated in Fig. 1, in which the binding energy shifts for the simple alcohols from Table 1 are plotted against the proton affinities of these alcohols,[9-11] listed in Table 2.

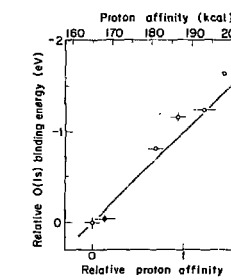

Fig. 1. Oxygen 1s binding energies vs. proton affinities for simple alcohols (open circles) and CF_3CH_2OH (filled circle), all in the gas phase. Relative E_B (1s) and PA values are referred to H_2O. The values and references are given in Tables 1 and 2. Compounds in order are: H_2O, CF_3CH_2OH, methanol, ethanol, isopropyl alcohol, and *tert*-butyl alcohol (for which two values of PA are plotted). The straight line has unit slope and goes through the H_2O point. (XBL 7312-7033)

Table 2. Proton Affinities in Simple Alcohols(kcal)

Compound	PA	Compound	PA
H_2O	165 (2)[a]	Ethanol	186 (2)[a]
CF_3CH_2OH	168 (3)[b]	Isopropyl alcohol	193 (3)[a]
Methanol	181 (2)[a]	*tert*-Butyl alcohol	198,206[a]

[a]These proton affinities are adopted values, from Refs. 9-11, with the estimated error in the last digit given parenthetically. Two values have been given for *tert*-butyl alcohol; both are listed.

[b]J. L. Beauchamp, private communication.

Also plotted is the CF_3CH_2OH point, to be discussed below. The good agreement between these two quantities provides a striking illustration of the close connection between core-level binding-energy shifts and chemical properites. We note that this is not just an empirical correlation of unknown origin but a straightforward consequence of a molecule's electronic charge distribution relaxing to shield an excess positive charge in two similar processes.

Before seeking to generalize the above results we must issue a *caveat*. The confirmation of Eq. 14 in Fig. 1 does not guarantee that the above argument is completely correct. In particular it does not imply that the quantities plotted are almost entirely variations in relaxation energies, as Eqs. 12 and 13 would imply. For this comparison of $\Delta(PA)$ with $\Delta E_B(O\ 1s)$, inductive (initial-state) effects would also make these two parameters tend to vary together. This is readily illustrated by rewriting Eq. 6b for this case and its proton-affinity analog derived from Eq. 9 and 19.

$$\Delta E_B(O\ 1s) = -\Delta\varepsilon(O\ 1s) - \Delta E_R(O\ 1s) \qquad (6b')$$
$$-\Delta(PA) = -\Delta E(H^+) - \Delta E_R(PA) \qquad (15)$$

If, in going from one alcohol to another, the oxygen becomes more negative, for example, then $\varepsilon(1s)$, which is always negative for bound states, will increase, thereby decreasing $E_B(O\ 1s)$. The "rigid molecule" (inductive) contribution to the proton affinity, $E(H^+)$, will of course increase, as will PA, and $-\Delta(PA)$ will also be negative. Thus inductive effects as well as relaxation effects would shift $-\Delta(PA)$ and ΔE_B similarly, and Eq. 14 would still tend to hold.

From the above reasoning we can make, as a first step toward generalizing, the rather tentative suggestion that proton affinities and core-level binding-energy shifts may be comparable among a wider range of compounds than just the

essentially nonpolar simple alcohols. The comparison can be extended in two steps. First, a wider variety of functional groups could be considered. Thus methoxy, phenyl, or CF_3 groups could be attached to the α carbon, for example, and the resulting O(1 s) binding-energy shifts could be compared with known proton affinities, to test the prediction that $\Delta E_B(O\ 1s) = -\ \Delta(PA)$. Data on only one compound proton affinity and O(1s) binding-energy shift in CF_3CH_2OH. When plotted on Fig. 1, the CF_3CH_2OH point shows excellent agreement with the trend for the simple aliphatic alcohols.

A second, larger extension would include other oxygen-containing functional groups in the comparison. Thus the proton affinities and O(1s) binding-energy shifts in alcohols and acids could be compared, for example, to test the predicted $\Delta E_B(O\ 1s) = -\ \Delta(PA)$ relation. Unfortunately, there are not enough O(1s) binding energies and proton affinities available for the same molecules to test the validity of either of these extensions. It seems probable that the first prediction should hold, but the second is less likely to, because molecular geometries of different functional groups can change on proton attachment, while there is no geometry change on X-ray photoemission.

A somewhat different case is readily tested. This is the relation between the nitrogen 1s binding energy shifts, $\Delta E_B(N\ 1s)$,[12] and the variation in proton affinities[9,14] of the series NH_3, CH_3NH_2, $(CH_3)_2NH$, and $(CH_3)_3N$. Very good agreement between these two quantities is found, as indicated in Fig. 2. This agreement is particularly impressive because in this case methyl groups are directly substituted for hydrogens on the photoemitting nitrogen atom.

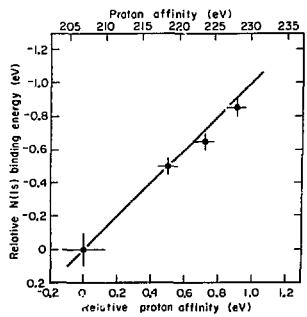

Fig. 2. Nitorgen 1s binding energies vs. proton affinities for (from left) NH_3, methylamine, dimethylamine, and trimethylamine. The PA values plotted are average of those given in Refs. 13 and 14. The error on the NH_3 point is absolute, while the others are relative. The straight line through the NH_3 point has unit slope. (XBL 7312-7032)

In the original work, the analysis developed above was used to formulate an explanation of the change in the first ionization potential within these series of alcohols and amines. It was argued that relaxation effects dominate the observed variations. In addition, the Lewis definition of basicity was extended to include the core orbitals and several examples of the connection between core-level binding energy shifts and the Lewis basicity were given. Finally, the inverted acidity order of the aliphatic alcohols in solution (relative to the gas phase) was rationalized in terms of an extramolecular relaxation; a polarization of the solvent that is active in ionization processes in solution. More detailed discussions can be found in the full report of this work.*

Footnotes and References

*Condensed from LBL-234; published in J. Am. Chem. Soc., 96, 5299 (1974).

1. R. B. Woodward and R. Hoffmann, "The Conservation of Orbital Symmetry," Academic Press, New York, N. Y., 1970.

2. G. N. Lewis, "Valence," Dover Publications, New York, N. Y., 1966, p. 142.

3. (a) K. Siegbahn, et al., "ESCA Applied to Free Molecules," North-Holland Publishing Co., Amsterdam, 1969; (b) D. W. Davis, M. S. Banna, and D. A. Shirley, J. Chem. Phys., 60, 237 (1974).

4. D. W. Davis, D. A. Shirley, and T. D. Thomas, J. Amer. Chem. Soc., 94, 6565 (1972).

5. See, for example, D. A. Shirley, Advan. Chem. Phys., 23, 85 (1973).

6. D. A. Shirley, Chem. Phys. Lett., 16, 220 (1972).

7. J. I. Brauman and L. K. Balir, J. Amer. Chem. Soc., 90, 6561 (1968).

8. J. I. Brauman and L. K. Balir, J. Amer. Chem. Soc., 92, 5986 (1970).

9. J. L. Beauchamp and M. J. Caserio, J. Amer. Chem. Soc., 94, 2638 (1972).

10. J. Long and B. Munson, J. Amer. Chem. Soc., 95, 2427 (1973).

11. D. H. Aue. University of California at Santa Barbara, private communication.

12. P. Finn, R. K. Pearson, J. M. Hollander, and W. L. Jolly, Inorg. Chem., 10, 378 (1971).

13. D. H. Aue, H. M. Webb, and M. T. Bowers, J. Amer. Chem. Soc., 94, 4726 (1972).

14. W. G. Henderson, M. Taagepera, D. Holtz, R. T. Melver, Jr., J. L. Beauchamp, and R. W. Taft, J. Amer. Chem. Soc., 94, 4728 (1972).

THEORY OF SATELLITE STRUCTURE IN PHOTOEMISSION

R. L. Martin and D. A. Shirley

The growing application of ESCA spectroscopy, in which atomic core levels are photo-ionized with monochromatic X rays and the orbital binding energies measured through spectrometric analysis of the photoelectrons' kinetic energies, has led to renewed interest in calculations of photoemission spectra for atomic and molecular core levels. Most calculations have focused on the lowest-binding-energy peak observed in the characteristic spectrum from each core level; i.e., the adiabatic or fully-relaxed (FR) peak. The relaxation energy,

$$E_R^i = -\ \epsilon_i - E_B^i \ , \qquad (1)$$

has received considerable attention recently; enough indeed to exaggerate the significance of the FR peak at the expense of the rest of the characteristic spectrum. Here ϵ_i is the ith orbital energy and E_B^i the binding energy of a given orbital i.

In this report we capsulize the results of work describing a full theory of photoemission. Emphasis is placed on core-level photoionization and the many-body aspects of the process.

In photoemission an N-electron system in an initial state $\Psi_i(1,2,\ldots N)$ interacts with the radiation field. A photon is absorbed, taking the system to to a final state $\Psi_f(1,2,\ldots N)$, in which at least one electron has been ejected into a continuum state. We shall restrict the discussion below to those events in which only one electron is ejected.

Kinetic-energy analysis of the photoelectron spectrum reveals peaks at energies

$$K_j = h\nu + E_i(N) - E_f^j(N-1) \qquad (2)$$

where $E_i(N)$ is the initial-state energy and $E_f^j(N-1)$ is the total energy of the remnant $N-1$ electron system. The spectrum is usually dominated by states at the "one-electron binding energies",

$$E_B^j = E_f^j(N-1) - E_i(N) \qquad (3)$$

each of which corresponds approximately to the orbital energy ϵ_j of a one-electron atomic or molecular orbital j -- the simplest one-determinant description of the initial state [Eq. (2)]. Closer inspection of the spectrum reveals a set of satellite states, at higher energies $\{E_f^j(N-1)\}$, associated with each main peak. In the literature on the subject these satellites have been variously termed "shake-up", "monopole-excitation", and "correlation" states. Unfortunately they have also been treated as if they were qualitatively different from, or were reached in a different way than, the main $N-1$ electron state. The apparent differences are in fact artificial, the consequence of using certain basis sets to describe the initial and final systems, together with single-determinant wave functions. While the heuristic descriptions have a certain pedagogic value, they must not be taken literally. The satellites do not arise through a two-step process, and they do not correspond to one electron being ejected as a photoelectron and a second electron being excited to a higher bound state. Such descriptions are intuitively appealing but fundamentally incorrect. They confuse the eigenstates of the $(N-1)$-electron Hamiltonian with a particular set of one-electron orbitals.

A photoemission experiment is just a special case of optical absorption in which the N electron system absorbs a photon of energy $h\nu$ and is raised from its initial state to a final state with one unbound electron. The act of observing the kinetic energy of the photoelectron (the N^{th} electron), in anticipation of using Eq. (2) to study the $N-1$ electron system, should also focus our attention on the fact that the final state is really that of an N-electron system. If dipole selection rules are operative, which is often the case, they apply to the *total* N electron system. This means, for example, that a $^1S \rightarrow {}^1P$ transition is allowed for the *total* system; any combination of $N-1$ electron final state plus photo electron final state symmetries that couple to ^1P (e.g., $^1S + p$, $^1P + s$, etc.) would satisfy this criterion. Among the ^1S final states of the $N-1$ electron system none has preference. The main lines and the satellites are qualitatively exactly equivalent. Each is reached directly via a one-step, "one-electron" dipole transition.[1] The intensity differences arise, as shown below, because of quantitative differences in cross-sections.

The above general comments are made without reference to basis sets, configuration interaction, or even electron correlation. We emphasize their basis-set independence. While one-electron molecular orbitals provide a convenient basis set, which we shall use below, they are in no way necessary.

N-Electron Sudden Approximation

The first application of the sudden approximation to hole-state excitation was made by Bloch.[2] Many authors have contributed to the literature on this subject. Åberg has given a recent comparative discussion of the sudden approximation in connection with x-ray satellite spectra.[3-4] Åberg's work is now the standard reference in the field of inner-shell ionization phenomena, especially in connection with x-ray spectra. For general use in photoelectron spectroscopy it is not directly applicable, however, because in inner-shell ionization, per se, attention is focused on the ionic $N-1$ electron system. The photoelectron is disposed of quickly in these discussions by taking the high-energy limit $k \rightarrow \infty$. We are interested primarily in the behavior of the (N electron plus photon) system under the constraint of constant total energy; i.e., the photoelectron has a finite energy determined by Eq. (2). Even if the sudden approximation is used a new derivation is required.

It is outlined below.

Let us assume that the initial state can be described by a single-determinantal wave function

$$\Psi_i(N) = (N!)^{-\frac{1}{2}} \left| \phi_1(1)\ \phi_2(2)\ \cdots\ \phi_N(N) \right| \qquad (4)$$

where $\{\phi_i\}$ is some appropriate basis set of molecular orbitals. The final state is described similarly, but a continuum function χ_f replaces ϕ_1, the orbital from which the photoelectron is ejected. Thus

$$\Psi_f(N) = (N!)^{-\frac{1}{2}} \left| \chi_f(1)\ \phi'_2(2)\ \phi'_3(3)\ \cdots\ \phi'_N(N) \right|. \qquad (5)$$

The orbitals $\{\phi_i'\}$ are primed to note that they are similar, but not idential, to the initial-state basis functions.

With the wavefunctions so defined, one finds that the cross section for a transition from state Ψ_i to Ψ_f is given by

$$\sigma_{SA} = \frac{1}{N}\ \rho(E_f) \left| \langle \chi_f | \phi_1 \rangle\, S_{11} + \sum_{j=2}^{N} (-1)^{1+j} \langle \chi_f | \phi_j \rangle S_{1j} \right|^2 . \qquad (6)$$

Here $\rho(E_f)$ is the density of final states and S_{1j} is an (N-1) electron overlap integral defined by Eq. 7

$$S_{1j} = \left\langle \prod_{k=2}^{N} \phi'_k(K) \middle| \Psi_i(N\text{-}1, \phi_j, 1) \right\rangle, \qquad (7)$$

where $\Psi_i(N\text{-}1\ ,\ \phi_j, 1)$ is the minor of $\phi_j(1)$ in $\Psi_i(N)$.

Many electron effects are apparent even in the crude level of theory employed thus far: the transition matrix element is not separable into an "active" times a "passive" electron part. Expansion of the overlap integral in Eq. (7) yields for the transition moment

Here the abbreviated notation $\langle 2'|2\rangle = \langle \phi'_2 | \phi_2 \rangle$ has been used in the determinants. If unrefaxed orbitals were used to describe the passive electrons in the final state, we would have $\langle i'|j\rangle = \delta_{ij}$, and Expression (8) would reduce to $\langle \chi_f | \phi_1 \rangle$. Using real (relaxed) orbitals, the first term will usually be altered somewhat. The diagonal elements $\langle j'|j\rangle$ are typically of the order of a few percent less than unity, while the off-diagonal elements are very small. Thus the first term might typically have a value of ~(0.8-0.9) $\langle \chi_f | \phi_1 \rangle$, only 10 - 20% different from the frozen orbital approximation.

The second term in (8) is more problematical. Each of the determinants in the sum can be rearranged so that all but one of the diagonal elements are nearly unity. The remaining diagonal element will have the form $\langle j|1\rangle$, where the orbital ϕ'_j is the final state function which most closely resembles ϕ'_1. If we retain only the diagonal product (which yields the largest term by far in each determinant), and divide the sum in (8) by the first term, we find

$$\text{Ratio} = \sum_{j=2}^{N} (-1)^{1+j}\, \frac{\langle j'|1\rangle \langle \chi_f | j\rangle}{\langle j'|j\rangle \langle \chi_f | 1\rangle}.$$

It is safe to assume that the ratio $\langle j'|1\rangle / \langle j'|j\rangle \ll 1$ for all j, but the ratio $\langle \chi_f | j\rangle / \langle \chi_f | 1\rangle$ may be significantly larger than unity, thereby necessitating the retention of the sum in Eq. 6. This sum can be regarded as arising from an "internal shakeup" mechanism: in fact it is rather similar in structure to "conjugate shakeup". An electron appears to be ejected from the j^{th} orbital and replaced by an electron from orbital ϕ_1. In fact this mechanism requires both exchange in the initial state (to make the product $\langle j'|1\rangle \langle \chi_f | j\rangle$) and relaxation (to make $\langle j'|1\rangle \neq 0$). Further discussion of this interesting term lies outside the scope of this paper, but we note that it was not apparent in Åberg's treatment because the photoelectron was not explicitly included in the final state.

An important advantage of the present N-electron formulation of the SA is that the factor $\langle \chi_f | \phi_1 \rangle$ contains an explicit dependence of the

$$\langle \chi_f | 1 \rangle \begin{vmatrix} \langle 2'|2\rangle & \langle 2'|3\rangle & \cdots & \langle 2'|N\rangle \\ \langle 3'|2\rangle & \langle 2'|2\rangle & \cdots & \langle 2'|N\rangle \\ \vdots & & & \\ \langle N'|2\rangle & \langle N'|3\rangle & \cdots & \langle N'|N\rangle \end{vmatrix}$$

$$+ \sum_{j=2}^{N} (-1)^{1+j} \langle \chi_f | j \rangle \begin{vmatrix} \langle 2'|1\rangle & \langle 2'|2\rangle \cdots \langle 2'|j\text{-}1\rangle \langle 2'|j\text{+}1\rangle \cdots \langle 2'|N\rangle \\ \langle 3'|1\rangle & \langle 3'|2\rangle \cdots \langle 3'|j\text{-}1\rangle \langle 3'|j\text{+}1\rangle \cdots \langle 3'|N\rangle \\ \vdots & \\ \langle N'|1\rangle & \cdots \quad \cdots \quad \cdots \quad \cdots \quad \langle N'|N\rangle \end{vmatrix} \qquad (8)$$

photoemission cross-section on the orbital symmetry of χ_f and the photon energy. By using even such approximate wave functions as plane waves (of the right wavelength) for χ_f and Slater orbitals for ϕ_i, most of the crudest physical features of photoemission cross-section ratios could be derived using this approach. Thus, for example, we can easily deduce the well known result that $\sigma(^1s)/\sigma(2p)$ for second-row elements is small for very soft (~100 eV) photons but larger for harder (~1000 eV) photons, which is readily understandable in terms of the deBroglie wavelengths in the final state χ_f.

The above discussion has shown that the SA can give qualitatively reasonable results for photoemission cross-sections when applied properly. We do not, of course, advocate using the SA when other methods are available, as described below.

The N-Electron Dipole Approximation

The dipole approximation is derived by taking account of the photon field explicitly by adding a term

$$p_i \rightarrow \vec{p}_i - \frac{e}{c}\vec{A}$$

to the momentum operator of each electron. Here $\vec{A}$ is the vector potential of the photon field. After making the dipole approximation and carrying out several standard manipulations, it can be shown that the introduction of H_ϕ inserts an operator $\sum_{k=1}^{N} \vec{p}_k$ into the transition matrix element and adds a multiplicative factor of $(\hbar\omega)^{-1}$. The cross-section thus becomes[5]

$$\sigma_{DA} \propto (\hbar\omega)^{-1} \left| \langle \Psi_f(N) | \sum_{k=1}^{N} \vec{p}_k | \Psi_i(N) \rangle \right|^2 \rho(E_f) \qquad (9)$$

Expansion of the matrix element yields terms that differ from those in the sudden approximation only in including a matrix element of the momentum operator p_1. There are also additional terms arising from the rest of the momenta, $\sum_{k=2}^{N} p_k$. This result can be arranged in the form

$$\langle \Psi_f(N) | \sum_{k=1}^{N} p_k | \Psi_i(N) \rangle = \langle \chi_f | p | \phi_1 \rangle \, S_{11} + \sum_{j=2}^{N} (-1)^{1+j} \langle \Psi_f | p | \phi_j \rangle \, S_{1j} + \sum_{j=1}^{N} (-1)^{1+j} \langle \Psi_f | \phi_j \rangle \, P_{1j} \qquad (10)$$

Here P_{1j} denotes an (N-1) electron transition matrix similar to S_{1j},

$$P_{fj} = \left\langle \prod_{\ell=2}^{N} \phi_\ell^*(\ell) \mid \sum_{k=2}^{N} p_k | \Psi_i(N\text{-}1, \phi_j, 1) \right\rangle . \qquad (11)$$

The first two terms in Eq. (10) arise from the p_1 operator and the rest from the $\sum_{\ell=2}^{N} p_\ell$ sum. Thus Eq. (10) approaches the argument of the RHS of Eq. (6) if only the first two terms are retained and p is replaced by unity. Another comparison with the SA is obtained by approximating χ_f with a plane wave. In this case we may replace $\langle \chi_f | p | \phi_j \rangle$ by $\hbar k_f \langle \chi_f | \phi_j \rangle$, etc. Furthermore, by energy conservation

$$\hbar\omega = E_B + \hbar^2 k_f^2 / 2m .$$

After some rearranging of Eq. (9), it follows that

$$\sigma_{DA} \propto \left(\frac{k_f^2}{k_f^2 + \frac{2mE_B}{\hbar^2}} \right) \left| \langle \chi_f | \phi_1 \rangle \, S_{11} + \sum_{j=2}^{N} (-1)^{1+j} \langle \chi_f | \phi_j \rangle \, S_{1j} + (\hbar k_f)^{-1} \Sigma[p] \right|^2 \qquad (12)$$

k becomes large the coefficient term in Eq. (12) approaches units, the last term goes to zero, and Eq. (12) approaches Eq. (6); i.e., the dipole approximation result approaches the SA result. Again, however, the form given here contains an explicit expression for the momentum matrix elements of the active electrons.

The results given in Eqs. (6), (10), and (12) are straightforward, but to our knowledge they have not been given explicitly before, and most molecular core-level photoemission spectra are interpreted using even more approximate expressions. The deficiencies of the SA, the DA, and the plane-wave (or OPW) approximations are too well known to require discussion. Nevertheless, for the purposes at hand -- the calculation of core-level correlation-peak intensities -- any of these approaches is usually adequate provided that electron correlation is treated properly. In numerical work on HF to be discussed in the following report, we found that the first term in Eq. (10) dominated all others at photon energies well above threshold ($h\nu \cong 1500$ eV). It was also found that for the purposes of computing relative correlation peak intensities the slowly varying energy dependent factors cancel and a comparison of the overlap integrals (S_{11}) is all that is necessary. The wavefunctions used to compute this overlap integral, however, must be much more sophisticated than the single-determinantal functions we have used so far. For this reason we have extended the formalism outlined above to include configuration interaction. Both initial and final state configuration mixing were found to be very important in the F(1s) "shake-up" spectrum of HF.

Footnotes and References

1. Semantic confusion is possible here. By a one-electron transition we mean a transition caused by a one-electron operator or a linear combination of one-electron operators. Thus $\sum \vec{p}_i$ would cause a one-electron transition, but not $\vec{s}_i \cdot \vec{s}_j$.

2. F. Bloch, Phys. Rev., 48, 187 (1935).

3. T. Aberg, Phys. Rev. 156, 35 (1967).

4. T. Aberg, Ann. Acad. Sci. Fenn. A VI, 308 (1969).

5. There is, of course, a dependence of the cross section on the photon polarization properties. For the purposes of this report we assume that all angular dependence, etc., has been averaged away.

FLUORINE 1s CORRELATION STATES IN THE PHOTO-IONIZATION OF HYDROGEN FLUORIDE: EXPERIMENT AND THEORY

R. L. Martin, B. E. Mills, and D. A. Shirley

Introduction

Photoemission spectra of atomic core levels in atoms and molecules yield for each core level j a main peak at an electron kinetic energy

$$K_j = h\nu - E_B^{(o)} \qquad (1)$$

where $h\nu$ is the photon energy and $E_B^{(o)}$ is the binding energy of the primary peak. This corresponds to an atomic or molecular ion that is described theoretically to first approximation by removing an electron from orbital j and allowing the passive electrons to relax adiabatically (i.e., without changing their quantum numbers). If $h\nu$ is substantially larger than $E_B^{(o)}$, additional satellite peaks may also be observed at higher binding energies $E_B^{(n)}$. Qualitatively, one usually describes these states as arising from at least a two electron excitation from the ground state (ionization accompanied by "shakeup"). A quantitative theoretical treatment of the transition cross section to such states, however, shows that one electron descriptions may be misleading. The cross section for such a transition owes much of its strength to manybody effects. In particular, configuration interaction (CI) in both the initial and final state is required; hence the latter are more accurately described as "correlation states", and the satellite peaks as "correlation peaks".

The theoretical formalism for calculating correlation state spectra was described in the preceding paper[1] (hereafter called I). We report in the present paper a complete study of the fluorine 1s correlation-state spectra in gaseous HF. To our knowledge this is the first in which several of the theoretical nuances developed in I have been applied. It is also the first case showing quantitative agreement between experiment and theory.

The gaseous sample was obtained by evaporation of 99.9% + pure liquid HF, obtained from Matheson Gas Products, Inc. The photoelectron spectra were obtained using Al $K\alpha_{1,2}$ x-rays (1486.6 eV) on the 50 cm radius Berkeley iron-free magnetic spectrometer. Spectral data points were taken at pressures of ~ 50 and ~ 350 microns (Fig. 1). The analyzer chamber was maintained at a pressure of approximately 10^{-5} Torr. The high pressure spectrum was used to determine which of the satellite peaks of the F(1s) main line were caused by inelastic collisions of the electrons passing through the sample after photoemission. The intensities of these peaks should increase

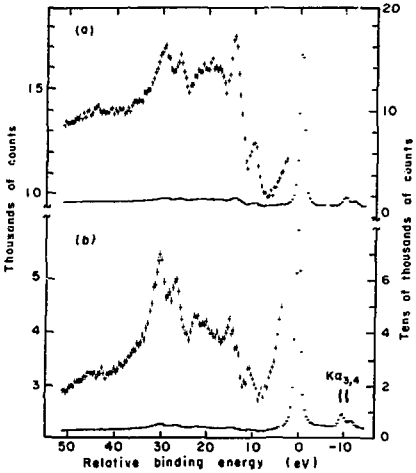

Fig. 1. The high (a) and low pressure (b) photoelectron spectrum of gaseous HF. The binding energy is measured relative to the main peak, the F(1s) hole state. (XBL 7411-8298)

with pressure. If the low pressure spectrum (Fig. 1b) is subtracted from the high pressure spectrum (Fig. 1a) with appropriate weighting to equalize the main F(1s) peaks, the result is an inelastic electron loss spectrum.

The low pressure spectrum was fitted (Fig. 2) using a non-linear least squares program which automatically took into account the (weak) Al $K\alpha_{3}$ and $K\alpha_{4}$ peaks as well as the slight change of the the energy window caused by the fact that the magnetic spectrometer produces spectra linear in momentum. The main peak, corresponding to the F(1s) hole state, was fitted best by a sum of three Lorentzian peaks and these were used as the fundamental form for the "correlation" peaks.

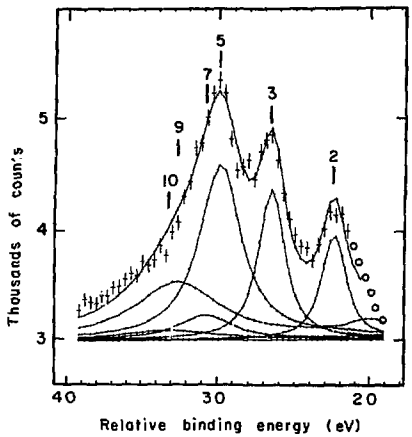

Fig. 2. Expanded spectrum of HF at low pressure and experimental fit; numbered states correspond to those in Table 1. The circles represent data corrected for pressure dependent peaks.
(XBL 7412-8360)

The results in Table 1 indicate the theoretical intensities of the peaks are in excellent agreement with experiment. Theoretical energies, relative to the main line, are 2.1 to 3.5 eV higher than experiment. Note that the width of the peaks increases with greater separation from the main peak, or alternatively, the width increases as you approach the double ionization ("shake-off") limit.

The correlation-peak spectrum was calculated using the theoretical formalism described in I. Two major levels of sophistication were used for the wavefunctions necessary in this work. First configuration interaction among the ionic final states was considered, with the ground state represented by a single Slater determinant. In the next step, CI in the ground state was also included. For each of these cases, the relative intensities of the correlation peaks were computed in the overlap approximation. It was shown in I that except for terms which are small for core-level satellites, [2] the dipole and the N-electron sudden approximations give identical results in the overlap approximation. These are displayed in Table I for final state CI (Method A) and for initial state CI (Method B).

A complete description of the means used to obtain the wavefunctions necessary in this study is presented in the full account of this work. Here we simply note that the wavefunctions for the correlation states were obtained as the eigenvectors of a configuration expansion based on one-

Table 1. Correlation peak intensities in the overlap approximation

State[a]	$(S_n^{11})^2$ Method A	$(S_n^{11})^2$ [b] Method B	I(expt) [c]	FWHM (eV)	E(theor) [d] (eV)	E(expt) [d] (eV)
0	(1.000)	(1.000)	(1.000)	1.4	(693.5)	
1	0.000	0.020	–	–	23.89	
2	0.012	0.020	0.019(3)	2.1(3)	25.90	22.4(2)
3	0.015	0.030	0.030(4)	2.3(3)	29.57	26.50(5)
4	0.000	0.000	–	–	30.89	–
5	0.036	0.062	0.057(5)	3.7(3)	32.35	29.90(7)
6	0.000	0.001	–	–	32.72	–
7	0.007	0.012	0.010	4.7(3)	33.31	30.87
8	0.000	0.000	–	–	33.74	–
9	0.028	0.041	0.038(5)	7.1(9)	34.84	32.7(3)
10	0.005	0.007	0.007	7.9(9)	35.43	33.3
11	0.000	0.000	–	–	35.72	–

a) In order of increasing energy "Reference state" is numbered 0, as in Fig. 1 and text.

b) All intensities normalized to peak 0. Absolute values of S^{11} are 0.78115 (Method A), 0.71970 (Method B).

c) Error in last pace given parenthetically.

d) First entry is the absolute binding energy of the reference state; the others are incremental energies relative to this.

electron molecular orbitals. These orbitals were optimized for the F(1s) hole state and were themselves linear combinations of atomic orbitals. The basis set of atomic orbitals is thus a very important parameter in the calculation. Not all of the excited states that can be calculated for a given basis set will have physical significance. Our final choice gave stable energies and transition moments with respect to addition of further orbitals and slight modifications of the exponents of existing orbitals for those excited states which we felt were physically reasonable.

An indication of the completeness of the basis set for at least two of the states of interest here is afforded by comparison with previous work. We found an SCF energy of -100.0553 a.u. for the $1\Sigma^+$ ground state of HF. The near Hartree-Fock result of Cade and Huo is -100.0703 a.u. The same basis yields an energy of -74.5670 a.u. for the F(1s) hole state, to be compared with Schwartz's result of -74.5365 a.u. The calculated F(1s) binding energy is 693.5 eV, which is slightly higher than the value of 693.3 eV reported by Schwartz. Our $^3\Pi$ shakeoff limit falls at -73.2872 a.u. or 34.8 eV above the primary hold state. The compositions of the molecular orbitals which are most important for describing shakeup phenomena in HF are given for the ground state and the ionic states in Table 2a and Table 2b respectively.

Table 2. Basis set of Slater functions and selected one electron orbitals used in the CI wavefunctions.

Slater Function[a] Type	ξ	Molecular Orbitals 1σ	2σ	3σ	4σ	5σ	6σ	7σ	1π	2π	3π	4π
A. HF Ground State:												
1. F(1s)	7.716	-0.6768	0.2873	0.0665	-0.0729	0.1185	0.0143	-0.0384				
2. F(1s')	10.514	-0.3313	-0.0154	-0.0031	-0.0054	-0.0250	0.0038	0.0039				
3. F(2s)	1.933	-0.0034	-0.4249	-0.1301	0.4412	0.1233	-0.2966	0.1057				
4. F(2s')	3.120	0.0021	-0.6228	-0.1699	0.2847	-0.2811	-0.1380	0.1436				
5. F(2p)	1.847	0.0005	-0.0885	0.6050	0.4963	0.2023	-0.0010	0.0957	-0.7149	-0.2956	-0.0323	0.1401
6. F(2p')	4.175	-0.0012	-0.0266	0.2852	0.3050	0.1327	0.0056	0.0509	-0.3386	-0.2534	-0.0143	0.0958
7. F(3d)	2.500	0.0001	-0.0216	0.0453	-0.0232	-0.0300	0.0878	0.0201	-0.0263	0.0116	-0.0552	-0.0003
8. F(3s)	1.000	-0.0001	-0.0417	-0.0024	0.2278	1.1467	-0.6601	-0.0954				
9. F(3p)	1.000	-0.0009	-0.0193	0.0238	0.0163	-0.2236	-1.1454	-0.0880	-0.0600	1.0978	0.1275	-0.7086
10. F(3d')	0.800	-0.0002	-0.0080	0.0034	0.0244	-0.1275	0.1289	0.6961	-0.0157	0.1735	-0.9574	0.1114
11. F(4s)	0.600	-0.0001	0.0051	0.0036	-0.0292	-0.0576	-0.1121	0.7936				
12. F(4p)	0.600	0.0002	-0.0016	0.0015	0.0245	0.0023	-0.2400	0.3504	0.0089	-0.0814	0.1208	1.2224
13. H(1s)	1.000	0.0028	0.1841	-0.0297	-1.7194	-0.5649	1.5561	-0.7593				
14. H(1s')	1.500	-0.0018	-0.2311	0.3042	0.3169	0.0954	-0.3849	0.3402				
B. HF^+, F(1s) Hole State:												
1. F(1s)	7.716	-0.5892	0.3055	0.0909	-0.0403	0.0588	-0.0087	0.0258				
2. F(1s')	10.514	-0.4178	0.0035	-0.0038	-0.0125	-0.0177	-0.0119	-0.0024				
3. F(2s)	1.933	-0.0305	-0.2378	-0.0022	0.5674	0.1979	0.3954	-0.0922				
4. F(2s')	3.120	0.0071	-0.8100	-0.2620	0.1700	-0.0562	0.1087	-0.0539				
5. F(2p)	1.847	-0.0005	-0.1273	0.5742	0.4799	0.2672	0.0312	-0.0984	0.6168	0.2489	0.0288	0.2153
6. F(2p')	4.175	0.0005	-0.0714	0.4383	0.1111	0.0615	-0.0147	0.4970	0.4970	0.0996	0.0046	0.0638
7. F(3d)	2.500	-0.0008	-0.0252	0.0474	0.0057	-0.0168	-0.0349	-0.0062	0.0282	-0.0067	0.0159	-0.0035
8. F(3s)	1.000	-0.0023	-0.0435	0.0635	0.0661	1.3143	0.4695	0.4624				
9. F(3p)	1.000	-0.0065	-0.0111	-0.0084	0.0563	0.1808	1.0704	0.3730	-0.0571	-0.0613	-0.1002	-0.9615
10. F(3d')	0.800	-0.0022	-0.0073	0.0192	-0.0409	-0.1653	0.1510	-0.5887	0.0051	-0.2936	0.9282	0.2020
11. F(4s)	0.600	-0.0007	0.0062	-0.0079	-0.0189	0.0819	0.1583	-0.9247				
12. F(4p)	0.600	0.0011	-0.0046	0.0145	-0.0146	-0.0501	0.4501	-0.1900	0.0201	-0.1271	-0.2970	1.1986
13. H(1s)	1.000	0.0238	0.1929	-0.2628	-1.7866	-1.3668	-1.3129	0.1798				
14. H(1s)	1.500	-0.0134	-0.2196	0.3289	0.3656	0.3365	0.4841	-0.1434				

[a] $\chi_n = r^{n-1} e^{-\xi r}$, where n is the principal quantum number.

The intensity of each final-state peak relative to that of the main peak was first calculated in the overlap approximation. If only final-state CI was considered (Method A), the relation

$$\frac{I(n')}{I(o)} = \frac{\left|\sum_n C_{n'n} S_n^{11}\right|^2}{\left|\sum_n C_{on} S_n^{11}\right|^2} \qquad (2)$$

is appropriate. The extension of the theory to include configuration interaction in the initial-state (Method B) leads to

$$\frac{I(n')}{I(o)} = \frac{\left|\sum_{n,m} C^*_{n'n} D_{om} S^{11}_{nm}\right|^2}{\left|\sum_{n,m} C^*_{on} D_{om} S^{11}_{nm}\right|^2} \qquad (3)$$

Here $C_{n'n}$ and D_{om} are the coefficients of the configurations (n and m) in the eigenvectors of the final and initial states, respectively. For HF these would have the form

$$|\Psi_f^{(n')}\rangle = C_{n'0}\,|1\sigma\ 2\sigma^2\ 3\sigma^2\ 1\pi^4\ (^2\Sigma^+)\rangle + C_{n'1}\,|1\sigma\ 2\sigma\ 3\sigma\ 4\sigma\ 1\pi^4\ (A\ ^2\Sigma^+)\rangle + C_{n'2}\,|1\sigma\ 2\sigma^2\ 3\sigma\ 4\sigma\ 1\pi^4\ (B\ ^2\Sigma^+)\rangle + \ldots$$

$$|\Psi_i^{(o)}\rangle = D_{00}\,|1\sigma^2\ 2\sigma^2\ 2\sigma^2\ 1\pi^4\ (^1\Sigma^+)\rangle + D_{01}\,|1\sigma^2\ 2\sigma^2\ 3\sigma\ 4\sigma\ 1\pi^4\ (^1\Sigma^+)\rangle + \ldots$$

where, for the final state $|\Psi_f^{(n')}\rangle$, the two linearly independent doublet spin functions which can be constructed from the orbital occupancy are denoted by A and B.

The overlap functions S_{nm}^{11} were discussed in I. Here they actually refer to a sum of determinantal overlap integrals, the nature of the sum being determined by the expansion coefficients of the Slater determinants in the configuration. For HF the superscripts "11" refer to the deletion of the column containing electron 1 and the row containing the basis function $1\sigma\beta$ from the ground state determinant(s).

The conclusions drawn below refer specifically to the F(1s) correlation-state peaks in the high-energy XPS spectrum of HF. We believe that most of them are more generally true for comparable spectra, but the exact extent to which they apply can be ascertained better following theoretical analysis of additional cases.

First and perhaps of most importance, the excellent agreement between experiment and Method B (Table 1) provides strong evidence that the overlap approximation embodied in Eq. (3) is adequate to describe such a high-energy core-level correlation-state spectrum. Since Eq. (3) could be derived from Eq. I (10) without reference to the dipole operator itself, this implies that even the sudden approximation (SA) would give an adequate representation of the relative intensities in the experimental spectrum.

The corollary conclusion is that initial-state CI must be included, since Method A (Table 1) gives poor intensity predictions. This is entirely expected in view of the discussion in I, but it has been recognized in previous work on core level satellite spectra.

Finally, it is of interest to interpret the correlation peak intensities in terms of "shake-up" excitations into virtual orbitals. An examination of the eigenvectors shows that the first two correlation states (1 & 2) can be described fairly well as arising from the $3\sigma \rightarrow 4\sigma$ transition. These two final states are describable as molecular valence states, the remainder of the spectrum corresponding primarily to Rydberg-like states. Only state 2 of this pair is predicted to have an observable intensity, and it is the first peak observed in the experimental spectrum. It seems reasonable to assert that the relatively low intensity of this transition is attributable to the charge transfer nature of the excitation. The 3σ orbital is the bonding combination of the F(2p) and H(1s) orbitals and is largely localized on the fluorine atom, while the 4σ is the anti-bonding combination and is primarily hydrogen like. Since the orbitals have their large components in different regions of space, you would expect a small overlap. This interpretation seems plausible, but one should realize that there are much more subtle effects which contribute substantially to the cross section. These are the small admixture of the $1\pi \rightarrow 2\pi$ excitation into state 2, the even smaller admixture of the reference state, and the effect of configuration interaction in the initial state. This last effect is very important and can be seen quite clearly in Table 1. The inclusion of initial state CI (Method B) nearly doubles the predicted intensity of state 2 relative to the primary hole state.

The most intense peak in the spectrum, state 5, corresponds to the $1\pi \rightarrow 2\pi$ or $F(2p\pi) \rightarrow F(3p\pi)$ excitation. Its counterpart, state 3, is also relatively intense. The next most intense peak in the spectrum is state 9, the $F(2p\pi) \rightarrow F(4p\pi)$ excitation. These results, of course, would be expected on the basis of a simple one electron overlap model.

The states with smaller intensities are less predictable. State 7 is primarily attributable to the $3\sigma \rightarrow 5\sigma$ excitation. It would be tempting to say that since the 5σ orbital is F(3s) like, there should be very little overlap with the 3σ orbital in the ground state (which is mainly $F(2p_\sigma)$ like), and this causes the small intensity of state 7. These arguments, however, are probably oversimplified since there is a fairly large amount of the $3\sigma \rightarrow 6\sigma(F2p_\sigma \rightarrow F3p)$ excitation in the wavefunction. Configuration mixing in these states makes it nearly impossible to make rough *a priori* estimates of intensities. For example, the $3\sigma \rightarrow 6\sigma$, or $F(2p_\pi) \rightarrow F(3p_\sigma)$ excitation is important in state 8, and you might therefore expect it to be rather intense. It is not. The

$F(2p_\sigma) \rightarrow F(4s)$ excitation, state 10, on the other hand, has a much larger intensity. The reasons for these differences in overlap are complex and tied into the specific nature of configuration mixing in these excited states. Since the configuration enter into the wavefunction with a phase, they can either add intensity to the predominant configuration, or cancel what intensity the dominant configuration might supply.

These configuration mixing problems are expected to be more severe in molecules than in atoms since you generally have a much denser excited state manifold in the molecular species.

In summary, the correlation peak spectrum of HF can be calculated quite satisfactorily in the overlap approximation. The intensities of the correlation peaks are very dependent upon the effects of configuration interaction in both the initial and final states. At the present time, quantitative predictions of such spectra based on simple one-electron models seem doomed to failure. Even qualitative estimates and assignments are very difficult considering the importance of configuration interaction in the final state. The effect of CI in the initial state is to increase the intensities of the shakeup states at the expense of the primary hold state. For HF, the shakeup states are all roughly twice as intense once initial state CI is included.

Footnotes and References

1. R. L. Martin and D.A. Shirley, preceding report.

2. These corrections were computed and discussed in the full report of this work to be published in J. Chem. Phys.

MULTIPLET SPLITTING OF THE MANGANESE 2p AND 3p LEVELS IN MnF_2 SINGLE CRYSTALS*

S. P. Kowalczyk, L. Ley,† F. R. McFeely, and D. A. Shirley

Multiplet splitting of core-level peaks in x-ray photoemission (XPS) spectra is of interest both as a probe of the interactions between electrons in atoms, molecules, and solids, and as a diagnostic tool for acquiring information about unpaired spin in chemical systems. Multiplet splitting is expected to be observed in an XPS spectrum if the specimen possesses unpaired electrons in its outer valence shells. The splitting arises when upon ejection of a core electron, the resulting partially filled core shell can couple with the open valence shell to form several multiplets of different energy.[1] The simplest spectrum is expected for a core s level. This should result in two peaks with an energy separation given by Van Vleck's theorem[2] and the relative intensities expected from this simple picture are given by the multiplicity ratio (S+1)/S. This level of interpretation neglects electron correlation and is only approximately correct. Only recently have the 2p levels in transition metal compounds been given a comprehensive theoretical treatment.[3] The few reports of experimental evidence for splittings in these levels have been largely indirect.[5] The XPS spectra of 3p levels of the transition metal compounds exhibit very complex spectra for which the Hartree-Fock one-electron model gives a poor description.[4,6,7] As a step toward understanding the multiplet structure in XPS spectra of non-s levels, we have studied the multiplet splitting of the Mn 2p and 3p levels obtained in high resolution XPS measurements of MnF_2 single crystals.

To facilitate analysis of multiplet structure, we have subtracted the inelastic background and characteristic energy loss structure by means of a suitable response function.[8] The resulting corrected spectrum for the Mn 2p level in MnF_2 is shown in Fig. 1. The most striking feature of Fig.1 is that the Mn $2p_{3/2}$ peak is asymmetric toward higher binding energy and the Mn $2p_{1/2}$ peak is asymmetric to lower binding energy. This agrees qualitatively with early x-ray emission data on the 3d metals and their compounds, in which the $K\alpha_1$ ($2p_{3/2}$ - 1s) emission line has an asymmetry index α of greater than 1.0 and the $K\alpha_2$ ($2p_{1/2}$ - 1s) emission line has α close to but less than 1.0.[9-11] Here α is defined as the ratio of the

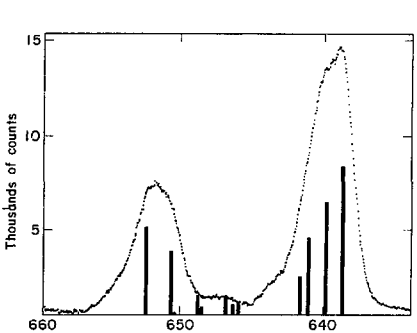

1. Corrected Mn 2p spectrum (points) and spectrum calculated by GS (bars) for MnF_2. The energy scale of the calculated spectrum has been reduced by a factor of 0.96. (XBL 748-4056)

half-width at half-maximum on the high binding-energy side, W_H, to the half-width at half-maximum on the low binding energy side, W_L. The spectrum of Fig. 1 yields $\alpha(2p_{1/2}) = 0.8$ and $\alpha(2p_{3/2}) = 1.6$ in good agreement with the x-ray emission work. It was proposed by the x-ray workers that the asymmetry of the Kα lines arose from multiplet splitting. In the first XPS work on MnF_2, Fadley and Shirley[4] postulated the existence of multiplet effects in their Mn 2p spectra from indirect arguments based on line widths. Later, Frost et al.[5] studied the 2p levels of cobalt ion complexes. These workers observed that the separation of the peak maxima between the Co $2p_{1/2}$ and Co $2p_{3/2}$ levels was systematically larger by 1 eV in the high spin (S = 3/2) complexes than in the low spin (S = 0) complexes. This was interpreted as indirect evidence of multiplet splitting, in which the degeneracy of J is broken by the exchange interaction with the states of higher J shifting to lower binding energy for the $2p_{3/2}$ and to higher binding energy for the $2p_{1/2}$, thus yielding an apparent increase in the spin-orbit splitting. For MnF_2, we found the splitting of the $2p_{3/2}$ - $2p_{1/2}$ peak maxima to be 13.0 (1) eV and the mean peak separation to be 12.1 (1) eV, versus 11.18 (25) for both in Mn metal.[12] It has already been shown that there is less uncompensated spin in the metal than in MnF_2[13] so the interpretation of increased splitting being due to multiplet effects is in the same direction as in Co. Similar results have been obtained for the oxides of Ni and Co in comparison to the metals; however, diamagnetic ZnF_2 has the same splitting (within experimental error) as Zn metal. These data, provide further support for the multiplet interpretation.

Besides the asymmetry of the peaks and the enhanced 2p 1/2 - 2p 3/2 splitting, two other features of Fig. 1 should be noted. First, a rather substantial area remains between the two main peaks after background correction. If our correction procedure is right, this area must represent structure. A similar correction procedure for ZnF_2 gave no intensity in this region, reinforcing the interpretation that the additional intensity in the MnF_2 spectrum is intrinsic. Secondly, the tops of the 2p 1/2 and 2p 3/2 peaks show signs of possible structure.

Recently Gupta and Sen[3] (GS) have calculated the expected 2p XPS spectrum for MnF_2 by working out the levels of the p^5d^5 system, employing Hartree-Fock results on the Mn^{+2} ground states. The solid bars in Fig. 1 show the positions and intensities of the twelve eigenstates found by GS. Their energy scale was reduced by 4% to match the experimental spectrum. Adjustments of this magnitude are not surprising, because GS did not do a relaxed hole-state calculation. Figure 1 shows the GS calculation to be compatible with our XPS spectrum in considerable detail. The two peaks are asymmetric in direction that agree with the GS results. In fact, when the latter were broadened with Lorentzian functions of appropriate intensities the resulting simulated spectrum showed asymmetries of $\alpha(3/2) \sim 1.7$ and $\alpha(1/2) \sim 0.5$ in fair agreement with the experimental values of 1.6 and 0.8, respectively, mentioned above. On the basis of the comparison shown in Fig. 1, we conclude that the GS calculation explains the essential features of the $2p_{1/2}$ - $2p_{3/2}$ XPS spectrum of MnF_2.

Figure 2 shows the $K\alpha_1$ x-ray emission spectrum of MnF_2, after Nefedov.[10] This spectrum is to be compared to the $2p_{3/2}$ part of Fig. 1. The spectra are qualitatively very similar with the x-ray spectrum appearing to show more resolved structure. Both spectra have a FWHM of 3.7 eV. The components in Nefedov's spectrum are about 1.0 eV apart. A least-squares fit of our XPS $2p_{3/2}$ spectrum with four Gaussian functions restrained to have the relative intensities given by the GS results are separated by a similar amount

Figure 3 shows the high resolution XPS spectrum of the Mn 3p region of MnF_2. The features of this spectrum are summarized in Table 1. Fadley et al.[4] demonstrated the inadequacy of the Koopman's theorem approach in explaining the 3p multiplet structure. Multiplet-hole theory (MHT) gave some improvement but the agreement was still somewhat less than satisfactory. It was suggested by Fadley et al.[4] that part of the discrepancy between the experimental results and theory might be due to spin-orbit and crystal-field effects. These two effects were studied by GS and found to have a negligible effect.

The next step would appear to be the inclusion of electron-correlation effects. Correlation should be more important for the 3p-3d interaction than for the 2p-3d interaction analogous to the situation that obtains in the 3s and 2s levels.[14] Electron correlation effects are crucial in understanding the Mn 3s spectrum in MnF_2.[14] Inclusion

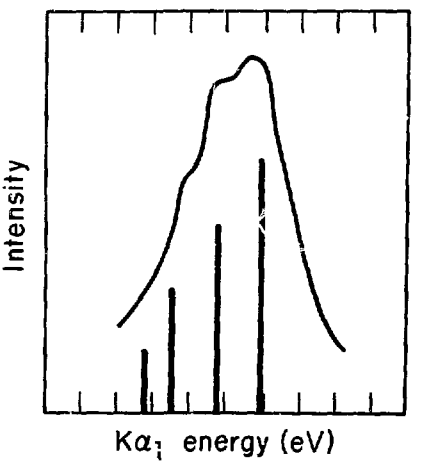

Fig. 2. The $K\alpha_1$ x-ray profile of Mn in MnF_2, after Nefedov (Ref. 10). Bars indicate states calculated by Gupta and Sen. Each division on the abscissa is 1 eV. (XBL 748-4058)

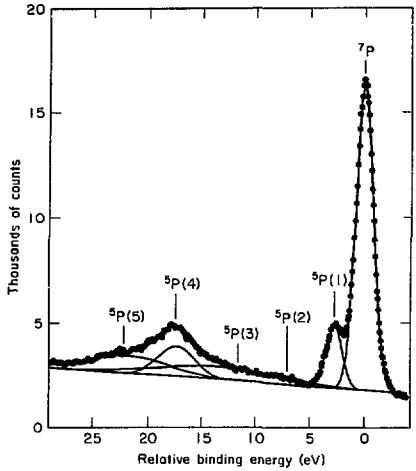

Fig. 3. Mn 3p XPS spectrum in MnF_2, together with fitted peaks. The very broad peaks probably represent several states. (XBL 748-4054)

of correlation effects leads to more 3s peaks than the Hartree-Fock one-electron model and affects the distribution of intensity among the peaks. These predictions have been confirmed by experiments.[14] Intra-shell correlations are thus usually important in XPS multiplet spectra, while inter-shell correlations are not. Thus correlation must be considered in the Mn 3p spectrum even though the 2p spectrum could be explained without taking correlation into account.

Correlation can be introduced into a Hartree-Fock multiplet-hole calculation by including configuration interaction.[15] This approach, which worked very well in explaining the anomalies in the Mn 3s spectrum, does not appear to work for 3p spectra.[7] Bagus and Wahlgren[7] have performed a Hartree-Fock calculation with configuration interaction to predict the Ni 3p spectrum in a NiO_6^{10-} molecular cluster. This calculation gave satsifactory agreement with XPS results. The new peaks in the cluster calculation were attributed to the symmetry of the cluster being lower than in the free ion, enabling the nickel d electrons to re-arrange themselves in more ways than possible in the free ion. These results suggest that perhaps the XPS results of MnF_2 can be explained in similar terms.

While a detailed comparison with theory is not yet possible, the good resolution in the 3p spectrum in Fig. 3 allows to perform a sum-rule test that has not been feasible before. The weighted average of the energy of the satellites, $\bar{E}(^5P)$ can be used to define an average ^5P - ^7P energy separation $\Delta\bar{E}$, given by

$$\Delta\bar{E} = \bar{E}(^5P) - E(^7P).$$

From the data in Fig. 3, we obtained $\Delta\bar{E} = 14.5$ eV in MnF_2. This should be comparable to Koopman's theorem results which predict only two 3p peaks. Values of 13.5 and 13.7 eV have been obtained with the Koopman's theorem description.[4] Also the intensity ratio of the area of the ^7P peak to the sum of the areas of ^5P peaks was 1.1 or fairly close to the multiplicity ratio of 1.4. This good agreement provides further support to the multiplet-hole theory of the 3p spectrum even though we do not as yet have a theory that can predict the positions, or even the number, of final-state ^5P peaks.

Besides attempting to understand these spectra as a problem in atomic physics, we can try to use these spectra as a probe of unpaired spin density in transition metal compounds. While the presently available XPS resolution does not yet allow the intense 2p lines in transition metals to be used as a definitive spin "fingerprint," these lines can still be used to probe spin density in two ways. The asymmetry of the $2p_{1/2}$ and $2p_{3/2}$ line should scale with spin, as should the separation of the $2p_{1/2}$ and $2p_{3/2}$ maxima. The 3p spectra were also shown to have possible diagnostic value by converting the "CI spectrum" into a "Koopman's theorem spectrum." It would be very valuable if this approach could be systematically applied to a series of transition metal salts, because the separation of the high- and low-spin

Table 1. Summary of the observed splitting and relative intensities of the Mn3p levels in MnF_2

Mn3p final state	^7P	$^5P(1)$	$^5P(2)$	$^5P(3)$	$^5P(4)$	$^5P(5)$
Energy (eV)[a]	0.0	2.75(5)	7.6(5)	12.75(30)	17.5(2)	21.8(1)
Relative Intensity[b]	1.0	0.19		~ 0.28[c]	~ 0.21	~ 0.26

[a] The energies are given relative to the ^7P state.

[b] The intensities are relative to ^7P level.

[c] This is the sum of the $^5P(2)$ and $^5P(3)$ intensities.

centroids in the Koopman's theorem spectrum should be a good measure of the total 3d spin.

Footnotes and References

*Condensed from LBL-2976; published in Phys. Rev. B 11, 1721 (1975).

†IBM Fellow.

1. For a review of multiplet splitting in XPS see: C. S. Fadley in Electron Spectroscopy, ed. D. A. Shirley, (North-Holland Amsterdam, 1972) p. 781; and D. A. Shirley, Advances in Chemical Phys. 23, 85 (1972).

2. J. H. Van Vleck, Phys. Rev. 45, 405 (1934).

3. R. P. Gupta and S. K. Sen, Phys. Rev. B10, 71 (1974).

4. C. S. Fadley, D. A. Shirley, A. J. Freeman, P. S. Bagus, and J. V. Mallow, Phys. Rev. Lett. 23, 1397 (1969); C. S. Fadley and D. A. Shirley, Phys. Rev. A2, 1109 (1970).

5. D. C. Frost, C. A. McDowell, and I. S. Woolsey, Chem. Phys. Lett. 17, 320 (1972).

6. A. J. Freeman, P. S. Bagus, and J. V. Mallow, Internat. J. Magnetism, 4, 35 (1973).

7. P. S. Bagus and U. I. Wahlgren, private communication.

8. C. S. Fadley, Ph.D. Dissertation, University of California (Lawrence Radiation Laboratory, Report UCRL-19535 (1970) unpublished, Appendix A.

9. L. K. Izraileva, Akad. Nauk, (Phys. Ser.) 25, 965 (1961).

10. V. I. Nefedov, Akad. Nauk. (Phys. Ser.) 28, 724 (1964).

11. J. Finster, G. Leonhart, and A. Meisel, Jour. de Phys. 32, C4-218 (1971).

12. The Mn metal results are from the unpublished data of the authors.

13. F. R. McFeely, S. P. Kowalczyk, L. Ley, and D. A. Shirley, Sol. St. Comm. 15,1051 (1974).

14. S. P. Kowalczyk, L. Ley, R. A. Pollak, F. R. McFeely, and D. A. Shirley, Phys. Rev. B7, 4009 (1973).

15. P. S. Bagus, A. J. Freeman, and F. Sasaki, Phys. Rev. Lett. 30, 850 (1973).

EVIDENCE FOR A LOCALIZED MAGNETIC MOMENT IN PARAMAGNETIC α-Mn FROM MULTIPLET SPLITTING

F. R. McFeely, S. P. Kowalczyk, L. Ley,† and D. A. Shirley

Alpha manganese is unusual among metals of the 3d transition series. It has a complex bcc lattice with 29 atoms per unit cell. Its magnetic structure is also unusual. Shull and Wilkinson found[1] that α-Mn is antiferromagnetic below ~ 100 K, and they reported an average magnetic moment of 0.5 μ_B in the parmagnetic phase up to 500 K, using neutron diffraction. Recent NMR[2] and neutron diffraction[3] studies have indicated at least four different magnetic moments below T_N with a weighted average of 0.63 μ_B, but dc susceptibility measurements[4] on the parmagnetic phase have been analyzed to yield an average moment of 2.37(7) μ_B/atom, in contrast to the neutron diffraction value. To elucidate the nature and magnitude of the atomic moment in the parmagnetic phase we have carried out x-ray photoemission experiments. Multiplet splitting of the 3s and 2s lines reveal the presence, on the 10^{-15} sec time scale, of a localized 3d spin, corresponding to a localized magnetic moment of ~ 2.5 μ_B.

The spectra reported below were obtained in a Hewlett-Packard 5950A electron spectrometer using monochromatized AlKα radiation (1486.6 eV). The instrument was modified for ultrahigh vacuum operation and operated with a pressure of 6×10^{-11} Torr in the analyzer chamber.

Spectra of the valence bands, the 3s region and the 2s region are shown in Fig. 1.

The 3s and 2s spectra both show doublet structures due to multiplet coupling of the final 3s (2s) hole state with the incomplete valence shell of Mn. The 3s peaks were fitted to Lorentzian lineshapes by a non-linear least squares procedure. The analysis of spectra obtained from two different samples yielded values of 4.12(10) eV and 4.05(10) eV for the separation of the two peaks. The intensity ratio of the peaks was approximately 1.3 in each case. Due to the high degree of inelastic scattering associated with the 2s photoemission lines, we were not able to fit these spectral features to analytic peak shapes; however, the two components of this feature appear to be separated by ~ 3.5 eV.

Since the discovery of antiferromagnetism in α-Mn by Shull and Wilkinson, the exact nature of the magnetic moments, both in the ordered and paramagnetic states, has been a subject of considerable controversy. The problem is complicated by the fact that the α-Mn structure has four crystallographically inequivalent sites, with 1, 4, 12 and 12 atoms respectively. These sites may of course carry different moments. On the basis of neutron

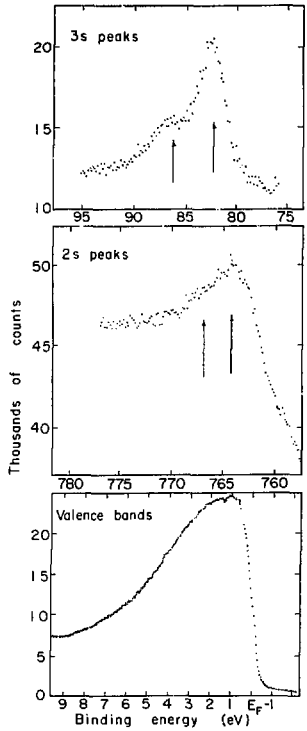

Fig. 1. Uncorrected photoemission spectra of Mn 3s (top), 2s (middle), and valence bands (bottom). (XBL 741-251)

diffraction data, several models for their magnitude in the antiferromagnetic state have been proposed.[5] However, the NMR work of Yamagata and Asayama[2] indicates that atoms even on crystallographically equivalent sites may carry different moments. This result, along with the suggestion by Sato and Arrot[6] that the wavevector characterizing the magnetic ordering might deviate from [1,0,0], would necessitate a spin-density wave treatment of the antiferromagnetic state. However, the single-crystal neutron diffraction work of Yamada[3] et al. revealed no such deviation, and these workers suggested a localized-moment model, with a weighted average moment of 0.63 μ_B.

In the paramagnetic state, the first determination of the average moment was made by Shull and Wilkinson on the basis of the paramagnetic diffuse neutron scattering intensity. They deduced an average moment of ~0.5 μ_B and suggested that this was due to a mixture of atoms with moments 0 and 1 μ_B. Recently, however Nagasawa and Uchinami[4] measured the magnetic susceptibility of α-Mn in the paramagnetic state below 300 K and determined a value of 2.37(7) μ_B for the average magnetic moment. These two observations are not necessarily contradictory. Neutron scattering would detect moments with correlation times of ~ 10^{-12} sec or longer. The dc susceptibility--a macroscopic quantity--is independent of correlation time.

Multiplet splitting in the core-level spectra of manganese salts is well known.[7-12] The simplest interpretation of the 3s multiplet splitting ΔE would neglect electron correlation and employ van Vleck's theorem,[13] which has the form

$$\Delta E(3s) = (2S + 1)\,\frac{G^2(3s\ 3d)}{5}\ , \qquad (1)$$

for exchange splitting of a $3s^1\ 3d^n$ final state in which the d electrons couple to spin S. Given the essential constancy of the exchange integral G^2(3s 3d)--an atomic parameter--Eq. (1) can be used to deduce S from ΔE(3s), if G^2 is known. In fact the situation is substantially complicated by electron correlation,[12,14] and the relation

$$\Delta E(3s) \cong (\text{const.})\ (2S + 1), \qquad (2)$$

is expected to be only approximately correct even in salts. In a metal such as Mn, further complications are introduced by the partially itinerant nature of the 3d electrons and by the presence of the s-p conduction bands. Electrons in these bands can screen the 3s - 3d and 3d - 3d interactions, reducing both the correlation effects responsible for additional satellite peaks[14] and thus the intensity ratio of the two observed peaks in Mn relative to Mn^{2+},[12] as observed.

It is difficult to assess the importance of these complications. We note that the 3s-4s exchange integral G^0(3s 4s) is small relative to G^2(3s 3s). Also, the sp band is probably itinerant and largely unpolarized. Thus we shall neglect the effect of sp bands on ΔE(3s). Since the 3s orbital lies well within the atom (as evidenced by the value of $\langle r \rangle_{3s}$ = 0.465 Å[15]). The dominant contributions to the exchange integrals should come from within the atomic core and thus be relatively insensitive to changes in bonding. To the extent that this is true, ΔE(3s) should be proportional to (2S + 1). On this basis we have plotted ΔE(3s) of MnF_2, MnF_3, and MnO_2 against the nominal value of (2S + 1) in Fig. 2, and plotted a line through these three points, obtaining ΔE(3s) = 1.0 (2S + 1) + 0.6. The non-zero intercept necessitated by this fit must be regarded as an empirical parameter, and reflects the insufficiency of the Van Vleck's Theorem treatment. From this equation the ΔE(3s) = 4.08 of α-Mn corresponds to a 2S+1 value of 3.50, hence to a "spin only" magnetic moment of ~ 2.5 μ_B. This is in excellent agreement with the susceptibility value of 2.37 μ_B. The multiplet splitting spectrum provides a spectroscopic measurement of this localized moment, albeit with low resolution: we can infer from the

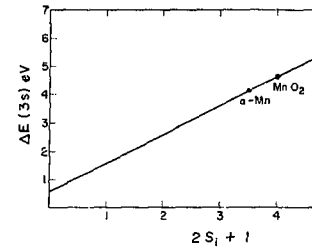

Fig. 2. E(3s) plotted against $2S_i + 1$, where S_i is the initial-state spin for MnF_2 (Ref. 12), MnF_3 (Ref. 10), and MnO_2 (Ref. 8). (XBL 743-2707)

spectrum that most or all of the sites in α-Mn have a moment near the nominal value of 2.5 μ_B.

Both the excellent agreement of this derived moment with the susceptibility data and the agreement between ΔE(2s)/ E(3s) in Mn and MnF_2 (~0.9 in each case) support our interpretation. We believe, however, that this agreement may be in part fortuitous, and we do not wish to emphasize its quantitative aspects. These observations appear to establish the following attributes of paramagnetic α-Mn: (1) localized spins exist on the Mn atoms on the time scale of 10^{-15}sec, (2) they have an average spin S ~ 1.25, and presumably a moment μ ~ 2.5 μ_B, and (3) most or all of the Mn sites have values of S not too far from this average value. Any viable theoretical model for α-Mn should be consistent with these three features.

Footnotes and References

*IBM Fellow.

1. C. G. Shull and M. K. Wilkinson, Rev. Mod. Phys. 23, 100 (1953).

2. H. Yamagata and K. Asayama, J. Phys. Soc. (Japan) 33, 400 (1972).

3. T. Yamada, N. Kouitomi, Y. Nakai, D. E. Cox, and G. Shirane, J. Phys. Soc. (Japan) 28, 615 (1970).

4. H. Nagasawa and M. Uchinami, Phys. Letters 42A, 463 (1973).

5. J. S. Kasper and B. W. Roberts, Phys. Rev. 101, 537 (1956).

6. H. Sata and A. Arrot, Proc. Intern. Conf. Magnetism and Crystallography, Kyoto, 1961, J. Phys. Soc. (Japan) 17 (1962), Suppl. B-I, p. 147.

7. C. S. Fadley, D. A. Shirley, A. J. Freeman, P. S. Bagus, and V. J. Mallow, Phys. Rev. Letters 23, 1397 (1969).

8. C. S. Fadley and D. A. Shirley, Phys. Rev. A2, 1109 (1970).

9. T. S. Fadley, in Electron Spectroscopy, ed. by D. A. Shirley (North-Holland, 1972), p. 781.

10. J. C. Carver, G. K. Schweitzer, and T. A. Carlson, J. Chem. Phys. 57, 973 (1972).

11. G. K. Wertheim, S. Hüffner, and H. J. Guggenheim, Phys. Rev. B 7, 556 (1973); S. Hüffner and G. K. Wertheim, Phys. Rev. B 7, 2333 (1973).

12. S. P. Kowalczyk, L. Ley, R. A. Pollak, F. R. McFeely, and D. A. Shirley, Phys. Rev. B 7, 4009 (1973).

13. J. W. Van Vleck, Phys. Rev. 45, 405 (1934).

14. P. S. Bagus, A. J. Freeman, and F. Sasaki, Phys. Rev. Letters 30, 850 (1973).

15. P. S. Bagus, A. J. Freeman, and F. Sasaki, Phys. Rev. Letters 30, 850 (1973).

16. C. C. Lu, T. A. Carlson, F. B. Malik, T. C. Tucker, and C. W. Nestor, Jr., Atomic Data 3, 1 (1971).

MULTIPLET SPLITTING OF X-RAY PHOTOEMISSION SPECTRA CORE LEVELS IN MAGNETIC METALS*

S. P. Kowalczyk, F. R. McFeely, L. Ley,† and D. A. Shirley

Measurements of core-level binding energies and valence band density-of-states by x-ray photoemission spectroscopy (XPS), has proved very valuable to the understanding of the electronic structure of solids. For systems with unpaired spin, information about the initial state spin S can in principle be obtained by correlation with the measured splitting of a core level caused by the phenomenon of multiplet splitting.[1] The basis of obtaining S is the use of Van Vleck's Theorem,[2]

$$\Delta E_{n\ell} = \frac{2S+1}{2\ell+1} G^{n\ell}(n\ell, n'\ell'), \qquad (1)$$

where $\Delta E_{n\ell}$ is the splitting of the $n\ell$ level, $G^{n\ell}$ is the appropriate atomic exchange integral, and n and n' are the principle quantum numbers of the level measured and the level with the unpaired spin respectively. Unfortunately the situation is not so straightforward. Using (1) overestimates $\Delta E_{n\ell}$ by a factor of ~ 2 when $n = n'$. It is now understood that this discrepancy is due to intra-shell electron correlations.[3,4] It will be shown that by using systems where the correlation effects are nearly the same, measured ΔE_{ns} can still be used to obtain S.

The 3d metals can be divided into 3 classes according to their magnetic properties: paramagnetic (Sc,Ti,V), antiferromagnetic (Cr, Mn), and ferromagnetic(Fe,Co,Ni). Figure 1 shows a typical 3s spectrum of a metal from each of these classes. The Sc spectrum shows a single peak as expected from a band theory explanation of Pauli paramagnetism. Paramagnetic Ti and V exhibit 3s spectra similar to Sc. Antiferromagnetic Cr and α-Mn show sizeable 3s splittings (2.8 and 4.1 eV, respectively). Likewise ferromagnetic Fe, Co and Ni show multiplot structure.

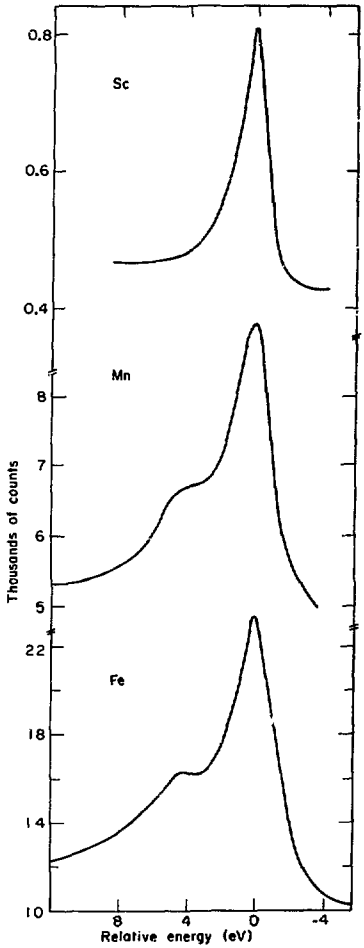

Fig. 1. XPS 3s spectra of Sc, Mn, and Fe.
(XBL 7410-4348)

Figure 2 demonstrates how S can be obtained from measured ΔE_{ns} despite large correlation effects. The integral in (1) should be dominated by the atomic core region and be relatively insensitive to bonding effects outside the atomic core. Thus for an atom in various environments, ΔE_{ns} should still be proportional to 2S+1. By plotting measured ΔE_{ns} vs 2S+1 of ionic systems, where S is well defined, one obtains in effect a "calibration curve" on which one can place an observed ΔE_{ns} of a metal or an atom in an alloy or a compound and get a value for 2S+1 or the localized moment. Using this calibration procedure for Fe with an observed $\Delta E_{3s} = 4.3$ eV yields a magnetic moment $\mu = 2.2\ \mu_B$ which agrees quite well with the

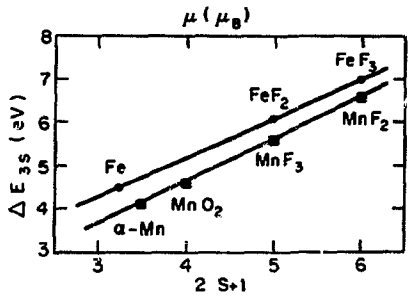

Fig. 2. Calibration curves for Fe and Mn. Fe, α-Mn, FeF_2 and MnF_2 from data of the authors. FeF_3 and MnF_3 are taken from J. C. Carver, G. K. Schweitzer, and T. A. Carlson, J. Chem. Phys. 57, 973-982 (1972). (XBL 7410-4429)

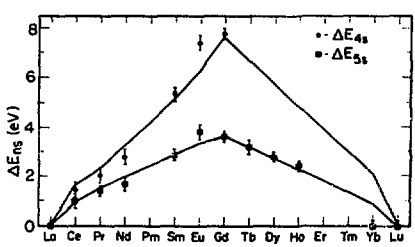

Fig. 3. Observed 4s (●) and 5s(■) multiplet splitting in the rare earth metals. The solid curves are estimates based on Eq. 1. The 4s estimates have been reduced by a factor 0.55.
(XBL 7410-4347)

generally accepted value of 2.22 μB.[5] This agreement suggests the correlation factor is roughly constant for Fe atoms in different surroundings. Our α-Mn measurements were obtained at room temperature and from the above procedure implied a localized moment with an average value of ~ 2.5 μB. This is at odds with neutron diffraction measurements above 100°K. This is due to the fact that the XPS time scale (10^{-15}sec) is several orders of magnitude faster than neutron diffraction. The XPS observation of two well defined peaks indicates that all the Mn atoms have a moment close to the average value.

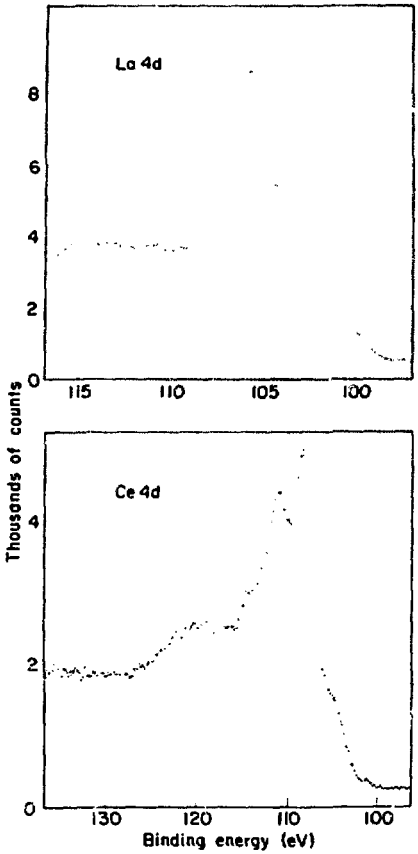

Fig. 4. La and Ce 4d spectra. (XBL 7410-4357)

Figure 5 summarizes the results for the 4s and 5s measured splittings for the rare earth metals. The solid lines are Van Vleck's theoretical estimates for the metals in their trivalent state. The estimates for ΔE_{4s} have been scaled by 0.55 to account for correlations. The observed values follow the theoretical curve quite well which supports the idea of the near constancy of correlation. Only Eu and Yb significantly deviate and this is due to their divalent character. This suggests the ΔE_{ns} measurements could be applied to the problem of determining valency ratios in mixed valency rare earth compounds. Levels with nonvanishing orbital angular momentum often possess very complicated multiplet structures.[4b,6] This structure can be useful as a valency fingerprint. The 4d spectra of La($4f^0$) and γ-Ce($4f^1$) metals are displayed in Fig. 4. One could for instance determine if Ce was tetravalent ($4f^0$) or trivalent ($4f^1$) in a particular compound or alloy. A trivalent Ce 4d spectrum would resemble that of γ-Ce, while tetravalent Ce would exhibit a 4d spectrum similar to La metal which just shows spin-orbit splitting.

Footnotes and References

*Condensed from LBL-3430; published in the "Proceedings of the 20th Annual Conference on Magnetism and Magnetic Materials".

†IBM Fellow.

1.C. S. Fadley and D. A. Shirley, Phys. Rev. A 2, 1109-1120 (1970).

2. J. H. Van Vleck, Phys. Rev. 45, 409-419 (1934).

3. P. S. Bagus, A. J. Freeman, and F. Sasaki, Phys. Rev. Lett 30, 850-853 (1973).

4. a) S. P. Kowalczyk, L. Ley, R. A. Pollak, F. R. McFeely, and D. A. Shirley, Phys. Rev. B 7, 4009-4011 (1973).

b) S. P. Kowalczyk, L. Ley, F. R. McFeely, and D. A. Shirley, Phys. Rev. B, 11, 1721 (1975).

5. C. Kittel, Introduction to Solid State Physics, 3rd Edition (John Wiley & Sons, Inc., New York, 1968)p. 461.

6. S. P. Kowalczyk, N. Edelstein, F. R. McFeely, L. Ley, and D. A. Shirley, Chem. Phys. Lett. 29, 491 (1974).

X-RAY PHOTOEMISSION STUDY OF THE ELECTRONIC STRUCTURE OF THE 3d TRANSITION METALS Sc TO Zn†

L. Ley,* F. R. McFeely, S. P. Kowalczyk, and D. A. Shirley

The 3d transition elements comprise an interesting group of metals, exhibiting a wide variety of structural, electronic, and magnetic properties. Since many theories of the magnetic properties of the transition metals take d-bandwidth, total bandwidth, and density of states at the Fermi level as essential one-electron properties responsible for the magnetic behavior, clearly detailed, quantitative information over the entire occupied range of the density-of-states N(E) is essential. It is just such information which is supplied by x-ray photoemission spectroscopy.

All spectra reported here were taken with a Hewlett-Packard 5950A electron spectrometer modified to operate at a base pressure of 2×10^{-10} Torr. The use of a high energy photon source, monochromatized Al K_α radiation of 1486.6 eV, insures a featureless density of final states in the photoemission process. The samples were thin films prepared *in situ* by standard methods.

The valence band spectra of the non-magnetic metals Sc and Ti are rather free-electron-like in appearance, having less pronounced structure than other members of the series. The valence bands also exhibited the strongest plasmon energy loss structure, which is indicative of a free-electron-like metal.[1]

Vanadium and chromium, with 5 and 6 valence electrons, respectively, both crystallize in the body centered cubic structure. Chromium at room temperature is an antiferromagnet with a spin-density wave periodicity slightly less than twice that of the lattice. For computational simplicity, Asano and Yamashita[2] treated antiferromagnetic chromium with a magnetic superlattice with exactly twice the ordinary lattice constant. The antiferromagnetic splittings were found to be of the order of 0.4 eV. Since they varied for different bands over the entire range of N(E), however, their effect on N(E) should be small. This is demonstrated by the calculations of Connolly.[3] We therefore in Fig. 1 compare the spectrum with N(E) for paramagnetic Cr.[4] Note especially the plateau of low density of states near E_F indicated by the spectrum. This important feature was not observable by ultraviolet photoemission[5] or soft x-ray emission[6] techniques. The theoretical N(E) shown for vanadium is that of Cr, with E_F shifted to account for the change in number of valence electrons. As can be seen, the agreement between this rigid-band approach and experiment is quite remarkable.

The success of this rigid band approach indicates that the theoretical N(E) for Cr, with E_F shifted to account for the addition of 2 electrons would be a good model for Fe. This is shown in Fig. 2(a). Figure 2(b) shows the same N(E) adjusted for spin polarization by allowing for the appropriate magnetic moment in the ferromagnetic state and assuming a k-independent exchange splitting ΔE.

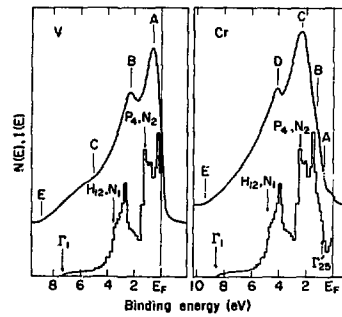

Fig. 1. XPS spectra of V and Cr compared with the theoretical N(E) for paramagnetic Cr. (XBL 747-3647)

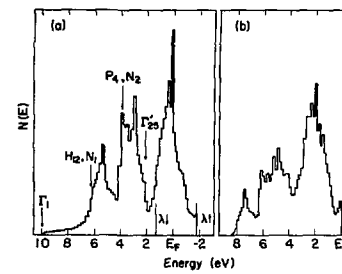

Fig. 2. N(E) for Fe generated from (N(E) for Cr by assuming rigid bands, (a) without spin polarization (b) with spin polarization. (XBL 747-3644)

Instead of a peak in N(E) at E_F, this procedure predicts a low value of N(E) at E_F with a peak at 1.8 eV below E_F. This prediction is fulfilled by the photoemission spectrum shown in Fig. 3 along with the spin-polarized N(E) curve of Connolly.[3] The heavier members of this series yield photoemission spectra generally in good agreement with existing calculations.

Briefly, we can make the following general points based on our spectra. 1) The d-bands are seen to evolve systematically across the series

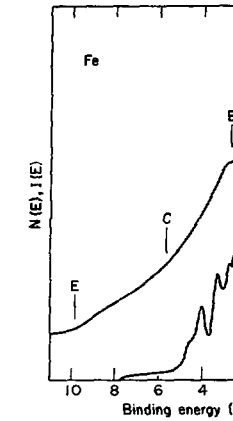

Fig. 3. XPS spectrum of Fe compared to the N(E) curve of Connolly. (XBL 747-3643)

from bands reflecting a high degree of free-electron-like behavior in Sc to bona fide core levels in Zn. 2) A rigid-band-model extrapolation of the theoretical densities of states between isostructural nearest neighbors in the series works very well. 3) The spectrum of iron can be explained by shifting theoretical nonmagnetic N(E) plots to align the chemical potentials of the spin-up and spin-down sub-bands. This is strong support for the validity of the spin-polarized band model.

Footnotes and References

†Condensed from "Proceedings of the 20th Annual Conference on Magnetism and Magnetic Materials."

*IBM Fellow.

1. R. A. Pollak, L. Ley, F. R. McFeely, S. P. Kowalczyk and D. A. Shirley, J. Electr. Spectros. 3, 381-398 (1974).

2. S. Asano and J. Yamashita, J. Phys. Soc. (Japan) 23, 714-736 (1967).

3. J. W. D. Connolly, Electronic Density of States, Nat. Bur. Std. Special Publication 323, 27-32 (1971).

4. R. P. Gupta and S. K. Sinha, Phys. Rev. B3, 2401-2411 (1971).

5. D. E. Eastman, J. Appl. Phys. 40, 1387-1394 (1969).

6. D. W. Fischer, Phys. Rev. B4, 1778-1786 (1971).

CRYSTAL-FIELD EFFECTS ON THE APPARENT SPIN-ORBIT SPLITTING OF CORE AND VALENCE LEVELS OBSERVED BY X-RAY PHOTOEMISSION

L. Ley,† S. P. Kowalczyk, F. R. McFeely, and D. A. Shirley

A feature readily observed in x-ray photoelectron spectroscopy (XPS) of heavier elements is a splitting of core levels, commonly referred to as spin-orbit (s-o) splitting. This splitting reflects the two possible couplings of the core hole spin $\vec{s}$ with its angular momentum $\vec{\ell}$ forming total angular momentum eigenstates differing in energy by the difference in the expectation value $\langle \vec{\ell} \cdot \vec{s} \rangle$ multiplied by a factor ξ, the coupling strength. Improvement in the resolution obtained in XPS and the availability of UV sources in an energy range that gave access to the least-bound core levels improved the accuracy with which these splittings could be measured to an extent that made it possible to measure small deviations of the spin-orbit splitting in solids from those measured in the gas phase. Furthermore even changes in the splitting of the outermost d-levels in Zn and Cd have been observed in going from the metal to binary compounds containing one of these elements.[1,2]

It is convenient to compare the splittings observed in solids to those for the free ions as a secure starting point for the discussion of various solid-state effects. To do this, we have compared the free-ion spin-orbit splitting from the observed term values of the configuration $(d^9)^2D$ in the optical spectra of the ions.[3] While rendering the determination of the spin-orbit splitting straightforward and reliable, this method has the disadvantage that we have to deal in some cases with very highly ionized atoms. Results for the spin-orbit splitting given in Dunn's compilation[4] makes two points clear; 1) for a given d-shell configuration the spin-orbit splitting increases with increasing ionic charge by not more than 2% per unit charge; 2) a change in the d-configuration $(d^9 \rightarrow d^8)$ affects the spin-orbit splitting considerably more than the corresponding increase in ionic charge. These two points are consequences of the approximate form of the spin-orbit Hamiltonian-operator:

$$H_{s.o.} = \frac{\alpha^2}{2}\left(\frac{1}{r}\frac{\partial V}{\partial r}\right)\vec{l}\vec{s} \ ,$$

neglecting exchange effects and the mutual spin-orbit and spin-spin interaction of electrons in unfilled shells.[5] Here α is the fine-structure constant and V is the shielded nuclear potential. The dependence of the expectation value $\langle l_{s.o.} \rangle$ mainly on the inner part of the electronic wavefunction ψ has been pointed out by many authors. The variation in the operator $\frac{1}{r}\frac{\partial V}{\partial r}$ upon charge transfer in outer shells is very small in this region.

Data obtained from solids are given in Tables 1 and 2 and can be summarized as follows:

1) Core-like d-levels of elements in tetrahedral surroundings show no, or only a very small (> 1%), increase in the apparent $\Delta E_{s.o.}$ compared to free-atom values. The only exceptions are the Te compounds with an average increase of ~ 2.8%.

2) In, Te, Cd and Zn metals have an apparent $\Delta E_{s.o.}$ in the outermost d-levels which exceed the free atom values by 4.7, 7, 45, 59% respectively.

3) Pb and Sb show no such increase.

4) Valence d-bands in Ag and Au are split by amounts far exceeding the free-atom $\Delta E_{s.o.}$ value, in contrast to the valence p-bands (Bi, Pb) which are split by energies close to $\Delta E_{s.o.}$ for the free atoms.

We will now discuss the influences on the apparent spin-orbit splitting of "core-like" d-levels of an atom surrounded by other atoms in a solid. We note at the outset that we are dealing with final-state structure following photoemission from a closed shell. This is manifestly a one-electron (hole) problem. The appropriate d hole state Hamiltonian in the one-electron approximation has the form

$$H = h_0 + h_{cryst} + h_{s.o.} \quad . \qquad (1)$$

Here h_0 contains the kinetic energy operator and the spherical Coulomb potential of the nuclear charge Z screened by the inner electrons forming closed shells. The h_{cryst} term summarizes the potentials due to the neighboring atomic cores and the valence electrons including the valence electrons of the atom under consideration, and $h_{s.o.}$ is the one-electron spin-orbit hamiltonian.

We wish to show that the differences in the value for the d-level splittings, $\Delta E_{s.o.}$ observed in different solid environments is a result of the influence of h_{cryst} rather than of a modification in $h_{s.o.}$. The spin-orbit interaction is a first order effect in the expansion of the relativistic energy expression for a spinning electron in an electric field U.[6] The non-relativistic form generalized to a many electron system can be written as[7]

$$h_{s.o.} = \frac{\alpha^2}{2} \left\langle \frac{1}{r} \frac{\partial U_{eff}}{\partial r} \right\rangle \Sigma_i \; \ell_i \cdot s_i$$

+ terms which include mutual spin-orbit interactions and spin-spin interactions in the unfilled shell. (2)

So far we have dealt with the effects of charge transfer in the valence shell of the central atom on $\langle h_{s.o.} \rangle$. We must also consider direct changes in the wavefunction of the d-electrons itself upon entering a solid or molecule. These changes can be considered in two parts:

1) Renormalization of ψ_d due to the necessary orthogonalization of ψ_d with respect to wavefunctions on neighboring atoms. In the simplest case of orthogonalization to one other orbital, this leads to a renormalization-factor of $(1-S^2)^{-\frac{1}{2}}$, where S is the overlap integral between the two orbitals. This leads to an increase in the coefficient of ψ_d and therefore in the Lande factor ζ_d. The components added to the wavefunction upon orthogonalization make only vanishing contributions for small r, the region which determines ζ_d.

2) A mixing of the d-electrons with electrons of different symmetry located at the same atom. This mixing is always possible throughout the Brillouin zone but at k = 0 it is possible only for certain symmetry components of the potential. This effect leads to a decrease in the spin-orbit splitting, because the orbital that will mix most strongly to the nd wavefunction is (n+1)p, with a Lande factor smaller than that of the d orbital. We can therefore dispense with the second effect in explaining increases in the apparent $\Delta E_{s.o.}$.

Since direct changes in the expectation value of $h_{s.o.}$ can not be responsible for the observed increases in the apparent $\Delta E_{s.o.}$ over their free-atom values. The explanation must therefore be sought in the h_{cryst} term if we are to explain the enhancement within the framework of the Hamiltonian in Eq. (1).

The matrix element of h_{cryst} can be expanded into a series of spherical harmonics $Y_{LM}(\theta,\phi)$. The angular momentum $\hat{L}$ of the state under consideration limits this expansion to a sum over even orders in L. For d electrons the last nonvanishing term has $L_{max} = 4$, while for p-electrons $L_{max} = 2$. The matrix element $\langle h_{cryst} \rangle_i$ has the symmetry of the point group of the lattice and is in general given by

$$\langle h_{cryst} \rangle_i = \sum_{L=0,2,4,} A_L T_L(i) \quad , \qquad (3)$$

where $T_L(i)$ is the linear combination of spherical harmonics of order L that transforms as the symmetrical irreducible representation of the point group of the lattice at the center of the Brillouin-zone. A_L is the expansion coefficient, which contains the radial integral of the Coulomb and exchange interaction of the electron i with the valence electrons and the surrounding ion cores. We shall ignore the term with L = 0 which corresponds to a generalized Madelung energy and cannot contribute to a splitting in the atomic levels. In solids which crystallize in lattices of cubic symmetry the A_2 T_2 term in expression (3) vanishes. This applies to the face centered cubic (f.c.c.) lattices of Ag, Au and Pb and to the tetrahedrally coordinated binary compounds. All other symmetries encountered in this investigation require the retention of the L = 2 term.

Table 1. Spin-orbit splittings in the free atoms and solids. Errors are given parenthetically. The Roman numerals indicate the ionization state of the atoms (ZnII = Zn^+).

Element	Shell	Lattice	Splitting (eV)	Reference
Zn II	Zn3d	free ion	0.337	3
Zn metal	Zn3d	hex	0.54(2)	a
CdII	Cd4d	hex	0.669	3
Cd Metal	Cd4d	hex	0.95(3)	a
Cd Metal	Cd4d	hex	0.99(5)	1
CdTe	Cd4d	z.b.[g]	0.70(5)	b
CdTe	Cd4d	z.b.	0.83(20)	c
CdS	Cd4d	z.b.	0.76(12)	c
CdSe	Cd4d	z.b.	0.87(16)	c
AgCd alloy	Cd4d	cubic	0.70(8)	this work
InIII	In4d	free ion	0.849	3
In metal	In4d	tetragonal	0.90(1)	1
In metal	In4d	tetragonal	0.88(15)	b
In metal	In4d	tetragonal	0.86(3)	a
InSb	In4d	z.b.	0.83(3)	d
InSb	In4d	z.b.	0.85(5)	b
InSb	In4d	z.b.	0.84(8)	2
InP	In4d	z.b.	0.84(8)	2
Sb V	Sb4d	free ion	1.239	3
Sb metal	Sb4d	rhombohedral	1.25(4)	1
GaSb	Sb4d	z.b.	1.21(4)	2
InSb	Sb4d	z.b.	1.22(4)	2
InSb	Sb4d	z.b.	1.15(10)	d
InSb	Sb4d	z.b.	1.25(5)	b
Te VII	Te4d	free ion	1.409	3
Te metal	Te4d	hex	1.51(1)	1
ZnTe	Te4d	z.b.	1.47(2)	2
CdTe	Te4d	z.b.	1.47(2)	2
HgTe	Te4d	z.b.	1.44(2)	2
PbTe	Te4d	NaCl	1.46(2)	2
PbTe	Te4d	NaCl	1.35(10)	d
Hg I	Hg5d	free atom	1.800	3
Liquid Hg	Hg5d	-	1.83(9)	2
HgTe	Hg5d	z.b.	1.77(2)	2
HgTe	Hg5d	z.b.	1.91(10)	c
HgSe	Hg5d	z.b.	1.81(10)	c
HgS	Hg5d	z.b.	1.79(10)	c
Pb IV	Pb4d	free ion	2.643	3
Pb metal	Pb4d	f.c.c.	2.62(2)	f
Pb metal	Pb4d	f.c.c.	2.66(9)	a
PbS	Pb4d	NaCl	2.58(2)	e
PbSe	Pb4d	NaCl	2.61(2)	e
PbTe	Pb4d	NaCl	2.62(2)	e

(continued)

Table 1. (continued)

[a] R. T. Poole, P. C. Kemeny, J. Liesegang, J. G. Jenkin, and R. C. G. Leckey, J. Phys. F., 3, 1146 (1973).
[b] D. E. Eastman, W. D. Grobman and J. Freeouf (unpublished) D. E. Eastman, J. Freeouf and M. Erbudak, Congres du Centenaire de la Societe Francaise de Physique, Vittel, France, (1973) unpublished.
[c] C. J. Veseley, R. L. Hengehold and D. W. Langer, Phys. Rev. B 5, 2296 (1972).
[d] N. Cardona, C. Penchina, N. Schevchik, and J. Tejeda, Solid State Commun. 11, 1655 (1973).
[e] F. R. McFeely, S. P. Kowalczyk, L. Ley, R. A. Pollak, and D. A. Shirley, Phys. Rev. B 7, 5228 (1973).
[f] L. Ley, R. Pollak, S. P. Kowalczyk and D. A. Shirley, Phys. Lett. 41A, 429 (1972).
[g] z.b. = zincblende structure.

Table 2. Free atom spin-orbit splitting and the apparent splitting of valence-band peaks in Ag, Au, Pb and Bi.

Element	Shell	Lattice	Splitting (eV)	Reference
Ag I	4d	free atom	0.555	3
Ag metal	4d	f.c.c.	1.6(1)	1
Au I	5d	free atom	1.522	3
Au metal	5d	f.c.c.	3.8(2)	a
Pb I	6p	free atom	1.746	3
Pb metal	6p	f.c.c.	1.80(5)	c
Bi I	6p	free atom	2.163	b
Bi metal	6p	rhombohedral	2.16(8)	c

[a] D. A. Shirley, Phys. Rev. B5, 4709 (1972).
[b] C. C. Lu, T. A. Carlson, F. B. Malik, T. C. Tucker and C. W. Nestor Jr., Atomic Data 3, Nr. 1 (1971).
[c] L. Ley, R. Pollak, S. P. Kowalczyk, and D. A. Shirley, Phys. Lett. 41A, 429 (1972).

It is evident from the data in Table 1 that all cases which exhibit an increase in $\Delta E_{s.o.}$ for the core d-levels fall into this latter group with the possible exception of the tellurium salts. The nonvanishing A_2T_2 term in expansion (3) seems therefore a necessary condition for an increase in $\Delta E_{s.o.}$.

Let us explore this possibility in more detail using Zn and Cd as examples. Zn and Cd crystallize in a hexagonal lattice. In this case it is convenient to divide the L = 2 term into three factors:

$$\langle h_{cryst} \rangle_i = f(\tfrac{c}{a}) \cdot A_2^{hex} \cdot T_2^{hex} + A_4^{hex} T_4^{hex} \qquad (4)$$

The geometrical factor $f(\frac{c}{a})$ depends on the ratio of the crystalline axes c and a. For c/a = 1.63, the ideal hexagonal lattice, $f(\frac{c}{a})$ is zero and the A_2T_2 vanishes for geometrical reasons. In Zn and Cd however, c/a is equal to 1.86 and the L = 2 term enters with a considerable geometrical advantage ($f(\frac{c}{a}) > 1$ in the point-ion model). We have diagonalized the two operators $h_{s.o.} + h_{cryst}$ in the sub-space of the d-electrons. The method employed for this calculation uses standard angular momentum algebra as outlined in Edmonds.[6] Figure 1(a) shows the level scheme for a d^9 configuration in the ideal hexagonal field ($f(\frac{c}{a}) = 0$) as a function of A_4. All degeneracies are lifted, yet the increase in the apparent spin-orbit splitting is negligible for values of A_4 which preserve the observed pattern of two d-peaks, that is for

$|A_4| < 0.4|\xi|$. Lifting the restriction of $c/a = 1.63$ introduces the A_2T_2 term, which changes the level pattern appreciably (Fig. 1(b)). As mentioned above, A_2 is expected to be greater than A_4 and we have therefore plotted the level scheme under the assumption that $A_4 = 0$. For positive values of A_2 the spin-orbit split doublets evolve into a pattern of two nondegenerate doublets and a single level, which would result in a three peak spectrum with relative intensities 1:2:2. For $A_2 < 0$ a drastic increase in apparent $\Delta E_{s.o}$ is possible without destroying the general appearance of a spin-orbit split d-doublet with the correct intensity ratio of 2:3. The value of A_2 which gives the observed spin-orbit splitting in Zn and Cd is about $1.4 \mid 5/2\xi \mid$. A spectrum generated from the level scheme at this point does indeed resemble the observed Cd spectrum closely.

This direct evidence that the increase in apparent $\Delta E_{s.o.}$ in Cd and Zn is symmetry-induced is supported by three pieces of additional experimental data.

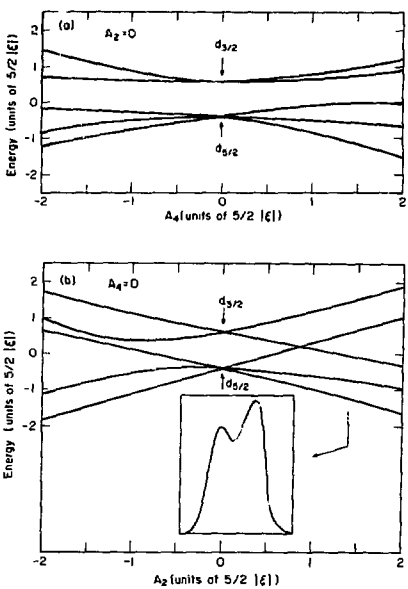

Fig. 1. Energies of a d^9 configuration as a function of the generalized crystal field parameter A_2. (a) ideal hexagonal field: $c/a = 1.63$, $A_2 = 0$; (b) general hexagonal field; A_4 is assumed to be zero. The insert shows a spectrum for $A_2 = 1.4 \mid 5/2 \ \xi \mid$. The line width of each component is equal to ξ. (XBL 746-3462)

1) Figure 2 shows the Cd 4d double[†] and for Cd metal and a AgCd alloy (10% Cd). The substitutional introduction of the Cd atom into the cubic surrounding of the Ag lattice reduces $\Delta E_{s.o.}$ to the free atom value.

2) The photoemission spectrum of Cd deposited in submonolayer coverage onto a Au single crystal shows no increase in spin-orbit splitting of the 4d level (compare Fig. 2). We interpret that as

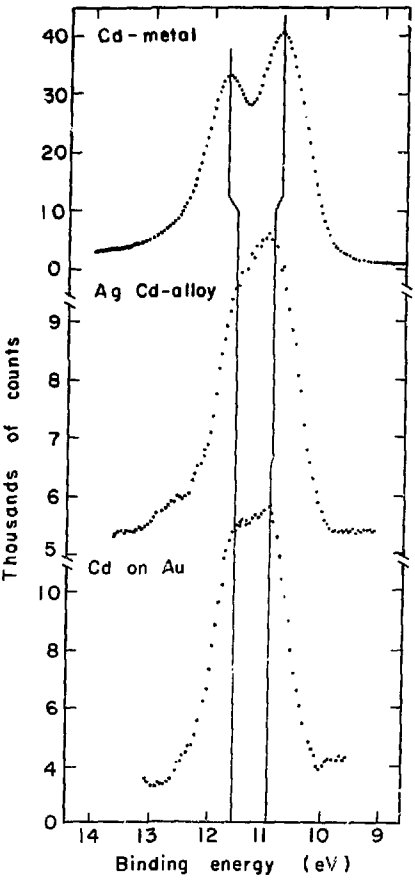

Fig. 2. The Cd 4d spectrum of (a) Cd metal, (b) a AgCd alloy (10% Cd), and (c) surface isolated Cd atoms. (XBL 744-2979)

the observation of single Cd atoms which are subjected to no crystal field. When the Cd coverage is increased to the extent, that the formation of Cd clusters becomes possible, the d-level splitting increases to the value in Cd metal.

3) Another physical property that is known to be proportional to the $L = 2$ term in an expansion similar to that of expression (3) is the electric field gradient at the nucleus. This field gradient can be measured by observing the interaction of the nuclear quadrupole moment Q with the field gradient q. Values of the coupling constant eqQ/h for ^{111}Cd in host lattices of Pb, In, Zn and Cd[9] are plotted against the increase in apparent $\Delta E_{s.o.}$ for these metals in Fig. 3. The plot shows a quite convincing correlation between the excess splitting and the quadrupole interaction of the few points available.

Let us turn now to the splittings observed in the valence d shells of Ag and Au and the p shells in Pb and Bi. These cases cannot be treated rigorously without taking the band character of these states into account. That is, level ordering at $\vec{k} = 0$ is not necessarily representative of the appearance of the density of states $\rho(E)$ as observed in an XPS-spectrum. The elements Ag, Au, Pb, and approximately also Bi crystallize in the fcc structure; that is, the symmetries throughout the Brillouin zone are the same for all four elements. Nevertheless, the observed differences in the apparent $\Delta E_{s.o.}$ between d bands (increase) and p bands (no increase) is striking they can be understood in terms of the symmetry induced splittings at representative points of the Brillouin zone. The d-electrons of Ag and Au are already split into two groups of bands, Γ_{12} and Γ'_{15}, at Γ the center of the BZ which has the full octahedral

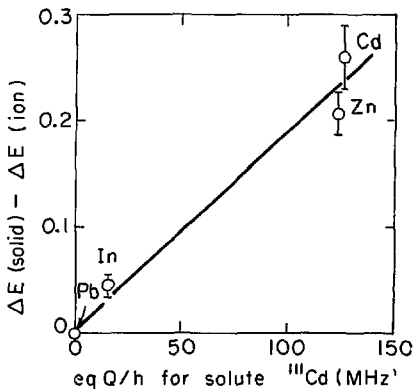

Fig. 3. The excess in apparent spin-orbit splitting $\Delta E_{s.o}$ versus the electrical quadrupole interaction strength eqQ/h of ^{111}Cd for a number of metals. (XBL 744-2975)

symmetry. Towards the outer parts of the BZ, these bands split further accompanied by a rearrangement of levels according to the various irreducible representations at symmetry points of lower than cubic symmetry. The maximum splitting occurs at X the center of the square face of the BZ. The pattern set by Γ and X can be regarded as representative for the two peaked structure in the density of states of Ag and Au. The spin-orbit interaction enhances this splitting further without being the dominant factor, however. The lower angular symmetry of the p-valence electrons in Pb and Bi preserves their orbital degeneracy at Γ. Along the symmetry directions on the surface of the BZ this degeneracy is partially lifted forming a single and a doublet level at each symmetry point except K.

The energy dispersion of these bands along the surface of the BZ is in general smaller than their splitting, giving rise to a two peaked density of states. In Pb and Bi, with 2 and 3 p-electrons respectively, only the bands in the lower peak of $\rho(E)$ are occupied, so that we would observe a single peak in the XPS-spectrum in the absence of spin-orbit interaction. In the presence of spin-orbit interaction however the two fold degenerate level at W splits and an inspection of the relativistic band structure of Pb by Loucks[10] reveals, that this splitting is preserved over much of the surface of the BZ giving rise to the observed doublet in the occupied part of $\rho(E)$. In the tight binding approximation, and in the absence of s-p hybridization the splitting at W equals the atomic splitting, a result that is in good agreement with experiment.

FOOTNOTES AND REFERENCES

*Condensed version of LBL-2901 and Phys. Rev. B10, 4881 (1974).

†IBM Fellow, present address: Max Planck Institut für Festkörperfonschung, Stuttgart.

1. R. A. Pollak, S. P. Kowalczyk, L. Ley, and D. A. Shirley, Phys. Rev. Letters 29, 274 (1972).

2. L. Ley, R. A. Pollak, F. R. McFeely, S. P. Kowalczyk and D. A. Shirley, Phys. Rev. B9, 600 (1974).

3. C. E. Moore, Atomic Energy Levels (U. S. Department of Commerce, NBS Circular No. 467 (1958).

4. T. M. Dunn, Trans. Faraday Soc. 17, 1441 (1961).

5. M. Blume and R. E. Watson, Proc. Roy. Soc. AZ70, 127 (1962).

6. P. A. M. Dirac, The Principles of Quantum Mechanics, (Oxford University Press, New York, 1947).

7. L. I. Shiff, Quantum Mechanics (McGraw Hill, New York, 1955).

8. A. R. Edmonds, Angular Momentum in Quantum Mechanics, (Princeton University Press, Princeton, N.J. (1957).

9. H. Haas and D. A. Shirley, J. Chem. Phys. 58, 3339 (1973).

10. T. L. Loucks, Phys. Rev. Letters 14, 1072 (1965).

THE STRUCTURAL NATURE OF AMORPHOUS Se AND Te*†

M. Schlüter, J. D. Joannopoulos, M. L. Cohen
L. Ley, S. P. Kowalczyk, R. A. Pollak, and D. A. Shirley

Recent X-ray (XPS) and ultraviolet (UPS) photoemission measurements on Se[1] and the new experiments presented here on Te show some remarkable differences between their trigonal and amorphous phases. One of these differences corresponds to a seemingly sharper structure in the s-like states of the amorphous phase of Se which is very unusual for an amorphous spectrum. Other important differences appear as interchanging strengths in the two peaks of the p-like bonding states. To explain these differences in terms of the possible structural nature of the amorphous phase we must first understand the origins of the structure in the crystalline spectrum.

Electronic charge distributions obtained from pseudopotential calculations on Se and Te[2] indicate that (1) the splitting of the two peaks in the p-like bonding states is related to the amount of mixing and hybridization of p_x, p_y, s and d states and (2) the relative strengths of these two peaks is related to the relative amount of intrachain and inter-chain bonding. The s-like region of the density of states is of considerable importance since these states are very sensitive to topology. The structure in the s-like region of the density of states of trigonal Se is very similar to that of a one-dimensional chain and thus reflects the definite chain-like nature of this phase. In trigonal Te, however, the structure in the s-like region is more similar to the superposition of a one-dimensional chain density of states and a three dimensional simple cubic density of states.

Let us examine the changes occurring in the amorphous phase. Figure 1 (top) shows the photoemission results of Shevchik et al.[1] for trigonal and amorphous Se. In the "lone-pair" region (between -2 eV and 0 eV), the amorphous spectrum has lost some fine structure and is shifted slightly to higher energies. However in the bonding p-like region (between -6 eV and -2 eV) rather interesting changes have occurred. The lower energy peak has become weaker whereas the higher energy peak has become stronger in the amorphous phase. This reversal corresponds to a decrease of the number of pure intra-chain bonding states. There are now more electrons occupying states localized outside the chains. The splitting of these peaks is very sensitive to the bond angle and hence to the hybridization. In the amorphous phase this splitting remains essentially unchanged, suggesting that bond angle variations are relatively small.

In the s-like region (between -18 eV and -7 eV) for Se there is a very unusual effect. The dip seems to be bigger in the amorphous phase than

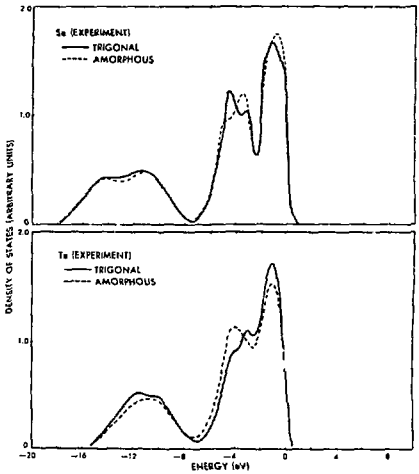

Fig. 1. X-ray and ultraviolet photoemission results (top) on trigonal (solid line) and amorphous (dashed line) Se as obtained from ref. 1. The amorphous sample was prepared by d.c. sputtering at room temperature. X-ray photoemission results (bottom) on trigonal (solid line) and amorphous (dashed line) Te as obtained in this work. Here the amorphous Te sample was obtained by Argon bombardment. The "lone-pair" states lie between -2 eV and 0 eV. The bonding p-like states lie between -6 eV and -2 eV and the s-like states are below -8 eV. (XBL 756-1566)

in the trigonal phase. This suggests some interesting structural properties. The change could not be caused by breaking of the infinite chains, which would only tend to fill up the dip. A reasonable alternative is the formation of rings. In particular the dip would increase if the rings were of order three, five, six or seven. Rings of order four, eight, or five and seven together, would certainly tend to fill up the dip.[3] Furthermore, since the bond angles in the trigonal phase are around 104°, the most likely ring structures

are five-fold and six-fold, or six-fold and seven-fold. To demonstrate the effect of the existence of rings on the density of states we have carried out two model calculations on Se containing only six-fold and only eight-fold rings respectively. On the basis of these results we propose that the amorphous Se samples contain a substantial number of atoms in ring-like configurations of order six. This suggestion seems to be consistent with Rechtin's and Averbach's[4] interpretation of their radial distribution function data.

The photoemission results for amorphous and trigonal Te obtained by Shevchik et al.[5] using the same sputtering technique as in the Se case give similar results. However these results differ from our photoemission data on amorphous and trigonal Te. Our experimental procedure was as follows. The x-ray photoemission spectra of Te were measured with a Hewlett-Packard ESCA-spectrometer 5950A utilizing monochromatized Al K_α x-rays (1486.6 eV) with a resoltuion of 0.6 eV (FWHM). A single crystal of Te was cleaved just prior to insertion into the spectrometer in an atmosphere of dry nitrogen. The amorphous sample was obtained after 2 hours of Ar^+-ion bombardment. The results are shown in Fig. 1 (bottom). In the bonding p-like region (-2 eV to -6 eV) we now find, in contrast to Se, a shift of strength to lower energies in the amorphous case. This suggests an increase in the number of the pure intra-chain bonding electrons, which would be consistent with an increase in the covalency of Te in the amorphous phase.

Footnotes and References

*Supported in part by the National Science Foundation, Grant GH 35688.

†Short version of a letter published in Solid State Communications 15, 1007 (1974).

1. N. J. Shevchik, J. Tejeda, M. Cardona and D.W. Langer Solid State Comm. 12, 1785 (1973).

2. M. Schlüter, J. D. Joannopoulos and M. L. Cohen, Phys. Rev. Letters 33, 89 (1974).

3. J. D. Joannopoulos, F. Yndurain, L. Falicov and M. L. Cohen, IBM International Tetrical Conference on Tetrahedrally Bonded Amorphous Semiconductors (to be published).

4. M. D. Rechtin and B. L. Averbach, Solid State Comm. 13, 491 (1973).

5. N. J. Shevchik, M. Cardona and J. Tejeda, Phys. Rev. B8, 2833 (1973).

AN IONICITY SCALE BASED ON X-RAY PHOTOEMISSION VALENCE-BAND SPECTRA OF A^NB^{8-N} AND A^NB^{10-N} TYPE CRYSTALS*

S. P. Kowalczyk, L. Ley,† F. R. McFeely, and D. A. Shirley

In general the spectra of the valence band region of A^NB^{8-N} and A^NB^{10-N} crystals show a three-peak structure, occasionally with a sharp core d peak intruding. Figure 1 shows the raw XPS-VBDOS spectra of some typical Group IV and Group V elements, and III-V, II-VI, IA-VII, and IV-VI compounds. Walter and Cohen[1] calculated electronic charge densities for several diamond zincblende semiconductors from pseudopotential band-structure wavefunctions. These charge densities give the distribution of the valence electrons in each band in real space: they can be related to peaks in our spectra. Peak I (PI) consists of electrons centered around the anion atomic site; i.e., an "s-like" distribution. Peak II (PII) consists of electrons basically centered around the cation, and located in the bonding region. Peak III (PIII) results from electrons concentrated between the atomic sites in the bonding region, i.e., a "p-like" distribution. With this in mind, and realizing that the *valence-band peaks cannot be truly described* with such a simple atomic picture, we shall refer to PI and PII as "s-like" bands and PIII as "p-like". Fuller discussions of the atomic derivation of the valence-band peaks are available in Refs. 2 and 3.

It was noted previously in an XPS study of the VBDOS of the isoelectronic series Ge, GaAs, and ZnSe[4] that the PI - PII splitting, ΔE_S^{XPS}, increased with increasing ionicity. This increasing splitting was attributed mainly to an increasing localization of electrons around the stronger anion potential. However, to devise a quantitative scale of ionicity, a covalent fiducial point is necessary. The need to treat ionic and covalent contributions on an equal footing has been cogently put forth in several articles by Phillips and Van Vechten.[5-8] Ley et al.[9] in an XPS-VBDOS study of groups IV and V covalent elemental crystals observed a rather simple relationship between the covalent splitting of PI and PII, ΔE_S^C, and the nearest-neighbor distance, d. The observed relation is

$$\Delta E_S^C = 8.0 - 2.2\,d \quad , \qquad (1)$$

with ΔE_S^C in eV and d in A. The measured ΔE_S^C and d for these crystals are listed in Table 1.

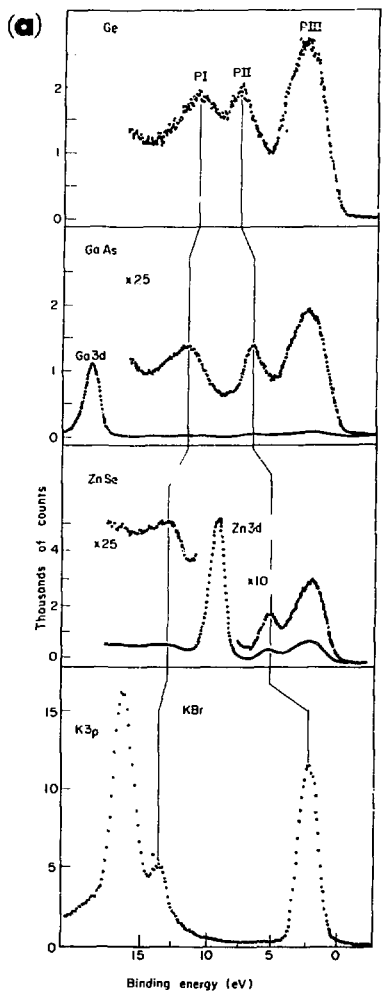

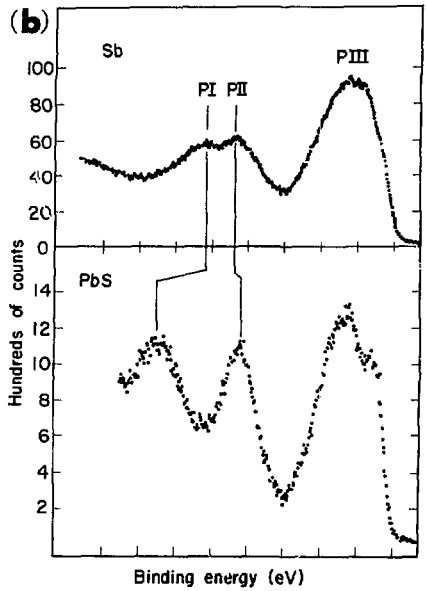

Fig. 1. (a) X-ray photoemission valence band spectra of several typical A^NB^{8-N} type crystals, Ge, GaAs, ZnSe, and KBr; and (b) A^NB^{10-N} type crystals, Sb and PbS. (a) XBL 745-3033) (b) XBL 745-3035)

Table 1. Nearest-neighbor distance and ΔE_S^C splitting for group IV and group V elemental crystals.

Crystal	Structure	d(Å)[a]	ΔE_S^C(eV)	Ref.
C	diamond	1.54	4.7	10
Si	diamond	2.34	2.6	8
Ge	diamond	2.44	3.1	8
α-Sn	diamond	2.80	1.8[b]	—
As	A7	2.50	2.6	11
Sb	A7	2.86	1.7	11
Bi	A7	3.10	1.2	11

[a] R.W.G. Wyckoff, Crystal Structures (Wiley, Interscience, New York, 1965).

[b] Predicted value from Eq. (1).

The fact that ΔE_S^C depends on d in such a simple way for the homopolar crystals suggests that it is a strong function of overlap and could serve as a covalent fiducial point. The fact that the group V semimetals fall on the "universal curve" of Ref. 9 suggests that the ionicity of the A^NB^{10-N} as well as the A^NB^{8-N} crystals might well be included in an XPS-derived scale of ionicity.

We are now in a position to decompose our measured splitting of the "s-bands", ΔE_S^{XPS} into an ionic and a covalent contribution. ΔE_S^C is arrived at by simply inserting d(A) of the crystal under analysis into Eq. (1). To obtain the ionic contribution, ΔE_S^i, we suggest that the relationship

$$\Delta E_S^i = \Delta E_S^{XPS} - \Delta E_S^C \qquad (2)$$

be employed. Now an ionicity number can be simply defined as

$$\mathcal{f}_i^{XPS}(AB) \equiv \frac{\Delta E_S^i}{\Delta E_S^{XPS}} . \qquad (3)$$

For example let us consider the isoelectronic series Ge, GaAs, and ZnSe, the members of which have nearly constant d. Germanium with d = 2.44 A, is of course purely covalent and $\mathcal{f}_i^{XPS}(Ge) = 0.0$. GaAs also has d = 2.44 A and Eq. (1) yields $\Delta E_S^C = 2.6$ eV. ΔE_S^{XPS} was measured to be 4.8 eV, which yields $\Delta E_S^i = 2.2$ and $\mathcal{f}_i^{XPS}(GaAs) = 0.46$. In a similar manner for ZnSe (d = 2.45 A), $\Delta E_S^C = 2.6$ eV, $\Delta E_S^{XPS} = 7.8$, $\Delta E_S^i = 5.2$ and $\mathcal{f}_i = 0.67$.

Table 2 summarizes the structures, the various parameters used, the the derived $\mathcal{f}_i^{XPS}(AB)$ for the crystals used in this study. Before discussing the results in detail, let us compare this empirical ionicity scale with the dielectric-based scale of Phillips. Our ΔE_S^i, ΔE_S^C, and ΔE_S^{XPS} are analogous to the C, E_h and E_g, respectively, of Phillips. His E_g is the gap between bonding and antibonding states. Here E_h is the homopolar energy and is equal to E_g for homopolar crystals and determined by the empirical relationship

$$E_h \propto d^{-2.5}$$

for heterpolar A^NB^{8-N} crystals. C is the ionic contribution to E_g.

Phillips has discussed in detail the correspondence between ionicity and coordination for the A^NB^{8-N} crystals.[5,7] In his study of seventy A^NB^{8-N} crystals Phillips found a critical ionicity F_i such that for $\mathcal{f}_i < F_i$ the crystals are four-fold coordinated and for $\mathcal{f}_i > F_i$ the crystals are six-fold coordinated. With $F_i = 0.785$, Phillips' scale had 100% accuracy in predicting crystal structure, far superior to any other then available quantitative scale of ionicity. In

Table 2. Nearest-neighbor distances, energy of XPS splitting of lowest two valence bands ΔE_S^{XPS}, the covalent splittings ΔE_S^C, ionic splitting ΔE_S^i and ionicity number $\mathcal{f}_i^{XPS}(AB)$. These parameters are explained in the text. All energies are given in eV.

Crystal	d(A)[a]	Structure[b]	ΔE_S^{XPS}	ΔE_S^C[c]	ΔE_S^i	$\mathcal{f}_i^{XPS}(AB)$[d]	Ref.
GaAs	2.44	Z	4.8	2.6	2.2	0.46	13
ZnSe	2.45	Z	7.8	2.6	5.2	0.67	13
InSb	2.81	Z	4.1	1.8	2.3	0.56	13
CdTe	2.81	Z	~ 5.2	1.8	~ 3.4	~ 0.65	13
GaSb	2.65	Z	3.6	2.2	1.4	0.39	13
ZnTe	2.64	Z	6.5	2.2	4.3	0.66	13
AlI	3.53	R	8.3	0.2	8.1	0.97	15
InAs	2.61	Z	4.7	2.3	2.4	0.51	13
CdSe	2.63	W	~ 5.7	2.2	~ 3.5	0.61	13
InP	2.54	Z	4.3	2.4	1.9	0.44	13
CdS	2.53	W	~ 5.5	2.4	~ 3.1	~ 0.56	13
MnCl	3.29	R	10.7	0.7	10.0	0.94	h
AlSb	2.66	Z	4.3	2.2	2.1	0.49	g
MgI	3.24	R	8.1	0.9	7.2	0.89	15
MgBr	2.99	R	9.9	1.4	8.5	0.86	15
GaP	2.36	Z	3.0	2.8	1.0	0.26	13
ZnS	2.34	Z	7.5	2.9	4.6	0.61	13
KCl	3.15	R	11.8	1.1	10.7	0.91	15
ZnO	1.95	W	9.1	3.7	5.4	0.59	13
KF	2.67	R	20.9	2.1	18.7	0.90	15
MgO	2.10	R	13.5	3.4	10.1	0.75	g
MgP	2.32	R	21.1	2.9	18.3	0.86	15
PbS	2.97	R	4.4	1.5	2.9	0.67	12
PbSe	3.06	R	4.3	1.3	3.0	0.70	12
PbTe	3.23	R	3.5	0.9	2.6	0.74	12
SnTe	3.14	R	4.4	1.1	3.3	0.75	g
$Pb_{0.8}Sn_{0.2}Te$	3.23	R	3.1	0.9	2.2	0.70	g
$Pb_{0.4}Sn_{0.6}Te$	3.18	R	3.5	1.0	2.5	0.71	g
$Pb_{0.2}Sn_{0.8}Te$	3.16	R	4.3	1.1	3.2	0.74	g
LiF	2.01	R	19.7	3.6	16.1	0.82	15
KBr	3.30	R	15.0	0.7	14.3	0.95	15
NaCl	2.82	R	10.0	1.8	8.2	0.82	15
$CdSnAs_2$	2.64[e]	2^f	~ 5	2.2	~ 2.8	~ 0.56	14
$ZnGeP_2$	2.37[e]	2^f	6.8	2.8	3.0	0.42	14
CsCl	3.51	CsCl	10.6	0.3	10.3	0.97	42
CsF	3.00	R	20.9	1.4	19.5	0.93	42
CsBr	3.71	CsCl	9.6	~0.2	9.6	1.00	42
MgTe	2.76	Z	~ 3.5	1.9	1.6	~ 0.46	13
BeO	2.57	R	~ 13	2.6	10.6	~ 0.82	g

[a] R. W. G. Wyckoff, Crystal Structures (Wiley-Interscience, Inc., New York, 1963).

[b] Z - zinc-blende, R - rocksalt, W - wurtzite, CsCl - cesium chloride.

[c] From Eq. (3).

[d] From Eq. (3).

[e] A. S. Borschevskii, N. A. Goryunova, and F. P. Kesamanly, Phys. Stat. Sol. 21, 9 (1967).

[f] Chalcopyrite structure is analogous to zincblende structure with the cation site being occupied alternately by group II and group IV cation.

[g] Unpublished work of this laboratory.

[h] C. J. Vesely, D. L. Kingston, and D. W. Langer, Phys. Letters 44A, 137 (1973).

Fig. 2, we have plotted the ionicities of several A^NB^{8-N} crystals common to studies for each scale, with the structure noted by symbols. We have added to both scales several A^NB^{10-N} crystals, the lead salts and SnTe, which have the rocksalt structure. We have also added to our scale several $Pb_xSn_{1-x}Te$ alloys and two ternary semiconductors. If for the dielectric scale we keep $F_i = 0.785$, the $\mathcal{F}_i^{DT}(AB)$ scale will make four wrong predictions with the inclusion of the A^NB^{10-N} crystals. If we lowered F_i to 0.71, $\mathcal{F}_i^{DT}(AB)$ would make two errors but would no longer have

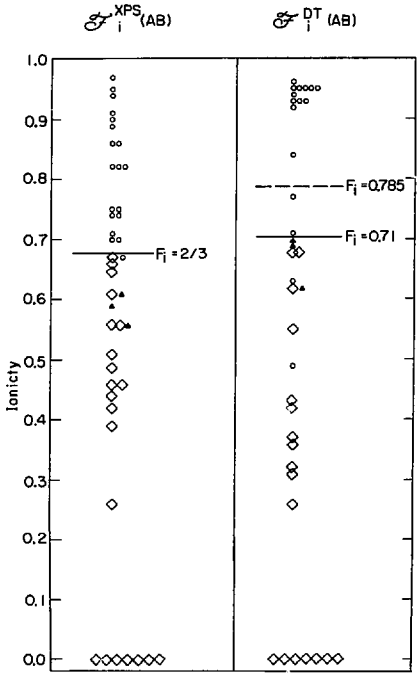

Fig. 2. Comparison of the XPS-derived scale of ionicity, $\mathcal{F}_i^{XPS}(AB)$ from Table 2 and the Phillips-Van Vechten ionicity, $\mathcal{F}_i^{DT}(AB)$ (Ref. 5) illustrating the ability to predict structural phase transformation. $\mathcal{F}_i^{DT}(AB)$ for crystalline materials of average V valence was obtained from P. J. Stiles, Solid State Commun. 11,1003 (1972). Vertical line indicates critical ionicity, F_i. Dashed vertical line for $\mathcal{F}_i^{DT}(AB)$ is the F_i derived in Ref. 5. Crystals with diamond, zinc-blende or chalcopyrite structure are indicated by •; wurtzite structure by ▲ and rocksalt structure by ○. (XBL 745-3032)

a perfect score for the 70 A^NB^{8-N} crystals of Ref. 5. The $\mathcal{F}_i^{XPS}(AB)$ scale with $F_i = 2/3$ is able to predict 100% of the structures correctly. However, within the accuracy of the data $\mathcal{F}_i^{XPS}(ZnSe)$ and $\mathcal{F}_i^{XPS}(PbS)$ should be considered equal; thus $\mathcal{F}_i^{XPS}(AB)$ makes one error. Thus $\mathcal{F}_i^{XPS}(AB)$ appears to be superior to $\mathcal{F}_i^{DT}(AB)$ when IV-VI crystals and ternary alloys are included. The lead salts present an interesting case because they can indicate whether the $\mathcal{F}_i^{XPS}(AB)$ scale can be generalized beyond A^NB^{8-N} crystals and because both ionic and covalent bonding have been proposed for them.[10] $\mathcal{F}_i^{XPS}(AB)$ predicts the lead salts to have the ionic rocksalt structure, which is correct. Recent charge density calculations on PbTe strongly support an ionic interpretation.[11]

The cesium halides have the eight-fold coordinated CsCl structure. Citrin and Thomas have reported XPS data for several of these compounds.[12] If we apply our treatment to these data we obtain: $\mathcal{F}_i^{XPS}(CsF) = 0.93$, $\mathcal{F}_i^{XPS}(CsCl) = 0.97$, and $\mathcal{F}_i^{XPS}(CsBr) = 1.00$. All these values are in the upper range of the alkali halide data. In Fig. 2 we have also plotted data from two $A^{II}B^{IV}C_2^V$ (chalcopyrite-type) crystals. These are ternary analogs of the binary $A^{II}B^V$ crystals, i.e., $ZnGeP_2$ is the analog of GaP, and $CdSnAs_2$ of InAs.

We shall not discuss the other scales of ionicity in detail since this has already been done by Phillips.[5] The major problems with the other scales, notably Coulson's molecular orbital approach,[13] $\mathcal{F}_i^{CRS}(AB)$, and Pauling's thermochemically based scale,[14] $\mathcal{F}_i^{P}(AB)$, derive from the lack of symmetrical treatment of ionic and covalent contributions. Both Pauling's and Coulson's scales tend to bunch groups of crystals with respect to ΔZ; i.e., III-V crystals are clustered at one value and II-VI at another. Phillips stated that his dispersion theory does not work too well for crystals such as alkali halides with $\mathcal{F}_i \gtrsim 0.9$, which is where Pauling's scale is best because the covalent contribution is very small. The Phillips-Van Vechten theory uses optical and dielectric data. Optical data are not always straightforward to interpret and this approach includes some approximations. $\mathcal{F}_i^{XPS}(AB)$ appears to have wider applicability than the other scales. It appears that $\mathcal{F}_i^{XPS}(AB)$ needs a correction factor for the anion size in the case of the alkali halides. There is need for further work especially in the expansion of classes of crystals studied. This study shows promise in the application of XPS to study of the problem of the nature of the chemical bond in solids.

Footnotes and References

*Condensed from LBL-2902; published in J. Chem. Phys. 61, 2850 (1974).

†I.B.M. Fellow.

1. J.P. Walter and M.L. Cohen, Phys. Rev. B 4, 1877 (1971).

2. S.P. Kowalczyk, F.R. McFeely, L. Ley, R.A. Pollak, and D.A. Shirley, Phys. Rev. B 9, 3573 (1974).

3. R.G. Cavell, S.P. Kowalczyk, L. Ley, R.A. Pollak, B. Mills, D.A. Shirley, and W. Perry, Phys. Rev. B 7, 5313 (1973).

4. R.A. Pollak, L. Ley, S.P. Kowalczyk, D.A. Shirley, J.D. Joannopoulos, D.J. Chadi, and M.L. Cohen, Phys. Rev. Lett. 29, 1103 (1972).

5. J.C. Phillips, Rev. Mod. Phys. 42, 317 (1972).

6. J.C. Phillips and J.A. Van Vechten, Phys. Rev. B 2, 2147 (1970).

7. J.C. Phillips, Bonds and Bands in Semiconductors (Academic Press, New York, 1973).

8. J.C. Phillips and J.A. Van Vechten, Phys. Rev. Lett. 22, 705 (1969).

9. L. Ley, R.A. Pollak, S.P. Kowalczyk, F.R. McFeely, and D.A. Shirley, Phys. Rev. B 8, 641 (1973).

10. R. Dalvin, Solid State Physics, 28, 179 (1973).

11. M.L. Cohen, International Conference on Narrow Gap Semiconductors, Nice, France (1973), unpublished.

12. P.H. Citrin and D.T. Thomas, J. Chem. Phys. 57, 4446 (1972).

13. C.A. Coulson, L.B. Redei, and D. Stocker, Proc. Roy. Soc. (London) 270, 352 (1962).

14. L. Pauling, The Nature of the Chemical Bond (Cornell University Press, Ithaca, New York, 1960).

X-RAY PHOTOEMISSION SPECTRA OF THE 4d LEVELS IN RARE EARTH METALS*

S. P. Kowalczyk, N. Edelstein, F. R. McFeely, L. Ley,† and D. A. Shirley

The photoemission spectra of core levels in materials possessing unpaired electrons often exhibit satellite structure. This phenomenon, which is usually attributed to multiplet splitting, was first observed in x-ray photoemission spectra (XPS) of solids by Fadley et al.[1,2] It is interpreted as arising from the multiplicity of final states formed by the coupling of an open core shell with partially filled outer shells. Rare-earth metals and rare earth compounds, with their large number of unpaired 4f electrons, should present particularly interesting cases for study of multiplet structure.

Figure 1 shows the 4d spectra of La and Lu, which have a completely empty and a completely filled 4f shell, respectively. These spectra exhibit only well-defined spin-orbit split doublets with separations of 2.85(10) and 10.0(2) eV, respectively, in reasonable agreement with theoretical values of 3.2 and 10.2 eV.[3] Also shown is the 4d spectrum of Yb, which is a divalent metal with a $4f^{14}$ ion-core configuration. Here again the 4d spectrum consists simply of a $4d_{5/2}$ - $4d_{7/2}$ spin-orbit doublet split by 8.90(15) eV.[4] The simple spin-orbit doublet character of the 4d doublet in Yb is interpreted as further confirmation of the $4f^{14}$ configuration in this metal.

Figure 2 shows the XPS spectra in the 4d region of Ce, Sm, and Eu. These spectra are typical of the rest of the rare-earth series in exhibiting complex structure due to the $4d^9 4f^n$ interaction. We shall discuss only the $4d^9 4f^7$ cases, Eu and Gd, as only these have as yet been analyzed in detail. The discussion below applies particularly to Eu. The Gd spectrum has not been as well resolved as yet. For these two metals the initial open-shell configuration and level is $4f^7$; ^8S. Thus emission of an $n\ell$ electron can lead only to the two terms $n\ell^{4\ell+1}4f^7$; ^9L and $n\ell^{4\ell+1}4f^7$; ^7L, where $|L| = |\ell|$. For the $\ell = 2$ case of interest here, each term consists of five levels with J ranging from $|S-2|$ to $|S+2|$. The configuration $f^7(^8S)d^1$ was treated by Judd.[4] By reversing the sign of the d-shell spin-orbit coupling constant ζ, we can use his discussion essentially verbatim for $f^7(^8S)d^9$, noting that the d-f exchange terms require no modification because the 4f shell is exactly half full. Figure 3 is a plot of the level ordering within the ^9D and ^7D multiplets using the reduced variables η and ξ defined by Judd[4] (cf his Fig. 5). The parameter η scales as energy for any particular value of ξ, which is, itself, an index of the degree of j-j coupling in the 4f shell:

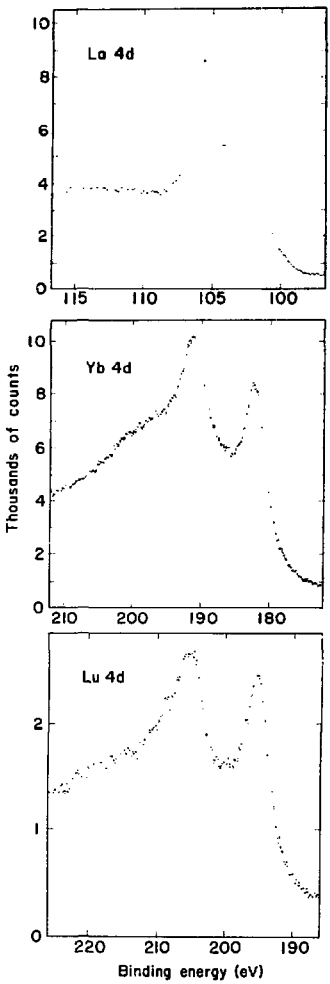

Fig. 1. XPS spectra of the 4d levels of La, Yb, and Lu metals, showing only spin-orbit doublets. (XBL-746-3513)

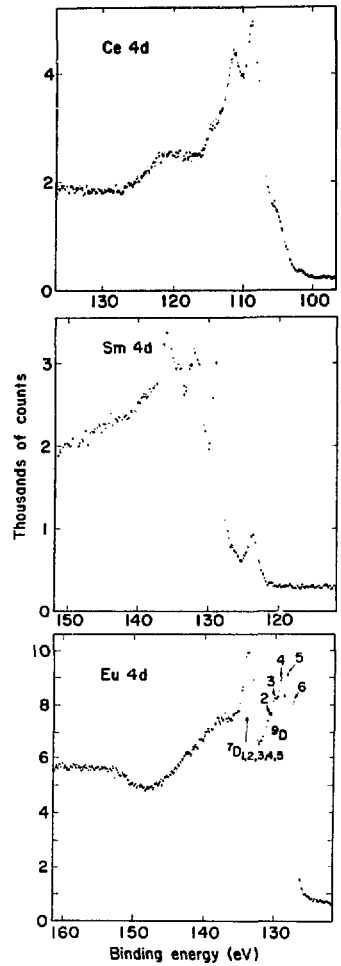

Fig. 2. XPS spectra of the 4d regions of Ce, Sm, and Eu metals exhibiting structure due to final-state coupling. The Eu spectrum has been analyzed as discussed in text. (XBL-746-3514)

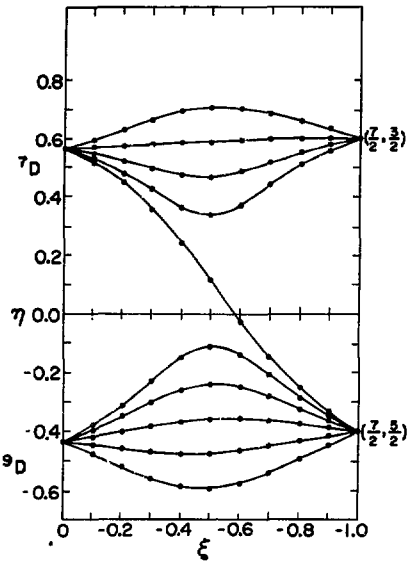

Fig. 3. Levels of the configuration f^7d^9 that derive from the core level $8_{S7/2}$. The axes are labeled as follows: $\eta = (E(J) - \frac{35}{80}G)[G^2 + (\frac{5}{2}\rho)^2]^{-1/2}$; $\xi = \frac{\chi}{1+|\chi|}$, where $\chi = \frac{5}{2}\zeta/G$. The matrix elements were calculated for the f^7d configuration so, for our case, $\zeta < 0$, $G > 0$, and therefore $-1 < \xi < 0$. The LS extreme is given for $\xi = 0$ on the left, and the Jj extreme is given for $\xi = -1.0$ on the right. (XBL-746-3551)

$\xi = 0$ for pure L-S and -1 for j-j coupling. The five-peak fine structure on our ^9D peak in the Eu spectrum (Fig. 2) shows excellent agreement with this interpretation, while the ^7D fine structure is unresolved. Judd attributed a similar effect in the GdI spectrum to a contraction of the ^7D multiplet through interaction with an excited term ^7D of f^7d, derived from the level ^6p of the core.

We can qualitatively explain the difference in appearance and structure of the ^7D and ^9D terms but cannot account quantitatively for the contraction of the ^7D term on the basis of our simple model. However we can set a lower limit on ξ of -0.87 (Fig. 3). The main uncertainty is in the value of G for which we can set a lower limit $G \geq 4.4$ eV. Energies calculated on Judd's model are compared with experimental values in Table 1. The derived value of the effective 4d spin-orbit coupling constant within the ^9D manifold is $\zeta_d = 1.4(2)$ eV. This is somewhat smaller than estimates based on theory ($\zeta_d = 2.2$ eV) or obtained by interpolation using the La, Yb, and Lu experimental values ($\zeta_d = 1.8(3)$ eV). Again this contraction within the ^9D manifold is probably attributable to interaction with excited states.

Table 1. The $4d^94f^7$; ^9D multiplet energies in Eu metal (in eV).

Level	E(expt)	E(fitted)[a]
$^9D_6$[b]	0	0.1
$^9D_5$	0.78(04)	0.8
$^9D_4$	1.52(04)	1.4
$^9D_3$	2.22(04)	2.2
$^9D_2$	2.85(08)	2.9
^7D[c]	6.33(10)	6.3

[a] After Ref. 4.

[b] The binding energy of $^9D_6$ relative to the Fermi energy is 127.70(15) eV.

[c] Mean energy only.

A noteworthy feature of the Eu spectrum is the apparent reduction in multiplet separation between the ^7D and ^9D terms. According to simple theory,[4] this separation would be given by

$$G = \frac{24}{35}G^1(4d,4f) + \frac{32}{105}G^3(4d,4f) + \frac{528}{1524.6}G^5(4d,4f) ,$$

or 18.91 eV, using Mann's[5] exchange integrals. The lower limit we give for G is 4.4 eV, corresponding to a reduction factor of 0.23. A large reduction factor is expected for multiplet splitting cases involving two subshells with the same principal quantum number, because of the large intrashell correlation energy. A factor of 0.6 has previously been observed for 4s 4f multiplets in rare-earth salts[6] and metals.[7] Closure of the multiplet energy gap arises primarily through configuration interaction of the low-spin term (^7D in this case) with excited states of the same symmetry. This should lead to two other observable spectral features: the

$^7D/^9D$ intensity ratio should be less than the multiplet value of 7/9, and "correlation peaks" should be present at higher binding energies, as observed[8] in Mn^{2+}. Large background intensities in our spectra, arising from elastic scattering, preclude a really quantitative interpretation, but both of the above features appear to be present.

Footnotes and References

*Condensed from LBL-2937; published in Chemical Physics Letters 29, 491 (1974).

†I.B.M. Fellow.

1. C.S. Fadley, D.A. Shirley, A.J. Freeman, P.S. Bagus, and J.V. Mallow, Phys. Rev. Lett. 23, 1397 (1969).

2. C.S. Fadley and D.A. Shirley, Phys. Rev. A2, 1109 (1970).

3. T.A. Carlson, C.C.C. Lu, T.C. Tucker, C.W. Nestor, and F.B. Malik, Oak Ridge National Laboratory Reprint No. ORNL-4614, 1970 (unpublished).

4. B.R. Judd, Phys. Rev. 125, 613 (1962).

5. J.B. Mann, Atomic Structure Calculations I. Hartree-Fock Energy Results for the Elements Hydrogen to Lawrencium, Los Alamos Scientific Laboratory Report LASL-3090 (1967).

6. R.L. Cohen, G.K. Wertheim, A. Rosencwaig, and H.J. Guggenheim, Phys. Rev. B5, 1037 (1972).

7. F.R. McFeely, S.P. Kowalczyk, L. Ley, and D.A. Shirley, Phys. Lett. 49A, 301 (1974).

8. S.P. Kowalczyk, L. Ley, R.A. Pollak, F.R. McFeely, and D.A. Shirley, Phys. Rev. B7, 4009 (1973).

MULTIPLET SPLITTING OF THE 4s AND 5s CORE LEVELS IN THE RARE EARTH METALS

F. R. McFeely, S. P. Kowalczyk, L. Ley,* and D. A. Shirley

Since the first observation of multiplet splitting of core levels in x-ray photoemission spectra (XPS) of solids by Fadley et al.,[1,2] many interesting applications have been made[3-7] and a deeper understanding of this phenomenon has developed.[8-11] In this Letter, we report the observation of multiplet splitting of the 4s and 5s core levels in the rare earth metal series La through Lu.

Our measured 4s and 5s splitting of the metals are given in Table 1 and compared with earlier work on several trifluorides.[5] The values for the splittings were obtained by least-squares fitting of Lorenztian or Gaussian functions to the spectra. The good agreement of the metal results with those of the trivalent ions is not surprising, since it has been shown earlier that the XPS spectra of the 4f region of the metals compare well with optical data of the trivalent ions and with XPS results on the trifluorides.[12]

The simplest estimate of the splitting $\Delta E(ns)$ is obtained by invoking Van Vleck's theorem[13] which yields

$$\Delta E_{VV}(ns) = \frac{(2S+1)}{7} G^3(ns,4f) \qquad (1)$$

where S is the initial-state spin. These results are given in Table 1 and plotted in Fig. 1 along with the experimental results. The use of Mann's[14] atomic Slater integrals, G^3, is justified because the 4f states are essentially core-like. Equation (1) reproduces $\Delta E(5s)$ quite well;

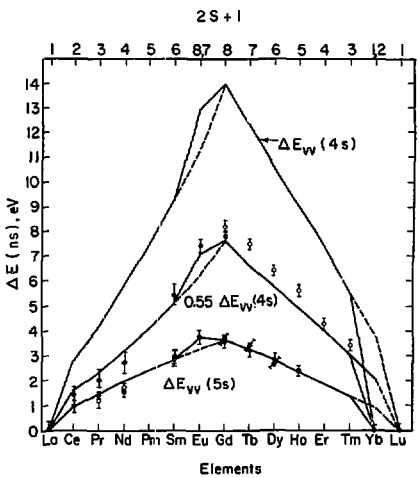

Fig. 1. Comparison of the experimental values of the 4s and 5s multiplet splitting with the Van Vleck theorem values (Eq. (1)). Filled circles are for the metals (this work), while open circles are trifluoride values (Ref. 5).

(XBL 746-3504)

Table 1. Experimental and calculated 4s and 5s splittings (eV) of the rare earth metals and trifluorides.

	2S+1	ΔE(4s)[a]	ΔE(4s)[b]	$\Delta E_{vv}(4s)$[c] Full	×0.55	ΔE(5s)[a]	ΔE(5s)[b]	$\Delta E_{vv}(5s)$[c]
La	--	0.0(2)	--	0.00	0.00	0.0(2)	--	0.00
Ce	2	1.4(3)	--	2.85	1.56	1.0(3)	0.0	0.93
Pr	3	2.0(3)	--	4.14	2.26	1.4(2)	1.2	1.46
Nd	4	2.7(3)	--	5.78	3.16	1.6(2)	1.7	1.92
Pm	5	--	--	7.52	4.11	--	--	2.38
Sm	6	5.4(3)	--	9.35	5.10	2.9(2)	2.8	2.83
Eu	8,7	7.4(3)	--	12.88,11.27	7.03,6.15	3.8(3)	--	3.76,3.29
Gd	8	7.8(2)	8.2	13.91	7.59	3.6(2)	3.7	3.62
Tb	7	d	7.5	12.17	6.64	3.2(3)	3.4	3.16
Dy	6	d	6.4	10.51	5.74	2.8(2)	2.7	2.78
Ho	5	d	5.6	8.98	4.90	2.4(2)	--	2.32
Er	4	d	4.3	7.35	4.01	d	--	1.85
Tm	3	d	3.4	5.51	3.01	d	--	1.39
Yb	1,2	0.0(3)	--	0.0,3.84	0.0,2.10	0.0(1)	--	0.0,0.93
Lu	--	0.0(2)	--	0.00	0.00	0.0(1)	0.00	0.00

[a] This work.

[b] Reference 5.

[c] Equation 1.

[d] These values could not be obtained due to intense Auger transistions in the energy region of interest.

however, it systematically predicts a value that is 80% too high for ΔE(4s). This result is analogous to that in the 3d metal ion series, where it has been theoretically shown[10] and experimentally verified[8] that intra-shell correlations are extremely important, while inter-shell correlations are much smaller because elections in different principal shells are already spatially correlated. The reason for the overestimate of ΔE(4s) by Van Vleck's theorem is quite simple. In the high-spin final state, the 4s and 4f elections are spatially separated by the antisymmetry requirements of the Pauli Principle. Thus inclusion of correlation will lower the energy of the low-spin final state more than of the high-spin final state, reducing the splitting. To obtain an accurate theoretical value for ΔE(4s), it would be necessary to do a configuration interaction calculation on the final state as was done for the transition metal ions.[10]

Figure 1 confirms the divalent character of metallic Eu and Yb cores, and demonstrates that at room temperature Ce is trivalent rather than tetravalent.

Footnote and References

*I.B.M. Fellow

1. C.S. Fadley, D.A. Shirley, A.J. Freeman, P.S. Bagus and J.V. Mallow, Phys. Rev. Lett. 23, 1397 (1968).

2. C.S. Fadley and D.A. Shirley, Phys. Rev. A 2, 1109 (1970).

3. D.T. Clark and D.B. Adams, Chem. Phys. Lett. 10, 131 (1971).

4. J.C. Carver, G.K. Schweitzer and T.A. Carlson, J. Chem. Phys. 57, 973 (1972).

5. R.L. Cohen, G.K. Wertheim, A. Rosencwaig and H.J. Guggenheim, Phys. Rev. B5, 1037 (1972).

6. S. Hüfner and G.K. Wertheim, Phys. Lett. 44A, 113 (1973).

7. F.R. McFeely, S.P. Kowalczyk, L. Ley and D.A. Shirley, Solid State Comm., to be published.

8. S.P. Kowalczyk, L. Ley, R.A. Pollak, F.R. McFeely, and D.A. Shirley, Phys. Rev. B7, 4009 (1973).

9. A.J. Freeman, P.S. Bagus and J.V. Mallow, International J. Magnetism 4, 35 (1973).

10. P.S. Bagus, A.J. Freeman and F. Sasaki, Phys. Ref. Lett. 30, 850 (1973).

11. P.S. Bagus, M. Schrenk, D.W. Davis and D.A. Shirley, Phys. Rev. A9, 1090 (1974).

12. F.R. McFeely, S.P. Kowalczyk, L. Ley, and D.A. Shirley, Phys. Lett. 45A, 227 (1973).

13. J.H. Van Vleck, Phys. Rev. 45, 405 (1934).

14. J.B. Mann, Los Alamos Report No. LA-3690 (1967), unpublished.

3. Physical, Inorganic, and Analytical Chemistry

X-Ray Crystallography

Physical and Inorganic Chemistry

Geochemistry

CRYSTAL AND MOLECULAR STRUCTURES OF THORIUM AND URANIUM TETRAKIS (HEXAFLUOROACETONYLPYRAZOLIDE) COMPLEXES

K. Volz, A. Zalkin, and D. H. Templeton

Polymeric pyrazolide compounds of the type $M(Pz)_n$ can be formed in the reaction of pyrazole (Pz) with ions of transition metals, lanthanides, and actinides. In 1966, Mahler[1] discovered that hexafluoroacetone (hfa) can react with the pyrazolide compounds in a 1:1 ratio to yield metal ion pyrazolide-hexafluoroacetone complexes $[M(hfaPz)_n]$. Several actinide tetrakis(hfaPz) compounds were synthesized by Andruchow and Karraker.[2] We have studied two of these with x-ray diffraction methods to verify their composition and to establish their molecular structure, which can be represented:

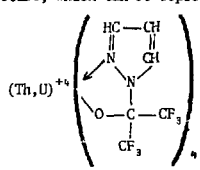

Crystalline samples of $Th(C_6H_3ON_2F_6)_4$ and $U(C_6H_3ON_2F_6)_4$ were kindly provided by D. G. Karraker. The thorium crystals were well-formed colorless prisms. The dark violet uranium crystals after recrystallization from toluene were fragile hexagonal plates. X-ray diffraction experiments with MoKα radiation showed that both are triclinic, space group $P\bar{1}$, with the following lattice dimensions:

$Th(C_6H_3ON_2F_6)_4$,

$a = 11.282(5)$, $b = 16.245(7)$, $c = 10.836(5)$ Å,

$\alpha = 90.14(5)$, $\beta = 108.75(5)$, $\gamma = 107.07(5)°$.

$U(C_6H_3)N_2F_6)_4$,

$a = 11.302(5)$, $b = 16.377(8)$, $c = 11.000(5)$ Å,

$\alpha = 87.85(5)$, $\beta = 111.02(5)$, $\gamma = 109.95(5)°$.

X-ray diffraction data for both crystals were measured with a scintillation counter and an automatic diffractometer. Absorption corrections were made using the analytical formulas with crystal dimensions which were calibrated by comparisons of the same reflection measured for various values of the azimuthal angle. The structures were solved by Fourier and least-squares methods and were refined to $R = 0.026$ for 2,966 unique reflections for the thorium compound and $R = 0.027$ for 4,125 unique reflections for the uranium compound. Coordinates of all the atoms including in each case the twelve hydrogen atoms were found by these calculations.

The molecular structure of the thorium compound is shown in Fig. 1. The thorium and uranium compounds have essentially the same structure except for an average difference of 0.06 Å in the actinide-ligand bond lengths because of the actinide contraction. The compounds crystallize as discrete molecular complexes which are sufficiently volatile to be sublimed at 140°C under vacuum.[2] The structure of one of the ligand groups is shown in more detail in Fig. 2. Each metal atom has four oxygen neighbors and four nitrogen neighbors at average distances Th-O = 2.291(4), Th-N = 2.637(5), U-O = 2.237(3), U-N = 2.574(5) Å. In each case the eight neighbors are at the corners of an irregular dodecahedron.

Footnotes and References

1. W. Mahler, U.S.Patent 3,265,705 (August 9, 1966), assigned to E. I. duPont de Nemours and Co., Inc.

2. W. Andruchow and D. G. Karraker, Inorg. Chem. 12, 2194 (1973).

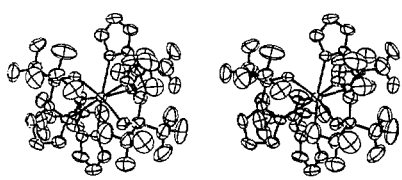

Fig. 1. Stereoscopic view of the molecular structure of the thorium complex. The hydrogen atoms have been omitted for clarity. (XBL 738-1019)

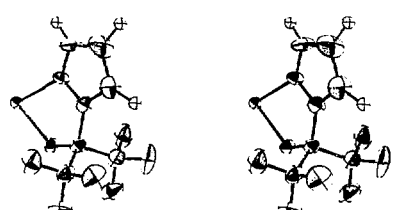

Fig. 2. Stereoscopic view of one of the ligands. (XBL 738-1016)

THE CRYSTAL STRUCTURE AND ABSOLUTE CONFIGURATION OF A BROMOHEXAACETYL DERIVATIVE OF VITEXIN*

F. A. Jurnak and D. H. Templeton

Although the C-glycosyl flavone compounds occur widely in nature and were isolated as early as 1851, the elucidation of the chemical structure was hampered by the nature of the C-glycosylic side chain. The resistance of the C-C bond to acid hydrolysis prevented the identification of the sugar moiety. In 1964, Horowitz and Gentili[1] first overcame these obstacles when they deduced the basic structure of vitexin from chemical and NMR data. Later Eade, Hillis, Horn, and Simes[2] inferred the existence of two rotational isomers of acetylated vitexin from temperature-dependent NMR studies. We undertook a study of a bromohexaacetylated derivative of vitexin to test these predictions and to investigate some new procedures for solving a difficult crystallographic problem which had been studied without success in another laboratory. Our study confirmed the chemical structure of vitexin but showed that our crystals were a mixture of two chemical derivatives containing respectively one and two bromine atoms. We also showed that an acetyl group of the original heptaacetate was lost somewhere in the recrystallizations.

The derivative, of material isolated from the wood of *Vitex lucens*, was made available by R. Horowitz of the Fruit and Vegetable Chemistry Laboratory, Pasadena, California. Pale yellow crystals, obtained from methanol-acetone solution, were given us by K. Palmer of the Western Regional Agricultural Laboratory, Albany, California. We obtained diffraction data with MoKα radiation for 3,512 reflections of which 2,669 were significantly above background. The latter included 1,104 Friedel pairs which permitted unambiguous determination of the absolute configuration of the structure.

It had been expected to exploit the anomalous dispersion effects to determine the structure, but this became unnecessary when more conventional Fourier and least-squares methods yielded the solution. The disorder concerning the bromine atoms, and large thermal motion of some of the side chains, caused the refinement to be laborious. The final result reduced R to 0.099, a value close to the estimated accuracy of the data.

The molecular formula is shown in Fig. 1. The bromine atom indicated as Br(2) is estimated to be present in 30% of the molecules. Figure 2 shows a stereoscopic view of the molecular structure. Figure 3 shows how these molecules are packed into the unit cell, in space group $P6_5$, with dimensions a = 21.602(7) and c = 13.869(7)Å. It is confirmed that the sugar ring is a β-D-glucosyl moiety, attached through C-C bonds to the eight position of the flavone nucleus, and is approximately perpendicular to the flavone plane.

Footnotes and References

*Condensed from LBL-2335.

1. R. M. Horowitz and B. Gentili, Chem. Ind. (London), (1964) 498.

2. R. A. Eade, W. E. Hillis, D. H. S. Horn, and J. J. H. Simes, Aust. J. Chem. 18, 715 (1965).

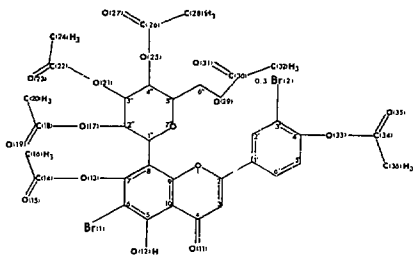

Fig. 1. Molecular formula of the vitexin derivative. (XBL 735-664)

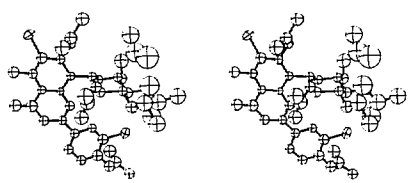

Fig. 2. Stereoscopic view of the molecular structure. (XBL 735-665)

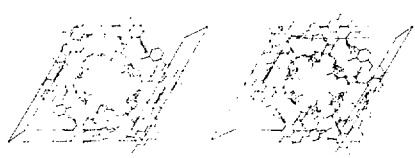

Fig. 3. Crystal structure of the vitexin derivative. (XBL 7311-1409)

CRYSTAL STRUCTURE AND CONFORMATION OF A MULTI-SULFUR HETEROCYCLE

H. Ruben, D. H. Templeton, and A. Zalkin

On the basis of nuclear magnetic spectroscopy it is known that some substituted tetrathianes exist in solution as equilibrium mixtures of chair and twist conformations, with slow rates of interconversion.[1] To complement this work we determined the crystal structure of 3,3:6,6-bis(pentamethylene)-s-tetrathiane to learn its structure and conformation in the solid state. Because of the high quality of the crystals, an exceptionally accurate result was obtained.

The crystals are triclinic, space group $P\bar{1}$, with cell dimensions $a = 6.632(6)$, $b = 8.462(6)$, $c = 6.446(6)$ Å, $\alpha = 93.92(6)$, $\beta = 103.23(6)$, and $\gamma = 96.90(6)°$. The structure was solved by statistical phasing of the strongest reflections from a data set including 2,715 independent observed reflections. After least-squares refinement, R was reduced to 0.025. The model that was used in the calculations makes an allowance for polarization of the bonded hydrogen atoms, so that the hydrogen coordinates represent the actual position of the proton rather than the center of the electron density. The molecular structure, shown in Fig. 1, is centric with all three rings in chair conformations. Average bond distances are S-S = 2.035(2), C-S = 1.842(2), C-C = 1.525(1), and C-H = 1.05(1) Å. The bond angles at C(1) deviate from regular tetrahedral in such a way that the molecule is more extended and the cyclohexane rings are farther from the center than if these angles were tetrahedral. This bending of the molecule brings C(6) closer to sulfur than is C(2), and it is noteworthy that the C(1) - C(6) distance [1.537(2) Å] is longer than the other C-C bond lengths.

Reference

1. C.H. Bushweller, G. Bhat, L.J. Letendre, J.A. Brunelle, H.S. Bilofsky, H. Ruben, D.H. Templeton, and A. Zalkin, J. Amer. Chem. Soc., 97, 65 (1975).

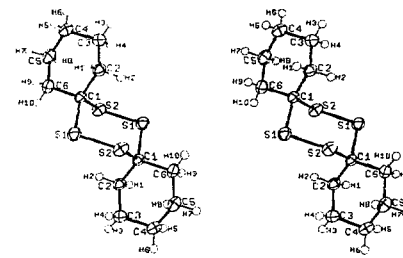

Fig. 1. Molecular structure of 3,3:6,6-bis(pentamethylene)-s-tetrathiane. (XBL 717-1196)

CRYSTAL STRUCTURE OF AMMONIUM HYDROGEN MALONATE

G. Chapuis, A. Zalkin, and D. H. Templeton

Recent developments in ^{13}C nuclear magnetic resonance spectroscopy make is possible to find the chemical shielding tensors of crystalline substances and to correlate the orientations of these tensors with respect to the molecular structure determined by x-ray diffraction. The results may give better understanding of the relation between electronic structure and magnetic shielding. If consistent results are found for the same groups in various crystals, then the NMR technique may be used with confidence as a probe of orientation in other phases.

We studied the crystal structure of ammonium hydrogen malonate by x-ray diffraction to complement an NMR study by Chang, Griffin, and Pines.[1] The combined study yields orientations for the tensors for carbon in the methylene group and in two independent carboxyl groups, and shows that the latter orientations are significantly affected by the non-equivalence of the oxygen, one of which is involved in strong hydrogen bonding.

The diffraction data, recorded with a scintillation counter and MoKα radiation, showed the crystals to be monoclinic, space group C2/c, with cell dimensions at 22°: $a = 11.214(3)$, $b = 8.647(3)$, $c = 11.507(4)$ Å, $\beta = 107.29(2)°$. The structure was solved by statistical phasing. It was refined by least-squares to $R = 0.042$ for 794 independent observed reflections.

The configuration of the malonate, Fig. 1, is similar to that found in malonic acid with the two carboxyl groups nearly perpendicular to each other. In contrast, these groups are nearly coplanar in the potassium acid salt. In both the ammonium and potassium salts, the ions are connected by strong symmetrical hydrogen bonds into infinite chains. The result is that the two crystallographically independent carboxyl groups in our crystal are chemically equivalent, and each can be regarded as half ionized. The bond distances clearly differentiate the carbonyl oxygen atoms (C-O = 1.232 or

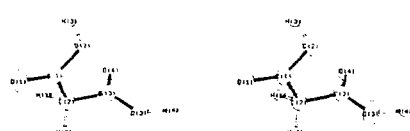

Fig. 1. Structure of the malonate ion in ammonium hydrogen malonate. (XBL 741-240)

1.223 Å) from those bonded to hydrogen (C-O = 1.284 or 1.288 Å). In the hydrogen bonds the O-O distances are 2.487 and 2.476 Å. Other average bond distances are C-C = 1.51, C-H = 1.05, and N-H = 1.00 Å. The ammonium ion is hydrogen bonded to four neighboring oxygen atoms with N-O distances ranging from 2.80 to 2.99 Å.

The relation of the shielding tensors to the geometry of the molecule is described by Chang, Griffin, and Pines.[1]

Reference

1. J. J. Chang, R. G. Griffin, and A. Pines, J. Chem. Phys., in press (1975).

BACKBENDING AND OTHER DEVIATIONS FROM IDEALITY IN EXTRACTION SYSTEMS*

J. J. Bucher and R. M. Diamond

Slope analysis is an often-used method for interpreting and analyzing data from extraction equilibria in order to obtain information on the nature of the extracting species. Central to the application of this method is the assumption that any deviation from the law of mass action is due to the formation of a new chemical species. But as has been pointed out,[1,2] it is unreasonable to ignore all nonspecific non-idealities of the extracted species and blame all deviations on new chemical species.

The extraction of a strong acid, H^+X^-, by a solution of trilaurylamine (TLA) in a low dielectric-constant medium that induces association of the resulting salt to an ion pair or higher aggregate can be written

$$\log[(TLA\cdot HX)_n]_o \approx \log K + n \log[TLA]_o (H^+X^-) + \log y^n_{TLA}/y_{(TLA\cdot HX)_n} . \quad (1)$$

Thus, a log-log plot of the stoichiometric concentration of the organic-phase amine-salt vs the product $[TLA]_o(H^+X^-)$ should yield a curve whose tangent is the value of n at that point, if the activity-coefficient ratio is a constant.

The results of the present study of the TLA extraction of $HClO_4$ into 1-bromooctane and into CCl_4 and of $HClO_4$ and HI into cyclohexane are shown in Fig. 1. When determined at low amine-salt concentrations the log-log plots are straight lines with unit slope, indicating predominantly ion pairs and

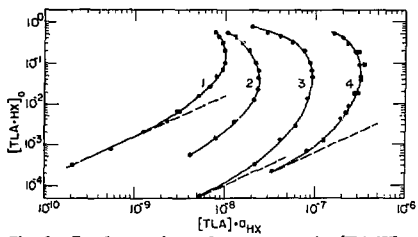

Fig. 1. Total ammonium salt concentration $[TLA\cdot HX]_o$ vs $[TLA]_o(H^+X^-)$ for various diluents. Curve 1 is the $TLA\cdot HClO_4$, 1-bromooctane system; curve 2 is the $TLA\cdot HClO_4$, CCl_4 system; curve 3 is the $TLA\cdot HClO_4$, cyclohexane system; and curve 4 is the $TLA\cdot HI$, cyclohexane system. (XBL 751-2017)

the validity of the assumption that the organic-phase activity-coefficient ratio is constant. But at higher concentrations, the curves deviate upward from the line of unit slope. This is the region that has been of most interest in the literature,[3] and this behavior has almost always been ascribed to a further association of the ion pairs. The average value of this aggregation, n, at any point, can be determined by the tangent of the curve, or the whole curve can be fitted to a small number of oligomers, if the activity-coefficient ratio of the various oligomers are still assumed constant. But as can be seen in Fig. 1, with "poor" diluents the curves for these TLA salts actually "backbend" for concentrations above 0.1M, yielding negative values for the slope. This behavior is completely unexplainable in the context of an aggregation model with ideal activity coefficients for the salt associations. The simplest, and we believe the correct, explanation is that at these large concentrations of amine salt we are dealing with a new diluent, consisting of amine salt and solvent. This new more polar phase has properties more favorable for the extraction of the salt. The value of the organic-phase activity $y_{(TLA\cdot HX)_n}$ decreases with the increase in amine-salt concentration. However, no amount of tinkering with the amine-salt coefficient alone can yield the results of Fig. 1. One must take into account another component too. And we think it is the amine coefficient that is important. The activity coefficient of TLA should increase with increasing salt concentration in the mixed diluent, and both activity coefficient changes should cause a very marked lowering in the ratio $y_{(TLA\cdot HX)_n}/y^n_{TLA}$. Even though the molar concentration of amine in the organic-phase is small (10^{-2}–10^{-3}M), so that one might think its activity coefficient would not vary much, the change in the nature of the diluent can cause large changes.

Are there other types of extraction systems that do not allow for simple slope analysis, and if so treated, lead to wrong conclusions? The answer appears to be yes. Consider the extraction of $HReO_4$ by trioctylphosphine oxide (TOPO) solutions in isooctane. The equilibrium constant for extraction as an ion pair can be expressed

$$K^a_n = \frac{[H^+\cdot n\text{TOPO}\cdots ReO_4^-]_o y_{n\text{TOPO}\cdot HReO_4}}{(H^+ReO_4^-)[\text{TOPO}]^n_{\text{TOPO}}} .$$

To determine the value of n, the number of TOPO molecules coordinated to the extracted acid, one can study the dependence of the extracted acid on the TOPO concentration. To exclude the possibility of

aggregation beyond the ion pair, tracer concentrations of $HReO_4$ can be used. Figure 2 shows the distribution of 1×10^{-6}M $HReO_4$ in 1.0M HCl with TOPO in isooctane. The initial slope drawn is two (n=2), but the raw data show deviations from this line even at TOPO concentrations as low as $2\text{-}3\times10^{-5}$M. The organic-phase $HReO_4$ concentration at these TOPO concentrations is 10^{-8}M, so no aggregation beyond the ion pair is expected. Extension of the line of slope two is shown by a dashed line, and the subtraction of this line from the raw data is indicated by the dashed line connecting the filled triangles. This resultant line has a slope of three. By all the normal rules of slope analysis this indicates that at the initial low TOPO concentrations there are two TOPO molecules coordinated per extracted acid, but that over most of the TOPO concentration range studied the slope of three indicates a three-to-one complex.

Yet infrared spectroscopic results[4] over the whole TOPO range studied indicate that the species is a $2TOPO\cdot HReO_4$ complex like the one known in other diluents.[5] In this case, dependence on simple slope analysis leads to the wrong result (although there are warning inconsistencies). What can be the cause of this error in the simple mass-law analysis? We believe it is due to the presence of the polar TOPO molecules when dissolved in very inert ("poor") diluents. That is, the addition of the polar TOPO molecules makes the inert diluent isooctane into a new and more polar solvent. It is surprising, however, at least to us, what a small amount of TOPO is necessary to cause deviations from the line of slope two. Figure 2 shows significantly enhanced extraction at as low as $2\text{-}3\times10^{-5}$M TOPO. At such a concentration there is only one TOPO for approximately 4000 isooctane molecules; to have any marked effect the TOPO must selectively solvate (be in the vicinity) of the even rarer $H^+(TOPO)_2ReO_4^-$ species. This process leads to a lowering of the extracted acid activity coefficient, but without the formation of a higher TOPO complex or aggregation of the $H^+(TOPO)_2ReO_4^-$ species.

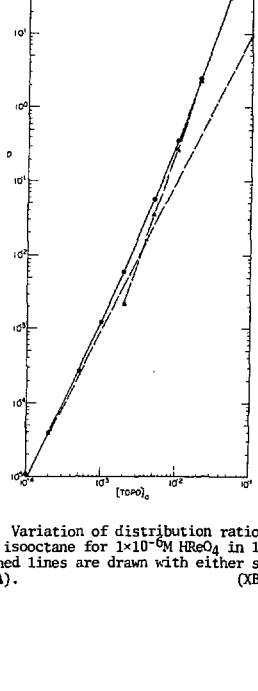

Fig. 2. Variation of distribution ratio, D, with TOPO in isooctane for 1×10^{-6}M $HReO_4$ in 1.0M HCl. The dashed lines are drawn with either slope two or three (▲). (XBL 751-2016)

In this paper we have described several examples of systems that do not follow the behavior expected for extraction models based on the simple application of mass action to step-wise equilibria. Types of studies included are the formation of higher complexes with the extractant molecule, as the extractant concentration is increased, and stepwise aggregation of the extracted amine salt, as the salt concentration is increased. In the former case, neglect of possible organic-phase activity coefficient variations leads to the suggestion of higher complexes than actually exist. In the latter case, ignoring possible activity coefficient variations suggests a greater degree of ion aggregation and higher types of ion aggregates than really exist, especially with "poor" solvents. We believe that the origin of the difficulties experienced in applying simple mass-law slope analysis to these systems comes from not giving consideration to the change in the properties of the diluent as it goes from the initially pure solvent to a mixture of extractant and/or extractant complex and solvent.

Footnotes and References

*Condensed version of LBL-3453.

1. Y. Marcus, J. Phys. Chem. 77, 516 (1973); Y. Marcus, Pure Appl. Chem., 2085 (1969).

2. W. Muller and R. M. Diamond, J. Phys. Chem. 70, 3469 (1966).

3. See for example: Y. Marcus and A. S. Kertes, "Ion Exchange and Solvent Extraction of Metal Complexes" (Wiley-Interscience, N.Y., 1969) pp. 737-815.

4. J. J. Bucher and R. M. Diamond, J. Inorg. Nucl. Chem. 34, 3531 (1972).

5. J. J. Bucher, M. Zirin, R. C. Laugen and R. M. Diamond, J. Inorg. Nucl. Chem. 33, 3869 (1971).

LUMINESCENCE FROM THE PEPTIDE GROUP*

M. Daniels† and M. E. Jayko

Previous work in the excited states of proteins has concentrated exclusively on absorption and emission by the "aromatic" group, phenylalanine, tyrosine, and tryptaphane, and the properties of the peptide group have been studies in absorption only. We report now the detection of emission characteristic of the peptide group using apparatus constructed specifically for this purpose. The excitation source was a 1 kw hydrogen discharge (Hinteregger type), dispersed by a McPherson Model 225 1 meter scanning vacuum UV monochromator. The exciting beam was monitored by a sodium salicylate screen and an RCA 6199-Keithley 417 picoammeter-Speedomax recorder combination. Excitation wavelengths between 1900 Å and 2400 Å were used at a bandwidth of 3.3 nm. The emitted radiation was collected by a 50 mm Spectrosil lens system and analyzed by a Jarrel-Ash 0.25 meter scanning monochromator equipped with a grating blazed at 3000 Å, also at a bandwidth of 3.3 nm. The dispersed radiation was detected by an EMI 6256 photomultiplier, cooled with liquid nitrogen and operated in the photon counting mode. Signal counts were then transferred to a 400 channel analyzer (RIDL 32-1213) operated in the multiscaling mode. At 1750 Å a dark count rate of 12 counts/sec was observed. Emission spectra have routinely been measured from 200 nm to 612 nm and excitation spectra from 200 nm to 280 nm.

Very similar spectra have been observed for N-acetylglycine, N-acetylalanine, acetamide, and N-methylacetamide. Apart from obvious scatter peaks, the spectra are complex. Most prominent is an emission obtained on exciting at 240 nm and hence is tentatively assigned to an $\pi\pi^*$ state. At lower energies a broad shoulder is observed from 325 nm-380 nm (3.8 eV-3.2 eV) and a clear but weak peak at 480 nm (2.6 eV). On exciting at higher energies (1950 Å) a stronger, narrower peak is observed at 240 nm. Present data do not allow us to determine the head of this emission which indeed may be structured but its position and intensity is consistent with it originating from a $\pi\pi^*$ state.

No emission has been observed from N-diethylacetamide.

Footnotes and References

*Abstract of invited paper presented at the International Conference on Excited States of Biological Molecules, Lisbon, Portugal, 18 April 1974 (see LBL-2383).

†Chemistry Department and Radiation Center, Oregon State University, Corvallis, Oregon.

RADIOPOLAROGRAPHIC STUDIES OF Cf, Es, AND Fm

F. David* and K. Samhoun†

The radiopolarography proposed by Love in 1958[1] is a developed technique using radioactive isotopes. In this technique the diffusion current i measured in the classical polarography is replaced by the radioactivity reaching the dropping mercury cathode after the electroactive ions have been reduced to the metallic state. The variation of this radioactivity with the negative potential imposed during a given time constitutes the radiopolarogram.

Since the diffusion current is not measured in this method the reduction of hydrogen ions, if it interferes with the studied reduction, has no effect on the measurement of the radioactivity of the amalgam. It follows from this that potentials of half-wave more negative than-1.6 V/SCE could be measured for elements in very low concentration even at tracer scale. It is clear therefore that radiopolarography is a convenient method for studying redox properties of 5f elements.

Principles

Since the number N of reduced ions to the metallic state during a time θ is a related with the mean diffusing current i by $N = i/nF \times \theta \times \mathcal{N}$ ($\mathcal{N}$ is the Avogadro's number) the fundamental equation of Ilkovic giving the limiting diffusion current is easily transformed as follows:

$$A_d = 0.627 \times m^{2/3} \times t^{1/6} \times D^{1/2} \times A_s \times \theta = KA_s\theta$$

where A_d is the radioactivity of the mercury collected during θ seconds. It is found by measuring the height of plateau of the radiopolarogram $A = f(E)$. A_s is the volume radioactivity of the solution, and D and t have the same significance as in classical polarography.

In addition to this, the linear dependence of the mean diffusing current on the square-root of the height of the mercury head, $A_d = K'\sqrt{h}$, is still the principle criterion to verify the Ilkovic equation. On the other hand the number n of electrons exchanged in the electrode process disappears in the modified Ilkovic equation. However, this could be determined from the polarographic wave equation, which is:

$$E = E_a^o + \frac{RT}{nF} \operatorname{Ln} \frac{A_d - A}{A}$$

for a reversible electrode process, and

$$E = E_a^o + \frac{RT}{\alpha nF} \operatorname{Ln} \cdot 886 K_e^o \left(\frac{t}{D}\right)^{1/2} + \frac{RT}{\alpha nF} \operatorname{Ln} \frac{A_d - A_{irrev}}{A_{irrev}} \quad \text{for an}$$

irreversible electrode process. E_a^o is the standard potential including the energy of amalgamation, K_e^o denotes the heterogeneous rate constant of the electrode process at the standard potential E^o, expressed in cm sec^{-1} and α is the transfer coefficient. In order to compare the measured value A_d^* and the calculated one for A_d, R is defined as follows:

$$R = \frac{A_d^* \text{ (measured)}}{A_d \text{ (calculated)}} = \frac{A_d^*}{KA_s\theta} .$$

Experimental Procedure

An automatic apparatus of radiopolarography has been built in the Institut de Physique Nucleaire in Orsay.[2] The same apparatus slightly modified has been set up at LBL (Fig. 1).

Three ml of radioactive solution are introduced in the small cell (A) where the reference electrode compartment and the platinum anode are literally connected. The aqueous solution remains on carbon tetrachloride occupying the canalizations of Section (B). The drops of mercury flow through the radioactive solution and are stored in the inert medium of CCl_4. No effect of CCl_4 on the stored amalgam was noticed. The drops of mercury already polarized are mostly surrounded with a thin film of aqueous solution. In order to eliminate this parasite radioactivity, the drops are shaken when flowing through column (D) by two rotating magnets. In addition, a pump (P) ensured a permanent circuit of CCl_4 through Section (B) in the direction shown in Fig. 1. The mercury is stored at an electromagnetic gate (V) during a time θ. Through this time the operating apparatus (E) orders simultaneously the opening of (V) and the change of potential, so that the mercury collected at a fixed potential is taken down in a test tube and its radioactivity A is measured. The apparatus was tested with a solution of ^{54}Mn and LiCl 0.1 M at pH 2.85 and t = 25°C. The potential of half-wave was -1.47 V/SCE, which is in agreement with the known standard potential of Mn^{+2}/M^o (3). The Ilkovic equation was verified and $R = A_d^*/A_d = 100\%$ with a value of $D_{Mn^{+2}} = cm^2\ s^{-1}$. The standard deviation of the experimental points at the plateau is 2%. The background of the radiopolarogram is 3% of the height of plateau.

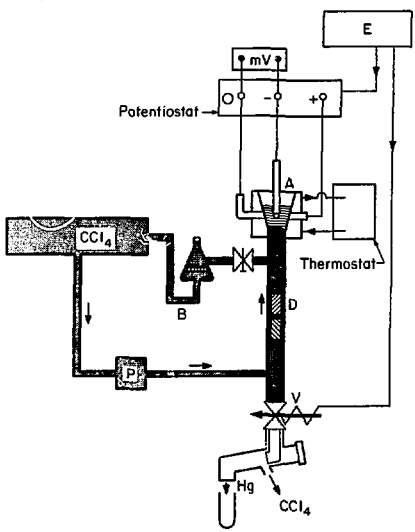

Fig. 1. (XBL 751-2035)

Experiments on Cf, Es, and Fm

3.4×10^5 α/min/2π of $^{254-255}Es$, 9.4×10^4 α/min/2π of $^{249-250-252}Cf$ and 3.4×10^2 α/mn/2π of ^{255}Fm are mixed in 3 ml of HCl 4×10^{-3}M and LiCl 0.10 M. ^{54}Mn was added to this mixture, so that its radiopolarogram is used to standardize those of Es and Cf and to check the normal functioning of the apparatus. The radiopolarograms obtained at 25°C are presented in Fig. 2. The potentials of half-wave are measured and standardized using -1.470 V as E^o of Mn^{2+}/M^o(Hg). It follows from this that E 1/2 (Cf) is -1.770 V/SCE which is in agreement with previous preliminary results.[4] E 1/2 (Es) = -1.713 V and E 1/2 (Fm) = -1.70 V. The potentials of Cf and Es are measured with ± 1 mV. E 1/2 for Fm was less precise. It is due to the fact that the ratio Fm/Es by activity was only 1/1000 in the mixture and its measurements was disturbed by the decay of ^{255}Es. A precise value for Fm requires a preliminary separation $^{255}Fm/Es$. The Ilkovic equation was verified so that $A_d = f(\sqrt{h})$ is a linear functions (Fig. 3). The ratio $R = A_d^*/A_d$ for ^{54}Mn was 100%.

Since R = 100% for Mn in the mixture of Cf and Es and the standard deviation at the plateau is less than 2% the determination of the diffusion coefficient D seems to be possible by fitting the measured height of the plateau A_d in the Ilkovic equation. The diffusion coefficient for Cf is $(6.26 \pm .4) \times 10^{-6}$ $cm^2 s^{-1}$ and for Es $(6.5 \pm .4) \times 10^{-6}$ $cm^2 s^{-1}$. These values are practically so close to those measured or calculated for trivalent ions of lanthanides[5] that Es^{3+} and Cf^{3+} are assumed to be diffusing at the dropping mercury cathode.

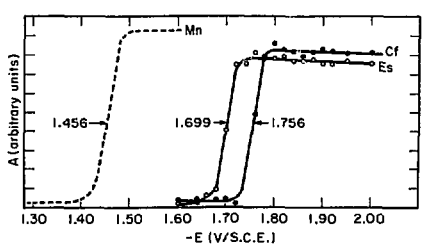

Fig. 2. (XBL 751-2034)

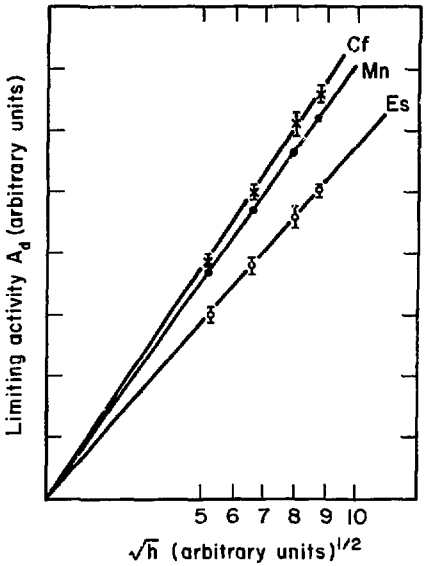

Fig. 3. (XBL 751-2033)

The mechanism of the electrode process and its reversibility require more experiments, which are in *progress*.

Footnotes and References

*On leave from Institut de Physique Nucleaire, Orsay, France.

†On leave from CNRS (Lebanon) and Institut de Physique Nucleaire, Orsay, France.

1. D. Love, Anal. Chem. Acta 18, 72 (1958).

2. P. Rogelet, F. David, Radio Chem. Anal. Lett. 18, 6, 387 (1974).

3. J. N. Gaur, N. K. Goswami, Electrochim. Acta 12, 1483 (1967).

4. F. David, Radiochem. Radioanal. Lett. 5, 279 (1970).

5. E. H. Spedding, P. E. Porter, J. M. Weight, J. Am. Chem. Soc. 74, 2055 (1952).

STUDY OF SOME THERMODYNAMIC PROPERTIES OF 5f ELEMENTS

F. David,* K. Samhoun,† R. Guillaumont,‡ and L. J. Nugent§

Nugent, Burnet, and Morss recently published[1] the values of the sublimation enthalpies ΔH^o_s and the values of the formation enthalpies ΔH^o_f for the aquo ions M^{3+}_{aq} for each member of the 4f and 5f series. The data were obtained through theoretical considerations and by correlation of P(M) and ΔH^{o*}_s functions.

P(M) is defined by $P(M) = \Delta H^o_s - \Delta H^o_f$ if $\Delta E(M) < 0$

and $P(M) = \Delta H^o_s - \Delta H^o_f + \Delta E(M)$ if $\Delta E(M) > 0$.

ΔH^{o*}_s is defined by $\Delta H^{o*}_s = \Delta H^o_s$ if $\Delta E(M) < 0$ · $\Delta H^{o*}_s = \Delta H^o_s + \Delta E(M)$ if $\Delta E(M) > 0$.

$\Delta E(M)$ is the difference between the lowest electronic energy level of the $f^n s^2 d^1$ configuration and the lowest energy level of the $f^{n+1} s^2$ configuration in the neutral gaseous atom.

We have examined these functions for the 5f series using new experimental data and estimating ΔH^o_f for fermium, mendelevium and nobelium from amalgamation data.[2-4] Although P(M) = f(Z) varies linearly and parallel for the first seven terms of the 4f and 5f series it looks different for the last terms (Fig. 1).

For lanthanides P(M) = f(Z) is represented by a "V" curve with a minimum at gadolinium while P(M) seems to decrease linearly with Z throughout the 5f series. In both cases however P(M) is a slow-varying function of Z as expected.[1]

By taking into account this observation, new values of ΔH^o_s and ΔH^o_f are estimated for each element of the 5f series (Table 1). On the other hand the estimation of the entropy of formation ΔS^o_f of M^{3+}_{aq} ions (Table 1) allowed the determination of the free energy change and the redox potential E^o corresponding to the couple M^{3+}_{aq}/M (Table 1). With this basic result $E^o(M(X)/M)$ for all known X redox state are derived. The comparison of redox stabilities from Fig. 2 predicts the relative stability of Pa(III) (E^o [Pa(IV)/Pa(III)] ≃ -1.9 V), Cm(V) (E^o[Cm(V)/CM(IV)] ≃ +1.3V) and Cf(V) (E^o [Cf (V)/Cf(IV)] ≃ +0.8 V).

reasonable delay range following the muon stopping signal, but the data are insufficient to permit calculation of a meaningful, precise lifetime value. It is also unfortunate that the observed energy of 2614 keV is within experimental precision (±2 keV) equal to that of the well-known first excited state of ^{208}Pb (2614.5 keV). It is possible that time-correlated, inelastic excitation of this level in the ever-present lead shielding could occur to the extent observed, and cannot yet be excluded. (A priori, of course, the possibility of an accidental energy overlap is on the order of 1%.)

Although single gamma-ray intensities are not sufficient to permit lifetime measurements, they can be made for ranges of gamma-ray pulses in the Ge(Li) detector. The only presently reportable values were made in several short runs using 128 time channels. An example of such a time spectrum is shown in fig. 5. The periodic, beam-associated background is evident both in the prompt and the delayed times. After subtraction of the periodic background measured at negative times, the delayed counts can be fitted (with excellent χ^2) to a single exponential as shown in fig. 6. A single-run example of the experimental lifetimes measured in this manner is shown in Table 2. The increase in the lifetime at the higher energy ranges is attributed to an increased relative background from electron bremsstrahlung; however, at the present time, we have not yet tried to fit these data to other than a single exponential.

In conclusion, our lifetime measurements are in excellent agreement with the electron measurement of Hashimoto et al.[2] and several standard errors larger than the results from fission measurements[3], thereby adding some weight to Bloom's hypothesis, despite our inability to obtain definitive lifetime measurements on individual gamma rays.

THE MAGNETIC SUSCEPTIBILITY OF ^{249}Cf METAL

D. K. Fujita, T. C. Parsons, J. R. Peterson,*
M. Noe,* and N. Edelstein

Magnetic measurements of the transplutonium metals are of great importance because it is in this region of the actinide series that the metals exhibit the localized magnetic behavior characteristic of the lanthanide metals. It should then be possible to correlate the chemical valences of the transplutonium elements with their structural properties as determined by crystallographic studies. Such correlations have been proposed by Zachariasen[1] and modified by Cunningham and Wallman[2] for the first half of the actinide series. The basic assumption inherent in this model is that the f electrons in these metals are non-bonding and do not contribute to the formation of chemical bonds between metal atoms. This assumption as applied to the early actinide metals has been questioned.[3,4] However the model may be applicable to the transplutonium metals.

Very few magnetic measurements have been reported for the transplutonium metals because of the major experimental difficulties encountered in obtaining pure, well-characterized samples and the small amounts of materials available. In this paper we report the first magnetic susceptibility measurements on two different preparations of ^{249}Cf metal.

The two ^{249}Cf metal samples were synthetized and characterized by x-ray powder diffraction techniques at ORNL. Both samples were the expanded fcc phase. The mass of the first sample LI-48-A was 8.85±0.15 μg. This mass was determined after the magnetic measurements by dissolution of the sample and a subsequent alpha assay. This number agreed with an earlier determination of the mass obtained by a gamma ray assay. The mass of the second sample LI-54 was 6.12±0.14 μg obtained only by a gamma ray assay.

The apparatus used for the magnetic measurements was a Faraday balance of the type first suggested by Cunningham,[5] which has been described previously.[6] The temperature was varied by flowing cold N_2 or He gas around the sample chamber, which was filled with the He exchange gas. The temperature was monitored by a calibrated GaAs diode installed in the sample chamber less than 1 cm below the sample. The apparatus was calibrated with $HgCo(NCS)_4$ used as a standard.

The reciprocal deflections of the two samples as a function of temperature at various magnetic fields are shown in Figs. 1 and 2. From this data the magnetic susceptibility of the samples at each temperature may be obtained. The data showed no magnetic field dependence over the entire temperature range measured. Plots of the reciprocal gram susceptibility vs temperature for the two samples are shown in Figs. 3 and 4. As can be seen from these plots the data for both samples follow the Curie-Weiss law[7]

$$\chi_M = \frac{C}{T + \Delta} .$$

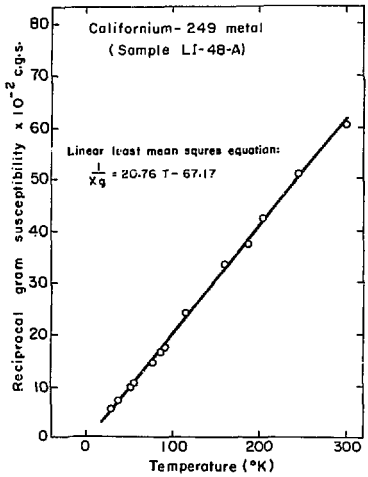

Fig. 1. Reciprocal deflection vs temperature of ^{249}Cf metal (sample LI-48A). (XBL 751-2003)

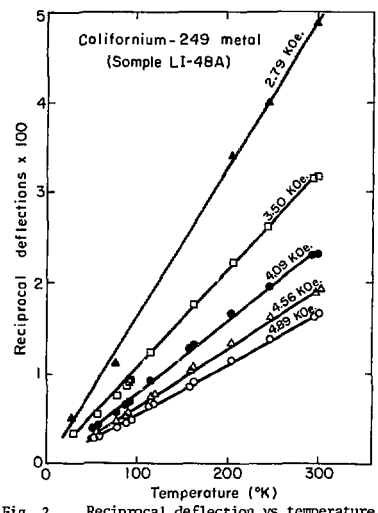

Fig. 2. Reciprocal deflection vs temperature of ^{249}Cf metal (sample LI-54). (XBL 751-2004)

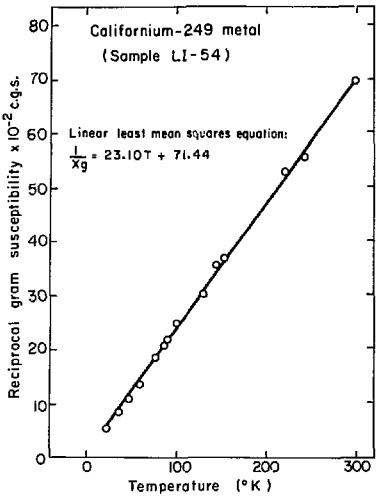

Fig. 3. Reciprocal gram susceptibility vs temperature of ^{249}Cf metal (sample LI-48A). (XBL 751-2005)

Since Δ is small we may calculate the effective magnetic moments for these samples by[7]

$$\mu_{eff} = 2.828(C)^{1/2} \text{ BM}.$$

These results are shown in Table 1.

The two likely valance states for Cf metal are $5f^{10}$, Cf^{2+}, or $5f^{9}$, Cf^{3+}. We may estimate the free ion Landé g values for the ground term and then calculate the effective free ion magnetic moments for Cf^{2+} J = 8 and Cf^{3+} J = 15/2. The results are also shown in Table 1.

Table 1. ^{249}Cf metal.

Sample	Phase	Mass (μg)	μ_{eff} (BM)	Δ (°K)	T
LI-48	fcc	8.85	9.84	-3.24	28°K - 298°K
LI-54	fcc	6.12*	9.32	3.00	22°K - 298°K

Calculation: $\mu_{eff}(Cf^{3+}) = 10.22$ BM

$\mu_{eff}(Cf^{2+}) = 10.18$ BM

The experimental values for the two samples differ by approximately 5%. These samples were from different preparations so it is possible this difference could be due to different impurities in the samples. We estimate the reliability of each measurement to be about 2%. The samples were of identical phases as determined by x-ray crystallography but the diffraction pattern could not be obtained from part of the sample while another part could be amorphous. The measured effective moments are lower than calculated for which we have no explanation. It is unfortunate that for this particular case the magnetic susceptibility measurements do not differentiate between the dipositive and tripositive ion due to their effective moments being accidentally the same. Therefore we can reach no conclusion from these measurements about the correlation of the structure (ionic radius) with valence state.

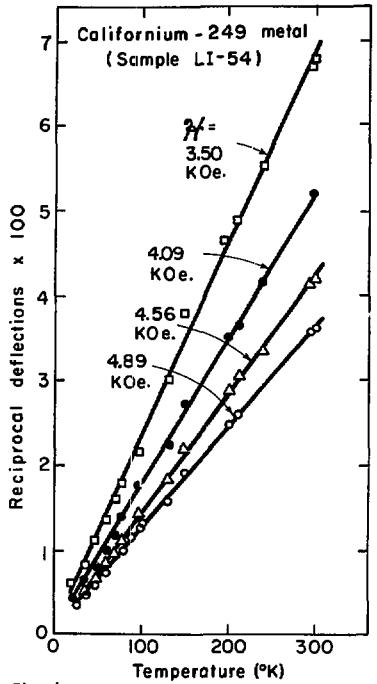

Fig. 4. Reciprocal gram susceptibility vs temperature of ^{249}Cf metal (sample LI-54). (XBL 751-2006)

Footnotes and References

*Oak Ridge National Laboratory

1. W. H. Zachariasen, J. Inorg. Nucl. Chem. 35, 3487 (1973).

2. B. B. Cunningham and J. C. Wallman, J. Inorg. Nucl. Chem. 26, 271 (1964).

3. H. H. Hill in "Plutonium 1970 and Other Actinides," edited by W. N. Miner, The Metallurgical Society, New York, 1970, p.2.

4. A. J. Freeman and D. D. Koelling in "The Actinides: Electronic Structure and Related Properties, Volume I," edited by A. J. Freeman and J. B. Darby, Jr., Academic Press, New York, 1974, p.51.

5. B. B. Cunningham, J. Chem. Educ. 36, 31 (1959).

6. D. K. Fujita, UCRL-19507, 1969.

7. See for example B. N. Figgis, "Introduction to Ligand Fields," John Wiley and Sons, Inc., New York, 1966, for the details of this equation.

THE EPR OF Cf^{3+} IN OCTAHEDRAL SYMMETRY AND THE NUCLEAR DIPOLE MOMENT OF ^{249}Cf

N. Edelstein and D. G. Karraker*

The diamagnetic compounds Cs_2NaMCl_6 (M = Y^{3+} or Lu^{3+}) provide an excellent lattice for magnetic and optical investigations of the trivalent $4f^n$ and $5f^n$ ions.[1,2] The octahedral coordination about the f^n ion $(MCl_6)^{3-}$ particularly simplifies the analysis of the experimental results.[3] We report in this paper the electron paramagnetic resonance (epr) spectrum of $^{249}Cf^{3+}$ diluted in $Cs_2NaLuCl_6$. The spin Hamiltonian parameters of Yb^{3+} present in our sample as an additional impurity are also given. From an analysis of the spin Hamiltonian parameters of Cf^{3+} the value of the nuclear magnetic dipole moment of ^{249}Cf is determined. This work is the first report of the magnetic properties of Cf^{3+} in a well defined symmetry site.

$Cs_2NaLuCl_6$, doped with ^{249}Cf, was prepared by adding stoichiometric amounts of CsCl, NaCl, and $LuCl_6 \cdot XH_2O$ to 6M HCl, adding a 6M HCl solution of ^{249}Cf, evaporating to a solid, drying this material in quartz to 400°C, and then fusing by lowering in a sealed quartz tube at 2 mm/hr through a 950°C vertical furnace. The product was a polycrystalline material; the sample used for epr measurements contained approximately 0.5 wt% ^{249}Cf. The epr spectra were measured at 4.2°K and at a frequency of approximately 35GHz with the equipment previously described.[4]

The epr spectrum of the polycrystalline Cf^{3+} in $Cs_2NaLuCl_6$ sample is shown in Fig. 1. The seven hyperfine lines confirm the nuclear spin I of ^{249}Cf as 9/2. The measured parameters of the applicable spin Hamiltonian

$$H = g\,\mu_B \vec{H}\cdot\vec{S}' + A\,\vec{I}\cdot\vec{S}' \qquad (1)$$

where the effective spin S' = 1/2 and I = 9/2, are given in Table 1. The only other strong lines in

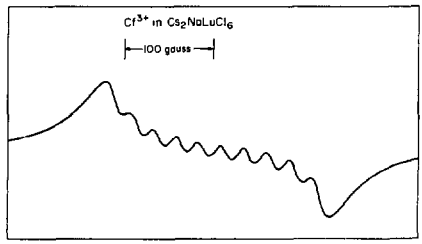

Fig. 1. EPR spectrum of Cf^{3+} in $Cs_2NaLuCl_6$, T = 4.2°K, the frequency is approximately 35GHz.

Table 1. Spin Hamiltonian parameters of $^{249}Cf^{3+}$ and various Yb^{3+} isotopes diluted in $Cs_2NaLuCl_6$. (XBL 744-2905)

Ion	I	|g|	$\left\|\frac{A}{g\mu_B}\right\|$ (gauss)	|A| ($cm^{-1}\times10^3$)
$^{249}Cf^{3+}$	9/2	6.273±0.010	25.7±0.7	7.52±0.2
Yb^{3+}	0	2.586±0.004		
Yb^{3+} [a]	0	2.584±0.002		
$^{173}Yb^{3+}$ [a]	5/2	2.584±0.002	157.4±0.5	18.99±.06
$^{171}Yb^{3+}$ [a]	1/2	2.584±0.002	577.4±1	69.66±.12

[a] From unpublished measurements at 4.2°K at a frequency of ~ 9.2 GHz.

the sample appeared at high magnetic fields and were assigned to Yb^{3+} from the measured g value (Table 1) and the characteristic hyperfine patterns. For the Yb^{3+} ion the effective spin is $S' = 1/2$ and $I = 0$ for the even-even isotopes which are 69.56% abundant, $I = 1/2$ for ^{171}Yb (14.31% abundant), $I = 5/2$ for ^{173}Yb (16.31% abundant).

Let us consider an isolated J level for an f transition ion in O_h symmetry. The energy levels and eigenvectors then depend only on the ratio and sign of the sixth order crystal field term to the fourth order term.[3] Lea, Leask, and Wolf[3] have tabulated these eigenvalues and eigenvectors for all J manifolds of the f^n series (n = 1-13) and predicted the crystal field ground states for the rare earth ions in cubic and octahedral symmetry. We may use this formulation of the problem for actinide ions; however we have to calculate the effects of intermediate coupling on the fourth and sixth order operator equivalent factors, β and γ, and on the free ion Landé g value, g_J. These parameters are shown in Table 2. We have used the electrostatic and spin orbit parameter values obtained by Carnall et al[5] to calculate these numbers. We did not use their configuration interaction parameters which will not greatly affect the ground state wave function. As can be seen from Table 2 the signs of the operator equivalent factors are not changed by the inclusion of intermediate coupling effects. Therefore the crystal field state should be either a Γ_6 or Γ_7 doublet which will give an isotropic epr spectrum.

The calculated g value for the Γ_6 state, $-5g_J$, is equal to -6.395 for Cf^{3+}. The calculated g value for the Γ_7 state is $5.667g_J$. Therefore we assign the epr spectrum to the Γ_6 state which allows us to set a limit on the ratio of the sixth to the fourth order crystal field parameter $B_0^6/B_0^4 < 1.32$.[6,7,8] This ratio is consistent with the limits found by Hendricks et al.[1]

If we use the relationship

$$\frac{A}{g} = \frac{a}{g_J}$$

we find the free ion hyperfine coupling constant

$$|a| = 1.50 \pm .04 \text{ MHz}.$$

Table 2. Operator equivalent factors and free ion g values for the ground state of the f^9 ions.

Ion	$\beta \times 10^6$	$\gamma \times 10^6$	g
$4f^9$ Dy^{3+} [a]	-.5920	1.0350	1.333
$5f^9$ Cf^{3+}	-.5602	0.4494	1.279

[a] From Reference 3.

The nuclear dipole moment is related to the free ion hyperfine coupling constant by[9]

$$a = \frac{2\mu_B\mu_N\mu}{I} \left\langle \frac{1}{r^3} \right\rangle \langle LSJ || N_i || LSJ \rangle ,$$

where μ_B and μ_N are the Bohr and nuclear magneton respectively, μ is the nuclear dipole moment, and $\langle 1/r^3 \rangle$ the expectation value of the radial wave function.

We have assumed the core polarization term is negligible. The operator $\vec{N}_i$ is defined.[8,9]

$$\vec{N}_i = \sum_i [\vec{I}_i - 10^{1/2}(\vec{s}C^2)_i^{(1)}]$$

where $\vec{I}_i$ and $\vec{s}_i$ are the spin and orbital angular momentum vectors and $C^{(2)}$ is a second rank tensor. We calculate

$$|\mu| \ (^{249}Cf) = .28 \pm .06 \ \mu_N$$

where we have corrected the $\vec{I}_i$ part of the tabulated N matrix element for the effects of intermediate coupling. The value of $\langle 1/r^3 \rangle$ was obtained from Lewis et al.[10] The error is estimated from uncertainties in the parameters used.

The ^{249}Cf nuclear ground state has been assigned to 9/2-[734] Nilsson level.[11] The formalism for calculating nuclear dipole moments for single neutron states from Nilsson wave functions is well known.[12] If we use for effective g values[13] $g_s^{eff} = -2.4$, $g_\ell^{eff} = -0.03$, $g_R = 3.5$, and a deformation parameter $\eta = 4$ we find

$$\mu \ (^{249}Cf) = -0.49 \ \mu_N .$$

The absolute value calculated for nuclear moment depends to some degree on the deformation parameter chosen. The agreement between the experimental and the theoretical result is fair.

Footnote and References

*Savannah River Laboratory, E.I. duPont de Nemours and Company, Aiken, South Carolina 29801.

1. M. E. Hendricks, E. R. Jones, J. A. Stone, and D. G. Karraker, J. Chem. Phys. 60, 2095 (1974).

2. R. W. Schwartz and P. N. Schatz, Phys. Rev. B 8, 3229 (1973).

3. K. R. Lea, M. J. M. Leask, and W. P. Wolf, J. Phys. Chem. Solids 23, 1381 (1962).

4. W. Kolbe, N. Edelstein, C. B. Finch, and M. M. Abraham, J. Chem. Phys. 56, 5432 (1972).

5. W. T. Carnall, S. Fried, and F. Wagner,Jr., J. Chem. Phys. 58, 1938 (1973).

6. In the notation of Lea Leask, and Wolf $x < -.45$.

7. We are using the tensor operator notation given by Wybourne (Ref. 9). The crystal field potential for O_h symmetry is

$$V_c = B_a^4[C_0^{(4)} + (5/14)^{1/2}(C_{-4}^{(4)} + C_4^{(4)})] + B_0^6 [C_0^{(6)} - (7/1)^{1/2}(C_{-4}^{(6)} + C_4^{(6)})];$$

$$C_Q^{(k)} = [\frac{4\pi}{(2k+1)}]^{1/2} Y_q^{(k)},$$

the $Y_q^{(k)}$ and normalized spherical harmonics.

8. B. G. Wybourne, "Spectroscopic Properties Rare Earths," (Interscience, New York, 1965).

9. A. Abragam and B. Bleaney, "Electron Paramagnetic Resonance of Transition Ions," Claredon Press, Oxford, 1970.

10. W. B. Lewis, J. B. Mann, D. A. Liberman, and D. T. Cromer, J. Chem. Phys. 53, 809 (1970).

11. E. K. Hyde, I. Perlman, and G. T. Seaborg, "The Nuclear Properties of the Heavy Elements," Vol. I, Prentice Hall, Inc., New Jersey, 1964.

12. M. A. Preston, "Physics of the Nucleus," Addison-Wesley Publishing Co., Inc., Palo Alto, 1962.

13. S. Nagamiya and T. Yamazaki, Phys. Rev. C4, 1961 (1971).

REACTIONS OF DITHIOLATE LIGANDS WITH URANIUM (IV) HALIDES

R. Gradl and N. Edelstein

Introduction

During the past decade there has been considerable interest in d transition metal -1, 2- dithiolene complexes, particularly because of their application to analytical, industrial, and bio-organic problems.[1] The unusual chemical properties of the dithiolene chelates have been thoroughly studied both theoretically and experimentally by several groups and the results have been summarized by McCleverty[2] and Hoyer and Dietzsch.[3]

In contrast to the d transition series, very little is known about actinide 1, 2- dithiolene complexes. The anionic uranyl (VI) chelates, $(R_4N)_2UO_2(mnt)_2$, where R is C_2H_5 or n-propyl, mnt = maleonitriledithiolate dianon, have been prepared.[4] Contradictory results existed about a U(IV) dithiolene complex until Dietzsch and Hoyer[5] synthesized $[As(C_6H_5)_4][U(mnt)_4]$ from the reaction of UCl_4 with Na_2mnt. They also found that neither the reaction of UCl_4 in methanol with the disodium salt of 1,2-dimercaptoethylene or with 4,5- dimercapto-o-xylene led to stable compounds. Very recently the synthesis of $(C_5H_5)_2U(tdt)$, tdt = toluenedithiol dianon, has been isolated from the reaction of $(C_5H_5)_2U(Net)_2$ and H_2tdt.[6] The proton NMR data indicate a monomer-dimer equilibrium below room temperature.

We present here the details of the reactions between UCl_4 and UI_4 and the ligands 3,4 -dithiotoluene (H_2tdt) and bis-trifluoromethyl 1,2 dithietene ($S_2C_4F_6$).

Results and Discussion

Reactions with 3,4 - toluenedithiol

UI_4. Uranium tetraiodide reacts with 3,4 -toluenedithiol in refluxing hexane to give a red-brown compound which is insoluble in methylene chloride, benzene, or toluene. It is very soluble in THF or DMF giving a yellowish-red solution, but it cannot be recovered from these solvents. The compound immediately decomposes in air and dissolves completely in water giving a green solution. Total elemental analysis of the compound shows its composition to be $U_2I_4(tdt)_2(H_2tdt)$. In agreement with this formulation the infra red spectrum shows a ν_{S-H} absorption at 2425 cm^{-1} which, when compared with the free ligand (H_2tdt: ν_{S-H} = 2545 cm^{-1}), corresponds to a weaker S-H bond. Sublimation at 160°C and 10^{-5} torr gives a yellow-brown product which does not show any IR absorption bands characteristic of the H_2tdt ligand.

The proton nmr spectrum exhibits two different bands corresponding to two sets of ligands, as shown in Table 1. The upfield resonances contain the $H(CH_3)$ and $H(CH_{ring})$ bands of two tdt ligands. This large upfield shift relative to TMS shows these protons are strongly affected by the paramagnetic U(IV) ions which have the $5f^2$ open shell configuration. The low field group (2.3 to 7.33 ppm downfield from TMS) exhibits two H(S-H) peaks in addition to the $H(CH_3)$ and $H(CH_{ring})$ peaks. These resonances are at the same frequencies as in the spectrum of the free ligand. We suggest the $U_2I_4(tdt)_2(H_2tdt)$ complex partially dissociates upon dissolving in THF due to a replacement of the H_2tdt ligand by two THF molecules. Note that in Table 1 the H(S-H) resonances of the free ligand in d_8-THF and $CDCl_3$ are different while the $H(CH_3)$ and $H(CH_{ring})$ resonances are very similar. This fact may be due to hydrogen bonding of the protons in the S-H group by THF.

A possible structure for $U_2I_4(tdt)_2(H_2tdt)$ is given in Fig. 1. In this structure each uranium ion is surrounded by four sulfurs and two iodines in a distorted octahedral configuration.

An appropriate reaction mechanism can be postulated which would lead to this structure. One molecule of H_2tdt reacts with UI_4 to give an intermediate UI_2tdt by replacement of two iodide ions as $2HI$. The insufficient coordination about the U(IV)

Table 1. H-NMR frequencies of 3,4-toluenedithiol and $U_2I_4(tdt)_2(H_2tdt)$.

Assignments	3,4-toluenedithiol In d_8-THF[a]	3,4-toluenedithiol In $CDCl_3$[a]	$U_2I_4(tdt)_2(H_2tdt)$ In d_8-THF[a]
CH_3	-2.16	-2.30	-2.30
S_1H	-4.00	-3.50	-4.10
S_2H	-4.40	-3.66	-4.20
ring H_1	-6.60	-6.66	-6.76
	-6.73	-6.80	-6.83
ring H_2	-7.06	-7.03	-7.13
	-7.16	-7.18	-7.33
ring H_3	-7.03	-7.06	-7.10
CH_3			9.35
ring H_1			11.64
			11.72
ring H_2			56.69
			56.85
ring H_3			56.45

[a]Units are ppm referenced to TMS.

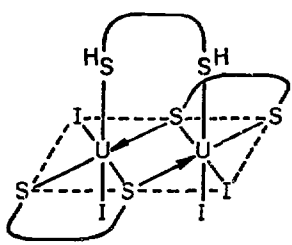

Fig. 1. Proposed structure for $U_2I_4(S_2C_7H_6)_2$ $(H_2S_2C_7H_6)$. The curved line represents the $C_6H_3CH_3$ backbone of the 3,4-toluenedithiol ligand. (XBL 7411-8303)

causes a dimerization with another molecule of H_2tdt, with one sulfur of each ligand bridging between the two U ions. However, a third ligand is needed to give each uranium ion the favored six fold coordination, but this ligand cannot be reduced to a dianion without giving the uranium ions a formal oxidation state (+V). Therefore the third ligand is easily replaced. The lability of the neutral H_2tdt ligand is the main cause of the thermal instability, the reactivity towards air, and the reason the compound cannot be recrystallized from THF or DMF due to its reactions with these solvents.

The proposed structure is supported by the report of a monomer-dimer equilibrium for $Cp_2U(tdt)$.[6] The π-bonded cyclopentadienyl ion is a much better coordinating ligand than I^- so at room temperature the complex is monomeric. At lower temperatures the dimer becomes stabilized. By contrast, the iodo complex even at room temperature coordinates a neutral ligand in order to become coordinatively saturated.

UCl_4. Uranium tetrachloride reacts with H_2tdt in refluxing CCl_4 or ethylcyclohexane to give a brown compound. Total elemental analysis showed the main part was unreacted UCl_4 and decomposition products of the ligand. Part of the material dissolves in THF to give a green solution leaving a brown residue. A red complex is precipitated from the green solution after several days at -10°C but in insufficient quantity for characterization.

Reactions with bis (trifluoromethyl -1,2 dithietene)

UCl_4. Uranium tetrachloride was treated with bis(trifluoromethyl) -1,1-dithietene in boiling ethylcyclohexane for several days to give a dark brown material of the empirical formula $U_2Cl_4S_2C_4F_6$ as determined by total elemental analysis. The mass spectrum only exhibited bands with very low intensity in the range between 840 and 860 mass units (molecular weight of $U_2Cl_4S_2C_4F_6$ = 844). The stretching frequency of the C = C bond (1607 cm^{-1}) showed shift is similar to that found in various dinuclear species containing a bridging dithiolene ligand, M-L-M, M = Fe,[7] M = V, Cr, Mo[8] and suggests the dithiolene ligand in this U complex may also be bridging. The material $U_2Cl_4S_2C_4F_6$ is very slightly soluble in THF and DMF but slowly decomposes in showed only a small shift of -14 cm^{-1} from the free ligand. This small shift is similar to that found in various dinuclear species containing a bridging dithiolene ligand, M-L-M, M = Fe,[7] M = V, Cr, Mo[8] and suggests the dithiolene ligand in this U complex may also be bridging. The material $U_2Cl_4S_2C_4F_6$ is very slightly soluble in THF and DMF but slowly decomposes in these solvents. Sublimation of this material yielded only UCl_4. We are presently unable to suggest a plausible structure for this material but it is possibly polymeric.

UI_4. Uranium tetraiodide was treated with $S_2C_4F_6$ in ethylcyclohexane at 130° for several days to give a brown material which was insoluble in common solvents. Total elemental analysis showed this material had an empirical formula $U_3F_3I(S_2C_4F_6)_2$. The excess of fluorine in this material indicates some of the ligand decomposed. The stretching frequency of the C = C bond (1618 cm^{-1}) is similar to that found for $U_2Cl_4S_2C_4F_6$. This material appears polymeric and no reasonable structure can be suggested for it.

Conclusion

Uranium tetrachloride and uranium tetraiodide react with the ligands bis(trifluoromethyl) -1, 2 dithetene and 3,4 toluenedithiol in a very specific fashion which is dependent on the particular halide and ligand used. In the reactions studied no anionic species were found and no general formula can be given for the different reaction products. The only common feature of the reactions is that dinuclear or polynuclear species were formed.

References and Footnotes

1. For a discussion and references to these applications, see Refs. 2 and 3.

2. J. A. McCleverty, Prog. Inorg. Chem. 10, 49 (1968).

3. E. Hoyer and W. Dietzsch, Z. Chem. 11, 41,(1971).

4. L. Zimmer and K. H. Lieser, Inorg. Nucl. Chem. Letters 5, 635 (1971).

5. W. Dietzsch and E. Hoyer, Inorg. Nucl. Chem. Letters 5, 635 (1969).

6. J. D. Jamerson and J. Takats, J. Organometal. Chem. 78, C23 (1974).

7. R. B. King, J. Amer. Chem. Soc. 85, 1584 (1963).

8. R. B. King, J. Amer. Chem. Soc. 85, 1587 (1963).

SOME REACTIONS OF NEPTUNIUM HEXAFLUORIDE AND THE SYNTHESIS OF $NpOF_4$

R. D. Peacock* and N. Edelstein

The discovery of Np(VII) in complex oxides and similar compounds[1,2] has led to renewed interest in the possibility that other Np(VII) compounds, formally analogous to well known Re(VII) and Te(VII) entities, might be synthesized. The most likely route to such compounds, lies in the oxidation of Np oxides, fluorides or oxide fluorides under drastic conditions. In the present work the oxidation of a neptunium oxide fluoride by krypton difluoride was attempted, and the opportunity was taken to study the stability of other high-valent neptunium compounds. The programme was divided into sections as follows: 1) the attempted synthesis of $CsNpF_7$ (with a view to ultimate oxidation to $CsNpF_8$), 2) the exchange reaction NpF_6 with BCl_3 (with a view to isolating a chloride of Np higher than the known $NpCl_4$), 3) the partial hydrolysis of NpF_6 and the attempted oxidation of the hydrolysis product.

Discussion

Although uranium salts of the types Na_3UF_9, K_2UF_8 and $CsUF_7$ have been known for some time,[3,4,5] the corresponding Np salts have not been isolated, and it appears that the reaction of NpF_6 with alkali metal fluorides generally leads to Np(V) salts.[6] However, strong colorations have been observed on previous occasions during the reaction between NpF_6 and NaF,[7] and the reaction between NpF_6 and NOF at -80°,[8] which may be ascribed to the formation of Np(VI) salts. From the present work it is evident that although the dry reaction between NpF_6 and CsF leads to $CsNpF_6$, the reaction in ClF_3 is more complicated and the initial product is probably an Np(VI) complex fluoride. Comparison with the U(VI) system suggests that the material initially formed is $CsNpF_7$, which then reacts with SiF_4 impurity in the system:

$$2CsNpF_7 + SiF_4 \rightarrow Cs_2SiF_6 + 2NpF_6.$$

Unfortunately the presence of the adventitious SiF_4 means that the solution experiments do not give precise information about the stability of the initial Np(VI) compound. Nevertheless, it is clear that $CsNpF_7$ is not stable at 25°, and it must also be concluded that any Np(VII) complex fluoro-anion will also prove to be very unstable indeed.

The highest certain chloride of neptunium is $NpCl_4$, though there is some slight evidence for $NpCl_5$ in the vapor state. Exchange reactions have proved successful in preparing tungsten and uranium hexachlorides from the corresponding fluorides and boron trichloride,[9,10] while the action of boron trichloride on rhenium hexafluoride certainly gives the pentachloride and just possibly a hexachloride as well.[11,12] The present work indicates that a competing reaction to give the tetrafluoride, which is also shown to some extent by uranium hexafluoride,[10] becomes exclusive with neptunium hexafluoride, even in the presence of chlorine and chlorine trifluoride.

$$3NpF_6 + 2BCl_3 \rightarrow 3NpF_4 + 3Cl_2 + 2BF_3.$$

The reaction of the NpF_4 with excess of BCl_3 leads to a change of phase, and it is likely that Np(IV) chloride fluorides, analogous to the known uranium compounds,[13] are formed. It is interesting that NpF_5, which has been fully characterized by x-ray photography,[14,15] is not isolated at any stage in this exchange reaction.

The hydrolysis of UF_6 has only recently been re-examined after early reports had suggested that UF_6 did not react with water in the vapor phase to give the oxide tetrafluoride.[16] However, two sets of workers have now independently shown that in anhydrous hydrogen fluoride solution the carefully controlled hydrolysis of UF_6 does give UOF_4, formally analogous to the well-known oxide tetrafluorides of Mo and W. Unlike UO_2F_2, this is an extremely reactive material; the structure is quite different from the 6-coordinated $MoOF_4$ and WOF_4, and in fact two different phases are known, one of which is isostructural with β-UF_5 and both of which contain uranium in high co-ordination.

In the present work it has been shown that a reactive material almost insoluble in anhydrous hydrogen fluoride is the first product of the hydrolysis of NpF_6. This reactive material has been identified by x-ray diffraction as parameters the trigonal form of $NpOF_4$. A least squares fitting[17] of the trigonal unit cell parameters to the observed data gives the lattice constants shown in Table 1. The more compressed unit cell for $NpOF_4$ as compared to UOF_4 follows the expected trend due to the decreased ionic radius of the higher Z element. When the $NpOF_4$ was allowed to stand in capillaries in incompletely dry conditions, it led to decolorization

Table 1. Lattice constants for UOF_4 and $NpOF_4$.

Lattice Parameters	UOF_4 [a]	$NpOF_4$ [b]
a(Å)	13.22	13.17 ± 0.02
c(Å)	5.72	5.70 ± 0.02

[a] Trigonal space group R3m (hexagonal setting), Ref. 4.

[b] Absorption corrections were made by the Nelson and Riley extrapolation procedure.

and the appearance of a further unidentified crystalline phase. The attempted oxidation of $NpOF_4$ with krypton difluoride did not lead to the hoped for $NpOF_5$ (which one might expect to be volatile), but only to the partial re-formation of NpF_6, perhaps according to the equation

$$NpOF_4 + KrF_2 \rightarrow NpF_6 + Kr + \frac{1}{2} O_2.$$

The residue was almost unchanged starting material.

It is now evident that a Np(VII) fluoride or oxide fluoride will not be easily prepared. To isolate NpF_7, or $NpOF_5$ will require stronger oxidizing conditions than those used, and it is difficult to see how these can be accomplished with materials presently to hand. NpO_2F_3 could have resulted from the direct fluorination of NpO_2 (cf ReO_2F_3), and the only remaining change here would be to attempt the oxidation of the rather unreactive NpO_2F_2. There appears on the surface to be a marginally better change of getting NpO_3F, since, with manganese and technetium, compounds of similar stoichiometry may be isolated without great difficulty.[16,17] Unlike MnO_3F and TcO_3F, however, it is not likely that an NpO_3F would prove to be volatile, so that the reaction conditions which might result in its isolation would need careful selection. It seems likely indeed that further progress in this field will have to await the isolation of complex oxides of Np(VII) more tractable than the presently known compounds towards fluorination.

Footnotes and References

*On leave from the Chemistry Department, The University, Leicester, England, January-June 1974.

1. (a) V. I. Spitsyn, A. D. Gelman, N. N. Krot, M. P. Mefodiyeva, F. A. Zakharova, Yu. A. Komkov, V. P. Shilov, and I. V. Smirnova, J. Inorg. Nuclear Chem., 31 2733 (1969). (b) C. Keller and H. Seifert, Inorg. Nuclear Chem. Lett., 5 51 (1969). (c) S. K. Awasthi, L. Martinot, J. Fuger and G. Duychaerts, Inorg. Nuclear Chem. Letters, 7 145 (1971). (d) M. Pages, E. Nectoux, and W. Freudlich, Radiochem. Radioanal. Lett., 7 155 (1971).

2. J. H. Burns, W. A. Baldwin, and J. R. Stokely, Inorg. Chem., 12 466 (1973).

3. J. G. Malm, H. Selig, and S. Siegel, Inorg. Chem., 5, 130 (1966).

4. N. S. Nikolaev and V. F. Sukoverkhov, Dokl. Akad. Nauk. SSSR. 136 621 (1961).

5. S. Katz, Inorg. Chem., 3 1598 (1964).

6. L. E. Trevorrow, T. J. Gerding, and M. J. Steindler, Inorg. Chem., 7 2226 (1968).

7. S. Katz and G. I. Cathers, Nuclear Appl., 5 206 (1968).

8. N. Bartlett and B. Zemva, unpublished observation, 1973.

9. T. A. O'Donnell and D. F. Stewart, Inorg. Chem., 5 1434 (1966).

10. T. A. O'Donnell, D. F. Stewart, and P. Wilson, Inorg. Chem., 5 1438 (1966).

11. J. H. Canterford, T. A. O'Donnell, and A. B. Waugh, Austral. J. Chem., 24 243 (1971).

12. J. Burgess, C. J. W. Fraser, I. Haigh, and R. D. Peacock, J. Chem. Soc., (Dalton Trans.), 501 (1973).

13. See D. Brown, Halides of the Lanthanides and Actinides (Wiley Interscience, London, 1968) p. 254.

14. S. Fried and J. H. Holloway, private communication quoted by R. P. Penneman, R. R. Ryan, and A. Rosenzweig, Structure and Bonding, 13 1 (1973).

15. J. H. Holloway, personal communication, 1974.

16. (a) L. H. Brooks, E. V. Garner, and E. Whitehead, "Chemical and X-Ray Crystallography Studies on Uranyl Fluoride," IGR-TN/CA 277 (1956). (b) M. G. Otey and R. A. Le Doux, J. Inorg. Nuclear Chem., 29, 2249 (1967).

17. D. E. Williams, Ames Laboratory Report IS-1052, (1964).

RECOIL TRITIUM REACTIONS WITH METHYLCYCLOHEXENE. A TEST OF THE ASSUMPTION OF ENERGY RANDOMIZATION PRIOR TO UNIMOLECULAR DECOMPOSITION*

D. C. Feet† and S. S. Markowitz

The reactions of recoil tritium atoms with the three methylcyclohexene isomers have been studied in the gas phase at 135°. T was produced by $^3He(n,p)T$. Recoil tritium atom abstraction, addition, or T-for-H substitution reactions accounted for 90% of the gas-phase products. Following activation by T-for-H substitution, the unimolecular decomposition of 4-methylcyclohexene-*t* (to give propylene-*t* or butadiene-*t*) and the unimolecular decomposition of 3-methylcyclohexene-*t* (to give ethylene-*t* or 1,3-pentadiene-*t*) was established from the pressure dependence of the product yield in the 300-1200-Torr pressure range. The apparent rate constants for these unimolecular decomposition processes was determined as 1×10^7 and 3×10^6 sec^{-1}, respectively. The rate constants for the unimolecular decomposition of cyclohexene-1-*t* and cyclohexene-3-*t* (formed by T-for-methyl substitution on 1-methylcyclohexene and 3-methylcyclohexene, respectively) were nearly equivalent. In addition, the average energy of excitation following T-for-methyl substitution is the same in cyclohexene-1-*t* and cyclohexene-3-*t*, namely, 6.0 to 6.5 eV. It was concluded that the RRKM (Rice, Ramsperger, Kassel, and Marcus) assumption of energy randomization prior to unimolecular decomposition is valud for the recoil tritium initiated unimolecular decomposition of cyclohexene.

Footnotes

*Condensed from Journal of Physical Chemistry, 78, 4 (1974).

†Present address: Argonne National Laboratory, Argonne, Illinois.

RECOIL TRITIUM REACTIONS WITH CYCLOHEXENE AND ALKENES. DETERMINATION OF RATE PARAMETERS*

D. C. Feet† and Samuel S. Markowitz

Kinetic rate parameters can be determined from recoil tritium reaction studies although the energy distribution of the reacting tritium atoms is not known. T is produced by $^3He(n,p)T$. Recoil T-for-*H* substitution on cyclohexene gives excited cyclohexene-*t* molecules. The dependence of product yield on pressure (in the 300 - 1500 Torr pressure range) showed that the excited cyclohexene-*t* molecules decomposed unimolecularly to give ethylene-*t* and butadiene-*t* with an apparent rate constant (at 135°) of $5 \sim 10^6$ sec^{-1}. The *s* parameter in the RRK (Rice, Ramsperger, and Kassel) treatment of the unimolecular decomposition of cyclohexene was determined as $s = 24$. Similarly, the pressure dependence of product yield showed that cyclohexyl-*t* radicals which are formed by recoil T atom addition to cyclohexene decomposed unimolecularly to give *n*-hexene-*t*, 1-butene-*t*, and methane-*t* with rate constant 8×10^3, 3×10^4, and 5×10^2 sec^{-1}, respectively. The relative rate of abstraction *vs.* addition of radicals in alkenes was determined from the scavenger dependence of the yields of products with a radical precursor.

Footnotes

*Condensed from Journal of Physical Chemistry, 78, 347 (1974).

†Present address: Argonne National Laboratory, Argonne, Illinois.

ION-MOLECULE REACTIONS IN RECOIL TRITIUM CHEMISTRY*

D. C. Feet† and S. S. Markowitz

The possibility of ion-molecule processes in recoil tritium reactions has been dismissed[1,2] through application of the adiabatic principle.[3] However, the energy defect was incorrectly evaluated from the unperturbed energy levels of the isolated particles.[4-6] Experimentally, Rowland and coworkers have established an upper limit of 10% for the contribution of excited electronic states in T-for-H substitution.[7] Experimentally, the yield of HT is higher in the presence of helium (versus other noble gases). To explain this, Seewald and Wolfgang[8] proposed that 6% of the total tritium reacted as unneutralized T^+ because of the high ionization potential of helium while Urch and Malcolme-Lawes[9-10] proposed greater stabilization of highly excited HT by helium.

Unexplained by Urch and Malcolme-Lawes is the higher yield of "polymer-t" accompanying the higher HT yield in helium (versus xenon) moderated T + cyclohexene reactions.[11] "Polymer-t" is backflushed from the chromatographic columns and washed from the walls of the sample capsule in which the recoil tritium reaction took place.[12,13] Recently, "polymer-t" has been characterized by Filatov and co-workers using thin layer chromatography.[14] Table 1 shows some "polymer-t" data. Irradiations and sample analysis are discussed elsewhere.[15,16] The key feature of Table 1 is that the "polymer-t" yield is non-zero with H_2S scavenging. The "polymer-t" yield was zero in an irradiated blank containing ^3He and scavenger but no hydrocarbon. The ^{35}S activity (due to

Table 1. T + alkene reaction data[a] at 25°C.

Parent	Scavenger	Yields		
		"Polymer-t"	Alkane-t	Gas Phase-t[b]
Cyclohexene[c]	H_2S	37	109	200
(Alkane-t = cyclohexane-t)	none	75	32	96
	SO_2	174	1	44
1-Butene[d]	H_2S	22	135	304
(Alkane-t = butane-t)	none	61	21	195
	SO_2	139	4	150

[a]Tritiated product yields relative to yield of tritiated parent compound as 100. Results of two samples that agreed to within 10%.

[b]Sum of all tritiated products monitored by radio-gas-chromatography except HT and the tritiated parent compound. For material balance of products with a radical intermediate, the decrease in gas phase product yields between H_2S and SO_2 scavenger should be accompanied by an identical increase in the "polymer-t" yield. The smaller change in the "polymer-t" yield indicates that "polymer-t" recovery is $[(174 - 37)/(200 - 44)] \times 100\% = 88\%$ complete for T + cyclohexene reactions (77% for T + 1-butene).

[c]Sample composition (cm Hg): ^3He 1.6, cyclohexene 5.6 (6 mole % scavenger).

[d]Sample composition (cm Hg); ^3He 1.7, 1-butene 14 (7 mole % scavenger).

$^{34}S(n,\gamma)^{35}S$ from H_2S) is less than 5% of the "polymer-t" yield with H_2S scavenging. Filatov et al. showed that "polymer-t" in unscavenged T + cyclohexene reactions was formed by chain addition initiated by cyclohexyl-*t* radicals. However, calculations show that radical-molecule (and radical-radical) routes to "polymer-t" formation are eliminated by H_2S, which donates a hydrogen atom to the radical. Rate constants used (units of cm^3 mole^{-1} sec^{-1}) were for methyl radicals reacting with H_2S [17] (3.0×10^9), with trans-2-butene[18] (for cyclohexene, 2.6×10^5), and with methyl radicals[19] (2.4×10^{12}). In the H_2S scavenged T + cyclohexene system, the estimated steady state concentration of: (1) tritium labeled radicals (chiefly cyclohexyl-*t* radicals, see Table 1) is 7×10^{-19} moles cm^{-3}; (2) unlabeled radicals (formed at one ion pair per 30 eV energy deposited by the $^3He(n,p)T$ reaction) is 6×10^{-14} moles cm^{-3}. The rate of reaction of tritiated radicals with H_2S is estimated to be three orders of magnitude larger than the rate of reaction of tritiated radicals with either 1) cyclohexene or 2) unlabeled radicals. Experimentally, the scavenger plateau of the cyclohexane-*t* yield[15] shows that cyclohexyl-*t* radicals react solely with H_2S rather than cyclohexene or unlabeled radicals in competition with H_2S.

The "polymer-t" yield not scavengeable by H_2S is 6% of the total yield of tritiated products (HT + parent-t + other tritiated gas phase products + "polymer-t") in T + cyclohexene reactions (4% in T + i-butene reactions). We propose that the "polymer-t" yield that is unscavengeable by H_2S results from ion-molecule processes. Typical ion-molecule reaction rate constants[20] are 10^{14} to 10^{15} cm^3 mole^{-1} sec^{-1}; which is larger by two orders of magnitude than radical-radical rate constants. In addition, tritiated ion chains, unlike tritiated radical chains, are not terminated by reaction with H_2S.[20]

Footnotes and References

*Accepted by Radiochimica Acta.

†Present address: Argonne National Laboratory, Argonne, Illinois 60439.

1. R. Wolfgang, Progress in Reaction Kinetics 3, 97 (1965).

2. D.S. Urch, MTP Int. Rev. Sci., Inorg. Chem. Ser. 8, 149 (1972).

3. H.S.W. Massey and E.H.S. Burhop, Electronic and Ionic Impact Phenomena, Clarendon Press, Oxford, 1952, pp. 513-4.

4. S. Dworetsky, R. Novick, W.W. Smith and N. Tolk, Phys. Rev. Lett. 18, 939 (1967).

5. H. Rosenthal and H.M. Foley, Phys. Rev. Lett. 23, 1480 (1969).

6. S.H. Dworetsky and R. Novick, Phys. Rev. Lett. 23, 1484 (1969).

7. G. Izawa, E.K.C. Lee, and F.S. Rowland, J. Phys. Chem. 77, 1210 (1973).

8. D. Seewald and R. Wolfgang, J. Chem. Phys. 47, 143 (1967).

9. D.J. Malcolme-Lawes and D.S. Urch, J. Chem. Soc., Chem. Comm. 18, 107 (1973).

10. D.J. Malcolme-Lawes, J. Chem. Soc., Chem. Comm. 18, 225 (1973).

11. R.W. Weeks and J.K. Garland, J. Phys. Chem. 73, 2508 (1969).

12. J.K. Garland, Anal. Lett. 1, 273 (1968).

13. D.C. Fee, University of California, Lawrence Berkeley Laboratory Report LBL-1687, Ph.D. Thesis, June, 1973.

14. E.S. Filatov, P.P. Kukin, and Yu. A. Ivanov, Radiochem. Radioanal. Lett. 15, 157 (1973).

15. D.C. Fee and S.S. Markowitz, J. Inorg. Nucl. Chem. 35, 2153 (1973).

16. D.C. Fee and S.S. Markowitz, Anal. Chem. 41, 1827 (1973).

17. N. Imai and O. Toyama, Bull. Chem. Soc. Japan 33, 652 (1960).

18. R.J. Cvetanovic and R.S. Irwin, J. Chem. Phys. 46, 1694 (1967).

19. P. Gray, A.A. Herod, and A. Jones, Chem. Rev. 71, 247 (1971).

20. Fundamental Processes in Radiation Chemistry, P. Ausloos, Ed., Interscience, New York (1968), p. 171.

DETERMINATION OF LEAD IN ATMOSPHERIC AIR AND IN ALUMINUM BY HELIUM-3-INDUCED NUCLEAR REACTIONS*

B. Parsa† and S. S. Markowitz

Helium-3 activation analysis has been applied to develop a very sensitive means of trace lead analysis. The procedure involves the bombardment of samples with ^3He particles to induce a Pb + ^3He + ^{207}Po reaction on lead isotopes. The 992-keV γ-ray of 5.84-hr ^{207}Po is used as the "signal" for lead determination. Only milligram amounts of sample are required. The excitation function for the production of ^{207}Po from the reaction of ^3He with lead of natural isotopic composition is presented. If necessary, destructive analysis may be carried out, and a radiochemical separation procedure to plate polonium onto a silver foil is discussed. The accuracy of the measurement is about 3 to 5% for comparative analyses. For absolute determinations, the error is estimated to be 9 - 12%. Under reasonable irradiation and counting conditions, the detection limit is approximately 50 pg/cm^2, corresponding to 0.5 ppb in a matrix 100 mg/cm^2 thick.

Footnotes

*Condensed from Analytical Chemistry 46, 186 (1974).

†Visiting Fulbright-Hayes Grantee. Permanent address: Tehran University Nuclear Center, Tehran, Iran.

HEAVY ION IRRADIATION OF SOLID GLYCINE

T. L. Tung, H. A. Sokol, W. Bennett-Corniea, G. P. Welch, and W. M. Garrison

To date, most of our detailed knowledge of the chemical actions of ionizing radiations has been derived from studies involving fast electrons produced either directly by an accelerator or secondarily through absorption of x- or γ-radiation. Recent interest in the possible biological and medical applications of heavy-ion beams has emphasized the need for more information on the effects of linear energy transfer (LET) in radiation chemistry. Relatively little systematic work has been done in this area of research -- particularly with reference to biochemical compounds in aqueous solution and in the solid state. We have initiated such a program at LBL using the 88-inch cyclotron as the radiation source. It is anticipated that this work will provide basic information that can also be applied in later studies using high-energy heavy-ion beams from the Bevalac. We report here preliminary findings of the effects of LET in the radiolysis of solid glycine. This is a well defined biochemical system and one that has been studied extensively with γ-rays.[1]

In the γ-radiolysis of solid glycine the over-all radiation induced step may be represented in the terms

$$NH_3^+CH_2COO^- \rightsquigarrow (NH_3^+CH_2COO^-)^+ + e^- \qquad (1)$$

followed by the proton stripping reaction

$$(NH_3^+CH_2COO^-)^+ \longrightarrow NH_3^+\dot{C}HCOO^- + H^+ \qquad (2)$$

With γ-rays (i.e., at low LET) the electron escapes the parent ion and subsequently is removed via

$$e^- + NH_3^+CH_2COO^- \longrightarrow NH_3 + \dot{C}H_2COO^- \qquad (3)$$

The radicals $NH_3^+\dot{C}HCOO^-$ and $\dot{C}H_2COO^-$ interact on dissolution of the solid in de-aerated water

$$NH_3^+\dot{C}HCOO^- + \dot{C}H_2COO^- \longrightarrow NH_2^+{=}CHCOO^- + CH_3COO^- \quad (4)$$

to give the imino acetic acid derivative and acetic acid. The imino acid then hydrolyzes spontaneously to give additional ammonia and glyoxylic acid

$$NH_2^+{=}CHOO^- + H_2O \longrightarrow NH_3 + CHOCOOH \quad (5)$$

Under γ-rays, charge recombination, i.e., the reverse of reaction (1)

$$e^- + (NH_3^+CH_2COO^-)^+ \longrightarrow (NH_3^+CH_2COO^-)^\ddagger \quad (6)$$

appears to be of relatively minor importance. The stoichiometry of reactions (1) - (5) gives $G(NH_3) \approx G(CH_3COOH) + G(CHOCOOH) \approx 5$ and $G(CH_3COOH) \approx G(CHOCOOH) \approx 2.5$ where G represents the number of product molecules formed per 100 eV absorbed energy. Column 1 of Table 1 summarizes the experimentally observed product yields obtained in the γ-radiolysis of solid glycine.

Table 1. Product yields (G) in the radiolysis of solid glycine with light and heavy particles.[a]

Radiation	$\gamma_{(^{60}Co)}$	H^+	He^{+2}	C^{+6}
LET(eV/A)[b]	0.1	1	4	30
Radicals[c]	5.2	4.7	3.2	1.7
Ammonia	5.0	4.4	3.8	3.7
Acetic Acid	2.3	2.3	2.1	1.3
Glyoxylic Acid	2.0	1.9	1.2	1.0
Methyl Amine	<0.2	—	0.4	0.6
Formaldehyde	<0.1	—	0.17	0.4
Formic Acid	<0.1	—	0.2	0.4

[a] Heavy particles at ~9 MeV per nucleon.

[b] Average overall value as given by energy range.

[c] Normalized to give G = 5.2 for the yield of long-lived free radicals in glycine under γ-rays as reported in Ref. 4.

We have now measured the contribution of reactions (1) - (5) in solid glycine under heavy-ion irradiation at energies corresponding to ~ 9 MeV per nucleon. The beams were wholly absorbed in the glycine which was irradiated in a circular Lucite cell having a diameter of ~ 6 cm. The glycine powder (10 g) was hydraulically compressed into the cell under an inert gas atmosphere. The cell was covered with a 1 mil Mylar film and sealed before removal from the inert atmosphere.

The heavy-ion beam as it exited the cyclotron vacuum was focused to a diameter of ~ 1 cm and then passed through an electromagnetic "beam-sweeper" so that the entire circular target area (~ 6 cm diameter) was uniformly irradiated. Dose was monitored with a secondary emission monitor located within the beam vacuum line. Calibration of the secondary emission monitor was by Faraday cup and electrometer. The beam current was approximately 10 nano amps to give an absorbed does of 1.55×10^{20} eV/gm in each case.

With the proton beam, as shown in Table 1, the yields of major products, including the long-lived radicals, are essentially the same as those obtained with γ-rays. However, as the LET of the particle increases above ~ 1 eV/A there begins a steady decrease in the yields of free radicals and of glyoxylic and acetic acids, which products are derived from the charge separation reaction sequence given Eqs. (1) - (5). At the same time, however, the ammonia yield does not decrease to the same extent. We are examining the possibility that radical dimerization, e.g.,

$$2\dot{C}H_2COOH \longrightarrow \begin{matrix} CH_2COOH \\ | \\ CH_2COOH \end{matrix} \quad (7)$$

becomes important at high LET.

Formic acid, formaldehyde, and methyl amine appear as the major products of new reaction modes which set in at high LET. It is of significance that these compounds are also formed as the major characteristic products of the photochemical decomposition of the simpler amino acids such as glycine and alanine and their peptide derivatives.[2,3] In radiolysis, the yield of excited molecular states formed via the charge-recombination step (6) would be expected to increase with increasing LET since the ion-pairs of reaction (1) would be produced closer and closer together. Although the above qualitative explanation for the observed effects of LET in the radiolysis of solid glycine appears to be self-consistent, it is clear that much more information both direct and indirect must be obtained before the role of excited-molecule reactions in the heavy-ion radiolysis of glycine is firmly established.

References

1. W.M. Garrison, Radiation Res. Rev. 3, 305 (1972).

2. M.E. Jayko, H.A. Sokol and W.M. Garrison, Lawrence Berkeley Laboratory Report LBL-1666 (1972).

3. K. Pfordte and K. Pohle, Stralentherapie 113, 140 (1960).

4. K.G. Zimmer and A. Miller, Current Topics in Radiation Research 1, 1 (1965).

SULFUR DETERMINATIONS ON SMALL BIOLOGICAL SAMPLES*

A. J. Hebert

Total sulfur contents of a series of toxic protein samples were determined with a recently described non-dispersive vacuum soft x-ray fluorescence spectrometer.[1] The spectrometer features six anodes which provide characteristic x-rays for sample excitation and determinations of the elements from oxygen to iron. The present experiments were primarily aimed at a sulfur determination and only a cursory examination was made to determine the presence of Na, Mg, Al, P, Cl, K, and Ca at the parts per million levels in several samples of protein.

An important consideration in performing vacuum soft x-ray analyses is the amount of incident radiation that may be converted to heat in the sample. This is especially true of biological samples that may contain easily decomposed or volatile components. The present spectrometer operates at anode power levels of 2 watts or less and the amount of exciting radiation reaching the sample after filtration is estimated to be less than 1 milliwatt per cm^2.

Repeated analyses with several of the present protein sample disks over periods of hours, and then again after several weeks, revealed no observable sample deterioration or decline in sulfur content.

Sample and Calibration Standard Preparation

Sample preparation requires 50 µℓ of aqueous solution or homogeneous suspension containing roughly 1 mg of sample per ml H_2O. The present group of unknowns were prepared with from 14 to 53 µg protein per sample.

A 50 µℓ portion of unknown solution or calibration standard (58.3 µg sulfur/ml) was pipetted onto the center of a 0.02 cm thick Lexan disk. (Lexan is an aromatic polycarbonate plastic.) The disks were made from sheet stock with a 2.54 cm diameter punch. Each has a 9 mm diameter circular scratch handscribed on center. When a disk was placed on a leveled hot plate surface at 60°C (circular scratch down), it took the shape of a very slightly dished flat-bottom saucer. A pipette rinse and sample fixing solution (1.20 g spectroscopic grade $LiBO_2$ plus 1.00 g acetic acid per liter) was then taken up and added to the sample droplet. The sample fixing solution also contains two drops (approximately 80 mg) of water soluble glue,[2] added to a 50 ml portion of the solution just prior to use.

The resulting dry-sample spots on the Lexan disks have an area of 0.7 cm^2 and a thickness of 2 to 5 µm. Several prepared samples and some blank disks are shown in Fig. 1. Each sample disk was placed in the spectrometer with an additional disk of Lexan as backing along with a disk of 0.5 mm pure aluminum and one of 0.2 mm copper also added as backing to provide a low noise background spectrum.

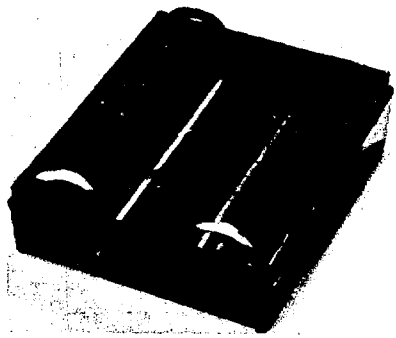

Fig. 1. Prepared samples and blank disks. (XBB 745-3564)

Results

Examples of some typical observed spectra using the silver anode (L x-rays) for excitation are shown in Fig. 2. The silicon peak (Si) was

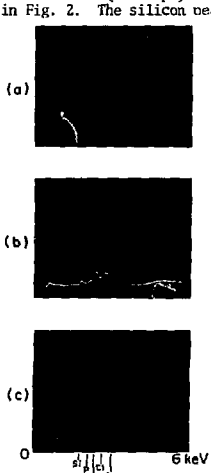

Fig. 2. Some typical four-minute spectra for (a) $LiSO_4$ standard solution (58.3 γ sulfur/ml), (b) Protein fraction 10-3, (c) H_2O rinse solution. The largest peak is due to scattered exciting radiation at E = 3 keV from silver L-X rays. The vertical scale corresponds to 10^4 x-ray pulses per channel at full scale. (XBB 757-4737)

caused by the Lexan. The observed sensitivity for sulfur was of the order to 50 ng in a typical four-minute run. Each sample was fluoresced for a total of 12 minutes or more.

Absorption corrections were applied to the observed sulfur intensities to correct for differences between the standard Li_2SO_4 solution and the various estimated sample weights and compositions. A variation in weight of protein in the sample of a factor of 3 (15 µg to 50 µg) resulted in a correction of about 3%, which in most cases is less than the estimated uncertainty in the analyses. The corrections were estimated using the coefficients tabulated by McMaster et al.[3]

Footnote and References

*Condensed from a manuscript in preparation and a paper entitled Chemical Structure of Bungarotoxins by V.A. Eterovic, L.E. Vickery, A.J. Hebert and E.L. Bennett presented at the X Reunion Nationale De La Sociedad Argentina De Investigacion Bioquimica, Nov. 1974, Buenos Aires.

1. A.J. Hebert and Kenneth Street, Jr., A Non-dispersive Soft X-Ray Fluorescence Spectrometer for Quantitative Analysis of the Major Elements in Rocks and Minerals, Anal. Chem. 46, 203 (1974).

2. Borden Inc., A Polyvinyl Acetate and Water Glue with the Residue Formula Closely Approximated by $(C_4O_2H_6)_n$. The glue is commonly referred to as "Elmer's Glue All". We are indebted to Mr. Flick of the Peabody, Mass. Office and Mr. Ziemann of the Bainbridge, NY Office for the general formula. The glue dries to a residue with roughly 1/3 of its original weight.

3. W.H. McMaster, et al., UCRL-50174 (May, 1967), distributed by the National Technical Information Service, U.S. Department of Commerce, 5285 Port Royal Road, Springfield, VA 22151.

ALAŠIYA OF THE AMARNA LETTERS

M. Artzy, F. Asaro and I. Perlman*

The exact geographical location of the ancient kingdom or city-state of Alašiya is unknown but it is in the general area of the eastern Mediterranean. There is considerable controversy about this location, with one thesis arguing that it was on Cyprus[1] (or Cyprus itself), and the other that Alašiya was located on or near the north Syrian coast.[2]

The king of Alašiya wrote a number of letters on clay tablets, including some to the Egyptian Pharoah which were found at the ancient site of Tell el-Armarna in Egypt. The purpose of the present work was to determine if the chemical composition of the clay of these "letters" might be homogeneous enough to identify the source of the clay, and hence the location of Alašiya.

The procedure for attempting to establish the provenience of clay products by means of neutron activation analysis has been described elsewhere[3] and will be reviewed here only in a cursory way. The analysis provides quantitative values for the abundances of many chemical elements, most of which may be classed as trace elements because of their very low concentrations. If one analyzes a considerable number of pottery pieces from a particular site, and finds that they are closely similar in composition, one may take as a working hypothesis that these came from local clays. The data are grouped element by element, and this results in a chemical profile or "fingerprint" for local ceramics. Finally, any other piece of clay product may be compared with this reference group to see whether or not the "fingerprints" fit each other. A discussion of complications and uncertainties which sometimes arise in the assignment of provenience is best left to the body of the report where the data on this particular problem are presented.

This report is concerned with two of the Amarna letters numbered 29788 and 29789 from the British Museum, which we sampled with the kind permission of Dr. Richard Barnett, the Keeper of the Asiatic Department.

The two tablets have chemical composition patterns which are very similar, and the agreement between them is as good, or even better than is usually found among a collection of sherds from one place (see Table 1). This indicates that the parts of the clay source from which these tablets were made were rather homogeneous, and other ceramics made from the same clay in the same way should have about the same composition.

Chemical abundance profiles for clays from a number of areas in Cyprus were available from pottery investigations. Some of these reference groups from ancient Enkomi in eastern Cyprus are shown in Table 1 along with the two Amarna letters. From Fig. 1, which shows some of the data as bar graphs, it can be seen that the two Amarna sherds are very much alike and different from the Enkomi material. Figure 2 shows the same type of information for three other sites on Cyprus and Fig. 3 shows comparisons with Egyptian reference groups. Thus none of our existing chemical profiles from Cyprus, or a meager sampling from Syria (not shown), or Egypt match that of the Amarna tablets.

The excellent agreement in chemical composition patterns of the two Amarna letters, however, indicates that further work developing additional chemical profiles of clay artifacts (or soils) in the eastern Mediterranean may be very fruitful.

Footnotes and References

*Now at the Institute of Archaeology, The Hebrew

Table 1. Chemical composition patterns of tablets and sherds.[a] The numbers for the respective elements are group mean values (M) and the standard deviations (± σ). All are in units of parts-per-million unless designated %.

	ELAM 13	ELAM 14	ENK α (30 pcs.) M ± σ	ENK β (18 pcs.) M ± σ	ENK γ (14 pcs.) M ± σ
Al%	5.18	5.20	6.40 ± 0.50[b]	6.58 ± 0.38[a]	6.43 ± 0.48
Ca%	12.3	10.4	9.1 ± 1.5	8.6 ± 1.6	11.3 ± 1.3
Mn	559	592	1065 ± 85	1067 ± 124	1034 ± 105
Na%	0.507	0.586	1.40 ± 0.19	1.20 ± 0.14	1.12 ± 0.20
U	1.66	1.74	*d*	*d*	2.07 ± 0.27
La	27.0	27.5	16.7 ± 1.3	20.5 ± 1.5	20.1 ± 1.5
Ti%	0.328	0.346	0.441 ± 0.043	0.465 ± 0.030	0.441 ± 0.025
Lu	0.278	0.292	0.313 ± 0.021	0.321 ± 0.016	0.310 ± 0.026
Co	14.16	16.03	29.50 ± 2.70	31.50 ± 2.60	30.10 ± 2.60
Sc	11.45	11.76	24.20 ± 1.30	23.13 ± 1.53	22.73 ± 2.33
Fe%	3.01	3.21	5.67 ± 0.35	5.69 ± 0.27	5.40 ± 0.45
Cs	4.52	4.37	3.72 ± 0.36	4.64 ± 0.60	4.07 ± 0.66
Cr	93	100	301 ± 50	334 ± 42	398 ± 64
Th	7.36	7.73	5.50 ± 0.37	6.76 ± 0.25	6.63 ± 0.49
Hf	2.91	3.25	2.73 ± 0.20	3.18 ± 0.22	3.12 ± 0.23
Ta	0.790	0.830	0.548 ± 0.043	0.677 ± 0.036	0.658 ± 0.079
Ni	73	116	201 ± 27	261 ± 41	208 ± 21
Rb	90	83	62 ± 16	76 ± 14	67 ± 24

[a]ELAM 13 is El-Amarna tablet #29789.
ELAM 14 is El-Amarna tablet #29788.
ENK α is a group of mixed local LB sherds from Enkomi.
ENK β is a group of mixed local LB sherds from Enkomi.
ENK γ is a group of Proto White Painted sherds from Enkomi.

[b]Of the 30 pieces, aluminum was measured in only 7 samples.

[a]Of the 18 pieces, aluminum was measured in only 4 samples.

[d]These sherds had been contaminated with silver, gold, and uranium.

University, Jerusalem.

1. F. Schachermeyr, Zum ältesten Namen von Kyprus, Klio 17, 230 (1920); C.F.A. Schaeffer, Enkomi-Alasia: Nouvelles missions en Chypre 1946-1950 (Paris: Librairie C. Klincksieck, 1952); H.G. Götterbock, The Hittite Conquest of Cyprus Reconsidered, J. Near Eastern Studies 26, 73 (1967); Y.L. Holmes, The Location of Alašiya, J. Ame. Oriental Soc. 91 (3), 426 (1971).

2. G.A. Wainwright, "Alashia-Alaša and Asy," Klio 14, 6 (1914-1915); H.W. Catling, Cyprus in the Neolithic and Bronze Age Periods, Cambridge Ancient History, 43 (Cambridge: Cambridge University Press, 1966), p. 61; G. Bass, Cape Gelidonya: A Bronze Age Shipwreck (Philadelphia: The American Philosophical Society, 1967), p. 78; R.S. Merrillees, Alasia, Proc. First Int. Congress on Cypriote Studies, Nicosia (1972), p. 111.

3. I. Perlman and F. Asaro, Pottery Analysis by Neutron Activation, Archaeometry 11, 21 (1969).

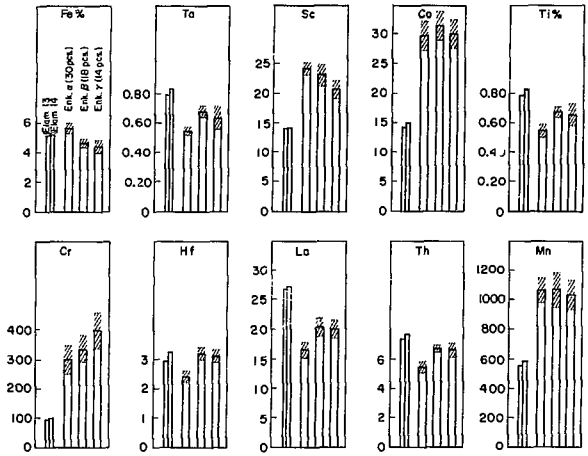

Fig. 1. Chemical abundance patterns of Amarna tablets and Enkomi pottery. The bars represent elemental abundance values for the individual Amarna sherds or mean values for pottery groups. The hatched zones reflect for each element the standard deviation in the abundances for all of the sherds in that group.

Elam. 13: Tell el-Amarna tablet #29789.
Elam. 14: Tell el-Amarna tablet #29788.
Enk. α: A group of 30 pieces of White Painted Ware, Plain White Ware, Mycenaean Ware excavated at Enkomi.
Enk. β: A group of 18 pieces of White Painted, Plain White Wares excavated at Enkomi.
Enk. γ: A group of 14 pieces of Proto White Ware excavated at Enkomi.

(XBL 742-2423)

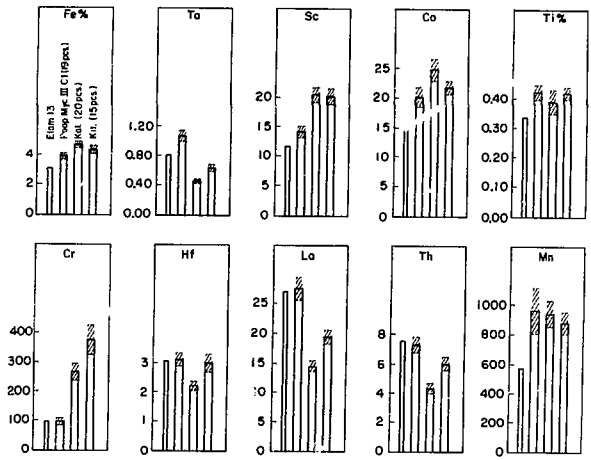

Fig. 2. Chemical abundance patterns of Elam. 13 and Cypriot pottery groups from Palaepaphos, Kalopsidha, and Kition. The bars and hatched zones have the same meaning as in Fig. 1.

Elam. 13: See Fig. 1.

Ppap Myc. IIIC1: A group of 19 pieces of Mycenaean IIIC1 excavated at Kouklia.

Kal.: A group of 20 pieces of Plain Ware excavated at Kalopsidha.

Kit.: A group of 15 pieces of Plain Ware excavated at Kition.

(XBL 742-2424)

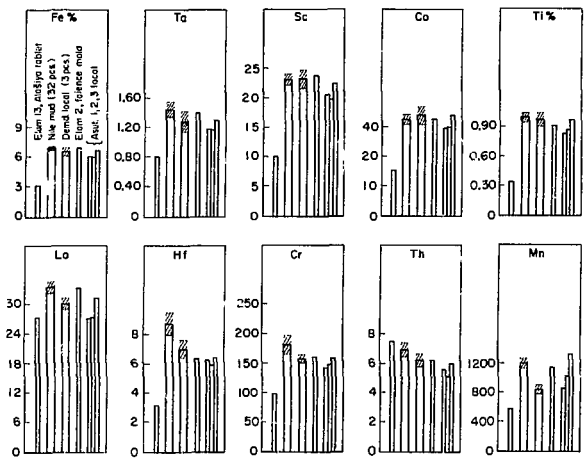

Fig. 3. Chemical abundance patterns of Elam. 13 and Egyptian pottery groups. The bars and hatched zones have the same meaning as in Fig. 1.

Elam. 13: See Fig. 1.
Nile Mud: A group of 32 pieces of Egyptian Wares excavated in Upper Egypt (El Ahaiwah, Nag-ed-Deir, Ballas).
Demd. local: A group of 3 pieces excavated at Deir el-Medineh.
Elam. 2: A faience mold from Tell el-Amarna.
Asut. 1,2,3: 3 pieces of Egyptian Wares excavated at Assuit. (XBL 742-2422)

CHRONOLOGY OF THE O. B. JAMES PLUTON

R. Drake,* H. R. Bowman, and A. J. Hebert

Odette B. James concluded that the ultramafic rock suite in the Emigrant Gap area of northern California was the result of fractional crystallization of a single magma. This complex may represent a classic example of a differentiation sequence of rock types resulting from fractional crystallization.

In the present work, the ages since the last melting of four fractions in the suite were determined by potassium-argon dating. The ages since the last differentiation had been measured by D. Noble[1] previously for three samples, using isotopic dating. The three whole-rock Rb/Sr analyses of the OBJ pluton agree closely with a 290-million year isochron and have an $^{87}Sr/^{86}Sr$ initial ratio of 0.7044. This age is nearly 100 million years older than the oldest recognized plutons in the Sierra and for this reason K-Ar age determinations were made on minerals separated from these whole-rock specimens. The results of the first four analyses are listed in Table 1.

Table 1. K-Ar age determinations.

Sample	Mineral	Age × 10^6 years
OBJ-21	plag.	179.2 ± 1
OBJ-22	plag.	152.1 ± 2.8
OBJ-23	biotite	152.5 ± 6.3
OBJ-24	biotite	160.7 ± 0.4

Although these dates vary by almost 30 million years, the ages are compatible with the general regional chronology. Other minerals from each of the whole-rock samples are being run to determine whether argon has been lost or inherited and to explain the different K-Ar ages.

We believe the whole-rock Rb/Sr isochron represents the age of differentiation and initial crystallization of the body, while the K-Ar ages represent the remobilization and recrystallization of minerals during final emplacement 152 - 180 million years ago. Thus we would predict that mineral groups from any single whole-rock sample would yield Rb/Sr isochrons of 150 - 180 million years. This interpretation implies that the Rb/Sr distribution in the body as a whole remained fixed after differentiation and layering, while during emplacement the mineral phases were re-equilibrated with respect to their immediate whole-rock environment. To achieve this, the body must have remained essentially solid and reacted metamorphic equilibrium during emplacement.

Footnote and Reference

*Department of Geology, U.C., Berkeley.

1. D. Noble, private communication.

TWENTY-FOUR MAJOR ELEMENT XRF ANALYSES OF LATE CENOZOIC VOLCANIC ROCKS FROM THE CHILEAN ANDES, 35 - 36°S LATITUDE

R. Drake* and A. J. Hebert

Twenty-four major element analyses of late Cenozoic volcanic rocks from the Chilean Andes at 35 to 36°S latitude are reported here. Analyses were made using x-ray fluorescence techniques.[1] Results of the analyses are shown in Table 1.

A plot of wt% K_2O vs wt% SiO_2 (Fig. 1) shows a narrow range of K_2O values for given SiO_2 content, which might be expected of samples representing a small volcanic province and time interval. The basic end-members of this suite are characteristically basaltic-andesites with about 55% SiO_2 and 1.5% K_2O. Few rocks from this region have less than 52% SiO_2 and all have greater than 1% K_2O. This volcanic suite is significantly higher in K_2O than corresponding island arc

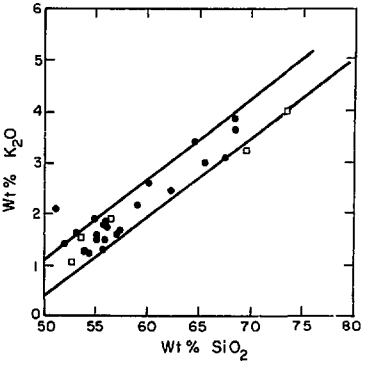

Fig. 1. Plot of wt% K_2O vs SiO_2 of samples of late Cenozoic volcanics from the Chilean Andes between 35 and 36°S latitude. Dots are for 24 XRF analyses. Squares are for chemical analyses from same region by other workers. (XBL 757-3546)

CHRONOLOGY OF THE O. B. JAMES PLUTON

R. Drake,* H. R. Bowman, and A. J. Hebert

Odette B. James concluded that the ultramafic rock suite in the Emigrant Gap area of northern California was the result of fractional crystallization of a single magma. This complex may represent a classic example of a differentiation sequence of rock types resulting from fractional crystallization.

In the present work, the ages since the last melting of four fractions in the suite were determined by potassium-argon dating. The ages since the last differentiation had been measured by D. Noble[1] previously for three samples, using isotopic dating. The three whole-rock Rb/Sr analyses of the OBJ pluton agree closely with a 290-million year isochron and have an $^{87}Sr/^{86}Sr$ initial ratio of 0.7044. This age is nearly 100 million years older than the oldest recognized plutons in the Sierra and for this reason K-Ar age determinations were made on minerals separated from these whole-rock specimens. The results of the first four analyses are listed in Table 1.

Table 1. K-Ar age determinations.

Sample	Mineral	Age × 10^6 years
OBJ-21	plag.	179.2 ± 1
OBJ-22	plag.	152.1 ± 2.8
OBJ-23	biotite	152.5 ± 6.3
OBJ-24	biotite	160.7 ± 0.4

Although these dates vary by almost 30 million years, the ages are compatible with the general regional chronology. Other minerals from each of the whole-rock samples are being run to determine whether argon has been lost or inherited and to explain the different K-Ar ages.

We believe the whole-rock Rb/Sr isochron represents the age of differentiation and initial crystallization of the body, while the K-Ar ages represent the remobilization and recrystallization of minerals during final emplacement 152 - 180 million years ago. Thus we would predict that mineral groups from any single whole-rock sample would yield Rb/Sr isochrons of 150 - 180 million years. This interpretation implies that the Rb/Sr distribution in the body as a whole remained fixed after differentiation and layering, while during emplacement the mineral phases were re-equilibrated with respect to their immediate whole-rock environment. To achieve this, the body must have remained essentially solid and reacted metamorphic equilibrium during emplacement.

Footnote and Reference

*Department of Geology, U.C., Berkeley.

1. D. Noble, private communication.

TWENTY-FOUR MAJOR ELEMENT XRF ANALYSES OF LATE CENOZOIC VOLCANIC ROCKS FROM THE CHILEAN ANDES, 35 - 36°S LATITUDE

R. Drake* and A. J. Hebert

Twenty-four major element analyses of late Cenozoic volcanic rocks from the Chilean Andes at 35 to 36°S latitude are reported here. Analyses were made using x-ray fluorescence techniques.[1] Results of the analyses are shown in Table 1.

A plot of wt% K_2O vs wt% SiO_2 (Fig. 1) shows a narrow range of K_2O values for given SiO_2 content, which might be expected of samples representing a small volcanic province and time interval. The basic end-members of this suite are characteristically basaltic-andesites with about 55% SiO_2 and 1.5% K_2O. Few rocks from this region have less than 52% SiO_2 and all have greater than 1% K_2O. This volcanic suite is significantly higher in K_2O than corresponding island arc

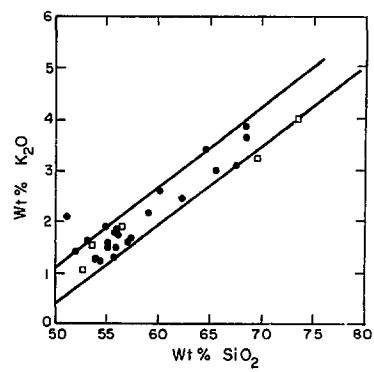

Fig. 1. Plot of wt% K_2O vs SiO_2 of samples of late Cenozoic volcanics from the Chilean Andes between 35 and 36°S latitude. Dots are for 24 XRF analyses. Squares are for chemical analyses from same region by other workers. (XBL 757-3546)

SOFT X-RAY ANALYSIS OF THE GRIZZLY PEAK VOLCANICS, BERKELEY HILLS, CALIFORNIA

R. N. Lambe,* D. G. Kosco,* A. J. Hebert, and G. H. Curtis*

Major oxide analyses of twelve flows of the Grizzly Peak Volcanics were made by nondispersive, soft x-ray, fluorescence analysis. Samples of approximately one-kilogram weight were ground to a particle size of less than 0.1 mm. The sample powder was mixed with spectroscopic grade $LiBO_2$, in a 1:10 ratio, fused, cast into a metal ringed pill, and annealed at 250°C for several minutes. Analyses were carried out on a nondispersive soft x-ray spectrometer.[1] The results are presented in Table 1, arranged in a tentative chronologic sequence of eruption, and represent the first modern analyses of the Grizzly Peak Volcanics. Previous analyses were made by C. Paluche (1896), using wet chemical techniques.

Samples GPV-1 through GPV-7 were collected from fresh exposures along California Route 24, and represent the complete sequence of andesitic flows in the Grizzly Peak Formation. GPV-11 represents a rhyolite averaging 20 feet in thickness, which separates the lower and upper units of the Grizzly Peak Formation. In almost all locations the rhyolite is pervasively altered to chlorite and clay minerals. GPV-11 was determined to be the least altered of all the rhyolite samples inspected. GPV-8 was sampled from a volcanic body in the Siesta Valley south of Route 24. The body measured approximately 305 by 390 meters and seems to cut the local structure suggesting that it may be some type of volcanic vent. GPV-9 was sampled from the Bald Peak Formation off Grizzly Peak Boulevard, a complex of flows younger than the Grizzly Peak Volcanics. GPV-10 was sampled from the uppermost flow in the Grizzly Peak volcanics off Grizzly Peak Boulevard and should be stratigraphically correlative to GPV-7. Sample GHC-374 represents one of the basaltic components of the Round Top Complex, for which there is good evidence indicating it is one of the volcanic vents supplying the Grizzly Peak Volcanics.

Plotting of the analyses on (FeO + Fe_2O_3) - MgO - (Na_2O + K_2O) and K_2O - CaO - Na_2O triangular diagrams suggests that the flows of the Grizzly Peak Volcanics form two genetic groups. The lower flows (GPV-1,3,4) demonstrate a progressive enrichment in CaO and MgO with decreasing age, reflecting the progressive accumulation of calcium-magnesian pyroxenes with depth in the magma chamber, and a calcium enrichment in the plagioclase reflecting the compositional change from An_{30-50} to An_{50-70}. The lowest flow, GPV-1, has been dated at 9.93 M.Y. and the fourth flow, GPV-4, at 8.85 M.Y. The chemical variation and geochronology seem to strongly suggest that the lower flows are genetically related.

The flows of the upper Grizzly Peak Volcanics along California Route 24 have been dated between 9.65 million years to 8.35 million years (M.Y.). The chemical variation seems to be oscillatory but reflects a general trend of enrichment in CaO, MgO and (FeO + Fe_2O_3). The general trend toward enrichment in (FeO + Fe_2O_3) is most obvious. GPV-9, sampled from the Bald Peak Flow (7.7 M.Y.) seems to fall on this trend. GPV-10 which should be stratigraphically correlative to GPV-7 appears to be chemically unrelated. Most noticeable are significant increases in K_2O, Na_2O, SiO_2, Al_2O_3, and decreases in MgO and CaO. It is seen in Figs. 1 and 2, that GPV-10 does not appear to be chemically compatible with the general trend displayed by the upper flows. The preliminary evidence suggests that the upper flows possess a more complex history than the lower flows.

The rhyolite, GPV-11, would plot off the differentiation trends of the lower and upper flows and does not appear to be petrologically or chemically related to the andesitic flows. It appears from mapping the rhyolite in the field that its source is to the west of the Grizzly Peak fault and presently several miles to the north of Round

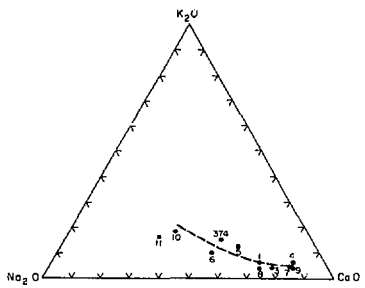

Fig. 1. Chemical variation in the Grizzly Peak Volcanic Series. (XBL 757-3544)

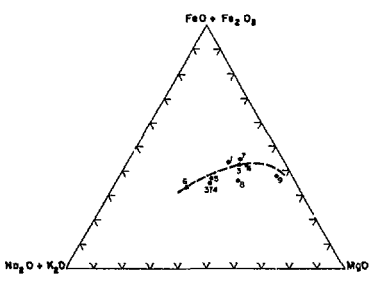

Fig. 2. Chemical variation in the Grizzly Peak Volcanic Series. (XBL 757-3548)

Table 1.

Oxides	Sample Number										
	GPV-1	GPV-3	GPV-4	GPV-11	GPV-5	GPV-6	GPV-7	GPV-10	GPV-8	GPV-9	GHC-374
SiO_2	50.509	50.974	48.278	69.063	57.420	57.770	50.717	58.259	51.999	50.281	60.376
TiO_2	1.130	1.339	1.116	0.414	0.856	0.820	1.126	0.890	0.813	1.004	0.636
Al_2O_3	16.229	17.810	18.264	13.126	17.060	17.004	17.914	15.155	18.303	16.106	15.456
FeO	7.659	7.820	6.862	2.017	5.794	5.742	7.024	7.456	6.863	7.607	5.026
MnO	0.139	0.142	0.129	0.042	0.124	0.136	0.151	0.130	0.136	0.155	0.096
MgO	6.243	7.366	6.742	1.459	5.251	4.584	6.325	1.475	8.280	11.497	4.834
CaO	9.462	10.172	11.089	3.142	7.237	7.850	11.498	3.723	10.668	8.736	5.224
Na_2O	(3.1799) 2.963	2.522	1.444	5.109	3.196	5.485	1.798	(5.1807) 4.704	3.560	(4.3850) 1.243	3.052
K_2O	(.6435) 0.856	0.528	0.427	1.542	1.464	1.457	0.608	(2.0713) 1.874	0.510	(0.6372) 0.448	1.421
Cr_2O_3	0.050	0.054	0.038	0.004	0.046	0.031	0.060	0.019	0.043	0.111	0.037
TOTAL	95.25	98.73	94.78	95.92	98.46	100.92	97.22	93.64	101.18	97.19	96.21

Values in parentheses are values determined by G.H. Curtis for K-Ar geochronology.

Top, the suggested source of the lower Grizzly Peak Volcanics.

The conclusions presented here are based on preliminary results and are subject to refinement. Further chemical analyses will be made in an attempt to obtain a better definition of the genetic relationships of the upper flows and to determine more accurately the differentiation trends presented here.

Footnote and References

*Department of Geology, University of California, Berkeley, CA.

1. A.J. Hebert and K. Street, Jr., A Nondispersive Soft X-Ray Fluorescence Spectrometer for Quantitative Analyses of the Major Elements in Rocks and Minerals, Anal. Chem. 46, 203 (1974).

EVIDENCE IN SUPPORT OF SIMILAR SOURCE MATERIAL IN THE GENESIS OF ALKALIC BASALTS

H. R. Bowman, F. Asaro, I. S. E. Carmichael,*
R. K. Mark,† and H.-U. Schmincke‡

Basalts exhibit a wide range of composition, from those that are tholeiitic (alkali poor) to those that have substantial amounts of alkali elements (called alkalic basalts). Precise abundance measurements for a large number of trace, minor, and major elements have been made on basalts from different geological environments: Quaternary basalts from behind the active Aleutian volcanic arc (Nunivak & Pribilof Islands, Alaska); Recent basalts from northern Baja California (erupted through continential crust, but also associated with subduction); and in contrast, the basalts of the Azores, east of the spreading mid-Atlantic ridge.

Earlier work by others had indicated a rough coherence in the Nunivak Island rocks between the overall alkali content and Rb, Ba, and Sr. In the present work with neutron activation analysis, the trace-element abundances were found to have a remarkable coherence when measured at high precision.

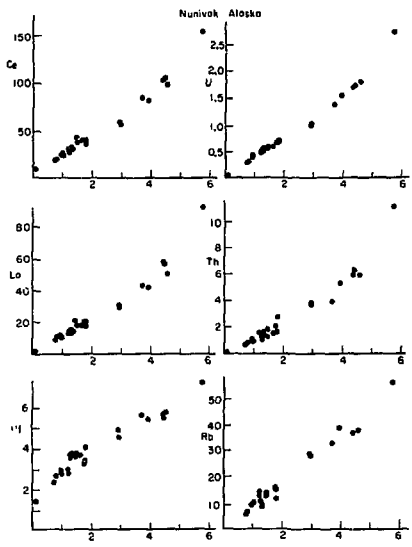

Fig. 1. The abundances of Ce, U, La, Th, Hf, and Rb plotted against Ta in basalts from Nunivak Island in the Bering Sea. The lowest Ta abundances on the first five graphs are for a megacryst from one of the other lavas. The Rb abundances are by R. Mar...[3] (XBL 753-2469)

In the most rigorous of the coherences of the trace-element abundances, two elements, U and Ta (Fig. 1), were nearly proportional to each other in the less alkalic Nunivak basalts, with some deviation in the more alkalic members. The general coherence between abundances extended over many of the trace elements for all the samples examined. The Rb abundances in Figs. 1 and 2 are from previous measurements by other workers and are plotted against neutron activation analysis Ta values.

Three of the four different locations studied in this work are widely separated. The trace-element abundance patterns, particularly when related to the tantalum abundance, are similar and agree much better with each other than with any tholeiitic-type basalts from the continents and island arcs that we have studied.

This study reinforces the concept that alkalic basalts from various geological environments exhibiting a range of chemical compositions all

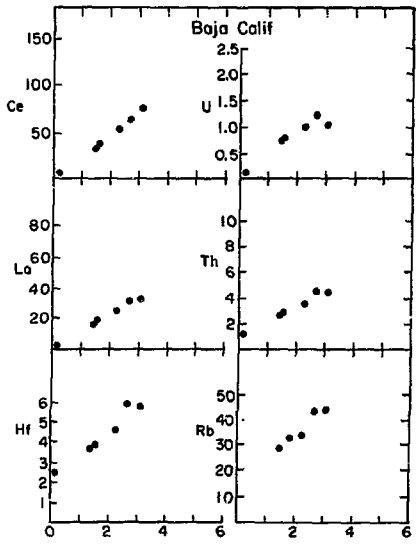

Fig. 2. The abundances of Ce, U, La, Th, Hf, and Rb plotted against Ta in basalts from San Quintin, Baja California. The lowest Ta point on the first five graphs is for a megacryst from one of the lavas. The Rb abundances were measured by Bacon and Carmichael.[2] (XBL 753-2494)

behave in a predictable and systematic way as regards their minor and trace elements. This suggests that in the regions in which these lavas were generated, they were formed by fusion of similar mantle material at similar pressures and temperatures.

The Nunivak lavas were erupted over a 6-million year period, and there is a high degree of correlation between tantalum and the ages of these lavas.

In Fig. 2 the Baja California trace-element results are plotted using the same elements as Fig. 1. Similar plots have been made in Fig. 3 for historic Azorean lavas[1] from five islands just east of the mid-Atlantic ridge. The Azorean each case the vertical and horizontal scales are the same so that absolute abundances can be compared.

Many alkalic basalts contain isolated crystals, or assemblages of crystals, that have grown during the ascent of the lava to the surface. Often these are large, and are called megacrysts. In addition, the lava may have incorporated foreign rock (often mantle) fragments plucked from the wall of its conduit, and these may have become disaggregated, to form xenocrysts, as they react with the hot lava. In Figs. 1 and 2 the rocks with the very low Ta abundances are pyroxene megacrysts. No megacrysts have been analyzed from the Azores.

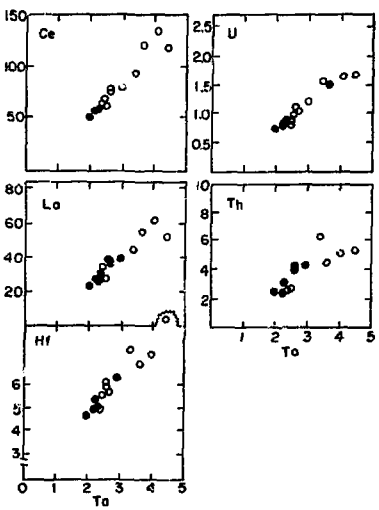

Fig. 3. The abundances of Ce, U, La, Th, and Hf plotted against Ta in basalts from 5 Azorean islands just east of the mid Atlantic ridge. No megacrysts have been analyzed from this area.
(XBL (XBL 757-3543)

Comparison of the trace-elements composition of the megacrysts and the related lavas leads to the partition coefficients for each of these elements, under the conditions of formation of the crystals at high temperature and pressure. Using experimental data on the temperature dependence of the partition coefficients, we can obtain the pressure dependence of the partition coefficients if the pressure-temperature conditions of the precipitation of the megacrysts is known. Estimates of these can be calculated from thermodynamic arguments using the major element composition of the megacrysts.[2]

Figure 4 shows the partitioning coefficients (megacryst abundances/lava abundances) for 23 elements of Baja California plotted against selected ionic radii. This curve is essentially a compatibility curve where ions the size of Mn^{2+} are accepted readily into the pyroxene lattice sites, and the smaller and larger ions are less compatible and tend to collect in the residual magmas. Ta, La, U, and Ce are quite incompatible (Fig. 4) in this sense, and the near proportionality of their abundances when plotted vs. each other is consistent with the crystalization process or subsequent partial melting. The coherence between trace elements and major elements found in lavas

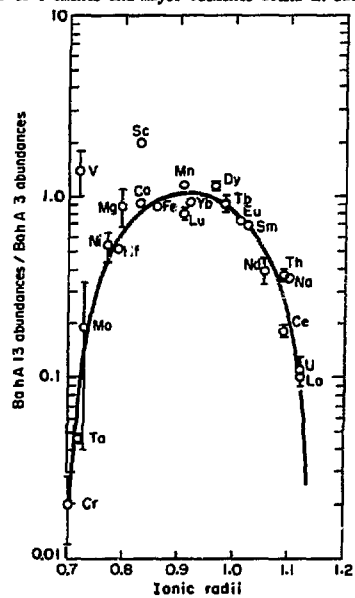

Fig. 4. The partitioning coefficients (elemental abundances in the megacryst ÷ those of the associated lava) for a Baja California lava plotted against selected ionic radii.
(XBL (XBL 757-3545)

places major constraints on the composition of the source material, for the stability of various minerals at depth is fundamentally controlled by the concentration of the major elements. By identifying coherences such as K, Th, Ta, etc., it is plausible to suggest that whatever mineral at depths held K (e.g., phlogopite[1]) also contained the coherent trace metals. Only in this way can the chemical composition of the mantle, on a fine scale, be obtained.

Footnotes and References

*University of California, Berkeley, Department of Geology and Geophysics.

†U.C.L.A., Department of Planetary & Space Sciences.

‡Ruhr-Universität, Institut für Mineralogie.

1. M.F.J. Flowers, H.-U. Schminke and H.R. Bowman, Rare Earth and Trace Elements in Historic Azorean Lavas, submitted to Earth Planet. Sci. Lett. (1975).

2. C.R. Bacon and I.S.E. Carmichael, Stages in the P-T Path of Ascending Basalt Magma: An Example from San Quintin, Baja California, Contrib. Mineral. Petrology (Balin) 41, 1 (1973).

3. R. Mark, private communication (1974).

4. J.M. Hoare, W.H. Condon, A. Cox, and G.B. Dalrymple, Geology, Paleomagnetism and Potassium-Argon Ages of Basalts from Nunivak Island, Alaska, Geol. Soc. Am. Mem. 116, 377 (1968).

OCEAN RIDGE-LIKE THOLEIITES IN THE NORTHERN GREAT BASIN OF NEVADA

H. R. Bowman, F. Asaro, R. K. Mark,* C. Lee Hu,*
E. H. McKee,† and R. R. Coats†

The trace element abundances of five rocks from the northern Great Basin of Nevada were measured by neutron activation analysis. The rocks were dated by the Rb-Sr and K-Ar methods.

These rocks were selected because previous petrographic studies and major element analyses had indicated they were rather primitive material (Olivine-tholeiites) and similar to basalts from the Snake River Plain in Idaho. In addition, they were all much younger (~ 8 - 10 million years old) than the usual Basin and Range formation in Nevada (~ 30 million years old). In the present work the quantitative abundance measurements on trace elements were made at LBL in Berkeley, Rb-Sr isotopic dates were determined at U.C.L.A. in Los Angeles, and the K-Ar dates were determined at the Isotope Geology Laboratory of the U.S. Geological Survey in Menlo Park, CA.

Neutron activation analyses were performed on samples made from 100 mg of powdered rock mixed with 50 mg of cellulose pressed into pellets. The samples were irradiated along with a composite standard in the Berkeley Triga Reactor once for ten minutes and later for eight hours. A detailed description of the method along with a description of the standard material has been given by Perlman and Asaro.[1] In this procedure 50 elements are searched for and 40 are usually found in rocks. The abundances of about 30 of these are measured with good precision. The abundances of the trace elements that we measured are shown in Table 1. Major element abundances (not shown) agreed well with previous work.

Samples were spiked with ^{84}Sr, ^{87}Rb, and ^{41}K for isotopic dilution measurements of concentration. The isotopic analyses were performed at UCLA on a single-filiment, 9-in., 60° mass spectrometer with a digital data acquisition system.

The rocks were dated by the K-Ar method (Menlo Park) by standard procedures.[2]

On the basis of rare earth element (REE) contents the basalt samples fall into two groups (Fig. 1). In one group (samples labeled E-15, 6238-2J, 54NC93 are referred to as "low REE"), the chondrite normalized REE pattern shows only minor light REE enrichment and about ten times chondritic concentrations. Such a pattern overlaps those reported for ocean ridge basalts,[3] (ORB) although lacking the commonly occurring light REE depletion. The pattern is almost identical to those reported for island arc tholeiites.[4] The other group (61NC18, 62NC133; referred to as "high REE") show a marked light REE enrichment typical of continental plateau tholeiites (e.g., Schilling[3]). The other LIL elements generally correlate with the REE, but Ba is an exception. Barium concentrations are variable, with no correlation to other LIL elements. The Ba concentrations are much greater than those commonly reported for ORB and some are even high for island arc tholeiites (e.g., Jakes and Gill,[4] and Philpotts et al.[5]).

The $^{87}Sr/^{86}Sr$ range for the Nevada tholeiites in this work is almost identical to the range reported by Leeman and Manton[6] for the tholeiites from the adjacent Snake River Plain to the north.

The samples in the present work are chemically distinct from (i.e., less alkalic) but Sr-isotopically similar to olivine tholeiites from the

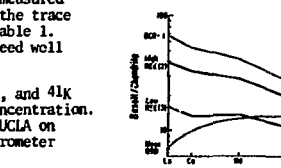

Fig. 1 Chondrite normalized rare earth element patterns plotted against atomic number.
(XBL 756-1582)

Table 1. Concentrations of Ba, REE, and other trace elements by instrumental neutron activation analysis. Standard Rock (BCR-1) is included for comparison.

	E15	6238-2J	54NC93	61NC18	62NC133	Typical σ	BCR-1
Ba	781.0	152.0	105.0	427.0	373.0	14.0	690 ± 33
La	6.4	6.6	5.2	13.5	16.4	0.4	25.3 ± 0.5
Ce	12.8	14.8	12.2	30.1	33.9	0.7	55.5 ± 1.6
Nd	10.1	8.2	10.3	20.2	19.8	1.5	30.5 ± 2.2
Sm	2.43	2.72	2.37	4.50	4.61	0.02	6.37 ± 0.13
Eu	1.06	1.12	0.98	1.61	1.64	0.02	2.00 ± 0.05
Tb	0.48	0.52	0.50	0.91	0.73	0.03	0.99 ± 0.13
Dy	3.82	4.27	4.09	5.86	5.14	0.20	6.33 ± 0.33
Yb	2.36	2.81	2.77	3.15	2.68	0.05	3.64 ± 0.08
Lu	0.358	0.424	0.368	0.481	0.364	0.019	0.538 ± 0.026
Hf	1.64	1.83	1.90	3.32	2.77	0.11	5.19 ± 0.38
Cr	342.0	306.0	427.0	369.0	559.0	8.0	15 ± 5
Mn	1350.0	1370.0	1420.0	1480.0	1435.0	30.0	1399 ± 35
Co	50.0	44.4	53.2	50.0	48.4	0.7	38.02 ± 0.46
Ni	150.0	120.0	200.0	105.0	120.0	25.0	15 ± 10
Sc	40.5	45.2	47.2	39.4	38.5	0.2	34.53 ± 0.58
U	0.152	0.302	0.122	0.330	0.384	0.023	1.65 ± 0.06
Th	0.47	0.56	0.51	1.06	1.08	0.13	6.07 ± 0.20
V	320.0	340.0	365.0	350.0	320.0	50.0	480 ± 60
Ta	0.257	0.284	0.204	0.585	0.508	0.004	0.717 ± 0.020
Zn	100.0	95.0	95.0	135.0	130.0	9.0	150 ± 21

The typical σ involves only the precision of the measurements. The errors on the BCR-1 Standard Rock include the calibration errors introduced by our standard as well as the statistical error introduced by counting radioactivities. All elements were calibrated against the same elements in Standard Pottery, except Zn which was calibrated against a Sc flux monitor.

adjacent Snake River Plain, and contain distinctly more-radiogenic Sr than the basalts from the adjacent Great Basin. The mean measured Rb/Sr (~0.02) of these samples would require about 10 billion years in a closed system to generate the radiogenic Sr they contain. The geochemistry of these basalts makes crustal contamination seem unlikely. If the magma is uncontaminated, the time-averaged Rb/Sr of the source material must have been ≥ 0.04. Thus, a significant decrease in Rb/Sr of the source material (≤ a factor of 2) most probably occurred in the relatively recent (≤ 10^9 y) past. Such a decrease of Rb/Sr in the mantle could accompany LIL element depletion produced by an episode of partial melting and magma extraction. By contrast, the source material of the ocean ridge basalts appears to have been depleted early in the earth's history.

Footnotes and References

*Department of Planetary and Space Science, UCLA, Los Angeles, CA.

†U.S. Geological Survey, Menlo Park, CA.

1. I. Perlman and F. Asaro, Pottery analysis by neutron activation, Archaeometry 11, 21 (1969).

2. G.B. Dalrymple and M.A. Lanphere, Potassium-Argon Dating: Principles, Techniques, and Applications to Geochronology (W.H. Freeman and Co., San Francisco, 1969).

3. J.G. Schilling, Sea-floor evolution: Rare-earth evidence, Phil. Trans. Roy. Soc. London, A, 265, 663 (1971).

4. P. Jakes and J. Gill, Rare earth elements and the island arc tholeiitic series, Earth Planet. Sci. Lett. 9, 17 (1970).

5. J.A. Philpotts, M. Martin and C.C. Schnetzler, Geochemical aspects of some Japanese lavas, Earth Planet. Sci. Lett. 12, 89 (1971).

6. W.P. Leeman and W.I. Manton, Strontium isotopic composition of basaltic lavas from the Snake River Plain, southern Idaho, Earth Planet. Sci. Lett. 11, 420 (1971).

RARE EARTH AND TRACE ELEMENT PATTERNS IN HISTORIC AZOREAN LAVAS

H. R. Bowman, M. F. J. Flowers,* and H.-U. Schmincke*

Analysis of rare earth element (REE) concentrations in volcanic rocks has become an important means of defining chemical differences that are produced by differentiation processes other than crystal fractionation at shallow depths. Within the north Atlantic region, as in other ocean basins, notable chemical differences exist between abyssal or ocean floor tholeiites. In a recently published petrogenetic model, Schilling[1], using REE concentrations, has further distinguished so-called 'primary mantle' plume material as a source for oceanic island magmas, and a low velocity layer deleted in large cations as a source for abyssal tholeiitic magmas. He has postulated that magmas of intermediate composition form by mixing, either of the magmas themselves or of the solid differentiated upper mantle fractions.

The Azores platform is one of the largest single topographic features of the Atlantic Ocean floor and is currently receiving considerable attention from geophysicists and geochemists. Within this region, the American, Eurasian and African plates come together at the Azores triple junction, formed by the intersection of the Azores-Gibraltar fracture zone (locally known as the East Azores fracture zone or EAFZ), and the mid-Atlantic rift (MAR). The Azores archipelago lies just to the north of the EAFZ, straddling the MAR from WNW (31°W, 40°N) to ESE (25°W, 37°N), with the islands Flores and Corvo to the west and Fayal, São Jorge, Pico, Graciosa, Terceira, São Miguel and Santa Maria to the east. Of the latter group, Graciosa, Terceira and the western part of São Miguel are believed to be associated with a WNW-ESE-trending trench known as the Terceira Rift.[2] The sub-parallel location of Fayal, Pico and São Jorge, and the strong evidence of tensional faulting, on Fayal and São Jorge especially, further suggest that the Terceira Rift is part of a larger zone of dilation which includes all of the central and eastern Azores.

In view of the interest in this region as a possible surface manifestation of a thermal plume in the upper mantle[3] we have initiated a geochemical study of the historic eruptions in the Azores archipelago. This is part of a larger study of historic lavas from islands in the eastern central Atlantic. Historic volcanism is particularly amenable to the detailed investigation of the geochemistry of low and intermediate pressure differentiation processes, which are often overprinted on more deep-seated processes taking place in the upper mantle. A study of historic eruptions from several volcanoes is also useful in making distinctions between chemical differences resulting from the sampling of a single time horizon in volcanoes at different stages of evolution (i.e., of different initial age), and those due to the regional heterogeneity of the mantle.

Rare earth and other trace element data have been obtained for 16 lava specimens of which 14 are historic and 2 are prehistoric eruptions from the islands of Pico, São Jorge, Terceira, Fayal, and São Miguel. The system of analysis used neutron activation analysis and has been described in Refs. 4 and 5. In brief, gram amounts of each rock were ground by hand into a powder. One hundred mg aliquots of these powders were mixed with cellulose, pressed into pills and irradiated along with calibrated composite standards in the Berkeley triga-type reactor.

This method is capable of qualitatively analysing for in excess of 50 elements in a sample. In rock samples, more than two dozen elements can be determined with precision of less than 5% and a number of these are determined to better than 1%.

All analyzed samples are characterized by highly fractionated, light REE-enriched patterns (Fig. 1), in strong contrast to the light REE-depleted basalts that characterize mid-ocean ridges.[6-9]

Model calculations by Varne and Graham[10] and Gast[9] indicate that liquids with such contrasting rare earth patterns as these are unlikely to have been produced by different degrees of partial melting of a single peridolitic source material. There is, therefore, strong evidence for chemical fractionation of the upper mantle in the vicinity of the mid-Atlantic ridge.

In Fig. 2 the La, U, Th and Hf are plotted against the Ta concentrations for the 15 different volcanic eruptions. The lines drawn thru the lower abundances demonstrate the average elemental-ratios of these samples. A simple model which involves the addition or subtraction of crystals, devoid in these elements, to a common source material can be used to explain these coherences. These elements are in general referred to as incompatible since they are not readily accepted into many crystal sites.[11] This rejection or acceptance is based on the ionic radii and is the general cause of the different rare-earth

patterns shown in Fig. 1. The average U/Ta and Th/Ta ratios of Fig. 2 are within 3% of those ratios measured at Nunivack in the Bering Sea, where a similar coherence is observed.

Footnote and References

*Institut für Mineralogie, Ruhr-Universität, D-463 Bochum, Germany.

1. J.G. Schilling, Iceland mantel plume existence, and influence along the Reykjanes Ridge: geochemical evidence, Nature (1973).

2. F. Machado, Submarine pits of the Azores plateau, Bull. Volcanol. 21, 109 (1959).

3. W.J. Morgan, Convection plumes in the lower mantle, Nature 230, 42 (1971).

4. H.R. Bowman, F. Asaro, I. Perlman, On the uniformity of composition in obsidians and evidence for magmatic mixing, J. Geol. 81, 312 (1973).

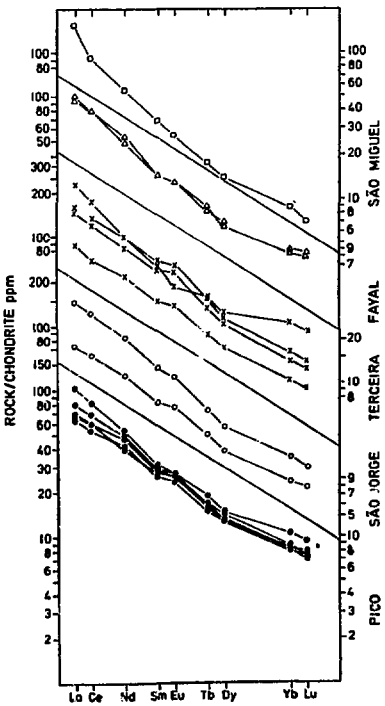

Fig. 1. Rare earth patterns (rock/chondrites) for historic and two prehistoric alkalic lavas from the Azores plotted against ionic radii. (XBL 756-1583)

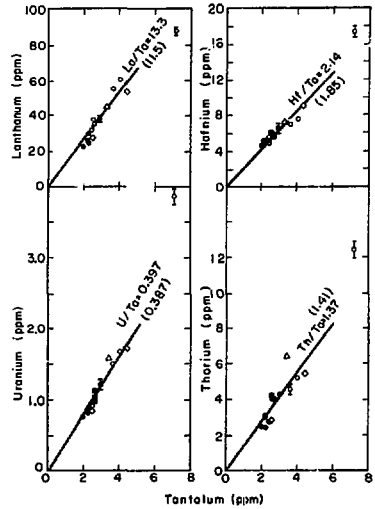

Fig. 2. The elemental abundances of La, Hf, U and Th plotted against Ta for basalt lavas from the island of Pico (solid circles), São Jorge (open squares), Terceira (open circles), Fayal (solid squares) and São Miguel (triangles) in the Azores. (XBL 757-3547)

5. I. Perlman, F. Asaro, Pottery analysis by neutron activation, Archaeometry, 11, 21 (1969).

6. J.G. Schilling, Sea-floor evolution; rare-earth evidence, Phil. Trans. Roy. Soc. Lond. A, 268, 663 (1971).

7. J.A. Philpotts, C.C. Schnetzler, S.R. Hart, Submarine basalts: some K, Rb, Sr, Ba, rare-earth, H_2O and CO_2 data bearing on their alteration, modification by plagioclase, and possible source materials, Earth and Planet. Sci. Lett. 7, 293 (1969).

8. A.L. Graham and G.D. Nicholls, Mass spectrographic determinations of lanthanide element contents in basalts, Geochim. Cosmochi. Acta 33, 555 (1969); D.H. Green and A.E. Ringwood, The genesis of basaltic magmas, Contrib. Mineral. Petrol. 15, 103 (1967).

9. P.W. Gast, Trace element fractionation and the origin of tholeiitic and alkaline magma types, Geochim. Cosmochim. Acta 32, 1057 (1968).

10. R.I. Varne and A.L. Graham, Rare earth abundances in hornblende and clinopyroxene of the hornblende lherzolite xenolity. Implications for upper mantle fractionation processes, Earth Planet. Sci. Lett. 13, 11 (1971)

11. A.E. Ringwood, Constitution of the Mantle, 3, Geochim. Cosmochim. Acta 15, 195-212 (1958).

4. Instrumentation

SuperHILAC 1974 OPERATIONS

E. L. Kelly

The SuperHILAC was operated at 15 shifts per week January through July, at 21 per week in August, and because of budget restriction at only 18 per week for the balance of the calendar year. The distribution of time is shown in Table 1.

There were three scheduled shutdowns for a total of ten weeks: April 27 - May 13 to install additional magnets in the experimental area and make high voltage tests on the 2.5 MV injector, June 23 - July 22 to install pulsed magnets in five drift tubes and other magnet changes in preparation for time-share operation, and December 5 - January 6 for major work on the line-item-funded SuperHILAC modifications, magnet changes in the experimental area, and installation of shielding.

The first quarter was largely devoted to ^{84}Kr (791 hours) and an on-target current of 0.1 particle μA average was obtained. An ^{18}O on-target beam of 2.1 particle μA average was also achieved.

In the second quarter there were only 190 hours of ^{84}Kr due to troubles with the 2.5 MV injector. However, ^{132}Xe was obtained for the first time and used for 50 hours; intensities of 5×10^8 pps at the target were reached. The intensities of ^{18}O were increased to 3.6 particle μA on target.

At the end of July the first Bevalac beam was obtained using $^{12}C^{+6}$ at 8.5 MeV per nucleon supplied by the SuperHILAC with an intensity of 29 μA (peak) at the start of the transfer line. Bevalac Ne beams were obtained in August and the first week of October saw completion of the first successful ^{40}Ar Bevalac run with 1.8 μA (peak) Ar^{+18} at the entrance to the transfer line. During the third and fourth quarters 173 hours of C, 368 hours of Ne, and 61 hours of Ar were supplied to the Bevalac.

Because of the failure of numerous scheduled runs with the 2.5 MV injector it was decided in September to take this injector off line. A group was formed to evaluate and make recommendations on the performance of the injector. December 24 was set as completion date for these studies. During this period many things were done. The accelerating tube was removed for cleaning and repair, and the electrode geometry was modified. HV tests were carried out while the accelerating tube was removed: operation for 1½ hours at 2.7 MV with infrequent sparking was demonstrated after modifying the rectifier structure which also greatly reduced diode board failures; several failure mechanisms of the 100 kHz oscillator coils were identified showing the way to improved coil design. Weaknesses still remain in the ion source telemetry system and power supplies.

Authorization to begin the line item modifications was received November 20, 1974 and work started immediately. However, FY-75 funding was only 850 K$, instead of the 1400 K$ expected, requiring delay in many items including the building addition, so that completion is not scheduled until FY-77.

A SuperHILAC Program Advisory Committee was established and held its first meeting on November 25, 1974.

TABLE 1. Operating time distribution for SuperHILAC, 1974.

Total research time	(4014 hours)	62%
Setup	11%	
Tuneup	11%	
Target time	40%	
Machine studies	(260 hours)	4%
Total maintenance	(2198 hours)	34%
Scheduled maintenance	19%	
Unscheduled maintenance	15%	
Total operation time	(6472 hours)	100%

88-INCH CYCLOTRON OPERATION, DEVELOPMENT AND STUDIES

J. Bowen, D. J. Clark, P. E. Frazier, D. L. Hendrie,
W. R. Holley, and D. Morris

During 1974 the cyclotron was scheduled for 20 eight-hour shifts per week for experiments in nuclear chemistry and physics, isotope production, and beam development. The time distribution is shown in Table 1. The particle distribution history is shown in Fig. 1. Table 2 shows most of the ions run and their energies, through December 1974. New beams in 1974 include C^{4+}, $^{18}O^{4+}$, F^{5+}, Ne^{6+}, and S^{7+}.

Trim coil solutions are calculated now for each new ion or energy run on the cyclotron, to give more reliable set-up parameters than existing approximate solutions.

TABLE 1. 88-Inch Cyclotron operation time distribution, 1974.

Tune-up		6%
Beam optics		5%
Experiments		57%
Beam development		9%
Operating time	(6383 hours)	77%
Planned maintenance		17%
Unplanned maintenance		6%
Total maintenance	(1889 hours)	23%
Total work time	(8272 hours)	100%

The heavy ion source change time has been reduced significantly by preparing and checking out a source and shaft while an alternate one is running. A facility has been constructed for separating ^{18}O from $H_2{}^{18}O$ by electrolysis, and loading it into bottles.

A cryogenic vacuum pumping system was installed in the cyclotron acceleration chamber. The system consists of a panel of helium gas at 20°K, with liquid nitrogen shielding. A refrigerator supplies the cool helium. First tests with beam gave a factor of at least 5 increase in intensity for sulfur beams, and 2 - 3 increase for oxygen beams.

A new design of ion source for heavy ions was built and prepared for testing. Its larger clearances should prevent some failures due to shorting. Its smaller bore size will provide a more reliable source for production of very high charge states. The small bore is presently being provided by tantalum insert sleeves which melt and cause maintenance problems.

The high power arc pulser was tested and proved to meet its design specifications for 10 A average current and pulsed current of 20 - 30 A peak for pulsed operation. Improvements were made in the regulator of the old filament source. The rf crowbar recycle system was redesigned. Design work was done on replacement of the rf modulator by a new tube to save power. Design and construction work was done on a multiplexer system for automatic

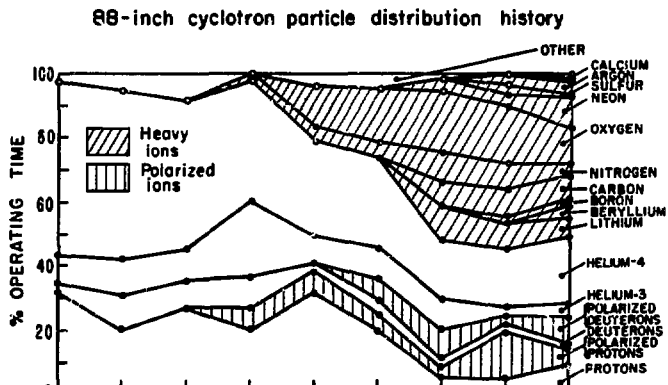

Fig. 1. 88-Inch Cyclotron particle distribution history. (XBL 751-2045)

TABLE 2. 88-Inch cyclotron beams, to December 1974

Ion	Energy[a] (MeV)	External beam[b]
p	10-55	100-20 μA
p(pol.)	13-52,55	.15 μA
d	3.5-65	100-20 μA
d(pol.)	15-20,65	.15 μA
^{3}He	25-140	100-10 μA
^{4}He	3-130	100-10 μA
$^{6}Li^{2+}$	60-80,93	5 μA
$^{7}Li^{2+}$	30-80	5 μA
$^{9}Be^{3+}$	110-120,140	1 μA
$^{11}B^{3+}$	40-115	5 μA
$^{12}C^{3+}$	50-105	5 μA
$^{12}C^{4+}$	90-187	5 μA
$^{14}N^{2+}$	34-40	2 μA
$^{14}N^{3+}$	50-90	10 μA
$^{14}N^{4+}$	60-160	5 μA
$^{14}N^{5+}$	250	1 μA
$^{14}N^{6+}$	360	10^{3} sec
$^{16}O^{3+}$	50-78	5 μA
$^{16}O^{4+}$	80-140	20 μA
$^{16}O^{5+}$	214-218	2 μA
$^{18}O^{4+}$	99,124	2 μA
$^{19}F^{4+}$	99,118	.3 μA
$^{20}Ne^{4+}$	50-108,112	2 μA
$^{20}Ne^{5+}$	130-150,175	1 μA
$^{20}Ne^{6+}$	170-252	.5 μA
$^{32}S^{6+}$	120-150,158	1 μA
$^{32}S^{7+}$	163-206,214	.2 μA
$^{40}A^{7+}$	130-165,171	.5 μA
$^{40}A^{8+}$	170-214,224	.2 μA
$^{56}Fe^{10+}$	180-220,250	1/sec
$^{84}Kr^{12+}$[c]	207,240	1/sec

[a]Energies run. Maximum possible shown after comma, if higher. First harmonic over 6 MeV/A. Third harmonic available down to about 1 MeV/A.

[b]Electrical microamps or particles/sec, total external.

[c]Filament source. Other beams used PIG source.

readout of cyclotron operating parameters. Modifications in the cyclotron control desk were started to provide additional digital readout of parameters. New oscillators were built for one of the polarized source rf transition sections.

Some beam development time was devoted to testing computer trim coil solutions and quick energy changes. Phase histories were measured on several third harmonic beams, and good agreement was obtained with computer predictions. Molecular ions such as D_2^+, D_2H^+, and HeH^+ were used to simulate heavy ions of the same charge/mass ratio, to give high intensity and long source life for the measurements. This information is being used to calculate a system of comprehensive solutions which will be adequate to run any requested particle and energy. For small energy changes, it was found that trim coil 17 should be varied, rather than the main coil.

Studies were also done on improving beam reproducibility of external beam, both directly out of the cyclotron and through an analyzing magnet. Several parameters were found to be unreproducible due to backlash or calibration changes, and improvements were made or planned on these items. A neutron monitor was very useful to distinguish well centered heavy ion beams from spurious beam.

ION SOURCE DEVELOPMENT*

S. Chintalpudi, D. J. Clark, C. Ellsworth,
B. Gavin, R. Gough, H. Grunder, W. R. Holley,
J. R. Meriwether, and F. Selph

The continued improvement of heavy ion sources is of particular importance at Lawrence Berkeley Laboratory, as at present four heavy ion injectors are used in LBL accelerator operations. Two of these serve the SuperHILAC[1] (a heavy ion Alvarez linac), another serves the Bevatron injector (a 20 MeV Alvarez linac operating in the 2$\beta\lambda$ mode), the fourth is used at the 88-Inch Cyclotron. All of these injectors use PIG sources at present, with modifications in each case to suit the special requirements of the accelerator. At the SuperHILAC the need is for large duty factor (15 - 50%), long lifetime sources. The present source supplies 3.0 μA, average of Kr^{6+} at 16% duty factor, measured after acceleration to 9.5 MeV. At the 2$\beta\lambda$ Bevatron injector requirements are for very high charge state of the lighter ions (up to neon), with low duty factor operation. At present 1 μA, peak of Ne^{6+} is achieved at 2.4 MeV. At the 88-Inch Cyclotron interest centers on usable beams of the highest possible charge state, because particle energy in the extracted beam varies as the square of the charge state. Currently 0.2 μA, average of 214 MeV Ar^{8+} is available.

The SuperHILAC

The SuperHILAC will accept beams of 113 KeV/nucleon from either of two injectors. One is a pressurized high voltage generator designed to accelerate ions to 2.5 MV of mass $A \geq 40$, while the other is a conventional 750 KV Cockcroft-Walton supply used for accelerating the lighter mass ions ($A \leq 40$). While Kr^{4+} (at 2.4 MV) and Xe^{6+} (at 2.5 MV) satisfy the linac acceptance requirements, the high voltage limitation of the injector necessitates higher charge states for the time being.

Both injectors use Penning type reflex discharges. Since emphasis lies with heavy ion production, and in as much as the low voltage, low mass injection system delivers adequate intensity beams (i.e., O^{3+}, Table 1), ion source improvement work is directed towards the 2.5 MV source. A test facility has been built to study source performance in an environment closely approximating that in the 2.5 MV source, and some results have been reported elsewhere.[3]

Recent emittance measurements made at the exit of the 2.5-MV injector, using $^{84}Kr^{6+}$ ions at 113 KeV/A, showed the areas to be 5.4 π-cm-mrad and 7.0 π-cm-mrad in the horizontal and vertical planes respectively.

Titanium cathodes are used in cold mode operation and allow for extended source lifetimes, typically, for krypton at 18% duty factor, about 27 hours. Plans are being made to accelerate ^{48}Ca using a sputtering electrode enriched with this metal. As this metal is extremely rare, it must be recovered by chemical reduction of the ion source. A 90% recovery efficiency is anticipated.

TABLE 1. Ion sources at Berkeley.[a]

Ion Species	2.5-MV injector (μA)	750-KV injector (μA)	Super-HILAC exit (nA)	Target (nA)
$^{18}O^{3+/7+}$		800	30,000	25,000
$^{40}Ar^{8+/13+}$		6.5	1,500	200
$^{48}Ti^{7+/13+}$		6	90	5
$^{40}Ar^{3+/13+}$	50		3,200	600
$^{84}Kr^{6+/21+}$	12		1,900	500
$^{86}Kr^{6+/21+}$ (natural gas)	0.9		40	5
$^{132}Xe^{8+/29+}$	2.3		52	2.5
$^{40}Ca^{3+/}$	21		projected values based on test stand performance	
$^{48}Ti^{3+/}$	25			
$^{93}Nb^{5+/}$	23 (hot mode)			
$^{197}Au^{10+/}$	0.3(hot mode)			

[a]Average current values are given.

In an effort to simplify isotope separation and improve the beam intensity of xenon, the SuperHILAC 2.5 MV source is using enriched xenon gas stored in small volume at low pressure. Two solenoids are pulsed open in unison for 20 msec, at rates of 1/sec to 1/min. The minute gas bursts are subsequently smoothed out by passing through a suitable length of porous metal rod. This gas source is in addition to and in parallel with a high pressure, high volume commercial proportional gas control device.

SuperHILAC performance data is shown in Table 1. The projected intensities of a few metallic ions are also included. Titanium, vanadium, and iron have also been accelerated from the 750 KV injector from cathode sputtering. Their intensities are expected to be increased about 50% upon installation of pulsed extractor power supply.

The 88-Inch Cyclotron

The LBL 88-Inch Cyclotron is a variable energy, multiparticle, sector-focused cyclotron that accelerates protons to energies up to 60 MeV, and heavier ions to 140 q^2/A MeV. It has an external polarized ion source for beams of polarized protons and deuterons which uses a quadrupole transport line to bring the ions down the pole axis of the cyclotron for injection. Heavy ion beams are run using a PIG source at the center of the cyclotron ("internal source").[4]

Early in the year the test facility on the vault roof was used to test a PIG source with a filament under the lower cathode, to supply heating independent of the arc. With the standard internal PIG source with self-heated cathodes, the arc needs at least a kilowatt to sustain itself, and source lifetimes are typically 4 - 6 hours. Using the filament the power can be reduced, and lifetimes as long as 40 hours for sources running with 500 watts arc power and N_2 gas and greater than 100 hours for 100 watt arcs and H_2 gas were determined. For beams which do not need high power levels to produce adequate intensity, use of a filament-heated cathode should substantially increase source lifetime and reliability. Installation in the cyclotron of a PIG source with a filament-heated cathode is planned.

Late in the summer, the heavy ion source test magnet and associated equipment was moved to the basement where a new facility for development of heavy ion sources was successfully put into operation. The test facility includes a magnet for PIG source operation and beam analysis, a Faraday cup and scanning wires for beam emittance measurements. The test facility can be used for testing regular internal PIG sources from the cyclotron and also for testing modifications and new developments in ion sources. A high power pulsed arc supply has been designed and built. The power supply has been used extensively in the test facility, and is being phased into operation on the cyclotron. The power supply can deliver a maximum of 30 kW average power and 10 A average current (40 A peak). It produces square wave current pulses with lengths as short as 10 μsec and with a duty factor variable from 0 to 100% (full DC operation).

Tests with the new arc supply show substantial increases in average intensities of high charge state beams from a PIG source under high power pulsed operation. Improvements by up to a factor of 10 in intensity of $^{14}N^{5+}$ ions were obtained with a wide bore anode. The production of $^{40}A^{7+}$ and $^{40}A^{8+}$ has also been studied using the pulsed arc supply and the test facility and beam intensity improvements by factors of 2 - 3 obtained.

Installation was completed and testing began of a "Mirror PIG" heavy ion source. The standard PIG source in use here and at many other laboratories has a uniform magnetic field. A mirror field shape, stronger at the ends than in the middle, is widely used in controlled thermonuclear fusion studies to reflect ions from the ends and provide longer confinement time. Increased confinement time is exactly what is needed to produce higher charge state heavy ions. In the present study here, the field at the cathodes can be increased to about twice the field at the center of the arc, where the ions are extracted. The additional field is produced by pole face windings in the test magnet. The field without the mirror coils being energized drops about 40% from the center of the arc to the cathodes, and thus is an "anti-mirror" field. This would be expected to be a poor situation for confinement.

First measurements agree with the prediction that the high charge states increase as the field goes from anti-mirror to uniform to mirror. Higher charge states show a greater increase in beam intensity than lower charge states. An intensity increase by more than a factor of 4 was obtained for $^{40}A^{7+}$. An interesting observation was that the gas flow could be reduced continuously to lower values as the mirror field increased. This indicates longer confinement time of the ions, as predicted. Tests are continuing with the long range goal in mind of incorporating the mirror field geometry into an external ion source for the cyclotron. In addition, the results obtained here can be used for sources at other heavy ion accelerators.

Some improvements were made on the polarized ion source at the 88-Inch Cyclotron. An unbaffled oil pump was tried on the first stage, in parallel with the blower pump. This greatly increased the pumping speed, permitting higher gas flow and giving more beam intensity. Contamination of the pump oil due to atomic hydrogen reaction was observed after a few hours. A cold cap would greatly reduce the oil problem, and another type of pump with a sight gauge and fill line would be more suitable.

Footnotes and References

*Condensed from LBL-3024.

1. Since August 1974, the SuperHILAC has been used occasionally as an injector to the Bevatron (as part of the Bevalac Project).

2. D. A. Spence, et al., "A 3-MV Injector for the SuperHILAC", 1971 Particle Accel. Conf., (also UCRL-20452).

3. B. Gavin, "Performance Characteristics of ...", Second Int. Conf. Ion Sources, Vienna, 1972 (also LBL-1219).

4. D. J. Clark, et al., "Cyclotrons - 1972", A.I.P. Conf. Proc. 9, 265 (1972),(also LBL-644).

A DIGITAL THERMOELECTRIC BEAM POWER METER

J. M. Nitschke

Introduction

The instrument to be described allows the measurement of the power generated in a target by a particle beam. This measurement can be performed over a wide power range, with great precision and linearity. For a given energy E (in MeV) and a measured power P (in watts) the number of particles per second (PPS) impinging on the target is given by the simple relationship

$$PPS = 6.24 \times \frac{P}{E} \times 10^{12}$$

The number of particles per second is one of the most important parameters of any accelerator.

A prototype of this instrument has been built and tested at the Heavy Ion Linear Accelerator (SuperHILAC).

The Principle of Operation

The principle of operation can best be understood by referring to Fig. 1. The particle beam strikes a suitable target and generates heat. The heat is pumped away on the back side of the target by a Peltier-module. (A Peltier module is a semiconductor device that can act as a refrigerator or heat pump depending on the direction of the current that is flowing through it.) The hot side of the Peltier module is attached to a cooling block which in turn is water-cooled. The target and the cooling block each contain a thermistor. These thermistors are electrically connected to a bridge circuit and a differential amplifier.

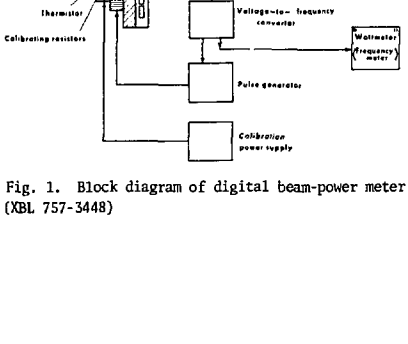

Fig. 1. Block diagram of digital beam-power meter. (XBL 757-3448)

When both thermistors are at the same temperature the output of the bridge and the amplifier is zero. This is the case in the absence of any beam when the whole assembly assumes the same temperature.

Even small amounts of beam will increase the temperature of the target (in particular since the unit is operated in vacuum), unbalance the thermistor bridge and produce an output voltage at the amplifier. This voltage is converted into a frequency and triggers a constant current pulse generator which is connected to the Peltier module. The module consequently cools the target until the thermistor in the target reaches the same temperature as the reference thermistor in the cooling block.

The fact that the power to the Peltier module is supplied in short pulses instead of DC is of no consequence for its performance since it has a very long thermal time constant. It leads, however, to a linear relationship between the frequency of the applied pulses and the cooling power generated since every pulse corresponds to a certain amount of energy (in watt-seconds or calories for example) and the pulse rate therefore corresponds to a certain amount of power (in watts or calories per second).[1] In the prototype instrument 1 kHz is equivalent to 1 watt of beam power. The beam power can therefore be read directly on a frequency meter.

Calibration

Since the instrument is linear over a wide range, a two point calibration is sufficient. The zero point is adjusted with the beam turned off or the digital beam power meter pulled out of the beam path. The second calibration point is obtained by a precise amount of heat generated by four resistors imbedded in the target. The thus simulated beam power can be calculated from a current and voltage measurement with a digital voltmeter.

Footnote

1. A direct DC-feedback without conversion into a frequency would result in a highly nonlinear instrument.

EXTRACTION OF $^{20}Na^{+}$ IONS FROM A He JET ION SOURCE

R. A. Gough, D. Littlejohn, D. J. Vieira and J. Cerny

This report describes a crucial experiment in our development of the RAMA facility[1] for on-line mass analysis of short-lived (≳ 50 msec) radioactivity at the 88-Inch Cyclotron. An overall description of the scope of this project can be found in ref. 1.

In this experiment, the $^{24}Mg(p,\alpha n)$ reaction was utilized to produce ^{20}Na, a β^{+}-delayed α emitter with a half-life ∿ 450 msec. A 40-MeV proton beam from the cyclotron was focused onto an 800-μg/cm² natural Mg foil located in a He jet target chamber charged with 1.5 atm of commercial grade He. The He was not deliberately seeded with impurities; however, no special care was taken to purge the gas system of contaminants prior to the run. Activity recoiling from the target was swept with a He flow rate of 15 - 20 Torr-ℓ/sec into a 1 mm inside diameter stainless steel capillary tube, 5.8 m long. The capillary terminated in a vacuum chamber maintained at ∿ 50 microns by a high capacity Roots blower/mechanical pump combination. A 1 mm diameter skimmer was located 5 mm downstream from the capillary which allowed 70-80% of the ^{20}Na activity to pass through it while deflecting most of the He carrier gas into the Roots blower to be pumped away.

Previous measurements[1] had indicated that ∿ 70% of the transmitted ^{20}Na activity was contained in a 2° opening cone. The He jet ion source,[1] modeled after the early Sidenius hollow cathode type,[2] was positioned so the filament (cathode) subtended a 2° cone from the end of the capillary. A thorough optimization of ion source operating parameters was not completed during this experiment. Throughout most of the run, however, the ion source conditions were: bias voltage V = 10.5 kV; arc voltage = 240 V; arc current = 1.5 A; filament voltage = 10 V; and filament current = 20 A. The arc was supported by an auxiliary source of He gas whose flow was ∿ 0.1 Torr-ℓ/sec. The beam was extracted by a grounded puller electrode positioned ∿ 1.5 mm from the exit hole of the ion source. Successful runs were made using exit hole diameters of both 1.0 mm and 1.5 mm.

An Einzel lens was used to focus the extracted beam into a Wien filter (crossed electric and magnetic fields) designed to provide a crude separation of the extracted beam components (e.g., He^{+}, Ta^{+}, $^{20}Na^{+}$). This filter had been calibrated prior to the run by feeding various gases (A) into the ion source arc and tuning the electric field (E) of the device for each gas at constant magnetic field (B) so the ion A^{+} passed through undeflected. The beam currents were monitored downstream by an on-axis, electron-suppressed Faraday cup. It is readily shown that, for ions of mass A and charge q to pass undeflected, the electric field must be given by

$$E = B\sqrt{2qV} \times A^{-\frac{1}{2}}$$

Figure 1 shows the linear relation observed between E and $A^{-\frac{1}{2}}$ for several measured ions.

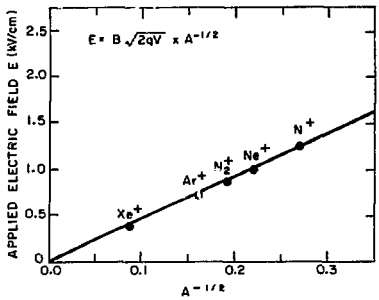

Fig. 1. Calibration of Wien filter at constant magnetic field. (XBL 757-3443)

During the ^{20}Na experiment, the Wien filter was tuned to direct the activity ($^{20}Na^{+}$) off-axis onto 0.63 micron Ni foil behind which was a well-shielded fully-depleted phosphorus-diffused detector. This counter/collector foil assembly was positioned at a distance from the extraction axis equal to ∿ 3 standard deviations of a Gaussian fit to a previously measured $^{20}Ne^{+}$ beam profile. About two counts per minute in the 2.15 MeV α group were observed resulting in the spectrum shown in Fig. 2. When the ion source filament was turned off (thereby extinguishing the arc) zero counts were observed in two 10-min counting intervals. The counting rate returned to normal when the ion source was turned on again.

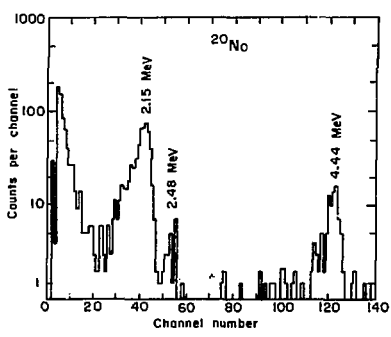

Fig. 2. Alpha-spectrum of ^{20}Na extracted as 10.5 keV $^{20}Na^{1+}$ ions and deflected to an off-axis detector. (XBL 757-3445)

Prior to turning on the ion source, but without interrupting the operation of the He jet, another detector/collector foil assembly was positioned to intercept the activity coming out of the skimmer. By comparing the yield before and after the ion source, the efficiency of the ion source was estimated to be ∿ 0.1%.

Present efforts are directed toward improving the on-line efficiency of both the He jet and the ion source. The installation of a magnetic analyzer is expected to be completed in 1975 with which on-line mass separation will become possible.

References

1. Nuclear Chemistry Division Annual Report for 1973, LBL-2366, p. 443.

2. G. Sidenius, First International Conference on Ion Sources, Saclay, France (1969), p. 401.

A CLUSTER BREEDER FOR He JET EXPERIMENTS

R. A. Gough, D. Littlejohn, L. Ho, D. Sherman, T. Raunemaa, D. Moltz, and J. Cerny

Until fairly recently, the importance of impurities in the He gas used for He jet transport systems has not been fully appreciated. In the last few years, however, many laboratories have reported[3] various additives that improve (in some cases dramatically) the efficiency of the He jet method for rapidly transporting radioactive atoms.

The probable explanation for these successes is the creation of large (10^3 - 10^8 amu)[1] molecular clusters that are formed when certain substances are subjected to ionizing radiation. This occurs, for example, when a charged-particle accelerator beam passes through the target chamber of a He jet experiment if the He has been seeded with an appropriate additive. Radioactive atoms recoiling from the target appear to attach themselves to these clusters.

If the He is then entrained in laminar flow along a suitable length of capillary tube, the interactions of the He atoms with the clusters will serve to concentrate the heavy clusters in the center of the flow stream[4] (reducing radioactive losses to the capillary walls). These interactions will further serve to accelerate the clusters until the axial velocity distributions of the clusters and He atoms become comparable. The clusters then possess considerable energy and momentum.

When the transported material reaches the end of the capillary tube an expansion occurs into vacuum. The angle of the expansion cone is very small (∿ 2°)[5] for sufficiently massive clusters but may be very large (∿ 30°) for the lighter He atoms. Thus, the nozzle-skimmer technique[4] can be used to effect a very efficient separation of the He gas from the radioactivity.

Of particular interest to our He jet program were two reports[6,7] which demonstrated the use of ultraviolet radiation (UV) as a means of cluster formation for off-line He-jet studies using both a ^{252}Cf fission source and a ^{228}Th α source. The UV can be generated by a carbon arc discharge or by a mercury vapor fluorescent lamp.

We have constructed a "cluster breeder" similar to the apparatus used in ref. 7 for testing purposes in our laboratory; it is shown schematically in Fig. 1. It has been used with a ^{225}Ra - ^{225}Ac α source (surveyed at 4×10^5 dpm) to collect samples of ^{221}Fr (E_α = 6.34 and 6.12 MeV; $t_{\frac{1}{2}}$ = 4.8 min), ^{217}At (E_α = 7.07 MeV; $t_{\frac{1}{2}}$ = 32 msec) and ^{213}Po (E_α = 8.38 MeV; $t_{\frac{1}{2}}$ = 4.2 μsec) on an aluminum collector foil. The foil was transferred to a counting chamber to measure the α particle yield. In one such test using CCl_4 as additive and a mercury vapor UV lamp to breed the clusters, the α-particle spectrum shown in Fig. 2 resulted from a 15-min collection, 2-min delay, 10-min counting sequence. Data from subsequent counting periods on this sample revealed that the ^{221}Fr and ^{217}At decayed with a half-life ∿ 4.8 min while the ^{213}Po group exhibited the half-life of its precursor ^{213}Bi (∿ 47 min). Zero counts were observed if either the UV lamp was turned off or if the apparatus was purged of CCl_4. With similar ongoing studies we hope to improve our understanding of the mechanisms necessary for efficient transfer of radioactivity as well as for efficient skimming. These studies will include the use of other additives and the transport of other activities.

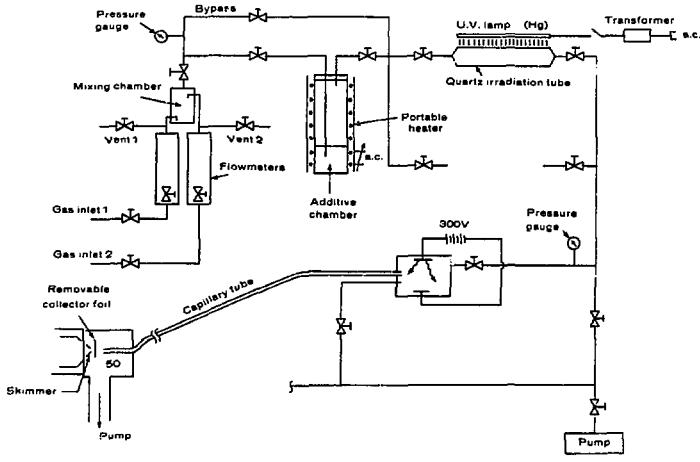

Fig. 1. A schematic diagram of the cluster breeder. (XBL 7412-8444)

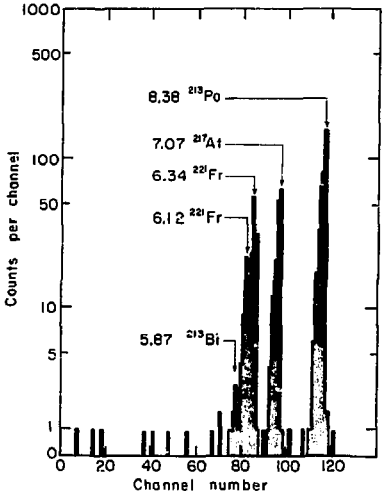

Fig. 2. Alpha-particle spectrum of activity transferred from a ^{225}Ra - ^{225}Ac source by a He jet using the cluster breeder. (XBL 757-3441)

References

1. H. Jungclas, R. D. Macfarlane and Y. Fares, Phys. Rev. Letters 27, 556 (1971).

2. J. Äysto, P. Puumalainen and K. Valli, Nucl. Instr. & Meth. 115, 65 (1974).

3. K. L. Kosanke, W. C. McHarris and R. A. Warner, Nucl. Instr. & Meth. 115, 151 (1974).

4. J. B. Arderson, R. P. Andres, and J. B. Fenn, Advan. Chem. Phys. 10, 275 (1966).

5. Nuclear Chemistry Division Annual Report for 1973, LBL-2366, p. 443.

6. K. Wien, Y. Fares, and R. D. Macfarlane, Nucl. Instr. & Meth. 103, 181 (1972).

7. H. G. Wilhelm, H. Jungclas, H. Wollnik, D. F. Snider, R. Brandt, and K. H. Lust, Nucl. Instr. & Meth. 115, 419 (1973).

A MODIFIED ^{8}Be IDENTIFIER

G. J. Wozniak, N. A. Jelley,* and J. Cerny

For several years we have been developing a general-purpose counter telescope technique[1] for studying transfer reactions which produce ^{8}Be nuclei ($t_{\frac{1}{2}} \sim 10^{-16}$ sec) as exit particles. Since initial investigation of the (α,^{8}Be) reaction at a bombarding energy of $\sim$ 65 MeV was hindered by low yields ($d\sigma/d\Omega < 50$ μb/sr) and a large α-α chance background, a "modified" ^{8}Be identifier has been developed[2] to improve the signal to noise ratio.

Figure 1 is a schematic of the modified identifier, illustrating its basic components; a divided collimator, twin transmission detectors (ΔE) and a position-sensitive stopping detector (E). The two α-particles from ^{8}Be decay are detected in subnanosecond coincidence in the ΔE detectors and, in addition, a comparison of their relative energy losses is made. The ^{8}Be is further identified by performing particle identification with the summed ΔE detector signals and the E signal. Finally the PSD is used to determine the direction of the ^{8}Be nuclei. A large solid angle is subtended to obtain a high probability of detecting the two breakup α-particles, while the energy resolution is improved by kinematically correcting the ^{8}Be energy by its direction.

When ^{8}Be decays, the two breakup α-particles have similar energies ($|E_1 - E_2|/(E_1 + E_2) < 10\%$) and thus similar flight times and differential energy losses (dE/dx). The maximum difference in the flight times of the two α-particles from a 35-MeV ^{8}Be is approximately 0.5 nanoseconds over a 12 cm flight path. Thus a ^{8}Be event can be characterized by a ΔTOF $\leq \Delta t_{max} = \pm 0.5$ nanoseconds. Similarly the energy loss of α_1 in ΔE_L is approximately equal to that of α_2 in ΔE_R (see Fig. 1). By calculating the ratio $R = \Delta E_L/(\Delta E_L + \Delta E_R)$, ^{8}Be events can also be characterized by a ratio signal of $\frac{1}{2}$.

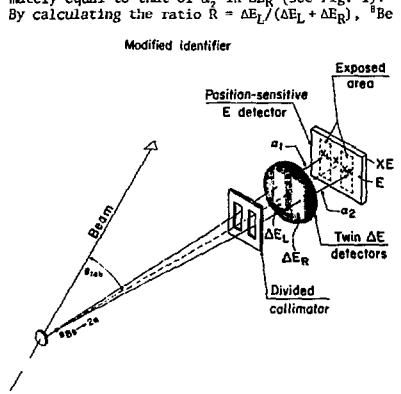

Fig. 1. Schematic diagram of the modified ^{8}Be identifier, illustrating the divided collimator, twin transmission detectors and PSD. (XBL 745-3062)

Figure 2 presents a ΔTOF spectrum [ΔE_L(start) - ΔE_R(stop)] of events originating from the same beam burst. The symmetric double peak is due to ^{8}Be events. Background counts are caused by fragmentation reactions and random chance coincident events associated with the high counting rate of 25 kHz in each of the ΔE detectors (intra-beam-burst rate 500 kHz). The full width at the base of the ΔTOF peak ($\sim$ 1 ns) reflects the minimum energy ($\sim$ 30 MeV) ^{8}Be event that could be detected, and the central dip is the effect of collimation on the breakup α-particle velocity distribution. If the identifier had 100% detection efficiency and perfect time resolution, then the ΔTOF peak would be rectangular with a width of $2\Delta t_{max}$. This is most closely realized for ^{8}Be nuclei emitted toward the center of the identifier. However, for those emitted off center, the first part of the breakup cone that is lost through collimation is the edge. Therefore, most of the ^{8}Be events emitted into the acceptance solid angle, that are not detected, correspond to the breakup α-particles having approximately equal velocities, and therefore equal times-of-flight, hence the central dip in the ΔTOF spectrum.

In the spectrum shown in Fig. 2, only events depositing more than 10 MeV in the E detector, and satisfying a ΔE_L - ΔE_R inter-beam-burst coincidence (2τ = 50 ns) and ΔE energy SCA's (set to eliminate Z = 1 and 3 particles), were recorded.

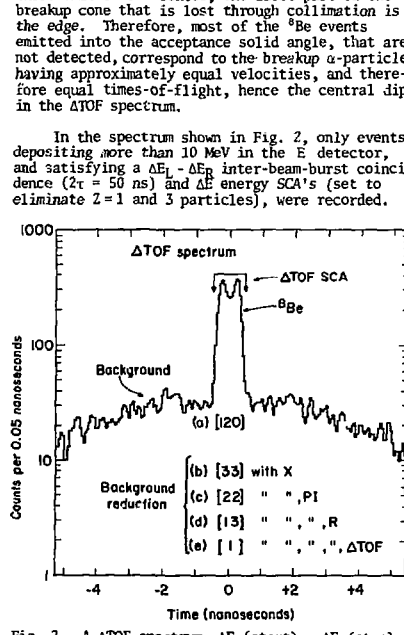

Fig. 2. A ΔTOF spectrum, ΔE_L(start) - ΔE_R(stop), of events originating from the same beam burst. The ratio of the total background to ^{8}Be events decreases from 120% to 1% as various SCA requirements are introduced. (XBL 742-2318)

The total number of intra-beam-burst background counts, expressed as a percentage of the number of ^{8}Be events, is 120% for the above conditions (see (a) in Fig. 2). As further SCA requirements are made: (b), (c), (d), and (e), the background decreases considerably with only a 25% loss in the number of ^{8}Be events which is almost entirely due to the setting of a restricted X gate. The lowest background is achieved when the position signal is restricted to fall within the ^{8}Be acceptance angle (X SCA); the PI falls in the calculated region for ^{8}Be events (PI SCA); the ratio is close to one-half (R SCA); and the ΔTOF signal corresponds to a time difference $\leq \Delta t_{max}$(ΔTOF SCA). All these conditions are characteristic of ^{8}Be events. With these requirements the total background in a ^{8}Be energy spectrum is 1% of the number of ^{8}Be events, at a counting rate of 25 kHz in each ΔE detector.

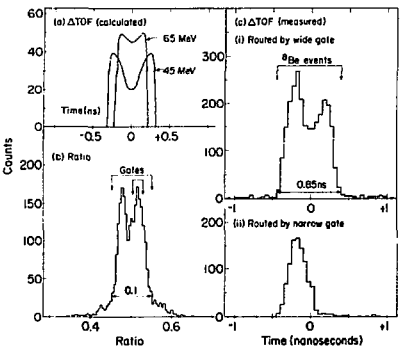

Fig. 3a) Calculated ΔTOF spectra, ΔE_L(start) - ΔE_R(stop), showing the effect of the divided collimator's shape on the relative velocity distribution. b) A ratio spectrum, $\Delta E_L/(\Delta E_L + \Delta E_R)$. c) Measured ΔTOF spectra routed by the ratio gates shown in part b). (XBL 742-2379)

A ratio spectrum is given in Fig. 3b. The double peaking in this spectrum corresponds to that seen in the ΔTOF spectrum shown in Fig. 2. If the lower velocity alpha from a ^{8}Be event traverses ΔE_L and the higher velocity one traverses ΔE_R, this corresponds to a negative time difference in the ΔTOF spectrum. It also corresponds to a higher ΔE_L energy loss ($dE/dx \propto E^{-1}$), and therefore a ratio greater than one-half. This equivalence is demonstrated in Fig. 3c(ii).

In Fig. 3c(i) a ΔTOF spectrum routed by the wider R SCA, is shown. The shape of this peak is closely predicted as can be seen from the calculated peak shapes for 45 and 65 MeV ^{8}Be events given in part (a). These ΔTOF spectra were calculated with the program EFFICR. (The asymmetry in the experimentally observed ΔTOF peak of Fig. 3c(i) is due to a slight asymmetry in the position gates).

To reduce the effect of kinematic broadening on the ^{8}Be energy resolution, three narrow position gates (X_L, X_C, X_R) were set. Each was equivalent to 0.4° and the summed gate (1.2°) had a detection efficiency (ε) of 20 - 36% for 35 - 70 MeV ^{8}Be events. In addition, a thin target (100μg/cm^2) was used and rotated to reduce the combined effect of the differential energy loss in the target and the beam spot size.

A ^{8}Be energy spectrum accumulated in two hours from the ^{11}B(α,^{8}Be) Li reaction at θ_{lab} = 20° and E_α = 72.5 MeV is shown in Fig. 4. This spectrum was obtained by summing the kinematically corrected energy spectra corresponding to the three position gates. Over 25 MeV of excitation in ^{7}Li is observed, and strong transitions to the ground and second excited states are seen as well as transitions to the 7.47 MeV; 5/2$^-$ and the 0.48 MeV; 1/2$^-$ states[5] (the latter only partially resolved). The 5/2$^-$ and 1/2$^-$ states are expected to be less strongly excited on the basis of calculated α-structure factors.[4] The absolute cross section to the ground state is 18 μb/sr at this energy and angle. The observed energy resolution is 400 keV and the counting rate in each ΔE detector was 25 kHz. At this counting rate the deadtime (observed with a pulser-triggered by a monitor counter) was 35%.

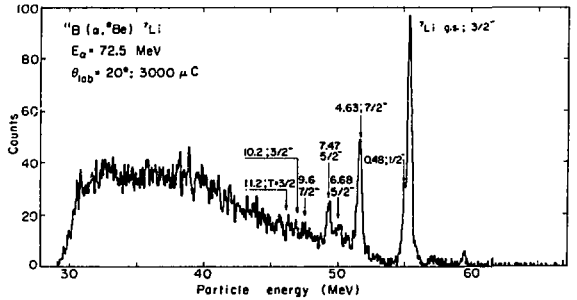

Fig. 4. A ^{8}Be spectrum from the ^{11}B(α,^{8}Be)^{7}Li reaction taken with the modified identifier. The locations of possible transitions to all states below 11 MeV are indicated.[4] (XBL 742-2411)

Using the modified identifier, data could be collected at twice the rate and with a lower background level than was possible with the simple identifier. The average background level above the impurity peak in Fig. 4 corresponds to an absolute differential cross section limit of ~ 0.1 μb/sr c.m. Lower cross section limits could be achieved if necessary by reducing the counting rate. There is no background from ^{8}Be* (2.9 MeV), when using a modified identifier, because its large breakup Q-value coupled with the restriction on the separation angle of the two α-particles imposed by the divided collimator causes α_1 and α_2 to have sufficiently different energies that the ΔTOF SCA and R SCA requirements eliminate ^{8}Be* events from the energy spectra.

The above counter telescope technique was developed for the spectroscopic study of low yield reactions producing ^{8}Be nuclei in the presence of a high chance α-α background. This technique should greatly simplify the study of single and multi-particle transfer reactions involving ^{8}Be, such as (^{9}Be,^{8}Be), (^{6}Li,^{8}Be), and (^{11}B,^{8}Be).

Footnote and References

*Present address: Nuclear Structure Laboratory, Oxford, England.

1. G. J. Wozniak, H. L. Harney, K. H. Wilcox, and J. Cerny, Phys. Rev. Letters 28, 1278 (1972); G. J. Wozniak, N. A. Jelley, and J. Cerny, Phys. Rev. Letters 31, 607 (1973).

2. G. J. Wozniak, N. A. Jelley, and J. Cerny, Nucl. Instr. & Meth. 120, 29 (1974).

3. F. Ajzenberg-Selove and T. Lauritsen, Nucl. Phys. A227, 1 (1974).

4. D. Kurath, Phys. Rev. C 7, 1390 (1973).

PERFORMANCE OF A SILICON PROTON POLARIMETER BETWEEN 19 AND 32 MeV*

J. Birchall,† H. E. Conzett, W. Dahme,‡ J. Arvieux,§
F. N. Rad, R. Roy, and R. M. Latimer

In the past few years interest has grown in the measurement of the so-called triple-scattering parameters.[1] These experiments require the scattering of a polarized beam from a target and the measurement of the polarization of the outgoing beam. The polarization is determined by scattering the beam from a suitable polarization analyzer and by comparison of the scattering yields at equal angles to the left and the right from the analyzer. Two nuclear scatterings are therefore involved, the first at the primary target and the second at the polarization analyzer. Count rates are generally low and increases in scattering efficiency have usually been made at the expense of energy resolution.

Recent progress in calculations for the three-nucleon system[2] and the relatively good agreement of the results of these calculations with measured cross-sections and analyzing powers[3] have spurred interest in experiments of the above type, which probe further our understanding of few nucleon systems. It is expected that precise determination of polarization transfer[4] and depolarization parameters for nucleon-deuteron elastic scattering will provide a sensitive test of the nucleon-nucleon interactions used in the calculations.

In the field of proton-nucleus elastic scattering it has been pointed out that detailed information on the nucleon-nucleus spin-spin interaction can be expected from the study of angular distributions of the depolarization parameter D.[5] In such experiments good energy resolution is required to separate elastically scattered protons from scattering from low lying states of the target nucleus.

A polarimeter has been designed for experiments of the above types, and for other experiments where a low yield of protons is expected. The polarimeter combines high scattering efficiency with good energy resolution.

As illustrated in Fig. 1, it comprises a polarization analyzer, labeled 'analyzer detector' and three silicon semiconductor detectors labeled 'left', 'right' and 'zero-degree'. The analyzer material is silicon in the form of a Si(Li) semiconductor transmission detector of 1-2 mm depletion depth. The zero-degree detector is centered on the polarimeter axis, while the left and right side detectors are positioned at ± 27° to the axis, and each subtends a solid angle of 12 msr at the analyzer. The side detectors, E_L and E_R, are operated together with the analyzer detector ΔE as two E-ΔE counter telescopes sharing the same ΔE detector. The summed pulse E + ΔE represents

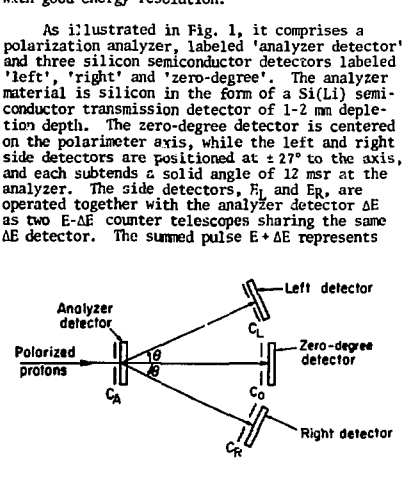

Fig. 1. Schematic diagram of the polarimeter, C_A, C_L, C_R, C_0 are collimators. (XBL 733-2368A)

the total energy of the particle incident on the analyzer detector. The polarimeter therefore has the advantage of good energy resolution even when the analyzer is made thick and the side detector solid angles are made large in order to increase count rate. Typically, energy resolutions of the order of 100 keV FWHM at 20 MeV are obtainable when the polarimeter is operated at analyzer count rates below about 5×10^4 sec^{-1}.

A typical energy spectrum is shown in Fig. 2 for ^{9}Be($\vec{p}$,$\vec{p}$) at E_p = 25.3 MeV and Θ_{LAB} = 45°. It was obtained with a 1 mm thick analyzer detector counting at $\sim 10^5$ counts per second. The elastic peak at channel 320 corresponds to a proton energy of 22.6 MeV. The peak at channel 285 is due to the 2.43 MeV state of ^{9}Be, while the small peak near channel 295 is from elastic scattering from ^{9}Be followed by scattering from the 1.78 MeV level of ^{28}Si of the analyzer detector. The cross-section for the 1.78 MeV state is approximately 4% of the elastic cross-section at 27° at this energy, but becomes comparable with the elastic cross-section at backward angles.

The polarimeter was designed with reference to recently published data on ^{28}Si($\vec{p}$,p) from 17 to 29 MeV.[6] Figure 3 shows a contour plot, derived from these data, of $A\sigma^{\frac{1}{2}}$ where A is the proton-^{28}Si analyzing power and σ is the differential elastic cross-section. The peak in this figure of merit, centered at E_p = 23 MeV and a scattering angle of 30°, is quite flat and reaches 5.4 (mb/sr)$^{\frac{1}{2}}$. The figure of merit of the present polarimeter could be increased by 5 - 10% of its present value by using a mean scattering angle of 30° instead of 27°. For the present arrangement, with an analyzer detector 2 mm thick and side detectors subtending

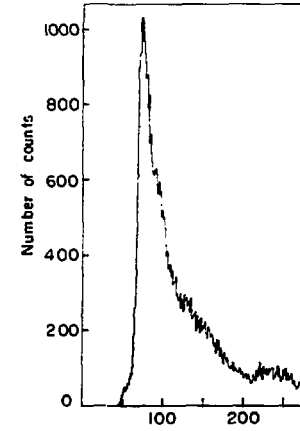

Fig. 2. Spectrum of ^{9}Be($\vec{p}$,$\vec{p}$) at E_p = 25.3 MeV, Θ_{LAB} = 45° with a 53.4 mg/cm^2 target.
(XBL 746-3549)

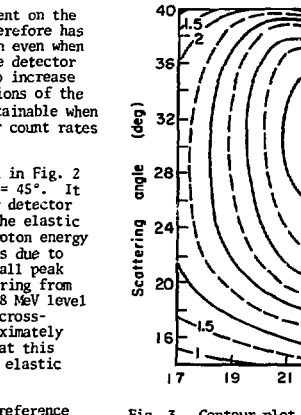

Fig. 3. Contour plot of the $\vec{p}$-^{28}Si figure of merit $A\sigma^{\frac{1}{2}}$ versus laboratory scattering angle and proton energy. The units of $A\sigma^{\frac{1}{2}}$ are (mb/sr)$^{\frac{1}{2}}$, with A measured as a fraction of 1.0.
(XBL 747-3632)

an angle of ± 3.5° at the analyzer, the left-plus-right scattering efficiency Y is $\sim 0.8 \times 10^{-4}$ per proton incident on the analyzer at 26 MeV. The integrated figure of merit $AY^{\frac{1}{2}}$ is $\sim 2.2 \times 10^{-3}$, with A measured as a fraction of 1.

The effective analyzing power of the polarimeter is determined in a calibration procedure which measures the asymmetry ϵ in the polarimeter produced by scattering a beam of polarization p_o from a target. ϵ is given by:

$$\epsilon = p_1 A_2 = A_2(Dp_0 + A_1)/(1 + p_0 A_1)$$

where p_1 is the polarization of the beam after scattering from the target, A_2 is the silicon polarimeter effective analyzing power and A_1 and D are, respectively, the analyzing power and depolarization parameter of the target. For direct elastic scattering the D-parameter is a measure of the spin-spin interaction occurring between the scattered proton and the target nucleus. D then takes on its maximum possible value of 1.0 for elastic scattering from a spin zero nucleus, such as ^{4}He or ^{12}C. A_1 is determined from the spin up-spin down asymmetry in the zero-degree detector, or from the combined asymmetries in two zero degree detectors when two polarimeters are in use, one at either side of the beam. Since ϵ, A_1 and p_0 are measured and D is known for ^{4}He or ^{12}C, A_2 can be determined. Results of such measurements are shown in Fig. 4.

The polarimeter has proven to be particularly useful in low yield experiments, such as in the determination of polarization transfer and depolarization parameters. The high efficiency coupled with inherently good energy resolution make it competitive with other polarimeters for proton

energies between 17 and ∿ 40 MeV. For experiments where energy resolution is important, involving the measurement of the polarization of protons scattered from complex nuclei with closely spaced levels or the measurement of polarization in breakup reactions, the present type of polarimeter is superior to others known to the authors.

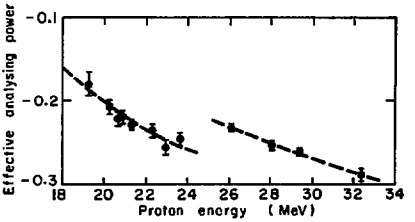

Fig. 4. Measured values of the polarimeter effective analyzing power versus proton energy for θ = 27°. A 1 mm analyzer detector was used, except for the points above 24 MeV where the analyzer was 2 mm thick. The dashed line is to guide the eye. (XBL 748-3845)

Footnotes and References

*Condensed from publication in Nucl. Instr. and Methods 123, 105 (1975).

†Present address: Physics Department, University of Basel, Switzerland.

‡Present address: Physics Department, University of Munich, West Germany.

§Present address: I.S.N., University of Grenoble, France.

1. L. Wolfenstein, Ann. Rev. Nucl. Sci. 6, 43 (1956).

2. J. C. Aarons, I. H. Sloan, Nucl. Phys. A182, 369 (1972), A198, 321 (1972); P. Doleschall, Phys. Lett. 40B, 443 (1972), Nucl. Phys. A220, 491 (1974); S. Pieper, Nucl. Phys. A193, 519 (1972), A193, 529, (1972), Phys. Rev. C8, 1702 (1973).

3. F. N. Rad, J. Birchall, H. E. Conzett, S. Chintalapudi, R. Roy, Phys. Rev. Letters 33, 1227 (1974), and references therein.

4. F. N. Rad, J. Birchall, H. E. Conzett, R. Roy, Phys. Rev. Letters 33, 1579 (1974).

5. A. Hussein, H. S. Sherif, Phys. Rev. C8, 518 (1973).

6. C. R. Lamontagne, B. Frois, R. J. Slobodrian, H. E. Conzett, Ch. Leemann, R. deSwiniarski, Phys. Lett. 45B, 465 (1973).

A VIEW OF THE PRESENT STATUS AND FUTURE PROSPECTS OF HIGH PURITY GERMANIUM*

W. L. Hansen and E. E. Haller

The present state of our knowledge of the properties of high purity germanium is reviewed. The role of excess vacancies, oxygen and high dislocation density in producing trapping in detectors is discussed. By the application of Fourier Transform Spectroscopy, the major impurities have been identified and aluminum has been found to be dominant in most crystals. Analysis has shown that the principal source of aluminum is the polycrystalline starting material. The material problems related to detector fabrication are surveyed and a spectrum taken with a 43 cm³ coaxial detector is presented. It is concluded that the important problems of material development are well delineated but that their solutions will require intensified effort.

The development of high purity germanium as a detector material has now progressed enough so that some general statements can be made about our present understanding, and the areas where further research is needed can be rather sharply defined. The recent application of Fourier Transform IR Spectroscopy has led to the identification of all the important impurities. Several hundred detectors of all sizes have been made, and in the process, crystal properties important to device performance have been illuminated. The evolution of our present understanding can be divided roughly into three areas; 1) the role of excess vacancies, 2) impurities and impurity distributions, and 3) the concern for dislocations and structural defects.

The Role of Excess Vacancies

An important acceptor level in high purity germanium can be produced by an excess of vacancies over the ambient temperature equilibrium value. Crystals grown from a melt incorporate a concentration of vacancies equivalent to their solubility at the melting temperature. As the crystal cools it becomes strongly super-saturated unless some low energy condensation nuclei are present. In germanium the vacancy solubility at the melting point is > 10^{15}/cm³ and at room temperature is insignificant.

If no condensation nuclei are present, (e.g.,

dislocations), the strong super-saturation of vacancies cause their precipitation as vacancy clusters or voids. These vacancy clusters, which can be revealed by chemical etching (Fig. 1) are always accompanied by acceptor centers with an activation energy of about 80 MeV and a concentration of 2 to $4 \times 10^{11}/cm^3$ (Fig. 2). Centers with this activation energy are efficient traps at 77°K and as a result, detectors containing vacancy clusters give completely unacceptable performance.

Impurities and Impurity Distributions

Most of our crystals have a background donor impurity which segregates toward the tail end so that this end is usually n-type. Many crystals exhibit a uniform net acceptor concentration along most of the length with the tail becoming n-type. Analysis of these crystals by Fourier Transform Spectroscopy (FTS) has shown that the n-type impurity is phosphorus and the p-type is aluminum.

A high concentration is sometimes found at the head ends of crystals. FTS shows that this is due to boron which always segregates to this end. Furthermore, these crystals have all been grown from the head ends of zone refined bars.

Occasionally crystals are found where the acceptor concentration increases from the head to the tail. FTS shows that this impurity is gallium or, in a few cases, indium.

On the basis of the distribution of the four impurities, we can explain all of our resistivity profiles. Indeed from an examination of the type of profiles, we can usually infer the nature of the impurities in a given crystal.

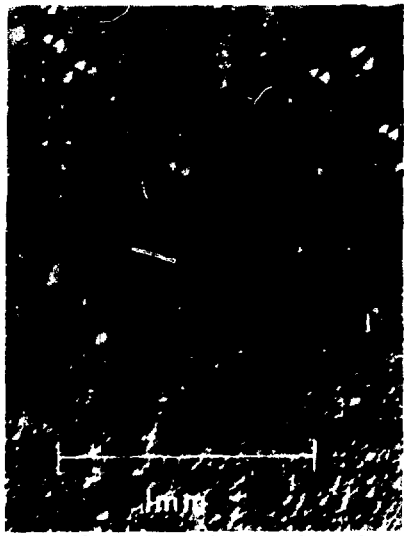

Fig. 1. Photograph of etch pits at the boundary of a dislocated and undislocated region of a crystal slice. In the upper portion are large pits due to dislocations and the lower, small pits due to vacancy clusters. The boundary region is free of pits. (XBB 7310-6167)

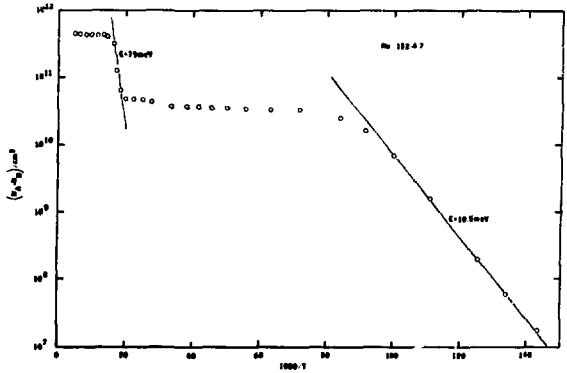

Fig. 2. Acceptor concentration vs temperature for a dislocation free crystal. The energy level at 79 MeV is associated with vacancy clusters and the level at 10.5 MeV has been determined by FTS as being due to aluminum. (XBL 7310-1380)

The Role of Aluminum

Once having taken into account the effects of excess vacancies, the most common type of impurity distribution that needs explaining is shown by the examples in Fig. 3. As can be seen in this figure, the conductivity of the crystals appears to be dominated by an acceptor with a segregation coefficient very close to 1.0. Low temperature measurements give an activation energy near 10 MeV for this acceptor. All of the group III and V impurities have activation energies near 10 MeV but have segregation coefficients far from 1.0 under our crystal growing conditions. The segregation coefficients of other common elements are known in germanium, and all are very far from 1.

Application of FTS to crystals exhibiting the non-segregating impurity proved that this impurity was always aluminum – even in the purest crystals. Since low temperature conductivity measurements indicated that the total impurity concentration was due to levels near 10 MeV, and FTS showed only the single dominant spectrum of aluminum, virtually all the electrical activity is accounted for without the need to invoke other sources such as vacancies, dislocations, strain, etc.

It is concluded then, that with the exception of aluminum, all the impurities are presently at a low enough concentration for any normal detector application. Now that we have an analytical technique in Fourier Transform Spectroscopy, we can hope that this impurity, too, will soon be controlled. We find, though, that even when the impurity concentration is sufficiently low, trapping effects are sometimes seen in detectors which can be attributed to structural imperfections. A more detailed report discussing the relation of dislocations and charge collection in detectors is in preparation.

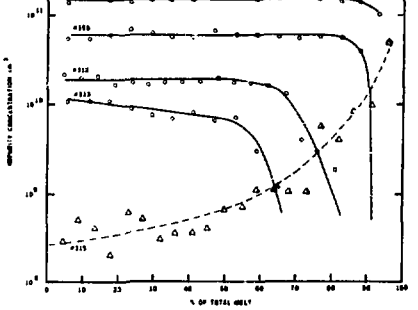

Fig. 3. A selection of crystal profiles which show the common constant impurity concentrations which have been shown by FTS as due to aluminum. The n-type portions are not shown. The lower dashed profile is of an n-type crystal which apparently contains little aluminum. (XBL 7310-1341)

Crystal Perfection and Growing Conditions

A strong correlation has been observed between poor charge collection in detectors and dislocation density. When the crystal contains $10^4/cm^2$ dislocations, detectable trapping appears which increases with dislocation density. The limits on dislocation density for crystals to make high quality detectors appear to be about 500 to 5000/cm^2 and these must be reasonably uniformly distributed.

The high or uneven distribution of dislocations is due to poor thermal conditions in the crystal grower. Enough is known historically about how to grow high-quality germanium crystals except for the fact that we are constrained to grow in hydrogen gas as the only ambient which will produce crystals free of trapping. Hydrogen has a very high thermal conductivity and a low viscosity so it is a source of strong thermal convection and surface cooling of the growing crystal.

Detectors

The process of making detectors from high purity germanium is remarkably free of art and complications when compared with making lithium drift devices. Stated simply, good germanium makes good detectors – any fussing with the fabrication is usually an attempt to compensate for some defect in the crystal.

If a crystal has sufficient purity to be depleted at a reasonable voltage, we find the device performance to be quite indifferent to typeness or even of mixed typeness (e.g., an n-type core in a p-type crystal). Since the field at the metal surface-barrier is lower with p-type crystals these often make devices capable of sustaining higher reverse bias than n-type. This may allow using poorer quality p-type than n-type crystals, but good quality crystals do not require high voltage. On the other hand, effectively thinner entry windows in x-ray detectors result from using n-type material.

As larger detectors are made, the crystal quality requirements become more stringent. Since spectral line widths are much more sensitive to differential than absolute charge collection efficiency, the inclusion of regions having a greater range of efficiencies in large devices makes their performance much poorer than small devices made from the same material.

In addition to the problem of material selection, coaxial detector fabrication presents more problems than do planar detectors due to the geometry of the surface barrier. Despite this, our group has made large coaxial detectors. Figure 4 shows a full energy spectrum of ^{60}Co made with a 43 cm^3 coax detector with an external surface barrier and a lithium-diffused core.

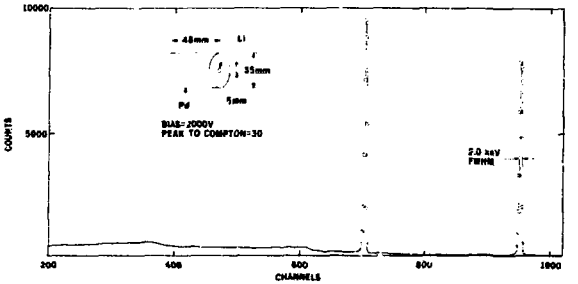

Fig. 4. Portion of a ^{60}Co spectrum taken with a 43 cm^3 coaxial high-purity germanium detector. Resolution and peak-to-Compton ratio were determined from expanded plots of this spectrum.
(XBL 7310-1372)

Conclusions

The principal source of contamination in much of our high-purity germanium has been shown to be aluminum in the starting material. Fourier Transform Spectroscopy permits analysis of polycrystalline germanium for very low concentrations of p-type impurities, so we are confident that the aluminum impurity can be controlled in the future.

Dislocation densities greater than about 10^4/cm^2 result in detectors with noticable trapping; consequently crystals used to make high quality detectors should have a dislocation density of 500 to 5000/cm^2 with reasonably uniform distribution.

As to detectors, the fabrication process presents no fundamental problems and the particular methods used are not by any means as critical as the choice of material. Excellent small detectors can be made from most high-purity germanium but routine production of large detectors such as coaxial units of > 50 cc volume awaits sufficient supply of crystals with good structural perfection over large volumes.

While this paper attempts to delineate the main problems in producing high-purity germanium for high quality detectors, we do not wish to imply that the solution of the remaining problems will be easy. In fact, we anticipate that considerable work will be needed to develop processes capable of producing substantial quantities of large diameter material suitable for large (50 cm^3) detectors.

Footnote

*Condensed from IEEE Trans. Nucl. Sci. 21, 251 (1974).

IMPURITIES IN HIGH-PURITY GERMANIUM AS DETERMINED BY FOURIER TRANSFORM SPECTROSCOPY*

E. E. Haller and W. L. Hansen

During the last few years a great deal of work has accumulated toward characterizing high-purity germanium in respect to detector fabrication. Many techniques were adapted and modified to complete this rather difficult task. Hall effect, conductivity measurements, and metal-point probing on bulk material as well as capacity-voltage dependences and alpha-particle probing of detectors and detector arrays helped to find the axial and radial distribution of donors and acceptors.[1,2] However, very little work was done on analysis to identify the impurities. The main reason was the lack of a method useful at net concentrations below 10^{10}/cm^3. Since the remaining impurities are usually accidental (i.e. not added intentionally) it is of crucial interest to find their nature and hence, perhaps, their source.[3]

Photothermal ionization of neutral acceptors/donors as discovered by Russian scientists,[4-6] combined with Infrared Fourier Transform Spectroscopy (FTS) takes, in a unique way, advantage of the properties of high-purity germanium. This was shown by S. D. Seccombe and D. M. Korn with n-type material produced by R. N. Hall at General Electric Research Center, Schenectady, New York. We have now applied the same method to p-type material down to net-acceptor concentrations below 10^9/cm^3.

It was shown theoretically and experimentally that impurities in semiconductors have more than one bound state for their holes/electrons and produce "hydrogen" like excitation spectra. Figure 1 presents the experimentally determined level schemes for neutral acceptors in germanium.[8] Similar sets of excited states are produced by group V impurities in n-type germanium[9] as well as

in any other electrically active centers.

Use of an interferometer instead of a spectrograph makes possible measurements of the required sensitivity in a short time. Interferograms are converted into frequency spectra by Fourier Transformation.

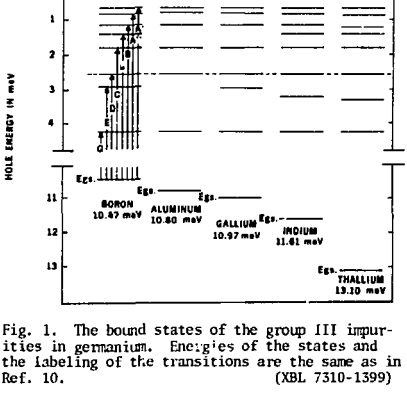

Fig. 1. The bound states of the group III impurities in germanium. Energies of the states and the labeling of the transitions are the same as in Ref. 10. (XBL 7310-1399)

The signal processing and data handling systems are shown schematically in Fig. 2b. Chopped infrared radiation enters the germanium sample causing photothermal excitation which changes the free carrier concentration. The change in voltage across the symmetrically biased sample is amplified with high common-mode rejection and fed into a conventional phase-lock amplifier (PAR model H-8). This unit filters, amplifies and synchronously rectifies the signal. It also controls the chopper motor. A voltage to frequency converter produces a frequency proportional to the signal.

The lower half of Fig. 2a shows a typical interferogram produced by a cube-shaped (0.57 cm^3) sample #313-0.2. The net acceptor concentration was about $10^{10}/cm^3$. Because we do not understand details of the signal formation process in the detector we can only state some experimental observations. In general the signal rises with increasing bias across the sample. We attribute this to multiple refilling and excitation of the acceptor states during the time light enters the sample. However, at a certain bias, breakdown occurs and the signal becomes very noisy. The critical value of the bias depends on the net-carrier concentration, sample surface preparation and on the temperature; a few hundred millivolts is a typical value for 8 mm thick samples. The signal amplitude does not depend on chopping frequency from a few cycles per second up to 200 Hz, the limit for the chopper motor. This means that carrier relaxation times in the sample are shorter than $\sim$ 1 ms ($\omega\tau \lesssim 1$).

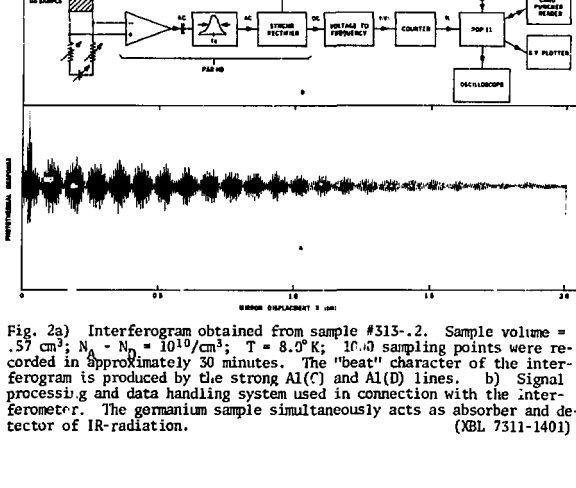

Fig. 2a) Interferogram obtained from sample #313-.2. Sample volume = .57 cm^3; $N_A - N_D = 10^{10}/cm^3$; T = 8.0°K; 1000 sampling points were recorded in approximately 30 minutes. The "beat" character of the interferogram is produced by the strong Al(C) and Al(D) lines. b) Signal processing and data handling system used in connection with the interferometer. The germanium sample simultaneously acts as absorber and detector of IR-radiation. (XBL 7311-1401)

Aluminum plays the most important role as an impurity in our high-purity germanium.[5] It was found to be the only important impurity in many crystals with net-acceptor concentrations ranging from > 10^{11}/cm^3 down to a few times 10^9/cm^3. A spectrum of the sample #313-0.2 containing mostly aluminum is displayed in Fig. 3. The lines of Al (A-G0, B(A-G), and Ga(A-G) correspond to those published by R. L. Jones and P. Fisher[8] within their experimental errors (≈ 0.2%). The continuum of Al starting at about 10.8 MeV is produced by holes which are excited directly from the ground state into the valence band.

The line-widths are limited by the instrument since the total mirror-advance is 2 cm. As can be seen in Fig. 2, the amplitude of the interferogram for this same sample does not decay to zero even at x = 2 cm. This means that the natural linewidth of some lines is smaller than 0.25/cm. The ratio of corresponding lines of different impurities approximately represents the ratio of their concentrations although a correction must be applied because of the variation of intensity of the exciting light with the wave number. This dependence is weak in the spectra region of the strong D and C lines.

Using this simple fact together with Hall-effect measurements of the samples we can observe the segregation of all impurities separately along the length of the crystal. The segregation coefficients for boron and gallium are very reasonable for the particular crystal growing parameters. The anomalous behavior of aluminum once again is evident.

The quality of spectra obtained with the full resolving power of the instrument is illustrated in Fig. 4 where four impurities are present (sample #291-14.0). The Al(C), In(D), and the Ga(C) lines are clearly separated. Their relative spacings are below 0.1 MeV. In addition to the impurities Al, In and Ga, a new unknown shallow acceptor X appears. The relative spacings between the (D), (C) and (B) lines of X are in agreement with the other shallow acceptor lines. We determined the ground state energy $E_{g.s.}$ as 0.18 MeV above the ground state of boron, i.e., (10.47 + 0.18) MeV. From measurements of several samples along crystal #291 we conclude that the segregation coefficient of X is somewhat smaller than that of Gallium and lies probably around 0.05. An n-type core makes a more precise estimate based on this particular crystal impossible.

The spectrum of an n-type sample #296.15.. is shown in Fig. 5. InGa contacts rubbed onto opposite surfaces of the polish-etched cubic sample were used. All the lines can be explained on the basis of phosphorous as an impurity.[9] Noise in the spectrum is due to current injection noise. Almost no improvement in current injection resulted from using lightly lithium-doped contacts, but this introduced the Li-lines. Only in Hoboken LMC material which was n-type did we find lines corresponding to antimony and to lithium without exposing the material to any heat treatment.

We were pleasantly surprised to discover that the method works also for polycrystalline material. Line splitting is observed in some samples, most probably due to stress, but it is not severe enough to make the analysis of the impurities questionable.

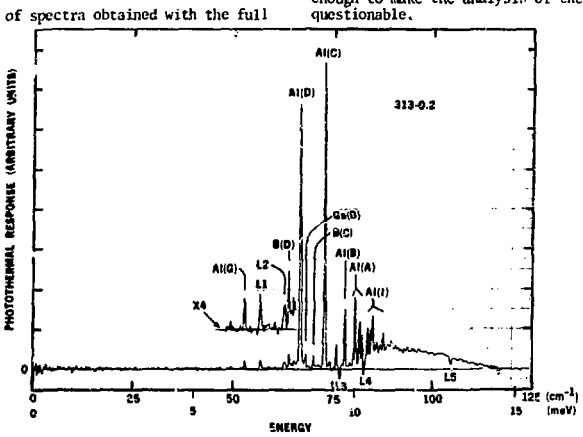

Fig. 3. Spectrum of sample #313-.2. The labeling of the lines is the same as in Ref. 10. Sample volume = .57 cm^3; $N_A - N_D = 10^{10}$/cm^3; T = 8.0°K; 1000 samples were recorded in approximately 30 minutes. A region below the Al(D) line is magnified by a factor of four with the baseline shifted. The aluminum concentration exceeds all other impurities (B,Ga) by a factor of more than 20. The explanation for the lines L_1 through L_5 is given in the text. (XBL 7310-1392)

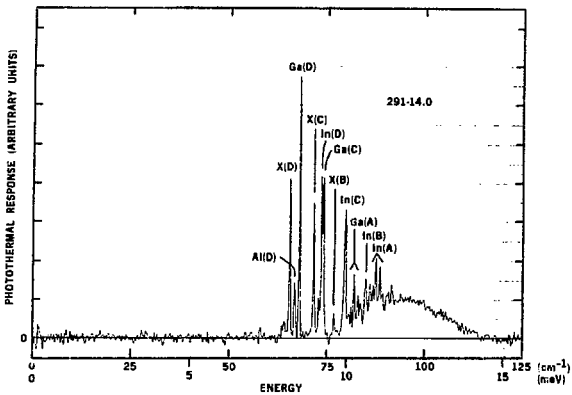

Fig. 4. Spectrum of sample #291-14.0. Sample volume = .47 cm^3; $N_A - N_D = 10^{11}/cm^3$; T = 8.0°K; 1024 sampling points were recorded in 30 minutes. Four impurities are present: X (unknown), Al, Ga, and In. The resolution allows the separation of the Ga(C) and In(D) lines. (XBL 7310-1396)

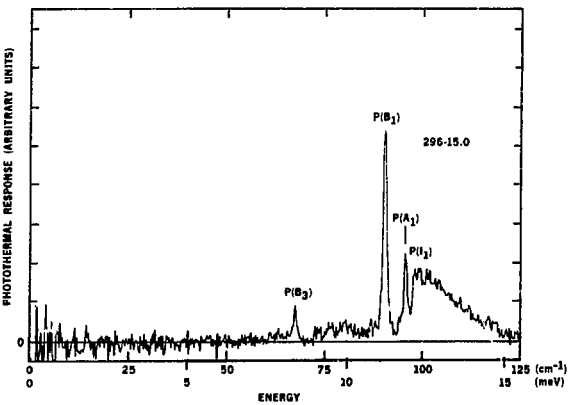

Fig. 5. Spectrum of the n-type sample #296-15.0. Sample volume = .42 cm^3; $N_D - N_A = 6 \times 10^{11}/cm^3$; T = 6.5°K; 700 sampling points were recorded in approximately 30 minutes. Phosphorous is the only detectable donor impurity in our n-type material. (XBL 7310-1395)

In order to test the method for "deep" acceptors we measured the photothermal response of high-purity, dislocation free germanium up to a wave number of 500/cm[1] (= 61.8 MeV). This is the upper limit for the instrument available to us. We were able to detect neutral beryllium[10] in dislocation-free material.

Conclusions

We have shown experimentally that the combination of Fourier Transform Spectroscopy (FTS) together with photothermal ionization of neutral impurities makes possible the analysis of acceptors and donors in high-purity germanium down to net-concentrations of $\sim 10^9/cm^3$ with a signal to noise ratio > 100. With the instrument available to us we did not reach a resolution comparable to the natural line-width of shallow acceptors. We believe, however, that a better resolution will not improve the analytical power of the method. Together with the Hall-effect, which is the best tool for the measurement of the net-concentrations, the segregation of each impurity separately along the axis of a crystal can be determined. That the method works especially well for shallow acceptors and donors is partially due to the fact that both the current through the sample and the temperatures involved are low. The only deep acceptor detected was neutral beryllium ($E_{g.s.}$ = 24.3 MeV). Whether the method will be applicable to deeper levels remains an unanswered question until instruments with a higher maximum wave number ν_{max} are used.

From measurements of over 50 samples we found that aluminum is the main impurity in p-type material. The presence of boron at the seed-end of some crystals can be predicted from the shape of the concentration profile obtained from conductivity measurements.

With the increase of the sample volume we would be able to analyze any impurities producing shallow levels down to the $10^7/cm^3$ range.

Footnotes and References

*Condensed from IEEE Trans. Nucl. Sci. 21, 279 (1974).

1. R. N. Hall, R. D. Baertsch, T. J. Soltys, and L. J. Petrucco, "High-Purity Germanium for Gamma Detectors", General Electric Co. Annual Reports, Numbers 1 through 5.

2. E. E. Haller, W. L. Hansen, and F. S. Goulding, IEEE Trans. Nucl. Sci. 20, No. 1, 481 (1973).

3. W. L. Hansen and E. E. Haller, IEEE Trans. Nucl. Sic. 21, No. 1 (1974) to be published.

4. T. M. Lifschitz and F. Ya.Nad', Sov. Phys. Doklady 10, No. 6, 532 (1965).

5. V. I. Sidorov and T. M. Lifshitz, Sov. Phys. Solid State 8, No. 8, 2000 (1967).

6. Sh. M. Kogan and Sedunov, Sov. Phys. Solid State 8, No. 8, 1898 (1967).

7. S. D. Seccombe and D. M. Korn, Solid State Comm. 11, 1539 (1972).

8. R. L. Jones and P. J. Fisher, Phys. Chem. Solids 26, 1125 (1965).

9. J. H. Reuszer and P. J. Fisher, Phys. Rev. A135, 1125 (1964).

10. H. Shenker, E. M. Swiggard and W. J. Moore, Trans. Metal, Soc. of AIME 239, 347 (1967).

HIGH RESOLUTION FOURIER TRANSFORM SPECTROSCOPY OF SHALLOW ACCEPTORS IN ULTRA-PURE GERMANIUM*

E. E. Haller and W. L. Hansen

The combination of photothermal ionization and far infrared Fourier Transform Spectroscopy circumvents the low sensitivity and resolution of transmission experiments using grating spectrometers. This was shown recently for shallow donors in ultra-pure germanium.[1] The strong dependence of the thermal ionization of a bound carrier from an excited state into the valence band on energy and temperature makes it possible to study selectively different regions of the excitation spectrum.

We report here the following new results:

a) the highest resolution spectra for the group III acceptors in ultra-pure germanium,

b) the separation of a number of excited states near the valence band,

c) the absence of the transition (8 + 0) → (8 + 1) leading to the earlier reported E line,

d) the discovery of two unknown shallow acceptors producing quasi-hydrogenic spectra like the group III acceptors,

e) the modulation of the free carrier mobility by optical and accoustical phonons excited by infrared radiation.

Experimental data were obtained from more than 50 high-purity germanium samples ranging in volume from 0.1 to 0.6 cm^3 and with net-acceptor concentrations between 10^9 and 10^{12} cm^3. These samples originated from 15 different crystals grown by the Czochralski method in our laboratory. Optical excitation of the neutral acceptors was done with a far infrared Michelson Interferometer. Using chopped excitation radiation, the bound carriers were raised to their various higher-lying states and thence thermally excited to the continuum. A PDP-11 computer performed all necessary storage and computations for Fourier transforms.

A new set of lines (impurity X) lying between

those of B and Al were found in samples from crystal 291 (Fig. 1). None of the unknown lines correspond to those already measured. The possibility that the observed acceptor X is created by a crystallographic defect is small since no correlation between the intensity of the most dominant defects (dislocations) and the line intensities could be found. It appears that the impurity X has a chemical character and segregates during crystal growth towards the tail end. Hall effect and IR-measurements of many samples taken from different sections along the crystal yield a segregation coefficient $k_X \sim 0.05 \pm 0.02$.

A second unknown shallow acceptor (impurity Y) was first observed in a polycrystalline sample from a very high-purity zone refined germanium bar and later in two crystals pulled from quartz, and in one crystal grown from a carbon crucible. In the latter crystal the impurity Y was present at a rather high concentration of $\sim 10^{10}$ cm^{-3}. From Hall effect and IR-measurements we found the segregation coefficient of Y to be $k_Y = 0.9 \pm 0.1$. This means that Y is nearly non-segregating in contrast to the dominant impurity aluminum, which segregates normally in crystals grown from carbon crucibles. This behavior could be explained by an impurity which diffuses out of the carbon crucible into the Ge-melt and quickly reaches its rather low maximum solubility.

By going to higher wavenumbers (500 cm^{-1}) and temperatures (17°K) many broad structures appeared in the spectra (Fig. 2). Comparison with optical and accoustical phonon modes[2] suggests that these

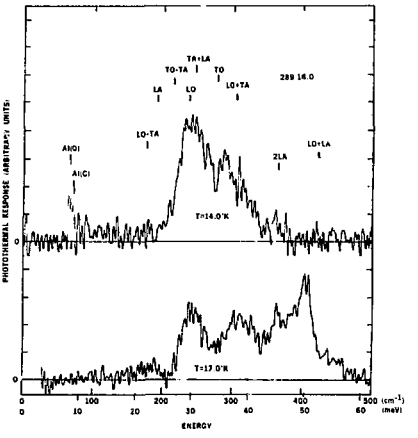

Fig. 2. Spectra of sample #289-16.0 at T = 14°K and 17°K. Sample volume V = 0.22 cm^3; $N_A - N_D$ = 1.7×10^{11}/cm^3. Phonon modes excited by broad band IR-radiation change the free carrier mobility and produce a number of broad features.
(XBL 7311-1431A)

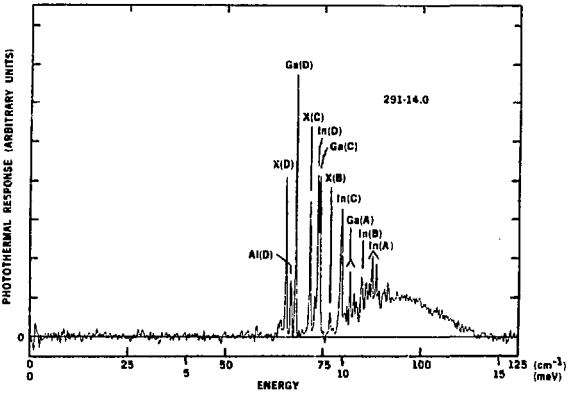

Fig. 1. Spectrum of sample #291-14.0. Sample volume V=0.47 cm^3; $N_A - N_D$ = 10^{11}/cm^3; T = 8.0°K; 1024 sampling points were recorded in 30 minutes. Four impurities are present: X (unknown), Al, Ga and In. The resolution allows the separation of the Ga(C) and In(D) lines. (XBL 7310-1396)

structures are created by interactions between phonons and free carriers. In this case the electrical signal is not produced by changes in the free carrier concentration, but rather by the modulation of the mobility of the free carriers. That the mobility modulation depends on long-range lattice order (crystal perfection) is shown by the fact that we could not observe these modes in dislocation free material (high-vacancy and vacancy-agglomerate concentration).

Footnotes and References

*Condensed from Solid State Comm. 15, 687 (1974).

1. S. D. Seccombe and D. M. Korn, Solid State Comm. 11, 1539 (1972).

2. S. J. Fray, F. A. Johnson, J. E. Quarrington and N. Williams, Proc. Phys. Soc. 85, 153 (1965).

A GAS IONIZATION COUNTER FOR PARTICLE IDENTIFICATION*

R. C. Jared, M. M. Fowler and S. G. Thompson

The advent of high energy heavy-ion accelerators has brought on a rapidly developing need for techniques to identify the products resulting from heavy-ion interactions. Many of the previously used particle identification methods have been reviewed by Goulding and Harvey.[1] One of these methods is the ΔE-E particle telescope. In an effort to extend the useful range of the ΔE-E system we have designed and built a gas ionization ΔE counter which allows determination of the atomic number of reaction products in the range $2 \leq Z \leq 40$.

The gas ionization counter is shown in Fig. 1. Ions, shown by a dotted line, pass through the window and traverse the gas losing energy, and are finally stopped in a gold surface barrier detector. The electrons formed along the path drift up through the grid (dashed lines) and are collected by the place shown at the top of the figure.

A magnetic yoke of mild steel is mounted around the entrance window of the counter. The yoke is fitted with a samarium-cobalt permanent magnet ($1 \times 1 \times 0.25$ inches) that supplies a magnetic field (∿ 1000 gauss) to remove any external electrons that could otherwise enter the counter. The entrance window forms the interface between the gas in the counter and the vacuum outside the counter. The window is made of VYNS[2] (40 ± 20 μgm/cm²) and is attached to the inner end of an Allen head capscrew. The fabrication and thickness measurement of the windows is described in LBL-3435 (see footnote *).

The gas in the counter must be maintained at constant density to ensure that the energy deposited by a given ion in the gas will remain constant. Regulation of the density is accomplished by a Cartesian manostat[3] as shown in Fig. 2. The Cartesian manostat and counter are kept in close proximity to minimize any temperature differential between them. Counting gas supplied from a tank at high pressure flows through a variable leak valve, then through the counter and to the Cartesian manostat that controls the density, and finally to a mechanical vacuum pump. An oil manometer is used to monitor the pressure.

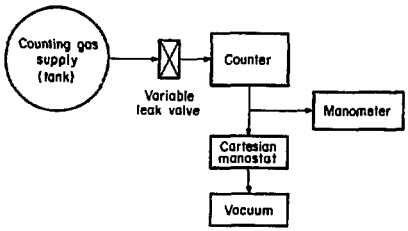

Fig. 2. Diagram of gas supply and regulation system. (XBL 7411-4594)

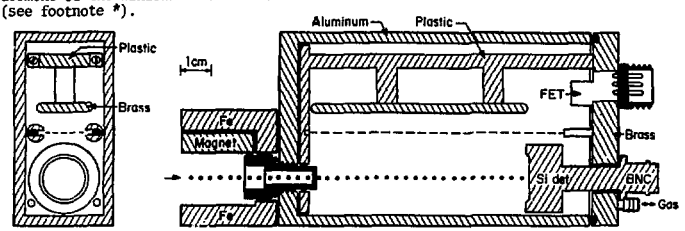

Fig. 1. A cross-sectional view of the gas ionization telescope. (XBL 7411-4588)

The time necessary to collect the electrons on the plate is determined by the drift velocity of the electrons in the gas. This drift velocity of electrons is a function of the field and the gas pressure in the counter. While the electrons are drifting to the plate they diffuse towards the walls of the counter. The average distance that electrons will diffuse while drifting a distance L in a uniform electric field x is given by:[4]

$$\bar{x} = \sqrt{\frac{4(0.0235)}{\pi}} \sqrt{\frac{L\eta}{x}}$$

where η is the ratio of the energy of agitation of the free electrons to that of the gas molecules. Unfortunately the value of η must be measured experimentally, and the value has not been found in the literature for the Ar-CH_4 counting gas mixture used. The value of η for pure argon is reported[5] to be $\sim$ 250 for $X/p = 1.0$ V·cm^{-1} Torr^{-1} while the value of η for pure methane is given as 8.6.[6] It seems likely that the value of η for the 90% Ar-10% CH_4 mixture used is between the values for the pure gases. Using the values of η for the pure gases as limits, the average lateral diffusion in uniform electric field typical of normal operating conditions (30 v-cm) is between 0.70 cm and 0.13 cm. This potential problem of electrons being lost in the walls of the counter was minimized by the focusing action of the electric field. Figure 3 is a plot of equipotential electrostatic lines in the center region of the counter. The parameters leading to the fields in Fig. 3 are typical operating conditions (grid at 100 V and plate at 350 V).

The end zones on the front and back of the counter create potential areas where the counter could fail to collect all the electrons that are generated in the gas by the passage of an ion through the counter. These effects have been investigated with alpha particles. The possibility of end zones was investigated by placing a ^{241}Am source in the front of the counter. The energy loss in the ionization counter and the surface barrier detector as a function of pressure was measured. From these measurements the dead layers were not experimentally observable and it is felt that they are less than 1% of the total path length in the gas. In addition, an alpha source mounted in the center of the chamber gave 26.1 ± 1 eV per ion electron pair, which is in good agreement with other measurements.[7]

The results of a third approach in which a ^{252}Cf alpha source was mounted in the front of the counter are shown in Fig. 4. This figure shows the width of the pulse height distribution in the surface barrier counter and in the gas counter as a function of the energy loss in the gas counter. The electronic noise of the two systems has been subtracted before plotting the data. The figure shows that the width of the energy spectrum in the gas counter is (within experimental errors) exactly that which is expected from straggling in the gas as is determined from that observed in the energy detector.

Six of the counters have been built at Berkeley and are being used in experiments. The performance of the six counters was found to be very uniform. Figure 5 is a map of energy deposited in the gas counter versus the energy observed at the surface barrier detector.

The gas ionization telescope has demonstrated ability to accurately measure the magnitude of energy losses using alpha particles. It has also been shown to be useful for experimental identification of reaction products by our group in the region ($6 < Z < 30$). Recent results using pure CH_4 as a counting gas have given better Z resolution than obtained within argon-methane mixtures.

The counter may also be useful in determining the atomic numbers of even heavier ions such as that of fission fragments. It now appears to be a very good replacement for thin silicon detectors in most applications. The ultimate value of these proposed applications will be revealed only after more investigation into the use of gas ionization counters as delta energy detectors.

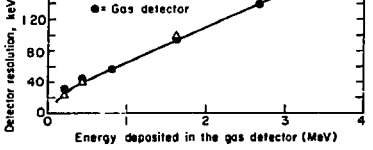

Fig. 3. Equipotential lines in the center section of the counter for typical plate and grid voltages. (XBL 7411-4592)

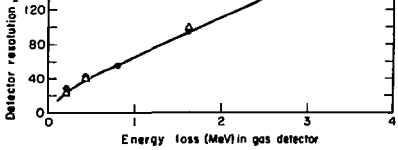

Fig. 4. Energy resolution of the gas detector and solid state detector as a function of the energy deposited in the gas detector. (XBL 7411-4590)

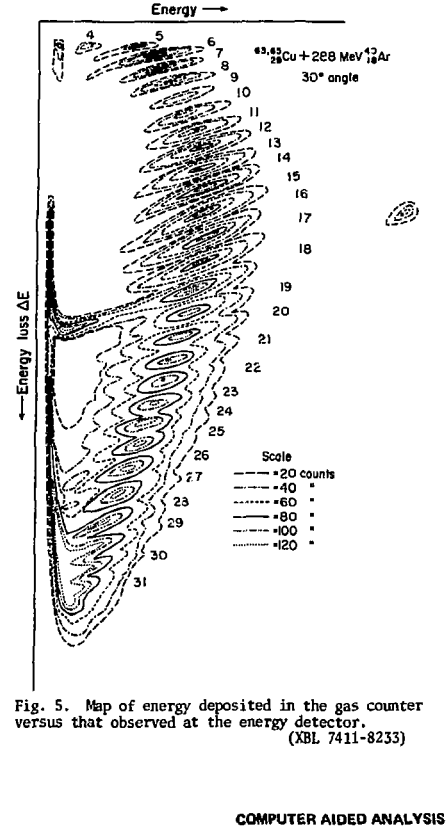

Fig. 5. Map of energy deposited in the gas counter versus that observed at the energy detector.
(XBL 7411-8233)

Footnotes and References

*Condensed from LBL-3435; published in Nucl. Instr. Meth. 124, 341 (1975).

1. F. S. Goulding and B. G. Harvey, LBL-2952 (1974), submitted to Annual Review of Nuclear Science.

2. This material is a polyvinylchloride-acetate copolymer (85% chloride, 15% acetate), supplied by Union Carbide, Bakelite Division.

3. Model No. 8 Cartesian Manostat supplied by the Manostat Corporation, 20 North Moore St., New York, New York.

4. W. N. English and G. C. Hanna, Am. J. Phys. 31, 768 (1953).

5. R. W. Warren and J. H. Parker, Jr., Phys. Rev. 128, No. 6, 2661 (1962).

6. L. W. Cochran and D. W. Forrester, Phys. Rev. 126, No. 5, 1785 (1962).

7. W. P. Jesse, Phys. Rev. 174, No. 1, 173 (1968).

COMPUTER AIDED ANALYSIS OF GAMMA-RAY SPECTRA

M. M. Fowler, D. Lee, R. J. Otto and I. Binder

The heavy-ion irradiations carried out in the radiochemical study of mass yields and the search for possible superheavy elements discussed elsewhere[1] in this report result in a large amount of gamma-ray spectral data to be sorted and correlated. A computer aided analysis scheme for this data has been described,[2] and it is the purpose of this report to indicate modifications and improvements of that procedure which have been made.

The general scheme of the data analysis is shown in the flow diagram in Fig. 1. As was previously reported, the computer code, AES1, is used to determine gamma-ray peak positions and net peak areas from experimental gamma-ray spectra measured with Ge(Li) spectrometers. Independently determined energy calibrations and absolute detection efficiencies are then used to calculate energies and disintegration rates associated with each peak. In prior analyses the output from the AES1 code consisted of punched cards. These cards were hand sorted and used as input to the code TAU1 which is used to determine the time and energy correlation of the gamma-ray peaks from spectrum to spectrum. An estimate is also made of the half-life associated with each peak and whether the decay is complex or simple.

We have modified and combined the AES1 and TAU1 codes so that the sorting is done during

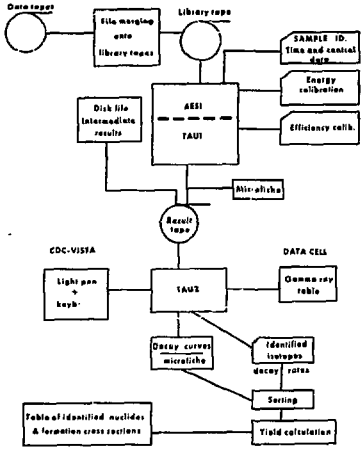

Fig. 1. Flow diagram for the analysis of gamma-ray spectra.

execution, thereby eliminating the need for punched cards. Furthermore, the code has been reorganized so that it can now be executed in the CDC-7600 computer rather than in the slower 6000 series machine. These changes result in a saving of ∿ 50% in execution cost and reduce the job turnaround time.

While these modifications are helpful from a data handling and cost viewpoint, perhaps the more significant improvements have been made in TAU2 code. This program is used to interpret the results from the AES1-TAU1 code. The CDC vista system is used to allow interactive analysis during the assignment of known nuclides to the various gamma-ray peaks. We have replaced the previously compiled table of gamma-ray emitting isotopes with the table of radioactive-decay gamma-rays compiled by W. W. Bowman and K. W. MacMurdo.[3] At the same time, the gamma-ray data were reformatted so as to reduce the necessary computer memory requirements resulting in a code requiring 40% less memory. Another improvement to the TAU2 code has been the introduction of weighting factors in the least-square fitting of the gamma-ray decay data. Previously all data points were weighted with the same absolute standard deviation, resulting in abnormally heavy weighting of points with high count rates. We have adopted a procedure of weighting all points with a constant fractional standard deviation (10% currently) as this more accurately describes the experimental data. The resulting decay curves show that this approach yields curves which more closely fit the experimental data, especially in cases where two components are present with one being much less intense than the other.

Past experience has shown the use of the light pen to be rather unreliable in some instances, possibly due to programming technique. In any case, we have transferred some of the light pen functions to the vista keyboard and have found this to be quite helpful.

The output of the TAU2 code remains as before. However, the final sorting and gamma-ray-isotope assignment is now checked by referring to the decay curves from TAU2 which are on microfiche and by corroboration with other gamma-rays from the same nuclide.

The set of programs has been extensively used during the past year for the analysis and interpretation of data obtained from heavy-ion bombardments. Experience in the use of the analysis method has shown that even with conditions which are not optimum for energy resolution (1.0 keV/channel, 2.6 keV FWHM) the half-life analysis has proven to be a powerful method for resolving components which are not well resolved in energy. The correlation of results from several gamma-rays associated with a single nuclide have been quite good even for weak transitions. These correlations give rise to confidence in yields which must be calculated from a single observed transition. Identification of reaction product nuclides and calculation of their corresponding formation cross sections have been made for products obtained by irradiation of uranium, bismuth, gold and silver targets with ^{12}C and ^{40}Ar using the SuperHILAC and Bevalac facilities at Berkeley.

We are in a continuing process of evolving the program set and in the future we plan to make improvements including the following: provision for online sorting of the isotope list so that only those elements of interest will be displayed to the vista operator. Effort will be made to improve the operation of the light pen so that ultimately all operations could be done from the pen. Statistical weighting factors for the least-squares fitting of the decay curves in TAU2 will be derived from the AES1-TAU1 code making the estimated uncertainties of the initial disintegration rates more meaningful. More input routines will be added to allow analysis of data from a larger variety of multichannel analyzers as they become available.

References

1. R. J. Otto, M. M. Fowler, D. Lee, I. Binder and G. T. Seaborg, "Radiochemical Mass Yield Distribution Studies in the Reaction of ^{40}Ar with ^{238}U and ^{209}Bi and 25.2 GeV ^{12}C with ^{238}U", Section I of this Report.

2. I. Binder, M. DeCasa, J. V. Kratz, J. O. Liljenzin and A. E. Norris, LBL-2366 (May 1974).

3. W. W. Bowman and K. W. MacMurdo, Atomic and Nuclear Data Tables 13, 89-292 (1974).

A SYNTAX ANALYZER FOR COMPLEX TECHNICAL TEXT

G. M. Litton, C. M. Lederer, and L. S. Vardas

General Description

A generalized syntax analysis system has been developed to check complex tabular data (entered via the IRATE input-editing keyboard system[1]) for the seventh edition of the Table of Isotopes. The system permits syntax definitions to be written in a language that is readily understood by someone familiar with the data to be analyzed; these definitions may be easily altered or extended with a minimum of reprogramming. The system consists of a syntax generator, encompassing a "meta-language compiler" that checks the definition of a syntax and translates it into a table of instructions for checking the data, and a syntax analyzer, encompassing a "parser", that applies these instructions to checking and, where desired, to reformatting of the data.

Figure 1 shows the structure and operation of the system. The syntax analyzer consists of subprograms appended to an existing data-processing program, whereas the syntax generator is a separate, complete program.

It has been part of the general philosophy underlying computerization of the Table of Isotopes[2] to use the computer to check the data, as well as to perform such standard operations as storage, sorting, and printout. Although it is not possible for the computer to know *a priori* of what the input data should consist (if it were, the "data" could be computed rather than entered), any data must nevertheless be comprised of a set of symbols or characters, ordered according to some specified set of rules (syntax). To illustrate this point, some examples of syntaxes

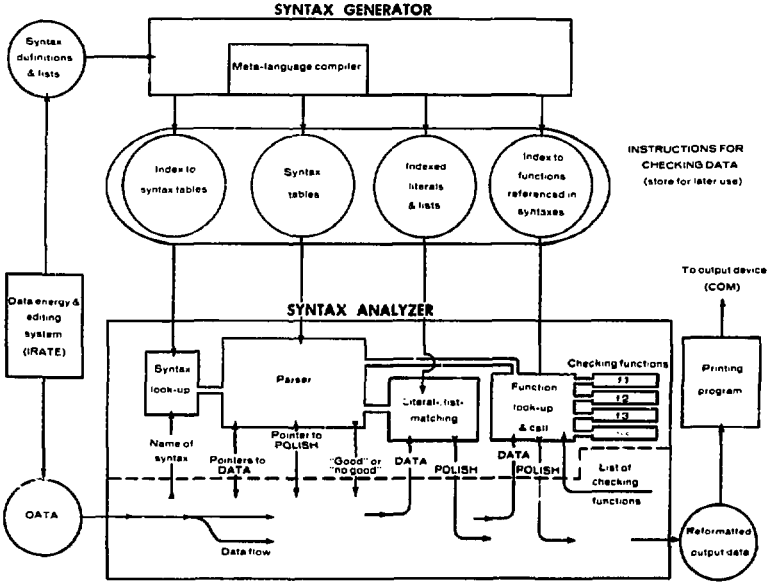

Fig. 1. Schematic illustration of the syntax analysis system. Syntax definitions, entered on the IRATE keyboard, are converted by the syntax generator to instructions for checking data, which may be stored for later use. Data, entered on the same keyboard (at another time), is processed by a data processing program, which may call the syntax analyzer to check whether a given segment of the data conforms to a specified syntax. The parser, the heart of the syntax analyzer, communicates with the rest of the program only via pointers (addresses of specified characters of data); it calls subsidiary functions to examine the actual data. Polish (translated data) is generated by the parser and subsidiary functions in a similar manner. (XBL 757-3450)

applicable to different types of data are illustrated in Table 1.

TABLE 1. Examples of syntaxes for several different types of data. (Syntaxes are described in English, not in the syntax language used by the syntax generator program.)

Type of Data	Defining Syntax
an integer	Either [a] an optional minus sign, followed by a non-zero digit, followed by a string of 0 to ∞ digits; or [b] the digit 0.
an element symbol	Any of the list of items H, He, Li, Be, ... Ha.
an isotope symbol	A superscript integer (mass number), followed by an optional [a] superscript m or m-subinteger ($1 \leq$ integer ≤ 4) or [b] superscript g, followed by an element symbol. (The Z-value corresponding to the element must be $\leq$ the mass number.)
English text	Words from an English dictionary, spaces, and punctuation marks, combined according to the rules of English grammar.

Definition of a Syntax

We have developed a syntax language that is broad enough to represent all possible syntaxes of interest for the present application. Many aspects of this language are not essential to the operation of the syntax analysis system, and could readily be modified for some other application. The outline below describes the syntax language, beginning with its smallest components:

1. Representation. Syntax definitions, like the data to be analyzed, consists of characters or symbols typed on the IRATE keyboard, and represented in the computer by a 12-bit number or byte.

2. Data elements. The syntax language references data elements in or of three different classes:

a) Literals: fixed characters or groups of characters. For example, "× 10" in a number in scientific notation (3.5×10^{7}). In the syntax language, most characters are automatically assumed to represent literals. Exceptions are characters fonted in italics or boldface [unless enclosed in the literal operators ('...')], and a few symbols reserved for syntactical operators.

b) Listable elements: elements that may be any item on a specified list. Examples are a digit (0, 1, 2, ... 9), an element symbol (H, He, Li, ... Ha), or a journal abbreviation (Nucl. Phys., Phys. Rev., ...). In the syntax language, an entire list is referenced by an arbitrary name in italics (*digit*, *element*, *journal*, etc.).

c) Functions: classes of variable data elements too large to be conveniently listed. For example, an integer or an isotope symbol (e.g., $^{179}_{72}Hf$). In the syntax language, a function is referenced by an arbitrary name in boldface characters. Such a function reference requires that a corresponding function subprogram ("checking function") of that name be added to the data processing program. Most functions could alternatively be defined in terms of syntax statements employing only listable elements and literals (e.g., the definitions of an integer and an isotope in Table 1). However, the analysis of simple or commonly-used data elements as functions is often more convenient and efficient.

3. Syntactical operators. These are a small set of superscript symbols listed in Fig. 2. They specify various ways in which the above types of data elements or syntax rules (see below) may be combined.

4. Syntaxes. A syntax is defined by one or more syntax rules, or statements, of the form:

rulename = (combination of data elements, syntactical operators, other "rulenames")

Superscript symbol	Interpretation	Sample expression	Valid data
⁰	or	a⁰b	a b
[...]	optional	a⁰b⁰c	abc ac
(...)	parentheses	(a⁰b)c	ac bc
		a⁰(bc)	a bc
$^{n_1,n_2-k}$	repeat n_1 to n_2 times	^{1,3}digit	5 28 370
"..."	rule name	"rule2"	
'...'	literal	'italic'	italic

Fig. 2. Syntactical operators. Additional operators (not illustrated) may be used to specify the generation of Polish (translated data) based on the data to be analyzed.

Each label enclosed in the rule operators "..." on the right-hand side of such a statement refers to another statement, which must be included as part of the same syntax. Definition of the syntax begins with the master rule "rule = ...". For example:

```
rule  = ..... "alpha" ..... "beta" .....
alpha = ..... "test2" ..... "beta" .....
beta  = .....
test2 = .....
  :
  :
```

With this type of structure it is possible to define a very complex syntax, containing many branches or options, with a relatively simple set of statements.

Application of the Syntax Analysis System

Syntaxes and lists referenced by them are entered on the IRATE keyboard, in the language described above. Each complete syntax is entered as a separate "syntax" section labeled by the name of the syntax; each list is entered in a labeled "list" section. Figure 3 shows an example – the syntax "thalf", applicable to half-life data, and the list "units" referenced by that syntax.

NAME= thalf

TYPE= syntax

rule = 'form1''form2''form3'

form1 = gnumber *units* comment

form2 = 'form4''lessthan'$t_{1/2}$'lessthan''form4'

form3 = '<'s'form4' or '>'z''form4'

form4 = number *units*

lessthan = '<'<'s'

NAME=units

TYPE=list

y

d

h

m

s

ms

μs

ns

ps

fs

as

Fig. 3. Example of a short syntax definition "thalf", applicable to half-life data. Three "functions", denoted by boldface labels, reference subroutines that check for specific data forms:

- gnumber - a "generalized number", which may have a preceding symbol (e.g., ≈, <, >), an uncertainty, and an exponent.
- number - same as gnumber, but no preceding symbol permitted.
- comment - permits any sequence of characters, i.e., a comment.

The lists *units*, referenced in the syntax definition, is shown in the right-hand portion of the figure.

The syntax generator then checks each of the syntaxes and lists for proper structure and completeness, and generates corresponding instructions for checking data. Whenever a given segment of data is to be checked to see if it corresponds to a particular syntax, the syntax analyzer, a group of subprograms added to the data processing program, is called. The syntax analyzer examines the data segment and returns a value that indicates whether or not the data conforms to the specified syntax. The operation of the preprocessor and syntax analyzer are shown in Fig. 1 in somewhat more detail than is provided by the above description.

If desired, the syntax analyzer may also output a "translated" version of the data segment ("Polish"). For example, words could be capitalized, symbols or abbreviations replaced by equivalent forms, etc.: "Co." can be replaced by "Company", "$L_1/L_2/M+N$" by "$L_{II}/L_{III}/M+N$...", "$10^3 e_K/\gamma = 15.7 \pm 1.3$" by "$e_K/\gamma$ 0.0157 *13*". Instructions for the generation of "Polish" may be contained within a list (as substitutions for given items on the list), in the checking functions, or within the syntax statements (by use of special instructions not described here).

The data processing program may call the syntax analyzer to check any part of the data. Use of the syntax analyzer does not preclude additional checking or manipulation of the data by other parts of the program. The syntax analyzer does not alter the data that it checks. (The "Polish", or translated data that it may generate is returned to a location specified by the data processing program.)

Other Applications

The syntax analysis system described here has potential for a broad range of applications. In fact, the initial design was intended as a generator of computer compilers, rather than a data analyzer. [In this design the syntax generator, consisting of the meta-language compiler only, checks the definition of the compiler language; the syntax tables that it generates and the syntax analyzer (parser) together comprise the new compiler; the "input data" to be analyzed is the program to be compiled; and the translated version of this data (Polish) is a set of machine-language instructions ("object code")].

Many other applications suggest themselves. One of the most interesting is a greatly simplified method for machine translation of languages, in which the syntax definitions encompass grammar rules, and the lists contain the dictionary.

References

1. E. Romascan, W. Greiman, C. M. Lederer, and A. Allen, LBL-2366, p. 453 (1974).

2. C. M. Lederer, J. M. Hollander, and L. P. Meissner, UCRL-18530 (1968).

5. Thesis Abstracts

PARITY NON-CONSERVING NUCLEAR FORCE

T. S. Chou

(LBL-2904)

The effect of parity non-conserving nuclear force is studied in a deformed nucleus, ^{180m}Hf. The big nuclear structure factor of the 501 keV gamma transition in the decay of ^{180m}Hf enables one to observe a big asymmetry of 1.5% at an average temperature of 20 mK°. The nuclear structure factor can arise by various mechanisms. For example, small energy spacing of the nuclear levels with opposite parity will cause a large mixing between them and/or the parity-allowed transition (in this case, M2) has an anomalously small matrix element while the parity-forbidden transition (E2) is not hindered. The low temperature necessary for producing polarized nuclei is achieved by adiabatic demagnetization of a chromium potassium sulfate-glycerin slurry which provides about 10 mK° heat sink. The ^{180m}Hf nucleus is polarized by a magnetic interaction of its dipole with the hyperfine field it sees in a cubic ferromagnetic compound, $ZrFe_2$, at low temperature.

The asymmetry is defined as the intensity ratio of the intensity difference in 180° and 0° with respect to its nuclear polarization direction to its average value:

$$a = 2 \cdot \frac{W(180) - W(0)}{W(180) + W(0)} = 2 \cdot \frac{G_1B_1A_1 + G_3B_3A_3}{1 + G_2B_2A_2 + G_4B_4A_4}$$

where G_k are determined from knowing the source-detector geometry; B_k are evaluated from the anisotropy of the 444 keV gamma transition in ^{180m}Hf; A_k are known from the transitions and the nuclear states involved; A_2 and A_4 are independent of parity mixing and their values can be obtained from an angular correlation experiment; A_1 and A_3 are proportional to the parity mixing ratio. So by measuring the asymmetry of the 501 keV gamma transition, one can evaluate the parity mixing ratio. Taking the slow warm-up of the sample into account, we derive the parity mixing ratio as 0.0290(19).

THE USE OF THERMALLY SENSITIVE ION-EXCHANGE RESINS OR ELECTRICALLY SENSITIVE LIQUID CRYSTALS AS ADSORBENTS

James A. Latty

(LBL-2913)

In Part I of this dissertation the desalting of aqueous solutions has been described as experimentally accomplished by thermally cycling a fixed bed of weak-acid and weak-base ion-exchange resins. A rate control model has been proposed which accounts for the observed properties of the mixed resin system. Using this model, several processes have been proposed and evaluated for eventual application to large scale brackish water desalting.

Part II of this work on cyclic sorption contains a description of the experimentally observed sorption properties of randomly oriented, nematic liquid crystal mesophases when subjected to a 3000 gauss magnetic field or a 1000 to 7800 volt per centimeter, D.C. electric field. These experimental observations are evaluated in light of published data for similar systems.

ATOMIC ELECTRONS SHAKE-OFF ACCOMPANYING ALPHA DECAY

'Ieir Shimshon Rapaport

(LBL-2978)

The α spectra associated with K-shell electron shake-off in ^{210}Po and ^{238}Pu decay have been determined by K x-ray - α coincidence measurements. Although the shapes of the spectra generally agree with theoretical expectations, some discrepancies are observed. From similar measurements the α spectra associated with L and M - shell electrons shake-off in ^{210}Po were determined. The abundances per α particle of the total K, L and M electron shake-off effects were determined in these measurements and found to be $P_K = (1.65\pm0.16) \times 10^{-6}$, $P_L = (7.23\pm0.65) \times 10^{-4}$ and $P_M = (1.84\pm0.37) \times 10^{-2}$ for ^{210}Po and $P_K = (0.75\pm0.09) \times 10^{-6}$ for ^{238}Pu. Also, the abundances per α particle of the L subshell electron shake-off effect were found to be $P_{L_1} = (5.11\pm0.40) \times 10^{-4}$, $P_{L_2} = (0.62\pm0.06) \times 10^{-4}$ and $P_{L_3} = (1.50\pm0.19) \times 10^{-4}$. Only limits on the ionizations probabilities of M subshells could be determined. These limits were: $P_{M_2} = 7 - 23\%$, $P_{M_4} < 24\%$, $P_{M_5} < 17\%$ and $P_{M_1} + P_{M_5} > 47\%$ of the total. These results are also compared with theoretical predictions. Further experimental and theoretical studies are suggested.

ELECTRONIC STRUCTURE QUANTUM MECHANICS APPLIED TO SOME SMALL POLYATOMIC MOLECULES

Dean Hemingway Liskow

(LBL-2980)

Quantum mechanics is used to compute ab-initio wavefunctions for several molecular systems in order to derive theoretical estimates for their structure and chemical behavior. The structure of the HO_2 radical is investigated with SCF and CI wavefunctions and is predicted to have a 106.8° bond angle. The bending potential energy for C_3, a species in carbon vapor, is investigated with SCF and CI wavefunctions and the results support the unusually low bending vibrational frequency previously determined experimentally. An SCF wavefunction is used to determine features of the $CH_3NC \rightarrow CH_3CN$ isomerization potential energy surface. And lastly, features of the $C^+ + H_2 \rightarrow CH^+ + H$ reaction potential energy surfaces are determined with CI wavefunctions.

α-TRANSFER STUDIES VIA THE (α, ^{8}Be) REACTION AT HIGH ENERGIES

Gordon John Wozniak

(LBL-2999)

The (α, ^{8}Be) reaction was investigated on ^{16}O, ^{15}N, ^{14}N, ^{12}C, ^{11}B, and ^{10}B targets at bombarding energies between 63.2 and 72.5 MeV with a ^{8}Be identifier of high detection efficiency. Differential cross sections were measured from $\theta_{c.m.} = 20° - 70°$ for solid targets and over a more restricted range for the nitrogen gas targets. An excitation function of the $^{12}C(\alpha, ^8Be)^8Be$ reaction at five bombarding energies between 63.2 and 67.3 MeV was obtained which conclusively demonstrated the direct nature of the (α, ^{8}Be) reaction at high bombarding energies. This reaction was found to proceed predominantly via a direct α-cluster pickup mechanism and to strongly populate only levels consistent with this mechanism. The angular distributions on spin 0 targets exhibited a strong dependence on the value(s) of L, the angular momentum transfer. Experimental distributions for L = 0 and L = 2

transfers were both oscillatory, but with the latter showing a much larger strength at back angles. The distributions for transitions where more than one L-transfer was allowed were approximately constant in magnitude with little structure.

A plane wave diffraction model was used to analyze the cross section data. This model which included finite-range and recoil effects adequately reproduced the L = 0 and L = 2 data from spin 0 targets. However, it failed to describe the shape of the angular distributions for transitions involving more than one L-transfer. The neglect of distortion in these calculations was investigated and found to be unimportant at forward angles ($\theta_{c.m.} < 70°$). Using the above model, relative α-spectroscopic factors were extracted which are in qualitative agreement with those of Kurath.

STUDY OF PARTIAL WAVE BRANCHING IN THE ALPHA DECAY OF ^{241}Am, ^{253}Es AND ^{255}Fm

Arthur James Soinski

(LBL-3411)

Nuclei of ^{241}Am, ^{253}Es and ^{255}Fm were oriented in single crystals of neodymium ethylsulfate at temperatures down to 11 mK. Orientation was detected by alpha particle angular distributions. The temperature dependences of these distributions are consistent with the lowest electronic states of these three actinide ions in the ethylsulfate lattice being similar to those of the corresponding lanthanide ions. Thus magnetic and axial orientation was observed in $Es^{3+}(5f^{10})$, as in $Ho^{3+}(4f^{10})$. Quadrupole orientation was observed in $Am^{3+}(5f^6)$, as in $Eu^{3+}(4f^6)$. In $Fm^{3+}(5f^{11})$ the orientation was magnetic and equatorial, as would be expected from the hyperfine interaction in $Er^{3+}(4f^{11})$. The hyperfine interaction constants were determined. For ^{253}Es we report $|A| = 0.26(3)$ cm^{-1}, for ^{241}Am, $P = -0.0033(6)$ cm^{-1}, and for ^{255}Fm, $|B| = 0.035(7)$ cm^{-1}. The ^{253}Es nuclear magnetic dipole moment was determined to be $|\mu| = 2.7(13)\mu_N$. The Am^{3+} data are consistent with an anti-shielding constant $\gamma_\infty \approx -10^2$, in good agreement with theory, and a shielding factor $\sigma_2 = 0.7$, similar to the value for Eu^{3+}. The nuclear results show that the s and d waves are in phase for the favored α decay branch in all three cases. The relative phase of the g wave was found to be negative for the ^{253}Es decay. Numerical integration of the coupled second-order differential equations describing the favored α decays of ^{253}Es and ^{255}Fm yielded partial wave amplitudes and phases. The results are compared with both intensity and angular distribution data. The measurement of the angular distribution of spontaneous fission fragments from aligned nuclei of ^{253}Es, ^{254}Es and ^{257}Fm are described in a separate appendix. The ^{257}Fm results are consistent with a K quantum number at the outer turning point of either 9/2 or 7/2.

ENZYMATIC UTILIZATION OF WASTE CELLULOSICS

Gautam Mitra and C. R. Wilke

(LBL-2334)

On the land area of the earth about 1.6×10^{10} tons of carbon are fixed every year by photosynthesis out of which about half appears in the form of cellulose. Hydrolysis of one pound of cellulose theoretically yields 1.11 lb. glucose which is equivalent to 0.56 lb. of ethyl alcohol. In the North American continent large amounts of cellulosic wastes are available for economic processing (1,2,3) with their energy equivalence almost equal to a fifth of current U.S. gasoline consumption (4).

In recent years cellulose degradation through enzymatic means has been investigated by various workers (5,6,7), the hydrolysis products being a mixture of simple reducing sugars. These investiagtions, however, have mostly been confined to the realm of basic research. This study presents experimental results on different aspects of the integrated process culminating in an economic process designed for manufacturing reducing sugar solution by enzymatic hydrolysis of waste cellulosic material.

The cellulose molecule is a high molecular weight polymer of β-1, 4 linked D-glucose residues. The chemical structure is represented as shown in Fig. 1.

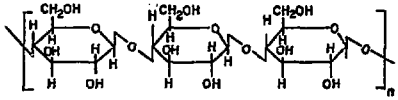

Fig. 1. (XBL 756-1597)

Degree of polymerization varies widely depending upon its origin. For chemical pulp and filter paper the degree of polymerization generally varies between 500 and 1000 whereas in wood cellulose it is about 8000-10,000. During enzymatic hydrolysis by cellulase enzyme β-1, 4 glucosyl bonds are split to produce reducing sugars according to

$$(C_6H_{10}O_5)_x + xH_2O \rightarrow x\ C_6H_{12}O_6.$$

The term "cellulase" is used to designate a complex system of enzymes (molecular weight range 12,000-68,000) showing various types of activities with respect to different kinds of substrates. The mechanism of degradation of crystalline cellulose by enzymatic means has been the object of intense study for the last 25 years. The most accepted postulate in this area has been the 2-step C_1-C_x theory proposed by Reese et al., (8). According to this theory the C_1 component of the enzyme first disintegrates the cellulose chain prior to its solubilization. The subsequent hydrolytic action at the β-1, 4 linked glucosyl bonds of the solubilized chain is attributed to the C_x component of the enzyme. Certain micro-organisms grow only on soluble cellulose, such as carboxymethyl cellulose, and synthesize only C_x components, whereas other microorganisms are capable of growing on highly ordered forms of cellulose and produce both C_1 and C_x. The fungus, Trichoderma viride was selected for the present study because of its high C_1 productivity during growth on insoluble cellulose (5, 7) along with an adequate production of C_x.

Cellulase activities are measured by interacting a given substrate with the enzyme and measuring the amount of reducing sugar produced in a given time. The tests are as follows:

C_1- Cotton: This test measures C_1 activity; 50 mg of adsorbent cotton is added to 1 ml appropriately diluted enzyme and 1 ml of 0.05 M sodium citrate buffer at pH 4.8. Reaction is carried out at 50°C for 24 hours and amount of reducing sugar produced measured by dinitrosalicylic acid test.

Filter Paper Activity: This test measures combined C_1-C_x activity. Fifty mg (1×6 cm) of Whatman filter paper no. 1 is added to a mixture of 1 ml of appropriately diluted enzyme and 1 ml of 0.05 M sodium citrate buffer at pH 4.8. Reaction is carried out ar 50°C for 1 hour and reducing sugar concentration determined by dinitrosalicylic acid test.

C_x Activity: This test determines β(1-4) glucanase activity. To 0.5 ml of 1.0% carboxymethylcellulose (CMC, 50T, Hercules Powder Co.) in 0.05 M sodium citrate buffer (pH 4.8) 0.5 ml of appropriately diluted enzyme is added and reaction carried out at 50°C for 1/2 hour followed by reducing sugar determination by dinitrosalicylic acid test.

Trichoderma viride, a highly productive mutant developed at the U.S. Army Laboratory at Natick, Massachusetts, was grown in a fermentation system (Figure 7) for the production of cellulase. Enzyme characteristics were examined in a stirred ultrafiltration cell and gel filtration column. Strong synergistic action among various fractions of C_x above and below molecular weight of 30,000 was noticed. C_1 activity was strongly dependent upon simultaneous presence of C_x activity in the enzyme solution. A low cost growth medium was developed (Figure 18). For the growth of the fungus, substituting chemical grade analytical reagents with commercial fertilizers. Specific oxygen demand for fungal growth on soluble sugars was determined to be 1.04 $\frac{\text{millimoles oxygen}}{\text{gm. dry weight} \times \text{h}}$. Single stage C.S.T.R. runs (Figure 21) with 1% soluble sugar yielded a maximum cell productivity of 0.92 $\frac{\text{mg. dry weight}}{\text{ml} \times \text{hr}}$ at a dilution rate of 0.21 hr^{-1}. The corresponding maximum specific growth rate from unsteady state observations

(Figure 20) was found to be 0.294 hr^{-1}. Two states C.S.T.R. runs were conducted with cell growth on glucose in the first stage and enzyme induction by cellulose addition in the second stage. From the results shown in Figure 24 the enzyme productivity for this mode of operation was determined to be 27.3×10^{-3} $\frac{\text{Filter paper activity for}}{\text{ml} \times \text{hr}}$ 1% dextrose as growth medium and 1% pure cellulose as inducer.

Hydrolysis of -200 mesh ball milled newsprint at 50°C and 4.80 pH with enzyme of 2.70 F.P. activity resulted in 82% conversion of cellulose in 40 hours. Adsorption characteristics of the enzyme on the fully ground solids and on the spent solids following hydrolysis were experimentally measured (Figure 31, Figure 32) at 50°C. Based on the experimental data a process for manufacturing reducing sugar solutions from waste paper was formulated.

Economic analysis was carried out for this process with a waste cellulosic feed of 833 tons/day (dry basis). Excluding the cost of the waste cellulosics the net manufacturing cost for reducing sugars was estimated at 1 ¢/lb with a total plant investment of $10,134,000.

6. 1974 Publications

PAPERS PUBLISHED AND LBL REPORTS ISSUED, 1974

ADOLPHE, A., (see Savigny, N., LBL-1656)

ALONSO, J., (see Tamura, T., LBL-1689)

ALONSO, C. T
The Dynamics of Viscous Nuclear Drops
LBL-2993, August 1974
(Presented in part at the International Colloquium on Drops and Bubbles, Pasadena, California, August 28-30, 1974)

ALONSO, C. T., (see Ghiorso, A., LBL-2998)

ALONSO, J. R., (see Ghiorso, A., LBL-2998)

ARTZY, M., Asaro, F. and Perlman I.
The origin of the "Palestinian" bichrome ware
LBL-1286, October 1972
J. Am. Oriental Soc. 93.4, 446 (1973)

ARTZY, M., Asaro, F., and Perlman, I.
Alašiya of the Amarna Letters
LBL-2375, June 1974
J. of Near Eastern Studies

ARTZY, M., Asaro, F., and Perlman, I.
Consideration of the Tel Nagila Bichrome Ware Krater as a Cypriote Product
LBL-2914, May 1974
J. Israel Exploration

ARVIEUX, J., Birchall, J., Conzett, H. E., Dahme, W., Haeberli, W., and Larimer, R. M.
Is the $^{12}C(\vec{d},d_0)$ Reaction a Good Polarization Standard?
LBL-2353, January 1974
Nucl. Instr. Methods 116, 605 (1974)

ARVIEUX, J., (see Birchall, J., LBL-2967)

ARVIEUX, J., (see Birchall, J., LBL-3425)

ASARO, F., (see Artzy, M., LBL-1286)

ASARO, F., (see Artzy, M., LBL-2375)

ASARO, F., (see Michel, H. V., LBL-2387)

ASARO, F., (see Artzy, M., LBL-2914)

ASARO, F., (see Rapaport, M. S., LBL-2962)

ASARO, F., (see Bowman, H., LBL-2966)

ASARO, F., (see Mark, R. K., LBL-3449)

ASCUITTO, R. J., (see Glendenning, N. K., LBL-1647)

ATCHER, R. W., (see Huizenga, J. R., LBL-2314)

ATCHER, R. W., (see Huizenga, J. R., LBL-2316)

BABINET, R., (see Nifenecker, H., LBL-1950)

BABINET, R. P., (see Moretto, L. G., LBL-2332)

BABINET, R. P., (see Thompson, S. G., LBL-2940)

BABINET, R. P., (see Moretto, L. G., LBL-3444)

BACHER, A. D., (see Macdonald, J. A., LBL-2317)

BACHER, A. D., (see de Swiniarski, R., LBL-2322)

BACON, F., (see Kaindl, G., LBL-1960)

BANNA, M. S., (see Davis, D. W., LBL-1909)

BANNA, M. S., Mills, B. E., Davis, D. W., and Shirley, D. A.
X-Ray Photoemission Molecular Orbitals of Hydrogen Fluoride and the Fluorinated Methanes.
LBL-2930, June 1974
J. Chem. Phys. 61, 4780 (1974)

BARTUNIK, H. D. and Kaindl, G.
Mössbauer Isomer Shifts in Chemical Systems of Gold
LBL-3438, September 1974
(To be published as a Chapter in book entitled, "Mössbauer Isomer Shifts," G. K. Shenoy and F. E. Wagner, eds., North-Holland Publishing Company)

BASKIN, C. P., Bender, C. F., Bauschlicher, C. W. Jr., and Schaefer, H. F. III
Reaction Pathways for the Triplet Methylene Abstraction $CH_2(^3B_1) + H_2 \rightarrow CH_3 + H$
LBL-2324, November 1973
J. Am. Chem. Soc. 96, 2709 (1974)

BASKIN, C. P., (see Yarkony, D. R., LBL-1969)

BASKIN, C. P., (see Schwenzer, G. M., LBL-1983)

BATES, H. (see Ruben, H., LBL-2358)

BAUSCHLICHER, C. W., Jr., (see Bender, C. F., LBL-2344)

BAUSCHLICHER, C. W., Jr., (see Baskin, C. P., LBL-2324)

BECCHETTI, F. D., Kovar, D. G., Harvey, B. G., Hendrie, D. L., Homeyer, H., Mahoney, J., von Oertzen, W., and Glendenning N. K.
Two-Proton-Transfer Reactions $^{208}Pb(^{12}C,^{10}Be)^{210}Po$ and $^{208}Pb(^{16}O,^{14}C)^{210}Po$
LBL-1972, August 1973
Phys. Rev. C 9, 1543 (1974)

BECCHETTI, B. G., Harvey, D., Kovar, J., Mahoney, J., and Zisman, M. S.
$(^{16}O,^{15}N)$ and $(^{12}C,^{11}B)$ Reactions on ^{54}Fe and ^{62}Ni at $E(^{16}O) = 104$ MeV and $E(^{12}C) = 78$ MeV.
LBL-2957, June 1974
Phys. Rev. 10, 1846 (1974)

BECCHETTI, F. D., (see DeVries, R. M., LBL-2363)

BEHKAMI, A. N., (see Huizenga, J. R., LBL-2314)

CERNY, J. (see Macdonald, J. A., LBL-2317)

CERNY, J. (see Jelley, N. A., LBL-2329)

CERNY, J. (see Wozniak, G. J., LBL-2374)

CERNY, J. (see Sextro, R. G., LBL-1955)

CERNY, J., Jelley, N. A., Hendrie, D. L., Maguire, C. F., Mahoney, J., Scott, D. K. and Weisenmiller, R. B.
A More Accurate Mass for ^{9}He
LBL-2984, August 1974
Phys. Rev. C 10, 2654 (1974)

CERNY, J. Weisenmiller, R. B., Jelley, N. A., Wilcox, K. H. and Wozniak, G. J.
^{7}Li + ^{7}Li Reaction Studies Leading to Multi-Neutron Final States
LBL-3407, September 1974
Phys. Letts 53B, 247 (1974)

CERNY, J. (see Jelley, N. A., LBL-3414)

CHINTALAPUDI, S., (see Rad, F. N., LBL-2959)

CHOU, T. S., (Ph.D. Thesis)
Parity Non-Conserving Nuclear Force
LBL-2904, March 1974

CHOU, T. S., Krane, K. S., and Shirley, D. A.
Another Nuclear Orientation Measurement of Parity Admixture in the 501-keV Gamma Transition in ^{180}Hfm
LBL-3408, September 1974
Phys. Rev. C

CHU, B., (see Bucher, J., LBL-611)

CLEM, R. G. and Sciamanna, A. F.
Styrene Impregnated ^{60}Co Irradiated, Graphite Electrode for Anodic Stripping Analysis
LBL-2108 (Rev.), September 1974
Analytical Chem., 47, 276 (1975)

CLEM, R. G., and Sciamanna, A. F.
"Styrene Impregnated, Cobalt-60 Irradiated, Graphite Electrode for Anodic Stripping Analysis)

COATS, R. R. (see Mark, R. K., LBL-3449)

COHEN, M. L., (see Varea de Alvarez, C., LBL-2330)

COLOMBANI, P., (see Ward, D., LBL-3446)

CONOCCHIOLI, T. J., (see Bucher, J. J., LBL-2351)

CONWAY, J. G., (see Van Deurzen, C. H. H., LBL-1975)

CONWAY, J. G., (see Van Deurzen, C. H. H., LBL-1986)

CONZETT, H. E., (see de Swiniarski, R., LBL-1620)

CONZETT, H. E., (see Lamontagne, C. R., LBL-1941)

CONZETT, H. E., (see Arvieux, J., LBL-2353)

CONZETT, H. E.
Polarization-Analyzing Power Theorem for (p,n) Transitions Between Members of an Isospin Multiplet
LBL-2371, February 1974
Phys. Letters 51B, 445 (1974)

CONZETT, H. E., (see Rad, F. N., LBL-2939)

CONZETT, H. E., (see Mayer, B., LBL-2340)

CONZETT, H. E., (see Rad, F. N., LBL-2959)

CONZETT, H. E., (see Birchall, J. LBL-2967)

CONZETT, H. E.
Polarization Phenomena in the Three-Nucleon System
LBL-2995, August 1974
(Presented at the Internation Confere ce on Few Body Problems in Nuclear and Particle Physics, Quebec, Canada August 27-31, 1974)

CONZETT, H. E., (see Rad, F. N., LBL-3418)

CONZETT, H. E., (see Birchall, J., LBL-3425)

CONWAY, J. G., Blaise, J., and Verges, J.
The Infrared Spectrum of Curium-44
LBL-3401, September 1974
Spectro Chimica Acta. B

CRAMER, J. G., (see DeVries, R. M., LBL-2363)

DAHME, W., (see Arvieux, J., LBL-2353)

DAHME, W., (see Mayer, B., LBL-2340)

DAHME, W., (see Birchall, J., LBL-2967)

DAHME, W., (see Birchall, J., LBL-3425)

DAVENPORT, I. F. and King, C. J.
The Onset of Natural Convection from Time-Dependent Profiles
LBL-1999, October 1973
Int. J. Heat Mass Transfer 17, 69 (1974)

DANIELS, M., and Jayko, M. E.
Luminescence From the Peptide Group
LBL-2383, March 1974
Presented at the International Conference on the Excited States of Biological Molecules, Lisbon, Portugal, April 18, 1974

DAVIS, D. W., Banna, M. S. and Shirley, D. A.
Core-Level Binding Energy Shifts in Small Molecules
LBL-1909, July 1973
J. Chem. Phys. 60, 237 (1974)

DAVIS, D. W., and Shirley, D. A.
The Prediction of Core-level Binding-energy Shifts from CNDO molecular orbitals
LBL-1970, August 1973
J. Electr. Spectrosc. 3 137 (1974)

GIAUQUE, R. D., Goda, L. Y., and Garrett, R. B.
X-ray-Induced X-Ray Fluroescence Analysis of Suspended Air Particulate Matter.
LBL-2951, July 1974
NFP as of yet.

GIZON, A., (see Gizon, J., LBL-1948)

GIZON, A , (see Proetel, D., LBL-2349)

GIZON, J., Gizon, A., Maier, M. R., Diamond, R. M., and Stephens, F. S.
Deformed States of Neutron-Deficient Cerium and Neodymium nuclei
LBL-1948, July 1973
Nucl. Phys. A222, 557 (1974)

GIZON, J., (see Proetel, D., LBL-2349)

GLENDENNING, N. K., and Nagarajan, M. A.
Exact Treatment of the DWBA by Analytic Means for Particle Transfer Between Heavy Ions
LBL-2378, March 1974
Nucl. Phys., A236 (1974)

GLENDENNING, N. K.
Classical and Quantum Mechanical Descriptions of Heavy-Ion Interactions
LBL-2905, June 1974
Invited paper for the International Conference on Reactions Between Complex Nuclei, Nashville, Tennessee, June 10-14, 1974

GLENDENNING, N. K., (see Becchetti, F. D., LBL-1972)

GODA, L. Y., (see Giauque, R. D., LBL-1697)

GODA, L. Y. (see Giauque, R. D., LBL-2951)

GOUGH, R. A., (see Sextro, R. G., LBL-1955)

GOULD, H., Marrus, R., and Mohr, P. J.
Radiative Decay of the 2^3S_1 and 2^3P_2 States of Helium-Like Vanadium (Z = 23) and Iron (Z = 26)
LBL-2906, June 21, 1974
Phys. Rev. Letts. 33, 676 (1974)

GOULDING, F. S., and Harvey, B. G.
Identification of Nuclear Particles
LBL-2952, February 1974
Ann. Rev. of Nucl. Sci.

GRADL, R., and Edelstein, N.
Reactions of Dithiolate Ligands with Uranium (IV) Halides
LBL-3404, September 1974
J. of Organometalic Chem.

GRÄF, H.
Parabolic Cylinder Functions W(a >, ± X): Expansions for All Arguments
LBL-2969, August 1974
Mathematics of Computation

GRANT, R. W., (see Varea de Alvarez, C., LBL-2330)

HADEISHI, T., (see Yellin, J., LBL-1602)

HAEBERLI, W., (see Arvieux, J., LBL-2353)

HALBACH, K.
A Magnetic Field Clamp with Beneficial Saturation Effects
LBL-2370, February 1974
Nucl. Instr. Methods 119, 327 (1974)

HALBACH, K.
Rapid Measurement of the Effective Field Boundary of Homogeneous Field Magnets
LBL-2388, March 1974
Nucl. Instr. Methods 119, 329 (1974)

HARDY, J. C., (see Macdonald, J. A., LBL-2317)

HARNEY, H. L., (see Macdonald, J. A., LBL-2317)

HARVEY, B. G., (see Becchetti, F. D., LBL-1972)

HARVEY, B. G., (see DeVries, R. M., LBL-2363)

HARVEY, B. G., (see Homeyer, H., LBL-2377)

HARVEY, B. G. (see Goulding, B. G., LBL-2952)

HARVEY, B. G., (see Becchetti, F. D., LBL-2957)

HARVEY, B. G., (see Scott, D. A., LBL-2996)

HAUSTEIN, P. E , (see Massmann, H., LBL-1693)

HEBERT, A., (see Bowman, H., LBL-2966)

HELD, E. R., (see Bucher, J. J., LBL-2351)

HENDRIE, D. L., (see Becchetti, F. D., LBL-1972)

HENDRIE, D. L., (see deSwiniarski, R., LBL-2322)

HENDRIE, D. L., (see Yagi, K., LBL-2982)

HENDRIE, D. L., (see Cerny, J., LBL-2984)

HENDRIE, D. L., (see Scott, D. A., LBL-2996)

HEUNEMANN, D., (see Moretto, L. G., LBL-1966)

HILF, E. R., (see Küpper, W. A., LBL-642)

HOLLANDER, J. M., (see Jardine, L. J., LBL-245)

HOLLANDER, J. M., (see Lederer, C. M., LBL-1261)

HOLLANDER, J. M., (see Lederer, C. M., LBL-1262)

HOMEYER, H., (see Becchetti, F. D., LBL-1972)

HOMEYER, H., (see DeVries, R. M., LBL-2363)

HOMEYER, H., Mahoney, J., and Harvey, B. G.
Improvements to Resistive-Wire Focal Plane Detector
LBL-2377, February 1974
Nucl. Instr. Methods (Letter to editor) 118, 311-312 (1974)

HU, C. L. (see Mark, R. K., LBL-3449)

MACDONALD, J. A., Cerny, J., Hardy, J. C., Harney, H. L., Bacher, A. D., and Plattner, G. R.
Analyzing Powers for Two-Nucleon Transfer Reactions in the lp-Shell
LBL-2317, October 1973
Phys. Rev. C9, 1694 (1974)

MAGUIRE, C. F. (see Yagi, K., LBL-2982)

MAGUIRE, C. F., (see Cerny, J., LBL-2984)

MAGUIRE, C. F. (see Scott, D. A., LBL-2996)

MAHONEY, J. (see Becchetti, F. D., LBL-1972)

MAHONEY, J. (see Homeyer, H., LBL-2377)

MAHONEY, J. (see Becchetti, F. D., LBL-2957)

MAHONEY, J. (see Yagi, K., LBL-2982)

MAHONEY, J., (see Cerny, J., LBL-2984)

MAHONEY, J. (see Scott, D. A., LBL-2996)

MAIER, M. R. (see Gizon, J., LBL-1948)

MAIER, M. R. (see Proetel, D., LBL-2349)

MAIER, M. R., (see Tjøm, P. O., LBL-2379)

MANG, H. J., (see Ring, P., LBL-2968)

MARK, R. K., Hu, C. L., Bowman, H. R., Asaro, F., McKee, E. H., and Coates, R. R.
Recently (< 10^9 Y) Depleted Radiogenic (87/86 Sr ~ 0.706) Mantle, Source of Ocean Ridge-Like Tholeiite, Northern Great Basin
LBL-3449, November 1974
Geochimica et Cosmochimica Acta

MARKOWITZ, S. S., (see Parsa, B., LBL-1901)

MARKOWITZ, S. S., (see Parsa, B., LBL-1902)

MARKOWITZ, S. S., (see Fee, D. C., LBL-1910)

MARKOWITZ, S. S. (see Fee, D. C., LBL-1949)

MARKOWITZ, S. S., (see Jacob, N. P., Jr., LBL-2381)

MARKOWTIZ, S. S. (see Jacob, N. P., Jr., LBL-2381 (Rev.))

MARRUS, R., (see Gould, H., LBL-2906)

MARSHALEK, E. R. (see Bose, S., LBL-2963)

MARTIN, R. L., and Shirley, D. A.
The Relation of Core-Level Binding Energy Shifts to Proton Affinity and Lewis Basicity
LBL-2341, December 1973
J. Am. Chem. Soc. 96, 5299 (1974)

MASSMANN, H., Rasmussen, J. O., Ward, T. E., Haustein, P. E., and Bernthal, F. M.
Configuration Mixing of Two-Quasiparticle States in Even-Even Deformed Nuclei
LBL-1693, June 1973
Phys. Rev. C9, 6 (1974)

MASSMANN, H., and Rasmussen, J. O.
Uniform Semiclassical Orbital Calculations of Heavy Ion Coulomb Excitation
LBL-3440, November 8, 1974
Nucl. Phys. B

MAYER, B., Conzett, H. E., Dahme, W., Kovar, D. G., Larimer, R. M., Leemann, C.
j-Dependence of the Vector Analyzing Power for (d,^{3}He) and (d,t) Reactions
LBL-2340, December 1973
Phys. Rev. Letters, 32, 1452 (1974)

MEYERHOF, W. E., (see Tjøm, P. O., LBL-2931)

MEYER ter VEHN, J., Stephens, F. S., and Diamond, R. M.
Evidence for Asymmetric Shapes From High-Spin Odd-A Spectra
LBL-2394, March 1974
Phys. Rev. Letters 32, 1383 (1974)

MEYER ter VEHN, J.
Rotational Band-Structures in Transitional Odd-A Nuclei
LBL-3416, September 19, 1974
Phys. Rev. Letts.

MICHEL, H. V., Frierman, J. D. and Asaro, F.
Chemical Composition Patterns of Ceramic Wares From Fustāt Egypt
LBL-2387, March 1974
Archaeometry

MICHEL, M. C., (see Yellin, J., LBL-1602)

MILLS, B. E., (see Banna, M. S., LBL-2930)

MITRA, G., and Wilke, C. R.
Enzymatic Utilization of Wastes Cellulosic
LBL-2334, January 1974
Ph.D. Thesis

MITRA, G., and Wilke, C. R.
Continuous Cellulase Production
LBL-2365, February 1974
Biotech. & Bioeng.

MOHR, P., (see Gould, H., LBL-2906)

MORETTO, L. G. and Kataria, S. K.
Superfluid Properties of Excited Nuclei Arising From a δ-Force Residual Interaction
LBL-1942, September 1973
Lettere al Nuovo Cimento 9, 190 (1974)

MORETTO, L. G.
Influence of Pairing and of the Spin Projection Distribution on the "Classical" Isothermal Rotations of a Nucleus
LBL-2321, January 1974
Nucl. Phys. A226, 9 (1974)

MORETTO, L. G., and Babinet, R. P.
Large Superfluidity Enhancement in the Penetration of a Fission Barrier
LBL-2332, January 1974
Phys. Letters 49B, 147 (1974)

MORETTO, L. G.
Statistical Properties of a Paired Nucleus With Fixed Quasi-particle Number
LBL-2368, March 1974
Phys. Letters 51B, 35 (1974)

MORETTO, L. G., Babinet, R. P., Galin, J., and Thompson, S. G.
Experimental Evidence of a Diffusion Process Associated with the Mass Asymmetry Degree of Freedom in Heavy Ion Reactions
LBL-3444, November 1974
Phys. Letters B

MORETTO, L. G., (see Thompson, S. G., LBL-2940)

MORETTO, L. G.
Thermodynamical Properties of a Paied Nucleus with a Fixed Number of Quasi-Particles
LBL-2994, September 1974
Nucl. Phys. A

MORETTO, L. G., Heunemann, D., Jared, R. C., Gatti, R. C., and Thompson, S. G.
Study of a Fission-Like Environment in Reactions With Very Heavy Ions
LBL-1966, July 1973
Third Symposium on the Physics and Chemistry of Fission, Rochester, New York, August 13-17, 1973)
Physics & Chem. of Fission, Vol II, 351, (1973)

MYERS, W. D., and Swiatecki, W. J.
The Nuclear Droplet Model for Arbitrary Shapes
LBL-1957, July 1973
Annals of Phys. 84, 186 (1974)

MYERS, W. D.
Macroscopic Aspects of Heavy-Ion Reactions
LBL-2945 June 1974
(Invited talk presented at the International Conference on Reactions Between Complex Nuclei, Nashville, Tennessee, June 1974)

NAGARAJAN, M. A.
Heavy Ion Induced Transfer Reactions Leading To Weakly Bound Final States
LBL-2918, May, 1974
Phys. Letters 52B, 395 (1974)

NAGARAJAN, M. A., (see Glendenning, N. K., LBL-2378)

NAGARAJAN, M. A., and Wang, W. L.
Pion-Nucleus Charge Exchange Reactions in the Isobar-Doorway Model
LBL-2934, June 1974
Phys. Rev. C10, 2125 (1974)

NAGARAJAN, M. A., and Wang, W. L.
Coupled-Channel Pion-Nucleus Charge Exchange Reactions
LBL-2958, June 1974
Phys. Rev. C

NAGARAJAN, M. A., (see Kleber, M., LBL-2973)

NAGARAJAN, M. A. and Wang, W. L.
A Separable Expansion for the Nuclear Form Factors
LBL-2986, August 1974
Phys. Rev. C10, 2206 (1974)

NAKAI, K., Proetel, D., Diamond, R. M., and Stephens, F. S.
Lifetimes and g-Factors in Decoupled Bands
LBL-2389, March 1974
Phys. Rev. Letters 32, 1380 (1974)

NAKAMURA, M., and Shalimoff, G. V.
Four Function Calculator Used to Automatically Compute Wavelength
LBL-2331 Rev., March 1974
Applied Spectroscopy (as a Note), 28, 581 (1974)

NARDI, E., (see Kataria, S. K., LBL-1905)

NAUMANN, R. A., (see Krien, K., LBL-1652)

NEWTON, J. O., Stephens, F. S., and Diamond, R. M.
Rotational Bands in the Light Odd-Mass Thallium Nuclei
LBL-2333, January 1974
Nucl. Phys.

NIFENECKER, H. (see Jared, R. C., LBL-1963)

NIFENECKER, H., Signarbieux, C., Babinet, R., and Poitou, J.
Neutron and Gamma Emission in Fission
LBL-1950, July 1973
Third Symposium on the Physics and Chemistry of Fission, Rochester, New York, August 13-17, 1973)
"Physics and Chemistry of Fission, 1973" Vol. II, 117 (1973)

NITSCHKE, J. M., (see Ghiorso, A., LBL-2998)

NIX, J. R., (see Krappe, H. J., LBL-1920)

NORRIS, A. E., (see Kratz, J. V., LBL-2947)

NURMIA, M., (see Eskola, P., LBL-2315)

NURMIA, M., (see Ghiorso, A., LBL-2998)

OLOVSSON, I., (see Ruben, H., LBL-1931)

OLSEN, C. E., (see Krane, K. S., LBL-2354)

O'NEIL, S. V., (see Yarkony, D. R., LBL-1969)

O'NEIL, S. . ., (see Schwenzer, M., LBL-1983)

OWAIS, M., (see Scott, A., LBL-672)

PARSA, B., and Markowitz, S. S.
Determination of Lead in Atmospheric Air and in Aluminum by Helium-3-Induced Nuclear Reactions
LBL-1901, June 1973
Anal. Chem. 46, 186 (1974)

PARSA, B., and Markowtiz, S. S.
The Half-Life and the α-Decay Branching Ratio of ^{207}Po
LBL-1902, June 1973
J. Inorg. Nucl. Chem. 36, 1429 (1974)

PARSONS, T. C., (see Starks, D. F., LBL-3422)

PEARSON, P. K. (see Dykstra, C. E., LBL-2983)

PEARSON, P. K., Schaefer, H. F., III, and Wahlgren, U.
Potential Energy Surface for the Model Unimolecular Reaction HNC → HCN
LBL-3402, September 1974
J. of Chem. Phys., 62, 350 (1975)

PERLMAN, I., (see Artzy, M., LBL-1286)

PERLMAN, I., (see Artzy, M., LBL-2375)

PERLMAN, I., (see Artzy, M., LBL-2914)

PERLMAN, I., (see Rapaport, M. S., LBL-2962)

PETROVICH, F., (see Scott, A., LBL-672)

PLATTNER, G. R., (see Macdonald, J. A., LBL-2317)

POITOU, J., (see Nifenecker, H., LBL-1950)

POLLAK, R. A., (see Ley, L., LBL-1688)

POLLAK, R. A., (see Kowalczyk, S. P., LBL-1916)

POLLAK, R. A., (see Kowalczyk, S. P., LBL-1945)

POLLAK, R. A., Ley, L., McFeely, F. R., Kowalczyk, S. P., and Shirley, D. A.
Characteristic Energy Loss Structure of Solids From X-Ray Photoemission Spectra
LBL-1971, September 1973
J. Electr. Spectrosc. 3, 381 (1974)

POLLAK, R. A., (see McFeely, F. R., LBL-1989)

POSKANZER, A. M., (see Bowman, J. D., LBL-1967)

POSKANZER, A. M., (see Zebelman, A. M., LBL-3427)

PROETEL, D., Diamond, R. M., Kienle, P., Leigh, J. R., Maier, K. H., and Stephens, F. S.
Evidence for Strongly Deformed Shapes in ^{186}Hg
LBL-1939, June 1973
Phys. Rev. Letters 31, 896 (1974)

PROETEL, D., Diamond, R. M., and Stephens, F. S.
High-Spin Excitation Modes in Even Hg Nuclei
LBL-2380, March 1974
Nucl. Phys. A231, 301 (1974)

PROETEL, D., Benson, D., Jr., Gizon, A., Gizon, J., Maier, M. R., Diamond, R. M., and Stephens, F. S.
Decoupled Bands in Odd-Mass Mercury Isotopes
LBL-2349, January 1974
Nucl. Phys. A226, 237 (1974)

PROETEL, D., (see Nakai, K., LBL-2389)

PRUSSIN, S. G., (see Jardine, L. J., LBL-245)

QUARLES, W. G., Templeton, D. H., and Zalkin, A.
The Crystal and Molecular Structure of Melatonin
LBL-1933, June 1973
Acta Cryst. B30, 99 (1974)

QUARLES, W. G., Templeton, D. H., and Zalkin, A.
The Crystal and Molecular Structure of 5-Methoxytryptamine
LBL-1934, June 1973
Acta Cryst. B30, 95 (1974)

RAD, F. N., Saylor, D. P., and Jain, M.
Final State Interaction in Three Nucleon System
LBL-2935, July 24, 1974
(To be presented at the International Conference on Few Body Problems in Nuclear and Particle Physics, University of Laval, Quebec, Canada, August 27-31, 1974)

RAD, F. N., Birchall, J., Conzett, H. E., Chintalapalli, S., and Roy, R.
The Vector Analyzing Power in d-p Scattering at 45.4 MeV and The Nucleon Nucleon Interaction
LBL-2959, July 1974
Phys. Rev. Letters 33, 1227 (1974)

RAD, F. N., Birchall, J., Conzett, H. E., and Roy, R.
Polarization Transfer in Proton-Deuteron Elastic Scattering
LBL-2939, June 1974
(To be presented at the International Conference on Few Body Problems in Nuclear and Particle Physics, Quebec, Canada, August 27-31, 1974)

RAD, F. N., (see Birchall, J., LBL-2967)

RAD, F. N., Birchall, J., Conzett, H. E. and Roy, R.
Vector-to-Vector Polarization Transfer in Deuteron-Proton Elastic Scattering
LBL-3418, September 1974
Phys. Rev. Letts., 33, 1579 (1974)

RANDRUP, J.
Spontaneous-Fission Inertial-Mass Functions in the Actinide Region
LBL-2385, February 1974
Phys. Rev. C

RANDRUP, J.
The Nuclear Seyler-Blanchard Model in the Hartree Approximation
LBL-3413, September 1974
Nucl. Phys. A.

RAPAPORT, M. S., Asaro, F., and Perlman, I.
K-Shell Electron Shake-Off Accompanying Alpha Decay
LBL-2962, July 1974
Phys. Rev. C

RAPAPORT, M. S., (Ph.D. Thesis)
Atomic Electrons Shake-Off Accompanying Alpha Decay
LBL-2978, September 1974

RASMUSSEN, J. O., (see Krien, K., LBL-1652)

RASMUSSEN, J. O., (see Ma, C. W., LBL-1677)

RASMUSSEN, J. O., (see Tamura, T., LBL-1689)

RASMUSSEN, J. O., (see Massmann, H., LBL-1693)

RASMUSSEN, J. O., (see Shihab-Eldin, LBL-3409)

RASMUSSEN, J. O., (see Massmann, H., LBL-3440)

RAY, S., Zalkin, A., and Templeton, D. H.
Crystal Structures of the Fluosilicate Hexahydrates of Cobalt, Nickel, and Zinc
LBL-1932, June 1973
Acta Cryst. B29, 2741 (1973)

RAY, S., Zalkin, A., and Templeton, D. H.
Crystal Structure of Copper Fluosilicate Hexahydrate
LBL-1935, June 1973
Acta Cryst. B29, 2748 (1973)

RESMINI, F. G., (see deSwiniarski, R., LBL-2322)

REZANKA, I., (see Tamura, T., LBL-1689)

RINNEBERG, H. H., and Shirley, D. A.
Perturbed Angular Correlation of $^{111}Cd^{m}$ in Antiferromagnetic MnF_2, FeF_2, CoF_2 and NiF_2
LBL-2398, April 1974
Phys. Rev. B11, 248 (1975)

REZANKA, I., (see Krien, K., LBL-1652)

RING, P., and Mang, H. J.
Attenuation of the Coriolis Interaction Within the Cranking Model
LBL-2968, July 1974
Phys. Rev. Letters 33, 1174 (1974)

RINNEBERG, H. H., and Shirley, D. A.
Supertransferred Hyperfine Interaction: Perturbed Angular Correlation of ^{111m}Cd in Antiferromagnetic NiO, CoO, and MnO
LBL-2900, April 1974
Physical Review B

RINNEBERG, H. H., Schwartz, G. P., and Shirley, D. A.
Paramagnetic Shifts and Spin-Flop in Superttransferred Hyperfine Structure of ^{111m}Cd in $RbMnF_3$
LBL-2979, August 1974
Phys. Letts. 50A, 69 (1974)

ROBINSON, C. W. and Wilke, C. R.
Simultaneous Measurement of Interfacial Area and Mass Transfer Coefficients for a Well-Mixed Gas Dispersion in Aqueous Electrolyte Solutions
LBL-2399, March 1974
A. I. Ch. E. J. 20, 285 (1974)

ROY, R., (see Rad, F. N., LBL-2939)

ROY, R., (see Rad, F. N., LBL-2959)

ROY, R., (see Birchall, J., LBL-2967)

ROY, R., (see Rad, F. N., LBL-3418)

RUBIN, H., Olovsson, I., Zalkin, A., and Templeton, D. H.
Sodium Chromate Tetrahydrate
LBL-1931, June 1973
Acta Cryst. B29, 2963 (1973)

RUBEN, H., Zalkin, A., and Templeton, D. H.
N,N'-Bis-(2,2,6,6-Tetramethylpiperidy1-4)-Succinic Acid Diamide Dihydrate
LBL-1936, June 1973
Acta Cryst. B30, 334 (1974)

RUBEN, H., Bates, H., Zalkin, A., and Templeton, D. H.
2, 4, 4-Triphenyl-1,2-Diazetidine-3-One-1-Carboxylic Acid, Ethyl Ester
LBL-2358, January 1974
Acta Cryst. B30, 1631 (1974)

RUBEN, H., Zalkin, A., Faltens, M. O., and Templeton, D. H.
Crystal Structure of Sodium Gold (I) Thiosulphate Dihydrate, $Na_3Au(S_2O_3)_2 \cdot 2H_2O$
LBL-2369, February 1974
Inorg. Chem. 13, 1836 (1974)

SALOMON, D., (see Kaindl, G., LBL-3427)

SAVIGNY, N., Adolphe, C., Zalkin, A., and Templeton, D. H.
Structure of NdSBr and Isotypical Rare Earth Sulfobromides
LBL-1656
Acta Crystallographica B29, Part 7, 1532-1535 (July 1973)
no reprints available

SAYLOR, D. P., (see Rad, F. N., LBL-2935)

SCHAEFER III, H. F., (see Yarkony, D. R., LBL-681)

SCHAEFER, III, H. F., (see Yarkony, D. R., LBL-1969)

SCHAEFER, III, H. F., (see Schwenzer, G. M., LBL-1983)

SCHAEFER, III, H. F., (see Liskow, D. H., LBL-2302)

SCHAEFER, III, H. F., (see Baskin, C. P., LBL-2324)

SCHAEFER, III, H. F., (see Bender, C. F., LBL-2344)

SCHAEFER, III, H. F., (see Yarkony, D. R., LBL-2345)

SCHAEFER, III, H. F., (see Liskow, D. H., LBL-2372)

SCHAEFER, III, H. F., (see Yarkony, D. R., LBL-2919)

SCHAEFER, III, H. F., (see Garrison, B. A., LBL-2911)

SCHAEFER, III, H. F., (see Ungemach, S. R. LBL-2948)

SCHAEFER, III, H. R., (see Dykstra, C. E., LBL-2983)

SCHAEFER, III, H. F., (see Schwenzer, G. M., LBL-2985)

SCHAEFER, III, H. F., (see Pearson, P. K., LBL-3402)

SCHAEFER, III, H. F., (see Siegbahn, Per, LBL-3403)

SCHAEFER, III, H. F., (see Schwenzer, G. M., LBL-3421)

SCHAEFER, III, H. F., (see Bender, C. F., LBL-3432)

SCHWARTZ, G. P., (see Rinneberg, H. H., LBL-2979)

SCHWENZER, G. M., O'Neil, S. V., Schaefer, III, H. F., Baskin, C. P., Bender, C. F.
Geometries of the Excited Electronic States of HCN
LBL-1983, September 1973
J. Chem. Phys. 60, 2787 (1974)

SCHWENZER, G. M., Schaefer, III, H. F., and Bender, C. F.
Excited Electronic States of HNC, Hydrogen Isocyanide
LBL-2985, August 1974
J. of Chem. Phys.

SCHWENZER, G. M., and Schaefer, III, H. F.,
The Hypervalent Molecules Sulfurane (SH_4) and Persulfurane (SH_6)
LBL-3421, October 1974
J. of the Am. Chem. Soc., 97, 1393 (1975)

SCIAMANNA, A. F., (see Clem, R. G., LBL-2308)

SCIAMANNA, A. F., (see Clem, R. C., LBL-2308 (Rev.))

SCOTT, A., Owais, M., and Petrovich, F.
Core Polarization in Inelastic Proton Scattering from ^{209}Bi at 61 MeV
LBL-672, September 1972
Nucl. Phys. A226, 109 (1974)

SCOTT, D. K.
Multinucleon Transfer Reactions
LBL-1991, August 1973
(Presented at the International Conference on Nuclear Physics, Munich, Germany, August 27- September 1, 1973)

SCOTT, D. K., (see Yagi, K., LBL-2982)

SCOTT, D. K., (see Cerny, J., LBL-2984)

SCOTT, D. K.
The Analysis of High Energy Heavy-Ion Transfer Reactions
LBL-3434, November 1974
(Presented at Symposium on Classical and Quantum Mechanical Aspects of Heavy Ion Collisions, Heidelberg, Germany, October 2-4 (1974)

SCOTT, D. K., Harvey, B. G., Hendrie, D. L., Kraus, L., Maguire, C. F., Mahoney, J., Terrien, Y., and Yagi, K.
Spectroscopy of Exotic Nuclei Using Heavy-Ion Transfer Reactions
LBL-2996, September 1974
Phys. Rev. Letts. 33, 1343 (1974)

SEABORG, G. T.
Status Report on the Transuranium Elements
LBL-2325, September 1973
Pure and Appl. Chem. Vol. 6, 1 (1974)

SEABORG, G. T., (see Kratz, J. V., LBL-2944)

SEABORG, G. T., (see Kratz, J. V., LBL-2947)

SEABORG, G. T., (see Ghiorso, A., LBL-2998)

SELPH, F. B., and Spence, D. A.
Computer Utilization for Design and Operation of the Super-HILAC
LBL-3431, October 1974
(Presented at the CUBE Symposium, Lawrence Livermore Laboratory, Livermore, California, October 23-25, 1974)

SEXTRO, R. G., Gough, R. A., and Cerny, J.
High-Resolution Measurements of Beta-Delayed Protons from ^{37}Ca and ^{41}Ti
LBL-1955, April 1974
Nucl. Phys. A234, 130 (1974)

SEXTRO, R. G., (see Zebelman, A. M., LBL-3427)

SHAKIN, C. M., (see Wang, W. L., LBL-1995)

SHALIMOFF, G. V., (see Nakamura, M., LBL-2331 Rev.)

SHELINE, R. K., (see Stephens, F. S., LBL-1911)

SHIHAB-ELDIN, A., (see Jardine, L. J., LBL-2943)

SHIHAB-ELDIN, A. A., Jardine, L. J., and Rasmussen, J. O.
Extension of Relative Alpha Decay Rate Theory to Spherical Odd-Odd Nuclei (^{210}At)
LBL-3409, September 1974
Nucl. Phys. A

SHIRLEY, D. A., (see Ley, L., LBL-1688)

SHIRLEY, D. A., (see Davis, D. W., LBL-1909)

SHIRLEY, D. A., (see Kowalczyk, S. P., LBL-1916)

SHIRLEY, D. A., (see Ley, L., LBL-2323)

SHIRLEY, D. A., (see McFeely, F. R., LBL-2350 Rev.)

SHIRLEY, D. A., (see Kowalczyk, S. P., LBL-1945)

SHIRLEY, D. A., (see Davis, D. W., LBL-1970)

SHIRLEY, D. A., (see Pollak, R. A., LBL-1971)

SHIRLEY, D. A., (see McFeely, F. R., LBL-1989)

SHIRLEY, D. A., (see Rinneberg, H. H., LBL-2398)

SHIRLEY, D. A.
Theory of Auger-Satellite Energy Shifts
LBL-1993, October 1973
(Phys. Rev. A 9, 1549 (1974)

SHIRLEY, D. A., (see Ley, L., LBL-2323)

SHIRLEY, D. A., (see Varea de Alvarez, C., LBL-2330)

SHIRLEY, D. A., (see Martin, R. L., LBL-2341)

SHIRLEY, D. A., (see McFeely, F. R., LBL-2350)

SHIRLEY, D. A.
ESCA, Results Versus other Physical and Chemical Data
LBL-2397, February 1974
(Presented at the International Conference on Electron Spectroscopy, Namur, Belgium, April 16-19, 1974)
J. Electr. Spectrosc. 5, 135 (1974)

SHIRLEY, D. A., (see Suzer, Sefik, LBL-2384)

SHIRLEY, D. A., (see Rinneberg, H. H., LBL-2900)

SHIRLEY, D. A. (see Ley, L., LBL-2901)

SHIRLEY, D. A., (see Kowalczyk, S. P., LBL-2902)

SHIRLEY, D. A., (see Soinski, A. J., LBL-2917)

SHIRLEY, D. A., (see Ley, L., LBL-2929)

SHIRLEY, D. A., (see Banna, M. S., LBL-2930)

SHIRLEY, D. A.
Hyperfine Interactions and ESCA Data
LBL-2936, June 1974
(Presented at the International Conference on Hyperfine Interactions Studied in Nuclear Reactions and Decay, Uppsala, Sweden, June 10-14, 1974; also submitted to Physica Scripta)

SHIRLEY, D. A., (see Kowalczyk, S. P., LBL-2937)

SHIRLEY, D. A., (see McFeely, F. R., LBL-2953)

SHIRLEY, D. A.
A Summary of the International Conference on Hyperfine Interactions Studied by Nuclear Reactions and Decay
LBL-2960, July 1974
(Presented at International Conference on Hyperfine Interactions Studied in Nuclear Reactions and Decay, Uppsala, Sweden, June 10-14, 1974)

SHIRLEY, D. A., (see Rinneberg, H. H., LBL-2979)

SHIRLEY, D. A.
X-Ray Photoemission and Surface Structure
LBL-3400, August 1974
(To be presented at the 21st Annual National Meeting of the American Vacuum Society, Anaheim, California, October 8-11, 1974)
J. Vac. Sci. Technol., 12, 280 (1975)

SHIRLEY, D. A., (see, Chou, T. S., LBL-3408)

SHIRLEY, D. A.
X-Ray Photoemission (ESCA) from Molecules and Solids
LBL-3410, September 1974
Proc. Of the Royal Australian Chem. Inst.

SHIRLEY, D. A., (see Kowalczyk, S. P., LBL-3430)

SHIRLEY, V. S., and Lederer, C. M.
Table of Nuclear Moments
LBL-3450, December 1974
(Proceedings of the International Conference on Hyperfine Interactions Studied in Nuclear Reactions and Decay, Uppsala, Sweden, June 10-14, 1974)

SIEGBAHN, P., and Schaefer, H. F., III
Potential Energy Surfaces for $H + Li_2 \rightarrow LiH + Li$ Ground State Surface from Large Scale Configuration Interaction
LBL-3403, October 1974
J. of Chem. Phys.

SIGNARBIEUX, C., (see Nifenecker, H., LBL-1950)

SIMON, R. S., (see Stephens, F. S., LBL-1911)

SLOBODRIAN, R. J., (see de Swiniarski, R., LBL-1620)

SLOBODRIAN, R. J., (see Lamontagne, C. R., LBL-1941)

SOINSKI, A. J., (see Kaindle, G., LBL-1960)

SOINSKI, A. J., and Shirley, D. A.
Nuclear Orientation Studies of ^{241}Am and ^{255}Fm
LBL-2917, June 1974
Phys. Rev. C10, 1488 (1974)

SOINSKI, A. J., (Ph.D. Thesis)
Study of Partial Wave Branching in the Alpha Decay ^{241}Am, ^{253}Es, and ^{255}Fm
LBL-3411, September 1974

SPENCE, D. A.
Drift Tube Alignment and Beam Emittance Codes in use at the Superhilac
LBL-3417, October 1974
(Presented at the CUBE Symposium, Lawrence Livermore Laboratory, Livermore, California, October 23-25, 1974

SPENCE, D. A., (see Selph, F. B., LBL-3431)

STAHEL, D. P., (see Jelley, N. A., LBL-3414)

STARKS, D. F., Parsons, T. C., Streitwieser, A., Jr., and Edelstein, N.
BIS(π-cyclooctatetraene) Protactinium
LBL-3422
Inorg. Chem., 13, 1307 (1974)

STEPHENS, F. S., Kleinheinz, P., Sheline, R. K., and Simon, R. S.
Backbending and Rotation Alignment
LBL-1911, November 1973
Nucl. Phys. A222, 235-251 (1974)

STEPHENS, F. S.
Rotation-Aligned Coupling Scheme
LBL-1968, July 1973
To be presented at the International Conference on Nuclear Physics, Munich, Germany, August 27-September 1, 1973

STEPHENS, F. S., (see Meyer ter Vehn, J., LBL-2394)

STEPHENS, F. S., (see Proetel, D., LBL-1939)

STEPHENS, F. S., (see Gizon, J., LBL-1948)

STEPHENS, F. S., (see Newton, J. O., LBL-2333)

STEPHENS, F. S., (see Proetel, D., LBL-2349)

STEPHENS, F. S.
Coriolis Effects and Rotation Alignment in Nuclei
LBL-2352, January 1974
Rev. Mod. Phys.

STEPHENS, F. S., (see Tjøm, P. O., LBL-2379)

STEPHENS, F. S., (see Proetel, D., LBL-2380)

STEPHENS, F. S., (see Nakai, K., LBL-2389)

STEPHENS, F. S., (see Tjøm, P. O., LBL-2931)

STEPHENS, F. S., (see Ward, D., LBL-3446)

STEYERT, W. A., (see Krane, K. S., LBL-2337)

STEYERT, W. A., (see Krane, K. S., LBL-2354)

STREITWIESER, Jr., A. (see Starks, D. F., LBL-3422)

SUDBURY, E. A., (see Bucher, J. J., LBL-2351)

SUZER, S., and Shirley, D. A.
Initial-State Configuration-Interaction Satellites in the Photoemission Spectrum of Cd
LBL-2384, February 21, 1974
J. Chem. Phys.(Note to Editor) 61, 2481 (1974)

SVENTEK, J. S., (see Huizenga, J. R., LBL-2314)

SVENTEK, J. S., (see Huizenga, J. R., LBL-2316)

SWIATECKI, W. J. (see Myers, W. D., LBL-1957)

SWIATECKI, W. J., (see Bowman, J. D., LBL-2908)

TAMURA, R., and Rezanka, I., Iwata, S., Rasmussen, J. O., and Alonso, J.
Levels in ^{165}Tm excited by decay of 10 Min ^{165}Yb and by the ^{158}Gd(^{11}B, 4nγ) Reactions
LBL-1689, May 1973
Phys. Rev. C8, 2425 (1973)

TAMURA, R., (see Yagi, K., LBL-2982)

TEMPLETON, D. H., (see Savigny, N., LBL-1656)

TEMPLETON, D. H., (see Ruben, H., LBL-1931)

TEMPLETON, D. H., (see Ray, S., LBL-1932)

TEMPLETON, D. H., (see Quarles, W. G., LBL-1933)

TEMPLETON, D. H., (see Quarles, W. G., LBL-1934)

TEMPLETON, D. H., (see Ray, S., LBL-1935)

TEMPLETON, D. H., (see Ruben, H., LBL-1936)

TEMPLETON, D. H., (see Ruben, H., LBL-2358)

TEMPLETON, D. H., (see Ruben, H., LBL-2369)

TERRIEN, Y., (see Yagi, K., LBL-2982)

TERRIEN, Y., (see Scott, D. A., LBL-2996)

THOMPSON, S. G., (see Kataria, S. K., LBL-1905)

THOMPSON, S. G., (see Jared, R. C., LBL-1963)

THOMPSON, S. G., (see Moretto, L. G., LBL-1966)

THOMPSON, S. G., (see Moretto, L. G., LBL-3444)

THOMPSON, S. G., Moretto, L. G., Jared, R. C., Babinet, R. P., Galin, J., Fowler, M. M., Gatti, R. C., and Hunter, J. B.
Macroscopic Aspects of Heavy Ion Reactions
LBL-2940, June, 1974
(Presented at the Nobel Symposium on Superheavy Elements, Ronneby Brunn, Sweden, June 11-15)

TJØM, P. O., Maier, M. R., Benson, D. Jr., Stephens, F. S., Diamond, R. M.
High-Spin States in ^{191,193,195}Au
LBL-2379, March 1974
Nucl. Phys. A231, 397 (1974)

TJØM, P. O., Stephens, F. S., Diamond, R. M., de Boer, J., and Meyerhof, W. E.
Angular-Momentum Effects on Continuum Gamma Rays Following Heavy-Ion Reactions
LBL-2931, May, 1974
Phys. Rev. Letters 33, 593 (1974)

TSANG, C. F.
Superheavy Element
LBL-2339, September 1974
The Physics Teacher, 13, 279 (1975)

TSANG, C. F (see Ma, Chin W., LBL-2347)

TSANG, C. F., (see Ma, Chin W., LBL-2347 (Rev.))

TSANG, C. F., (see Bowman, J. D. LBL-2908)

TSANG, C. F.
Nuclear Collisions with Friction
LBL-2928, May 1974

TSANG, C. F.
Similarities and Differences between Volume-Charge (Nuclear) and Drops and Charged Conducting (Rain) Drops
LBL-2970, August 1974
(To be presented at the International Colloquium on Drops and Bubbles at Pasadena, California, August 28-30, 1974)

UCHIYAMA, F., (see Wang, W. L., LBL-2313)

UNGEMACH, S. R., and Schaefer, III, H. F.
Model Studies of the Hydrophobiv Interaction: Watermethane
LBL-2948, July 1974 (J. Amer. Chem. Soc. 96, 7898 (1974)

UDAGAWA, R. (see Yagi, K., LBL-2982)

VAN DEURZEN, C. H. H., and Conway, J. G.
Excitation of Spectra of Multiply Ionized Atoms by Capacitor Discharges
LBL-1975, August 1973
Applied Spectroscopy, 28 3 (1974)

VAN DEURZEN, C. H. H., Conway, J. G., and Davis, S. P.
Spectrum and Energy Levels of Quadruple-Ionized Vanadium (V v)
LBL-1986, September 1973
J. Opt. Soc. Am. 64, 498 (1974)

VAREA de ALVAREZ, C., Cohen, M. L., Ley, L., Kowalczyk, S. P., McFeely, F. R., Shirley, D. A., and Grant, R. W.
Electronic Density of States and Bonding in Chalcopyrite-Type Semiconductors
LBL-2330, November 1973
Phys. Rev. B10, 596 (1974)

VERGES, J., (see Conway, J., LBL-3401)

VIOLA, V. E., Jr., (see Zebelman, A. M., LBL-3427)

von OERTZEN, W.
Some New Developments in Direct Reactions Induced by Heavy Ions
LBL-1678, April 1973
Presented at the Minerva Symposium on Physics in Rehovoth, Israel, 2-4 April 1973

von OERTZEN, W., (see Becchetti, F. D., LBL-1972)

von OERTZEN, W., (see DeVries, R. M., LBL-2363)

WAHLGREN, U., (see Pearson, P. K., LBL-3402)

WANG, W. L., and Lipes, R. G.
Heavy-Ion Elastic Scattering at High Energies
LBL-1964, August 1973
Phys. Rev. C9, 814 (1974)

WANG, W. L., and Shakin, C. M.
Angular Distribution and Polarization of $^{16}O(\gamma,n)^{15}O$
LBL-1965, October 1973
Phys. Rev. C9, 2144, 1974.

WANG, W. L. and Uchiyama, F.
Differential $L_1 \rightarrow K_S$ Regeneration Cross Section in Coherent Production Model and Optical Model
LBL-2313, October 1973
Nucl. Phys. B73 23-39 (1974)

WANG, W. L.
A Comment on the Giant Dipole Resonance of ^{16}O
LBL-2356, January 1974
Chinese J. Phys.

WANG, W. L.
Factorization in Relativistic Heavy-Ion Scattering
LBL-2359, April 1974
Phys. Letters 52B, 143 (1974)

WANG, W. L., (see Nagarajan, M. A., LBL-2934)

WANG, W. L., (see Nagarajan, M. A., LBL-2958)

WANG, W. L., (see Nagarajan, M. A., LBL-2986)

WARD, D., Bertschat, H., Butler, P. A., Colombani, P., Diamond, R. M., and Stephens, F. S.
High-Spin States in $^{127,129}La$; A Test of Backbending in the Even Ba and Ce Nuclei
LBL-3446, December 1974
Phys. Rev. B

WARD, T. E., (see Massmann, H., LBL-1693)

WEGMANN, G., (see Küpper, W. A., LBL-642)

WEISENMILLER, R. B., (see Jelley, N. A., LBL-2329)

WEISENMILLER, R. B., (see Cerny, J., LBL-2984)

WEISENMILLER, R. B., (see Cerny, J., LBL-3407)

WHITTAKER, B., (see Edelstein, N., LBL-2348)

WIDEMANN, F., Picon, M. Asaro, F., Michel, H. V., and Perlman, I.
A Lyons Branch of the Pottery-Making Firm of Ateius of Arezzo
LBL-1964, November 1973
Archaeometry, 17, 45 (1975)

WILCOX, K. H., (see Jelley, N. A., LBL-2329)

WILCOX, K. H., (see Jelley, N. A., LBL-3414)

WILCOX, K. H., (see Cerny, J., LBL-3407)

WILKE, C. R., (see Mitra, G., LBL-2334)

WILKE, C. R., (see Mitra, G., LBL-2365)

WILKE, C. R., (see Robinson, C. W., LBL-2399)

WILLIAMS, L. A., (see Garrison, B. A., LBL-2911)

WOLLENBERG, H., (see Bowman, H., LBL-2966)

WORTMANN, G., (see Kaindl, G., LBL-3437)

WOZNIAK, G. J., (see Jelley, N. A., LBL-2329)

WOZNIAK, G. J., Jelley, N. A., and Cerny, J.
A ^8Be Identifier and its Application to the $(\alpha,^8Be)$ Reaction
LBL-2374, March 1974
Nucl. Instr. Methods 120 (1974) 29

WOZNIAK, G. J., (Ph.D. Thesis)
α-Transfer Studies via the $(\alpha,^8Be)$ Reaction at High Energies
LBL-2999, August 1974

WOZNIAK, G. J., (see Cerny, J., LBL-3407)

YAGI, K., (see Scott, D. A., LBL-2996)

YAGI, K., Hendrie, D. L., Kraus, L., Maguire, C. F., Mahoney, J., Scott, D. K., Terrien, Y., Udagawa, T., Low, K. S., and Tamura, T.
One- and Multi-Step Processes in the $^{144}Nd(^{12}C,^{14}C)$ Reactions
LBL-2982, December 1974
Phys. Rev. Letts.

YARKONY, D. R., Hunt, W. P., Schaefer, III, H. F.
Relation between electronic structure and the chemiluminescence Arising from Collisions between Alkaline Earth Atoms and Halogen Molecules
LBL-681, June 1972
Mol. Phys. 26, 941 (1973)

YARKONY, D. R., O'Neil, S. V., Schaefer, III, H. F., Baskin, C. P., and Bender, C. F.
Interaction Potential Between Two Rigid HF Molecules
LBL-1969, August 1973
J. Chem. Phys. 60, 855 (1974)

YARKONY, D. R., and Schaefer, III, H. F.
Triplet Electronic Ground State of Trimethylenemethane
LBL-2345, January 1974
J. Am. Chem. Soc. 96, 3754 (1974)

YARKONY, D. R., and Schaefer, III, H. F.
Correlation Diagram for He + He → Be
LBL-2919, June 1974
J. Chem. Phys. 61, 4921 (1974)

ZALKIN, A., (see Savigny, N., LBL-1656)

ZALKIN, A., (see Ruben, H., LBL-1931)

ZALKIN, A., (see Ray, S., LBL-1932)

ZALKIN, A., (see Quarles, W. G., LBL-1933)

ZALKIN, A., (see Quarles, W. G., LBL-1934)

ZALKIN, A. (see Ray, S., LBL-1935)

ZALKIN, A., (see Ruben, H., LBL-1936)

ZALKIN, A., (see Ruben, H., LBL-2358)

ZALKIN, A., (see Ruben, H., LBL-2369)

ZEBELMAN, A. M., Poskanzer, A. M., Bowman, J. D., Sextro, R. G., akd Viola, V. E., Jr.
Fragments from Uranium Irradiated by 2.1 GeV/Nucleon Deuterons and Alpha Particles
LBL-3427, October 1974
Phys. Rev. C

ZISMAN, M. S., (see (Becchetti, F. D., LBL-2957)

ZUEHL, R., (see Bucher, J. J., LBL-2342)

7. Author Index

AUTHOR INDEX

☆GPO 884-428